BOND STRENGTH OF ULTRA-HIGH-PERFORMANCE CONCRETE UNDER DIRECT TENSION PULLOUT

Konstantinos Tsiotsias

A THESIS SUBMITTED TO
THE FACULTY OF GRADUATE STUDIES
IN PARTIAL FULFILLMENT OF THE REQUIREMENTS
FOR THE DEGREE OF
MASTER OF APPLIED SCIENCE

GRADUATE PROGRAM IN CIVIL ENGINEERING
YORK UNIVERSITY
TORONTO, ONTARIO

March 2019

Abstract

Bond occurs at the interface between the reinforcing bars and the cover concrete and enables force transfer between the two media.

Thirteen specimens comprising four distinct UHPC or ECC (Engineered Cementitious Composite) material compositions and two different values cover thicknesses to the embedded bar were tested. Experimental results were compared with bond strength values obtained from beam tests where anchorage length in the constant moment region and material properties were the same. Bond strength measurements obtained from the DTP setup were half the corresponding values obtained from beam specimens, whereas the DTP setup showed more sensitivity to the increase of the cover thickness.

Detailed nonlinear finite element analysis was conducted using two alternative levels of approximation in modeling the bar – matrix interface. The occurrence of unaccounted for confining pressures and restraint effects were shown in conventional pullout methods, while the DTP setup provided the most conservative estimate of bond strength.

Acknowledgements

I would like to express my deepest gratitude to my Professor and Supervisor, Dr. Stavroula J. Pantazopoulou, for her boundless support and guidance towards the fulfillment of my Master's Degree. My progress and accomplishments are indubitably as commensurate outcomes of my efforts as they are of hers. The contributions and knowledge that I am imparted with, thanks to Professor Pantazopoulou, have forged me into the better person and professional that I am today, and I consider myself very fortunate to have been her student. Great appreciation goes to Dr. Dan Palermo for the feedback and instruction he has offered me during the completion of my thesis, and to Dr. Liam Butler for the evaluation and endorsement of my work.

In respect, I would like to thank the Department of Civil Engineering of Lassonde's School of Engineering for providing me with the opportunity to advance my academic and scholarly career and the means to bring my research into fruition. I want to express my profound appreciation to Ms. Sindy Mahal for her indispensable advice and streamlining of crucial administrative matters that have optimized my experience and performance as a member of the graduate student faculty.

Many thanks to my friends and colleagues who have helped me during the entirety of my academic and research progress: Zoi, Mena, Adrien, Nicolas, Najmeh, Rita, Michael, Yuechen, Marina and Tintu. I would like to thank Lassonde's lab technician, Riad Rajab, for the invaluable contributions and assistance in the completion of my experimental work, as well as the head of Lassonde's Machine Shop, Adam McLean, for his involvement in the preparation of my experiments.

Last but not least, I would like to thank my family for their immeasurable support and faith in the pursuit of my goals and the encouragement they provided me in the realization of my studies. Their continuous confidence and backing has been a pillar of motivation and reassurance throughout my professional growth and personal cultivation.

Table of Contents

List of Tables

List of Figures

Chapter 1: Introduction

1.1 Objectives and scope

Reinforced concrete (RC) has become the established structural material of choice for the better part of the last two centuries. Being a composite material, it combines the compressive strength and formability of concrete with the tensile capacity and strain ductility of steel reinforcing bars. The resulting material provides sufficient strength to erect structures of great height and complexity that can withstand the spoils of time. However, the service life of RC structures is seriously impaired by the inability of conventional concrete to resist the development of cracking and deterioration of the embedded reinforcement due to corrosion. Corrosion is promoted by easy ingress of aggressive agents penetrating the cover through macropores and cracks, while oxidation generates expansive by-products on the surface of the exposed reinforcement leading to loss of bar section and cover delamination (Pantazopoulou and Papoulia 2001).

Recent advents in the improvement of the tensile strain ductility of concrete and resilience to cracking have led to the development of a new generation of strain resilient cementitious materials. Among those are the Engineered Cementitious Composites which are Cementitious materials with great strain capacity, obtained through synthetic fibers with controlled surface properties; another more popular class is the so-called Ultra-High-Performance Concrete (UHPC), which is actually a steel-fiber reinforced cementitious composite (UHPFRCC). UHPC composites incorporate fibers as mass reinforcement, that provide increased tensile capacity for concrete, intrinsic confinement and greater resistance to crack propagation by arresting the gap between the exposed surfaces of a crack. Structural members composed by UHPC have reportedly maintained their integrity after reaching their post-cracking branch, all the more while sustaining substantially increased tensile stresses. These qualities provide a new setting for the study of bond and anchorage behavior and for the establishment of commensurate design requirements for development of reinforcement.

Among the phenomena that govern structural behavior of UHPC, this thesis concentrates on the development of bond between the reinforcement bar and the surrounding cementitious matrix. Bond enables composite action between the two media and is responsible for transferring forces from the concrete to the reinforcement, and vice-a-versa. By applying tensile stress on the embedded bar, the bar tends to translate in the direction of the applied traction, whereas the ribs

that are interlocked with the matrix exert bearing action on the material encased in their path. This generates inclined pressures normal to the rib face, which are resolved into longitudinal and radial pressures on the cover concrete. It can be shown from classical mechanics that the radial pressures thus created are held in equilibrium with hoop tensile stresses of decreasing magnitude from the internal radius of the opening occupied by the bar, to the free surface of cover. Thus, the cover is susceptible to radial cracking upon exceedance of the tensile strength of concrete. Bond failure is manifested by longitudinal cracking on the free surface of cover along the length of the bar, which corresponds to loss of the hoop action and therefore loss of the bearing bond pressures leading to bar debonding. By introducing fiber reinforcement in the cementitious matrix, an additional mechanism of resistance to the proliferating cracks is provided (Figure 1-1), which in turn enhances the strength and resilience of bond, and the fracture energy of the cementitious matrix which in general benefits the development capacity of reinforcement (Chao, 2005). It is the objective of this research to assess and quantify the contribution of the tensile strength and post-cracking strain capacity of UHPC to the bond-slip law of the embedded reinforcement, to investigate the effect this has on the interpretation of the bond – slip law constitutive relations and to lay the foundations for a revised analytical approach towards the definition of bond strength.

Figure 1-1 Fiber reinforcement bridging the gap between cracks.

Past research has shown that the experimental setup interferes with the bond behavior causing spurious influences both on the strength of the bond mechanism as well as on the failure mode. In the effort to minimize these effects a direct tension pullout (DTP) specimen form has been proposed in the literature, wherein both the cementitious matrix as well as the bar are under longitudinal tension. The setup is commonly known as the DTP test and it requires that a support bar co-linear with the test specimen is cast so that conventional facilities for tension testing of

reinforcement may be used to conduct the tests. Because of the difficulties in eliminating any possible form of eccentricity between test and support bar in these tests, in the present study the DTP test setup has been modified so that only the test bar is embedded in the specimen block, whereas the support is provided by means of a spherical hinge.

Parameters of the investigation were, (a) The UHPC material used for the matrix, (b) the clear matrix cover over the bar. Additional important variables that could affect the generality of the findings (not examined experimentally) are (c) the diameter of the bar and (d) the embedment length of the pulled bar.

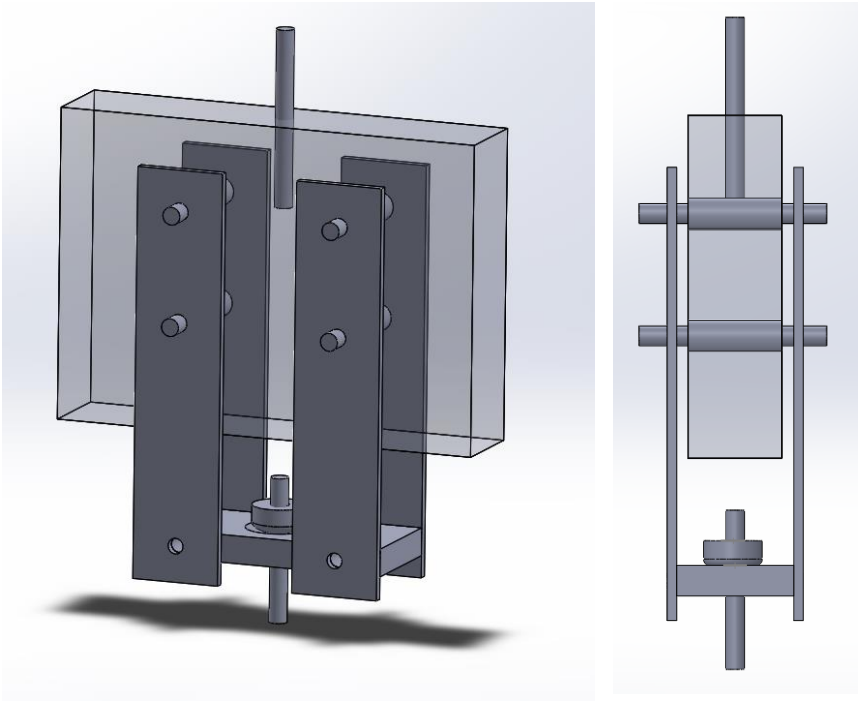

Figure 1-2 Preview of the designed test setup. The specimen is held vertically amidst the mechanical base. Left: Perspective view, Right: Side view.

Complementary to the experimental work, detailed nonlinear finite element analysis of bar anchorages in concrete (FEA) is conducted. The aim of this analysis is to simulate the behavior of the specimen, so as to estimate the distribution of the final stress fields developing in the modified DTP tests of this study's experimental program. In addition, it is an objective of the FE analysis to provide a framework for the study of structural members comprising UHPC materials. Appropriate material models are applied to reproduce the strength properties and absorbed fracture energy of conventional concrete and UHPC, respectively.

The objectives of this study are the following:

- Investigate the influence of specimen form in the acquired bond strength measurement from various experimental setups.
- Determine the contribution of fiber reinforcement in the overall bond – slip constitutive relationship of UHPC.
- Simulate the direct tension pullout experimental setup using the finite element approach.
- Review the parameters that construe the governing differential equation that describes bond behavior.
- Evaluate, through detailed finite element analysis the spurious influences exerted by support conditions on the anchorage zones, thereby affecting the phenomenological average bond strength obtained from various test forms.

1.2 Structure of the thesis

1.2.1 Chapter 1

Apart from a brief introduction to the essential concepts surrounding UHPC and the properties of bond behavior, Chapter 1 provides an overview of the scope and research approach utilized in this thesis. The bond properties of UHPC are examined through an experimental framework of isolating an embedded reinforcing bar in direct tension pullout and replicating the tensile stress conditions encountered in the tension zone of a bar anchorage. The experimental feedback is scrutinized to evaluate the obtained constitutive bond – slip relationship and the developing stress fields in the cover of a developed bar anchorage. Nonlinear finite element analysis (NLFEA) is employed to support the experimental findings and to illustrate the effect that spurious compressive fields may have on bond when tests are done without proper attention to the support conditions of the system comprising the specimen and the test-setup.

1.2.2 Chapter 2

In Chapter 2, past research and experimental studies are examined. It has become evident from vast differences in bond results, that the experimental setup greatly affects bond strength, owing to the unaccounted-for contribution of passive confinement generated due to the test arrangement. The balancing compressive forces work in favor of bond, securing the contact surface between reinforcement and concrete and ultimately increasing bond strength. To alleviate

this effect, the direct tension pullout (DTP) test is utilized where both the test bar and the surrounding concrete are stressed in tension.

Constitutive bond-slip models are investigated in this chapter, and the parameters that influence bond behavior are presented through review of the existing literature. Among the factors that engage bond, namely the surrounding concrete cover, embedment length, geometry and distribution of reinforcing bars, presence of confinement, available fracture energy, and concrete tensile strength, the latter has been the least contributing. Current models neglect the participation of concrete strain due to concrete's inherent brittleness and inability to sustain tensile stresses. However, in the case of UHPC, the cementitious matrix can suppress and arrest the propagating cracks owing to the incorporated fiber reinforcement, thus enhancing the bond capacity of the steel-to-concrete interface and post-cracking performance. It is within the scope of this study to answer whether analytical models ought to explicitly account for concrete strain in the constitutive differential equation of the bond-slip law.

1.2.3 Chapter 3

In Chapter 3, an overview of the experimental design and setup process is presented, and the finite element modeling approach is discussed. The experimental setup is planned in accordance to the DTP test mentioned in the previous chapter, in which a mechanical variation is introduced. Whereas in the conventional DTP test, both the test bar and the support bar are embedded within the test specimen, in this study's custom variation the support bar is externally hinged onto the specimen via a spherical seat on a connecting mechanical base. The base is attached on the concrete specimen through transverse steel cylinders that maintain the support bar in alignment with the test bar. A preliminary finite element analysis is presented using the commercial software ATENA and comparison with alternative experimental setups is conducted. In addition, the forthcoming experimental results are predicted by making qualitative assumptions regarding the magnitude of the expected bond strength and the corresponding fracture energy encompassed in the bond slip law of the UHPC or ECC test matrix.

A pressure sensitive model of the concrete bar interface is also considered in order to conduct a detailed finite element analysis in ATENA that enables interpretation of the effects of test setup on the characteristics of the resulting local bond – slip law. It is illustrated how vastly different bond strengths and bond-slip laws can be obtained by altering the size and support conditions of the specimen, thereby explaining the ambiguity and confusion in the state of the art, but also the vast differences obtained in the present study between DTP specimens and beam specimens

tested by a peer in order to also obtain the bond-slip properties of identical anchorages in the same matrices.

1.2.4 Chapter 4

Casting and fabrication of the specimens are presented in this chapter. The mold design and manufacturing procedure is described in detail and the characteristics of the material used for fabrication of each specimen are given. Four distinct material mix designs were used to construct a total of 13 specimens. The instrumentation and testing preparations are detailed in the end of this chapter, along with the resulting tensile strength properties attributed to the specimens of each material, obtained from prism and dog-bone tests conducted by peer researchers.

1.2.5 Chapter 5

In Chapter 5, the feedback from the experimental program is presented in detail and collectively reviewed. The constitutive bond-slip law is extracted from the bond and slip measurements obtained from the attached instrumentation. The acquired force – displacement properties, along with observations on the distribution of crack patters are discussed, and observations are made regarding the failure modes of all specimens. Bond strength properties are compared with corresponding bond measurements from four-point bending tests conducted by a peer researcher. Digital image correlation (DIC) is performed using the MATLAB module GeoPIV-RG to obtain the longitudinal and transverse strain levels on the surface of the specimens.

1.2.6 Conclusions

In the last chapter, a summary of the conclusions and outcomes of this study are presented. The principal finding of the research are discussed and a review is given in accordance to the results obtained from the experimental study and the Finite element analysis, particularly with reference to the importance of the test setup and specimen form for bond strength estimation.

Chapter 2: Literature Review

2.1 Introduction

In reinforced concrete (RC) structures, bond is the mechanism that ensures the composite behavior of concrete and the reinforcing bars. When a reinforcing bar is stressed in tension, as for example happens at a crack location, the resulting elongation causes sliding, relative to the surrounding cover. The lugs (or ribs, or deformations) on the bar's contact perimeter bear on the concrete as they attempt to displace the cover in order to pull-out, thus exerting bursting pressures on the inner perimeter of the cover (Figure 2-1). The pressure component is acting radially on the contact surface around the rib, which in turn supports longitudinal friction on the contact perimeter, parallel to the bar axis. The friction is the bond mechanism. A frequent consequence of the bursting pressure exerted by the bar is longitudinal splitting of the cover, leading to loss of bond, and to permanent destruction of the composite action of reinforced concrete.

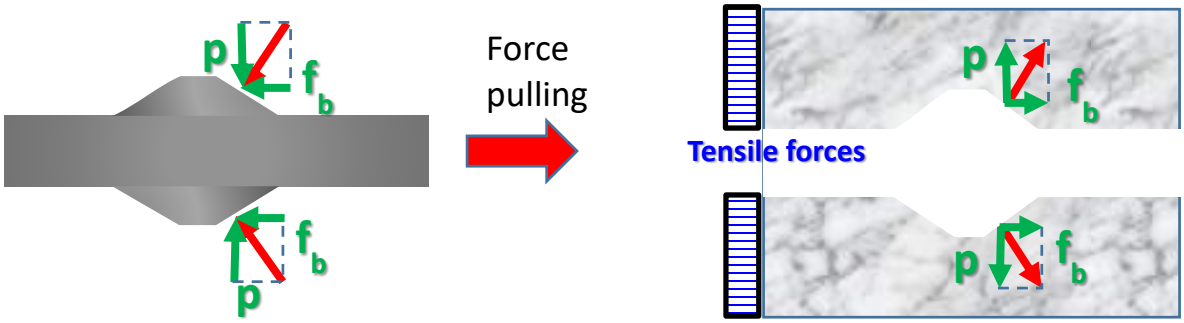

Figure 2-1 Exaggerated detail: (a) Forces exerted by concrete on the bar. (b) Forces exerted by the bar on the concrete cover.

Design for bond addresses this problem by regulating the clear cover on the bar, and the length of anchorage, which is the length required for a bar to develop its yielding force. For a given bond strength, f_{bd}, and assuming a uniform distribution of bond stresses along the contact surface between bar and concrete, the minimum length of anchorage required to yield a bar is obtained from equilibrium as $L_{b,min} = (D_b/4)\cdot(f_y / f_{bd})$. The value of f_{bd} is considered a mechanical property of concrete: Design Codes adapt empirical expressions to test data, for quantifying bond strength. Its magnitude is referred to concrete tensile strength which in turn depends on concrete compressive strength, f_c [Eurocode 2 (2004), ACI 318-14, CSA A23.3-14, Model Code 2010].

However, as this is an indirect measure of concrete's tensile strength and brittleness, the value of f_{bd} is mainly based on experimental evidence, although analytical investigations have been conducted to further understand its mechanics. This is a vast topic, that can by no means be fully exhausted in the present study. For this reason, the scope of Chapter 2 is to outline (a) relevant aspects of the mechanistic problem of bond as they have been understood so far, (b) essential experimental evidence that illuminate important aspects of the bond and anchorage mechanics with particular emphasis on the types of tests conducted to measure this property, (c) prominent code requirements, and (d) relevant experiments on bond of steel reinforcement in UHPC.

2.2 The mechanics of bond

Bond exists on the interface between the embedded bar and the surrounding concrete. It has been postulated and experimentally demonstrated that the capacity of this interface to transfer stresses between the two materials relies on the following mechanisms: 1) the chemical adhesion between steel and concrete, 2) the friction between the two surfaces, and 3) the mechanical interlock of the ribs against the concrete (Lutz et. al, 1967). Once the tensile capacity of the adhesion is exhausted, slip of the embedded bar will occur and friction takes over. As slip increases, the friction between bar and concrete diminishes and bond strength is sustained by mechanical interaction. Prior to the introduction of deformed bars, bond strength was primarily dependent on the first two mechanisms, and interlock was essentially a product of the roughness of the plain bar surface and the wedging action of the debris accumulated over the sliding smooth bar (*fib* Bulletin 10, 2000). However, bond strength that depends on adhesion and surface friction is inherently weak due to the low tensile strength of the interfacial zone. Deformed bars produce greater bond strength due to the interlocking bearing action that the inclined ribs impose on the neighboring concrete.

During the translation of deformed bars relative to concrete, the ribs will either split the concrete by pushing it away (wedging action) or crush the concrete by enclosing it in the spaces between them and it has been shown that for rib angles between 40^o and 105^o, the relative movement is almost entirely caused by the latter effect (Lutz et. al, 1967). Upon slipping of the bar, the concrete is crushed and adheres on the faces of the ribs, and the debris thus compacted and accumulated behave as pseudo ribs with angles between 30^o to 40^o (Figure 2-2). The resulting deformation creates comb-like "wedges" to appear on the surface of the concrete that resists this type of bar displacement through frictional and interlocking action. To counteract the compressive stresses

from the lugs, the pressurized concrete develops tensile stresses in the surrounding cover, thereby creating internal inclined cracks which are called “bond” cracks (Ciampi et. al 1982).

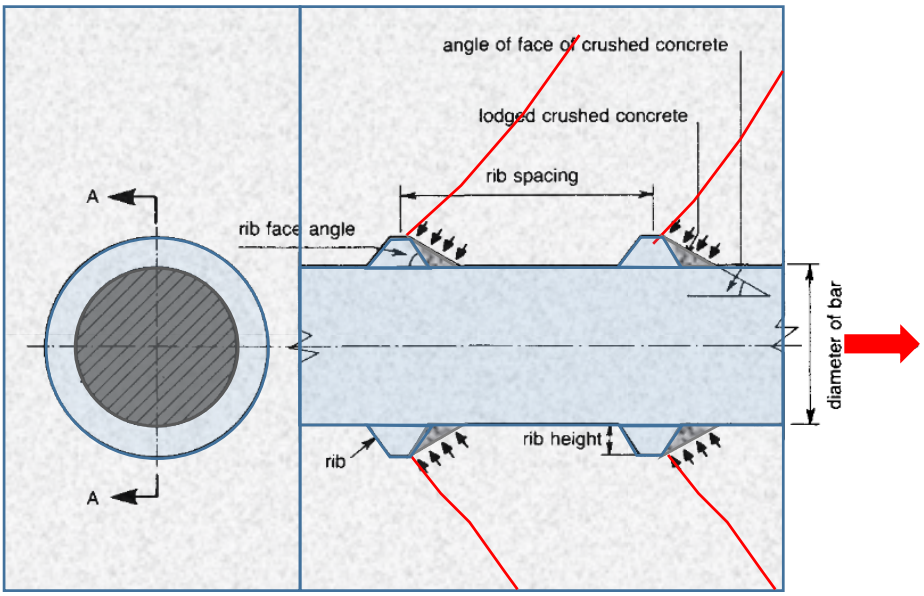

Figure 2-2 Geometry of a deformed reinforcing bar and the mechanical interaction between bar and concrete (modified from Tepfers 1979).

An illustration of these cracks has been achieved experimentally by Goto (1971) who injected ink into axially loaded tensile specimens through specially formulated narrow openings. The specimens were cut axially after the experiment and the crack patterns annotated by the ink were shown (Figure 2-3).

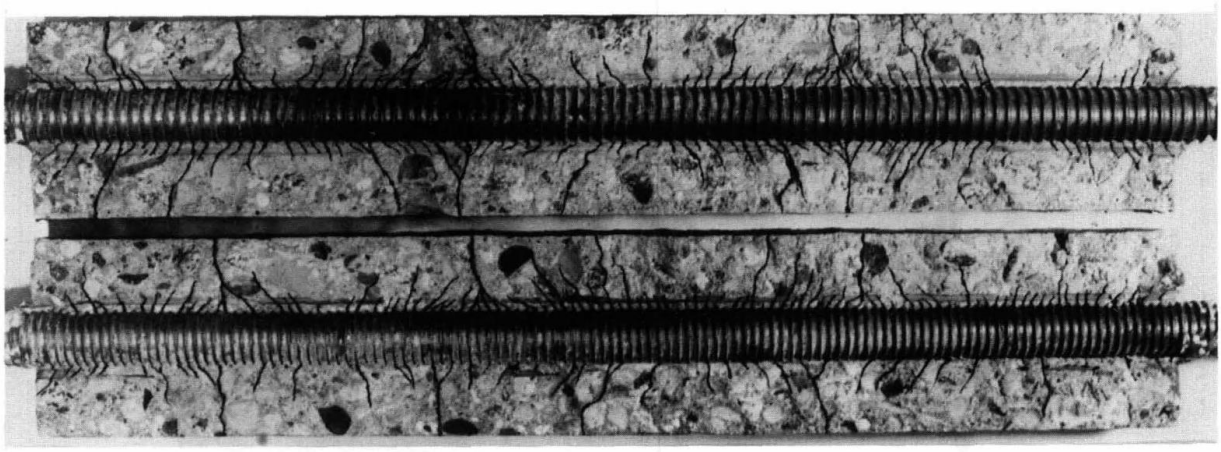

Figure 2-3 Goto’ s experiment to map the internal cracks around an anchorage using ink (Goto 1971).

A distinction is made here regarding the classification of bond cracks into their lateral and longitudinal components. Lateral cracks, also designated as “primary cracks”, occur near the locations of bar ribs caused by the tensile stress field that exists in the surrounding concrete as depicted in Figure 2-1. By increasing the applied load, inclined internal cracks will appear near the locations of the primary cracks and will progressively propagate away as the load continues to increase. At higher steel stresses, secondary cracks may also appear in the regions between the primary cracks. Longitudinal cracks follow the formation of the primary cracks and appear initially at the faces of primary cracks and grow to the extent of the lateral cracking space as the load increases (see Figure 2-4). The formation of longitudinal cracks is greatly influenced by the rib geometry and pattern distribution.

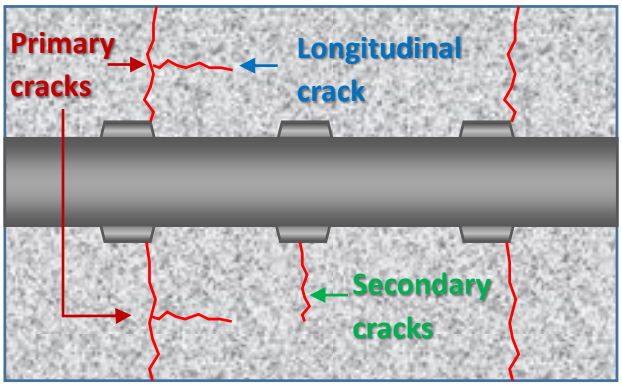

Figure 2-4 Characterization of crack patterns into primary, secondary and longitudinal cracks (Goto, 1971).

During the translation of the bar, the inclined pressures exerted by the ribs on the surrounding concrete mass, correspond to radial pressures p, and longitudinal tangential forces f_b, along the interface, as depicted in Figure 2-1 (b). The radial components of these pressures are resisted by hoop tension in the concrete cover which are limited by the tensile capacity of the concrete, as shown in Figure 2-5 (a). Splitting of concrete is a result of excessive radial pressures and is manifested externally by longitudinal cracking along the axis of the bar. If the engaged concrete cover is large enough to sustain the circumferential tensile forces, the failure mechanism is converted to bar pullout, which is the result of crushing of the concrete teeth against the bar lugs (see Figure 2-5 (b)). Primary, and secondary, cracks appear as a result of the radial pressures emanating in the concrete hoop. Longitudinal cracking is formed due to the deformation of the concrete “wedges” as the ribs bear against the inner surface.

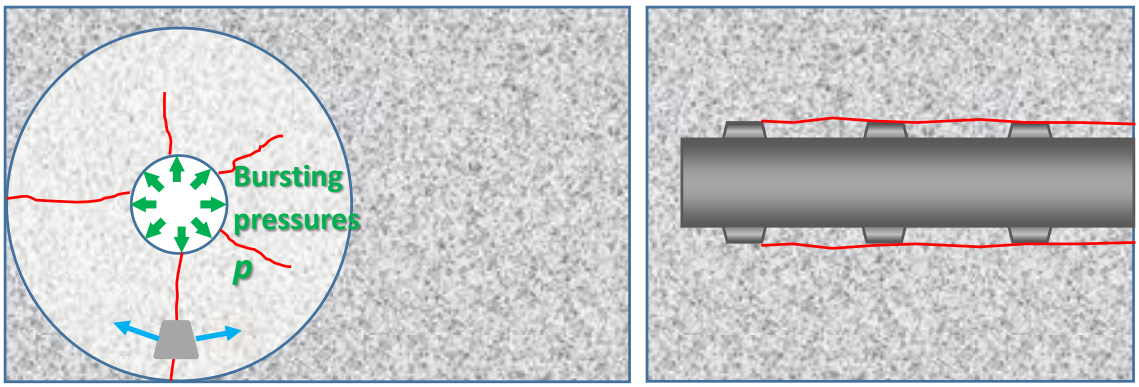

Figure 2-5 Illustration of the splitting failure (a) and pullout failure (b).

2.2.1 Governing Equations

Bond has been described in the literature in many different ways, ranging from qualitative mechanistic approaches to very involved computational models. It is however, rather instructive to review the basic equations that govern the mechanistic problem of bond – slip, and the findings that have been obtained based on that fundamental approach. The equations of force equilibrium of an elementary bar segment of length dx as depicted in Figure 2-6 [Tastani and Pantazopoulou (2013), Eleftheriou et al. (2017)] take the form:

$$F_s(x+dx) - F_s(x) + f_b(x)\cdot\pi\cdot D_b\cdot dx = 0 \Rightarrow$$

$$F_s(x) + (dF_s(x)/dx)\cdot dx - F_s(x) + f_b(x)\cdot\pi\cdot D_b\cdot dx = 0 \Rightarrow \frac{dF_s(x)}{dx} = -f_b\cdot\pi\cdot D_b \qquad \text{[2-1(a)]}$$

$$\Rightarrow \frac{df_s(x)}{dx} = -\frac{4}{D_b}\cdot f_b(x)$$

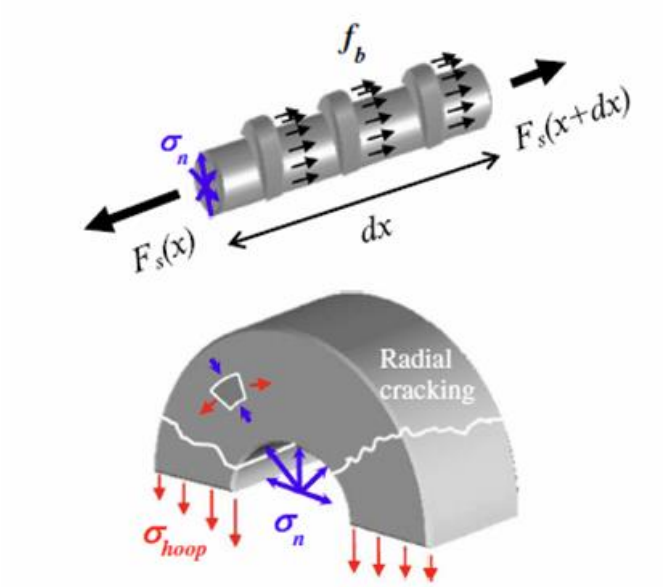

Figure 2-6 Bond stresses on an elementary bar segment (Tastani and Pantazopoulou, 2013).

From the kinematics of the relative translation between the two materials, slip is defined as:

$$s(x+dx)-s(x)=(\varepsilon_c-\varepsilon_s)\cdot ds \Rightarrow \frac{ds(x)}{dx}=-(\varepsilon_s-\varepsilon_c) \qquad [2\text{-}1(b)]$$

$$\frac{df}{dx}=-\left(\frac{4}{D_b}\right)\cdot f_b(x) \;\;,\;\; \frac{ds}{dx}=-(\varepsilon_s-\varepsilon_c) \qquad [2\text{-}1(c)]$$

In Eq. [2-1], f_s is the axial bar stress, f_b = is the bond stress, s is the bar slip relative to the surrounding concrete, ε_s is the bar strain and ε_c is the concrete strain.

Considering that the tensile strength of conventional concrete is negligible, the concrete strain ε_c has been customarily neglected and the closed form solution of the governing differential equation for an elastic bar with an elastic interfacial bond-slip property has been obtained as follows (Tassios 1979):

$$\frac{d^2}{dx^2}\varepsilon_s(x)=-\omega^2\varepsilon_s(x) \qquad [2\text{-}2]$$

where ω a pertinent physical parameter, which is a function of the bar elastic modulus E_s, the bond slip stiffness k, the bond strength f_b and the bar diameter D_b, (see Tastani and Pantazopoulou (2013) for detailed solutions of the coupled equations [Eqns. 2.1 (a) and (b)] for various material laws – see Appendix III (for the relevant solutions)). Important findings from these

solutions are, (a) that the bond stress and bar slip distributions are highly variable along the length of the anchorage; (b) average bond stress is less than the peak local bond stress, (c) that the assumption of a constant bond stress distribution only approximates reality in very short lengths of anchorage (less than 5 bar diameters); (d) that by definition (see Eqn. 2-1(a)) bar yielding (stress plateau) is necessarily associated with zero bond stress, which is only possible if it is assumed that a yielded bar debonds from its cover (due to the large effective Poisson's ratio at that stage); (e) the area under the local bond-slip relationship (which is intimately related to the fracture energy of concrete in unconfined anchorages) limits the maximum development capacity of a bar of a given size regardless of the available anchorage length, and that in order for an anchorage to be resilient, it is essential to increase this fracture energy property.

2.2.2 Parameters affecting bond

The review of the mechanistic problem presented in the previous section has illustrated clearly that the various modes of failure observed during the tests as well as the bond-slip law deduced from experiments depend greatly on the configuration of the bar anchorage, the intensity of the bar force and the material properties of the concrete and the bar – concrete interface. These parameters are discussed below in greater detail based on the relevant literature.

2.2.2.1 Cover and Bar spacing

As illustrated by Tepfers (1979), the radial pressures generated by the inclined ribs are resolved within the concrete hoop surrounding the bar. Internal cracks produced by the relative movement penetrate the concrete cover until the tensile strength in the hoop direction is exhausted (Figure 2-6). It can be shown from the mechanics of a thick ring under plane strain, which is a common idealization of the concrete cover under the bursting pressures p, that the larger the cover thickness or the spacing between successive bars, the greater the resistance in the hoop direction and the greater the bursting pressure p that may be supported by the ring [Tastani and Pantazopoulou 2013, Tastani (2006), Pantazopoulou and Papoulia (2001)]. Upon penetration of cracking through the thickness of the ring, failure is demonstrated on the surface in the form of longitudinal cracking along the axis of the bar (splitting). Failure mechanisms due to insufficient cover are common in structural members with reinforcement congestion. Darwin et al. (1996) have demonstrated that the correlation between cover thickness and bar spacing assumes a critical role in bond strength, as do the material properties. The following geometrical ratio has

been proposed to quantify this effect: bond strength of bars is increased from a reference base value by the factor:

$$\left(0.1\cdot\frac{\max(c_b,c_s)}{\min(c_b,c_s)}+0.9\right)\leq 1.25 \qquad [2\text{-}3]$$

where, c_b is the concrete cover, parameter c_s is defined as: $c_s=\min[c_{so},c_{si}+0.25\text{ in. }(6.4\text{mm})]$, c_{so} is the side cover and c_{si} is half the bar clear spacing. The above ratio moderates the bond strength of bars that are not confined by transverse reinforcement.

The strength of the cover is highly dependent on the presence of transverse reinforcement and confinement. The unbalanced compressive and shear forces imposed by the ribs are arrested by the transverse bars and attenuate the intensity of tensile stresses undertaken by the concrete ring. Recent efforts to increase the tensile capacity and tensile resilience of concrete have led to the introduction to mass reinforcement in the form of fibers that bridge the proliferating cracks within the cover. Being one of the major contributors to bond strength, the cover tensile capacity of fiber reinforced concrete is the next critical milestone of bond research.

2.2.2.2 Development length

Extensive experimental work on the contribution of development and splice length on bond capacity has been completed by Darwin et al. (1996), Eligehausen et al. (1983), Rehm (1979), Plizzari et al. (2003), Cairns et al (1979); several summary reports of the work on bond have been developed by the technical committees both in Europe (CEB/*fib* TG. 5.2) and the US (ACI Committee 408); the most notable being the *fib* Bulletin #10 on Bond (2000), the ACI 408 Recommendations (2003) and the *fib* Bulletin #72 (2014). After conducting statistical analysis on 133 unconfined and 166 confined specimens of various concrete strengths and bar geometries, specifically different relative rib areas, Darwin et al. (1996) developed a statistically-based model that considers the participation of cover, bar spacing as well as development and splice length. From calibration of the test data two important findings had emerged: (a) term $\sqrt{f_c'}$ does not accurately capture the experimental trend regarding the effect of concrete on bond strength, and (b) the yielding strength of the transverse reinforcement does not have any measurable effect on bond (i.e., stirrups do not yield during bond failure). Furthermore it was found that the development

capacity T_b of a bar splice of length l_d comprises contributions from transverse steel, T_s, and the concrete cover, T_c, as follows:

$$T_b = T_c + T_s \quad [2\text{-}4]$$

Another crucial finding of this study is that yielding of longitudinal reinforcement stressed in tension does not eliminate bond resistance, provided however that the bars are confined. In fact, confined anchorages show increased bond strength after yielding, since this process engages the interlocking stresses in the transverse bars (Darwin 1996). Thus, it follows that if transverse reinforcement is available, the design criteria regarding splice and development length should account for the amount of confinement and its effect on the bar development.

2.2.2.3 Confinement

The favorable effect of confinement in bond strength has been reported across multiple experimental studies (see f*ib* Bulletin #10, 2000 and #65, 2012). Confinement, being either direct (through transverse reinforcement) or indirect (through the presence of compressive stress fields around the bar), counteracts and therefore attenuates the radial stresses that develop on the concrete generated by the inclined ribs bearing on the concrete. It has been shown both through experiment and analysis that splitting of the cover eliminates bond strength (Figure 2-6). Malvar (1992) investigated experimentally the effect of confining pressures on local bond strength, by constructing cylindrical pull-out specimens with concentrically embedded reinforcement under applied hydraulic normal stresses. To ensure the locality of the readings, only 5 lugs were embedded into the confined concrete, with the remaining lugs being covered with a rubber sleeve. The experiment comprised two distinct phases. In the first phase, the concrete specimens were confined until longitudinal cracking ensued on the cover, in order to eliminate the active confining pressures from the concrete. Before the onset of the second phase, the specimens were unloaded. During the second phase, the specimens underwent monotonically applied hydraulic pressure, normal to the bar axis, up to a value of $0.2f_{ck}$, while the test bars were being pulled. The normal pressure in this phase was applied directly on the test bars since the surrounding concrete cover had been split. This experiment yielded two crucial findings regarding the effect of confinement on bond strength: firstly, while the measured bond strength values were double as compared to bond strength in unconfined concrete specimens, degradation of the bond mechanism was greater under higher levels of normal pressure. This denotes an upper limit in

the favorable effects of confining pressure on bond strength, beyond which bond was no longer affected. Secondly, it was found that as normal confining stresses increased, the lateral expansion due to Poisson's effect was attenuated, with expansions being reduced from 0.2mm to 0.05mm for an increase in normal pressure from $0.06f_{ck}$ to $0.2f_{ck}$.

2.2.2.4 Bar diameter

The bond capacity of reinforcement with different diameters has been investigated along lap splice locations in frame structures (ACI 318R-14 Fib Model Code 1990). It has been shown that bars with larger diameters are damaging to the concrete enclosed in the lap splices due to the larger radial stresses that are generated. Experimental evidence shows that the effect of bar diameter on bond strength is relatively small considering the other parameters influencing the problem (provided that the related rib area and surface roughness of the bar remain constant as bar diameter increases) [Eligehausen, Popov, Bertero (1982), Rehm (1979)]. Note that the related (or relative) rib area f_R, which is the ratio of the projected rib area normal to the bar axis to the product of the nominal bar perimeter and the average center-to-center rib spacing (ACI 408R-03) is a key parameter that is used to describe the deformation pattern of the bar lateral surface. For each bar, the related rib area index is calculated using:

$$f_R = (1/4)\cdot(d_e^2-d_i^2)/(ds);\ d_i=d_e-2a \qquad [2\text{-}5]$$

in which d_e is the external bar diameter (top of the rib), d_i is the core diameter (bottom of the rib), d is the nominal diameter, s is the longitudinal spacing of the ribs and a is the rib height. Eurocode 2 (CEN, 2004) prescribes a minimum bond index of 0.056 for bar diameters over 12 mm. Bars with higher related rib areas (0.085 to 0.119) show a stiffer bond response and failure is marked by strain localization [see Zuo and Darwin (2000); Eligehausen and Mayer (2000); Wildermuth and Hofmann (2012)]. Indeed, the plastic rotation capacity of members increases by more than 50% by reducing the f_R value to 0.02 (from 0.09).

2.2.2.5 Position

Early studies had established that the position of reinforcement during casting of concrete plays an important role on the development capacity of a given anchorage. For structural members made of conventional concrete this problem has been thoroughly investigated and introduced into the design codes (ACI 318R-14, EC2 2002). It was stated that for anchorage lengths of

longitudinal reinforcement that are located in sections with a concrete layer below that exceeds 300mm in thickness, the peak bond strength is reduced by 30%. This reduction is due to the entrapment of water that was intercepted in its upwards movement under the top bars during the hardening of concrete, which in turn reduces the local strength of concrete under the bars. This effect can be alleviated by increasing the available concrete cover, or the height of the bar ribs so that they penetrate deeper engaging into the cover. Similar studies conducted for SCC also illustrate the presence of a so-called top bar effect. This is probably mitigated in the presence of fibers (UHPC); however, no relevant information is available in the literature as of yet.

2.2.2.6 Fracture energy

The fracture energy of the concrete matrix quantifies the tensile resilience of the material and may be easily related to the bond slip law: energy conservation over the entire anchorage length L_b requires that the total strain energy stored in the concrete cover, U_c, equals the energy U_b, expended in bond-slip damage at the interface. Terms U_b and U_c are calculated from Eq. (2-6).

$$U_c = \int_0^{L_b} A_c \left[\int_0^{\varepsilon_{ct}(x)} f_{ct}(x) d\varepsilon_{ct} \right] dx = f_{ct} \int_0^{L_b} A_c \varepsilon_{ct}(x) dx \quad ; \quad U_b = \pi \cdot D_b \cdot \int_0^{L_b} \left[\int_0^{s(x)} f_b(x) ds \right] dx \quad \Rightarrow$$
$$\frac{A_c}{\pi \cdot D_b} \int_0^{\varepsilon_{ct}(x)} f_{ct}(x) d\varepsilon_{ct} = \int_0^{s(x)} f_b(x) ds \qquad [2\text{-}6]$$

where A_c is the cross sectional area of the concrete cover engaged by the anchorage (i.e. the cross sectional area of the concrete thick ring model used to emulate the state of stress in the cover). Generally, it was concluded that the greater the fracture energy absorption of the cementitious matrix, the greater the capacity for bond development.

2.3 Review of Experimental Studies on Bond

2.3.1 The effect of the test setup

Previous studies on bond development have demonstrated the sensitivity of bond strength measurements to the experimental setup (Tastani and Pantazopoulou 2010). Conventional tests such as the concentric and eccentric pullout tests generally overestimate the bond strength values by an excessive margin. The concentric pullout underlies the basic concept of the ASTM standard

for comparison of the bond strength of reinforcing bars in concrete (1999) also adopted by RILEM (1978). It is used by the industry (bar producers) for quick assessment of bond capacity. The test comprises a cubic block (having dimensions of $10D_b$) with a concentrically placed bar that is protruding at the center, which is pulled against a stationary supporting plate placed under the test surface. The resistance imposed by the supporting plate to the concrete generates longitudinal compressive stresses on the cover surrounding the bar (cracks parallel to the bar on specimen surface), as can be shown by equilibrium.

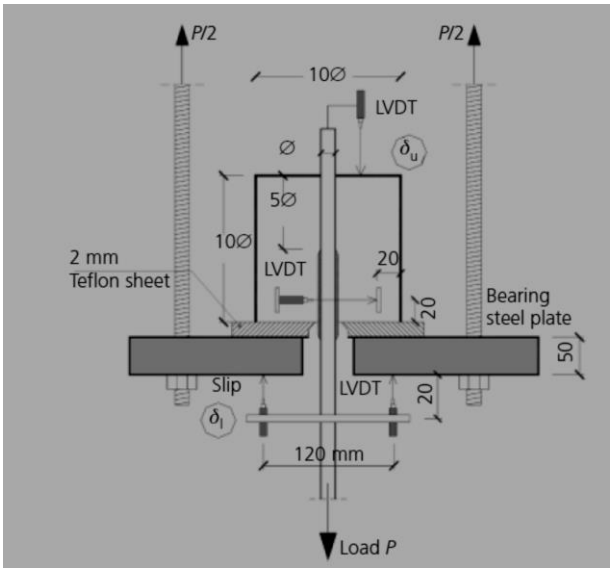

Figure 2-7 Illustration of the concentric pullout test (from Metelli and Plizzari, 2013).

The above figure depicts the presence of a Teflon layer between the concrete layer and the steel; this is meant to eliminate friction that would be generated between the steel plate and concrete, due to lateral dilation of the concrete in response to the imposed longitudinal compression. These pressures generate an inclined trajectory of stresses that converge towards the end of the anchorage, being eventually carried by the bar concrete interface. The effect is an unaccountable-for source of material bond strength enhancement leading to bond values that are two to three times larger than the normal values.

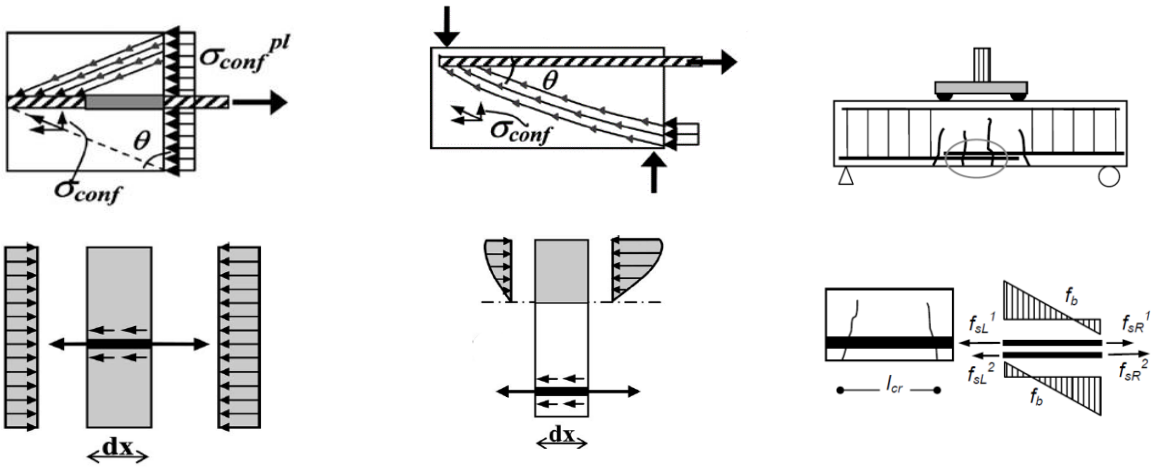

Figure 2-8 Left: Standard pullout test. Middle: Beam end test. Right: Lap splice test. [Tastani and Pantazopoulou (2006), Tastani et al. (2014)].

As a remedy to the problems of the standard pullout test setup, an eccentric arrangement has been considered. The modification does not alter the manner of loading (i.e. the concrete block containing the bar is supported against a steel plate (with a frictionless layer to minimize effects of restraint due to friction at the contact surface), with the cover on the smaller distance of the embedded reinforcing bar to the nearest surface being the test variable. Whereas this setup is believed to limit the effects of the confining pressures and ensures tensile stresses in the concrete at least in the proximity of the bar, the compressive stresses influence the experimental values in the post-peak branch where yielding has penetrated across the length of the bar and bond strength is limited towards the embedded end of the bar. The primary drawback of these methods involve the spurious interference at the interface on account of confining pressures in the cementitious matrix. The effective increase in bond strength leads to unconservative estimates (i.e. overestimates) of the average bond strength, especially for longer embedment lengths.

Figure 2-8 depicts two other prominent alternatives that have been considered for the study of bond and development. These include the beam end specimen shown in the center (Cairns and Plizzari 2003) and the lap-splice test shown in the right (the database of tests curated by ACI Committee 408 (2003) and the Bond Task Group of the *fib* (2012) comprises solely lap splice tests as they are considered to yield the most conservative values). The advantage of both of these tests is in that they develop the bar in a region where longitudinal concrete stresses are also tensile; a criticism in the case of the beam-end is the simultaneous presence of shear which places the end (free end) of the anchorage in transverse compression due to the support reaction.

However, bond values obtained from both of these tests are thought to be affected by the flexural response of the beam and in addition they are significantly more difficult to conduct.

In the effort to minimize the unaccountable effects of the confining pressures and to isolate bond from the effects of flexural curvature, a direct tension pullout (DTP) form has been proposed in the literature, wherein both the cementitious matrix as well as the bar are under longitudinal tension (Tastani 2006, Doctoral Thesis). The setup is commonly known as the DTP test and it requires that a support bar co-linear with the test specimen is cast so that conventional facilities for tension testing of reinforcement may be used to conduct the tests. This test provides the least possible estimate of bond strength, in which bond strength relies exclusively on the strength of the bar-to-concrete interface. Due to the difficulties involved in establishing this setup, an alternative version of the DTP test was initially introduced by Georgiou (2017) and was further improved in the present study, described in Chapter 3.

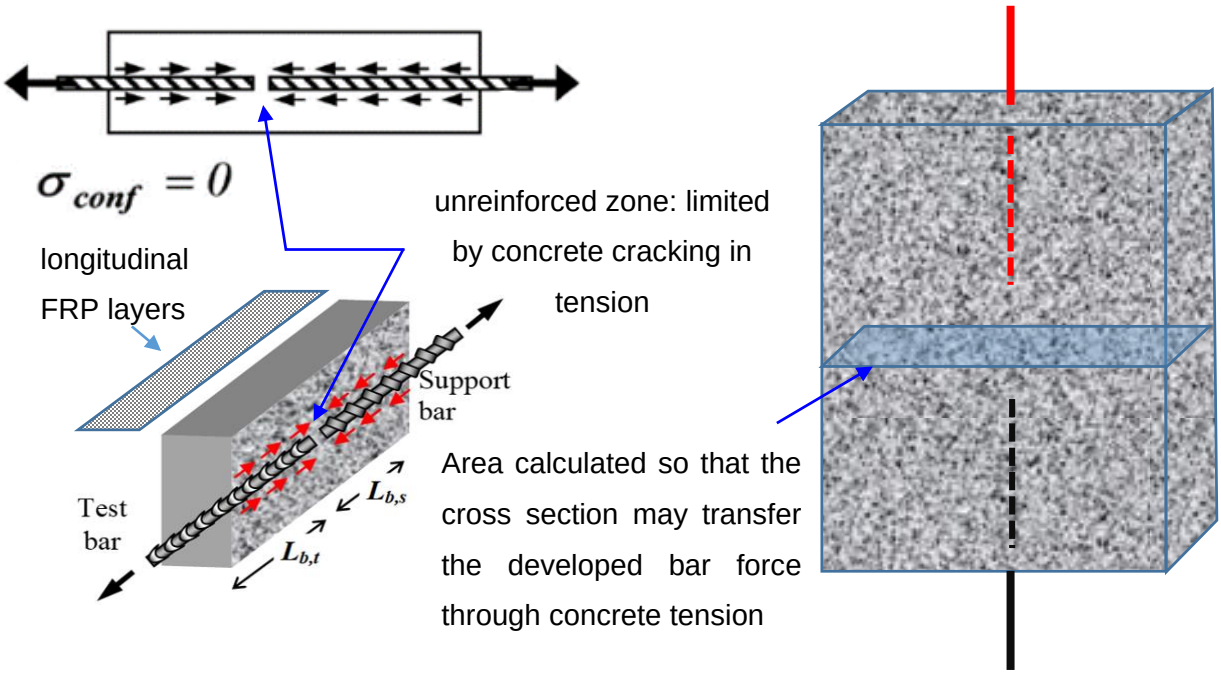

Figure 2-9 Unreinforced concrete zone sustaining tension.

The DTP specimen by Tastani (2006) is depicted in Figure 2-9, left. The concrete prism contains two bars, referred to as the test bar and the support bar, which are concentrically placed back to back in a concrete prism whose clear thickness is that of the concrete cover to be tested. The support bar is locked in place via a reaction wedge pulled against a support apparatus while the test bar is pulled in a similar fashion from the loading grip of the testing frame. This type of

specimen has a region of weakness in the center where the forces are transferred from the test region to the support region by concrete in direct tension. To avoid local failures two alternatives have been considered as depicted in Figure 2-9. In the specimen of Tastani (2006) (see also Tastani and Pantazopoulou 2010) longitudinal layers of FRP material were glued on the lateral surface of the specimen to act as a mechanism of reinforcement in the central tension zone. In this manner, the FRP fibers, being oriented parallel to the bars, acted as splicing whereas the concrete cover basically carried direct tension transferred through bond along the bar and the FRP interfaces. (This test setup facilitated the study of the effects of confinement also, wherein in some cases transverse FRP layers were also superimposed on the longitudinal layers to also provide additional confinement).

The advantages of the DTP test of Tastani and Pantazopoulou (2010) lie in the development of tensile stress fields around the test bar and the ability to isolate the confining pressures as a controlled study variable. The stress conditions derived from this test are in accordance to the ones encountered in flexural members where the concrete matrix undergoes tensile stresses. However, the application of such a test contains the risk of spurious effects from eccentricities due to possible misalignment of the test bar from the support bar, thereby making the preparation and casting of such specimens a sensitive process. The DTP specimen by Georgiou (2017) is depicted in the right of Figure 2-9. The specimen has an oblong rectangular cross section: the longer dimension is denoted here as b_c; the smallest dimension is controlled by the thickness of the cover being investigated, whereas the longer dimension is calculated so that the transfer section shown in light blue at the mid-height of the specimen may be able to transfer the tensile force of the bar through direct concrete tension:

$$b_c = \frac{A_b f_s}{(2C_{cov} + D_b) \cdot f_{ct}} \quad [2\text{-}7]$$

This type of specimen has many advantages, as it is easier to cast, and eliminates eccentricities between test and support bars during casting. A disadvantage is that its dimensions become very large if longer anchorages need to be tested, whereas the risk of premature through cracking of

the weak zone in tension prohibits its use in more demanding loading regimes (such as cyclic loading).

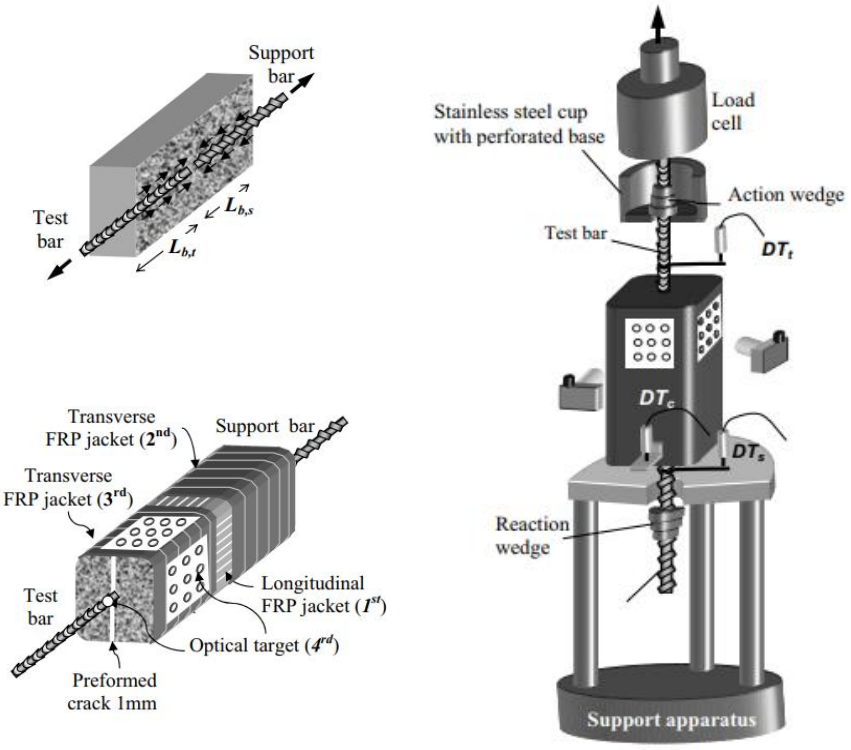

Figure 2-10 Configuration of the DTP bond test setup (from Tastani and Pantazopoulou 2010).

2.3.2 Mechanistic Interpretations of bond behavior

It was stated earlier that a commonly used approach to interpret the state of stress in the concrete cover of a bar being developed in concrete is to use the thick ring analogy. This model, originally suggested by Tepfers (1973) and later modified by Tastani and Pantazopoulou (2013) is based on the classical elasticity plane stress / plane strain solution of a pressurized vessel summarized in the following section. The primary difference between the two approaches is as follows: in the first case, the pressure exerted by the bar ribs, p, is considered as the input to the problem at the interior boundary of the ring, and therefore the limitation of the ring capacity by concrete strength in tension is used to calculate the limiting value of p that would be associated with through cover splitting. (Through the rib profile angle as per Fig. 2-1, the bond strength f_b that can be supported is evaluated). In the second case, the interior boundary of the ring is subjected to a radial translation u_r, (which again, is related to the amount of slip through the slope of the rib profile);

the pressure p that may be carried at the given input value of u_r is calculated from equilibrium, even past the exhaustion of the ring strength, so that a full bond stress – slip relationship may be calculated. So, the two approaches are basically a force and a displacement – based version of the thick ring solution. The following section summarizes the basic equations governing the thick ring with internal pressure problem.

2.3.3 Thick cylinder analogy

According to this model, the concrete cover surrounding the bar and supporting the radial pressures exerted by the bar ribs that are bearing on the interior cover with pressure p (see Figure 2-1) may be idealized as a thick cylinder with external radius C_c, whereas the inner radius R_b corresponds to the radius of the bar (Figure 2-11). In this approximation the longitudinal dimension (i.e. the bar axis and the bond stresses acting parallel to the bar axis) is not considered, although the kinematic and equilibrium conditions of Figure 2-1 have been used to link the radial pressure strength of the thick ring with the longitudinally oriented bond strength according to the tangent of the sloping angle of the effective rib.

Stress and strain conditions are expressed in polar coordinates - the equilibrium of forces on a cylinder section are expressed from Eqn. [2-8]:

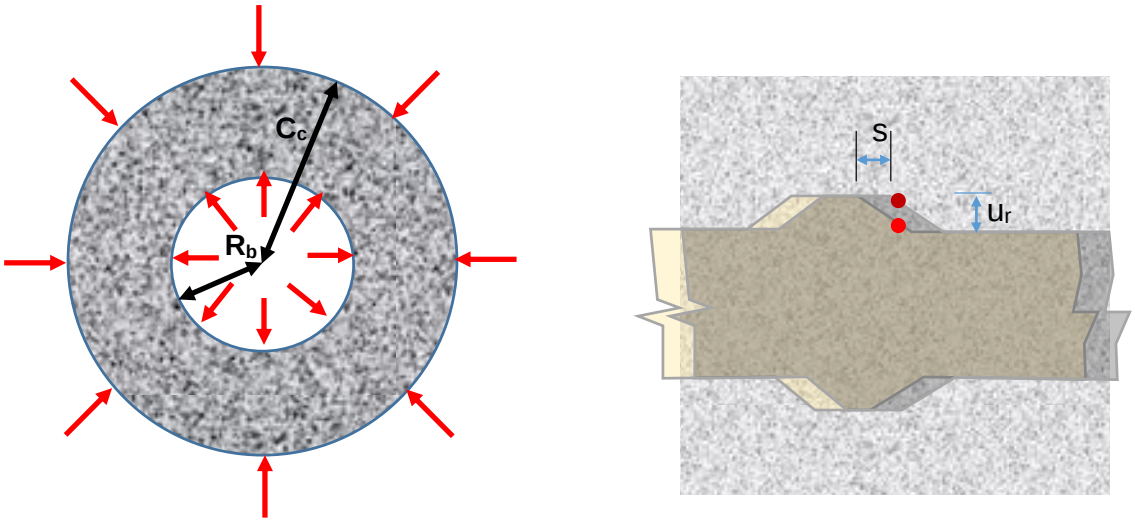

Figure 2-11 (a) The thick ring model: Definition of stress terms. (b) Geometric relationship between bar slip (s) and radial displacement, u_r: the red dot is a point in the concrete cover which displaces to the position of the burgundy dot when the bar slips by an amount s. The kinematic relationship is, $u_r = s \cdot tan(a)$.

$$\sigma_r - \sigma_\theta + \frac{\partial \sigma_r}{\partial r} \cdot r = 0 \qquad [2\text{-}8]$$

where σ_r is the radial stress (usually in compression) and σ_θ is the hoop stress (usually tensile) as a function of the radius r. Accordingly, the strain-displacement relationships are:

$$\varepsilon_r = \frac{du_r}{dr}\ ,\ \varepsilon_\theta = \frac{u_r}{r} \qquad [2\text{-}9]$$

where ε_r and ε_θ the corresponding radial and tangential (hoop) strains, and u_r the radial displacement. By relating stresses and strains by means of the generalized Hooke's law, Eqn. [2-10] is obtained:

$$\begin{aligned} \sigma_r &= \frac{E}{(1-2\nu)(1+\nu)}\left((1-\nu)\varepsilon_r + \nu\varepsilon_\theta\right) \\ \sigma_\theta &= \frac{E}{(1-2\nu)(1+\nu)}\left(\nu\varepsilon_r + (1-\nu)\varepsilon_\theta\right) \end{aligned} \qquad [2\text{-}10]$$

where ν is the Poisson's ratio, and E the modulus of Elasticity. Upon substitution of Eq. [2-9] in Eq. [2-8], the governing differential equation is obtained in terms of displacements:

$$\frac{d^2 u_r}{dr^2} + \frac{1}{r} \cdot \frac{du_r}{dr} - \frac{u_r}{r^2} = 0 \qquad [2\text{-}11]$$

2.3.4 Finite Element Approaches

With the availability of advanced computational methods for digital calculation and simulation of analytical data, several approaches using the finite element method have been introduced to study the behavior of bond. From among the various approaches published, two modeling approaches are at the core of the relevant literature:

2.3.4.1 The Bond link approach

One of the rudimentary approaches to the finite element modeling of reinforced concrete members is the bond link approach (Ngo and Scordelis 1967). To articulate the force-transfer mechanism between steel and concrete into mathematical interpretation, a "linkage" element is included at the nodal locations between the bar and the concrete cover, comprising of two linear springs, one in the horizontal direction (H) and one in the vertical direction (V). The nodal identifications on either end of the springs contain the same topological coordinates, while

representing the two materials independently. The spring stiffnesses can be expressed using the equation shown below:

$$\begin{Bmatrix} \sigma_H \\ \sigma_V \end{Bmatrix} = \begin{bmatrix} K_H & 0 \\ 0 & K_V \end{bmatrix} \cdot \begin{Bmatrix} \varepsilon_H \\ \varepsilon_V \end{Bmatrix} \quad [2\text{-}12]$$

where σ_H and σ_V, K_H and K_V, and ε_H and ε_V, represent the spring stresses, stiffnesses and strains in the horizontal and vertical directions, respectively.

The properties of the bond – slip constitutive law are embedded into the linkage elements in the form of a stiffness analytical function and a strength criterion: these properties are calculated over a tributary length spreading from the midpoints between successive nodes. This approach enables the representation and study of existing bond experiments where the properties of the spring elements are obtained via experimental measurements. However, this method requires the inclusion of the bond – slip relationship a priori and reduces the dimensionality of the problem into pointwise integration points where the springs are located.

2.3.4.2 Dimensionless contact element

An alternative approach to the finite element modeling of the bond – slip interface is with the use of the dimensionless contact element, initially introduced by Hoshino (1974) and Schäfer (1975) and developed by Dinges et al. (1985), while the present interpretation is obtained from Keuser et al. (1987). This element comprises of dimensionless, two-noded interface elements that connect the nodal stresses and strains of the two materials at geometrically coincident nodes as follows:

$$\begin{Bmatrix} \sigma_H^1 \\ \sigma_H^2 \\ \sigma_V^1 \\ \sigma_V^2 \end{Bmatrix} = \begin{bmatrix} 2K_H & K_H & 0 & 0 \\ K_H & K_H & 0 & 0 \\ 0 & 0 & K_V & K_V \\ 0 & 0 & K_V & 2K_V \end{bmatrix} \cdot \begin{Bmatrix} \varepsilon_H^1 \\ \varepsilon_H^2 \\ \varepsilon_V^1 \\ \varepsilon_V^2 \end{Bmatrix} \quad [2\text{-}13]$$

where σ_H and σ_V, K_H and K_V, and ε_H and ε_V, represent the spring stresses, stiffnesses and strains in the horizontal and vertical directions, respectively. Indices “1” and “2’ correspond to the node identification numbers of each side of the element. In the case of a multidimensional problem, interface elements containing the dimensionless contact element on each joint can be assigned on the contact surfaces of bonded elements. This approach holds the advantage that stress fields

normal to the contact surface can be represented by the contact elements as described in Eqn. [2-13], uses pressure sensitive constitutive models, and therefore enables monitoring the effects of confinement along the bar-to-concrete interface.

2.4 Code Approaches to Bond

2.4.1 ACI 318 and ACI 408

Design provisions regarding development and splice length are denoted in ACI 318, based on the original equations produced by Orangun, Jirsa and Breen (1975, 1977). The ratio of development length l_d to the bar diameter d_b equals:

Table 2-1 Development length provisions as specified by ACI 318.

$\frac{l_d}{d_b} = \frac{\frac{f_s}{\sqrt{f_c'}} - 200}{12\left(\frac{c + K_{tr}}{d_b}\right)}$	For $f_s < f_y$
$\frac{l_d}{d_b} = \frac{3}{40}\frac{f_s}{\sqrt{f_c'}\left(\frac{c + K_{tr}}{d_b}\right)}$	For $f_s \geq f_y$
where $c = c_{\min} + 0.5 \cdot d_b$ and $K_{tr} = \frac{A_{tr} \cdot f_{yt}}{1500 \cdot s \cdot n}$	

In the above table, $c_{\min}$ is the smaller value of the minimum concrete cover or ½ of the bar clear spacing; f_s is the bar tensile strength; f_c' is the concrete compressive strength; A_{tr} is the area of transverse reinforcement normal to the plane of splitting through the anchored bars; f_{yt} = yield strength of transverse reinforcement; S = spacing of transverse reinforcement; and n = number of bars developed or spliced at the same location [ACI Committee 408].

To account for pullout failure which controls failure in the presence of significant confinement, ACI 318 imposes the limitation that:

$$\frac{c + K_{tr}}{d_b} \leq 2.5 \qquad [2\text{-}14]$$

Additional phenomena such as bar location, epoxy coating, bar size and the use of lightweight concrete are incorporated by corresponding factors for the development length l_d, namely α, β, γ and λ.

Provisions for spliced or developed high relative rib area bars, with related rib area index ranging between $0.1 \leq f_R \leq 0.14$, were developed by ACI 480.3 according to the following expression:

$$\frac{l_d}{d_b} = \frac{\dfrac{f_y}{\phi f_c'^{1/4}} - 2130\left(0.1\dfrac{c_{\max}}{c_{\min}} + 0.9\right)}{80.2\left(\dfrac{c + K_{tr}}{d_b}\right)} \qquad [2\text{-}15]$$

These expressions are based on the work of Darwin et. al (1996) with the addition of a strength-reduction factor φ to account for the consideration of average bond stress. The reduction factor φ depends on the values used for tension (*0.6, 0.65*) at the ultimate limit state. For further simplification, Eq. [2-3] was later modified into the following:

$$\frac{l_d}{d_b} = \frac{\left(f_y / f_c'^{1/4} - 1900\omega\right)\alpha\beta\lambda}{72\left(\dfrac{c\omega + K_{tr}}{d_b}\right)} \qquad [2\text{-}16]$$

where *c* is as defined in Table 2-1 and:

$$\omega = 0.1\frac{c_{\max}}{c_{\min}} + 0.9 \leq 1.25 \qquad [2\text{-}17]$$

$$K_{tr} = C_R(0.72d_b + 0.28)\frac{A_{tr}}{sn} \qquad [2\text{-}18]$$

$$C_R = 44 + 330(f_R - 0.10) \qquad [2\text{-}19]$$

The ACI 408 Recommendations form the background to those adapted by the ACI 318 Code. The provisions presented by this committee follow the work of Zuo and Darwin (1998, 2000) which are a continuation of Darwin et. al (1996). Equation [2-9] employs the reduction factor φ in the similar fashion as in ACI 408.3 and can be applied for conventional and high relative rib area bars.

$$\frac{l_d}{d_b} = \frac{\left(\frac{f_y}{\phi f_c^{'1/4}} - 2400\omega\right)\alpha\beta\lambda}{76.3\left(\frac{c\omega + K_{tr}}{d_b}\right)} \quad [2\text{-}20]$$

A comparison of provisions ACI 318 (2002), ACI 480.3 (2003) and ACI 480R (2003) has demonstrated that the former approach leads to higher variability compared to test results than the two latter ones. Based on a statistical analysis of database test results, it was demonstrated that ACI 318 provisions lead to increased requirements for development and splice lengths and to lower estimated bond strengths (i.e. it is too conservative). In addition, being code requirements the ACI 318 provisions also incorporate additional clauses to limit the locations of spliced reinforcement so as to ensure structural redundancy.

2.4.2 CSA A23

Using a very similar approach to the ACI 318 requirements, in the Canadian code, bond design is incorporated in the development length l_d according to the expression:

$$l_d = 1.15\frac{k_1 k_2 k_3 k_4}{d_{cs} + K_{tr}}\frac{f_y}{\sqrt{f_c^{'}}}A_b \quad [2\text{-}21]$$

$$K_{tr} = \frac{A_{tr} \cdot f_{yt}}{10.5 \cdot sn} \quad [2\text{-}22]$$

2.4.3 EN-1988 (EC-2 2005)

According to European standards, bond failure is controlled by the ultimate bond stress f_{bd} which is calculated by the following expression:

$$f_{bd} = 2.25 \cdot \eta_1 \cdot \eta_2 \cdot f_{ctd} \quad [2\text{-}23]$$

where η_1 and η_2 are modifying factors related to the quality of bond conditions and the bar diameter, respectively. Factor f_{ctd} is the design value of the concrete tensile strength.

The calculation of the required anchorage length is based on the ultimate bond stress and on the type of reinforcement used, according to the expression:

$$l_{b,req} = \alpha \cdot \frac{D_b}{4} \cdot \frac{f_{sd}}{f_{bd}} \qquad [2\text{-}24]$$

where $l_{b,req}$ is the required anchorage length, D_b is the bar diameter and f_{sd} is the design stress on the bar, at the location where the anchorage begins; coefficient a is meant to account for the anchorage geometry (=1 for a straight anchorage, but =0.7 for anchorages with a hook).

2.4.4 Model Code 2010

From an analytical perspective, bond can be described, together with the link or interface element described in the F.E. modeling techniques in the preceding Section 2.3.4, using a properly calibrated constitutive model for the local bond-slip relationship. The Model Code 2010 presents such a model for use when studying structural members where bond is an essential attribute. The nomenclature of the model is given with reference to Figure 2-12 below. For the purposes of this study, bond behavior is described via a multilinear envelope, with each line segment representing the progressing stages of plastification. Through the longitudinal translation of the embedded reinforcement, the inclined ribs impose normal traction $\tau(s)$ on the periphery of the bar, where s corresponds to the relative slip of the reinforcement. Equation [2-25] provides the relationship between the bond strength τ and the relative bar slip s (Figure 2-12). Terms s_1, s_2 and s_3 represent milestone values of the relative slip which separate the multilinear model in accordance with the relevant stage. The following bond stress-slip model is used in the CEB-FIP Model Code 2010 and comprises four branches:

$$\tau(s) = \begin{cases} \tau_{\max} \cdot (s / s_1)^{\alpha} & 0 \le s \le s_1 \\ \tau_{\max} & s_1 \le s \le s_2 \\ \tau_{\max} - (\tau_{\max} - \tau_f) \cdot (s - s_2 / s_3 - s_2) & s_2 \le s \le s_3 \\ \tau_f & s > s_3 \end{cases} \qquad [2\text{-}25]$$

The ascending branch is affected predominantly by the relative slip, the surface geometry of the bar and the strength properties of the surrounding concrete. During this stage, the bar ribs begin to bear against the concrete surface and form concrete “wedges” that resist the bar displacement through interlocking action. Local crushing and micro-cracks occur at that stage. At peak bond strength, the ribs have penetrated into the concrete and the bar becomes locked against the wedges, while compressive and shear forces act on the encased concrete. In the presence of confinement and larger available concrete cover, the maximum bond strength is maintained over

a plateau before the concrete between the ribs is sheared off (*fib* Bulletin #65, 2012). Once the descending branch is reached, the bond strength between the bar and concrete is diminished and the bar is released from the concrete wedges. Bond strength is reduced up to a residual plateau which represents the dry friction of the bar against the concrete while it is being pulled outwards.

The local mechanistic properties of the bond – slip constitutive relationship between bar and concrete are described by Eq. [2-25]. However, accompanying phenomena such as bar yielding, transverse confining pressure, longitudinal cracking and cyclic loading are not explicitly described by this relationship. To account for the aforementioned phenomena, modifying factors are applied on bond strength $\tau_{b,0}$ as shown in Eq. [2-26]:

$$\tau_{b,m0} = \tau_{b,0} \cdot \Omega_y \cdot \Omega_{p,tr} \cdot \Omega_{cr} \cdot \Omega_{cyc} \qquad [2\text{-}26]$$

where $\tau_{b,m0}$ is the modified bond strength, $\tau_{b,0}$ is the reference bond strength obtained from DTP tests, whereas factors Ω_y, $\Omega_{p,tr}$, Ω_{cr} and Ω_{cyc} describe the effect of the bar yielding, transverse pressure perpendicular to the bar axis, longitudinal cracks parallel to the bar axis and cyclic loading, respectively. The definition of the above factors is described in detail, in (*fib* Bulletin #65, 2012).

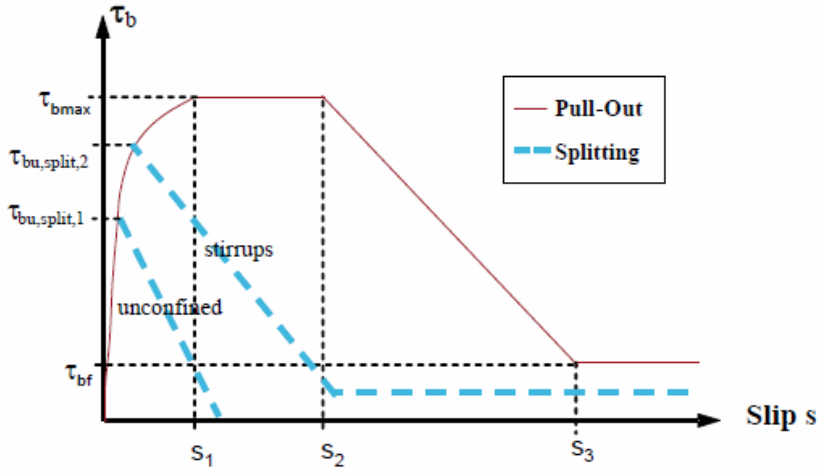

Figure 2-12 Bond stress-slip curve recommended by *fib* Model Code 2010 .

2.5 Bond in Ultra-High Performance Concrete (UHPC)

One of the most interesting findings of the previous experimental work on bond has been the

observation that in the absence of transverse reinforcement, increasing the length of anchorage cannot provide resilience and large strain capacity in the anchorage. The so called unzipping effect has been reported by Zuo and Darwin (2000) and by Tastani and Pantazopoulou (2006) among others, according to which, once the amount of slip exceeds the value of s_2 (Fig. 2-12) in unconfined anchorages (i.e. a sharp post-peak ensues the plateau in the bond slip law) then strain penetration ensues from the loaded towards the unloaded end of the anchorage and the stress developed by the bar can no longer increase. Instead, debonding propagates instantaneously and anchorage failure follows. This problem was explored by Tastani and Pantazopoulou (2006) through analytical investigation and it was shown that it can be mitigated only if the fracture energy of the matrix increases. This is very useful in the case of FRP reinforcements where the linear elastic strength of the bars can never be reached in unconfined concrete.

It has been shown through experiment that UHPC materials possess internal confinement by means of the distributed fibers. A few preliminary studies have been conducted showing that the magnitude of this confinement is equal in magnitude to the splitting strength of the UHPC material (Georgiou and Pantazopoulou 2017). The finding that UHPC's function is comparable to that of confined concrete has naturally led to experimental and analytical studies of the development capacity of reinforcement embedded in such materials.

UHPCs are an evolution of traditional fiber reinforced concrete (FRC), whereby the matrix, by means of fine aggregates and its self-consolidating mix design present a very dense, packed structure with minimal capillaries and generally very small size pores. These are orders of magnitude smaller than the multitude of embedded fibers which have an aspect ratio in the order of 100-200. The fact that fibers are very long enables them to arrest the propagation of flaws while they are still very small (this was not possible in the older versions of FRC where aggregates were of comparable size as the fibers); the very large aspect ratio of fibers enables a very large collective surface area of interaction with the matrix, where fiber bond may be developed (note for example a single 20 mm long Dramix type fiber having a volume of 1mm x 1mm x 20 mm = 20 mm^3 has a contact area of 80 mm^2, whereas a single NYCON brass-coated fiber of 12 mm length such as what is used in UHPC today would have a total volume of 0.1mm x 0.1mm x 12mm = 0.12mm^3, and a contact surface of 4.8 mm^2. For equal volumetric ratio of fibers (e.g. 2%), the contact surface area would be 4.8x(20/0.12) = 800mm^2, that is, 10 times greater than what is provided by standard fibers in conventional FRC.

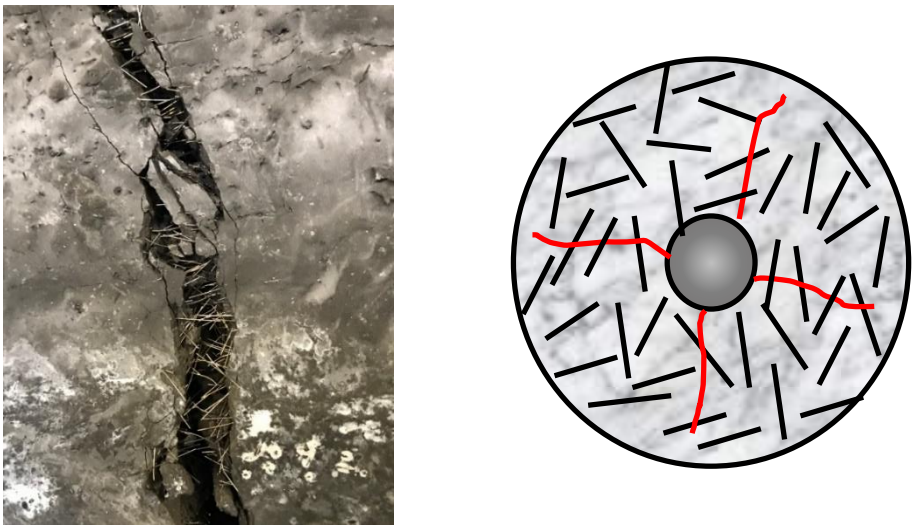

Figure 2-13 (a) Fibers crossing a localized crack in UHPC, (b) Visualization of the internal confinement effect by the fibers on the embedded bar.

UHPCs as well as ECCs (Engineered Cementitious Composites) can both be strain hardening in tension (known as SHFRCC for strain-hardening fiber reinforced cementitious composites). The strength of ECCs is generally lower to that of UHPCs, the former being reinforced with synthetic fibers. However, preliminary tests of bars embedded in both classes of materials [Billington (2016), Georgiou (2017), Tastani et al. (2018), Saikali (2019)] illustrate that a much shorter anchorage length is needed to develop a bar, with yielding requiring as little as $10D_b$ anchorage. Saikali (2019) found that even in very short anchorage lengths (in the order of $5D_b$) bond stress distribution is not uniform, and that even shorter lengths would be needed in order to capture the actual bond strength through experiment.

Chapter 3: Design of test setup and specimen form

3.1 Overview of modified direct tension pullout test setup

It has become evident from previous studies on bond behavior that the experimental setup greatly affects the acquired readings and interpretation of bond strength (Tastani and Pantazopoulou 2010). A detailed analysis on previous setups is presented in Chapter 2. As part of the experimental program of this study, direct tension pullout (DTP) tests are selected as they are devoid of the spurious effects of compressive stress fields around the bar. On account of the difficulties in eliminating any possible form of eccentricity in DTP tests, in the present study the DTP test setup has been modified so that only the test bar is embedded in the specimen block, whereas the support is provided by means of a spherical hinge. The main benefit of this setup is that it ensures a tensile stress field on the activated area around the test bar, similar to the conditions encountered in the tension zone of R.C. structural members, while simultaneously replacing the support alignment with mechanical interlock. The spherical hinge is held and allowed to freely rotate on a steel platform attached to the concrete specimen (Figure 3-1).

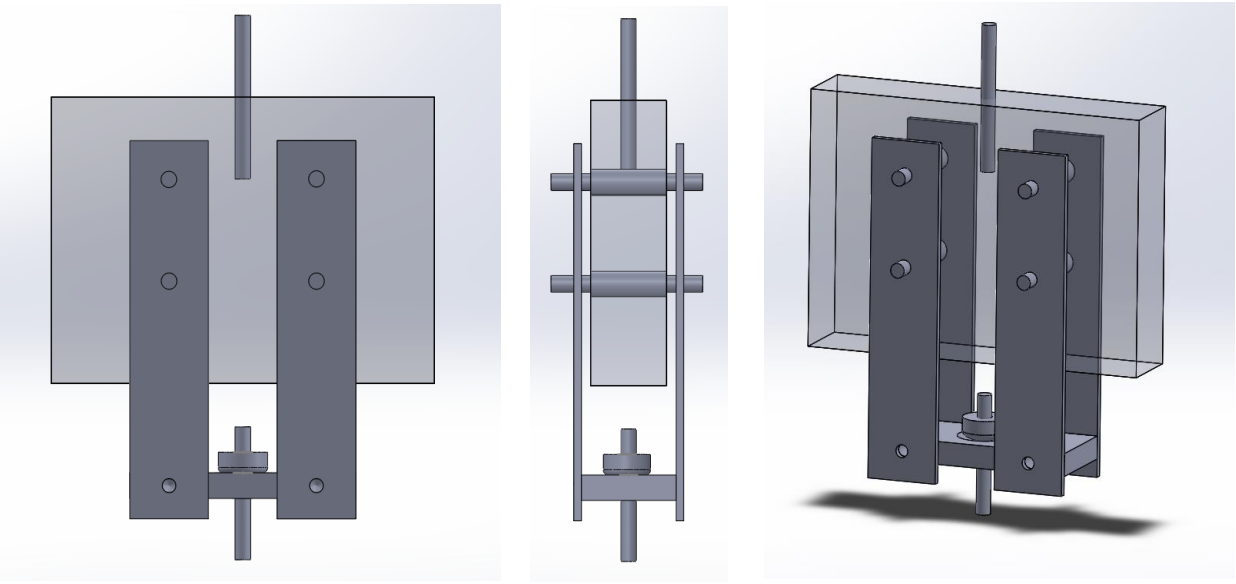

Figure 3-1 Direct tension pullout test with external support bar. Front view (left), Side view (middle), Perspective view (right).

The mechanical base was designed using the commercial software package Solidworks and later submitted to Lassonde's Machine Shop for manufacturing. The bottom, horizontal plate component consists of a steel rectangular base with a circular opening in the center, through which the support bar is held by means of a nut with a semispherical bearing surface. On the top face of the plate opening an elliptical concave surface is carved to allow for smooth rolling of the spherical nut. The vertical component of the steel hardware consists of four rectangular steel plates, attached to the bottom plate via one M16 structural bolt each. Each plate contains two openings through which horizontal transverse support bars that pass through the specimen's thickness will keep the specimen in a vertical position. To account for eccentricities during the casting of the specimens, four eccentric cylinders have been designed to adjust the horizontal support bars. The cylinders have an external diameter of 25.2mm and 1 mm thickness and they serve as a sleeve to an internally fit adjustment system. Thus, they contain a snugly fit internal cylinder of 24.2mm diameter as shown in Figure 3-2. The internal cylinder contains a through 16.0mm diameter hole, placed eccentrically from the center of the circular section. A circular opening of 1 mm diameter is placed diametrically opposite to the hole, to serve as anchor for an adjustment pin to rotate the cylinder. The internal cylinder rotates accordingly in order to correct the eccentricities of the horizontal openings.

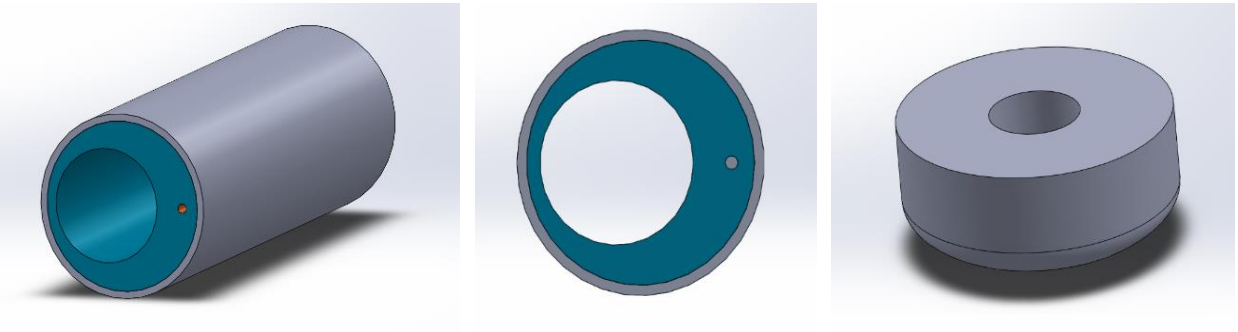

Figure 3-2 Two-component cylinders used for horizontal support and custom elliptical nut for vertical adjustlment. Perspective view of cylinders (left), Front view of cylinders (middle), custom elliptical nut (right).

The typical specimen is a rectangular plate (Figure 3-1), having adequate thickness to allow for the required clear cover over a test bar anchorage. Therefore, in this arrangement, the concrete is held down by the transverse bars described in the preceding paragraph, whereas the test bar is pulled in tension. This places both concrete and the anchored steel bar in direct tension and is therefore considered an adverse test (to yield conservative bond strength values).

3.2 Outline of the experimental study – scope and objectives

In the present work the test setup thus described is used in order to conduct an experimental investigation of reinforcement – to – concrete bond mechanics with the objective to derive a local bond-slip law for emerging UHPC materials used for the concrete matrix. Additional objectives are, to collect experimental data that can be used to calibrate analytical models for bond in this type of concrete including the evaluation of important assumptions needed in order to extend analytical solutions into this problem category, and to also evaluate the effect of the load test setup on the measured bond properties. The latter objective is achieved through comparison with the bond – slip results obtained by a parallel series of tests (conducted by peer R. Saikali (2019)) on beams comprising the same materials and containing the test anchorage in the constant moment region developed in a four-point loading setup.

Parameters of the experimental study include, apart from the material UHPC mix, the clear cover to the free surface of the surrounding cementitious material – which represents the trajectory of the anticipated splitting cracks observed in splitting-pullout failures of specimens in conventional concrete. Note that the total thickness of the specimens is, $t = D_b + 2c$, where D_b the diameter of the anchored bar and c the clear cover.

a) *UHPC materials used:* Four different mixture types were used in this study; two of those are made of commercial, prepackaged cementitious products, and two are mixed in-house; their individual properties are denoted in Chapter 4.
b) *Embedment length:* For all specimens, the embedment length was chosen to be $5 \cdot D_b$ based on experience with conventional concrete, according to which this is an estimate of the maximum anchorage length that can be used with the assumption of uniform bond stress (to reduce the bond strength by dividing the developed load with the lateral contact surface of the bar).
c) *Diameter of test bar:* The test bars used for this study were Canadian-type 15M bars with 16mm diameter.
d) *Clear Cover:* Two values were considered for the cover, namely $c_1 = 1 \cdot D_b$ and $c_2 = 2 \cdot D_b$.

Considering the parameters listed above, a total of 8 distinct specimen designs could be constructed. The geometry of the typical specimen is shown in Figure 3-3.

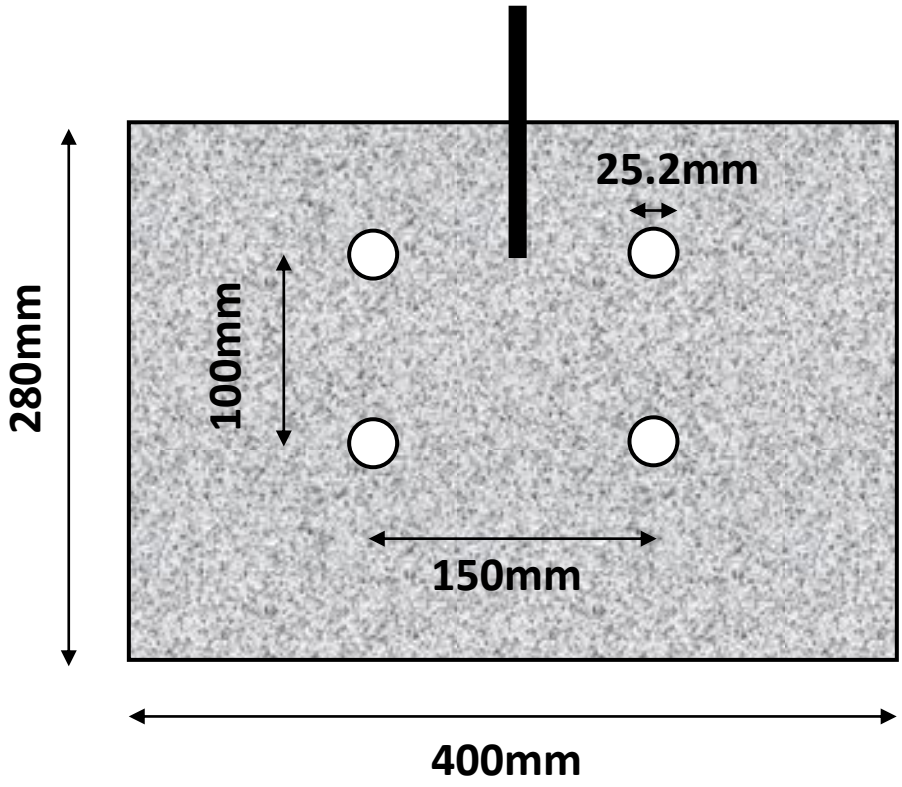

Figure 3-3 Geometry of Modified Tension Pullout test.

3.3 Modeling procedures

In order to assess the performance of the test setup and to design its various components, detailed modelling and computational evaluation of its response was carried out before the actual experiment. The modeling and finite element analysis of the specimen was carried out using the combination of the commercial software package ATENA 3D and ATENA Studio (ATENA Program Documentation, Parts 2-2 and 12). The original definition of the material properties, the modeling of the specimens, the boundary conditions, as well as the analysis steps and parameters are initially determined on ATENA 3D (ATENA Program Documentation, Part 2-2) whereas the analysis and post-processing are performed on ATENA Studio (ATENA Program Documentation, Part 12).

Bond modelling using detailed Nonlinear Finite Element Analysis (NLFEA) can be done using a variety of approximations and idealizations of the concrete – bar interface function. In the present study the presence of the ribs is represented implicitly through the local interfacial properties prescribed in the model. To be able to assess the relevance of the effect of the test setup it was

necessary to use a modeling approach wherein the interfacial action would be sensitive to spurious lateral pressure fields induced through the supports. However, this approach is rather complicated and impractical when it comes to analyzing larger bar assemblies. In this regard two alternative modelling approaches are studied here, namely the detailed interfacial model as a background benchmark for the simpler modelling approach which uses calibrated bond links (local springs in unidirectional action) to represent the interaction in larger scale problems where detailed interfacial modelling is not practical.

The detailed interfacial modeling is also used in the last part of the present chapter in order to explore in greater depth the effect of the test setup. The two alternative modelling approaches are outlined below as a precursor to the analytical exploration of the modified DTP specimen as well as its comparison with other, more conventional specimens such as the standard pullout and the eccentric pullout, and beam end [Tastani and Pantazopoulou (2010), Cairns and Plizzari (2002)].

3.3.1 Model “Link”

Model “Link” comprises the combination of three-dimensional solid elements representing the concrete volume and one-dimensional truss elements representing the bar’s action (only longitudinal action produces stress-transfer). In fact, a segmented sequence of co-linear truss elements modelling the anchored bar is connected with the concrete nodes with zero length one-dimensional springs that have been assigned nonlinear bond stress - slip properties. This arrangement enables the use of custom local bond - slip law curves which can be adjusted to include the fracture energy and confinement provided by the surrounding concrete by the area under the local bond – slip law. However, because the bond strength properties are assigned by the user and fixed throughout the analysis, this modelling approach cannot properly account for confining pressures and stress fields not proactively included in the bond law definition and therefore such effects cannot be studied using this approach.

3.3.1.1 Finite element arrangement

The finite element definitions are obtained from the ATENA Theory Manual (ATENA Program Documentation, Part 1). For the three-dimensional solid macroelements, brick and tetrahedral finite elements were used, named in the F.E. platform as CCIsoBrick and CCIsoTetra, respectively. Figure 3-4 shows the geometry, node numbering in the local system, and annotation of these elements. Linear shape functions are selected to optimize the computational load.

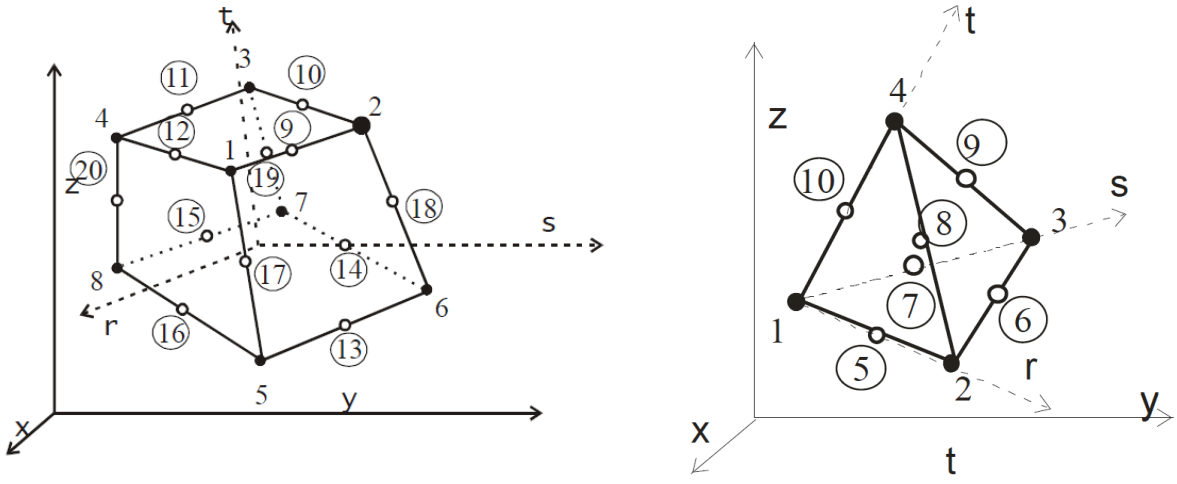

Figure 3-4 Geometry of CCIsoBrick elements (left), Geometry of CCIsoTetra elements (right) (ATENA Program Documentation, Part 1).

The reinforcing bars are modelled with truss elements (CCReinforcement) as depicted in Figure 3-5. To include the strength properties of the bond interface, the element CCBarWithBond is utilized. Figure 3-5 depicts the geometry and annotation of the bar with bond element. The bond - slip law properties are defined separately as material input.

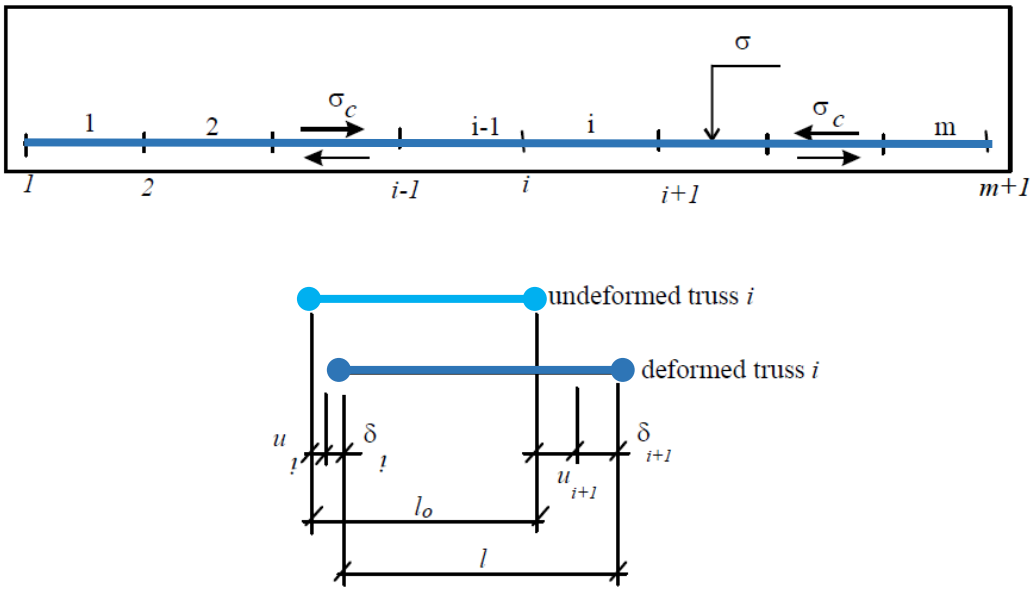

Figure 3-5 Reinforcement bar with bond-slip properties (ATENA Program Documentation Part 1).

To allow for the use of brick elements, the model is subdivided into zones of rectangular macroelements (Figure 3-6). The circular horizontal support openings are modeled within rectangular macroelements and meshed with tetrahedral finite elements. The reinforcing bar is placed concentrically on the top surface of the specimen with a small segment extending beyond the specimen. As denoted in the ATENA Program Documentation (ATENA Program Documentation, Part 11), the modeling of pullout specimens requires an undeformable, external macroelement that is attached to the “exposed” joint of the bar. No slip boundary conditions are imposed on the joint, whereas displacement control is applied concentrically on the external macroelement. To avoid wobbling effects, lateral movement is also restricted.

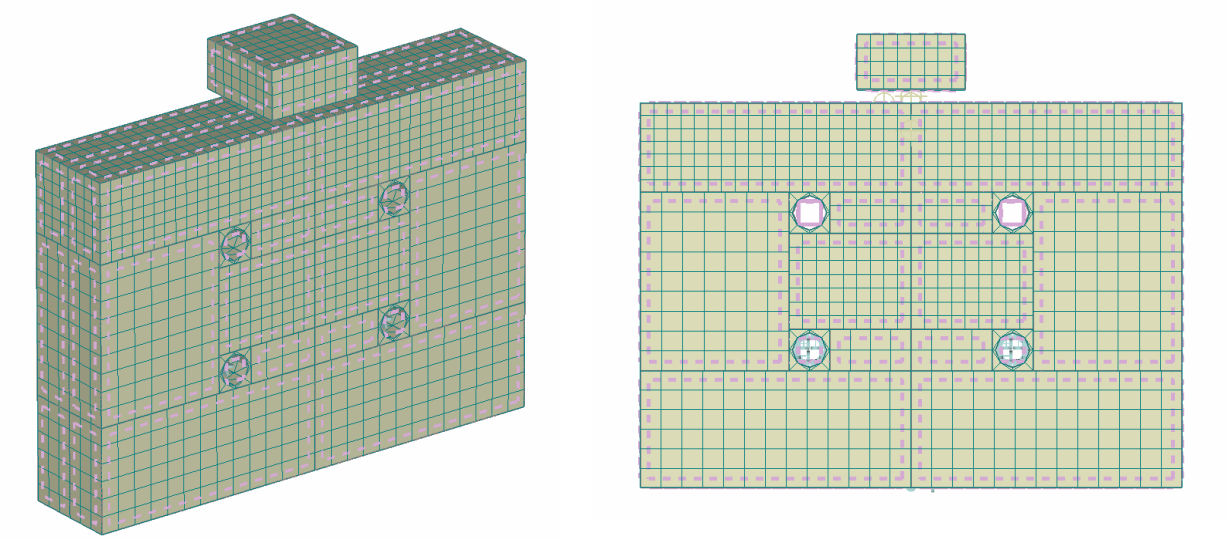

Figure 3-6 Mesh distribution and solid macroelement outline for Model “Link”: Perspective view (left), Front view (right).

Individual mesh properties are assigned to each macroelement, with a denser finite element distribution in close proximity of the reinforcing bar. Monitoring points are placed on the concrete and reinforcing bar to measure the incremental and total bond slip, the bond stress on the bar, the tensile and compressive stress fields on the concrete and the joint vertical displacements. For the analysis, the *Standard Newton-Raphson* iteration method is utilized with a maximum of 40 iterations performed be increment step. (ATENA Program Documentation, Part 1). Figure 3-7 shows the solution parameters included in the iteration method along with a visual representation of the convergence Criteria 1 – 4, representing the displacement increment, the normalized residual force, the absolute residual force and the energy dissipated, respectively. The Parallel

Direct Sparse Solver (PARDISO) is used for all the analysis executed in this study (ATENA Program Documentation, Part 1).

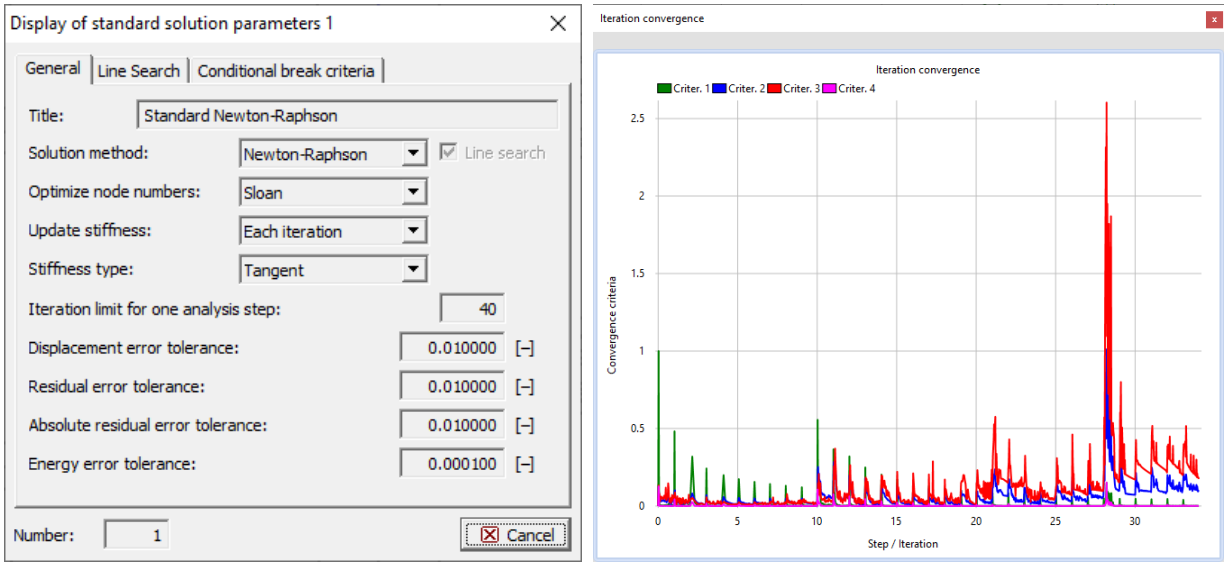

Figure 3-7 Parameters included in the Standard Newton-Raphson method and a visual example of the iterative procedure during a trail analysis.

A plasticity-based constitutive model is used for concrete equipped with fracture processes to simulate the brittle aspects of the material behavior (ATENA Program Documentation, Part 1). The model parameters refer back for calibration to the uniaxial stress-strain properties for tension and compression of concrete (elastic and fracture parts of the behavior) whereas the plasticity model refers to a Menetrey-Willam (1995) failure surface which passes through a standard Kupfer-Gerstle (1973) type biaxial failure envelope in the σ_{xx}-σ_{yy} plane (σ_{zz}=0).

In the following analysis two reference concrete examples are considered in determining the material properties required by the material model of ATENA: 1) Conventional Concrete and 2) Ultra-High Performance Concrete. Figure 3-8 denotes the material characteristics for conventional concrete and Figure 3-9 shows the tension and compression functions, in which ε_f is the tensile strain, σ_t the tensile stress, f_t the uniaxial tensile strength, ε_{pl} the plastic component of the compressive strain, σ_c the compressive stress and f_c the uniaxial compressive strength of the concrete. For the parametric study conducted the compressive strength of the concrete is assumed to be 25.0MPa whereas the tensile strength is taken as 2.5MPa (approximated 10% of f_c), with a corresponding modulus of elasticity E = 25.00GPa. The modulus of elasticity is obtained using the Eq. [3-1] for a value of γ_c = 2400kg/m^3 (CSA Concrete Design Handbook).

$$E = (3300 \cdot \sqrt{f_c'} + 6900) \cdot (\gamma_c / 2300)^{1.5} \qquad [3\text{-}1]$$

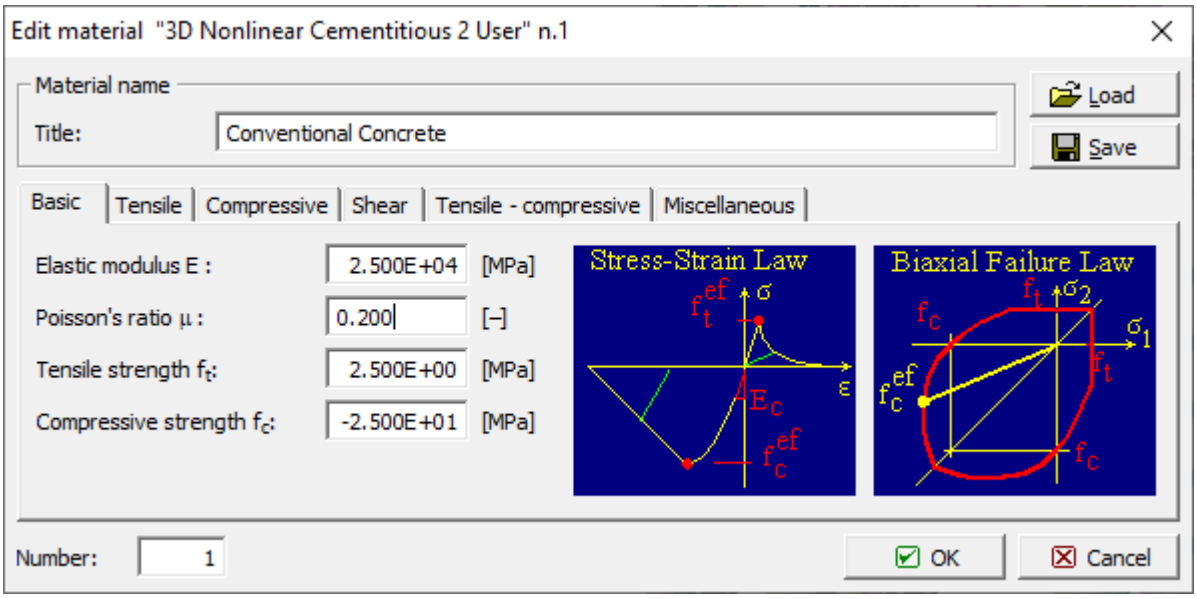

Figure 3-8 Constitutive properties for Conventional Concrete.

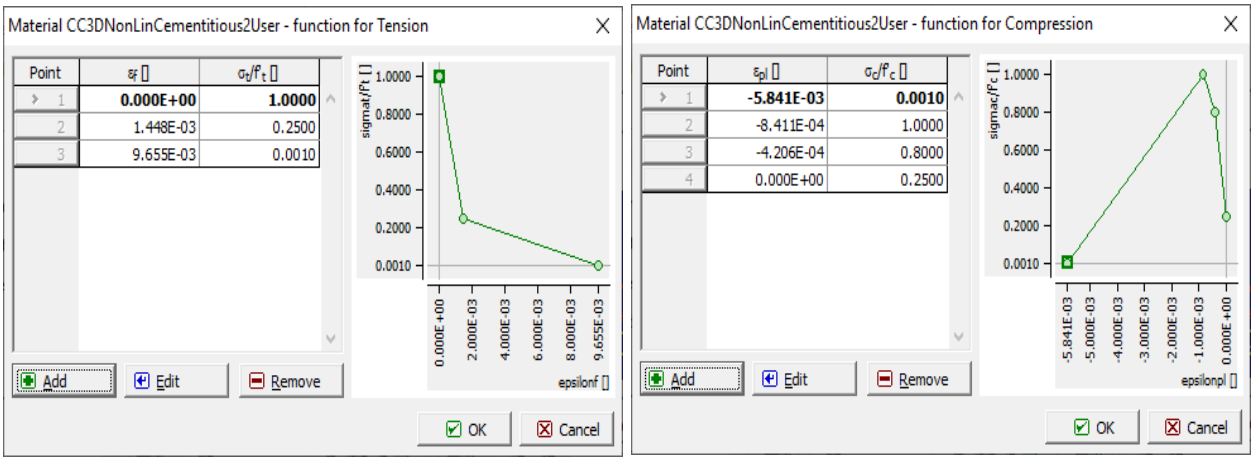

Figure 3-9 Tension and Compression constitutive functions for Conventional Concrete.

3.3.1.2 Material Constitutive Relationship for the Link Model

A custom bond – slip law is applied at the interface between reinforcement and concrete. The material code is CCReinforcementBondMaterial and the coordinates of the bond stress – slip properties are shown in Figure 3-10. The maximum bond strength assumed for Conventional Concrete is 4.5MPa, attained at a relative slip of 0.2mm. The model displayed below is constructed according with the Model Code 2010 (*fib* Bulletin 65, 2012). The starting point of the

bond – slip curve is chosen to be at 10% of the peak bond stress. That is because the program ATENA does not account for elastic deformations explicitly and slip is measured after the initial cohesion strength (represented by the starting coordinate of the ascending branch in Fig. 10) is exceeded.

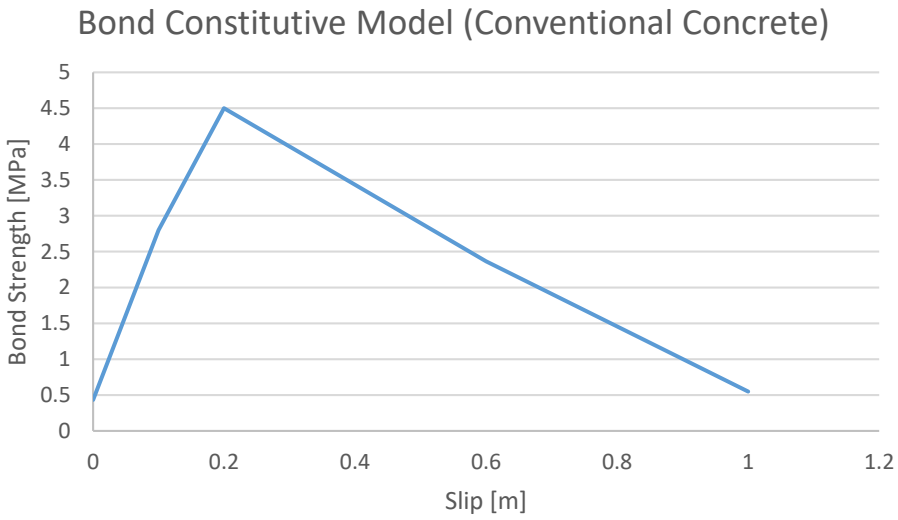

Figure 3-10 Coordinates of User Defined Bond-Slip curve for constitutive model on ATENA3D (Conventional Concrete).

The material constitutive properties for UHPC are shown in Figure 3-11. The compressive strength is assumed to be 120.0MPa and the tensile strength to be 15.00MPa (these values are not arbitrary, but represent the measured properties of one of the two commercial mixes used in the test program (Saikali, 2019)). During the tests the modulus of elasticity E reached values of 70GPa.

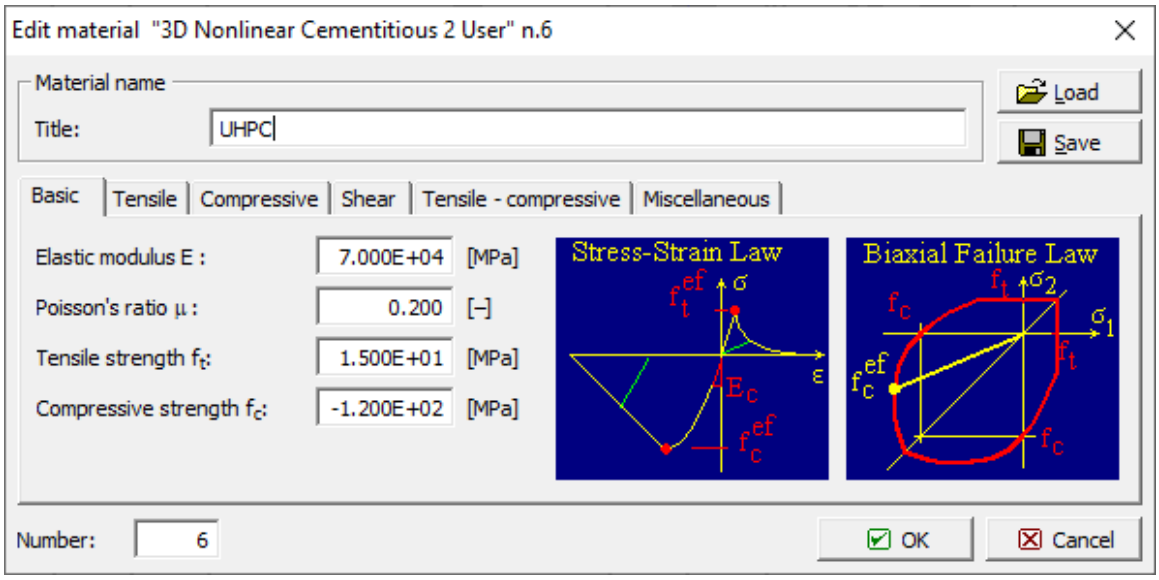

Figure 3-11 Constitutive properties for UHPC.

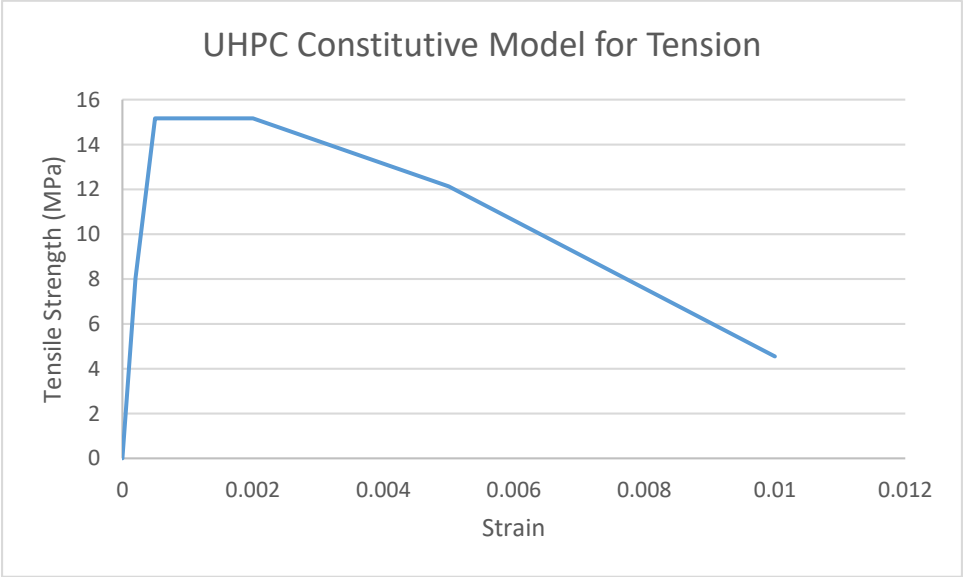

Figure 3-12 Coordinates of User Defined Tensile strength properties for UHPC constitutive model on ATENA3D.

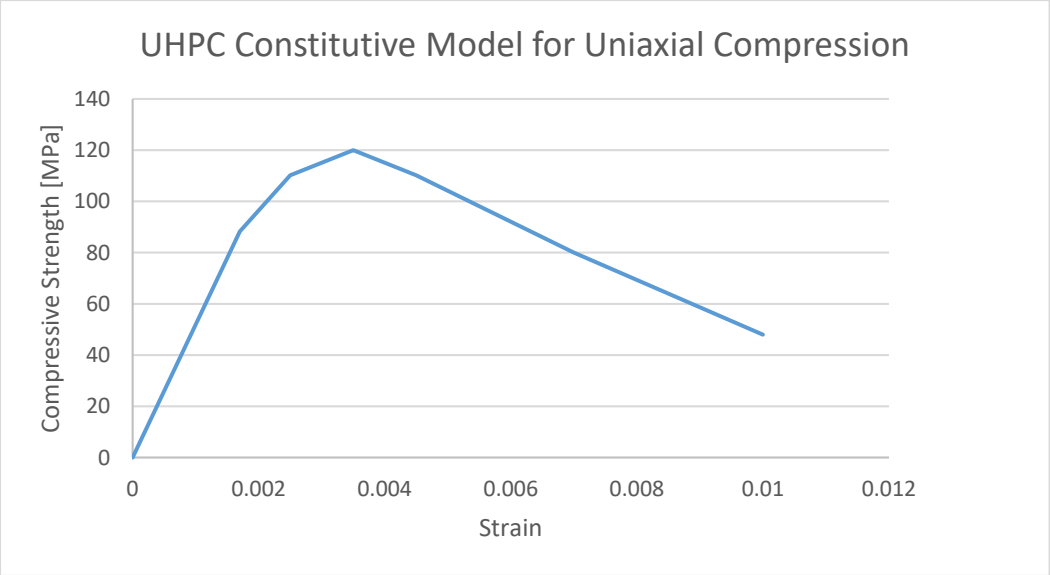

Figure 3-13 Coordinates of User Defined Compressive Strength for UHPC constitutive model on ATENA3D.

The bond constitutive model used for modeling the links in the case of UHPC specimens is shown in Figure 3-14. The assumed bond strength is 10.5 MPa, calculated as approximately the square root of the compressive strength f_c of concrete, reached at a relative slip of 1mm (approximated from the Model Code 2010).

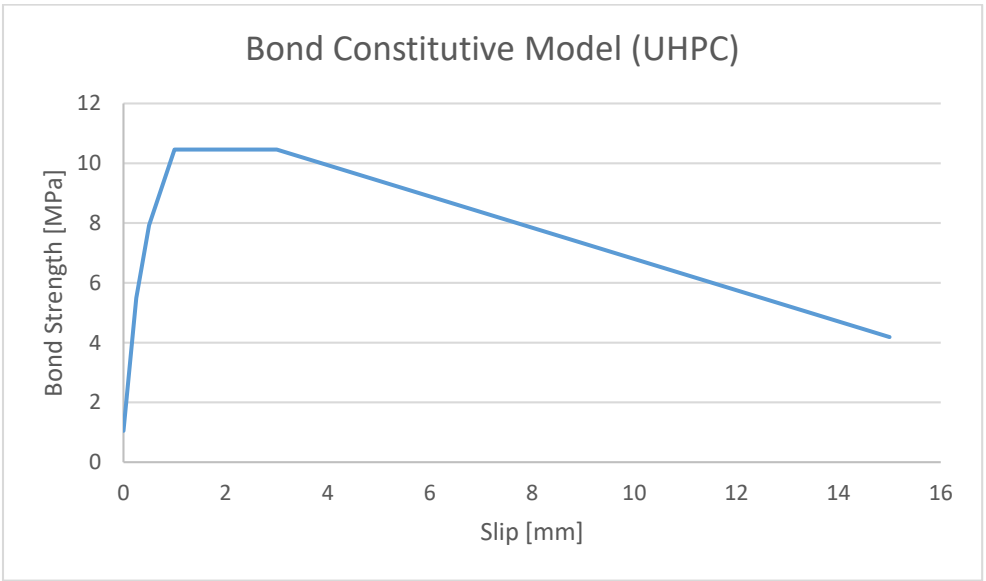

Figure 3-14 Coordinates of User Defined Bond-Slip curve for constitutive model on ATENA3D (UHPC).

For the reinforcing bar the material model with code CCReinforcement is used. Bilinear stress – strain law properties are assumed for the bar, with a yielding strength of σ_y = 400MPa (Figure 3-15).

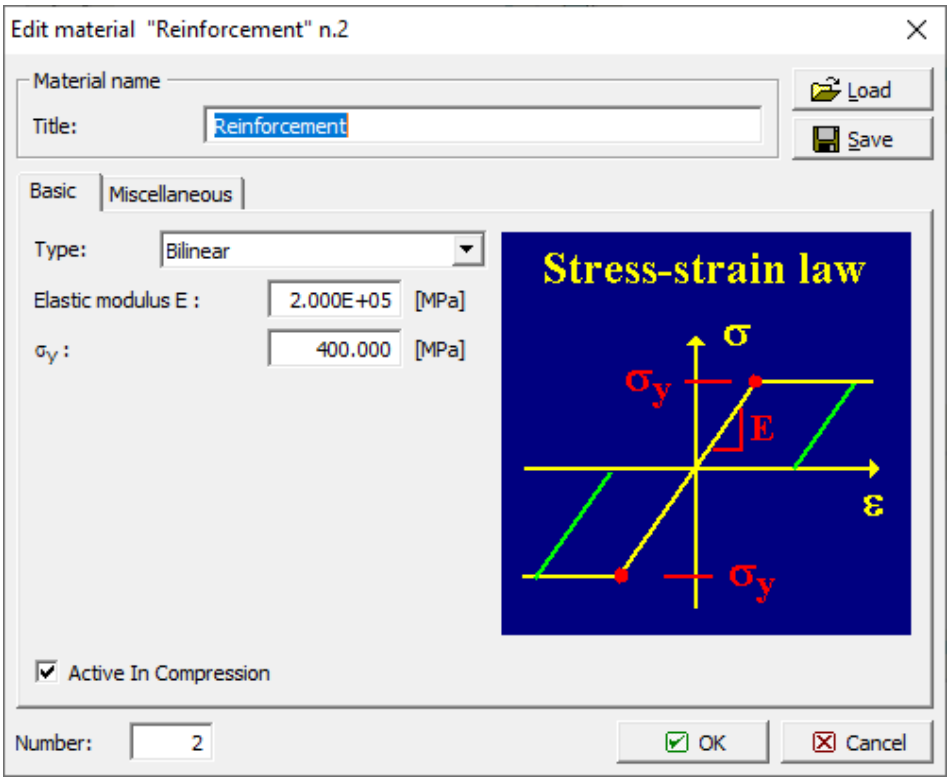

Figure 3-15 Constitutive properties for the reinforcing bar.

3.3.2 Model “Interface”

Model “Interface” is constructed using only three-dimensional elements. Both the main body of the concrete specimen and the reinforcing bar are modeled using brick and tetrahedral solid elements whereas the contact surface between the two materials is modeled using three-dimensional gap elements. Gap elements enable the customization of the interface properties between steel and concrete, thus taking into account the effects of normal stresses around the bar in the form of frictional computational models. While this method allows for the examination of confining pressures on the reinforcement, it increases the computational effort due to the finer mesh properties needed in the bar. To reduce this effect, the specimens are subdivided into their symmetrical components.

3.3.2.1 Finite element arrangement (Model “Interface”)

Interface elements exist in the contact areas between macroelements. They consist of isoparametric plane triangular or quadrilateral elements on each surface of the corresponding macroelements. The nodes of each of the two opposite sides of the interface are initially positioned in the same location. Figure 3-16 shows the geometry and annotation for the triangular and quadrilateral interface elements in local coordinates, respectively.

To model the embedded bar using three-dimensional interface elements, a distinct rectangular zone is first denoted containing the opening for the reinforcement. The bar is denoted as an independent macroelement, containing the same joint locations as with the concrete surface. The shared surfaces are then modified to incorporate the properties of the interface elements. Due to the irregular shapes of the macroelements, tetrahedral finite element meshing is used within the bar and the adjacent concrete macroelement while the remaining concrete body is modeled using brick finite elements. Finer mesh properties were assigned to the bar and the concrete macroelement adjacent to it, to ensure accuracy in the critical zone surrounding the interface. The concrete zone was assumed as approximately double the size of the bar (Figure 3-18).

Loading is imposed directly on the top surface reinforcement macroelement. To minimize the computational effort, the specimen model is reduced to its symmetric subcomponents and boundary conditions are placed on the planes of symmetry. Figure 3-17 shows the boundary conditions imposed on an axisymmetric specimen, where u_x and u_y are displacements in the x- and y- axis, respectively. In the case of two planes of symmetry, the specimen is reduced to 1/4 of its volume and for the case of one plane of symmetry 1/2 of the specimen is used for analysis.

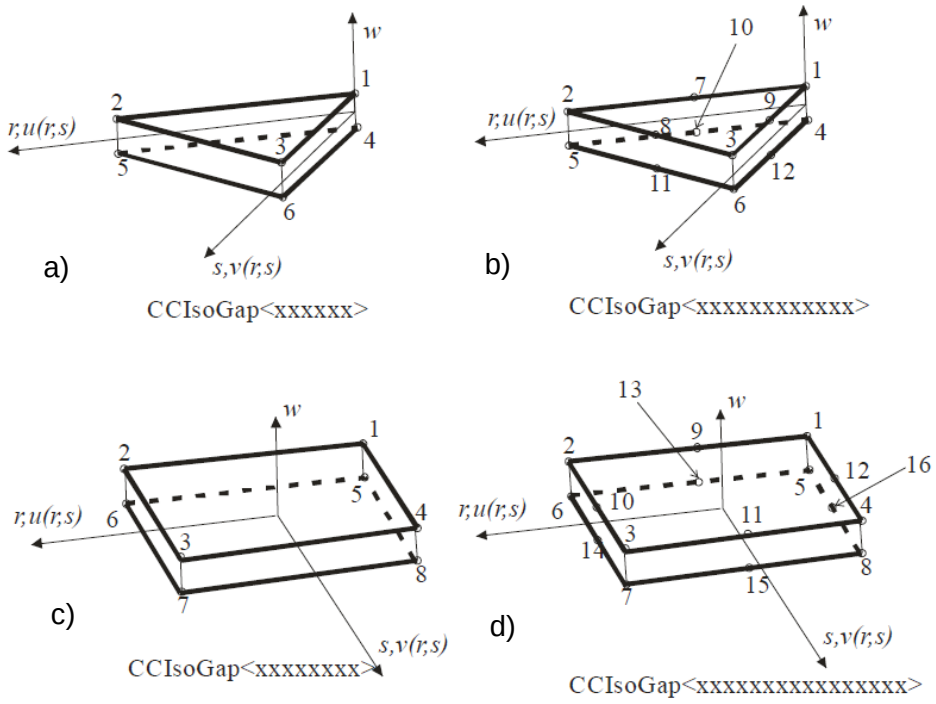

Figure 3-16 Geometry and annotation of the interface elements with a) triangular element w/ linear shape functions, b) triangular element w/ quadratic shape functions, c) quadrilateral element w/ linear shape functions and d) quadrilateral element w/ quadratic shape functions.

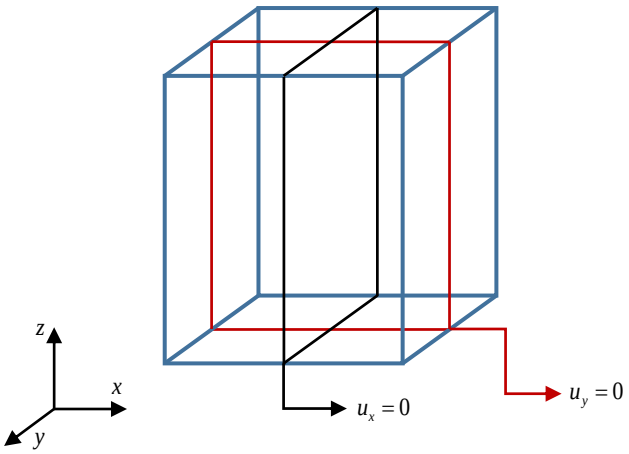

Figure 3-17 Boundary conditions for an axisymmetric rectangular element

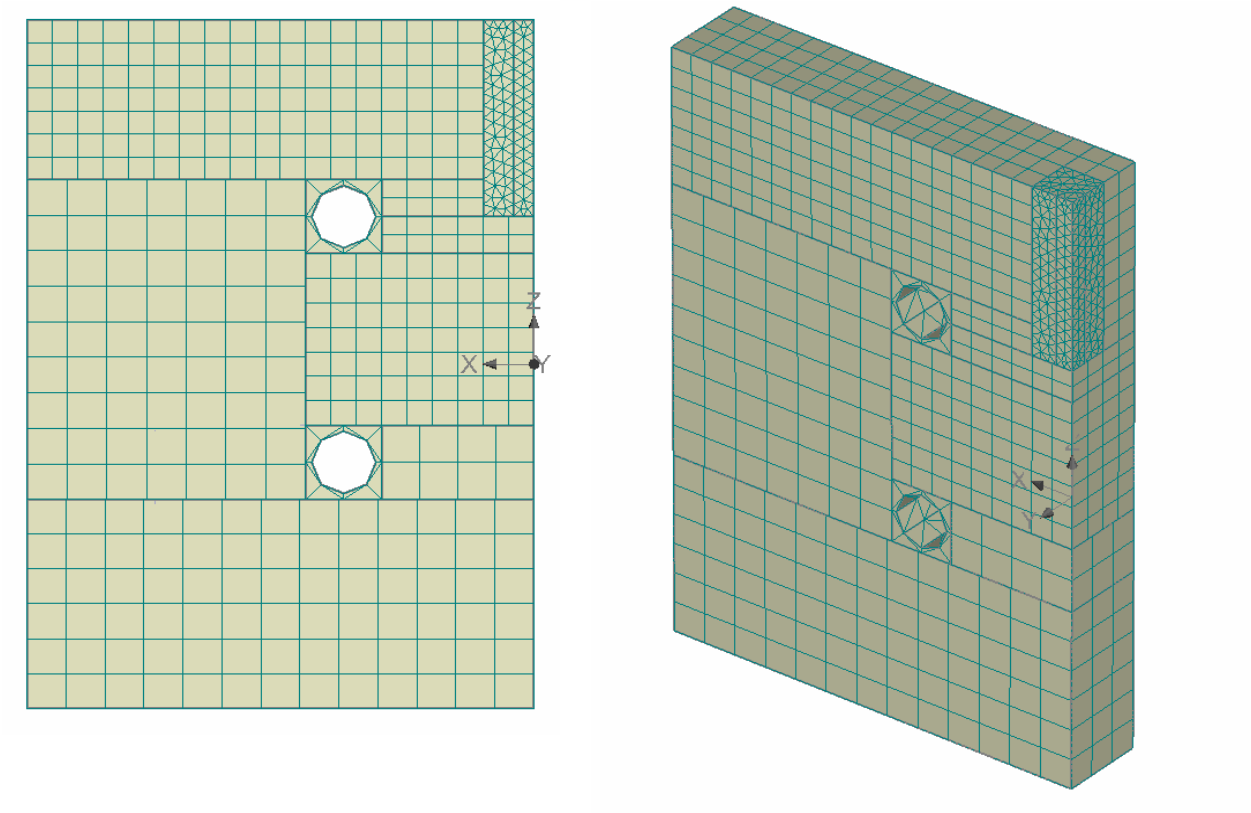

Figure 3-18 Mesh distribution and solid macroelement definition for Model “Interface”: Perspective view (left), Front view (right).

3.3.2.2 Material Constitutive Relationship for the Interface Model

The modelling approach used together with the interface model relies on the same material constitutive relationships for concrete and steel as denoted in Figure 3-8 and Figure 3-15. However, instead of bond links, the interface model is used to represent the interaction along the entire contact surface between bar and concrete (i.e. this is a 3-D surface – taken here as having zero thickness). This material utilizes the Mohr-Coulomb frictional criterion with a tension cut-off (ATENA Program Documentation, Part 1). In Equation (3), the relationship between the tangential stresses, τ_1 and τ_2, and the normal (to the contact surface) stress σ is shown in terms of relative sliding, Δv_1 and Δv_2, and the opening displacements normal to the contact surface, Δu. Terms K_{tt} and K_{nn} denote the tangential and normal stiffnesses, respectively.

$$\begin{Bmatrix} \tau_1 \\ \tau_2 \\ \sigma \end{Bmatrix} = \begin{Bmatrix} K_{tt} & 0 & 0 \\ 0 & K_{tt} & 0 \\ 0 & 0 & K_{nn} \end{Bmatrix} \cdot \begin{Bmatrix} \Delta v_1 \\ \Delta v_2 \\ \Delta u \end{Bmatrix} \quad (3)$$

Stiffness coefficients K_{tt} and K_{nn} are calculated based on the following expression:

$$K_{tt} = \frac{G}{t}, \quad K_{nn} = \frac{E}{t} \quad (4)$$

where G and E are the minimal shear and elastic moduli, per finite element, of the surrounding material, respectively. Term t corresponds to the thickness of the interface zone. In the case of a zero thickness interface zone, the established practice is to increase the shear and elastic moduli by a factor of 10 (ATENA Program Documentation, Part 11).

The corresponding failure surface follows the relationship displayed in Figure 3-19. The surface, initially starting from the normal tensile strength f_t, follows an ellipsoidal pattern until maximum cohesion c is reached. The envelope extends into the regime of compressive normal stresses with a proportional increase of the interface frictional resistance. However, once the Mohr-Coulomb condition is violated, the surface collapses to a residual surface that corresponds to dry friction (ATENA Program Documentation, Part 1). Tangent ϕ denotes the friction coefficient.

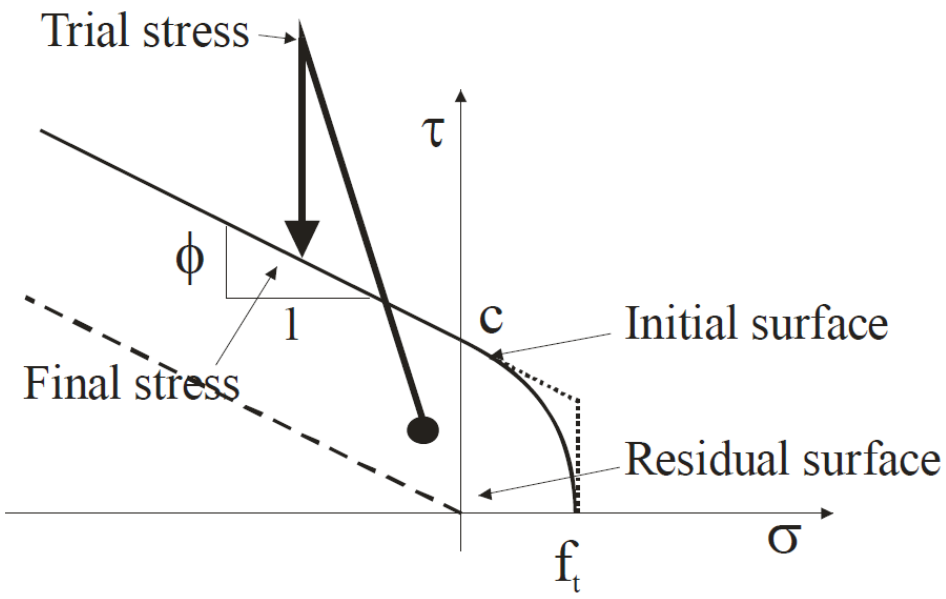

Figure 3-19 Failure surface for interface elements (ATENA Program Documentation, Part 1).

To satisfy the geometry of the assumed failure envelope of the interface model, parameters need to be interdependent as follows:

$$f_t < \frac{c}{\phi}, \quad f_t < c$$
$$c > 0, \quad f_t > 0, \quad \phi > 0 \tag{5}$$

The values used in this study are shown in Figure 3-20.

According to the recommendation found in the ATENA Program Documentation (ATENA Program Documentation, Part 1), $K_{tt}^{\min}$ and $K_{nn}^{\min}$ are taken as 0.001 times the initial stiffnesses since they are only used to enable the iterative calculations without the creation of zero pivots.

The post peak responses of the normal and tangential stresses are shown in Figure 3-21. For the sake of simplicity, custom fracture curves were used as shown in Figure 3-23.

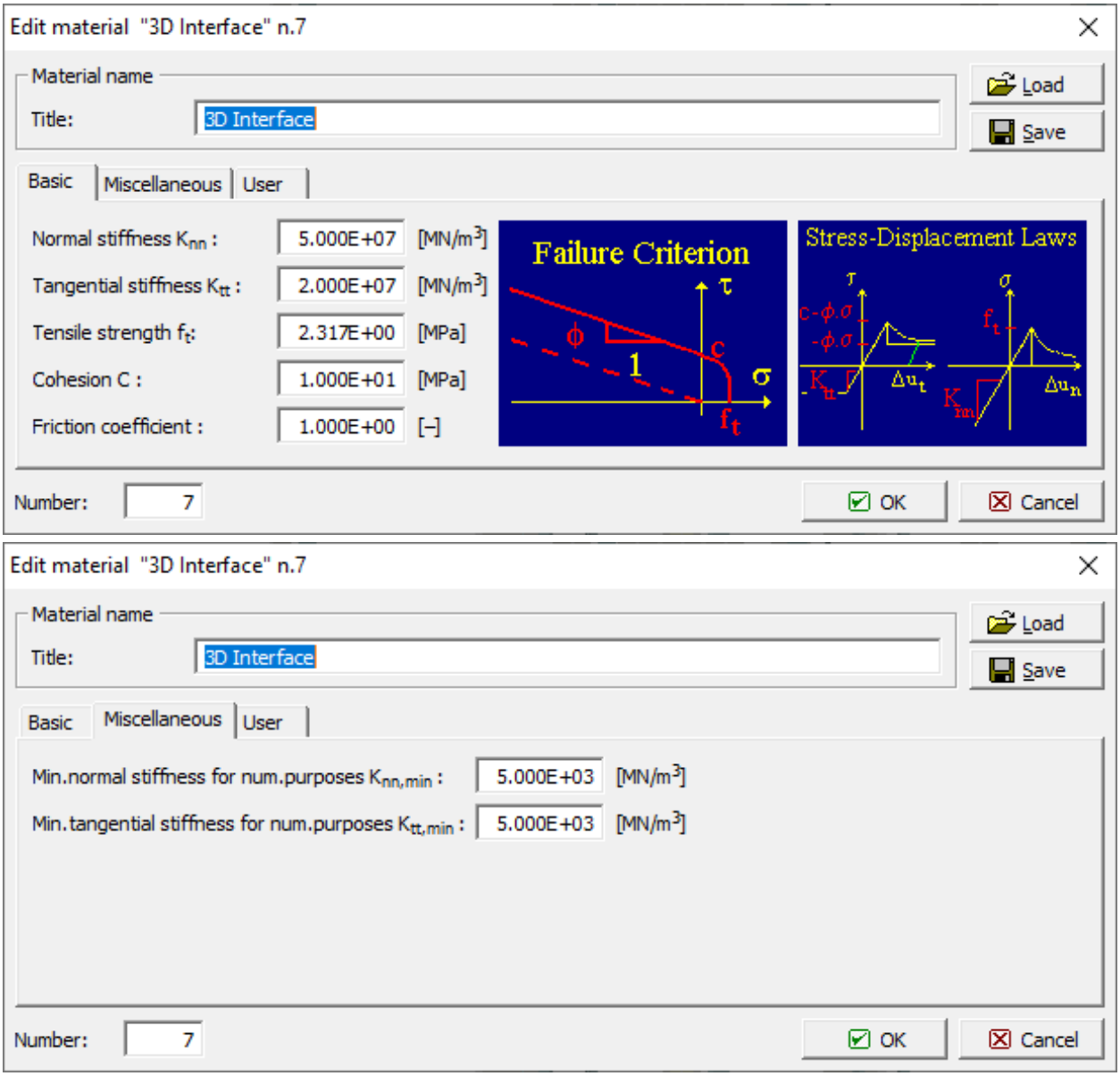

Figure 3-20 Material properties for the three-dimensional interface element.

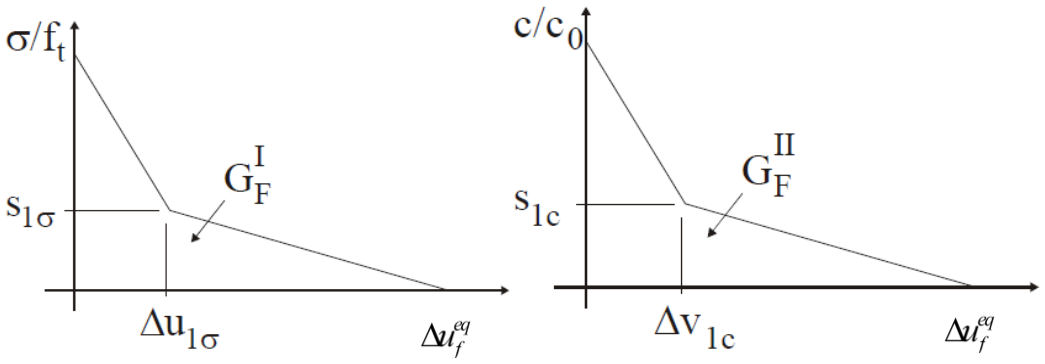

Figure 3-21 Softening law diagrams for tension and cohesion (ATENA Program Documentation, Part 1)

For the solid elements representing the reinforcement, the material model with code CC3DBiLinearSteelVonMises is used, which is based on the Von Mises Plasticity Model as denoted in the ATENA Theory Manual (ATENA Program Documentation, Part 1). The material input for this model is shown in Figure 3-22.

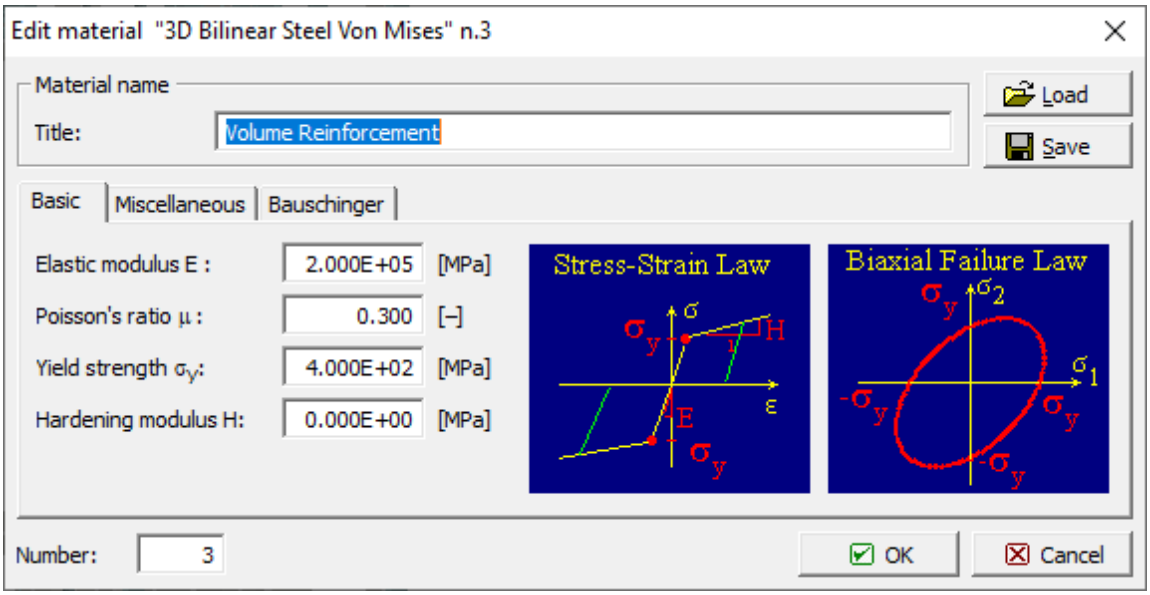

Figure 3-22 Constitutive properties for the 3D Bilinear Steel

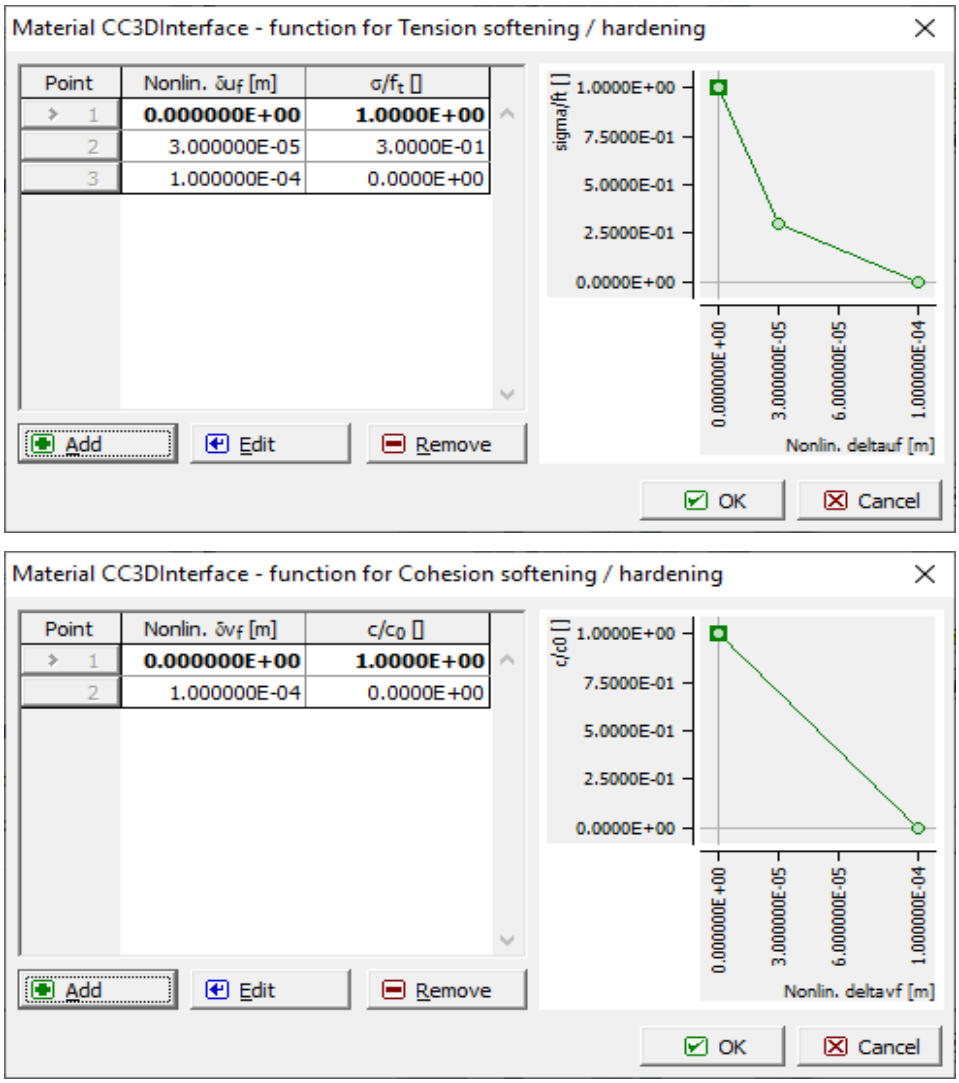

Figure 3-23 Coordinate input for the softening laws for tension and cohesion

3.4 Preliminary analysis (Model “Link”) of the Modified Tension Pullout Specimen

A preliminary analysis of the experimental setup of the DTP specimen is first performed in this section using the formulation of Model “Link”. Two cases are being analyzed with this model: the case with conventional concrete material properties and one case using ultra-high-performance fiber reinforced concrete material properties. The parameters of the material models are as denoted in Section 3.3.1.2.

3.4.1 Conventional Concrete

The model is initially analyzed using conventional concrete material properties and the corresponding bond – slip law properties. Displacement increments are applied on the external "box" surface with increments of 0.01 mm for displacements [0:0.1], and then continuing increments of 0.1 mm up to 3.0mm. Support conditions are applied on the bottom two horizontal cylinders ($u_x=u_y=u_z=0$), on the corresponding surfaces denoting the circular opening. To account for eccentricities later presented (during casting) in the horizontal cylindrical supports during the experimental program of this study, the upper horizontal supports were removed to relieve extra restraints and their resulting stresses in the experimental setup. This specimen is modeled according to the geometry shown in Figure 3-6 using the macroelements of Figure 3-24.

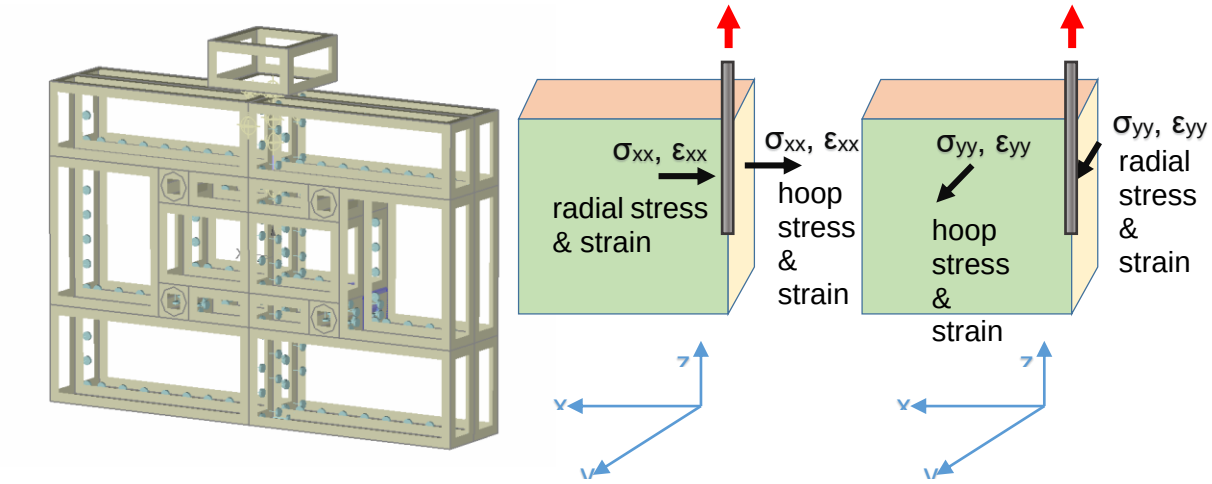

Figure 3-24 (left) Boundary conditions for Model "Link", (center) and (right): Nomenclature.

The analysis reached the total displacement of 3.0mm with a maximum applied load of 16.31kN. After reaching the peak strength, the curve proceeds to a precipitous descending branch immediately and levels out to a "plateau" around a load of 4kN.

Several monitor points have been placed along the bar length to measure the stress and slip levels at different locations of the bar. Three key locations have been monitored and named in reference to distance from the top surface, specifically as Z_1 = -20mm (green), Z_2 = -40mm (blue) and Z_3 = -80mm (red), where Z = 0 at the top surface of the specimen. For each location, the following diagrams have been drawn: the individual bond stress – slip relationship, the bond stresses of all monitors in reference to the total displacement, the transverse stresses σ_{xx} and σ_{yy}

and longitudinal stress σ_{zz} in reference to the total displacement. Distributions of stress fields are shown via screenshots obtained from the ATENA Studio graphical interface.

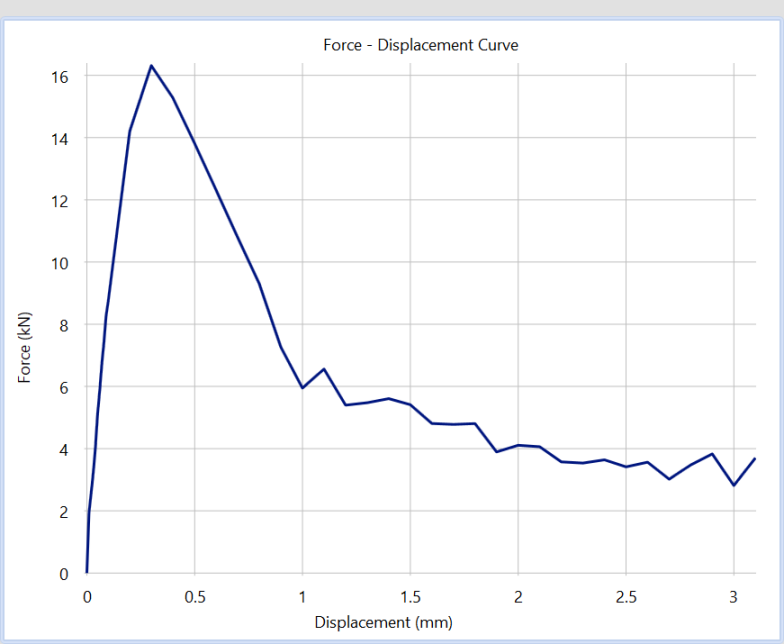

Figure 3-25 Force – Displacement curve for Model “Link” with Conventional Concrete.

3.4.1.1 Bond stress and slip distributions along embedded bar

Figures Figure 3-26, Figure 3-27 and Figure 3-28 depict the bond stress – slip relationships for monitor locations Z_1 = -20mm, Z_2 = -40mm and Z_3 = -80mm, respectively, and Figure 3-29 shows the comparison of the three monitors in reference to the total displacement of the test bar. The maximum bond strength, approximately 4.2MPa, was attained at the same analysis step, at a displacement of 0.3mm, for all bar locations (the same displacement at which the peak strength of the specimen was obtained). While all three bar locations fail practically simultaneously, there are minor differences in their constitutive bond – slip relationships. After reaching the peak bond strength, location Z_1 maintains a relatively small plateau before proceeding to the descending branch of the curve. Locations Z_2 and Z_3 decline immediately after reaching the peak bond strength. Incidentally, location Z_2 shows a change in local interface stiffness, in which the curve “breaks” to a smaller angle before reaching the peak bond value. Location Z_3 displays inconsistencies in the initial segment of the bond – slip curve, which can be presumably attributed to the appearance of cracking close to the free end of the bar because of the intense tensile stress levels that are generated in the cover at that location. All monitors exhibit essentially identical

descending branches, with the lower locations reaching lower bond stress measurements. Upon reaching the residual strength branch, the analysis displays variations in the bond – slip measurements, potentially owing to crack patterns appearing close to the monitored locations.

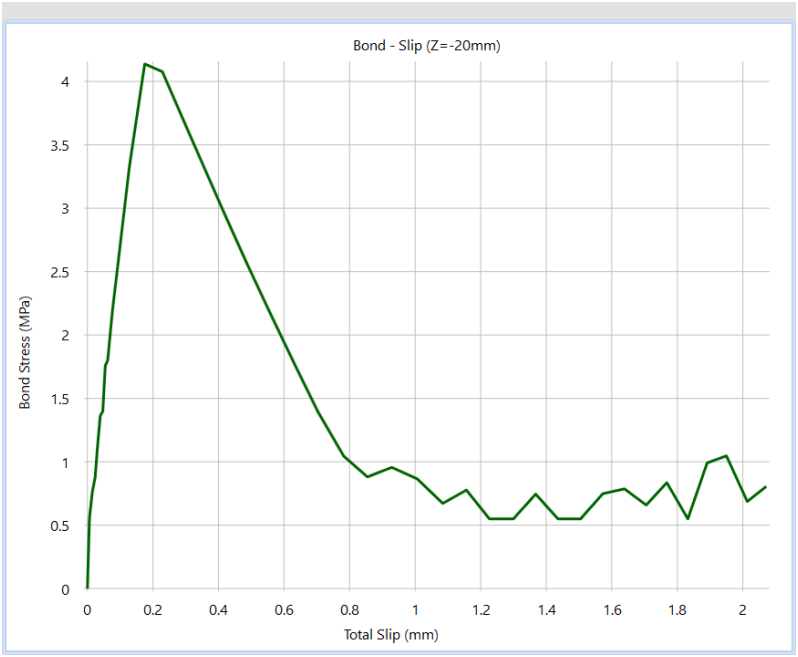

Figure 3-26 Bond stress – slip curve for location Z_1 = -20mm (Conventional Concrete).

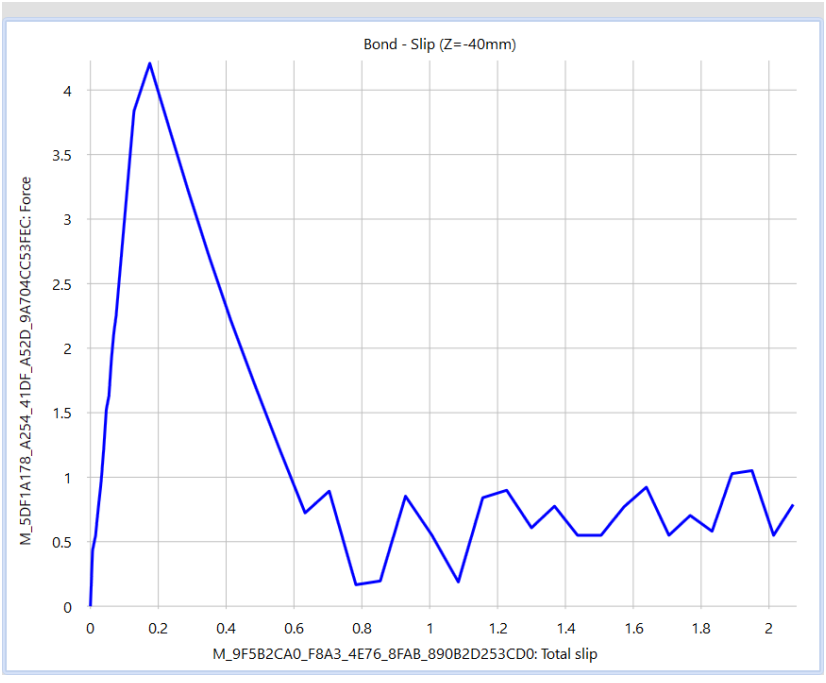

Figure 3-27 Bond stress – slip curve for location Z_2 = -40mm (Conventional Concrete).

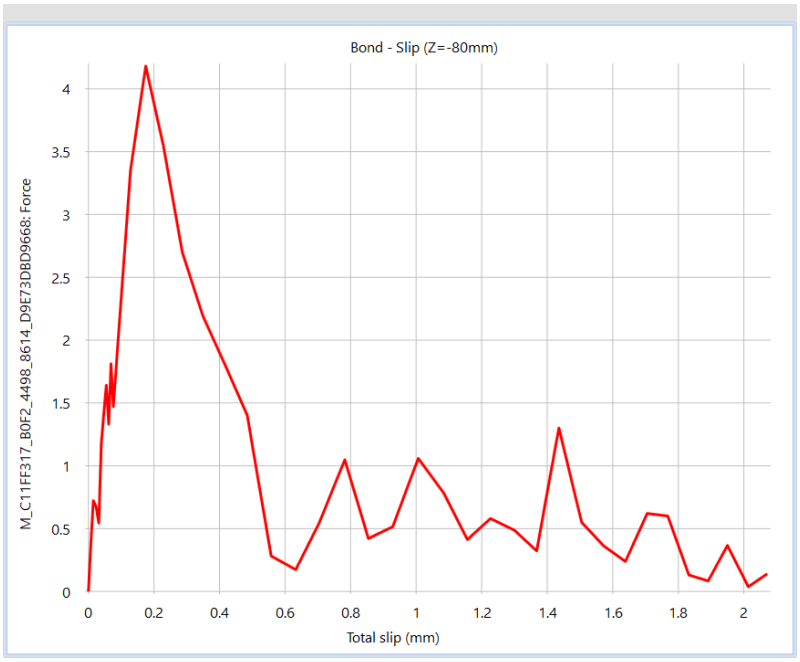

Figure 3-28 Bond stress – slip curve for location Z_3 = -80mm (Conventional Concrete).

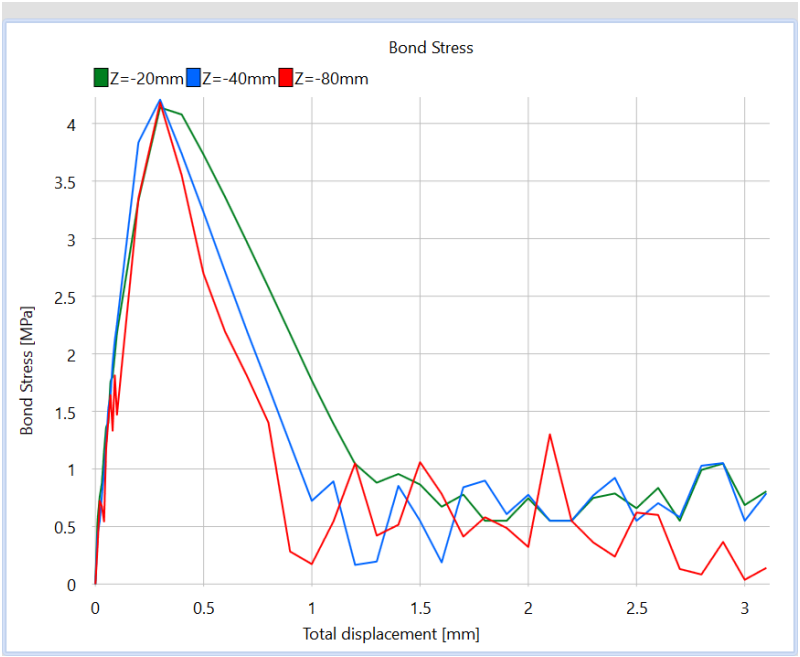

Figure 3-29 Bond stress of all monitors in reference to total displacement (Conventional Concrete).

Figure 3-30 shows the distribution of the Total Bond Slip along the anchorage at peak strength and at the end of the analysis. At peak strength the whole extent of the anchorage undergoes approximately equivalent dislocation from the concrete, at a value of 0.2mm. At the ultimate state, the maximum bond slip is accumulated on the bottom segment of the bar with the upper segment of the anchorage demonstrating lower values of slip. The lower values can be attributed to the loss of connection between the bar and the concrete, in which case the relative movement is effectively diminished as the anchorage displaces independently.

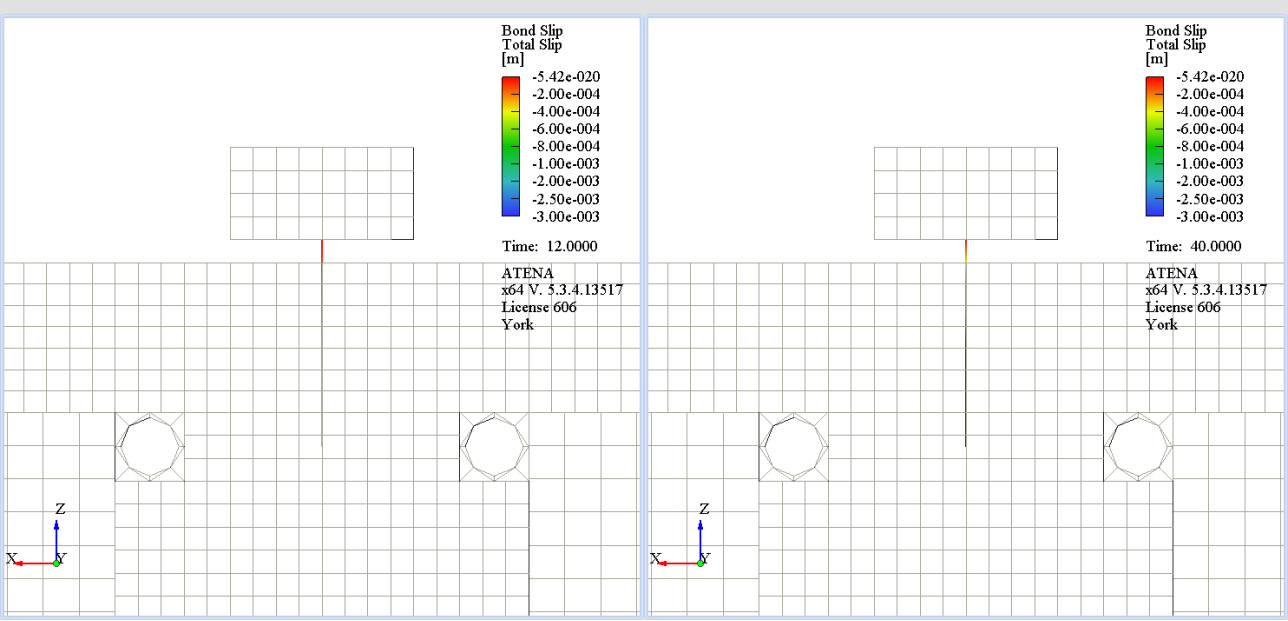

Figure 3-30 Bond Slip distribution along bar length at peak strength (left) and end of analysis (right) (Conventional Concrete).

3.4.1.2 Demonstration of transverse stresses σ_{xx} and σ_{yy}

Transverse stresses along the *x*-axis and *y*-axis are measured via the aforementioned monitor points in locations Z_1, Z_2 and Z_3. Figures Figure 3-31 and Figure 3-32 show the transverse stress to total displacement diagrams for σ_{xx} and σ_{yy}, respectively, along with the internal distribution of the transverse stresses at the peak strength of the specimen. Positive (tensile) stresses act in the hoop direction, normal to the cross section of the specimen that is parallel to the thickness. On the contrary, compressive stresses are exerted on the bar lateral surface in the x-direction (oriented in the radial direction in the thick ring analogy). The compressive stresses on the surface above the circular openings can be explained by the deformation of the anchorage due to the

Poisson's effect caused by the longitudinal tensile stresses. In the orthogonal plane, parallel to the width of the specimen, hoop stresses (σy) develop (see green zone) adjacent to the bar, as well as radial (in blue in the front and back of the bar) which correspond to the radial direction of the thick ring analogy. The surfaces of the anchorage facing the controlling cover of the section (in the *y*-axis), having been disconnected from the concrete due to the propagation of the inclined cracks, begin to translate internally, leading the surfaces in the perpendicular direction (*x*-axis) to expand outwards. The resulting deformed section imposes compressive stresses in the *x*-axis direction, thus generating the compressive stresses on the top surface of the concrete specimen.

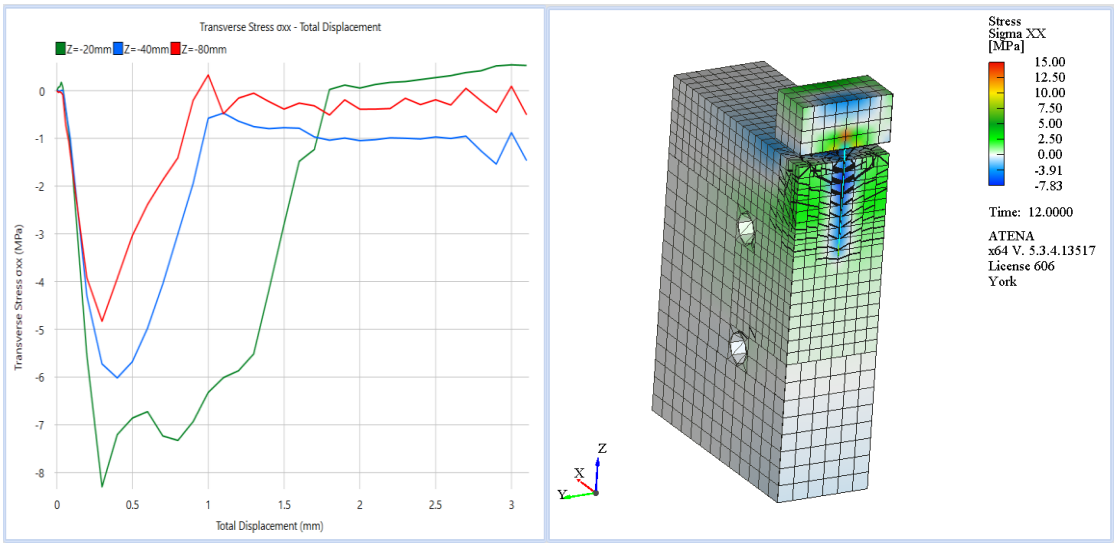

Figure 3-31 Transverse stresses σ_{xx} – Total Displacement curves (left) and distribution of σ_{xx} at peak strength (right) (Conventional Concrete).

3.4.1.3 Demonstration of σ_{zz} along the embedded bar

Figure 3-33 shows the longitudinal stress to total displacement diagrams for the control monitors and the distribution of stresses σ_{zz} along the specimen interior at peak strength. Tensile stress fields can be observed in the area denoted by the circular openings, with the orientation of the stress vectors towards the lower cylindrical supports. Minor compressive stresses congregate under the two supporting cylinders as a result of the resistance against the movement of the pulled bar. In Figure 3-34 the distribution of the longitudinal stresses at peak strength are displayed along the specimen height at locations extending 10mm, 20mm, 40mm and 80mm from the top surface of the specimen. An elliptical tensile stress zone is observed to originate from the

bar axis, extending up to the control cover surface and delineating the engaged concrete hoop where internal stresses are resolved. The hoop approaches the bar periphery as the section reaches the free end of the bar, where the tensile stresses have not yet exceeded the capacity of the inner radius of the hoop. At the free end of the bar, longitudinal tensile stresses can be observed extending between the circular openings.

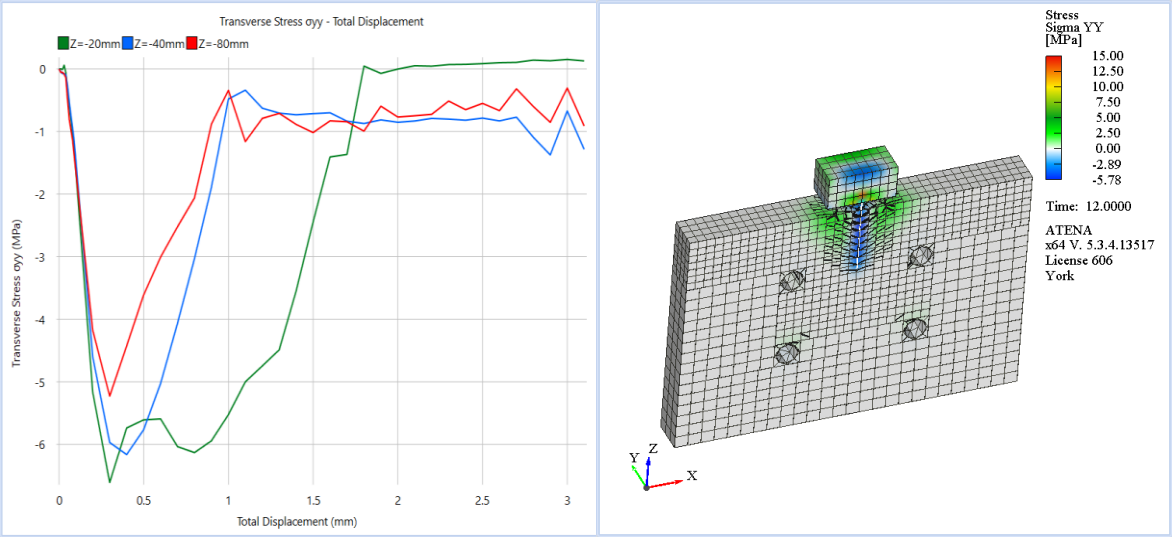

Figure 3-32 Transverse stresses σ_{yy} – Total Displacement curves (left) and distribution of σ_{yy} at peak strength (right) (Conventional Concrete).

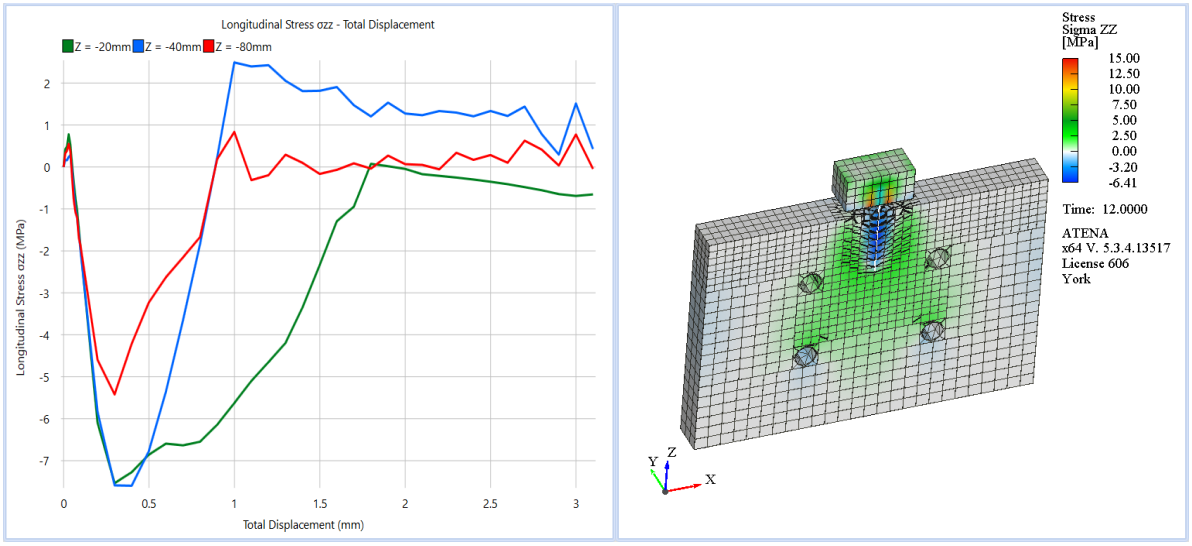

Figure 3-33 Longitudinal stresses σ_{zz} – Total Displacement curves (left) and distribution of σ_{zz} at peak strength (right) (Conventional Concrete).

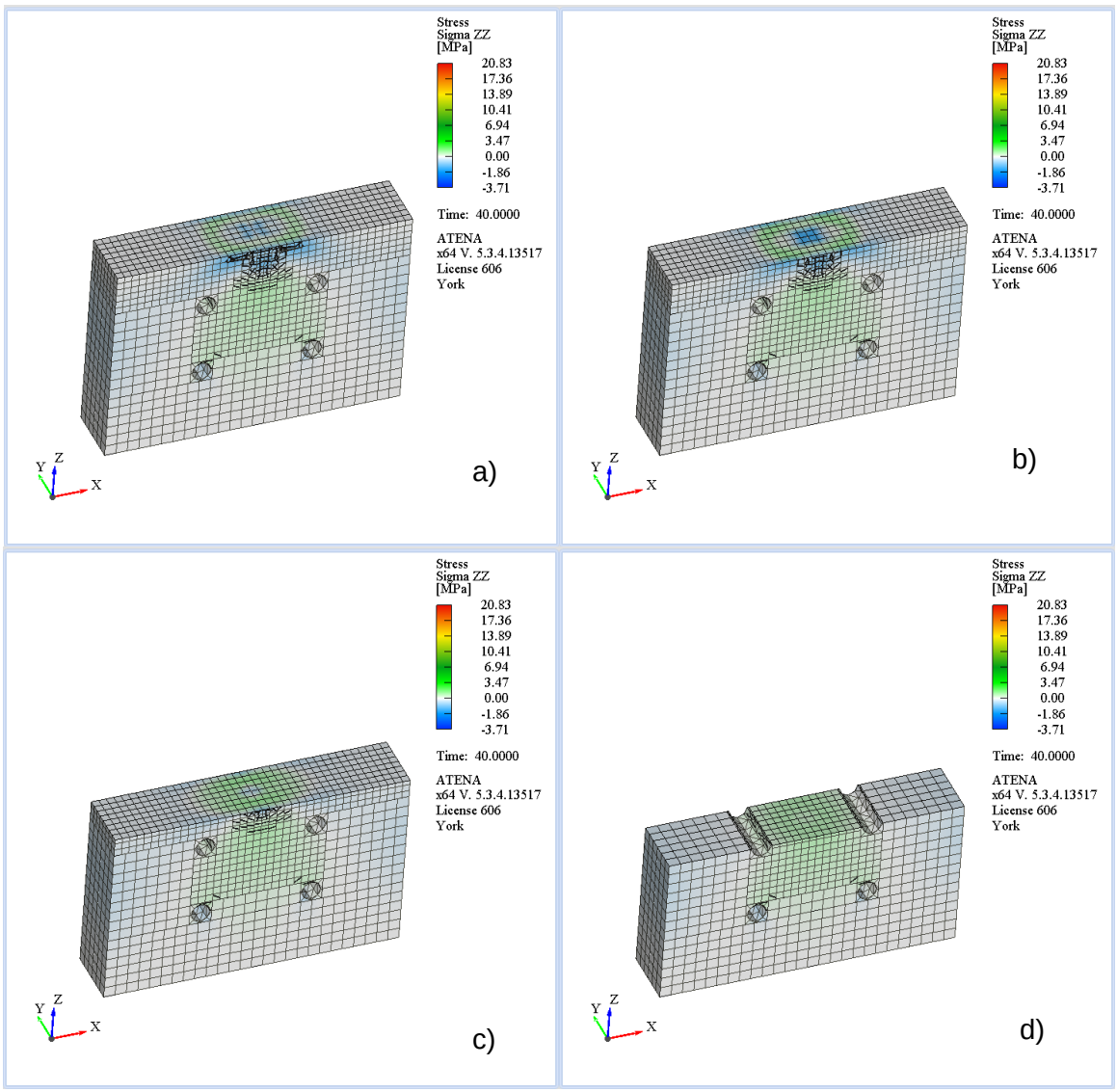

Figure 3-34 Distribution of transverse stresses σ_{zz} along specimen height at a) Z = -10mm, b) Z = -20mm, c) Z = -40mm and d) Z = -80mm (Conventional Concrete).

3.4.2 Predicted behavior when using UHPC Material

In this section, the same model is analyzed using the UHPC material properties and the corresponding bond – slip law properties, as denoted in Section 3.3.1.2. The following sections present the respective diagrams as in the case of the conventional concrete material. Displacement increments are applied on the external “box” surface with increments of 0.01 mm for displacements [0:0.1], and then continuing increments of 0.1 mm up to 6.0mm.

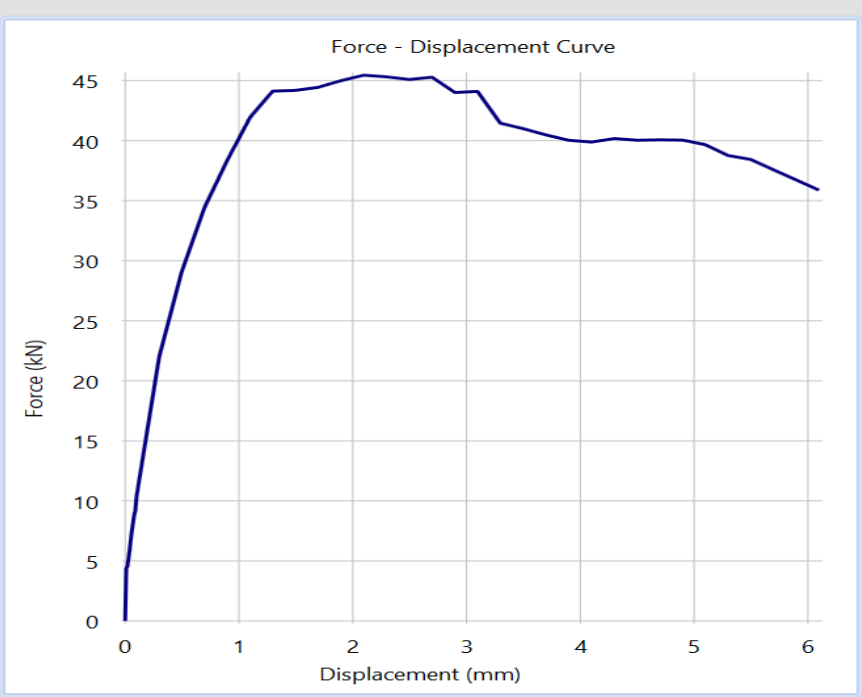

Figure 3-35 Force – Displacement curve for Model “Link” with UHPC.

The analysis reached the total displacement of 6.0mm with a maximum applied load of 45.5kN. After reaching the peak strength, the curve begins to degrade slowly, reaching 36kN before the analysis is terminated. An increase of 279% is observed in the case of the UHPC material, along with noticeable development of the absorbed fracture energy of the specimen response. While in the case of conventional concrete, peak strength is followed by an abrupt reduction of the total specimen strength, in the case of UHPC, softening occurs gradually with higher levels of ductility being achieved as loading increases.

Bond stress – slip is measured through monitors Z_1, Z_2 and Z_3 (Figs. Figure 3-36 – Figure 3-38) whereas the comparison between the bond stress responses is shown in Figure 3-39. The maximum bond stress is achieved at approximately 11MPa with a corresponding slip of 1mm. While monitors Z1 and Z2 demonstrate comparable responses, monitor Z3 shows reduced peak bond stress along with abrupt discontinuities in the ascending and descending branches of the bond stress – slip response. This can be attributed to the proliferation of cracking patterns around the free end of anchorage. Upon reaching the maximum attainable bond stress, all branches proceed to diminish gradually with the monitors located closer to the free end of the bar to be progressively reduced to lower stresses towards the end of the analysis.

3.4.2.1 Bond stress and slip distributions along embedded bar

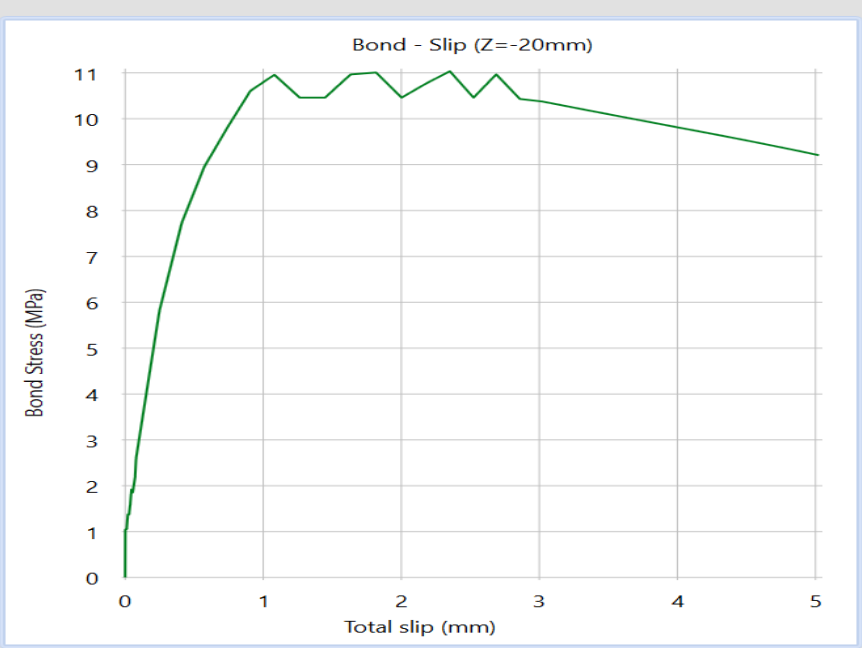

Figure 3-36 Bond stress – slip curve for location Z = -20mm (UHPC).

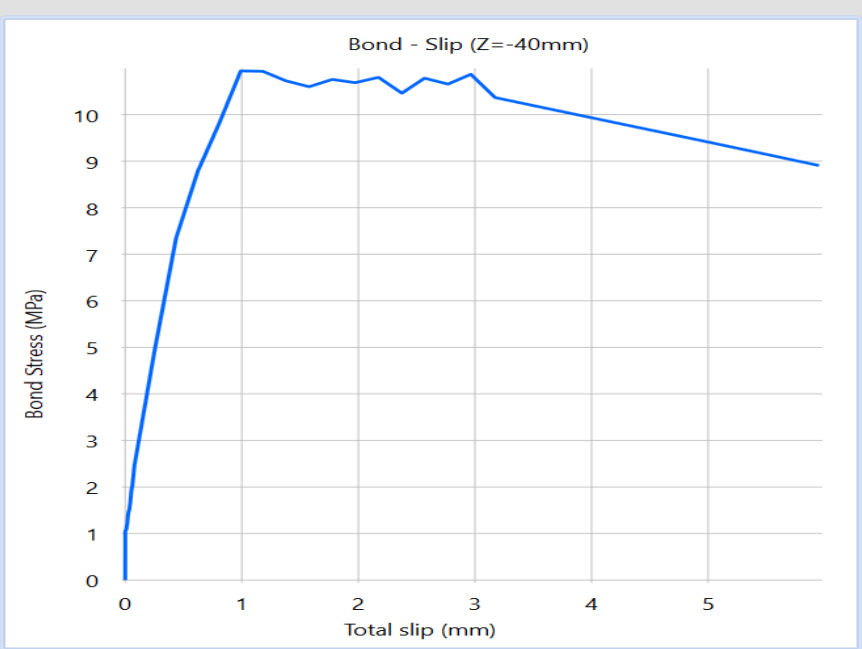

Figure 3-37 Bond stress – slip curve for location Z = -40mm (UHPC).

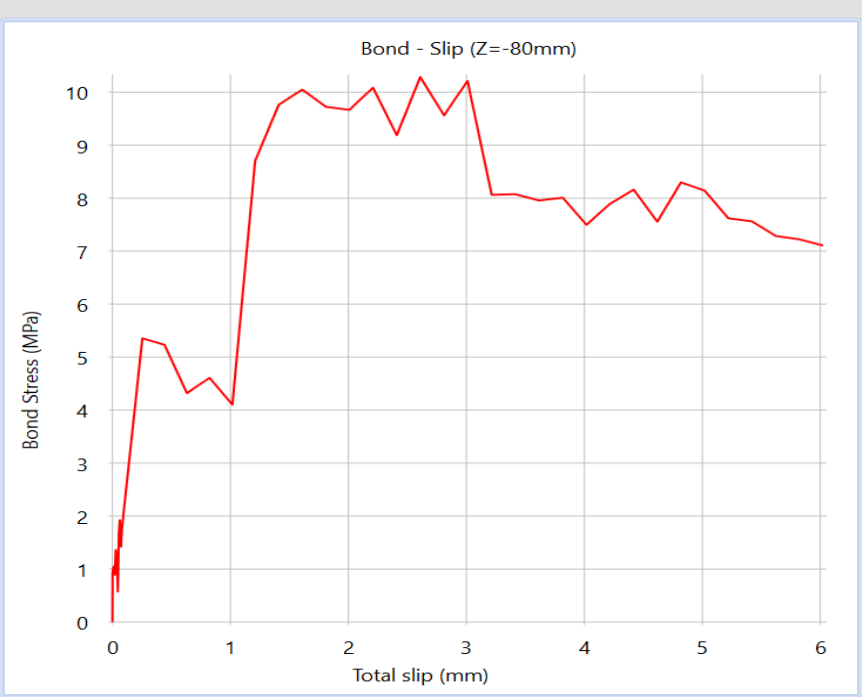

Figure 3-38 Bond stress – slip curve for location Z = -80mm (UHPC).

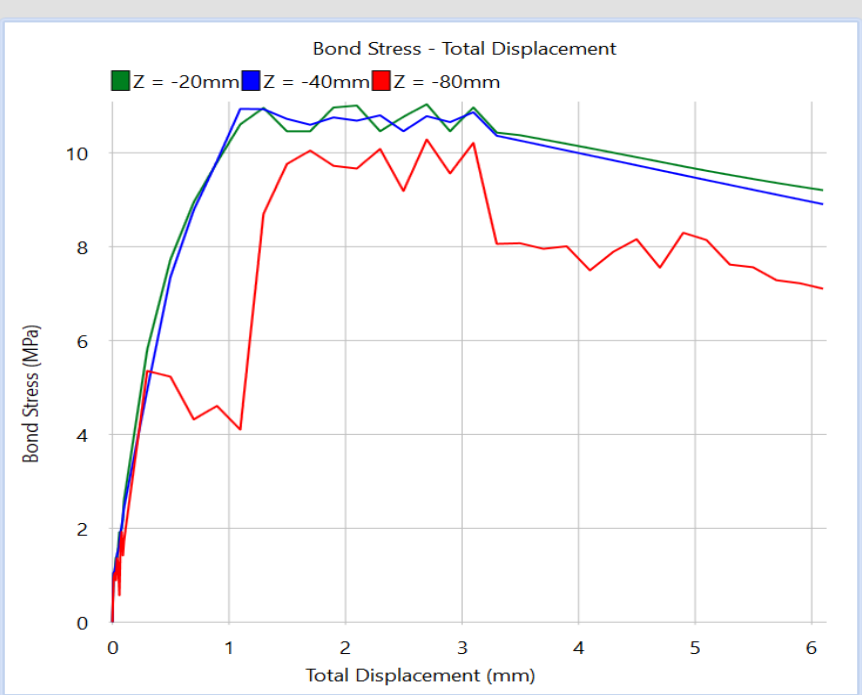

Figure 3-39 Bond stress of all monitors in reference to total displacement (UHPC).

In Figure 3-40, the bond slip distribution can be observed along the anchorage length at peak bond stress and at the termination of the analysis. In both cases, a seemingly unaltered green zone is denoted on the upper segment of the bar, starting from the top surface of the specimen, caused by the locally cracked concrete cover, leading to reduced relative slip measurements since the contact between the anchorage and the concrete has been severed. Incidentally, the relative movement measurements (slip) are progressively increased towards the free end of the bar. This can be explained by the dislocation of the upper segment of the bar from the concrete whereas the lower segment remains confined by the concrete surface, in which the relative movement can be measured over the whole extent of the bar.

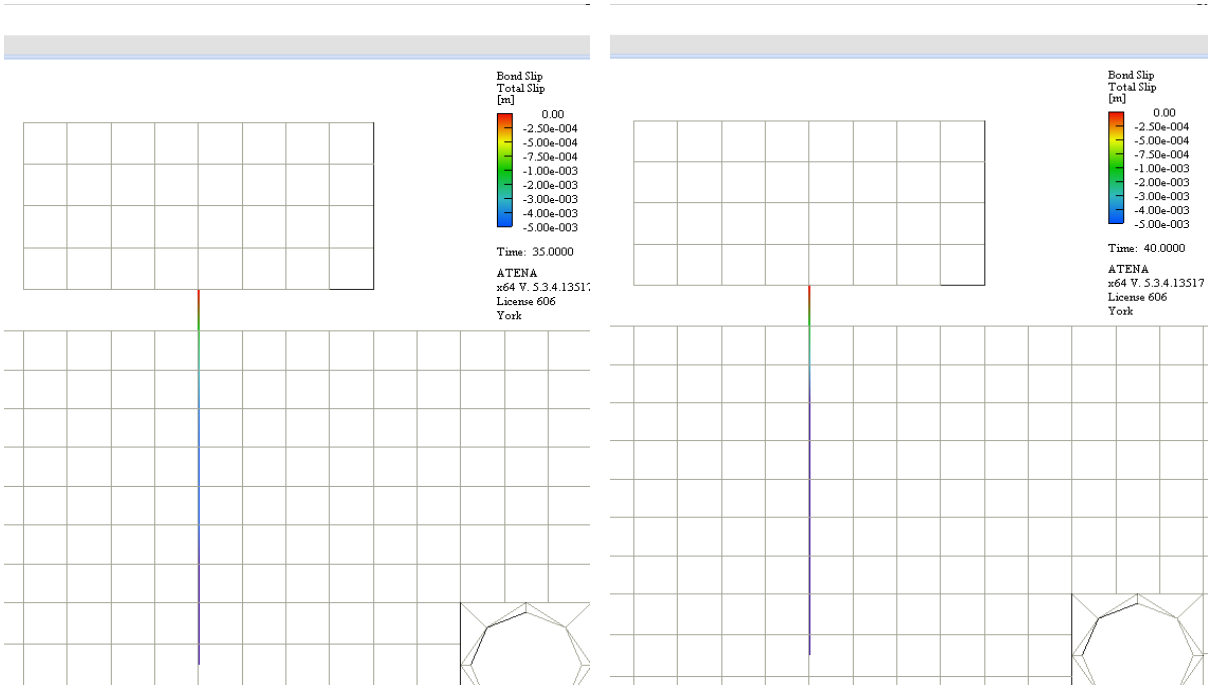

Figure 3-40 Bond Slip distribution along bar length at peak strength (left) and end of analysis (right) (UHPC).

3.4.2.2 Demonstration of σ_{xx} and σ_{yy} along the embedded bar

In Figures Figure 3-41 and Figure 3-42, the transverse stresses along the *x*-axis and the *y*-axis can be observed. As it was recognized in the case of conventional concrete, tensile stress fields accumulate on the concrete in the hoop direction around the bar whereas compressive stress fields develop on the location of the bar axis in the radial direction of the cover. Minor compressive stresses appear on the top surface of the specimen located above the circular openings as a result of the bar deformation. Contrary to conventional concrete, the engaged transverse concrete

zone over which development occurs, is limited to the upper segment of the bar where a conical crack surface plane is developed. The segment of the anchorage in the proximity of the free bottom end undergoes mild radial compressive stresses but hoop tension is negligible.

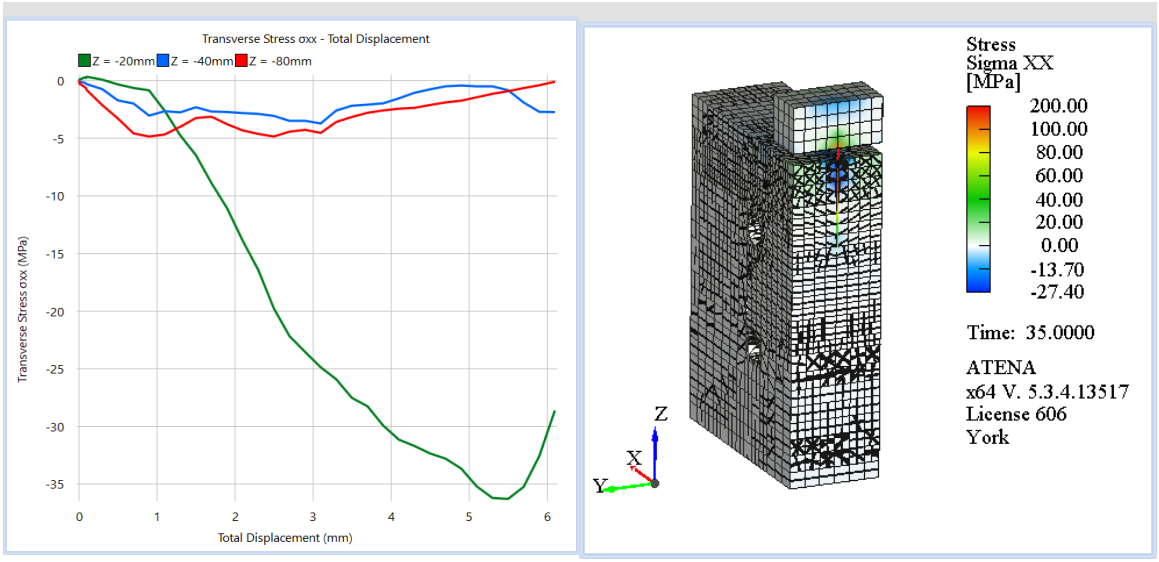

Figure 3-41 Transverse stresses σ_{xx} – Total Displacement curves (left) and distribution of σ_{xx} at peak strength (right) (UHPC).

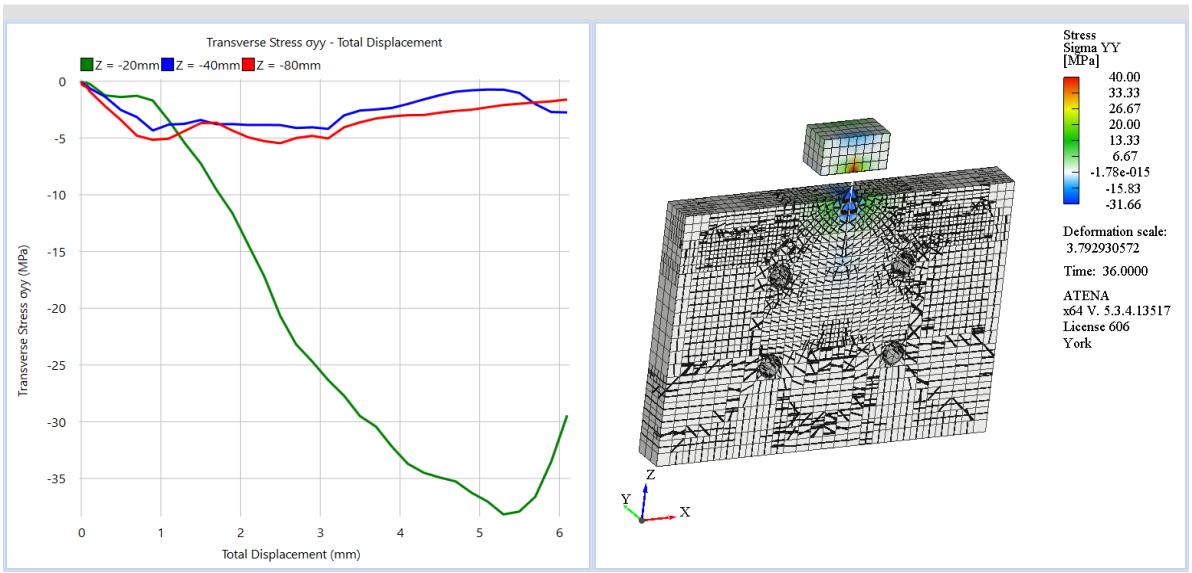

Figure 3-42 Transverse stresses σ_{yy} – Total Displacement curves (left) and distribution of σ_{yy} at peak strength (right) (UHPC).

3.4.2.3 Demonstration of σ_{zz} along the embedded bar

Longitudinal stresses in the UHPC model are distributed in a similar manner to the conventional concrete material modeling. The concrete enveloping the anchorage develops longitudinal tensile stresses reaching up to 35MPa, with the higher concentration of stresses located at the upper segment of the bar, in the proximity of the top surface of the specimen.

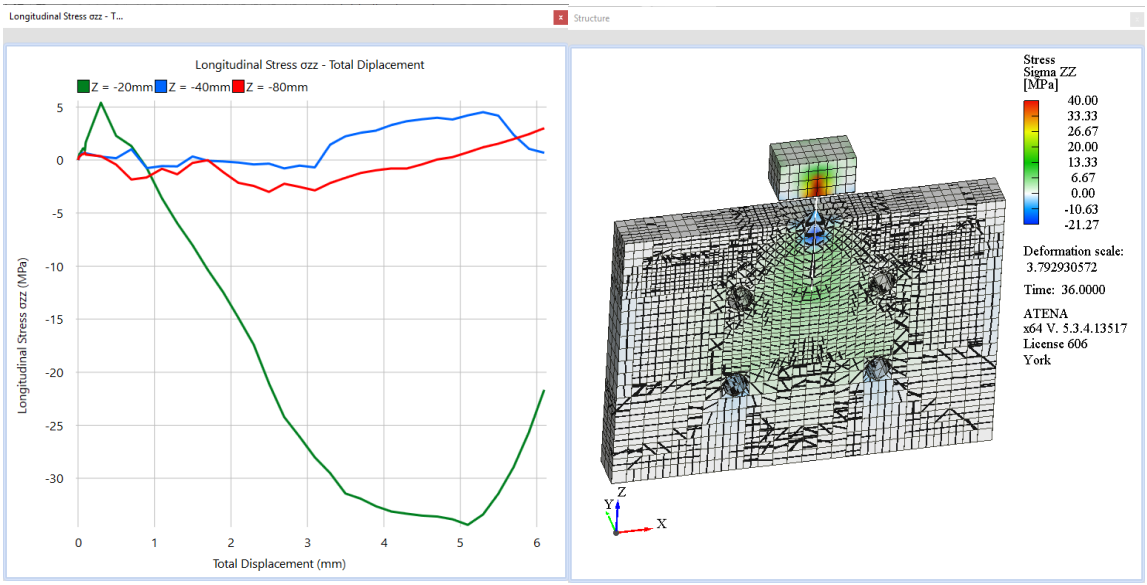

Figure 3-43 Longitudinal stresses σ_{zz} – Total Displacement curves (left) and distribution of σ_{zz} at peak strength (right) (UHPC).

The overall response of the UHPC model resembles that of conventional concrete regarding the distribution of the transverse and longitudinal stresses across the specimen volume. However, significant differences in magnitude can be observed in the case of the UHPC material properties leading to stresses in both directions to be greater by a factor of 4.5. The engaged concrete zone for the UHPC material is reduced to the upper segment of the bar where the conical crack remains prevalent, whereas in the conventional concrete model a major splitting crack propagates along the bar length. Several minor cracking patterns can be observed in the case of UHPC, which are dispersed in the whole extent of the concrete block. The extensive dispersion of the cracking patters across the specimen volume can be attributed to the higher levels of intrinsic confinement imposed by the included fiber reinforcement, which considerably increase the absorbed fracture energy of the concrete. In the case of conventional concrete, however, cracking is accumulated in the tensile zone surrounding the bar, where the major splitting crack remains prevalent (Figures Figure 3-31 and Figure 3-32). The bond – slip response of the UHPC is in accordance with the

greater incorporated fracture energy of the specimen, exhibiting a gradual decrease of bond strength after the peak stress has been attained. Even in the presence of cracking around the bar cover, the concrete-to-steel interface remains intact as a result of the confining forces acted on by the fibers, a response that is absent in the case of conventional concrete in which the bond interface is compromised after the appearance of the longitudinal (splitting) crack.

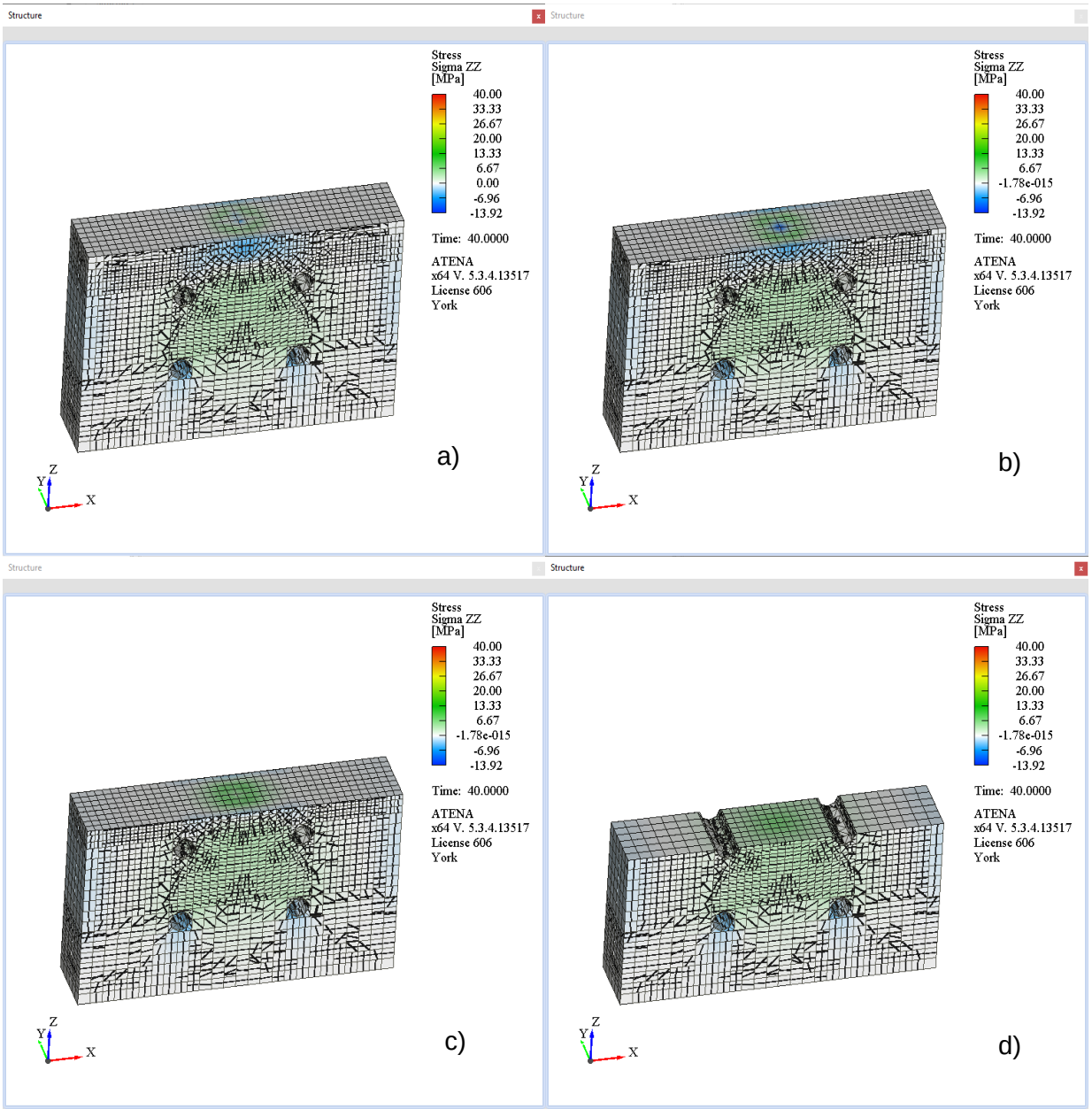

Figure 3-44 Distribution of transverse stresses σ_{zz} along specimen height at a) Z = -10mm, b) Z = -20mm, c) Z = -40mm and d) Z = -80mm (UHPC).

3.5 A study of the effect of the test setup on the apparent development capacity

The effect of experimental setup on bond behavior has been one of the most critical factors regarding the study of bond, being responsible for a great degree of discord and confusion in the bond community [Plizzari and Cairns (2003), Tastani and Pantazopoulou (2010), FIB Model Code (2010)]. Among the first tests conducted to study bond were the so-called standard pullout (RILEM 1978) on account of its simplicity of execution, which made it easy to use by steel manufacturers who wanted to assess quickly the improvements of a rib pattern design on bond. However, it was quickly recognized that the values for bond strength obtained from this type of test were excessive as compared to other setups. After several attempts to reconcile the differences, the ACI Committee 408 in collaboration with the Task Group 4.2 of CEB (now 2.5 in *fib*) created a database of bond anchorage tests to be used in the future for calibration of the various design proposals and specifications regarding bond and development capacity. The database only contained beam splice tests, i.e. beam specimens tested under four-point loading, where a splice would occur in the constant moment region. Splice tests generally yield much lower bond strength estimates as compared to the standard pullout test (about 40% of the value) and were therefore deemed more conservative for calibration of design expressions. However, there have been several reservations expressed regarding the relevance of a lap splice with the circumstances of an anchorage. Tastani et al. (2010) illustrated that a lap splice behaves identically to an anchorage, however this was a theoretical finding based on the mathematics of the solution of the differential equation of bond.

On the experimental front several attempts have been made to produce test results that are closer to reality without completely doing away with the simplicity of the standard pullout test. In this regard, several attempts at interpretation of the root of the increased bond strength provided by some test setups have been advanced (Tepfers 1979, Tastani and Pantazopoulou 2003). It was concluded that two fundamental differences occur between the standard pullout test and the lap-splice test: (a) The plate on which the concrete cube is bearing as the bar is being pulled out exerts friction on concrete resisting its attempt to expand laterally as the bar pulls out. (b) The plate exerts uniform compression on the concrete block surrounding the bar which generates confinement on the bar's lateral surface, leading to increased interfacial resistance, whereas unrealistically large concrete covers confine the bar in this occasion. The first problem has been addressed in practice and in the test standards by a request that a Teflon sheet or other lubricating

agent is placed between the concrete block and the steel plate to eliminate friction. To address (b), two alternatives have been suggested: (b.1.) to place the bar eccentrically with respect to the concrete block's centroid so that a realistic cover is possible, a test known as eccentric pullout, and (b.2.) pertinent support conditions are applied on the block so that it undergoes flexural moment as would occur on a bar anchorage near the support of a beam – known as "beam-end specimen" form.

This heuristic interpretation of the state of stress in any of the above test setups, advanced in order to explain the observed discord between otherwise identical bar anchorages, is tested in the present section through finite element analysis. To this end, several experimental setups are simulated, as follows: the concentric (Rilem standard) pullout test, the concentric specimen with a small cover, the eccentric pullout test, and the direct tension pullout test. For the latter case, the specimen is modeled according to the modified setup developed in this study. To account for the effects of normal pressures possibly effected due to the setup and creating spurious confinement effects over the anchorage, the Model "Interface" option is used in this part of the study, since the strength in this constitutive model is pressure sensitive, in order to enable the comparisons between the individual setups. Conventional concrete material properties are assumed for all models whereas the interface properties are displayed on Figures Figure 3-20 and Figure 3-23.

3.5.1 Concentric pullout test

The concentric pullout test is the conventional arrangement for the experimental investigation of bond specified by RILEM (1978) and ASTM 944-99 (1999). The test comprises cube specimens with an embedded test bar concentrically placed and extruding from the top surface. During the test, the specimens are pulled from the extending bar while the corresponding surface is pressed against an immovable plate. Depending on the surface roughness of the concrete cube and friction coefficient of the supporting plate against which the concrete is bearing, the concrete can either be assumed to expand freely in the lateral direction or that expansion is restricted due to the frictional resistance of the contact surface. Both conditions are considered as opposite extremes in the present study as separate models.

In total, four distinct variations of this test are simulated on ATENA 3D and ATENA Studio, namely the Standard 150x150 specimen with friction, the Standard 150x150 specimen with no friction (RILEM test), a modified 80x80 specimen with friction and a modified 80x80 specimen with no friction. For each case, the force-displacement curves are extracted and the stress, strain and bond – slip conditions are shown in key locations along the strength curve. Four milestone points

are selected in each the response curve to examine in greater detail the state of stress in both materials; these are denoted as Milestone Points A, B, C and D. All indicators of the state of stress are plotted for the milestone points in order to facilitate better understanding of how the confining effect interacts with bond: stresses σ_{zz} and σ_{xx}, strains ε_{zz} and ε_{xx}, shear stress τ_{xz} and vertical translation of the engaged bodies, Δ_z are shown (on account of axisymmetry, where it exists, the distributions of σ_{yy} and σ_{xx} are identical, and so σ_{yy} and ε_{yy} are not shown for brevity). For the sake of simplicity, the values $\sigma_{zz}/\varepsilon_{zz}$ will be referred to as "longitudinal stress/strain" whereas values $\sigma_{xx}/\varepsilon_{xx}$, will be referred to as "transverse stress/strain". Each of the aforementioned values will receive the annotation "positive" or "negative" which correspond to tensile and compressive properties, respectively.

All specimens are modeled considering identical anchorage lengths for 15M bars with 400 MPa yield strength. Two values for the clear cover thickness are considered, one to construct the section dimensions for the Standard 150x150mm pullout test and one according to the specimen dimensions used for this study. Respectively, the cover distances are $c_1 = 4.25 \cdot D_b = 67$mm and $c_2 = 2 \cdot D_b = 32$mm. The embedment length is chosen to be $5 \cdot D_b = 80$mm for all specimens and the material properties involve only those of conventional concrete. The analysis uses the *Standard Newton-Raphson* iteration method with displacement control, with an increment of 0.01 mm for displacements [0:0.1 mm] and then continuing with increments of 0.1 mm until failure of the specimen.

3.5.1.1 Standard 150x150 specimens with friction

This specimen is modeled with a rectangular 150x150mm section with the test bar placed in the center of the section. The modeling procedure follows the guidelines provided in Section 3.2.2. Due to symmetry, only a 1/4 of the specimen section is considered and boundary lateral restraints are enforced on the planes of symmetry, as shown in Figure 3-17. The top surface of the specimen is restricted in all directions, namely u_x, u_y and u_z. to account for the resistance imposed by friction against the surface of the opposing plate. The model is discretized in rectangular macroelements to maximize the distribution of brick finite elements, whereas the bar and the concrete macroelements immediately adjacent to it are modeled with tetrahedral finite elements to improve convergence on account of the steep gradients of the displacement field in that region. The bar axis is located at the intersection of the planes of symmetry. Figure 3-45 shows the geometry of the model and the corresponding mesh distribution. Solely finite elements with linear shape functions were used for this case.

The analysis reached the total displacement of 1.1mm with a maximum applied load of 63.5kN occurring at a displacement of 0.9 mm.

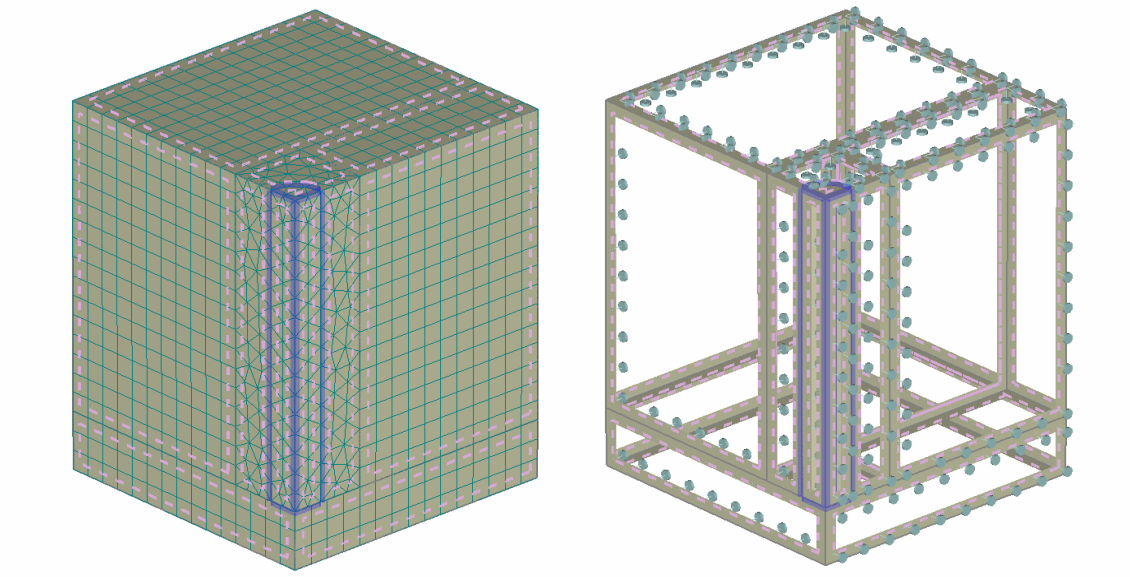

Figure 3-45 Geometry and mesh distribution for Standard 150x150 with friction.

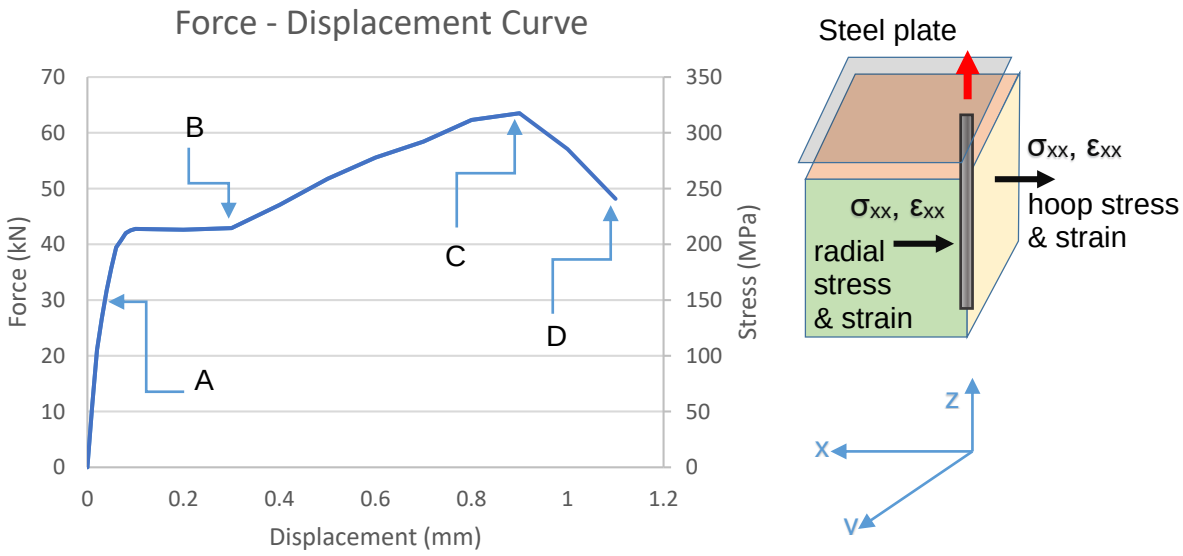

Figure 3-46: (a) Force – Displacement curve for Standard 150x150 with friction; (b) Nomenclature used in interpretation of results.

Figure 3-46 (a) shows the force – displacement curve for the Standard 150x150 specimen with friction and the corresponding stress that developed on the bar. The initial elastic response is followed by a plateau at approximately 66% of the peak strength before increasing to the maximum stress after the 0.3mm total displacement limit. The four distinct milestone locations are also shown in

Figure 3-46 (a). For the sake of the discussion that follows note the nomenclature of

Figure 3-46 (b).

Point A in the response curve – standard pullout, friction

At milestone A, the specimen has reached approximately 60% of the peak strength and bar displacement of 0.05mm. As depicted in Figure 3-47, tensile stresses σ_{zz} are being developed in the bar, not exceeding 225MPa at the loaded end and decreasing while progressing towards the free end. Because of its elastic state, tensile bar strains in the longitudinal direction (ε_{zz}) follow the same pattern as the stresses. Longitudinal compressive stresses not exceeding 20MPa are simultaneously being developed in the concrete around the uppermost segment of the development length. Radial cracks form, inclined at 45^o with respect to the longitudinal bar, with a width not exceeding the 0.013mm limit. The maximum crack width occurs under the free end of the bar, at the location of the major horizontal crack under the bar shown in the figure mentioned above. Concrete near the top develops transverse tensile stresses σ_{xx} and strains ε_{xx}, both in the hoop direction, as well as in the radial direction (the latter can be surmised by the color code on the y-face, in the neighborhood of the bar), whereas the sign is reversed near the free end which is subjected to transverse compression. Tensile stresses and strains do not exceed 1.5MPa and 0.001 respectively *(*Figure 3-48): The hoop tension (see green color in the figure to the left) extends to the outer fibers of the concrete specimen paving the prospect of splitting vertical cracks on the lateral surface of the pullout cube. Figure 3-49 presents the distribution of shear stresses τ_{xz}, which quantify the equivalent local bond stress developed at the interface between concrete and reinforcement. The negative sign displays the opposing direction of the shear stresses against the upwards movement of the bar. It is noted that bond stress is not distributed uniformly, with the peak occurring at the upper one third of the anchorage (10 – 15 MPa, with a relative slip at the loaded end of 0.05mm.)

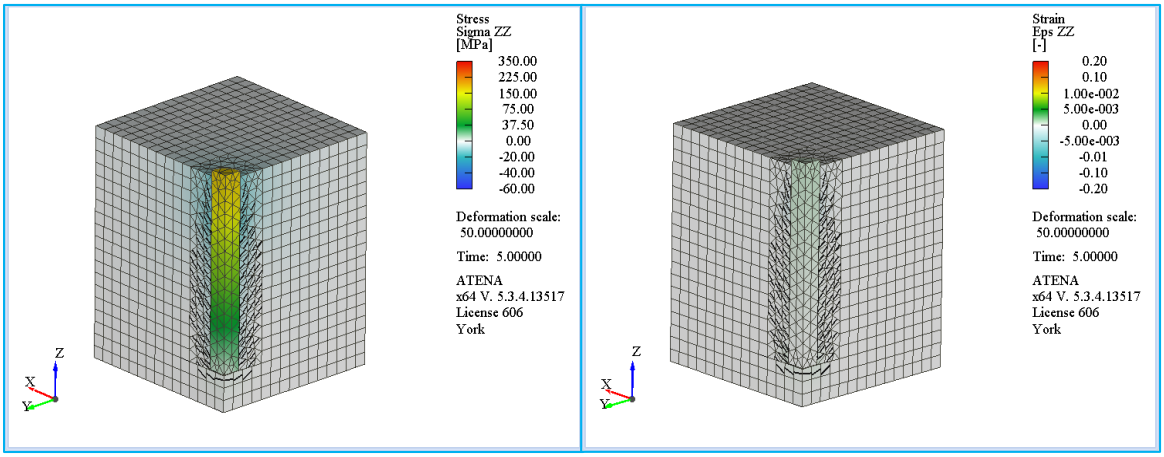

Figure 3-47 Stress σ_{zz} and strain ε_{zz} for Standard 150x150 with friction (Milestone A).

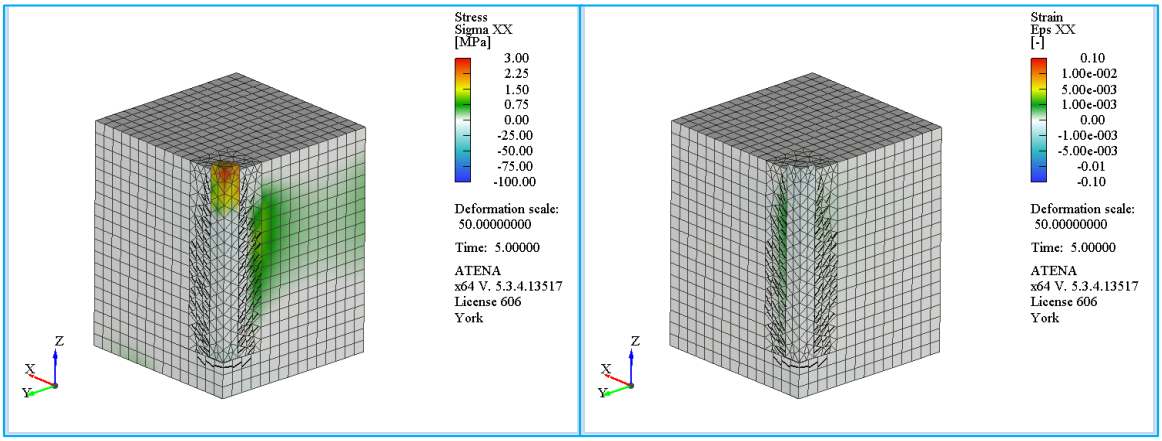

Figure 3-48 Stress σ_{xx} and strain ε_{xx} for Standard 150x150 with friction (Milestone A).

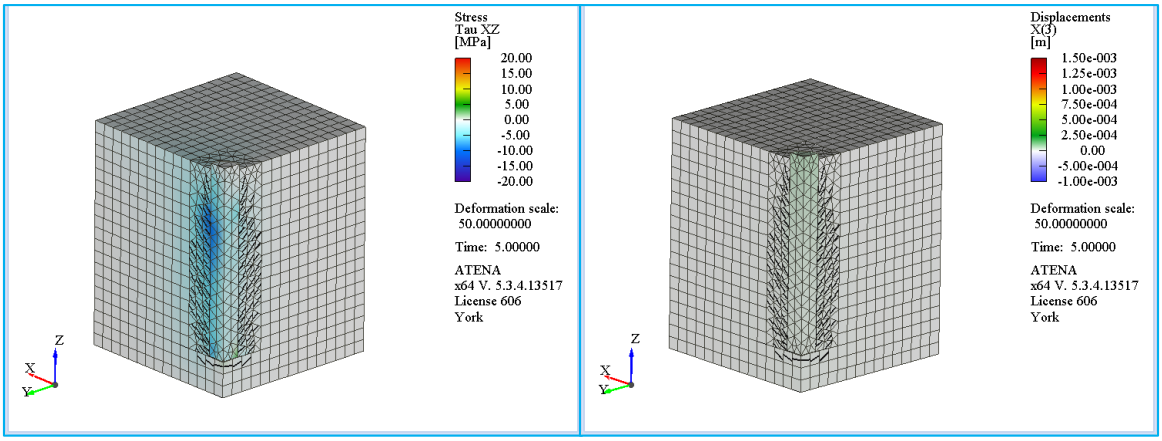

Figure 3-49 Shear stress τ_{xz} and slip Δ_z for Standard 150x150 with friction (Milestone A).

Point B in the response curve – standard pullout, friction

At milestone B, the specimen has reached approximately 67% of the peak strength and bar displacement of 0.1mm. The maximum crack width at this point is 0.032mm and it occurs under the free end of the pulled bar. Developed bar tensile stress σ_{zz} at the loaded end reaches 225MPa (Figure 3-50), whereas longitudinal compressive stresses in the concrete remain under the limit of 20MPa ($80\%f_c$). Cracking continues to propagate from the bar-to-concrete interface to the outer concrete perimeter at about 45° angle. Tensile strains ε_{zz} in the bar approach the value of 0.005 at the loaded end. Transverse stresses σ_{xx} and strains ε_{xx} in the concrete are tensile in the hoop direction (i.e. normal to the x-plane, around 1.5 – 2.5 MPa, Figure 3-51), and occurring around the mid-height of the anchorage. However radial stresses σ_{xx} are also visible in the y-plane behind the bar, that are compressive in magnitude (around 10 MPa). Shear stresses τ_{xz} propagate with increasing intensity from the upper segment towards the free end of the bar, with the bulk of the stress transfer (approximately 10 to 15 MPa) occurring in the lower 2/3 of the anchorage length. The relative slip between bar and concrete is 0.1mm at this point (Figure 3-52).

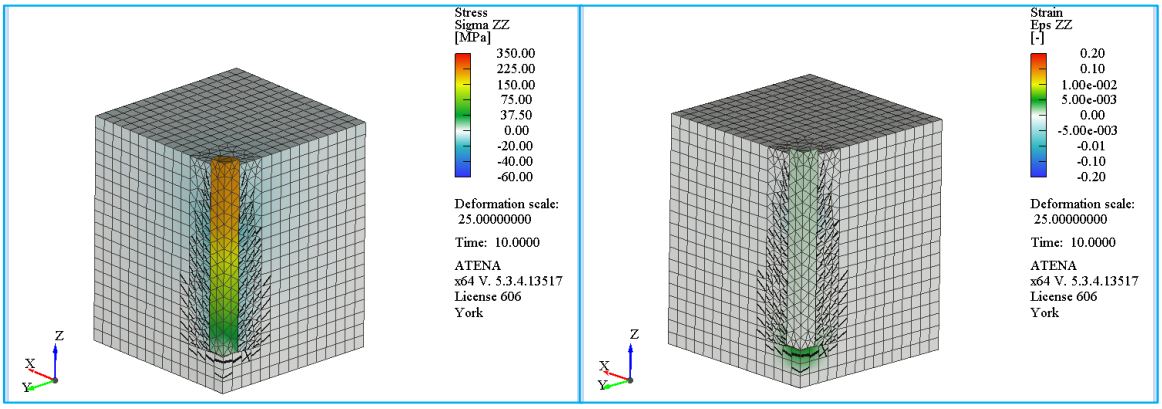

Figure 3-50 Stress σ_{zz} and strain ε_{zz} for Standard 150x150 with friction (Milestone B).

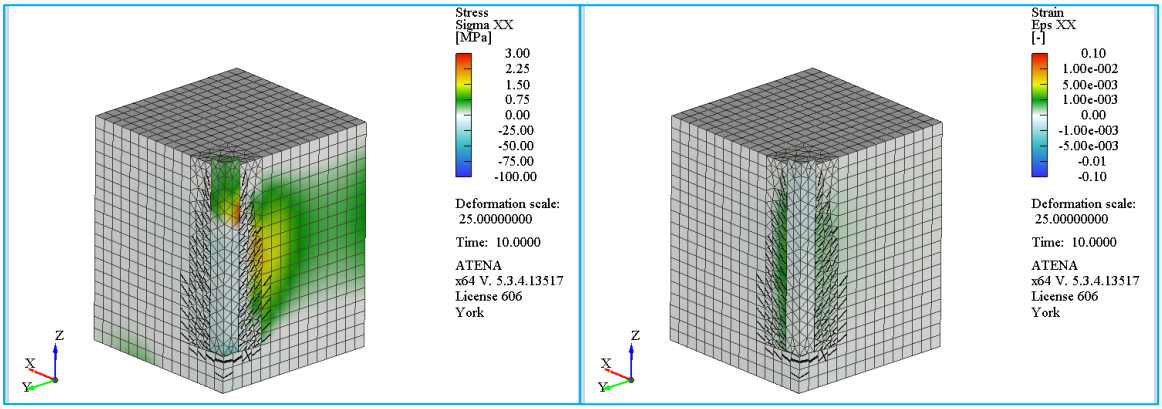

.

Figure 3-51 Stress σ_{xx} and strain ε_{xx} for Standard 150x150 with friction (Milestone B).

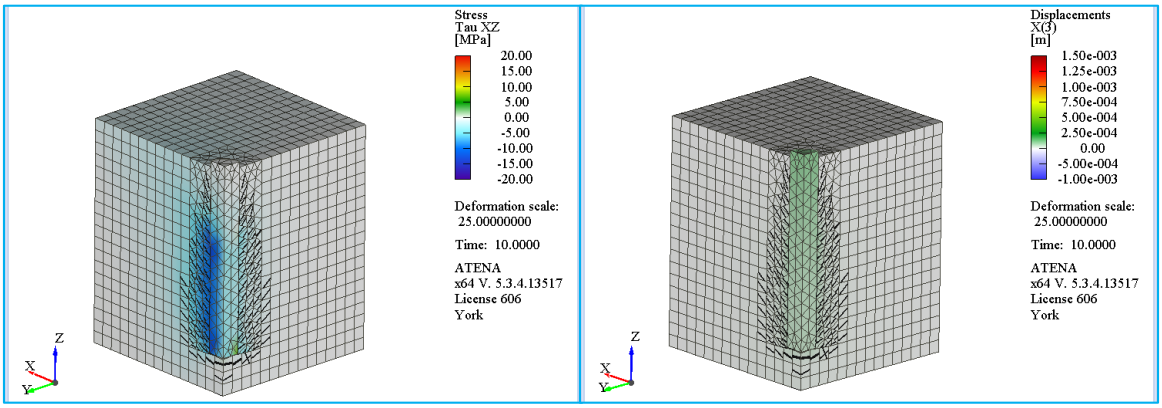

Figure 3-52 Shear stress τ_{xz} and slip Δ_z for Standard 150x150 with friction (Milestone B).

Point C in the response curve – standard pullout, friction

Milestone C corresponds to the peak development capacity of the bar, at a vertical bar displacement of 0.9mm. Peak bar axial stress developed is 317MPa whereas the longitudinal compressive stresses on the surrounding concrete have reached peak values in the range of 20 – 40 MPa and at about the mid-height of the anchorage the local compressive stress is 55MPa (Figure 3-53). Hoop (circular) cracking patterns develop on the top surface of the specimen while radial cracking extends with increased intensity in the concrete surrounding the free end of the bar. The maximum crack width at this point is 1.5mm. Local tensile strains of the concrete under the free end of the bar exceed the value of 0.20. At this point, the concrete has completely ceased to resist the movement of the bar. Transverse compressive stresses σ_{xx} have increased dramatically on the concrete located immediately around the bar, exceeding 25 MPa. Further beyond that immediate region hoop stresses are tensile in the range of 2.5 MPa, whereas radial strains are compressive with the exception being at the immediate interface where concrete has crushed and strains are residual tensile (open cracks, Figure 3-54). Very high values of shear stress (Figure 3-55) are recorded (in the neighborhood of 15 MPa to 20 MPa) extending over most of the anchorage length with the exception of the upper 1/5th of the available distance, whereas the relative slip at the loaded end is 0.9mm.

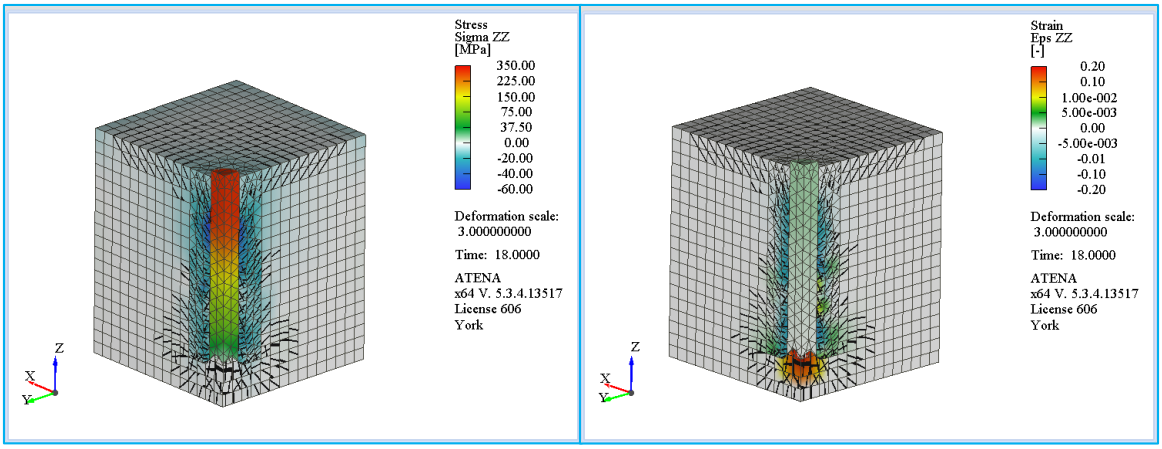

Figure 3-53 Stress σ_{zz} and strain ε_{zz} for Standard 150x150 with friction (Milestone C).

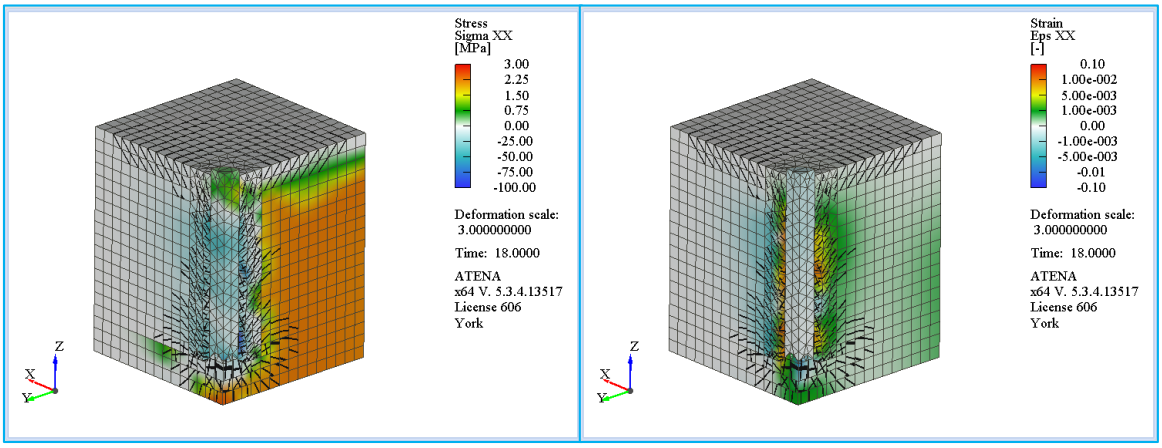

Figure 3-54 Stress σ_{xx} and strain ε_{xx} for Standard 150x150 with friction (Milestone C).

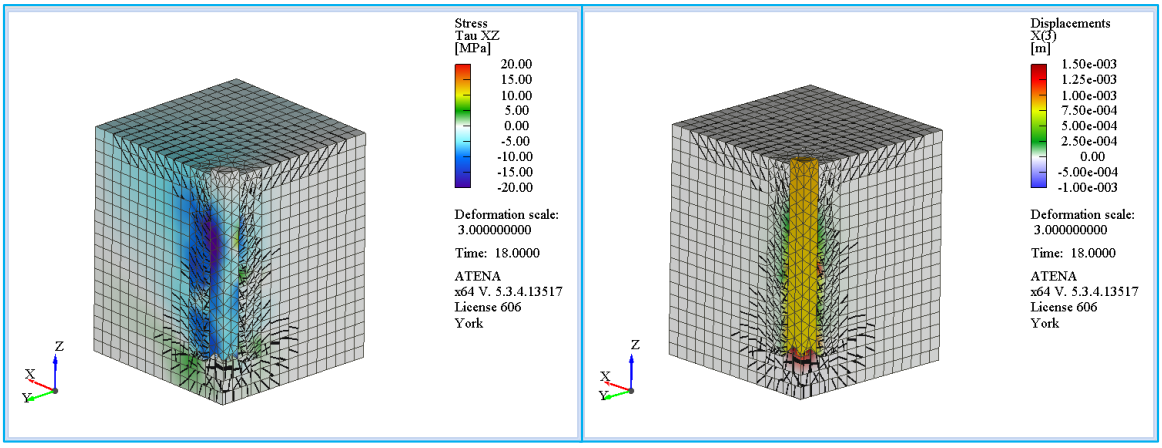

Figure 3-55 Shear stress τ_{xz} and slip Δ_z for Standard 150x150 with friction (Milestone C).

Point D in the response curve – standard pullout, friction

Milestone point D is near the end of the simulated test, when the residual development capacity of the anchorage is about 75% of peak strength, occurring at a bar displacement of 1.1mm. At this point, the bar has completely dislocated from the concrete and the stress that can be carried by the bar is steadily being reduced. The tensile stress σ_{zz} on the bar has attenuated to 240MPa and the longitudinal compressive stresses in the concrete are less than 25 MPa (Figure 3-56), accompanied with commensurate longitudinal compressive strains in the concrete in the upper 2/3 of the anchorage. A fine network of conical cracks is now formed practically emanating at a 45^o angle from the bar and extending over the body of the concrete. As was seen in milestone point C, normal stresses in the x-plane are tensile, lower than the cracking strength, which, when viewed in conjunction with the large values of the corresponding strains indicate that the material is in the softening part of its tensile stress-strain law. However, radial stresses acting on the bar (see *y*-plane) are residual compressive whereas in the same locations very large compressive strains in the radial direction exactly adjacent to the bar mark the local concrete crushing failure. These compressive stresses converging due to axisymmetry near the free end of the bar push down the bottom cover, leading to its delamination. Bond stresses develop in response to the radial compression (frictional mechanism) with an intensity at 15-20 MPa but extending over part of the anchorage only (Figure 3-57, Figure 3-58). Parts over which no bond is developing are considered debonded from concrete. The relative slip at this point is 1.1mm.

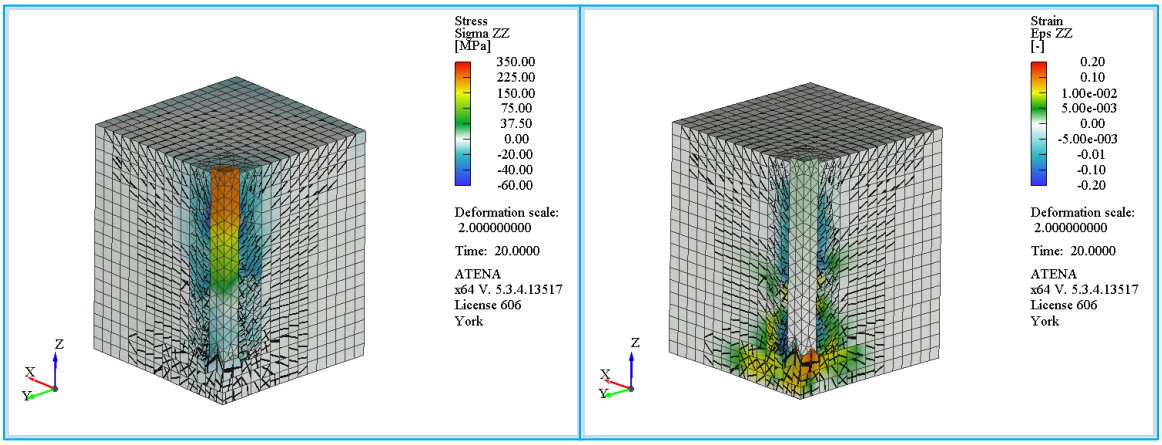

Figure 3-56 Stress σ_{zz} and strain ε_{zz} for Standard 150x150 with friction (Milestone D).

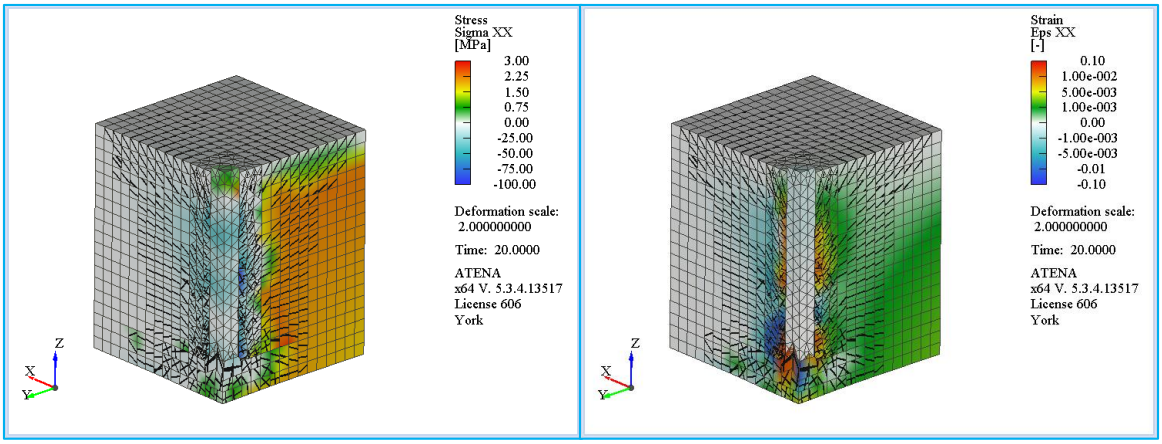

Figure 3-57 Stress σ_{xx} and strain ε_{xx} for Standard 150x150 with friction (Milestone D).

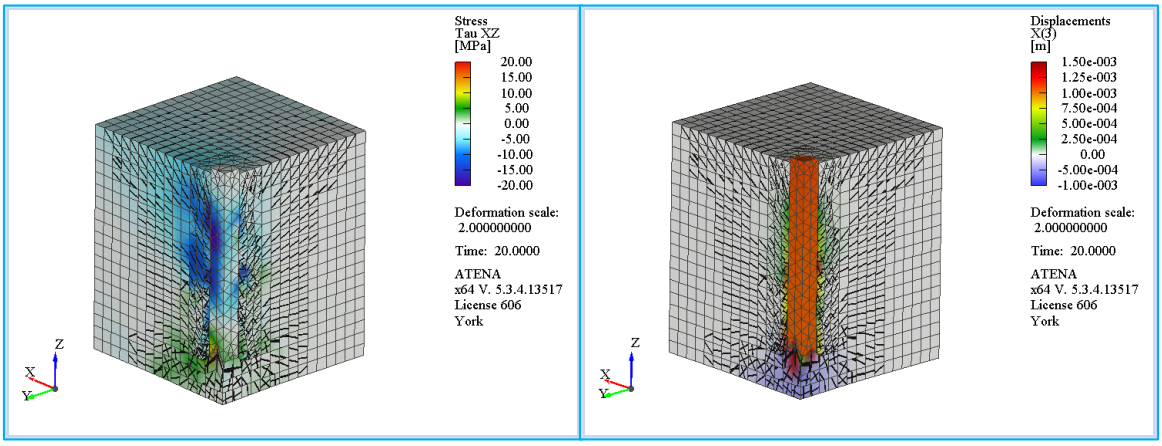

Figure 3-58 Shear stress τ_{xz} and slip Δ_z for Standard 150x150 with friction (Milestone D).

3.5.1.2 Standard 150x150 specimens with no friction

This specimen is modeled in the same way as the Standard 150x150 cube with friction. The only difference lies on the boundary conditions imposed on the top surface of the specimen in which displacements u_z are being restrained while u_x and u_y remain free. That is to allow the concrete to expand freely in the lateral direction without intervening with Poisson's effect as would occur with an intermediate Teflon layer. Figure 3-59 shows the boundary conditions imposed on the top surface and the planes of symmetry and Figure 3-60 shows the force – displacement curve for the specimen.

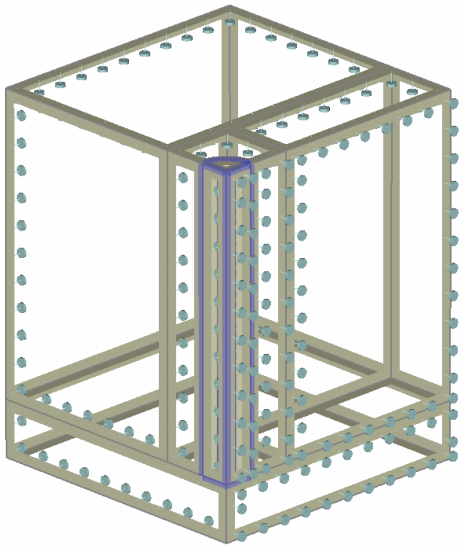

Figure 3-59 Boundary conditions imposed on Standard 150x150 with no friction.

The analysis reached the total displacement of 0.9mm with a maximum applied load of 45.778kN. After the initial branch reaches a strength of 42.6kN strength is reduced slightly, before increasing to the maximum load. Shortly after reaching the peak load, the curve begins to drop, signaling the disconnection of the steel from the concrete and the pullout of the bar.

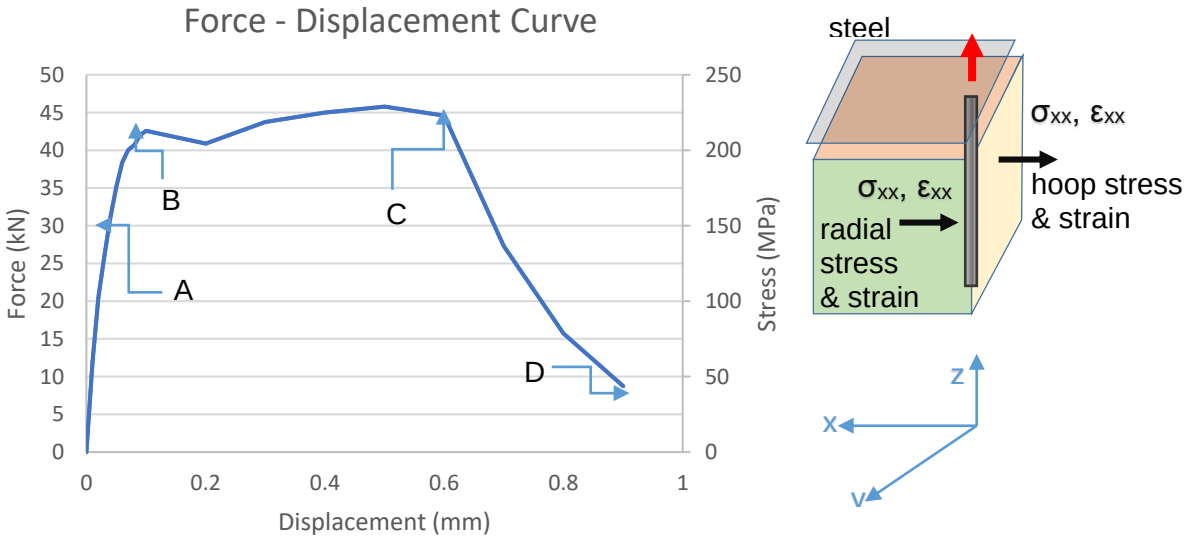

Figure 3-60: (a) Force–Displacement curve for Standard 150x150, no friction; (b) Nomenclature.

Point A in the response curve – standard pullout, no friction

At milestone A, the specimen has reached approximately 68% of the peak strength and a bar displacement of 0.04mm. Cracking starts to emanate in the proximity of the bar, not exceeding widths of 0.01mm. As shown in Figure 3-61, tensile longitudinal stresses (σ_{zz}) develop in the bar, reaching values of approximately 150MPa whereas compressive stresses develop on the concrete surrounding the bar, reaching values of approximately 20MPa. The tensile longitudinal strains (ε_{zz}) that appear on the bar do not exceed 0.000765 and decrease starting from the loaded end to the free end. Furthermore, tensile strains appear on the concrete under the free end and on the lower perimeter of the bar, whereas the concrete closer to the top pressed surface undergoes compressive strains of 0.001. These strains are the result of the bearing surface on the top of the specimen and mark the fact that the surrounding concrete in the development length is under compression while the bar is in tension. In the transverse hoop direction, tensile stresses (σ_{xx}) develop on the concrete reaching values of 2.5MPa (Figure 3-62, see the plane normal to the x-axis). Contrary to the case with frictional resistance on the top surface, in this case the tension is distributed along the top surface elements as well. Compressive transverse stresses act on the bar as part of the resisting concrete cover (radial stresses, parallel to the y axis seen on the plane normal to y), not exceeding values of 10MPa for this step. Transverse strains (ε_{xx}) acting on the bar are contractive (on account of the Poisson's effect), whereas for the same reason as well as on account of the shear strains at the interface the concrete surrounding the bar (which carries compressive σ_{zz}) reaches tensile strain values of 0.001. Shear stresses facing downwards around the concrete develop to values of -8.66MPa (direction opposite to the movement of the bar with relative slip of 0.04mm, Figure 3-63).

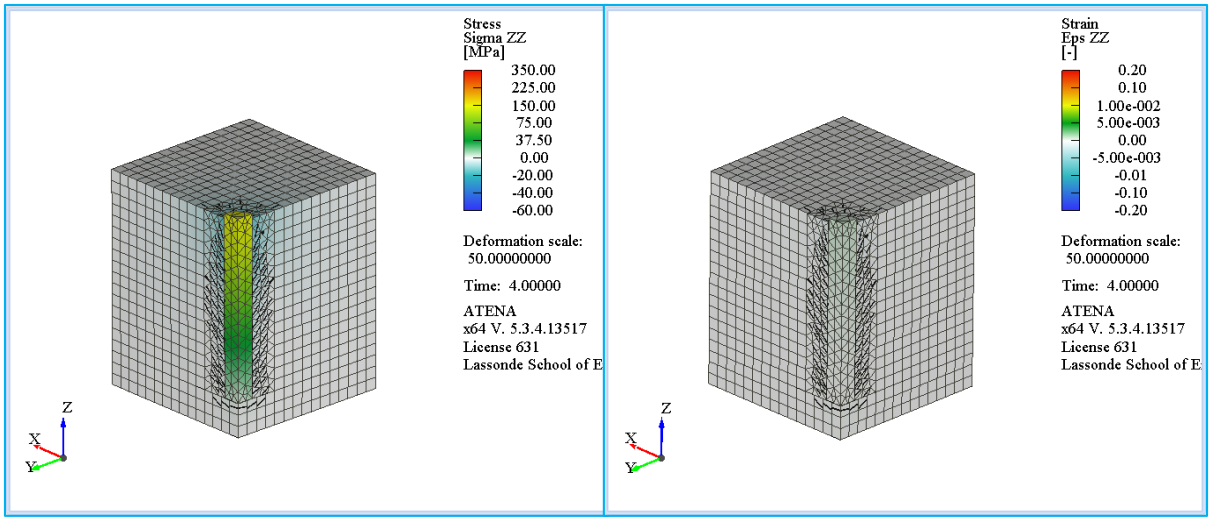

Figure 3-61 Stress σ_{zz} and strain ε_{zz} for Standard 150x150 with no friction (Milestone A).

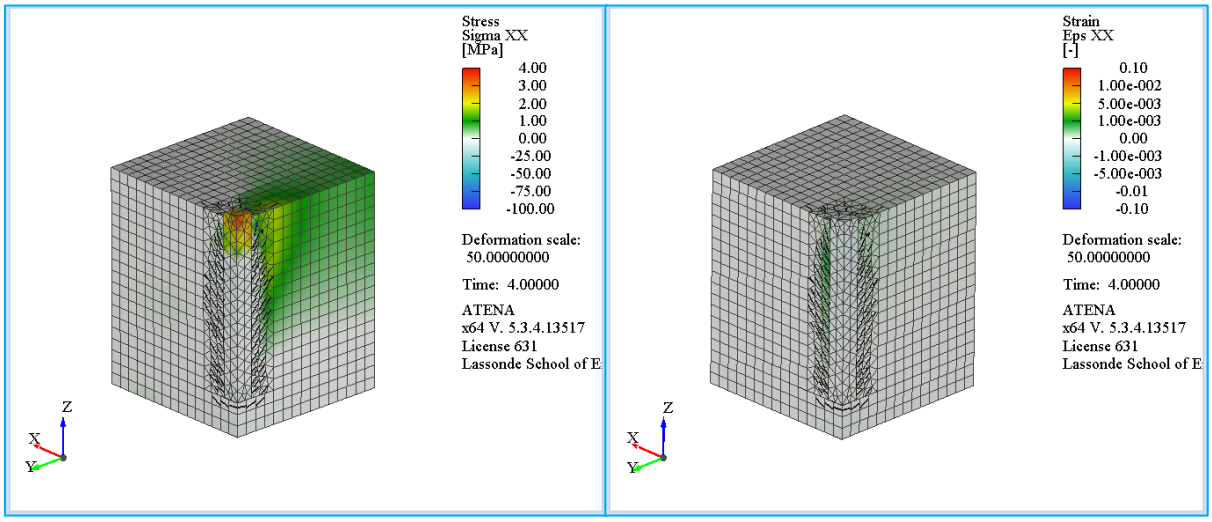

Figure 3-62 Stress σ_{xx} and strain ε_{xx} for Standard 150x150 with no friction (Milestone A).

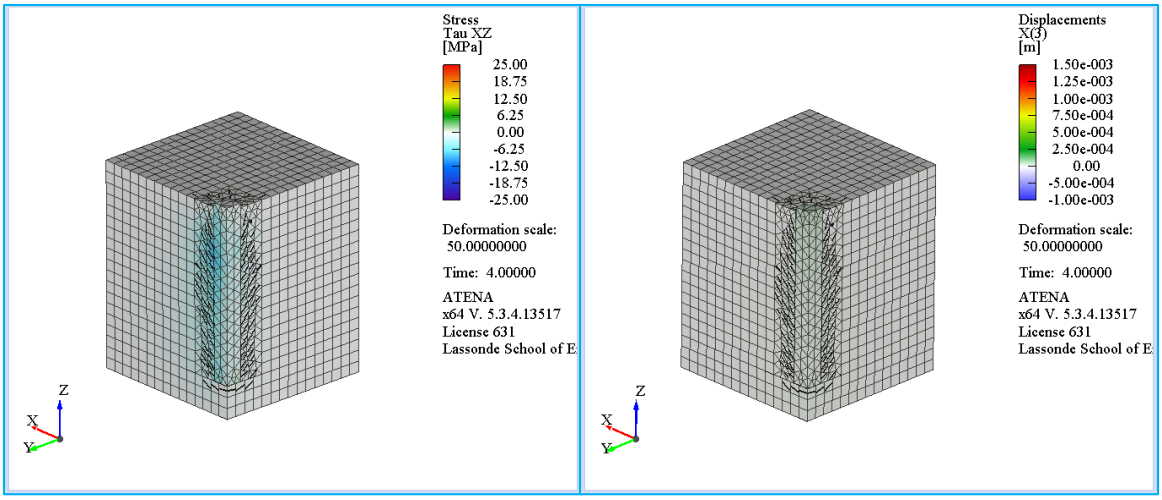

Figure 3-63 Shear stress τ_{xz} and slip Δ_z for Standard 150x150 with no friction (Milestone A).

Point B in the response curve – standard pullout, no friction

At milestone B, the specimen has reached approximately 93% of the peak strength and a bar displacement of 0.1mm. The longitudinal stresses on the bar reach 213MPa and parallel compressive stresses in the cover near of the bar reach 16MPa (Figure 3-64). Tensile longitudinal strains have exceeded the capacity of concrete by reaching values of 0.005 under the free end of the bar, whereas compressive strains still develop on the concrete surrounding the bar close to the top surface. In the transverse direction, stresses continue to increase in the hoop direction, but interestingly radial stresses are also tensile in the upper part of the cover. The corresponding tensile stresses on the bar begin to diminish on the upper segment close to the surface of the specimen, whereas the lower segment is compressed radially. Tension in σ_{xx} does not exceed 3MPa whereas compression reaches values of -34MPa (Figure 3-65). Shear stresses on the bar-to-concrete interface continue to increase, not exceeding values of -18.75MPa, with these values concentrated on the bar segment away from the top surface (Figure 3-66). That is due to bond failure on the top segment of the bar where the initial shear stresses had concentrated. The relative slip at this point is 0.1mm.

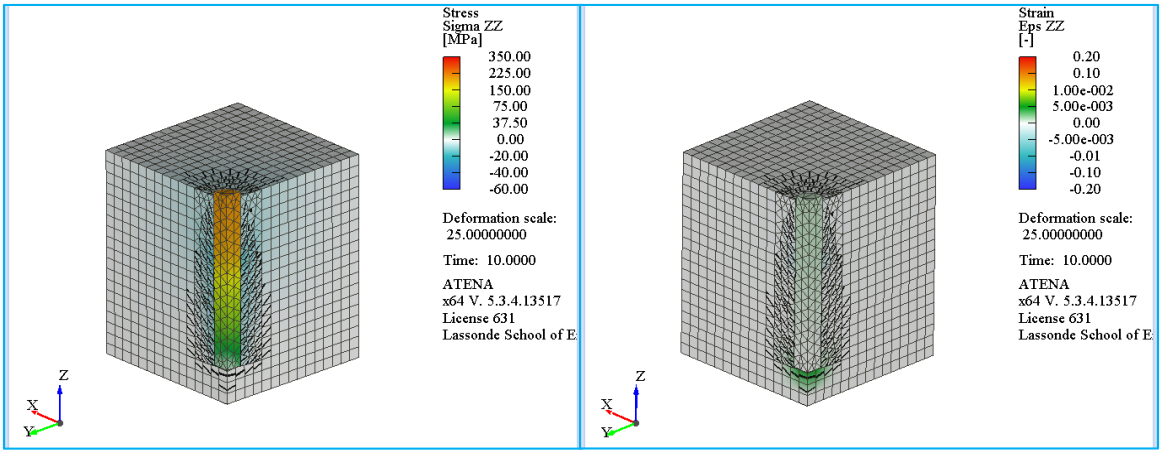

Figure 3-64 Stress σ_{zz} and strain ε_{zz} for Standard 150x150 with no friction (Milestone B).

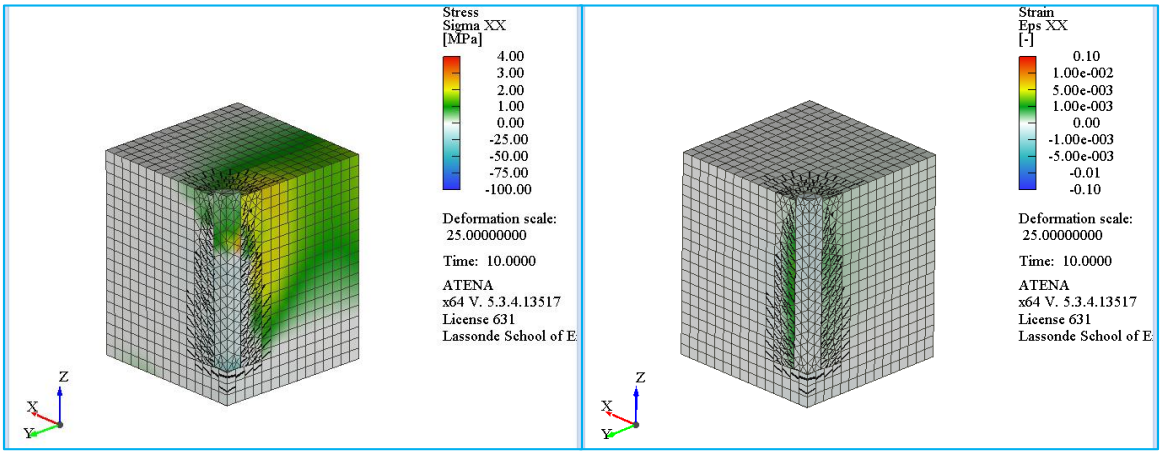

Figure 3-65 Stress σ_{xx} and strain ε_{xx} for Standard 150x150 with no friction (Milestone B).

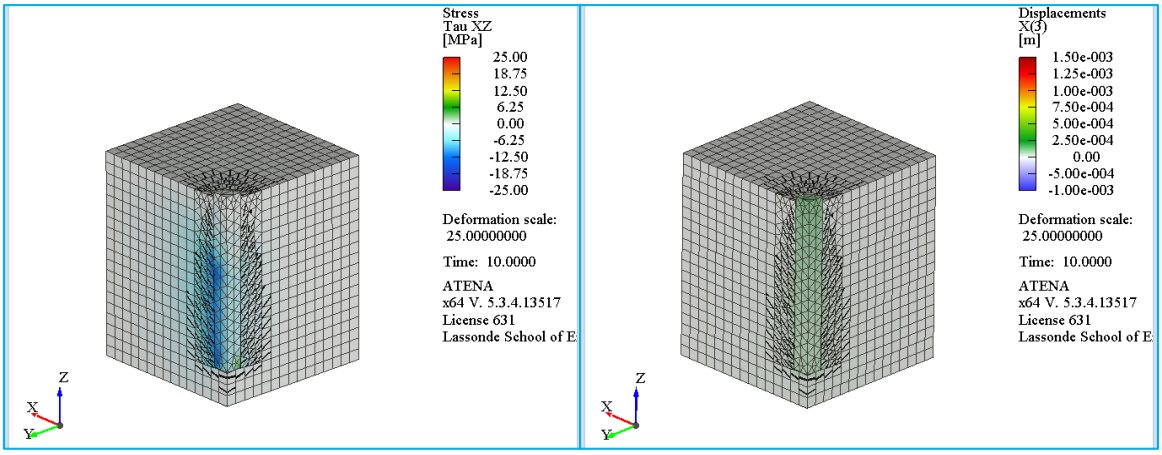

Figure 3-66 Shear stress τ_{xz} and slip Δ_z for Standard 150x150 with no friction (Milestone B).

Point C in the response curve – standard pullout, no friction

At milestone C, the specimen has reached approximately 97% of the peak strength and bar displacement of 0.6mm. Cracking has dispersed on the top surface of the specimen, denoting the equivalent concrete ring where radial stresses are resolved (note the radial pattern of cracking). Crack width at this step has reached a maximum of 1.1mm under the free end). According to Figure 3-67, tensile longitudinal stresses on the bar have begun to spread downwards while the compressive stresses on the concrete around the bar reach 40MPa, well beyond the concrete's uniaxial compressive strength of 25MPa. That is due to the passive confinement imposed by the bearing steel plate of the top of the test block. Compressive longitudinal strain levels around the bar reach values as high as -0.10 whereas the effective tensile concrete strains on the free end of the bar approach values of 0.20. Hoop tensile stresses on the concrete have extended to the edge of the concrete block with higher values in close proximity with the bar. The tensile values do not exceed 4.0MPa while horizontal tensile stress distributions also appear in the concrete below the free end of the bar (Figure 3-68). Compressive (radial) stresses on the bar have diminished due to loss of contact with the adjacent concrete as indicated by the strain penetration on the bar. Tensile hoop strains envelop the concrete surface normal to the corresponding axis of symmetry reaching values of 0.01. Compressive radial strains exist only on segmental zones of the concrete close to the bar since cracking has penetrated through the majority of the concrete volume. Shear stresses on the perimeter of the bar have been reduced in most of the bar surface and continuity has been lost (i.e. bond failure over that segment). This is due to the proliferation of cracking on the perimeter of the bar where contact with the concrete has started to diminish. Negative shear stresses do not exceed the values of 25MPa and are concentrated in segmented areas of the total interface (Figure 3-69). Additionally, positive shear stresses have started to appear on the concrete farther away from the bar perimeter. The relative slip at this point is 0.6mm.

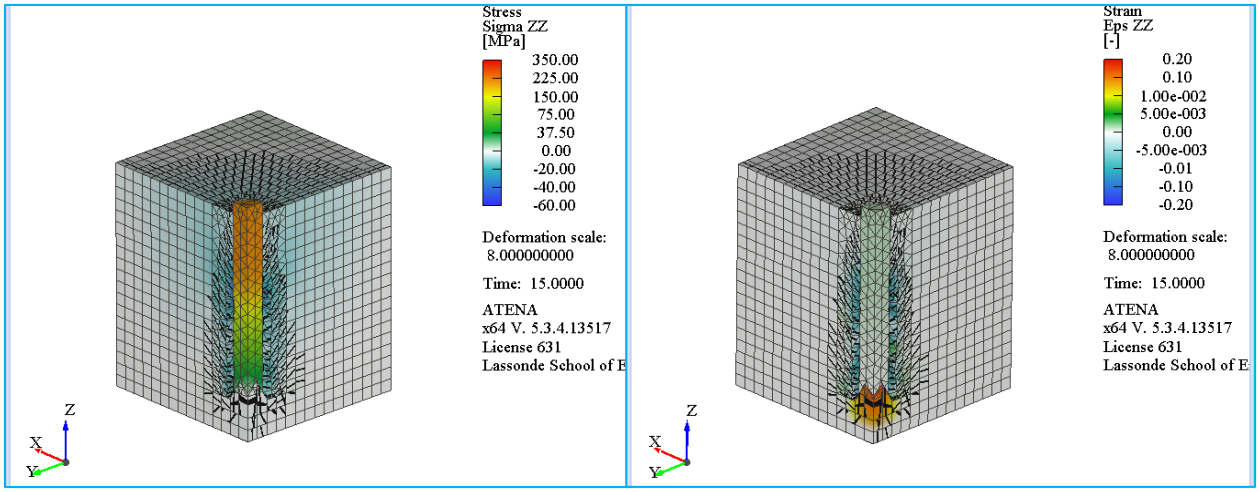

Figure 3-67 Stress σ_{zz} and strain ε_{zz} for Standard 150x150 with no friction (Milestone C).

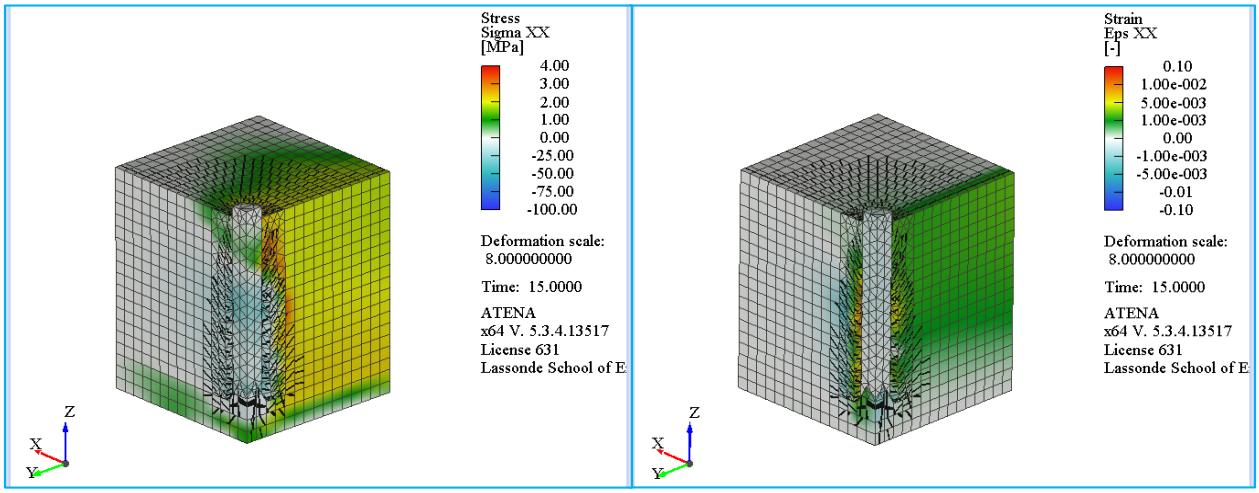

Figure 3-68 Stress σ_{xx} and strain ε_{xx} for Standard 150x150 with no friction (Milestone C).

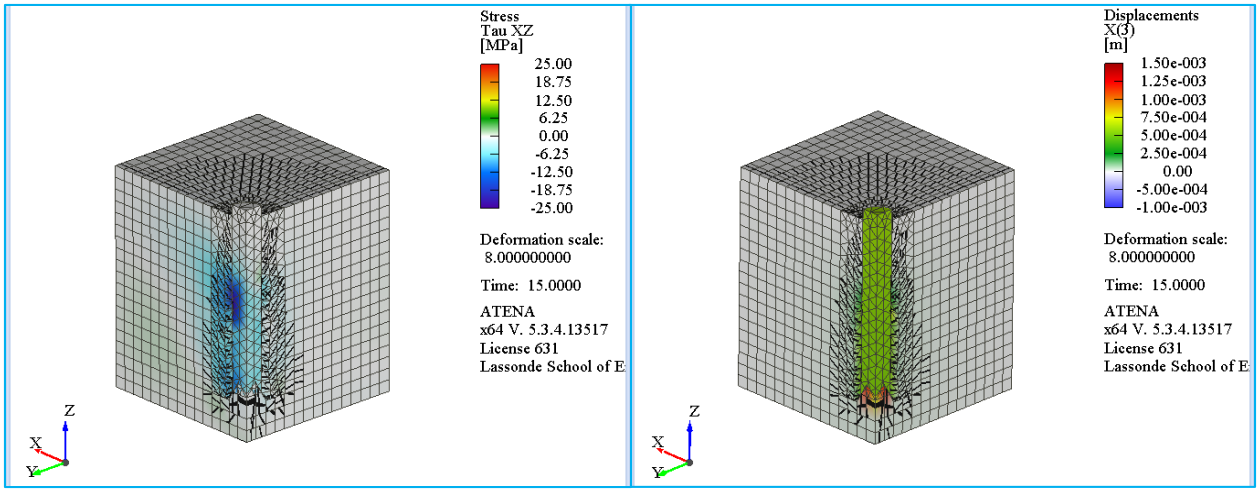

Figure 3-69 Shear stress τ_{xz} and slip Δ_z for Standard 150x150 with no friction (Milestone C).

Point D in the response curve – standard pullout, no friction

At milestone D, the specimen has reached approximately 34% of the peak strength and bar displacement of 0.8mm. The specimen has reached the end of the descending branch where significant loss of strength can be observed. Crack width has reached values of 1.8mm at this point. Tensile longitudinal stresses on the bar have diminished to no more than 75MPa and compressive stresses around the concrete have been reduced proportionately to approximately 20MPa (Figure 3-70). Corresponding longitudinal strains reach a maximum of 0.2 in tension before diminishing after the disconnection of the bar and concrete, while compressive strains reach values of 0.1 (i.e. the concrete has crushed locally). In the transverse hoop direction, tensile stresses σ_{xx} have engaged the majority of the concrete and have begun to diminish to 1.5 MPa as the bar is gradually pulling out of the specimen (Figure 3-71). Radial compression acting on the bar is around 25MPa. Strains ε_{xx} have increased to levels between 0.01 and 0.1 to the full extent of the concrete specimen with compressive values lying between 0.01 and 0.05. Shear stresses have declined significantly and below 12.5MPa since the contact of concrete with the bar has been reduced almost entirely and dry friction has taken over (Figure 3-72). Positive shear stresses develop on the concrete reaching values of no more than 6.25MPa. Relative slip is 0.8mm at this point.

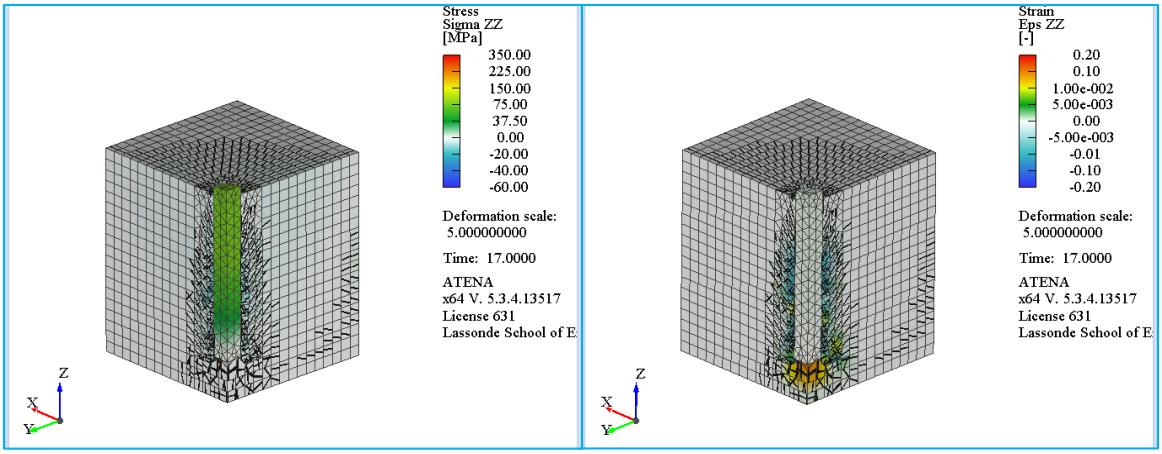

Figure 3-70 Stress σ_{zz} and strain ε_{zz} for Standard 150x150 with no friction (Milestone D).

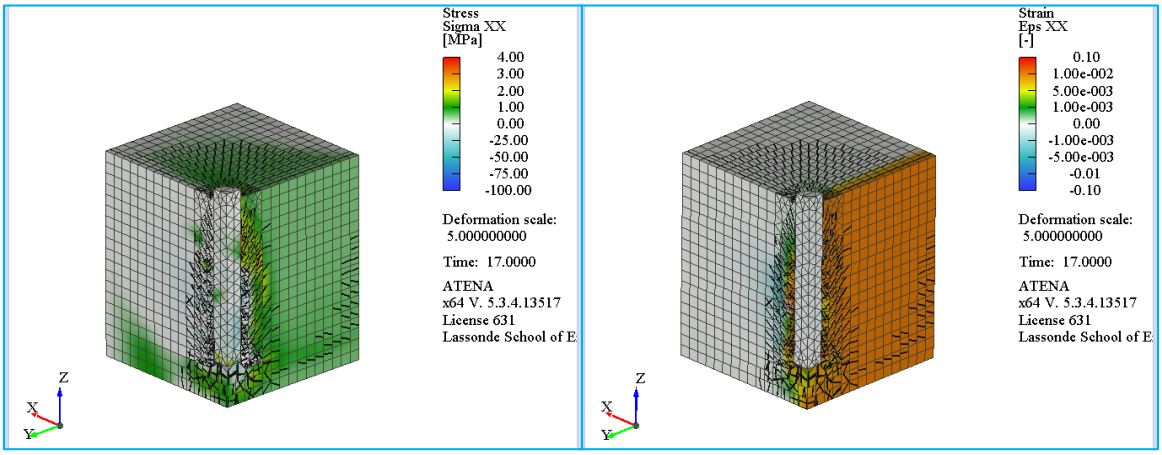

Figure 3-71 Stress σ_{xx} and strain ε_{xx} for Standard 150x150 with no friction (Milestone D).

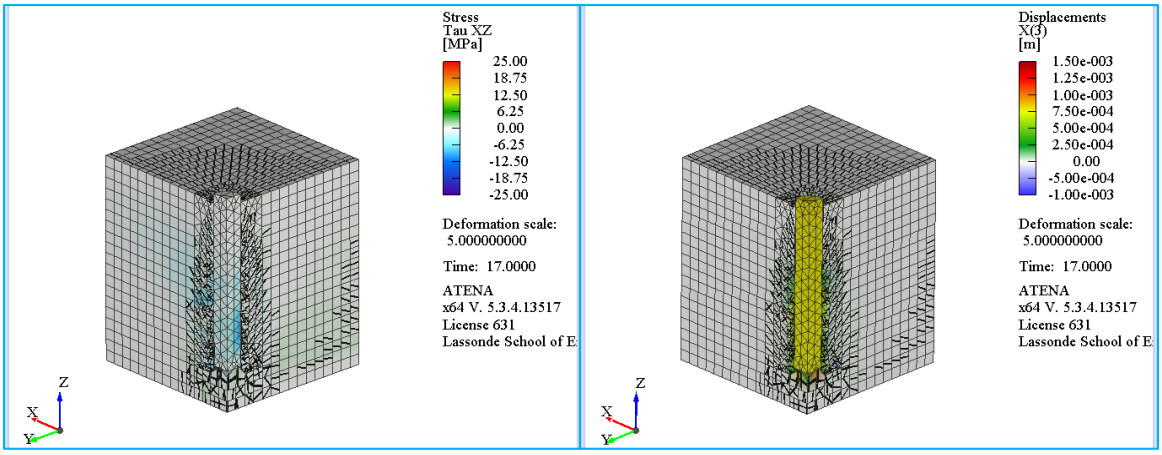

Figure 3-72 Shear stress τ_{xz} and slip Δ_z for Standard 150x150 with no friction (Milestone D).

3.5.1.3 Reduced size standard pullout (80x80) specimen with friction

This specimen follows the same formulation as the Standard 150x150 model with friction, however using the cover distance c_2 = 32mm instead of c_1. The total rectangular section has dimensions of 80x80mm for both sides. Analysis parameters and boundary conditions follow the procedure as denoted in 3.4.1. Figure 3-73 shows the mesh distribution and boundary conditions for this model and Figure 3-74 shows the force – displacement curve.

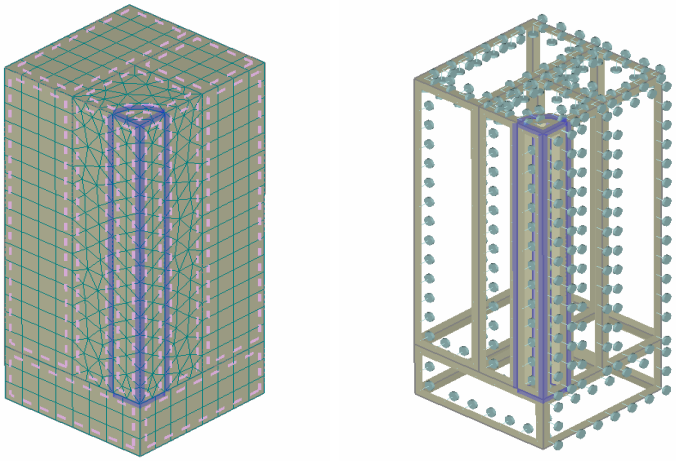

Figure 3-73 Mesh distribution and boundary conditions for Custom 80x80 with friction.

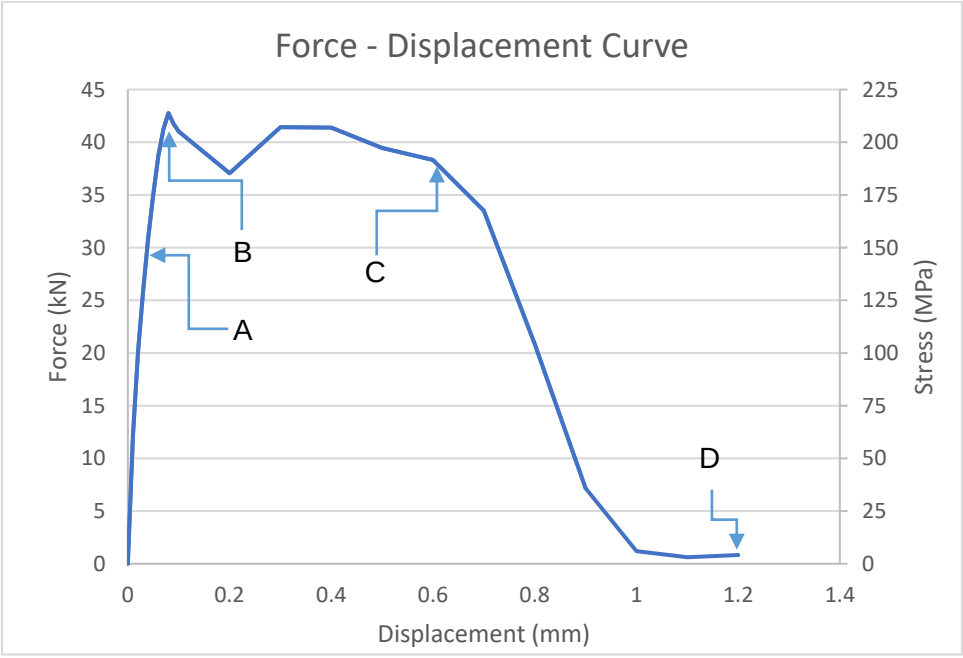

Figure 3-74 Force – Displacement curve for Reduced 80x80 with friction.

Point A in the response curve – reduced concentric pullout, friction

At milestone A, the specimen has reached approximately 72% of the peak strength and bar displacement of 0.04mm. Cracking develops in the same manner as in the Standard 150x150 specimens, with the higher concentration of upwards inclined cracks on the concrete closer to the bar element. Longitudinal cracks develop in the concrete under the free end of the bar. Crack width does not exceed 0.011mm. According to Figure 3-75, longitudinal tensile stresses developing on the bar reach a maximum of 150MPa and reduce gradually from the loaded end to the free end of the bar. Compressive stresses however develop on the surrounding concrete, particularly on the top surface of the specimen where restraints have been imposed. The anchorage is correspondingly strained in tension, not exceeding levels of 0.001, while the concrete sustains tensile strains on the bar perimeter and under the free end. The concrete surrounding the upper segment of the bar develops longitudinal compressive strains up to values of -0.0014. Transverse tensile stresses develop on the loaded end of the bar and upper segment of the concrete specimen, with the higher concentration on the bar to reach 4MPa (Figure 3-76). The concrete does not yet exceed 1MPa in tension. Radial transverse tensile strains appear on the concrete on the upper segment of the perimeter of the bar, reaching values up to 0.001, showing that the radial ring action is counteracted by the Poisson's effect. On the contrary, the bar develops compressive strains as a reaction against the pressures exerted against the surrounding concrete, reaching values much less than -0.001. Shear stresses envelop the interface between the bar and the concrete, with a maximum value between -7.5MPa and -15MPa (Figure 3-77). At this point, the distribution of bond stresses on the interface engages the entirety of the bar surface as the bond capacity has not been exceeded yet. The relative slip at this point is 0.04.

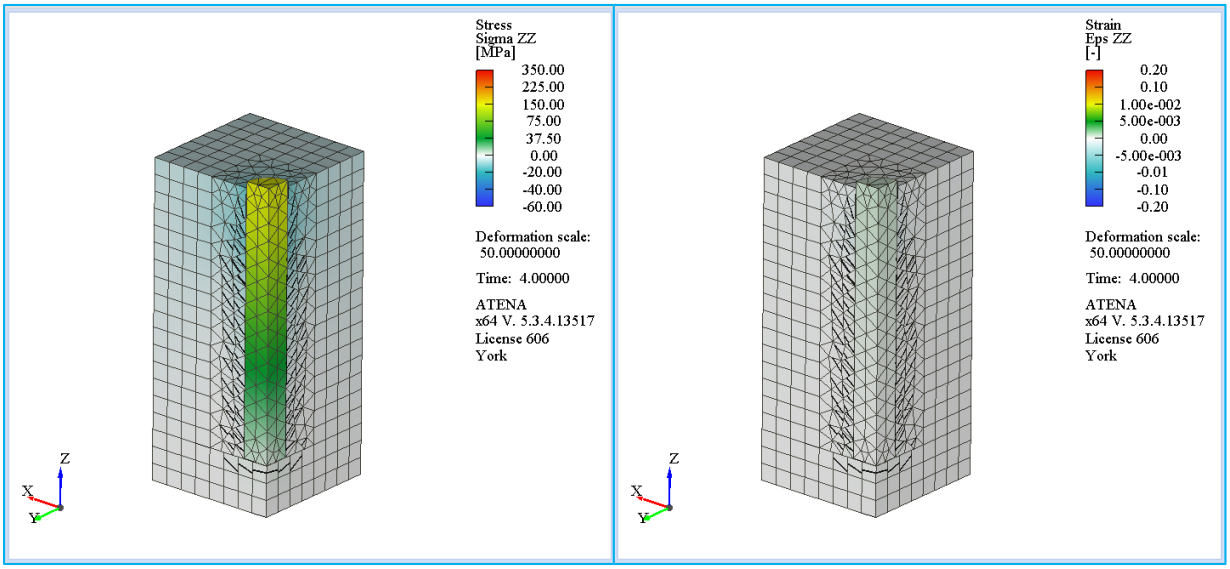

Figure 3-75 Stress σ_{zz} and strain ε_{zz} for Reduced 80x80 with friction (Milestone A).

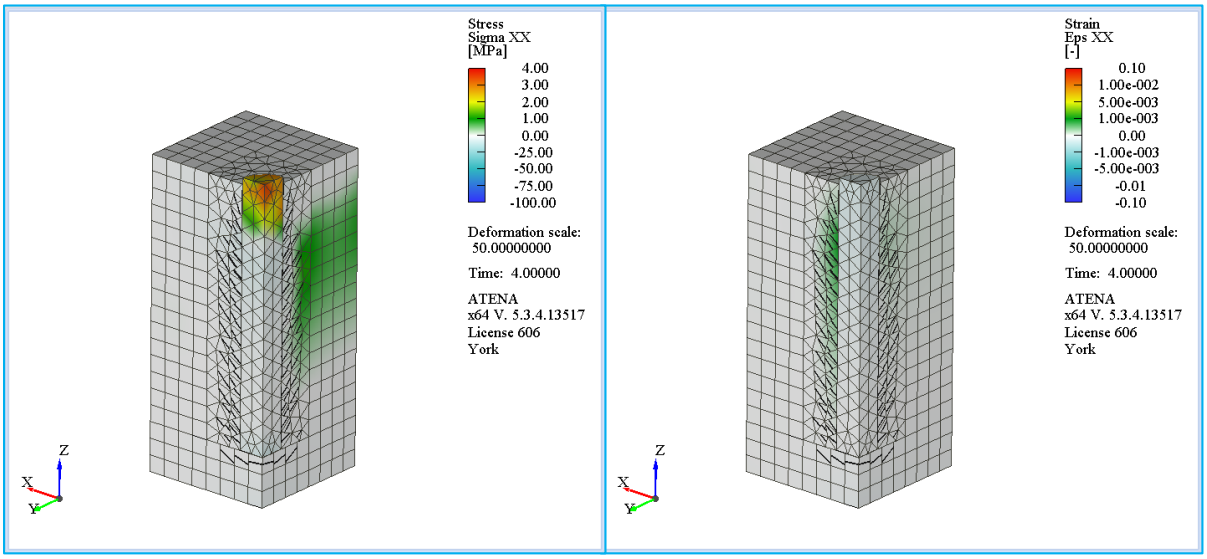

Figure 3-76 Stress σ_{xx} and strain ε_{xx} for Reduced 80x80 with friction (Milestone A).

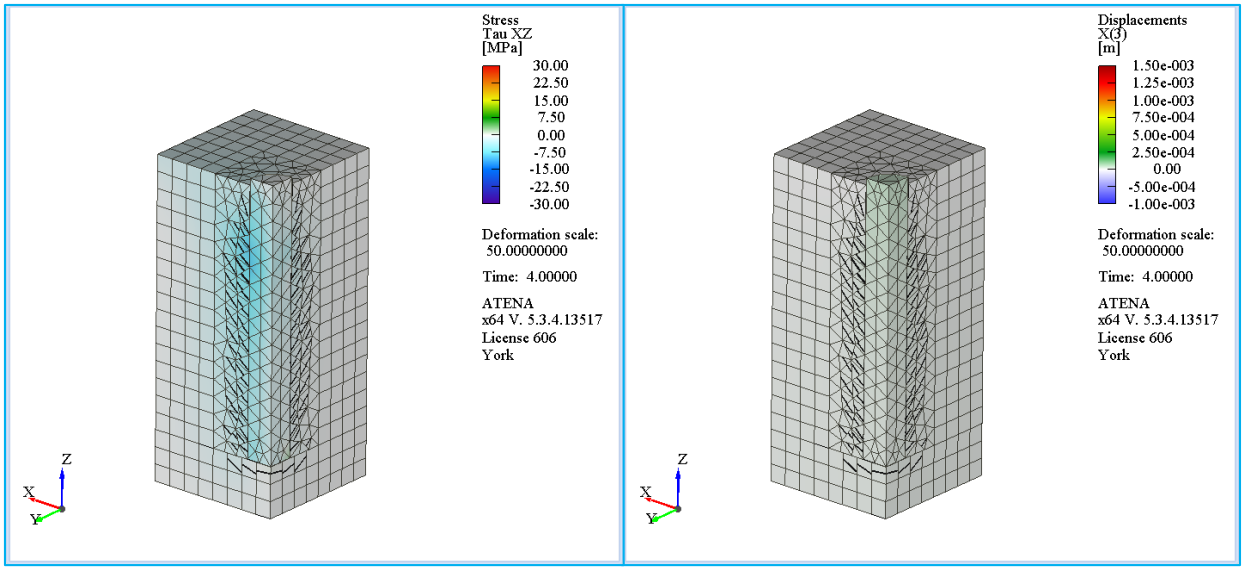

Figure 3-77 Shear stress τ_{xz} and slip Δ_z for Reduced 80x80 with friction (Milestone A).

Point B in the response curve – custom concentric pullout, friction

At milestone B, the specimen has reached 100% of the peak strength and bar displacement of 0.08mm. Inclined cracking has begun to extend further from the bar perimeter and engaging greater volume of concrete. Crack width shows a maximum value of 0.023mm. Longitudinal tensile stresses on the bar have reached their maximum capacity, which does not exceed the 225MPa limit, whereas compressive stresses have spread further into the concrete, with a higher concentration on the upper segment of the specimen and values that do not exceed -20MPa (Figure 3-78). Longitudinal tensile strains appear on the bar and on the concrete located under the bar reaching values of approximately 0.002. Compressive strains continue to engage the concrete close to the bar perimeter and on the upper segment of the specimen, not going beyond -0.003. In the transverse direction, low level tensile hoop stresses act on concrete with values that do not exceed the 2.5MPa. The bar stress at this point has been reduced due to loss of stress transfer between bar and concrete after the interface strength has been exceeded. Radial compressive stresses act on the free end of the bar, in the range of 25MPa (Figure 3-79). Tensile strains continue to increase on the concrete close to the bar and begin to extend to the outer surface of the specimen. The maximum tensile strain is not more than 0.002 at this point. Compressive strains appear on the upper segment of the bar and decrease moving from the loaded end towards the free end, with a maximum value of not more than 0.0003. The shear stress distribution has ceased to engage the upper segment of the bar due to loss of bond strength. The maximum negative values do not exceed the 15MPa at this point, with a higher

concentration of higher shear stresses on the top part of the engaged bar (Figure 3-80). The relative slip is 0.08mm at this point.

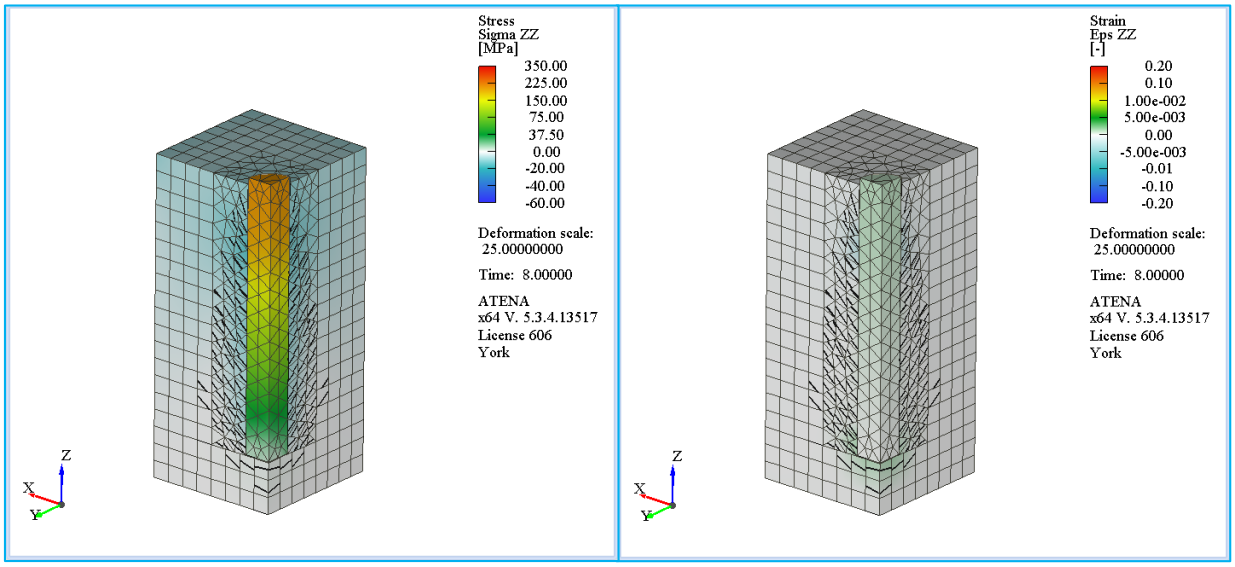

Figure 3-78 Stress σ_{zz} and strain ε_{zz} for Reduced 80x80 with friction (Milestone B).

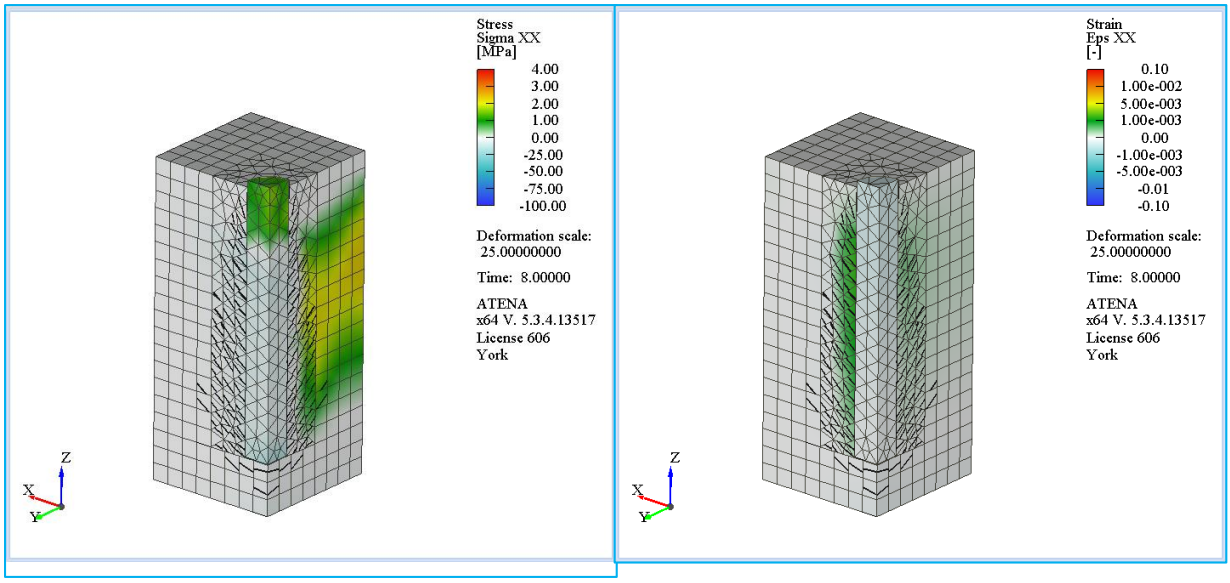

Figure 3-79 Stress σ_{xx} and strain ε_{xx} for Reduced 80x80 with friction (Milestone B).

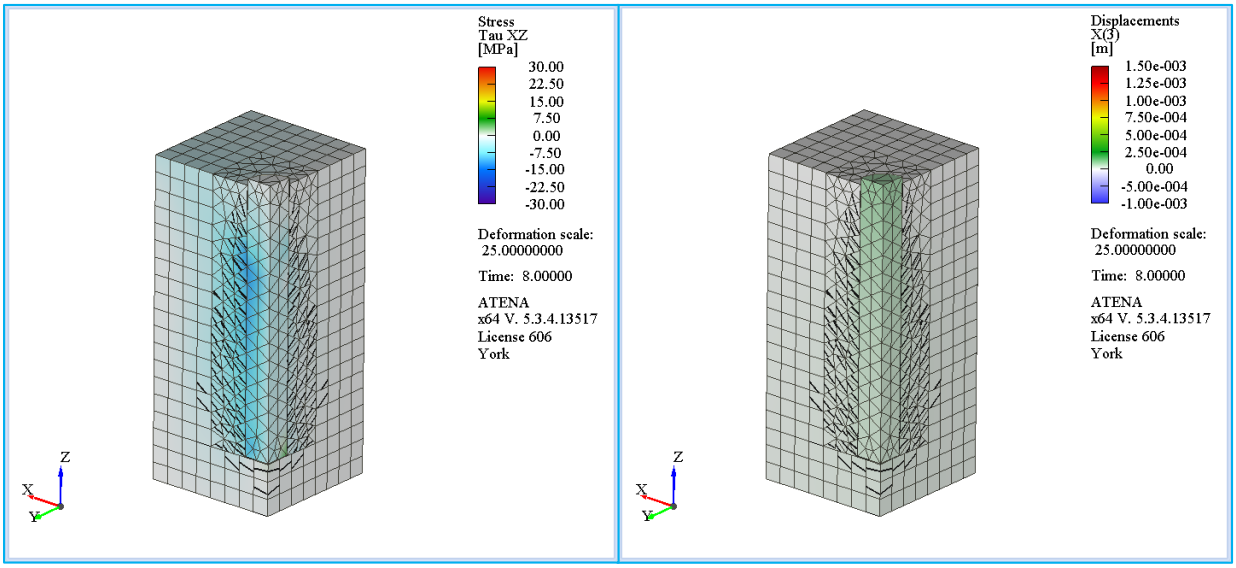

Figure 3-80 Shear stress τ_{xz} and slip Δ_z for Reduced 80x80 with friction (Milestone B).

Point C in the response curve – custom concentric pullout, friction

At milestone C, the specimen has reached approximately 90% of the peak strength and bar displacement of 0.6mm. Multiple cracking patterns have dispersed into the specimen, reaching the top and outer surfaces and weakening the concrete. Crack width has reached a maximum of 1mm under the bar tip at this point. The tensile stresses acting on the bar in the longitudinal direction have begun to decline and do not exceed the 200MPa limit (Figure 3-81). Compressive stresses have perpetrated into the concrete and have exhausted the extent of the available cover. Tensile strains on the bar do not exceed 0.005 whereas on the concrete below the free end of the bar strains reach levels between 0.1 and 0.2. Compressive strains appear on the circumference of the bar reaching values between 0.01 and 0.1. In the transverse direction, tensile stresses have exhausted the extent of the concrete specimen with the maximum values appearing closer to the bar perimeter. The maximum values are 4.0MPa (Figure 3-82). Compressive stresses appear close to the bar-to-concrete interface and reach values between 25MPa and 50MPa. Hoop tensile strains have reached the outer surface of the specimen and reach maximum values between 0.01 and 0.1. Compressive radial strains also exist on the concrete but beyond the process zone of intense cracking which occurs adjacent to the bar, and reach values between 0.001 and 0.005. Shear stresses have diminished on the bar-to-concrete interface signaling the reduction of available contact surface of stress transfer. Higher shear stresses appear in concentrated segments below the midlength of the bar anchorage, reaching a maximum value between -7.5MPa and -15MPa (Figure 3-83). The relative slip at this point is 0.6mm.

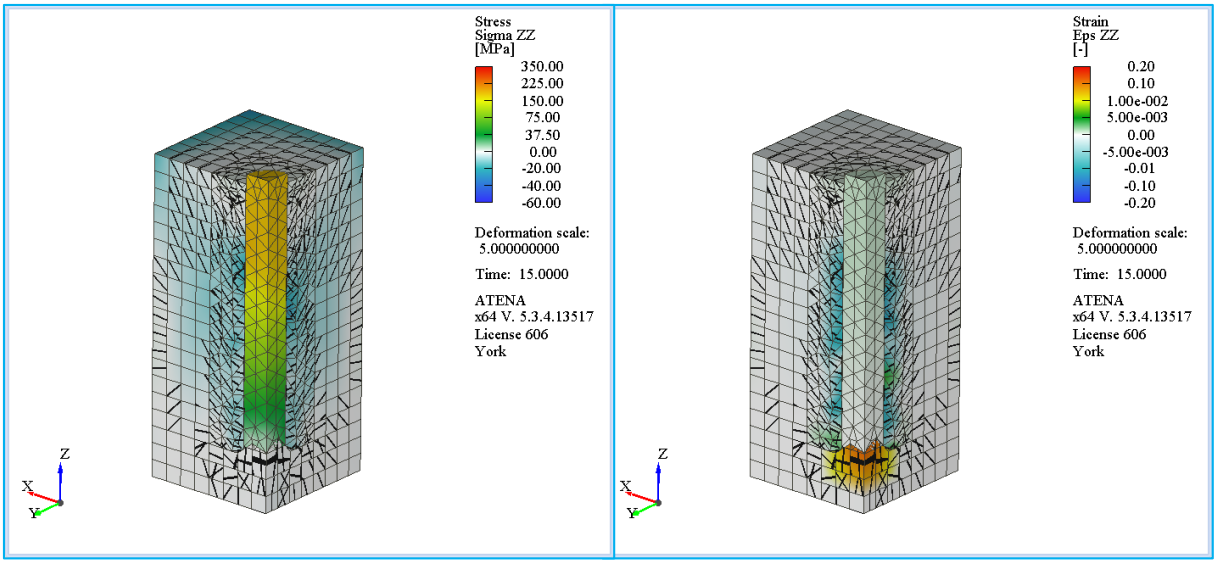

Figure 3-81 Stress σ_{zz} and strain ε_{zz} for Reduced 80x80 with friction (Milestone C).

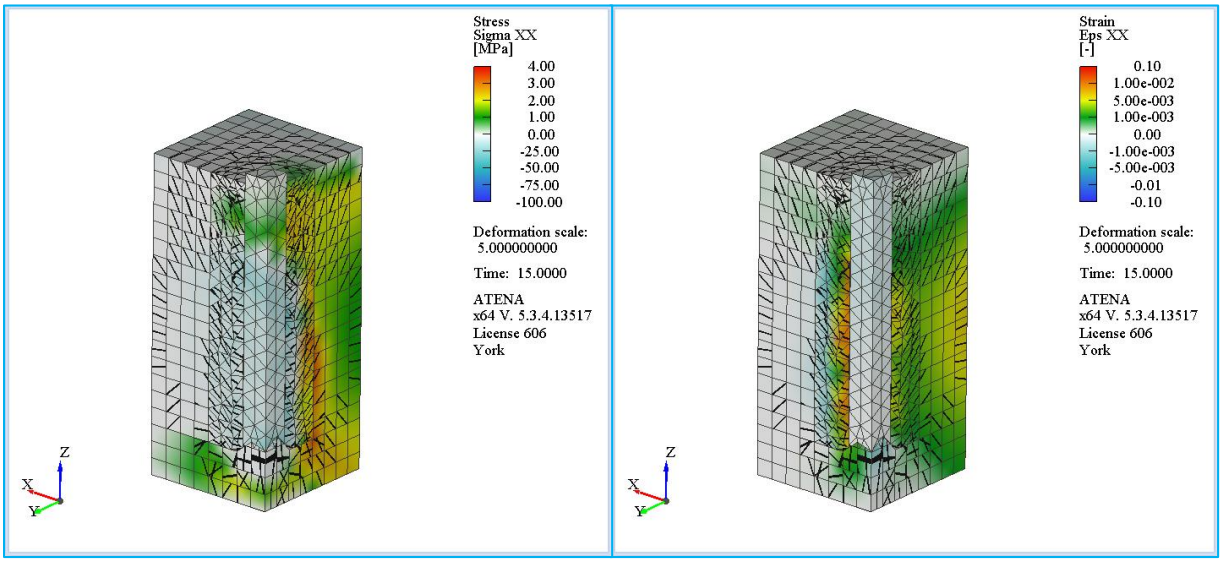

Figure 3-82 Stress σ_{xx} and strain ε_{xx} for Reduced 80x80 with friction (Milestone C).

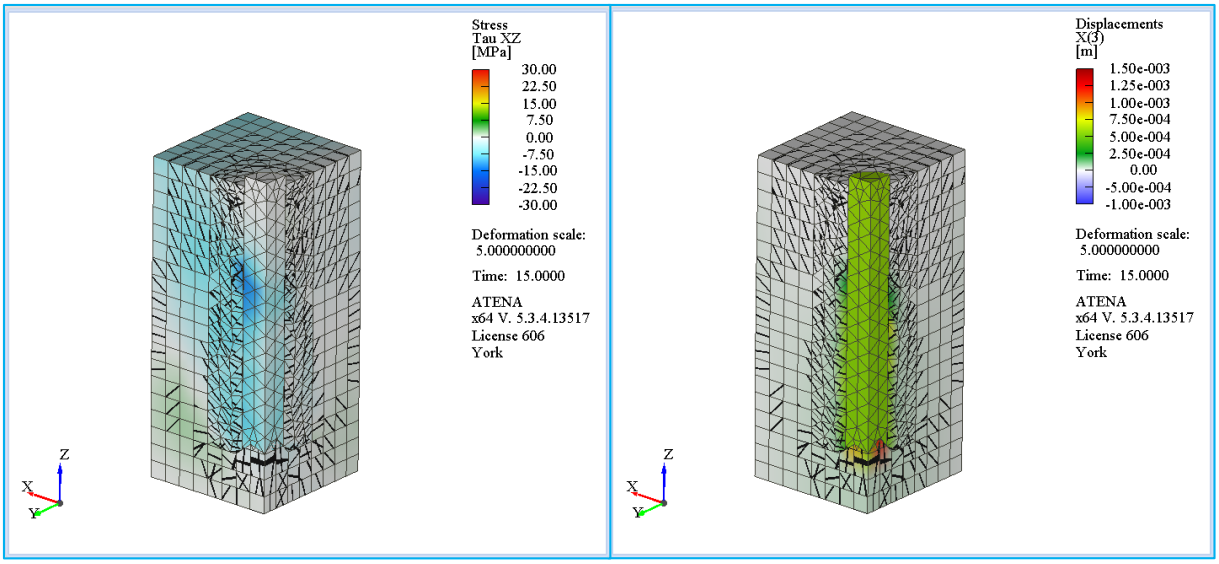

Figure 3-83 Shear stress τ_{xz} and slip Δ_z for Reduced 80x80 with friction (Milestone C).

Point D in the response curve – custom concentric pullout, friction

At milestone D, the specimen has reached approximately 14% of the peak strength and a bar displacement of 1mm. The cracks have essentially covered the entire specimen and no active resistance is obtained. It can be seen that the bar has effectively lost all strength and shows no resistance against the surrounding concrete. Tensile longitudinal strains have dispersed into the concrete with the higher concentration located under the free end of the bar. Values at this point of the analysis are not effectively exact. In the transverse direction, hoop tensile stresses in the concrete cover are residual values, whereas an arching action is clearly illustrated with transverse compressive stresses under the free end of the bar. While stress values have been reduced due to the absence of stress transfer through the bar-to-concrete interface, strain levels have increased to values beyond 0.1 (Figure 3-85). Compressive strains also exist on the concrete away from the process zone that has formed around the bar perimeter. Shear stresses have effectively diminished, as the interface between steel and concrete is eradicated. The bar is free to be removed from the concrete while encountering minimal resistance from the cover (see the uniform translation of the bar in Figure 3-86). The relative slip is 1mm at this point.

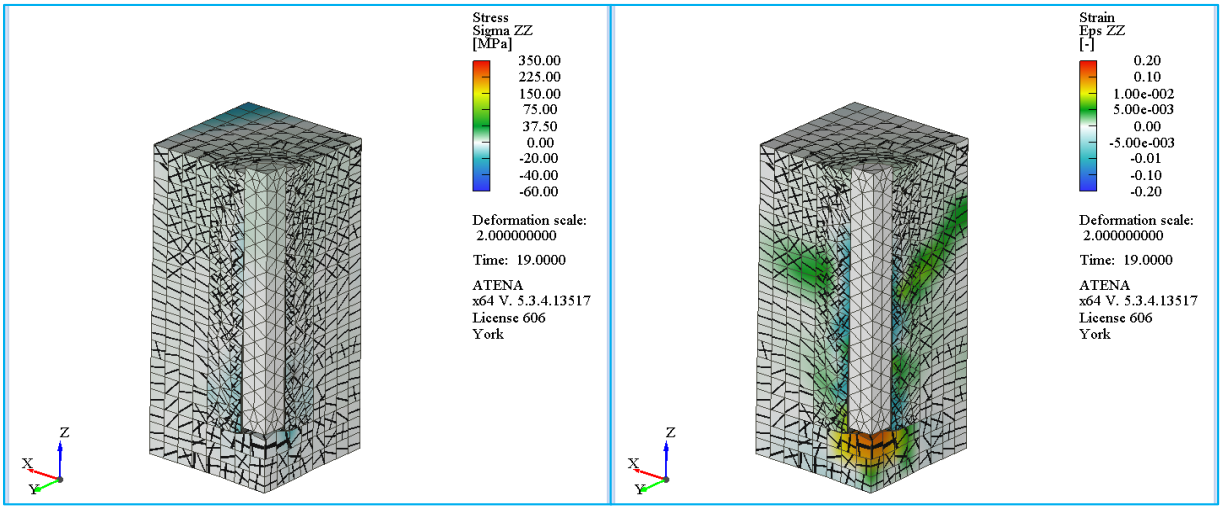

Figure 3-84 Stress σ_{zz} and strain ε_{zz} for Reduced 80x80 with friction (Milestone D).

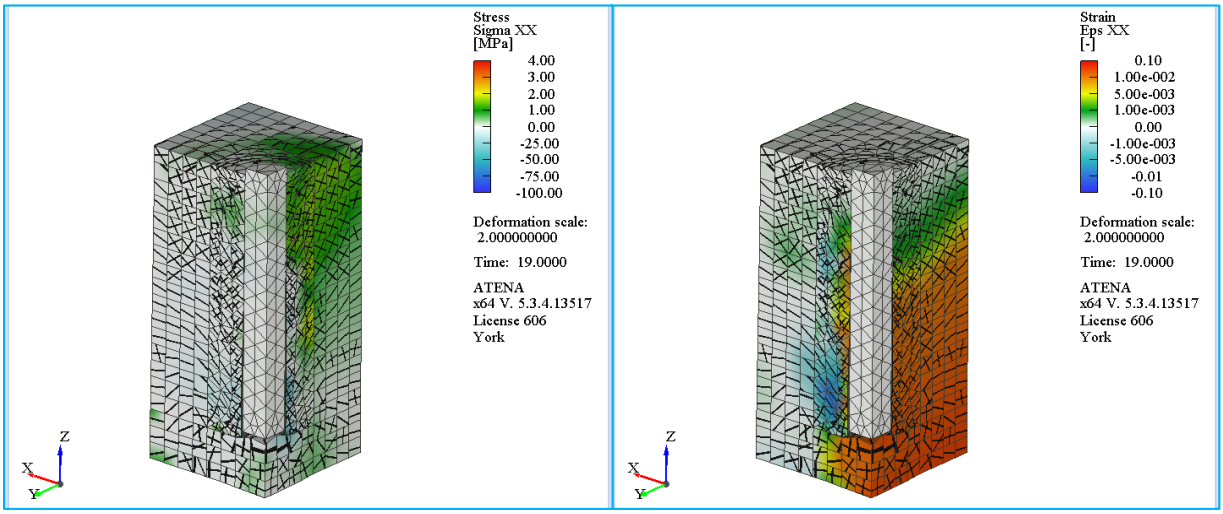

Figure 3-85 Stress σ_{xx} and strain ε_{xx} for Reduced 80x80 with friction (Milestone D).

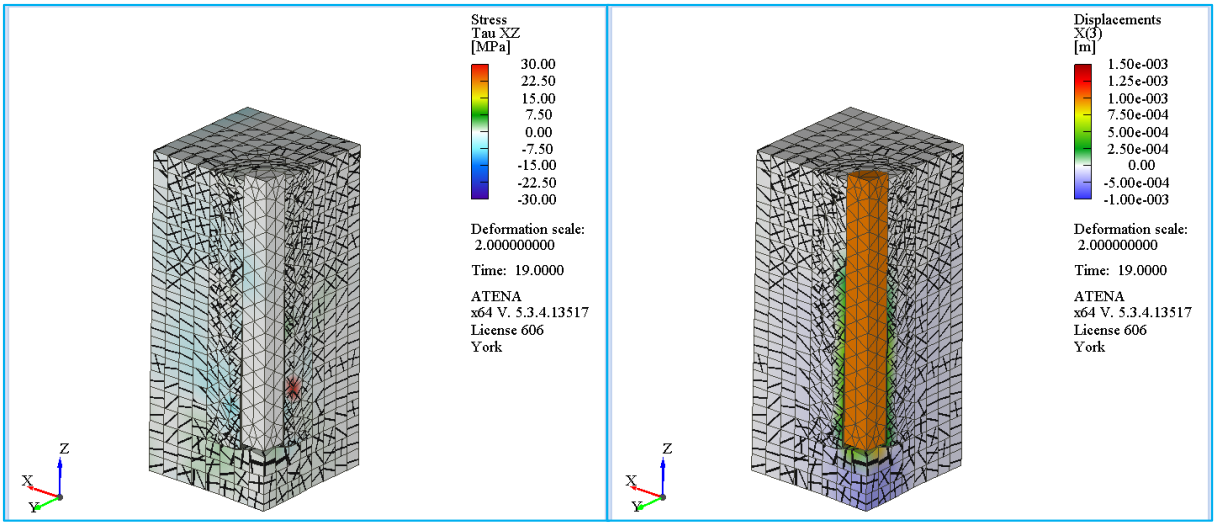

Figure 3-86 Shear stress τ_{xz} and slip Δ_z for Reduced 80x80 with friction (Milestone D).

3.5.1.4 Reduced 80x80 specimen with no friction

This specimen is modeled using the same formulation as the Reduced 80x80 specimen with friction with the only difference that there is no lateral restraint on the top surface of the concrete. Figures Figure 3-87 and Figure 3-88 show the boundary conditions applied on the Reduced 80x80 model with no friction and the force – displacement curve from this specimen, respectively.

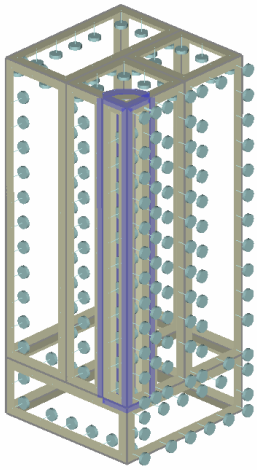

Figure 3-87 Boundary conditions for the Reduced 80x80 model with no friction.

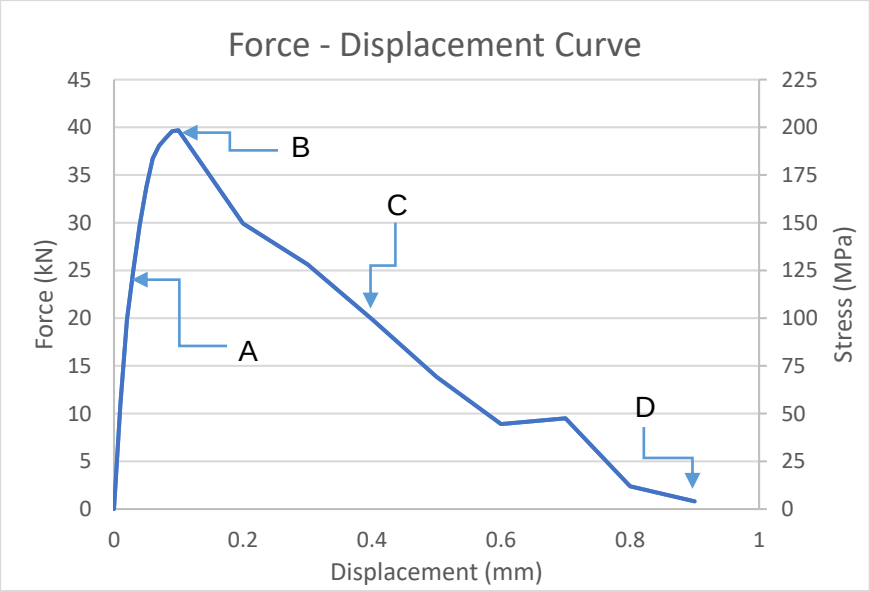

Figure 3-88 Force – Displacement curve for Reduced 80x80 with no friction.

The analysis reached the total displacement of 0.9mm with a maximum applied load of 39.7kN. The resistance increased until reaching the strength followed immediately by a post-peak descending branch. The analysis was terminated for strength values lesser than 2kN.

Point A in the response curve – custom concentric pullout, no friction

At milestone A, the specimen has reached approximately 63% of the peak strength and bar displacement of 0.03mm. Crack width does not exceed 0.0075mm at this point and the peak value occurs under the bar. According to Figure 3-89, tensile longitudinal stresses on the bar reach a maximum of 150MPa limit and they reduce progressively starting from the loaded end to the free end. Corresponding longitudinal compressive stresses accumulate on the top concrete surface reaching values up to -20MPa, due to the reactive stress imposed by the pressing plate. Inclined cracking patterns emanate on the concrete close to the bar, with some of them spread reaching the top surface of the specimen. Tensile strains follow the same pattern as the corresponding stresses, reaching values slightly less than 0.005. Hoop tensile strains accumulate on the perimeter of the bar and the bottom concrete under the free end of the bar. The upper segment of the concrete around the bar sustains compressive strains as the result of the bearing against the plate. In the transverse direction, tensile hoop stresses accumulate on the top segment of the bar and reach values up to 4MPa, and they have dispersed through the thickness of the concrete cover, not exceeding values of 1.5MPa (Figure 3-90). Compressive strains act on the bar as the reaction of the bar pressing and shearing at the same time on the concrete surface and do not

exceed values beyond 0.0002. Shear stresses appear on the interface engaging the major portion of the bar surface as the interface has not exceeded its tensile capacity yet; absolute values of the shear stress do not exceed the 10MPa (Figure 3-91). The relative slip at this point is 0.03mm.

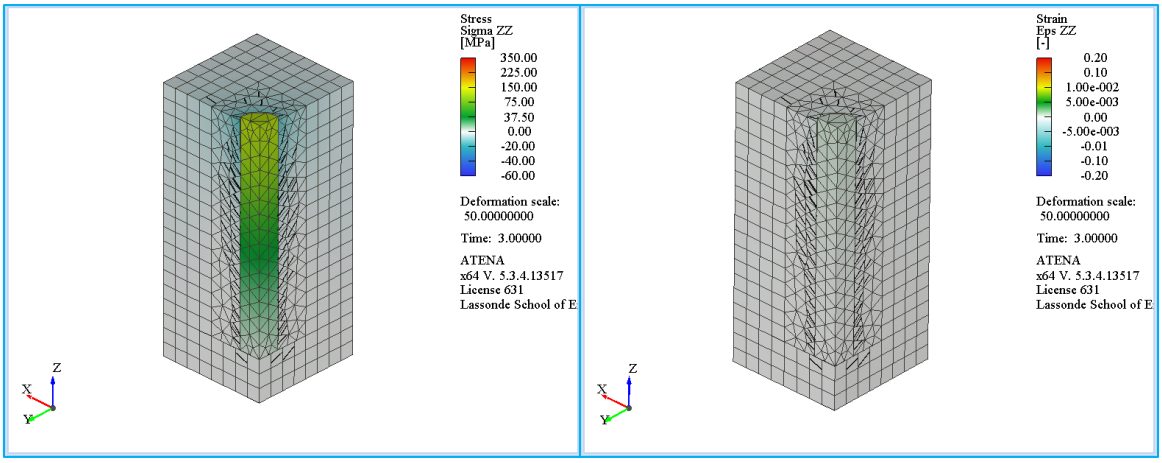

Figure 3-89 Stress σ_{zz} and strain ε_{zz} for Reduced 80x80 with no friction (Milestone A).

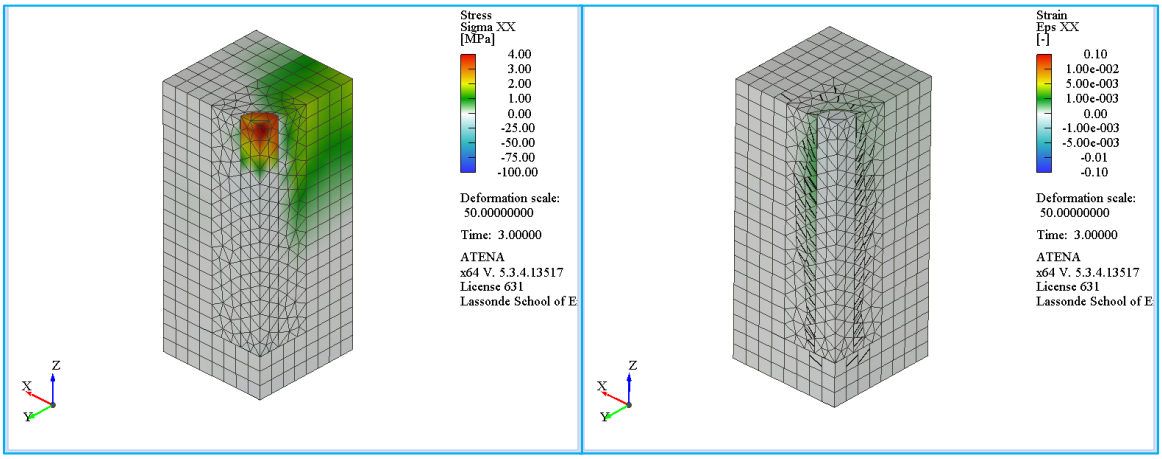

Figure 3-90 Stress σ_{xx} and strain ε_{xx} for Reduced 80x80 with no friction (Milestone A).

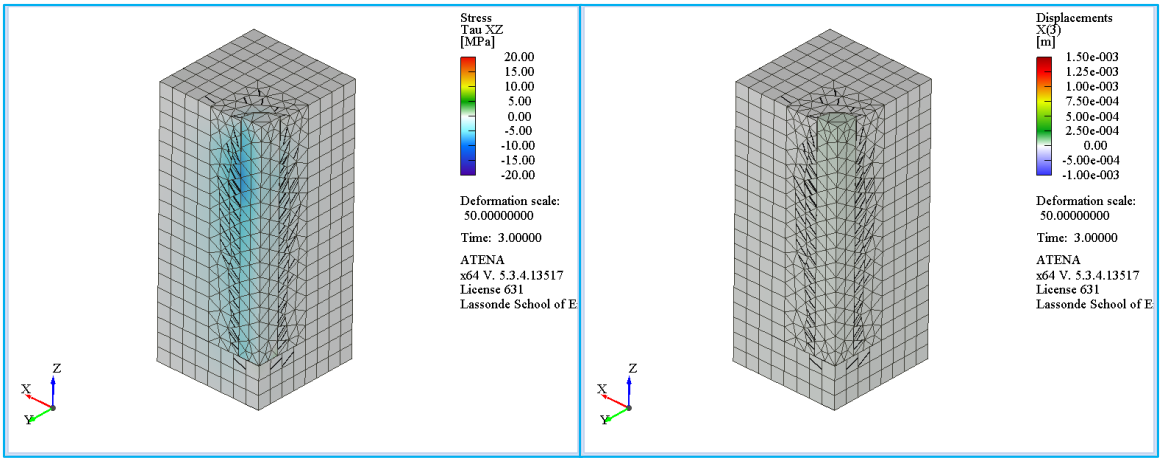

Figure 3-91 Shear stress τ_{xz} and slip Δ_z for Reduced 80x80 with no friction (Milestone A).

Point B in the response curve – Reduced concentric pullout, no friction

At milestone B, the specimen has reached 100% of the peak strength and bar displacement of 0.1mm. Cracking has spread to the outer surfaces of the specimen, resembling splitting cracks on the outer elements. Crack widths do not exceed 0.027mm. The longitudinal tensile stresses on the bar have reached 200MPa and they decrease from the loaded end towards the free end. Compressive stresses appear on the surface of the concrete, as the concrete ring becomes engaged against the resisting plate. Tensile strains increase both on the bar and the concrete with increasing values not more than 0.005 on the concrete under the free end of the bar. Minor compressive strains remain on the concrete surrounding the upper segment of the bar (Figure 3-92). Transverse hoop tensile stresses have dispersed across the larger part of the concrete specimen and values up to 4MPa appear closer to the bar stress zone. The stresses on the bar have incidentally been reduced due to the lesser resistance from the concrete. Compressive stresses gather under the free end of the bar creating arching, as the contact surface is resisting the movement of the bar. Transverse tensile strains appear in the same locations as the tensile stresses on the concrete with a higher accumulation closer to the bar perimeter, reaching values between 0.001 and 0.005 (Figure 3-93). Compressive strains act on the bar reaching minor values, lesser than 0.001. Shear stresses appear on the interface between bar and concrete with a greater accumulation to the lower part of the interface. This signals the loss of the interface strength in the upper part of the bar. The bond strength values reach up to -12MPa (Figure 3-94). The relative slip is 0.1mm at this point.

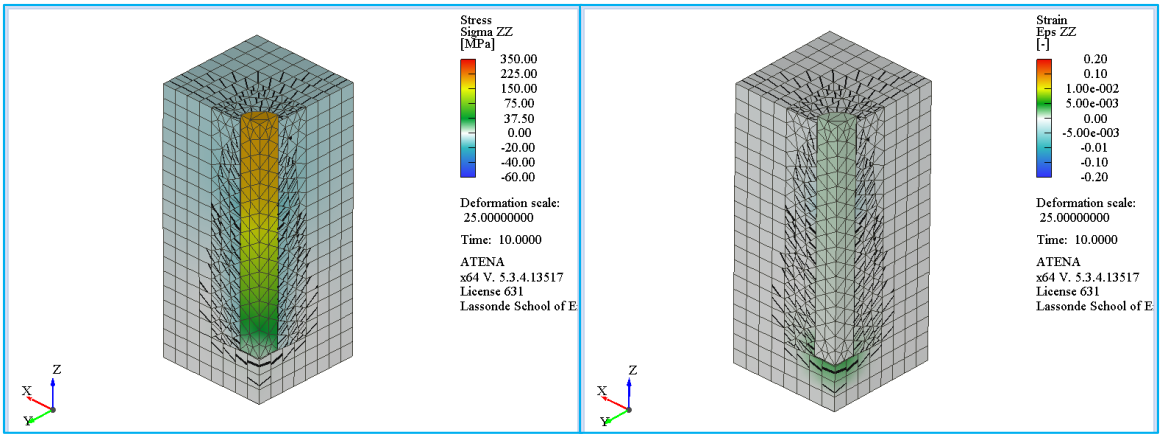

Figure 3-92 Stress σ_{zz} and strain ε_{zz} for Reduced 80x80 with no friction (Milestone B).

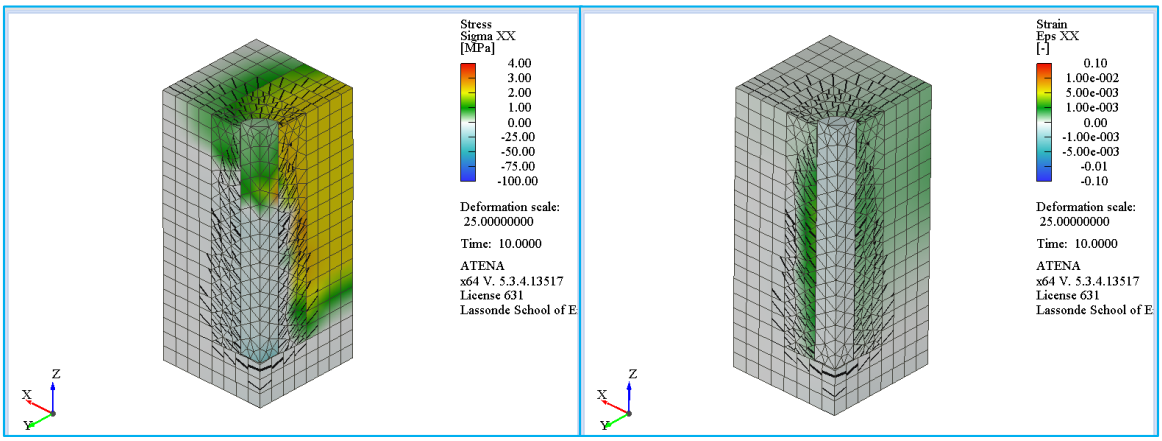

Figure 3-93 Stress σ_{xx} and strain ε_{xx} for Reduced 80x80 with no friction (Milestone B).

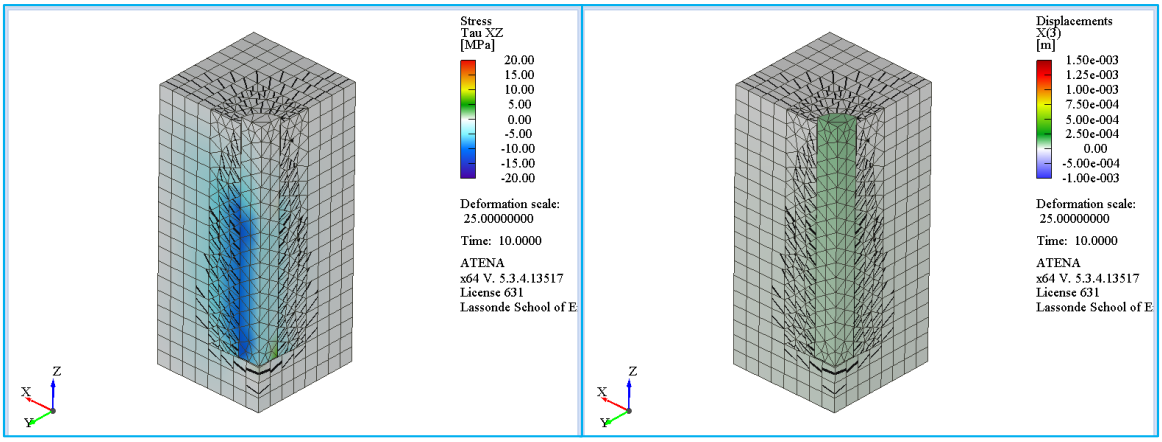

Figure 3-94 Shear stress τ_{xz} and slip Δ_z for Reduced 80x80 with no friction (Milestone B).

Point C in the response curve – reduced concentric pullout, no friction

At milestone C, the specimen has degraded to approximately 50% of the peak strength at a bar displacement of 0.4mm. Cracks have reached the outer surfaces of the specimen and have spread horizontally and vertically. The maximum crack width at this point is 0.53mm. It can be seen that the bar has lost strength and sustains no more than 100MPa. It can also be seen that a significant portion of the bar has been disconnected from the concrete as the cracks have proliferated through the specimen. Tensile longitudinal strains increase in concrete under the free end of the bar and reach values between 0.01 and 0.1 (Figure 3-95). Corresponding compressive strains appearing on the perimeter of the bar do not exceed values greater than -0.05. In the transverse direction, tensile hoop stresses have exhausted the strength of the engaged concrete and have redistributed to areas that have not yet exhausted the tensile strength of the concrete. The maximum tensile hoop stresses reach up to 4MPa whereas the concrete beyond the extent of the embedded bar develops stresses up to 1.5MPa (Figure 3-96). Tensile strains continue to engage the bigger potion of the concrete specimen, accumulating in segments that have not yet developed cracking. The maximum values appear on the lower part of the concrete surrounding the bar reaching values between 0.01 and 0.1. Compressive strains appear on the yet uncrushed concrete in close proximity with the bar but outside the process zone having absolute values as high as 0.05. Shear stresses have moved to the lower part of the bar as the interface between steel and concrete has exhausted its capacity. Shear stresses are in the range of -10MPa around the bar (Figure 3-97). The relative slip is around 0.4mm.

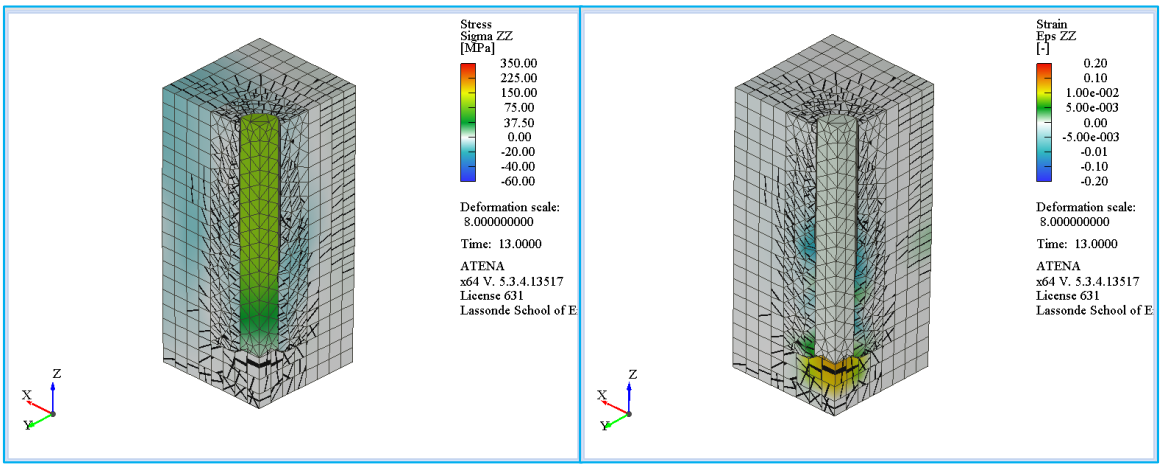

Figure 3-95 Stress σ_{zz} and strain ε_{zz} for Reduced 80x80 with no friction (Milestone C).

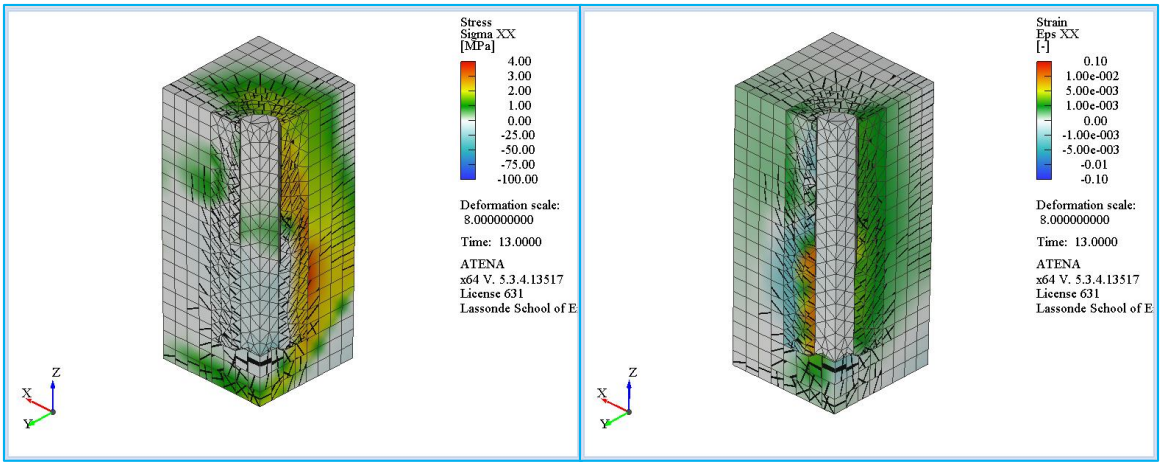

Figure 3-96 Stress σ_{xx} and strain ε_{xx} for Reduced 80x80 with no friction (Milestone C).

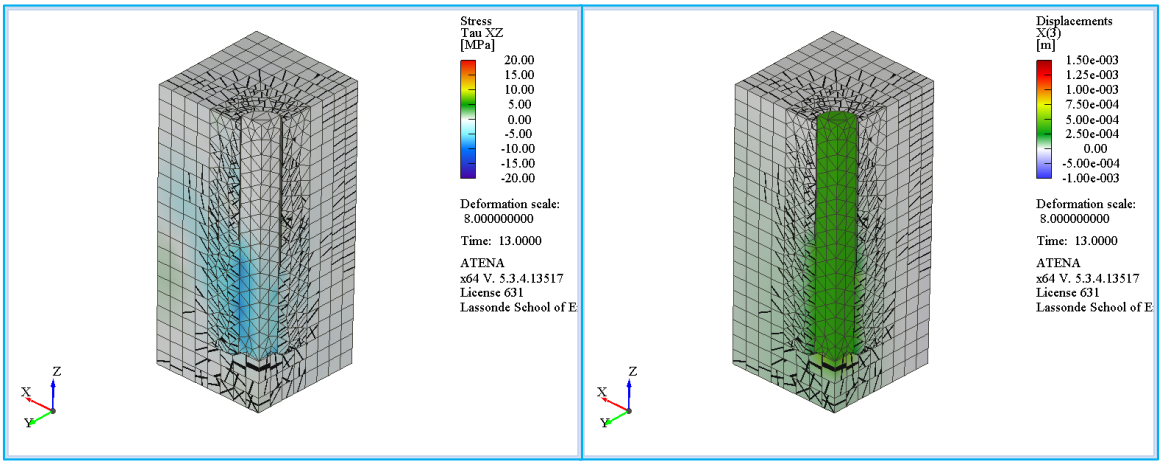

Figure 3-97 Shear stress τ_{xz} and slip Δ_z for Reduced 80x80 with no friction (Milestone C).

Point D in the response curve – Reduced concentric pullout, no friction

At milestone D, the specimen has degraded to approximately 6% of the peak strength and bar displacement of 0.8mm. Cracking has divulged in the majority of the concrete specimen and has exhausted the strength of the concrete ring. The maximum crack width at this point is 0.9mm. It is evident that the tensile stresses on the bar have been reduced as there is no bearing of the bar against the concrete. Tensile strains remain on the lower parts of the concrete volume with the higher intensities closer to the free end of the bar, reaching values of 0.1. Minor residual compressive strains remain close to the periphery of the bar reaching to values between -0.01 and -0.1 (Figure 3-98). In the transverse direction, hoop tensile stresses engage the yet active part of the concrete specimen with a significant portion of the outer ring to have lost its capacity

to carry stress. The maximum stresses are located near the lower part of the specimen and reach values up to 4MPa (Figure 3-99). Radial compressive stresses still act on the lower part of the specimen close to the bar free end, reaching a localized magnitude of -50MPa. Residual tensile strains still remain on the concrete and have retracted to the zones where concrete is still able to undergo deformation. The tensile strains peak at values between 0.01 and 0.1 while residual compressive strains that accumulate close to the bar perimeter reach values between -0.01 and -0.05 (at these strain levels the concrete cannot carry compression). Shear stresses have been reduced to the bottom part of the bar, which is the remaining segment of the interface that can still transfer load between steel and concrete. Positive and negative values of shear stress develop on the concrete further away from the bar and the maximum values for each do not exceed 5MPa and -10MPa, respectively (Figure 3-100). The relative slip at this point is 0.8mm.

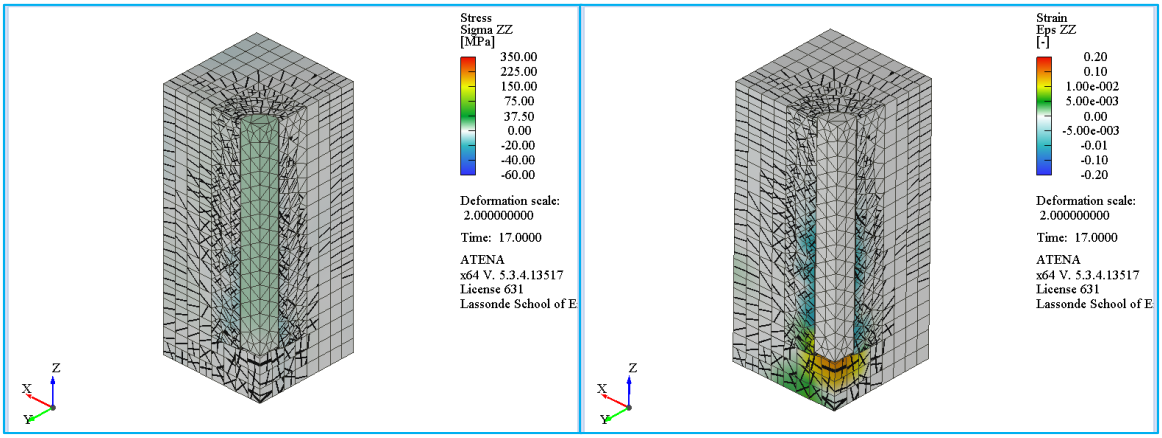

Figure 3-98 Stress σ_{zz} and strain ε_{zz} for Reduced 80x80 with no friction (Milestone D).

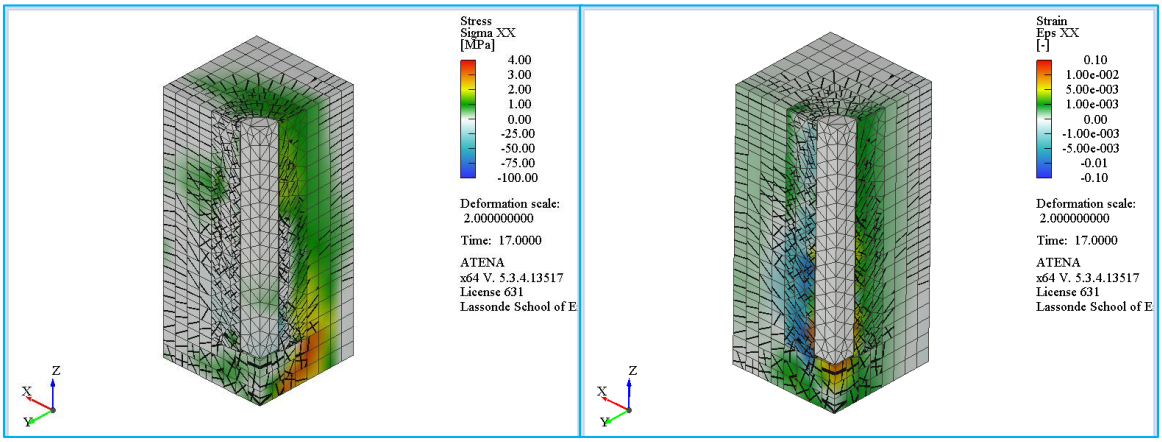

Figure 3-99 Stress σ_{xx} and strain ε_{xx} for Reduced 80x80 with no friction (Milestone D).

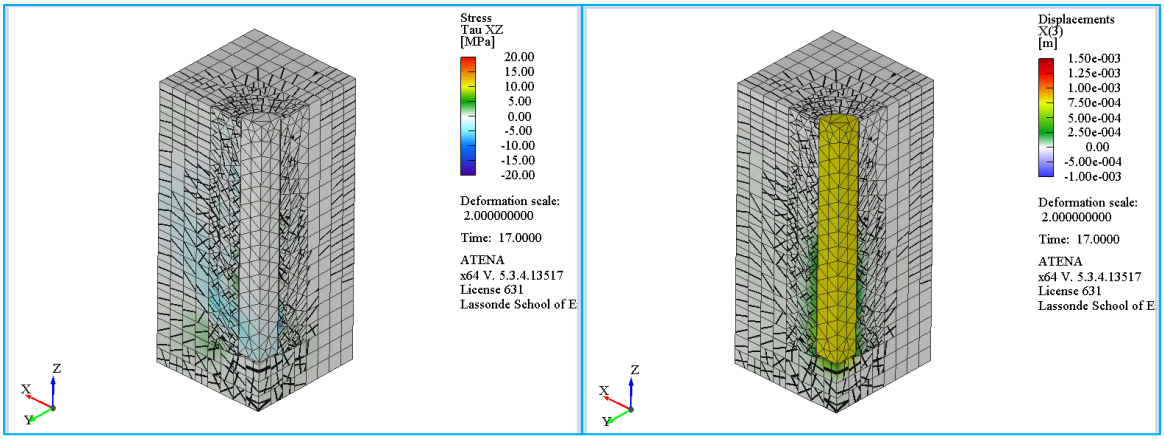

Figure 3-100 Shear stress τ_{xz} and slip Δ_z for Reduced 80x80 with no friction (Milestone D).

3.5.2 Eccentric Pullout Test

As the name suggests, the Eccentric Pullout Test comprises a specimen with an eccentrically embedded test bar. Rather than containing equivalent cover in all directions, in the Eccentric Pullout Test, the controlling cover is located on one side of the specimen. Figure 3-101 shows the section dimensions for this test. The controlling cover is c_2= 32mm is located on the bottom side of the section, whereas the opposing face contains a cover of 72mm. Due to the eccentric placement of the test bar, the section is symmetric in reference to the long edge and 1/2 of the total section area is considered in the model.

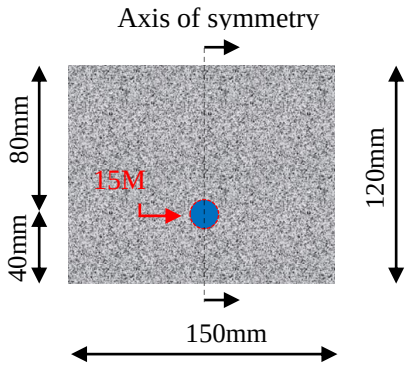

Figure 3-101 Section dimensions for the Eccentric Pullout Test.

The mesh distribution and boundary conditions for this test are shown in Figure 3-102. The model is divided in distinct rectangular macroelements that expedite the use of brick finite elements whereas the bar and the adjacent concrete macroelements are modeled using tetrahedral finite

elements. In this model, quadratic tetrahedral finite elements were used in the bar and concrete cover because of the high density of linear elements that were required.

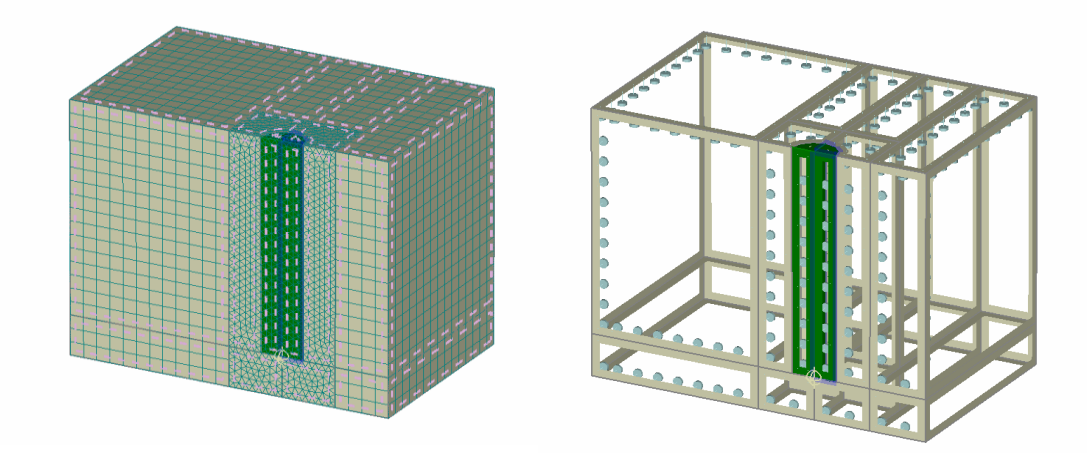

Figure 3-102 Mesh distribution and Boundary conditions for the Eccentric Pullout Test.

The analysis reached the total displacement of 0.8mm with a maximum applied load of 48.85kN. After reaching 44.602K (91.3%) of the total strength, the curve continues to reach the peak strength before rescinding into the descending branch.

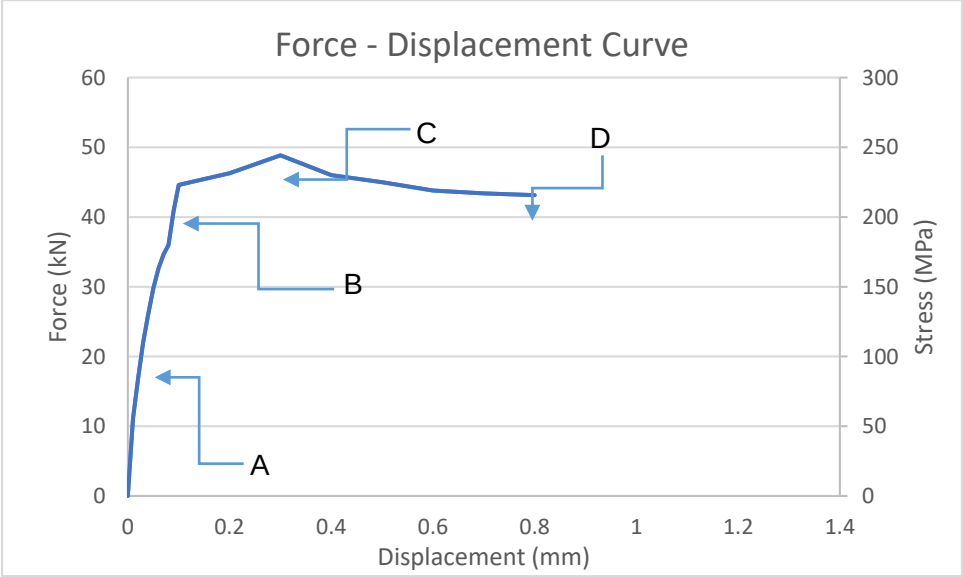

Figure 3-103 Force – Displacement Curve for the Eccentric Pullout Test.

Point A in the response curve – Eccentric pullout test

At milestone A, the specimen has reached approximately 54% of the peak strength and bar displacement of 0.04mm. Cracking emerges on the concrete surrounding the bar and expands to the top surface of the specimen. Vertical cracks reach the extent of the control cover surface whereas inclined cracking appears underneath the free end of the bar resembling the cone-shaped pattern mode encountered in pullout failure. Crack width does not exceed 0.036mm at this point.

Tensile longitudinal stresses accumulate on the bar reaching values of approximately 110MPa. Compressive longitudinal stresses acting on the concrete volume surrounding the bar closer to the loaded end reach values up to -40MPa (Figure 3-104) Tensile longitudinal strains act on the full extent of the bar and on the concrete underneath it. The maximum values of the tensile strains reach an average of 0.001 whereas tensile strain zones can be observed on the far edge of the specimen, opposite to the bar placement. Compressive longitudinal strains act on the top surface of the specimen as a result of the compressive stresses imposed by the bearing plate. The maximum values of these stresses reach between -0.001 and -0.01 and appear extensively on the concrete in close proximity with the bar. Tensile hoop transverse stresses act on the loaded end of the test bar and expand on the concrete specimen along the y-axis. The maximum positive values in the bar do not exceed 25MPa whereas the compressive transverse stresses acting on the free end of the bar reach values up to -75MPa (Figure 3-105). Compressive radial transverse stresses additionally appear on concrete surrounding the upper segment of the bar as a result of the lateral expansion of the concrete bearing against the supporting plate. Tensile transverse strains appear on the concrete surrounding the bar reaching values up to 0.02 whereas values up to 0.0001 appear on the specimen surfaces farther away from the bar. Compressive transverse strains congregate on the upper segment of the bar and the surrounding concrete with the highest values reaching up to -0.0025. Shear stresses of opposing directions appear anti-diametrically on the bar-to-concrete surface. The opposing signs are caused by the eccentric placement of the bar, providing an insight of the effect of bending on the pulled bar. Both positive and negative shear stresses do not exceed the absolute value of 10MPa (Figure 3-106). The relative slip at this point is 0.04mm.

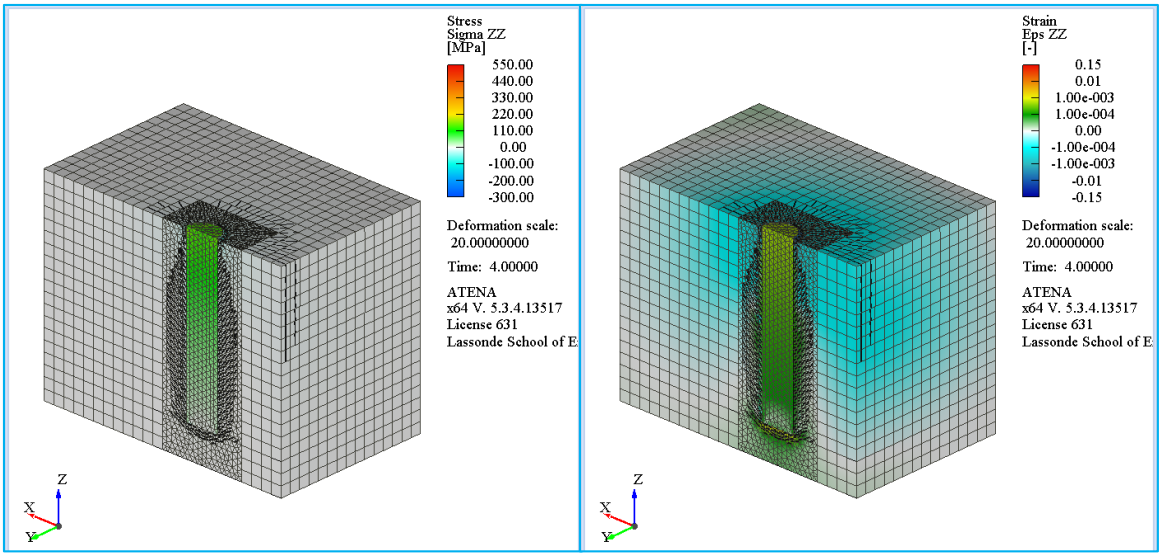

Figure 3-104 Stress σ_{zz} and strain ε_{zz} for the Eccentric Pullout Test (Milestone A).

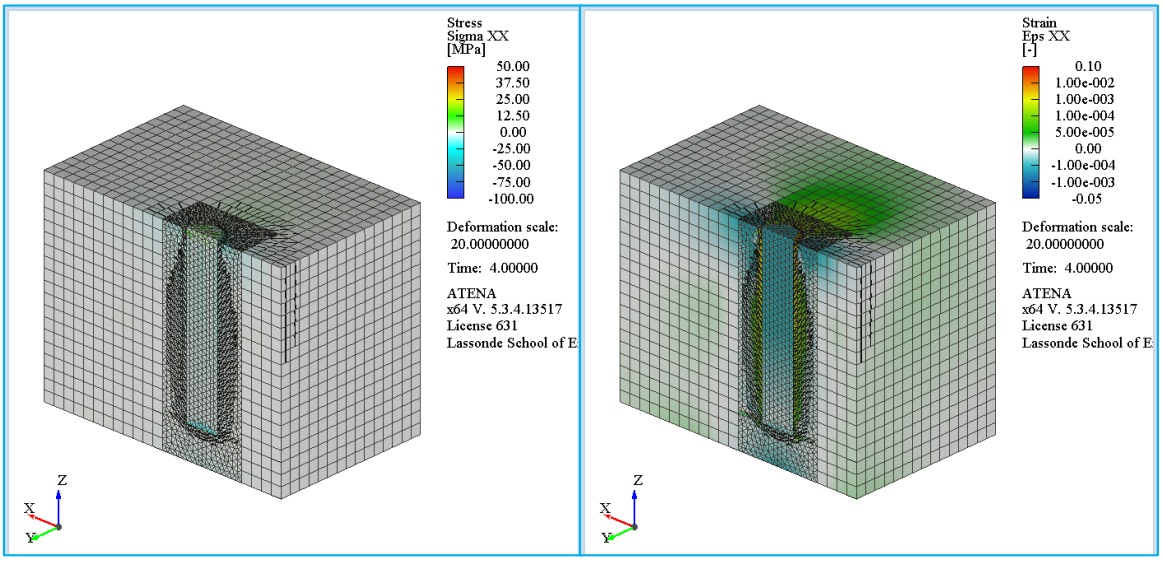

Figure 3-105 Stress σ_{xx} and strain ε_{xx} for the Eccentric Pullout Test (Milestone A).

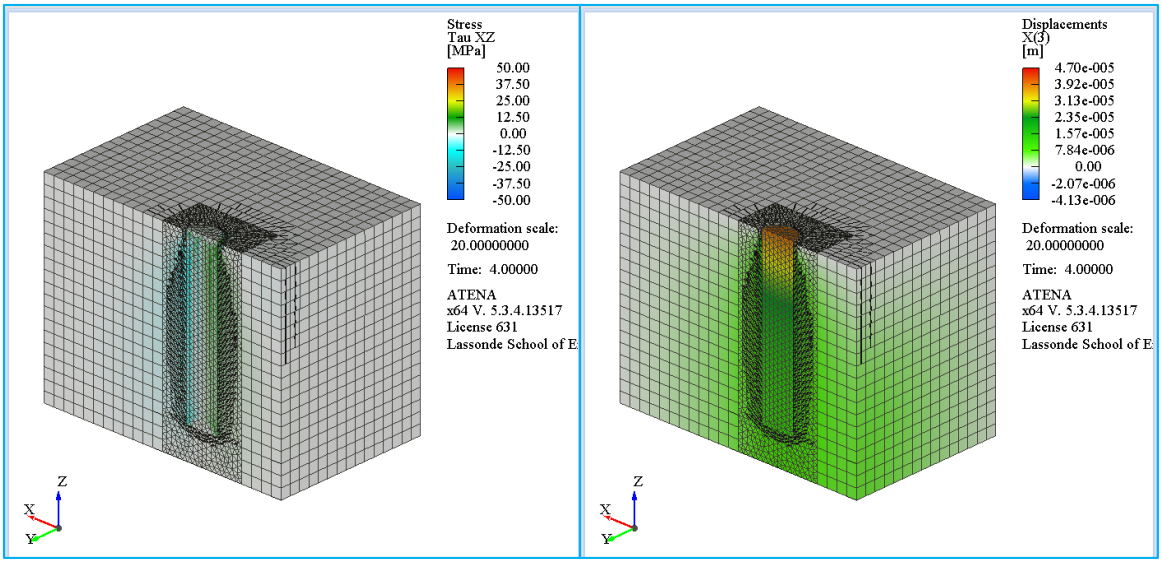

Figure 3-106 Shear stress τ_{xz} and slip Δ_z for the Eccentric Pullout Test (Milestone A).

Point B in the response curve – Eccentric pullout test

At milestone B, the specimen has reached approximately 91% of the peak strength and a bar displacement of 0.1mm. Inclined longitudinal cracking has dispersed further into the specimen, reaching the top surface, while the vertical cracks on the cover surface have progressed towards the free end of the bar. Crack widths do not exceed 0.09mm at this point. According to Figure 3-107, tensile longitudinal stresses acting on the bar have reach approximately 220MPa while the compressive stresses on the concrete surface around the upper segment of the bar reach approximately -180MPa. Tensile longitudinal strains penetrate further into the bar anchorage and in the concrete underneath the free end of the bar reaching to values up to 0.03. Tensile vertical strains also appear on the far edges of the top surface of the specimen. Compressive longitudinal strains increase in range and intensity, reaching up to values of -0.07, with the concentration of higher values closer to the bar-to-concrete interface. Tensile transverse stresses on the bar and upper segment of the concrete specimen have begun to diminish in intensity, caused by the exhaustion of the strength reserves of the interface closer to the loaded end of the bar. Compressive stresses act on the bar free end reach to values up to -87.5MPa (Figure 3-108). Tensile transverse hoop strains increase in range and intensity, reaching values up to 0.04 whereas the compressive radial transverse strains acting on the bar and the surrounding concrete of the upper segment of the specimen reach to values up to -0.008 (i.e. in the postpeak range of the concrete stress-strain behavior. Compressive transverse strains can also be observed on the concrete surrounding the lower part of the bar. Shear stresses appear on the opposing sides of

the bar continue to increase in range and intensity, reaching values up to 12.5MPa on both sides (Figure 3-109). The relative slip at this point is 0.1mm.

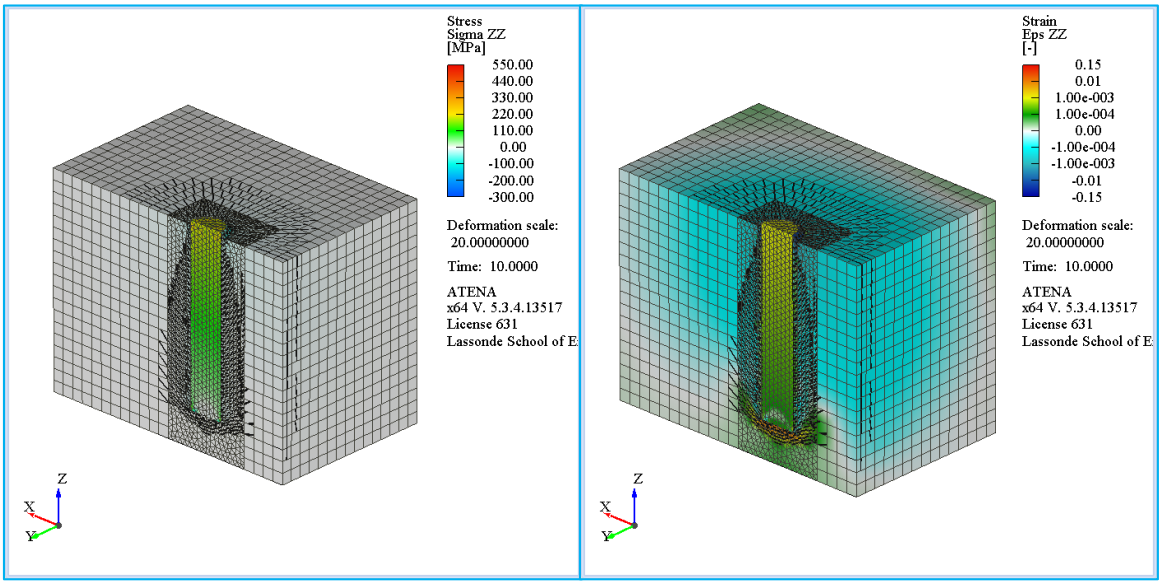

Figure 3-107 Stress σ_{zz} and strain ε_{zz} for the Eccentric Pullout Test (Milestone B).

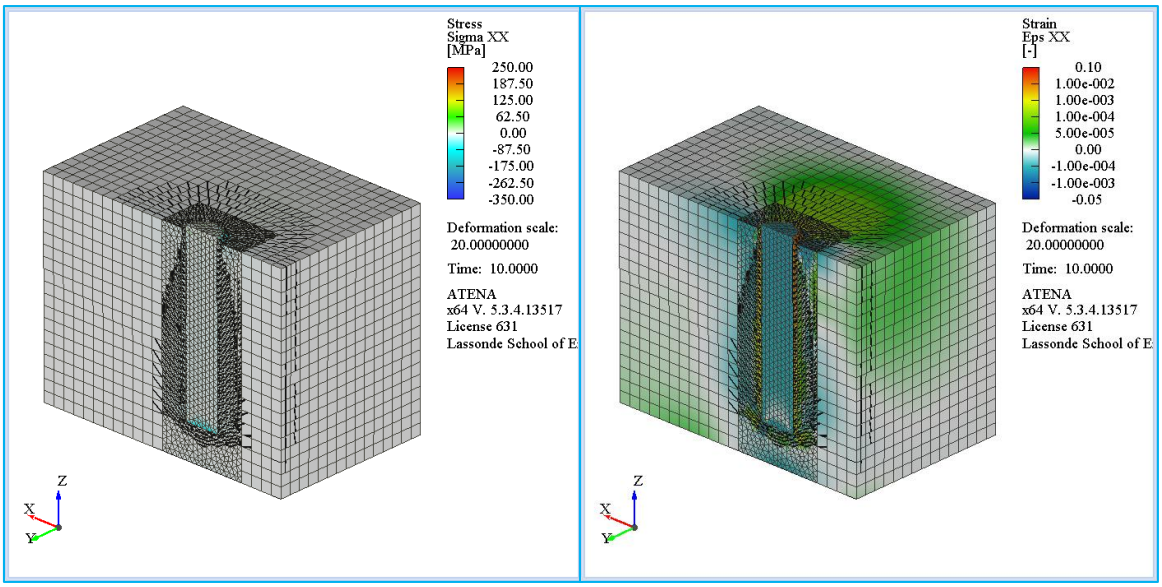

Figure 3-108 Stress σ_{xx} and strain ε_{xx} for the Eccentric Pullout Test (Milestone B).

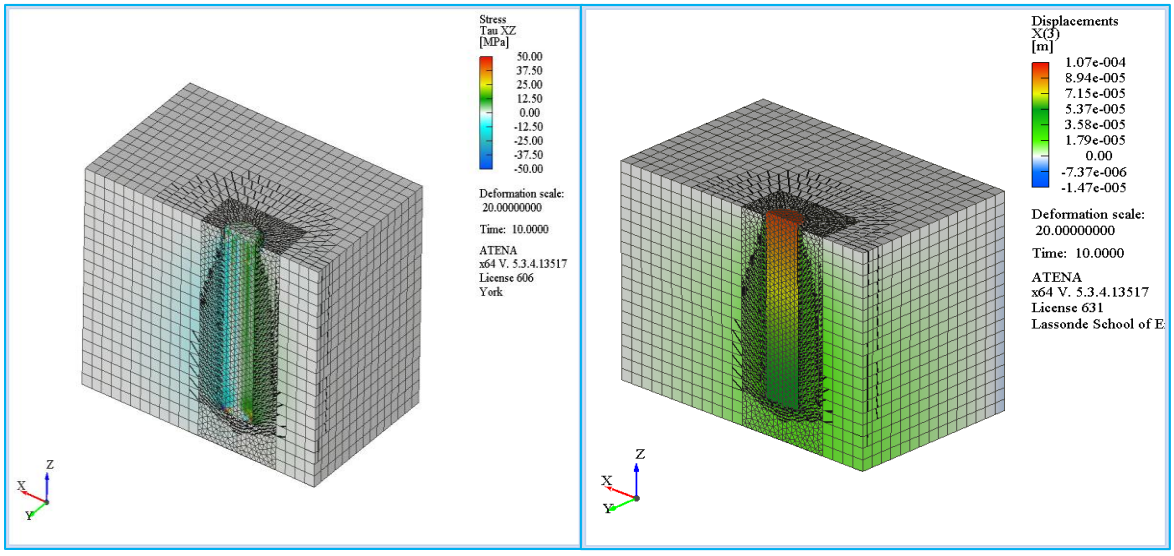

Figure 3-109 Shear stress τ_{xz} and slip Δ_z for the Eccentric Pullout Test (Milestone B).

Point C in the response curve – eccentric pullout test

At milestone C, the specimen has reached 100% of the peak strength and bar displacement of 0.3mm. Crack patterns continue to disperse on the top surface of the specimen, denoting an engaged zone of an elliptical section. Crack widths reach a maximum of 0.11mm at this point. The tensile longitudinal stresses on the bar have reached approximately 250MPa whereas the compressive stresses around the concrete reach -100MPa (Figure 3-110). The higher concentration of compressive longitudinal stresses occurring on the side of the bar facing the control cover surface. That is due to the partial detachment of the upper surface of the specimen from the bearing plate which lead to eccentric compressive stresses to be acting on the specimen. Tensile strains in the longitudinal direction, both on the bar and concrete, continue to increase with the maximum concentrated on the concrete underneath the bar free end, reaching to values of 0.04. Compressive longitudinal strains continue to expand and increase in intensity, reaching values of approximately 0.1. Tensile transverse stresses on the upper segment of the bar and concrete have diminished to values of 25MPa whereas the compressive transverse stresses on the free end of the bar reach -100MPa (Figure 3-111). Transverse strains continue to follow the same pattern as in the previous milestone, hereby increasing to positive (tensile) values of 0.05 and negative (compressive) values up to 0.01. Shear stresses continue to follow the same pattern, with values remaining below 12.5MPa on either side of the bar while the downwards shear stresses on the control cover side of the bar slowly overwhelm the opposing side on account of bending. The relative slip at this point is 0.3mm.

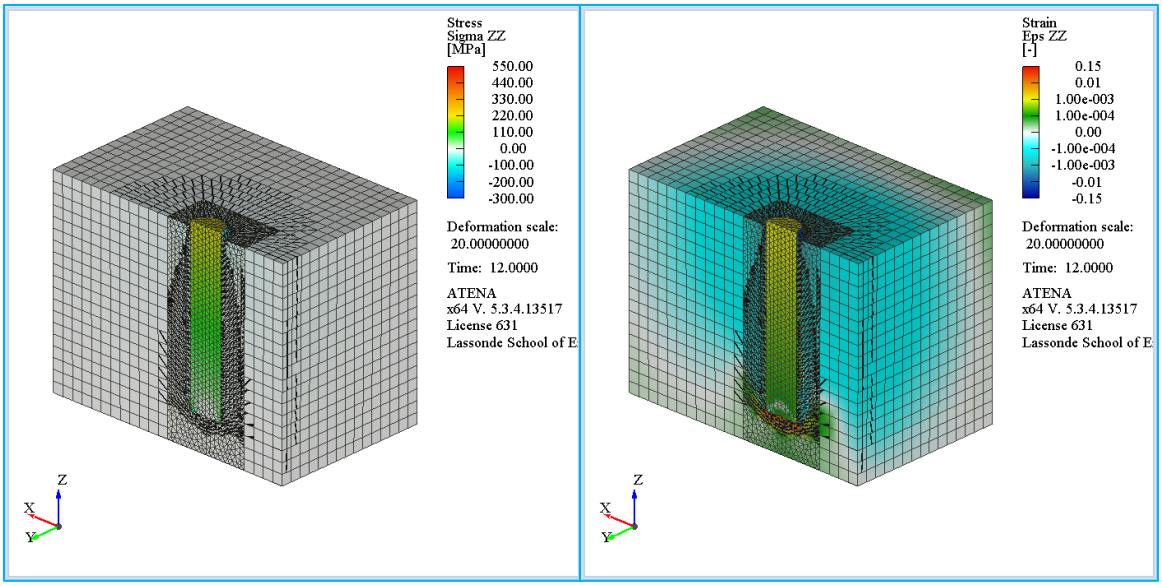

Figure 3-110 Stress σ_{zz} and strain ε_{zz} for the Eccentric Pullout Test (Milestone C).

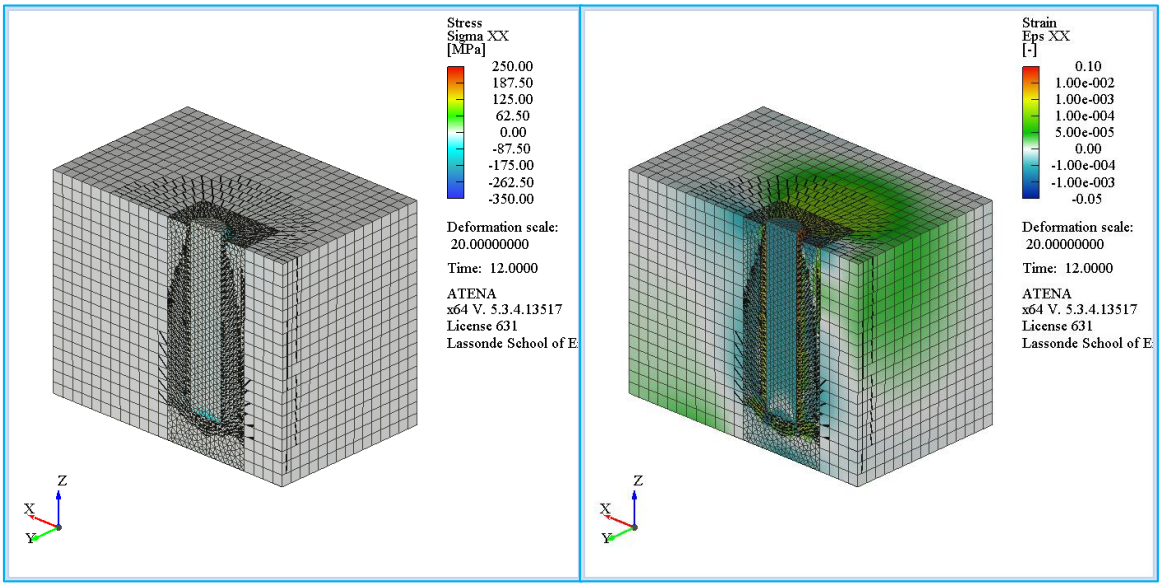

Figure 3-111 Stress σ_{xx} and strain ε_{xx} for the Eccentric Pullout Test (Milestone C).

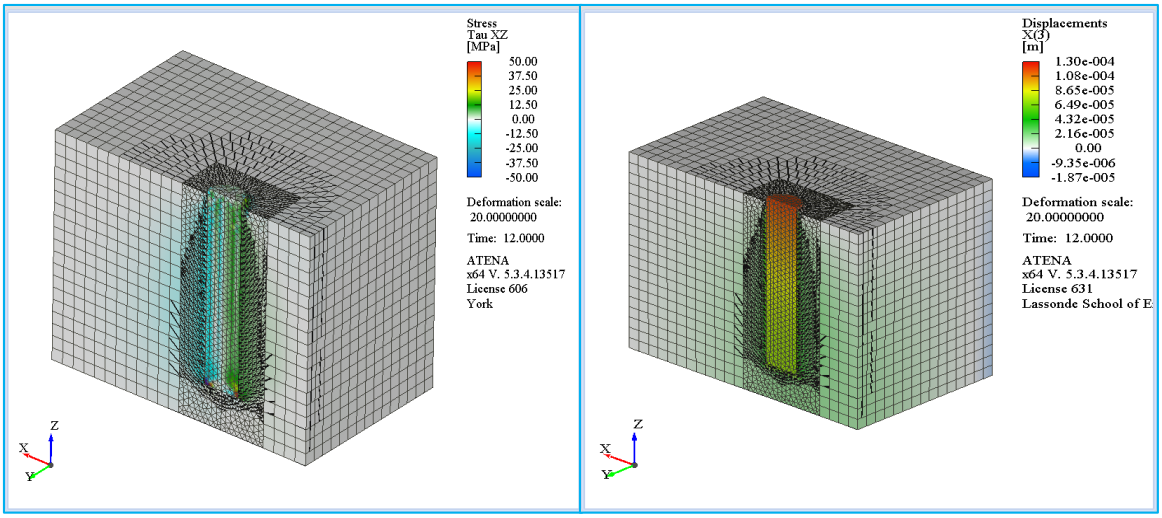

Figure 3-112 Shear stress τ_{xz} and slip Δ_z for the Eccentric Pullout Test (Milestone C).

Point D in the response curve – eccentric pullout test

At milestone D, the specimen has degraded to a residual resistance equal to 88% of the peak strength and bar displacement of 0.8mm. The crack path on the control cover surface has reached the bottom surface of the specimen, denoting the imminent splitting of the weakened surface. Crack width has reached a maximum of 0.21mm (Figure 3-113). Tensile strains in the longitudinal direction, following the same pattern, increase on the concrete underneath the free end of the bar up to values of 0.15 whereas compressive strains remain under 0.15 (both values are excessive so it may be safely surmised that stresses both in the hoop and the radial direction are practically zero (Figure 3-114). Transverse strains continue to follow the same pattern as in the previous milestone, hereby increasing to tensile values of 0.08 and compressive values up to 0.02. Shear stresses, while following the same distribution as before, now have diminished in the upper segment of the bar due to the exhaustion of the bond strength of the interface. This segment of reduced shear stress appears on the bar due to the reduction of the interface strength. The relative slip is 0.8mm.

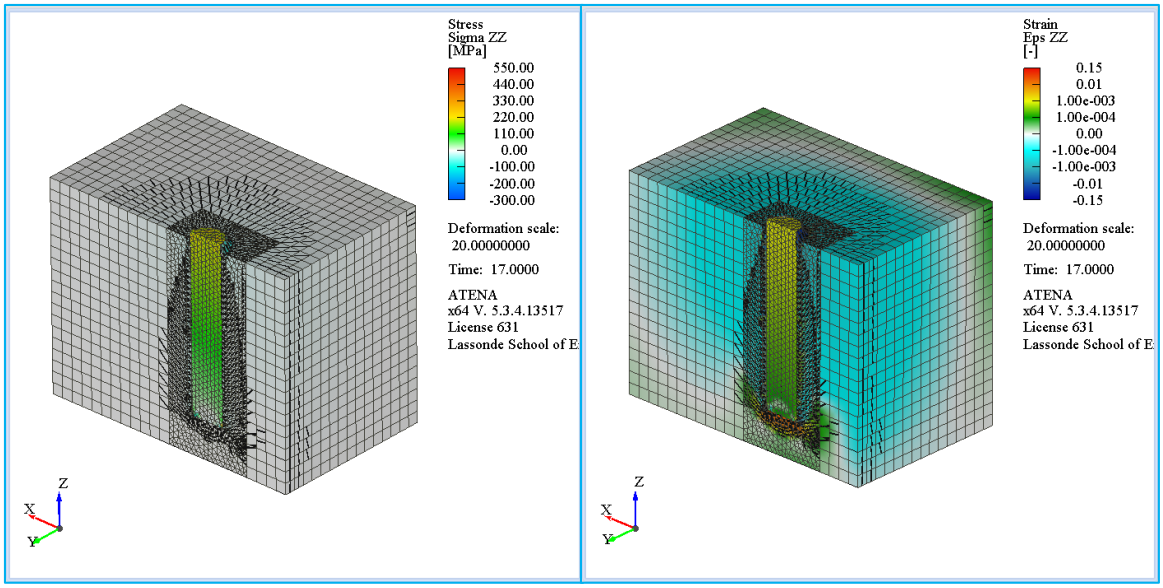

Figure 3-113 Stress σ_{zz} and strain ε_{zz} for the Eccentric Pullout Test (Milestone D).

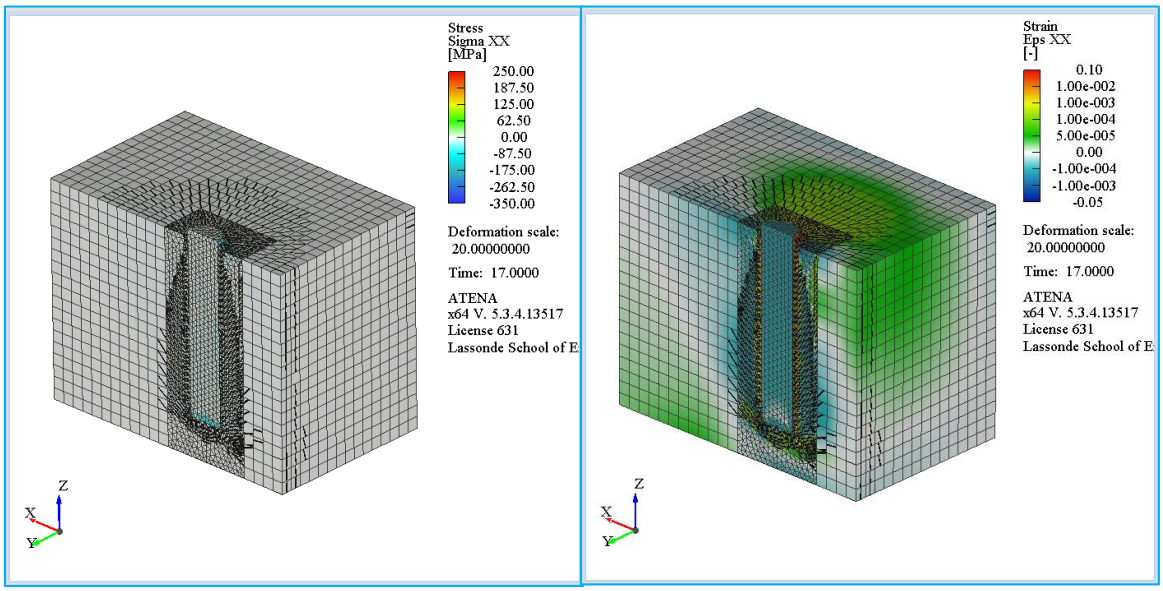

Figure 3-114 Stress σ_{xx} and strain ε_{xx} for the Eccentric Pullout Test (Milestone D).

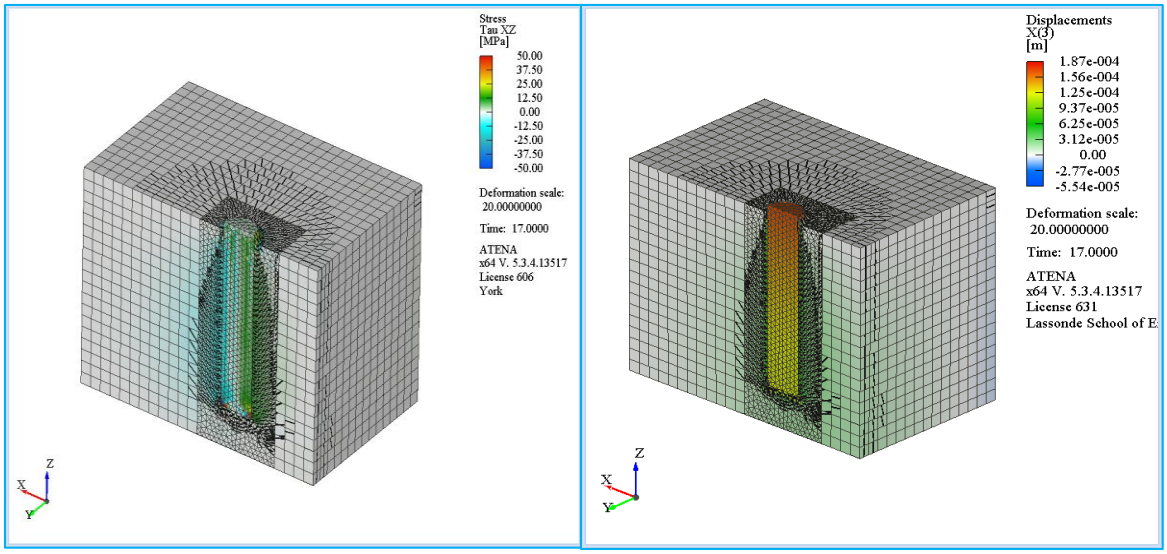

Figure 3-115 Shear stress τ_{xz} and slip Δ_z for the Eccentric Pullout Test (Milestone D).

3.5.3 Simulation of the Direct Tension Pullout test with the Interface Model

The Direct Tension Pullout test is modelled according to the formulation of Model "Interface" described in 3.2.2. The cover distance is c_2 = 32mm and the embedment length l_b = 80mm (=5D_b). The width of the section is 400mm while support conditions are placed on the bottom circular opening. The mesh distribution is shown in Figure 3-18 and the boundary conditions are shown in Figure 3-116.

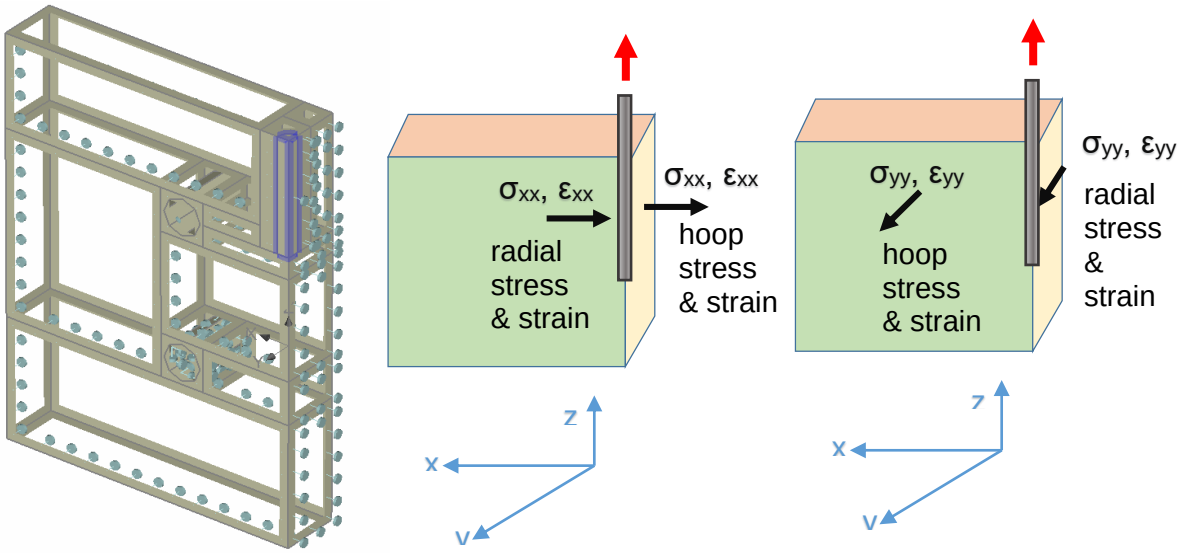

Figure 3-116 (left): Boundary conditions for the Direct Tension Pullout test, (center) and (right): Nomenclature.

The analysis reached the total displacement of 2.5mm with a maximum applied load of 25.844kN. After reaching the peak strength, the load immediately initiated the descending branch, reaching a “plateau” of approximately 7kN.

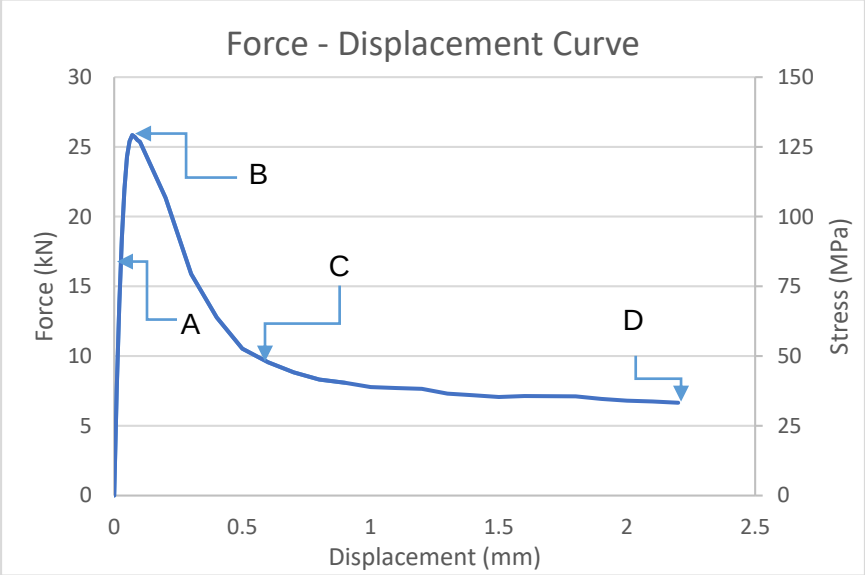

Figure 3-117 Force – Displacement curve for the Direct Tension Pullout test.

Point A in the response curve – direct tension pullout test

At milestone A, the specimen has reached approximately 72% of the peak strength and a bar displacement of 0.03mm. Cracking patterns have started to emanate from the engaged zone around the bar with cracks reaching the outer surface of the concrete specimen. The maximum crack width at this point is 0.0071mm, located on the concrete surface surrounding the test bar. According to Figure 3-118, tensile stress fields in the longitudinal direction have developed in the bar reaching to values no greater than 100MPa with lower stress intensities closer to the free end of the bar. Tensile strains develop on the bar following the same pattern as the tensile stresses. Longitudinal concrete tensile strains appear under the free end of the bar whereas compressive strains appear on the bottom of the lowest circular support and on the outermost concrete surface. Tensile strains do not exceed 0.0005 at this point and compressive strains remain under -0.00005. In the transverse direction, hoop tensile stresses develop from the top surface of the concrete, reaching the extent of the concrete cover and begin to spread towards the side faces of the specimen. Tensile zones begin to accumulate around the horizontal openings whereas the lower

side of the openings sustains a combination of orthogonal trajectories of both tensile and compressive stresses. The highest tensile stresses accumulate at the top of the test bar with a maximum of approximately 4MPa while the maximum compressive stress is located on the free end of the bar at the value of approximately -10MPa (Figure 3-119) Tensile strains develop on the top part of the concrete specimen reaching values not more than 0.0005. The bar sustains compressive strains as the result of the bearing against the concrete with a maximum of approximately -0.0001. Compressive strains additionally develop on the concrete reaching the top surface of the wider dimension, the concrete under the free end of the bar and the top segment of the horizontal support. Shear stresses develop at the interface between steel and concrete with the negative sign denoting the opposite direction along the z-axis: the highest shear stresses are located on the bar-to-concrete interface, reaching values up to -5.0MPa (Figure 3-120). At this stage, the majority of the bar interface is engaged in stress transfer, since the interface's stress limits have not yet been exceeded. Shear stresses also develop on the concrete zone denoted by the bar and the two circular openings. Positive shear stresses also appear on the outer side of the bottom circular support, not exceeding values beyond 1MPa. The relative slip at this point is 0.03-0.0265 = 0.0035mm.

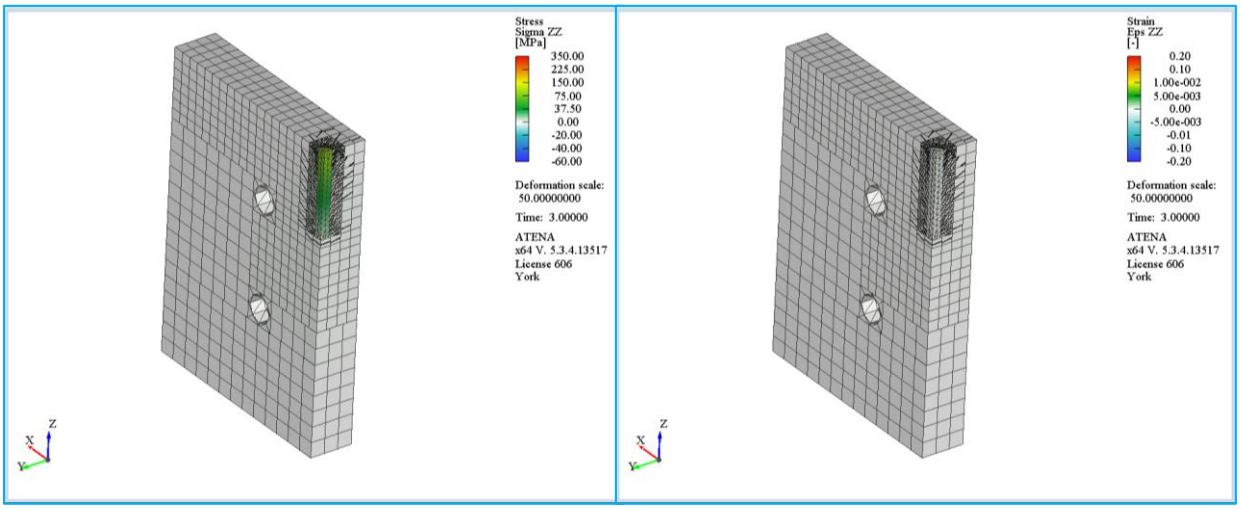

Figure 3-118 Stress σ_{zz} and strain ε_{zz} for Direct Tension Pullout test (Milestone A).

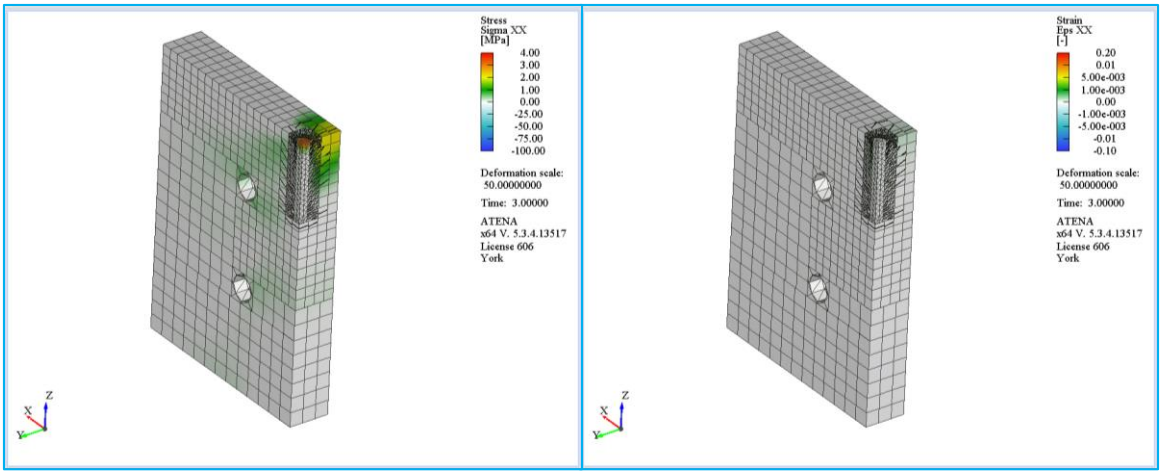

Figure 3-119 Stress σ_{xx} and strain ε_{xx} for Direct Tension Pullout test (Milestone A).

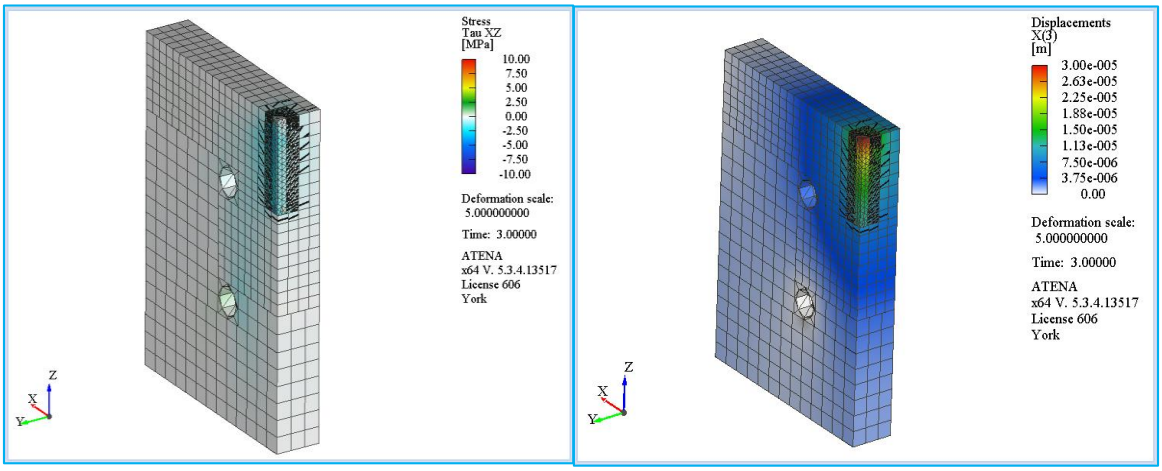

Figure 3-120 Shear stress τ_{xz} and slip Δ_z for Direct Tension Pullout test (Milestone A).

Point B in the response curve – direct tension pullout test

At milestone B, the specimen has reached 100% of the peak strength and bar displacement of 0.07mm. Cracks have proliferated to the cover surface of the specimen while horizontal cracks have reached the top layer of circular openings. The maximum crack width reaches 0.034mm at this point. Longitudinal tensile stresses in the bar have reached the maximum value of 130MPa while negative stresses (radial) act on the concrete perimeter zone around the bar, not exceeding -5MPa (Figure 3-121). Negative (compressive) values additionally appear on the outer surface of the farthest dimension and on the bottom of the lower horizontal opening. Minor tensile stresses appear on the concrete between the circular openings and the bar, not exceeding 3MPa. Tensile strains envelop the bar and the concrete adjacent to it. Contrary to the concentric and eccentric

setup, the concrete is not restrained to vertical displacement at the top and therefore no opposing compressive fields are developed during the displacement of the bar. The maximum tensile strains are located directly below the free end of the bar, where the concrete sustains strains up to 0.00043. Negative strains appear on the bottom side of the circular support and on the surface of the largest dimension, reaching a maximum strain lesser than -0.0001. Hoop tensile stresses in the transverse direction have enveloped both the bar and the concrete specimen, exceeding even the zone denoted between the circular openings and the test bar. The loaded end of the bar undergoes a maximum lateral stress of approximately 5MPa whereas the concrete around it reaches up to approximately 3MPa (Figure 3-122). Compressive radial transverse stresses are observed on the free end of the bar reaching up to values between -25 and -50MPa. Positive transverse strains appear on the concrete surrounding the upper segment of the bar and spread until the cover surface to a maximum of 0.004, located next to the bar-to-concrete interface. Negative shear stresses developing on the bar-to-concrete interface reach a value of -7.5MPa (Figure 3-123). The majority of the bar surface engages the specimen while a small portion on the top segment has become disconnected. This denotes exceedance of the local bond strength of the interface. Positive shear stresses are observed on the outer side of the bottom circular support and on the upper concrete specimen on the outer face of the largest dimension. The relative slip is approximately 0.07- 0.0612 = 0.0088mm.

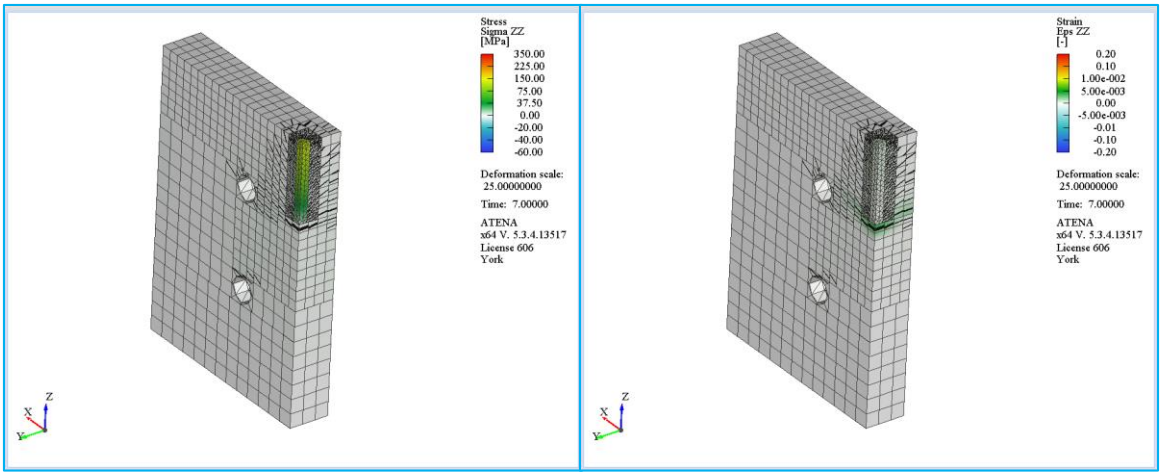

Figure 3-121 Stress σ_{zz} and strain ε_{zz} for Direct Tension Pullout test (Milestone B).

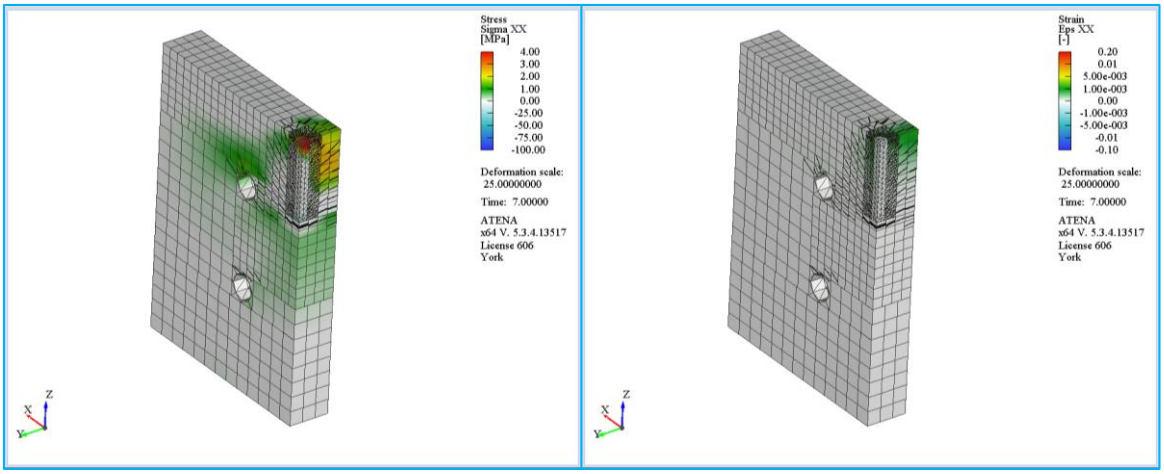

Figure 3-122 Stress σ_{xx} and strain ε_{xx} for Direct Tension Pullout test (Milestone B).

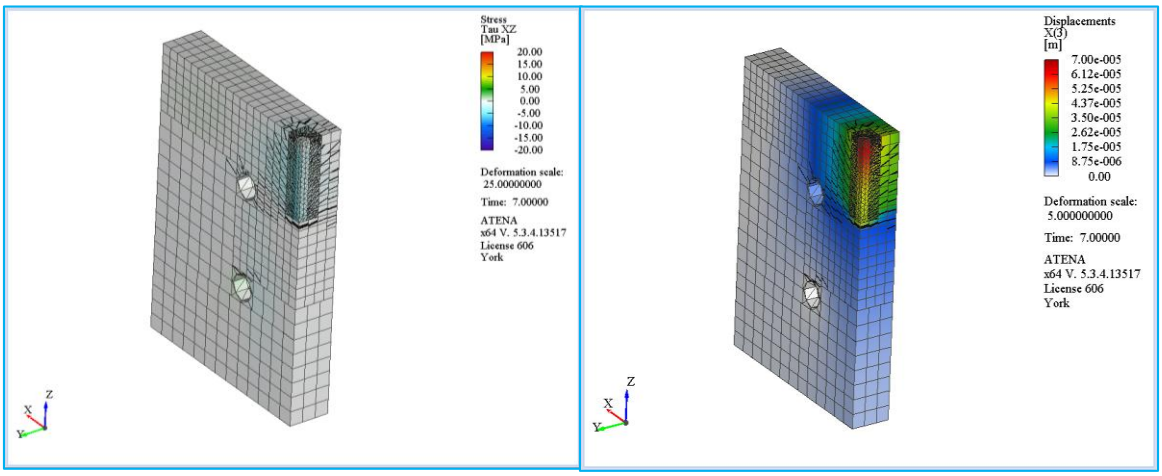

Figure 3-123 Shear stress τ_{xz} and slip Δ_z for Direct Tension Pullout test (Milestone B).

Point C in the response curve – direct tension pullout test

At milestone point C, the specimen has degraded approximately to 37% of the peak strength and bar displacement of 0.6mm. Cracks have proliferated towards the widest dimension, creating horizontal openings that start from the free end of the bar and penetrate through the top circular opening. The maximum crack width is 0.75 at this point. Tensile longitudinal stresses in the bar have been reduced to approximately 50MPa whereas the majority of the bar volume has reached the same value of stress indicating strain penetration and bond failure (Figure 3-124). Compressive stresses develop on the concrete surrounding the free end of the bar and on the outer surface of the widest dimension. Tensile hoop stresses that do not exceed 3MPa are distributed along the crack path. Tensile longitudinal strains appear on the concrete underneath

the free end of the bar reaching maximum values not more than 0.1 marking the development of a wide crack. The positive strains spread across the lateral crack path. Tensile transverse stresses appear on the upper concrete segment in close proximity to the bar and on the concrete zone underneath the extent of the bar. These strains do not exceed 2MPa (Figure 3-125). The bar undergoes positive transverse strains of not more than 10MPa. At the free end of the bar, negative lateral stresses reach up to -75MPa due to the pressures imposed by the concrete. Downwards shear stresses develop on the bottom segment of the bar. This denotes the exhaustion of the bond strength between the bar and the concrete, having values of $f_b = \tau_{xy}$= -10MPa and -15MPa (Figure 3-126). Upwards shear stress concentrations appear further away from the bar and closer to the outer surface of the widest dimension of the specimen. The relative slip is 0.618 -0.541= 0.077mm.

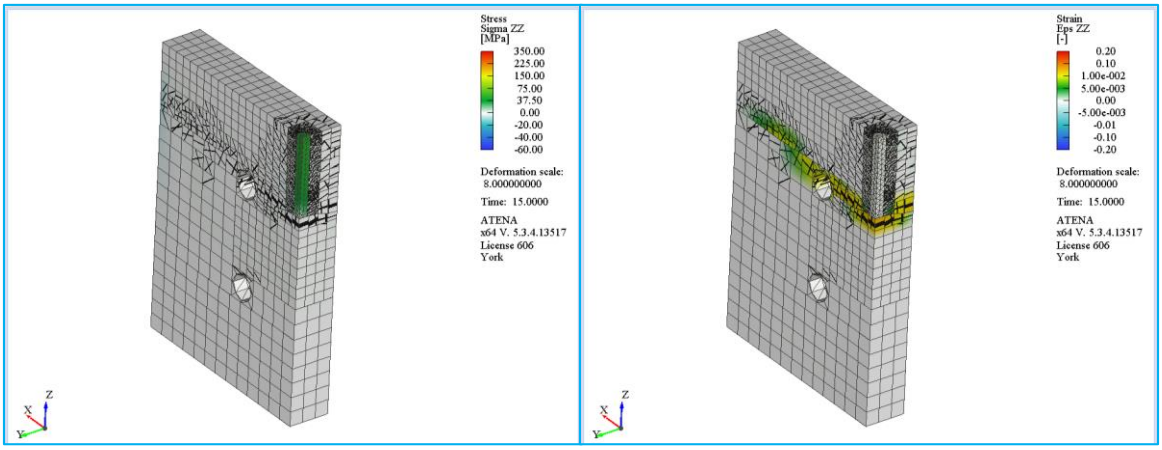

Figure 3-124 Stress σ_{zz} and strain ε_{zz} for Direct Tension Pullout test (Milestone C).

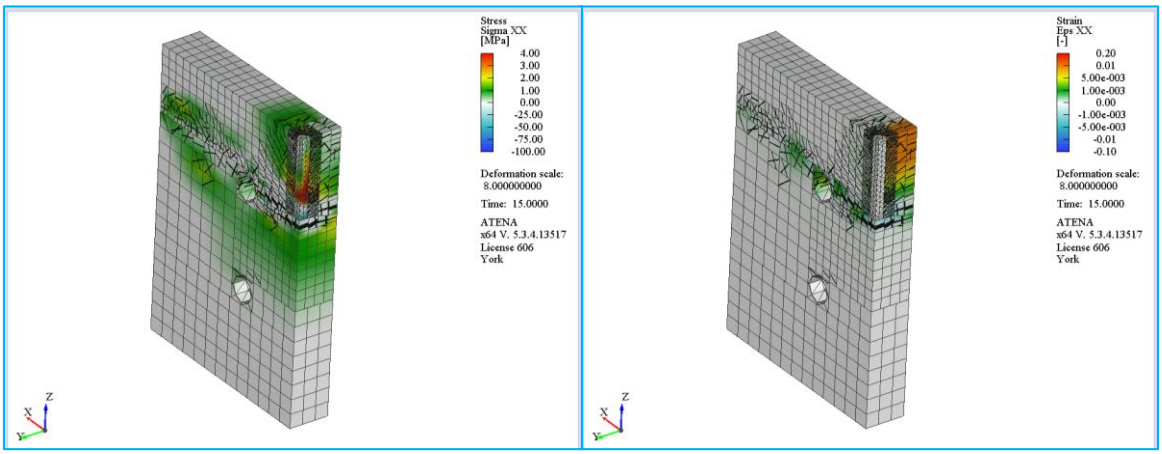

Figure 3-125 Stress σ_{xx} and strain ε_{xx} for Direct Tension Pullout test (Milestone C).

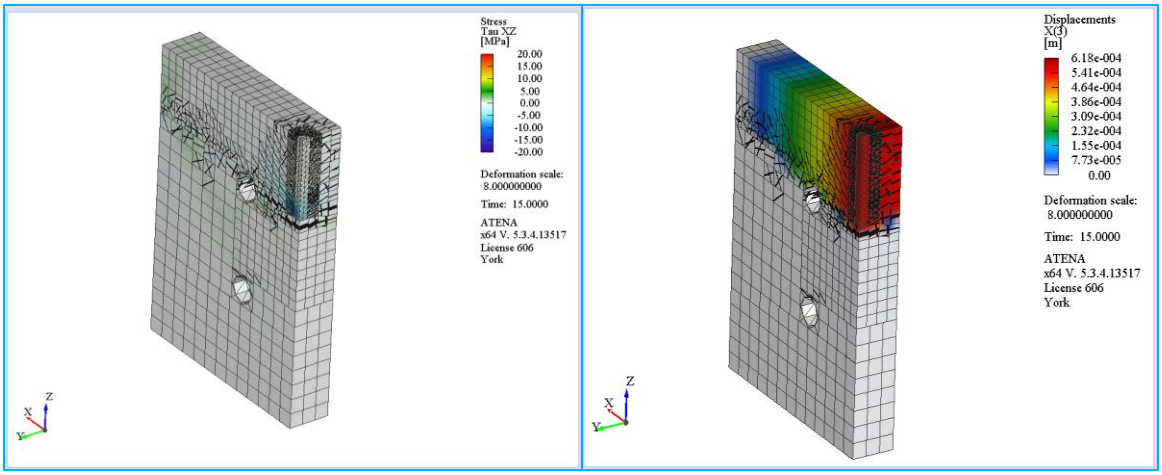

Figure 3-126 Shear stress τ_{xz} and slip Δ_z for Direct Tension Pullout test (Milestone C).

Point D in the response curve – direct tension pullout test

At milestone D, the specimen has degraded approximately to 27% of the peak strength at bar displacement of 2.5mm. The maximum crack width at this point is 2.7mm.

It is evident that the bar has almost completely disconnected from the concrete. This is shown from the constant tensile stress levels over the majority of the bar volume. Tension levels along the bar length remain at approximately 50MPa whereas a small segment in the free end of the bar retains values not more than 10MPa (Figure 3-127). Compressive longitudinal stresses appear on the concrete surrounding the free end of the bar and the outer surface at the end of the crack path and do not exceed -20MPa. Tensile strain levels are maximum at a value of 0.23 underneath the free end of the bar, at the location of the major horizontal crack, and extend with decreasing intensity towards the outer surface of the wider dimension. The maximum transverse hoop stresses in tension are located on the bottom segment of the bar. The yet uncracked concrete underneath the end of the bar anchorage develops tensile lateral stresses up to 1MPa (Figure 3-128). The maximum compressive radial stresses reach values up to -25MPa and are concentrated at the free end of the bar. This signifies the final attempt of the concrete cover to maintain contact with the displacing bar, since the remainder of the bar has been disconnected from the concrete. Transverse tensile strains maximize on the concrete located in the upper segment of the specimen and in close proximity with the bar at values reaching approximately 0.2 (i.e. in the post-peak tensile stress-strain branch, with no residual tensile strength). Having reached a plateau in the strength curve, the negative shear stresses appearing on the bottom segment of the bar have not changed significantly. The lower part of the bar remains yet

connected with the concrete, reaching extreme values of negative shear stresses between -10MPa and -15MPa (Figure 3-129). Upon exhaustion of the remaining interface, the bar will disconnect completely and the shear stresses will be diminished. The relative slip at this point is 2.5-2.19 = 0.31mm.

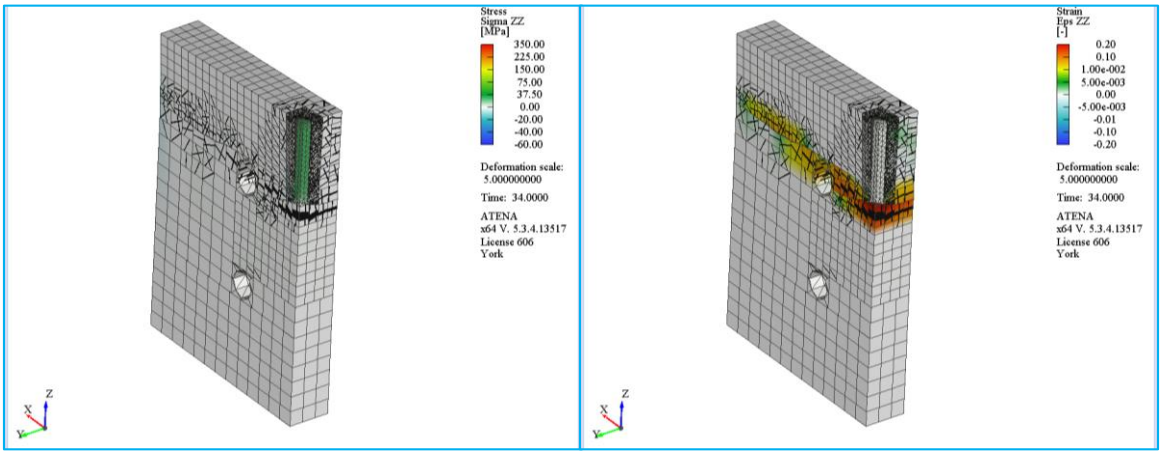

Figure 3-127 Stress σ_{zz} and strain ε_{zz} for Direct Tension Pullout test (Milestone D).

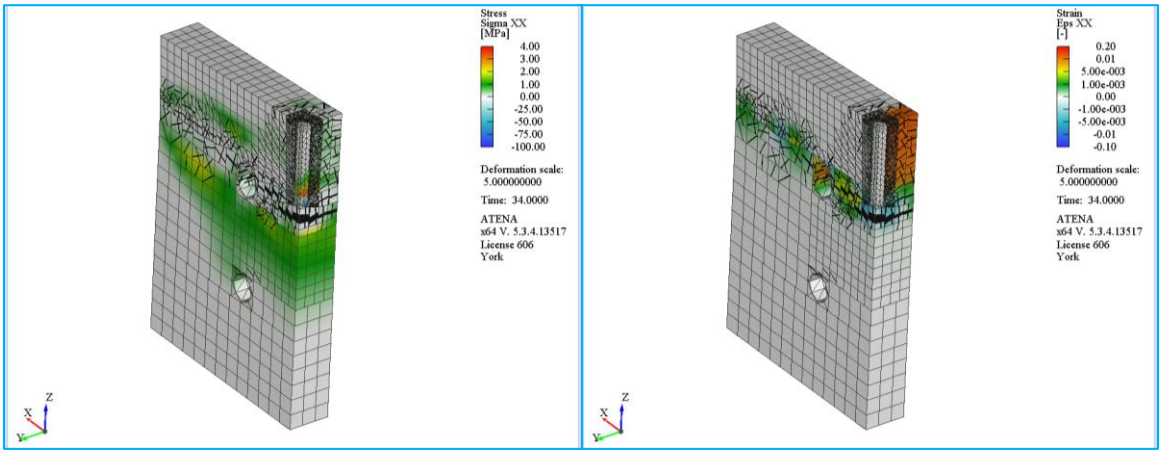

Figure 3-128 Stress σ_{xx} and strain ε_{xx} for Direct Tension Pullout test (Milestone D).

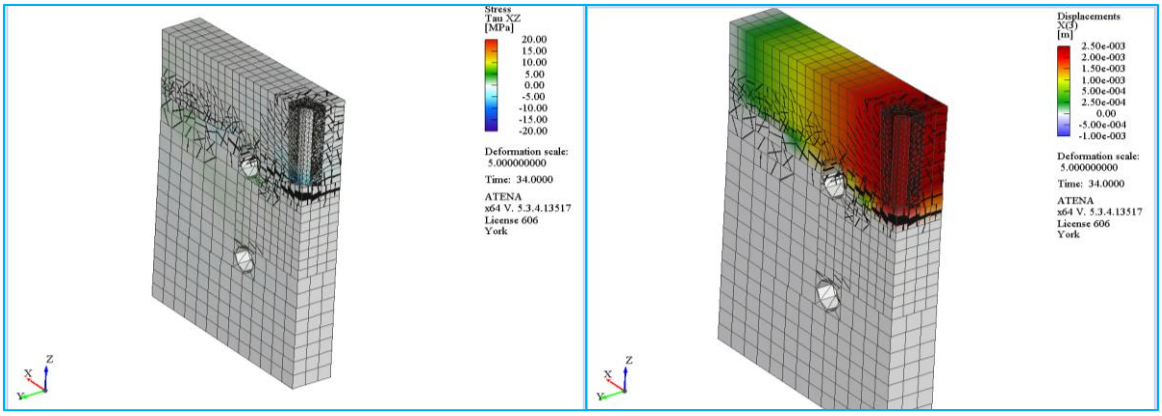

Figure 3-129 Shear stress τ_{xz} and slip Δ_z for Direct Tension Pullout test (Milestone D).

3.5.4 Comparisons between setups

It is evident from the finite element analysis of the various setups, that bond strength obtained from testing a bar embedded in a concrete block reading are greatly affected by the nature of the setup. Figure 3-130 shows the comparison of the force – displacement curves between the various setups and Table 3-1 summarizes the bar development capacities for all specimens and the corresponding displacements where peak stress is achieved. Note that in all cases displayed the anchorage length, bar size, interface model and concrete properties were identical.

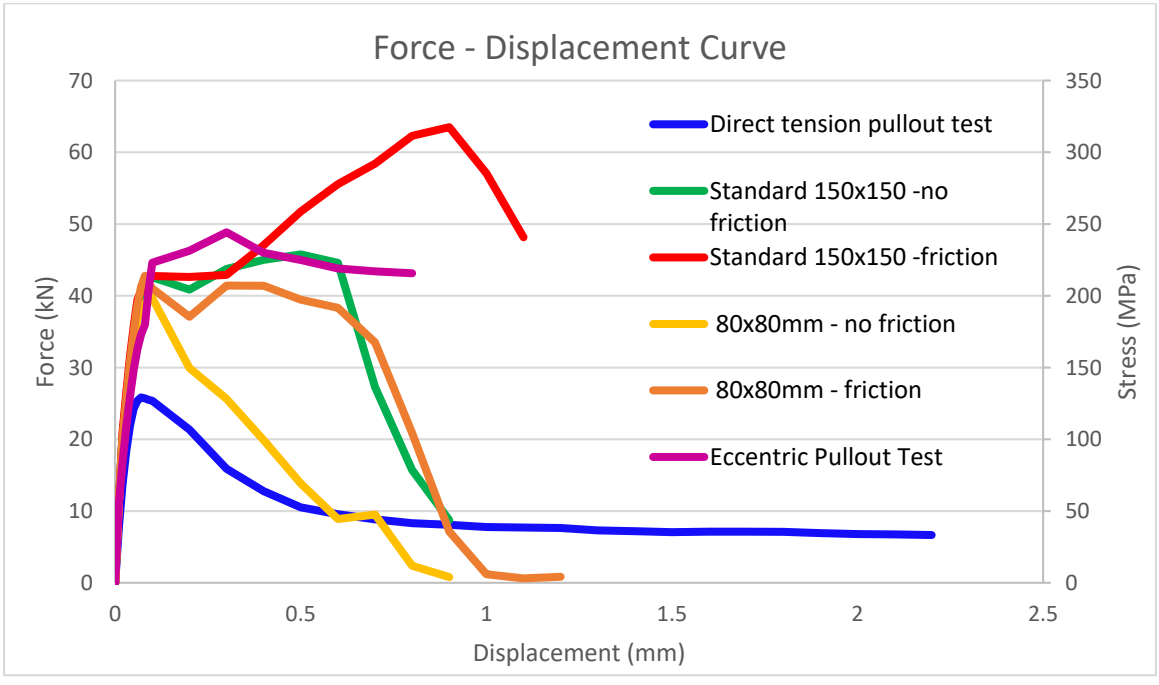

Figure 3-130 Comparison between Force – Displacement Curves for the various pullout setups.

Table 3-1 Comparison of peak values between the various pullout setups.

Type of test	Peak Load (kN)/ Stress (MPa)	Bar Displacement at Peak (mm)
Standard 150x150 w/ friction	63.5 / 317.51	0.9
Standard 150x150 w/o friction	45.78 / 228.89	0.5
Standard 80x80 w/ friction	42.78 / 213.89	0.08
Standard 80x80 w/o friction	39.69 / 198.43	0.1
Eccentric Pullout Test	48.85 / 244.25	0.3
Direct Tension Pullout Test	25.84 / 129.22	0.07

Comparison of σ_{zz}: A common element between the Concentric and Eccentric Pullout setups is the accumulation of compressive longitudinal stresses in the concrete cover surrounding the upper segment of the test bar. Due to the compressive forces imposed by the bearing plate of this setup, on the top surface of the specimens, the concrete zone that is in close proximity with the top surface develops stresses opposing the movement of the bar. This results in compressive stresses acting on the bar segment close to the top surface of the specimen, resembling the stress conditions appearing in the presence of confinement. Bond values obtained from these setups will lead towards greater strengths due to the favorable effect of these confining pressures on the reinforcement. On the contrary, in the Direct Tension Pullout test, the concrete stress zone around the bar develops only tensile longitudinal stresses in accordance to the bar displacement which resemble the tensile stress conditions encountered in the tension flexural zone of existing structural members, thus providing a more accurate representation of the actual bond capacity.

Comparison of ε_{zz}: While the longitudinal strains generated along the bar axis follow the same pattern in all of the setups, the strains on the concrete adjacent to the bar are opposing the movement of the bar in the Concentric and Eccentric Pullout setups. It is a common theme between the two aforementioned setups that a compressive longitudinal strain field encloses the bar which is in turn strained in tension. Effectively no strains appear on the upper segment of the concrete specimen during the DTP test, with the accumulation of compressive strains concentrating around the horizontal support cylinders. In all setups, tensile longitudinal strains appear on the concrete underneath the free end of the bar as a result of the bar disconnecting from the concrete surface. At this location, the major crack opening ensues spreading in the transverse direction and propagating towards the outer surfaces of the specimens.

Comparison of σ_{xx}: Transverse hoop tensile stresses appear on the concrete surrounding the bar and the upper segment of the bar itself. The tensile stresses on the concrete illustrate the proliferation of radial stresses caused by the relative movement of the bar with the concrete, with higher intensities accumulating in an elliptical “zone” around the bar. The dimensions of the ellipsis are determined by the specimen available covers, with the smallest one to be the controlling cover. As the tensile capacity of the tensile zone around the bar is exhausted, cracks begin to appear starting from the concrete adjacent to the bar. The cracks emanate until the full extent of the elliptical zone is covered. The limits of this zone can be seen in the rectangular edges of the Concentric and Eccentric Pullout tests. In the DTP test, the transverse pressures dispersed in the concrete area beneath the bar until the hole opening where the transverse support cylinder is located, albeit to a lesser intensity due to escalation of the crack pattern. Radial compressive transverse strains also occur in all circumstances where concrete bears on the bar during the bar’s displacement. This compressive stresses are responsible to a large extent for mobilizing the interface resistance that supports the frictional transfer along the interface of frictional shear.

Comparison of ε_{xx}: In all test setups, the concrete surrounding the bar undergoes tensile transverse strains, following the pattern of the tensile transverse stresses. Compressive transverse strains concentrate in the concrete underneath the free end of the bar indicating the tendency for arching, as a result of the reactions of the concrete surface against the pulling of the bar.

Comparison of Bond – Slip measurements: Bond stresses along the anchorage interface appear as negative shear stresses that oppose the upwards movement of the bar. In the early stages of the loading, shear stresses convey full engagement of the bar over the contact length, but as the load increases, the active zones translate towards the free end of the bar. This can be witnessed by the gradual degradation of the maximum shear stresses starting from the upper segment of the anchorage. When the bar dislocates from the concrete, shear stresses diminish and bond recedes into the descending branch of the bond – slip interface relationship. It was also evident from specimens with compressive stress fields around the anchorage that shear stress measurements, and therefore bond stress, demonstrated substantially higher values reaching to approximately double the bond capacity of the Direct Tension Pullout test. The restriction due to frictional forces on the resisting plate of the Concentric Pullout tests provide further increase of the shear stress measurements due to the compressive stresses that are directed towards the bar. Lateral expansion alleviated a portion of these stresses and reduced the shear pressure accumulating in the concrete. Shear stresses of opposing direction appeared on opposite the

sides of the bar in the case of the Eccentric Pullout test, as a result of the asymmetric dislocations of the bar. The forces developing due to the eccentric placement of the anchorage lead to the development of opposite shear stress flows on two opposite faces of the bar due to the bending action that was generated by the eccentricity, so that the rate of bar stress reduction per unit length would represent the average of the two extreme values; this explains the great difference in apparent development capacity of bars tested in beams under flexure (Saikali, 2019) and bars tested under direct tension. This is a characteristic encountered only in the Eccentric Pullout test.

Chapter 4: Experimental Program – Fabrication of Specimens

4.1 Introduction

The scope of the present investigation includes an experimental component in order to establish the bond strength of conventional reinforcement embedded in UHPC with minimal spurious influences from the test setup. To this end, a total of 13 specimens have been constructed over the course of 4 castings; specimens were designed to be tested in the custom setup, depicted in Fig. 3.1. This experimental study is part of a larger scope project intended to quantify the mechanical properties of various UHPC and ECC materials, with particular emphasis on the tensile strength and deformation resilience as well as on the bond – slip properties of conventional steel reinforcement embedded in these cementitious matrices. The material mixtures used for this study include two commercial mixes as well as two in-house mixes. During each casting, batching of the material for all the specimens of the study was done in a 200L mixer, making sure that for each direct pullout specimen there was at least a companion beam specimen having identical cover and test-bar anchorage region (tested by a peer), cylinders for compression testing and prisms or dogbone specimens for tension testing. Flowability tests were used to signal attainment of desirable fresh concrete properties, followed by pouring the final mix into the molds using a layered approach. Immediately after specimens were covered in plastic sheets and were left to rest for two days prior to placing them under wet burlap and plastic. In addition to the main test specimens, two additional specimens (comprising plain concrete) were used as dummy specimens for assessment of the test setup.

4.2 Preparation of the wooden formworks

Reusable molds were designed to accommodate casting of the specimens in the horizontal direction. The molds are fixed on a 600mm x 600mm spruce pine plywood base with a thickness of 19.00mm. A wooden panel with dimensions equal to the front face of the specimens (400mm x 280mm) is concentrically placed on top of the base. The front face panel has the same thickness as the base panel. On the perimeter of the wooden panel, four plywood sides with dimensions 525x99 (long face) / 280x99 (short face) for the specimens with $2D_b$ cover, and 525x67(long face) / 280x67(short face) for the specimens with $1D_b$ cover form the perimeter of the mold. The sides

rest on the base, directly bearing on the perimeter of the front face panel, without being fixed. On the outer face of the long vertical panels, a 2x4 (in.) piece of lumber is fixed on the base to ensure that the panels do not deform outwards during casting.

Each pair of long side panels are connected via two threaded steel rods which are tightened with nuts and washers on each side. The clamping pressure of the long side panels holds the short side panels in position. To ensure that the short side panels do not bent outwards due to the pressure from the fresh concrete after casting, aluminum L-brackets were fixed on the base, on the side of the short side panels. The test bar is held horizontally via a circular opening at the center of the short side panel resting on a wooden block that is fixed on the base. A descriptive arrangement of the formwork is shown in Figure 4-1 whereas Table 4-1 describes the annotation shown in the perspective view of the formwork.

On the top face of the front face panel, 4 circular openings, with a diameter of 25.2mm, were opened, to be used later for passage of the support rods that will keep the specimen in vertical position during testing (see Fig. 3.1). The openings penetrated to half the depth of the base panel. Through the openings, four hollow PVC cylinders were placed vertically and maintained in equidistant position via a wooden cardboard collar. To prohibit leakage of concrete through the edges of the enclosed space and the circular openings, a silicon layer was added on top of the edges of the openings and on the perimeters of the PVC tubes at the point of contact. Prior to pouring the concrete, all faces were oiled to ensure a smoother surface for specimen.

Table 4-1 Annotation description of Figure 4-1.

Annotation	***Description***	***Dimensions (mm) [2·D_b / 1·D_b]***
A	Base plate	600x600x19
B	Front face panel	400x280x19
C	Top / Bottom side plates	525x99x19 / 525x67x19
D	Side plates	280x99x19 / 280x67x19
E	Supporting wooden block	525x101.6x50.8
G	Hollow PVC tubes	150x25.2 (21mm inner)
H	Connecting threaded rods	500x9.5
I	Square L-brackets	36x36
J	Test bar	80x16

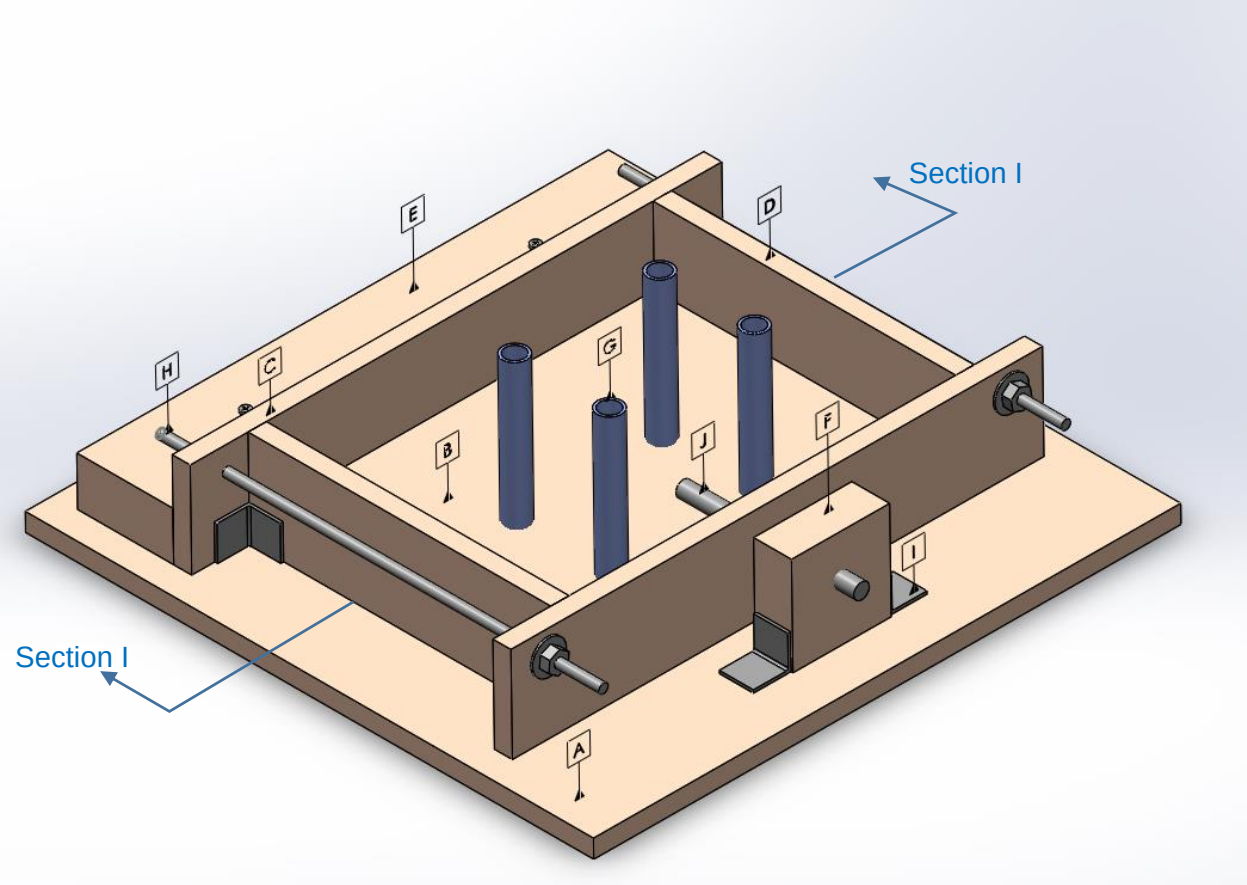

Figure 4-1 Perspective view of formwork design.

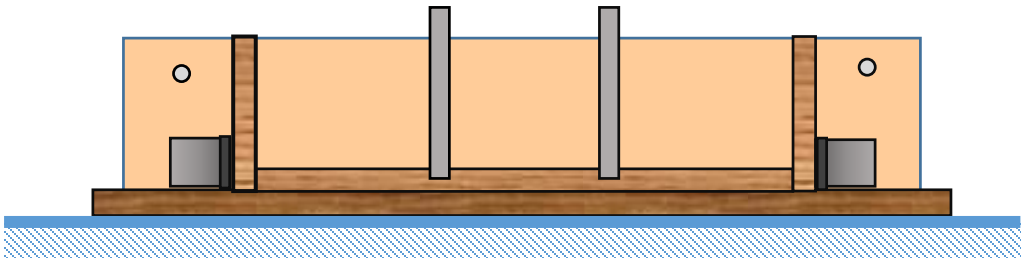

Figure 4-2 Section I-I view.

The same molds were used for all the castings that are included in this thesis. Minor curvatures of the vertical panels and of the front face panel were observed after the castings but were corrected with the aluminum L-brackets. Figure 4-3 shows one formwork for a specimen with $1 \cdot D_b$ and one formwork for a specimen with $2 \cdot D_b$. A total of four specimen molds were constructed with this design so only two identical specimens were prepared in each casting session.

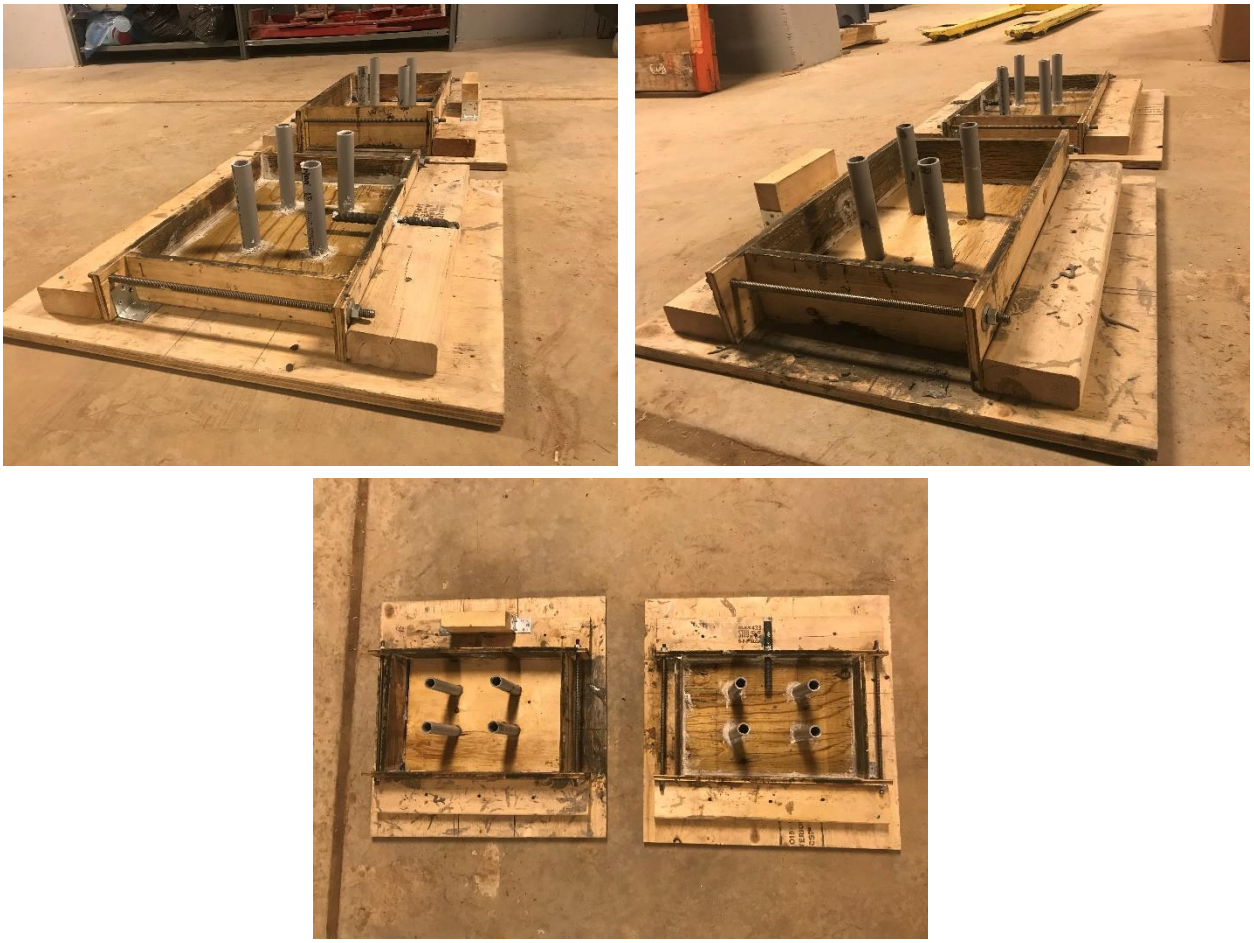

Figure 4-3 Top left: Perspective view from $1D_b$ cover mold, Top Right: Perspective view from $2D_b$ cover mold, Bottom: Top view.

4.3 Material design and batching procedures

Two of the different casting sessions concerned pre-blended, prepackaged commercial cementitious materials reinforced with brass-coated steel fibers, provided by two of the leading companies in the field of UHPC. These will be referred to henceforth as mix K and mix F, respectively. Casting was done as described in the following sections.

4.3.1 Commercial Mix K (CMK) – February 14th 2018:

The constituents for this mixture, along with their gravimetric analogies, are shown in Table 4-2. Material compositions were not provided by the supplier. A total of 25Kg of pre-packaged dry material, 20L of liquid admixtures mixed on site with ice-water and 20Kg of straight steel fibers

were provided. The steel fibers have a length of 13mm and a diameter of 0.2mm. A company representative was additionally present to ensure that the batching procedure was done according to the patent specifications of the mix.

Batching was initiated by mixing the pre-packaged powder and fine aggregate materials in dry condition and low speed for two minutes. After the allotted time, 50% of the water was added gradually along with 100% of Admixture A, and immediately after the rest of the water was added along with 100% of the ice. The use of ice ensured that the plastic temperature of the concrete would be kept between 20 ˚C and 30 ˚C. It was recommended that the speed of the mixer would be increased at this point. Mixing continued for a duration of approximately 3 minutes and then 100% of the Admixture B was added. After 1 minute of mixing, the steel fibers were added at a slow rate of approximately 15kg to 20kg per minute. Homogeneity and workability of the mixture was verified via a standard flow test after two minutes of mixing after the addition of the fibers as depicted in Figure 4-5. The diameter of the spread after the end of mixing and prior to casting was 227.5mm (ASTM-C230, 2010, see Figure 4-6). Note that the flow test comprises the following elementary steps: filling from the top an inverted squat cone mold with the material, then removing the mold with a slow rotational movement, and allowing it to spread laterally on the flow table for 2 minutes. Measuring the “static flow” of the sample along three axes. Continuing with 20 drops of the flow table by turning the hand crank. Measuring the “dynamic flow” of the sample along three axes (see Figure 4-7). The density of the fresh material was 23.3 kN/m^3. After hydration the material density was 24.7 kN/m^3. This mix created a crust on free exposed surfaces shortly after casting. To minimize this effect a plastic sheet or plexiglass plates were placed on top of all specimens immediately after casting.

Figure 4-4 Sample of short and straight steel fibers (l_o =13mm; Ø = 0.2mm; brass coated).

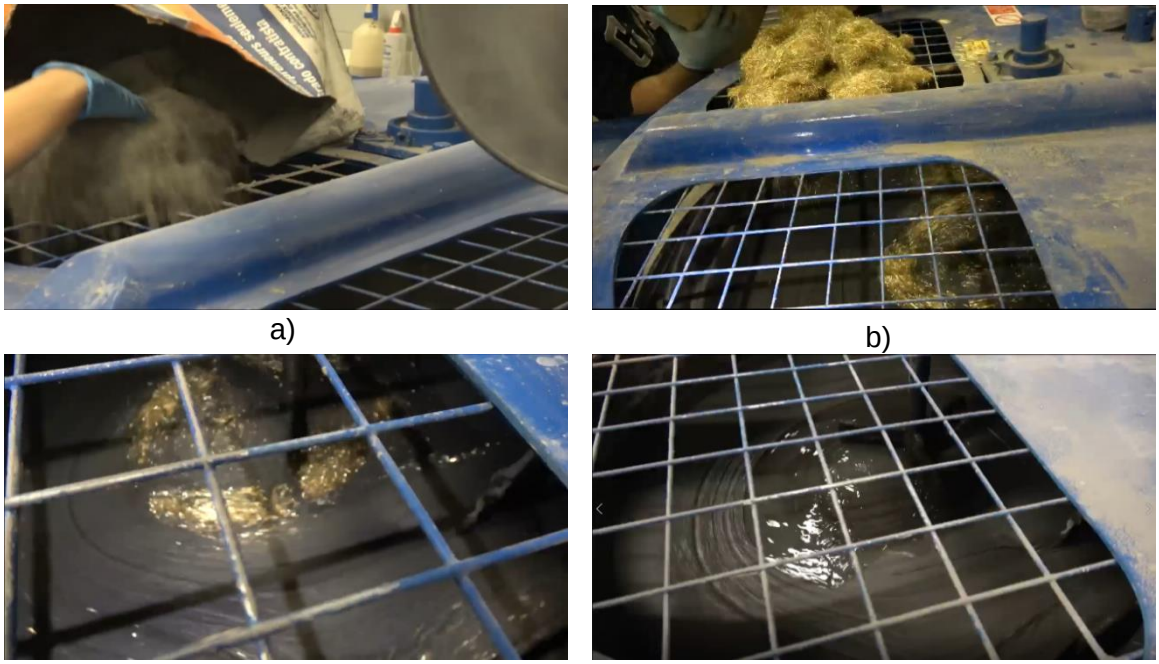

a) b) c) d)

Figure 4-5 Progressive stages of the batching procedure for the CMK mixture: a) Mixing of dry materials; b) Pouring of fibers into mixture; c) Mixing for distribution of fibers; d) Attainment of proper mixture consistency.

Figure 4-6 Flow table as specified by ASTM C230/230M standards.

Figure 4-5 shows the progressive stages of mix constitution and Figure 4-8 shows the specimen arrangement after casting. A stabilizing hardboard surface was used to cover the top surface of the specimens and secure the PVC tubes from misalignment.

Table 4-2 Material constituents and weight proportions for a 35L volume (CMK mix)

Materials	Kg/m^3	Kg
Pre-packaged Dry Material	1912.66	66.94
Water	147.32	5.16
Ice	49.11	1.72
Admixture A	47.96	1.68
Admixture B	25.13	0.88
Steel Fibers	156	5.46
Total Mass	2338.17	81.84

Table 4-3 Static and Dynamic Flow measurements for all Flow Test attempts (CMK).

Flow Test attempts	Static Flow (mm) [D_1 / D_2]	Dynamic Flow (mm) [D_1 / D_2]
1	220 / 205	220 / 235

Figure 4-7 Concrete sample within cylinder (left); Measurement of maximum and minimum diameters of sample after removal of the cylinder (right).

Figure 4-8 Specimens from CMK mixture covered with hardboard after casting.

4.3.2 Commercial Mix F (CMF) – February 29th 2018:

The constituents for this mixture, along with their gravimetric analogies, are given in Table 4-4. Binder material and admixture compositions were not provided by the supplier while the mixture components were pre-packaged in sealed bags and containers. A company representative was present during batching and casting to ensure that the batching procedure followed the requirements of the material patent.

Batching was initiated by blending the Dry-mix (containing both binders and fine aggregate) for approximately 1 minute before adding the Wet-mix. After adding the Wet-mix, the mixture was blended for 16 minutes. Once the allotted time expired, the mixing was stopped and a flow test was performed (ASTM-C230, 2010) to ensure the target flow, which in this case was 220 +/- 20mm. In the case that the mixture was determined to be too stiff, flowability was corrected through addition of small amounts of Wet-mix additive and mixing was repeated for two minutes before performing a flow test again. Similarly, in the case that the mixture was determined to be too fluid, a prepackaged bag of the Dry-mix powders was added and the process was repeated until the target flow was achieved. Once the target flow was attained (213.3mm), Steel fiber Types I & II were added gradually and mixing continued for two minutes. Type I steel fibers have the same shape and diameter as the ones in the CMK mixture, while having a length of l_o =19mm, whereas Type II steel fibers are longer, and with hooked ends, with an equivalent length and diameter of l_o =25mm and Ø = 0.3mm, respectively (Figure 4-9). After the mixing time ended, the

final flow test was repeated until the target flow was within the range indicated above. The wet density of the resulting material was 25.5kN/m^3.

Table 4-4 Material constituents and provided quantities for 80L volume (CMF mixture).

Materials	Provided Component	Quantity
Pre-packaged Dry-mix	Bulk bag	1
Pre-packaged Wet-mix	Gallon pail	5
Steel Fibers – Type I	Gallon pail	5
Steel Fibers – Type II	Gallon pail	5
Dry-mix additive	4” Cylinder mould	3
Wet-mix additive	1L Bottle	1

The results from all flow tests conducted are shown in Table 4-5. The final flow test measurement was 210mm. In Figure 4-11 various stages of the batching procedure are shown. The mixture progresses gradually from the dry state to the desired flow state through the addition of the Wet-mix and Wet-mix additive. Examples of the Static and Dynamic flow tests are shown in Figure 4-10.

Table 4-5 Static and Dynamic Flow measurements for all Flow Test attempts (CMF).

Flow Test attempts	Static Flow (mm) [D_1 / D_2 / D_3]	Dynamic Flow (mm) [D_1 / D_2 / D_3]
1	120 / 150 / 120	145 / 145 / 145
2	175 / 180 / 175	200 / 190 / 190
3	205 / 205 / 220	250 / 260 / 250
4	185 / 195 / 210	210 / 220 / 210

Figure 4-9 Sample of long steel fibers with hooked ends (l_o =25mm, Ø = 0.3mm; brass coated).

Figure 4-10 Examples of Static Flow measurements (left) and Dynamic flow measurements (right).

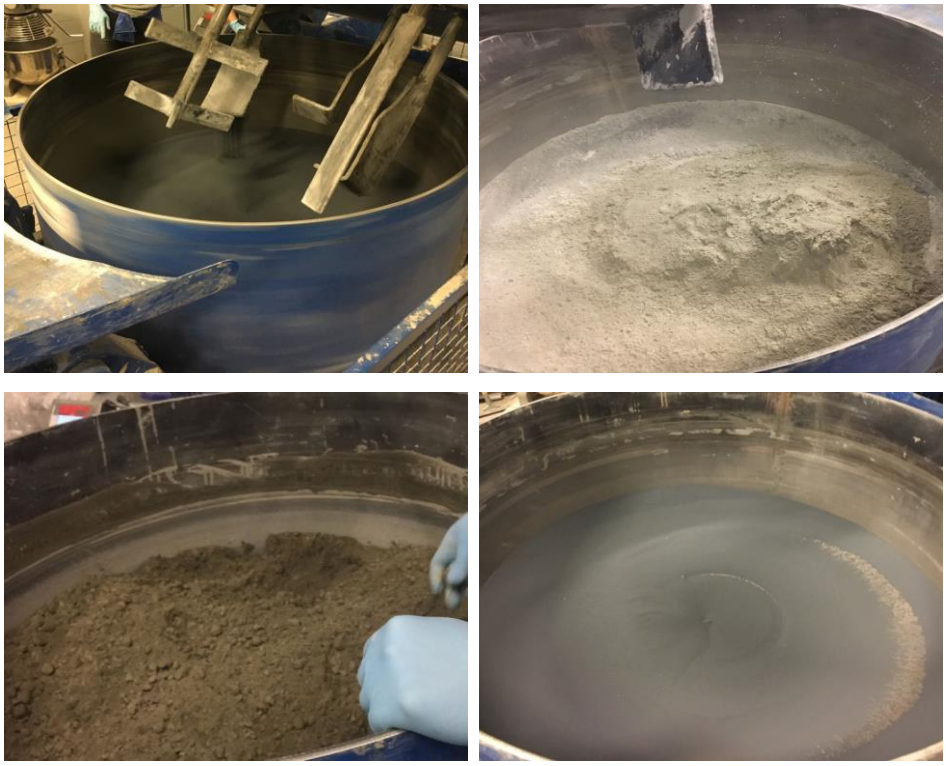

Figure 4-11 Progression stages of the batching process for CMF mixture.

4.3.3 In-house Mix NJ (IHNJ) – April 16th 2018:

The mix design for this in-house mixture is based on the work of Eshghi (2018). It was based on the ECC – M45 mix design, originally developed by Lepech and Li (2009), adopted to local material availabilities by Georgiou and Pantazopoulou (2017) where European type CemII-42 was used which is rich in Silica Fume, Slag and limestone content. With this type of cement being unavailable in Canada, a binder mix was created to replace its favorable properties. Further modifications were made with the use of a larger diameter PVA fibers (dtex -100 Kuralon K-II, imported from Japan, having a diameter of 0.1mm as compared to the fibers used by previous investigators with 0.039 mm diameter).

Details of the mixing procedure are given in the work of Eshghi (2018). Initially, all dry materials, namely the cement, fly ash, silica sand, slag and silica fume, are added into the mixer and mixed for 1~2 minutes. The superplasticizer is diluted into half of the water quantity and it is added gradually into the mix in a time span of 2~3 minutes. Mixing continues until no visible clumps and congregations appear into the mixture. Once the mixture changes color, the fibers are added at a slow pace of 5~10 minutes while the mixing pan is rotating. Finally, the remainder of the water

is added and mixing continues until the fibers are distributed evenly through the mixture. In the case of coated fibers, this recipe requires the addition of defoamer in the second half of the water, however it was not required in this experiment. The total duration of the batching procedure is approximately 30 minutes. Once the mix is terminated, the flow test is performed according to ASTM C230/230M standards, in which the mold is placed in a single layer atop the flow table shown in Figure 4-6. The diameter of the concrete sample is measured across the maximum and minimum diameters and the average value is calculated. The spread of the material for this batch was 210mm for the static flow and 240mm for the dynamic flow. Table 4-6 below gives gravimetric proportions of the ingredients for 35L of material volume.

Table 4-6 Material constituents and gravimetric proportions for 35L (IHNJ mixture).

Materials	Kg/m^3	Kg
GUL Cement (6 to 15% limestone powder)	400	14
Fly Ash	667.5	23.36
Silica Sand (Max. aggregate size 0.3)	445	15.58
Slag (Ground Granulated Blast Furnace)	45	1.58
Silica Fume (Densified)	110	3.85
Superplasticizer (MasterGlenium® 7700)	10	0.35
Water	311	10.89
PVA Fibers (dtex -100 Kuralon K-II)	25	0.875
Total Mass	2905.5	101.69

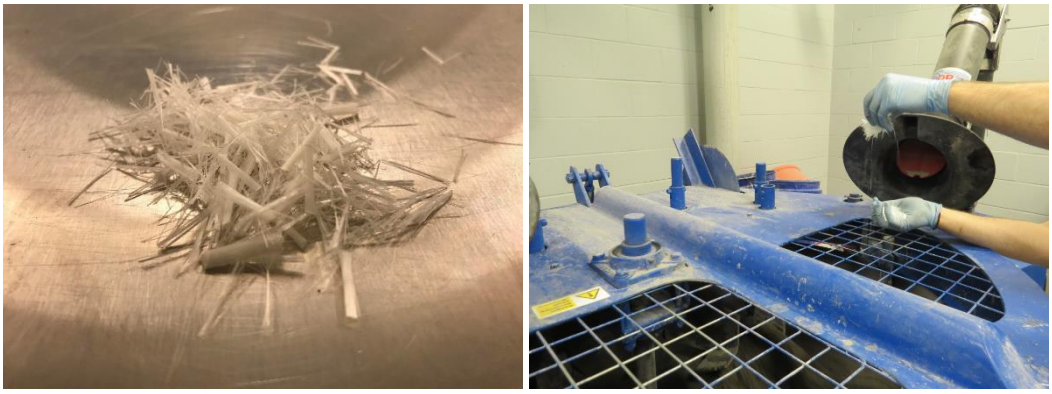

Figure 4-12 Short and straight PVA fibers (uncoated) (left); Pouring of synthetic fibers by "uncluttering" the batches (right).

A sample of the PVA 12mm fibers used in this mixture is shown in Figure 4-12. The fibers were uncoated and formed clumps which were dispersed during the addition into the mixture to allow for better distribution of the fiber mass.

Figure 4-13 Progression stages of the batching process for IHNJ mixture.

4.3.4 In-house Mix RT (IHRT) – June 13th 2018:

The design for this in-house mix is based on the work of Saikali (2019) and Yu et al. (2014). Table 4-7 denotes the materials and quantities used for 35L of the mixture (note: this is the volume of the four molds for the custom tension pullout specimens of the present study). All materials were stored in dry conditions and cold water was used during casting. The superplasticizer was divided into two equal portions, one to be cast along with the cold water and one to be added separately during the batching procedure.

Batching was initiated by placing all of the dry materials into the mixer, including the GUL cement, silica sand, slag and silica fume. After 5 minutes of mixing, the cold water containing half of the superplasticizer quantity was added gradually while the mixer was rotating. The water was mixed with the dry materials for a total of 5 minutes. Once the allotted time expired, the mixture was allowed to rest for a duration of 10 minutes to facilitate the chemical reactions between the

materials. At that stage, spherical particles could be observed across the mixture volume. After resting, the mixing process was restarted for 2 minutes and the second half of the superplasticizer was added gradually, until the desired flowability was achieved. Steel fibers were added only once a flow of 220 - 230 mm was achieved (average of two directions) and mixing continued for 5 minutes after the incorporation of the total volume of fibers. A second series of flow tests followed the completion of the mixing with the fibers until a flow of 210 mm was reached. For further addition of superplasticizer, the mixing continued for an additional 2 minutes before conducting the next flow test. Density of the fresh mix was 23.3 kN/m^3.

Table 4-7 Material constituents and gravimetric proportions for 35L (IHRT mixture).

Materials	Kg/m^3	Kg
GUL Cement (6 to 15% limestone powder)	724.13	25.35
Silica Sand (Max. aggregate size 0.542)	668.6	23.40
Slag (Ground Granulated Blast Furnace)	362.06	12.67
Silica Fume (Densified)	120.69	4.22
Superplasticizer (MasterGlenium® 3400)	12.0	0.42
Water	241.13	8.44
Steel Fibers (Coated SF Type I)	195.75	6.85
Total Mass	2324.9	81.372

Several flow test attempts were made in order to reach the target flowability for this mixture. Table 4-8 depicts the flow measurements for each test, with the last two tests conducted after the inclusion of the fibers into the mix.

Table 4-8 Flow test attempts for mixture IHRT

Flow Test attempts	Flow (mm) [D_1 / D_2]
1	160 / 155
2	175 / 185
3	210 / 195
4	220 / 225
5 (with fibers)	180 / 185
6 (with fibers)	210 / 207

4.4 Casting and demolding of specimens

A total of 13 specimens were cast during the experimental program. Immediately after casting a collar was placed on the protruding plastic tubes to ensure minimal disturbance from their original alignment. Two days after casting, the specimens were removed from the molds and were cured under soaked burlap for the remainder of the time until testing. The batching, casting and curing of the specimens were conducted in Lassonde's High Bay Structural Lab. All specimens were made using 15M bars and an embedment length of $l_b = 5 \cdot D_b$. Of the 13 specimens, 7 were made with a clear cover (in the thickness dimension) equal to $1 \cdot D_b$ whereas the rest were made with a $2 \cdot D_b$ clear cover. On the demolding phase, the PVC tubes were removed to allow for room for the attachment bars to the mechanical base.

Figure 4-14 Fabrication and demolding of specimens

Each specimen is named according to the code name assigned to their respective mix. The identification codes of the specimens contain 6 to 7 characters, with the last two divided by a hymen. The first two letters designating the type of material used, namely "CM" for a commercial mix and "IH" for an in-house mix. The third and fourth character contain the supplier code name. Letters "K" and "F" are assigned to the commercial mixes while "NJ" and "RT" correspond to the

in-house mixes. The number that follows denotes the clear cover with “1” corresponding to a cover of $1{\cdot}D_b$ and “2” for $2{\cdot}D_b$. The number between the hyphens shows the embedment length for each test bar with “5” for $5{\cdot}D_b$. The last character denotes the numbering of specimens associated with the same parameters, starting with the letter “A”. Table 4-9 shows the specimen identification codes associated with their respective parameters.

Table 4-9 Specimen code names and parameter specifications.

Specimen ID	Bar diameter	Embedment Length	Cover
CMK1-5-A	15M	$5{\cdot}D_b$	$1{\cdot}D_b$
CMK1-5-B			$1{\cdot}D_b$
CMK2-5-A			$2{\cdot}D_b$
CMK2-5-B			$2{\cdot}D_b$
CMF1-5-A	15M	$5{\cdot}D_b$	$1{\cdot}D_b$
CMF1-5-B			$1{\cdot}D_b$
CMF2-5-A			$2{\cdot}D_b$
IHNJ1-5-A	15M	$5{\cdot}D_b$	$1{\cdot}D_b$
IHNJ1-5-B			$1{\cdot}D_b$
IHNJ2-5-A			$2{\cdot}D_b$
IHNJ2-5-B			$2{\cdot}D_b$
IHRT2-5-A	15M	$5{\cdot}D_b$	$2{\cdot}D_b$
IHRT2-5-B			$2{\cdot}D_b$

Figure 4-15 All specimens prior to being placed under wet burlap.

Figure 4-16 Specimens constructed with the CMK material.

Figure 4-17 Specimens constructed with the CMF material.

Figure 4-18 Specimens constructed with the IHRT material.

Figure 4-19 Specimens constructed with the IHNJ material.

4.5 Tensile strength properties of materials

The tensile strength properties are shown in Table 4-10. The tensile tests denoted in the table (Dogbone, Splitting, Flexure) were conducted by peers. For the mixtures with steel fibers, two values for flexure were obtained, depending on the orientation of the fibers during casting. One-way and Random distributions were arranged in the casting process.

Table 4-10 Tensile capacities of specimens.

Material ID	Fiber type and percentage	Average Tensile Strength (MPa)			
		Dogbone	Splitting	Flexure [One-way]	Flexure [Random]
CMK	2% Steel 12 mm fiber	5.3	20.5	35.4	25.8
CMF	2% Mixed 19mm and 12mm Steel Fibers	8	25.5	36.18	39.85
IHNJ	2% 12 mm PVA fibers dtex 100	-	-	11.3	
IHRT	2.5% 12 mm Steel Fibers	-	18.86	28.83	24.485

Figure 4-20 Random distribution of fibers during casting.

4.6 Instrumentation and Testing Equipment.

Figure 4-21 depicts the setup in the servo-controlled testing frame where the tests were conducted. Specimens were monotonically loaded to failure at a displacement rate of 0.15mm/min until failure, or until the load carrying capacity of the specimen was reduced in the post-peak branch to 25% of the maximum load.

The specimens were initially secured on the mechanical base, along with their hardware components, before being placed on the testing frame. The instruments that were used are depicted in Figure 4-22. To measure the displacement of the test bar, a customized acrylic platform was fabricated and fastened around the bar perimeter. The platform would extend horizontally, with an additional metallic component attached on the bottom surface, against which the moveable arm of corresponding differential transducer (DT) would bear. To measure the displacement of the concrete surface, an additional metallic platform was cut and attached on the top surface of the specimen via hot glue. Both of the DTs for the measurement of the concrete and bar displacement were attached on an aluminum angle, that was hot-glued onto the vertical steel plates of the mechanical base. The vertical (splitting) crack was measured by a transversely oriented DT, glued on the back surface of the specimen, bearing against an accordingly aligned L-bracket. The complete setup of the DTs is depicted in Figure 4-23.

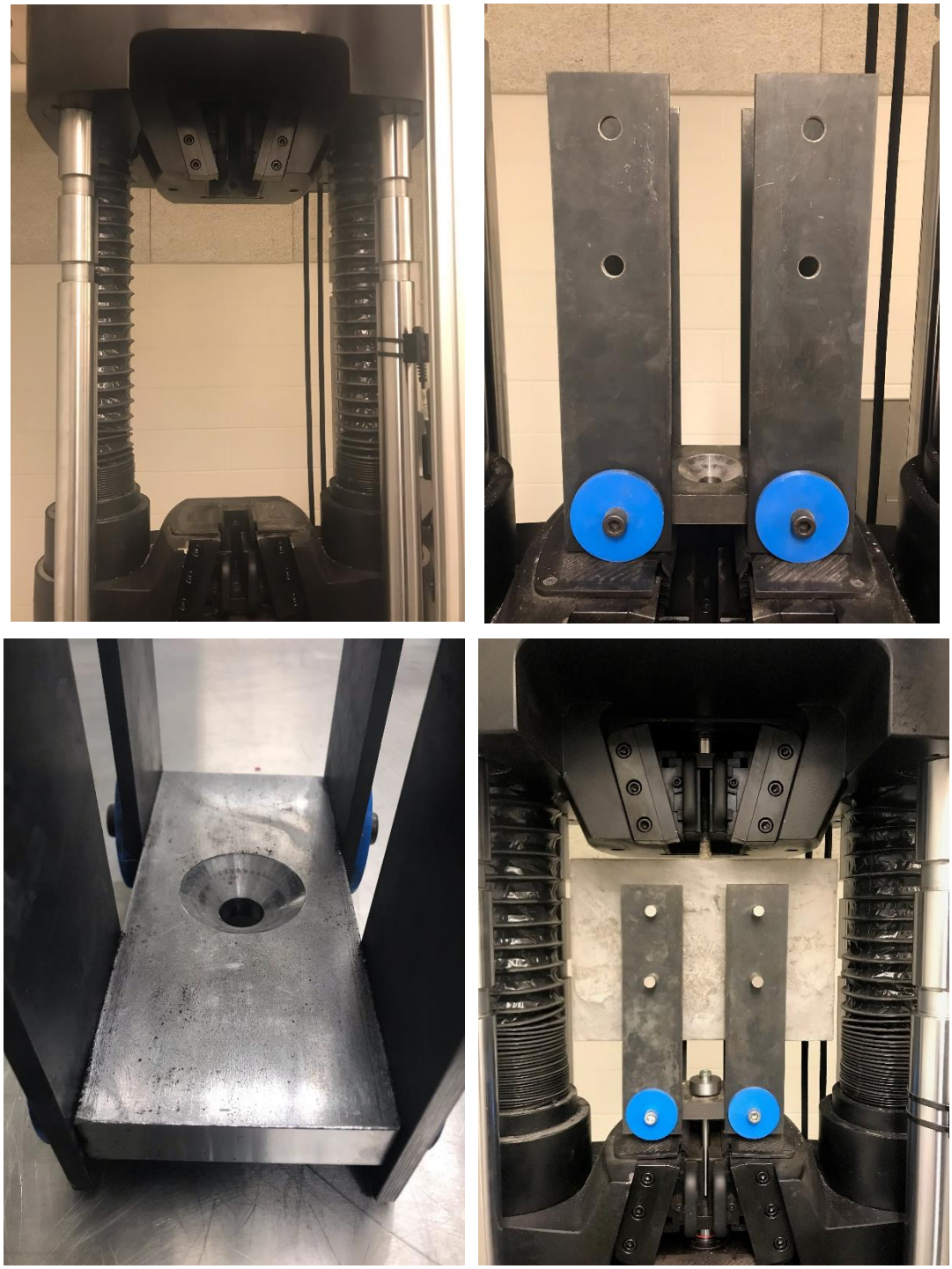

Figure 4-21 Test equipment and setup: (a) MTS Criterion test frame; (b) Lower part of the setup frame; (c) Concave rolling surface for bearing of the spherical nut of the lower gripping rod; (d) View of a dummy specimen in testing position

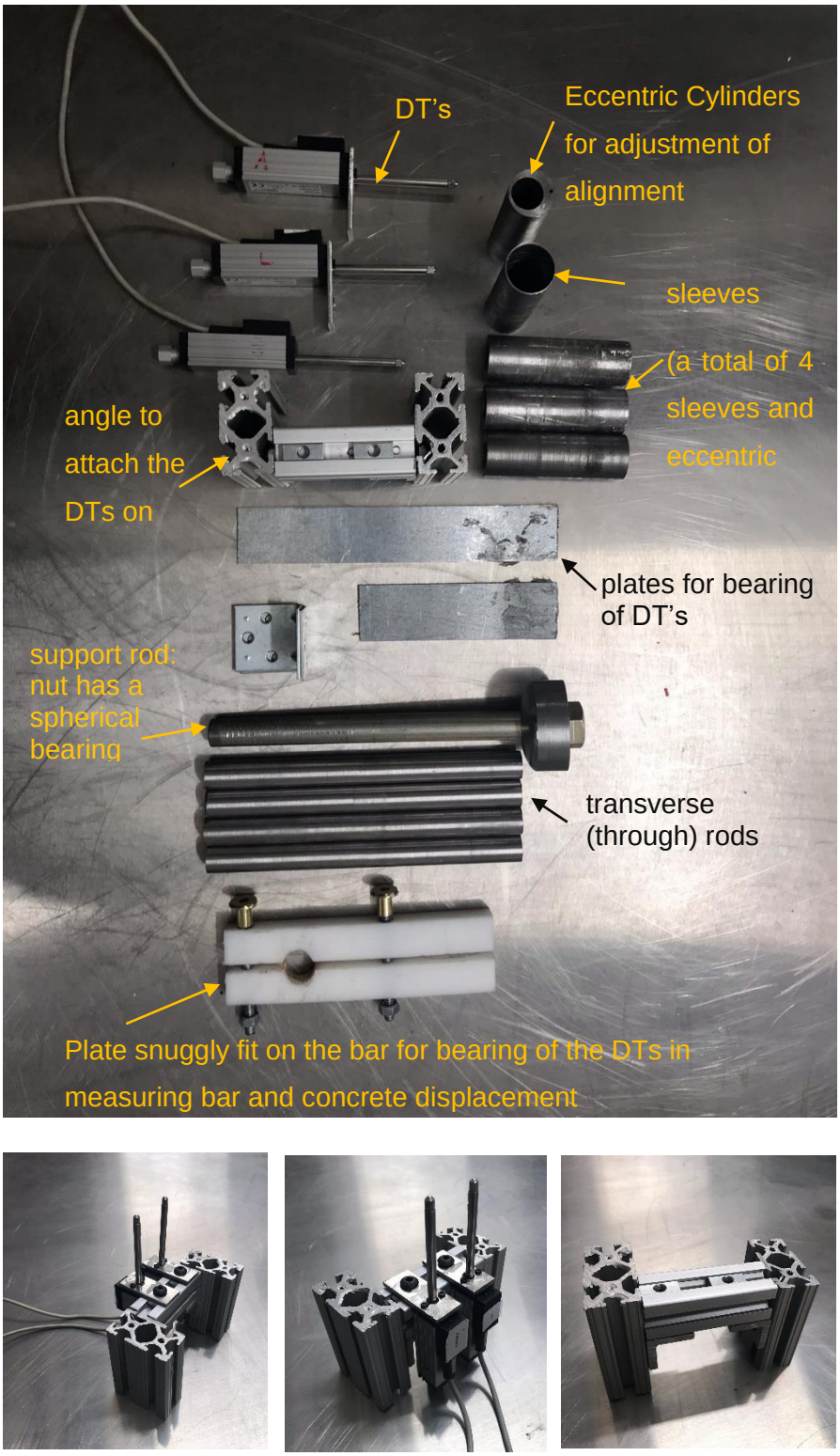

Figure 4-22 Hardware components used in the tests for instrumentation.

Figure 4-23 Setup of differential transducers (DT's) on the specimen to measure the bar displacement, concrete surface displacement and vertical (splitting) crack opening.

Prior to testing, the specimens were prepared for Digital Image Correlation (DIC) analysis by painting a contrasting speckled surface on their front façade in the region surrounding the length of anchorage. Figure 4-24 shows an example of a speckled surface as painted on the specimens. Each specimen was painted with a white, general purpose primer finish to allow for better observation of the crack patterns and black acrylic paint was used to create the speckled pattern.

Figure 4-24 Speckled painted surface of test specimens.

To perform the DIC analysis, the MATLAB module GeoPIV-RG (Stanier et al. 2015) was used by analyzing pictures taken during the experiments. The pictures were taken with a Canon DSLR camera mounted on a tripod overseeing the front façade of the specimens. Additional lighting was provided with a portable projector. A timer was attached on the camera that allowed for pictures to be taken every five seconds during the experiments. Figure 4-25 shows the camera and lighting setup used for the DIC analysis. The objective here was to map the field of strains on the surface of the specimen in order to correlate the longitudinal and transverse strain in the concrete specimen.

Figure 4-25 Camera and lighting setup for DIC analysis.

Chapter 5: Experimental results

In this chapter, the experimental output is presented and discussed. Force – displacement curves are obtained for each specimen, along with the displacement measurements of the attached differential transformers (DTs) for the bar displacement, top concrete surface displacement and the opening of the longitudinal crack. Digital Image Correlation (DIC) is used in the second segment of this chapter to monitor the displacement of surface locations. Strain levels along the longitudinal and normal directions are obtained from this analysis to be assessed and corroborated with the analytical models of Chapter 3 which represent the predictions made prior to the tests. Tests were done at full maturity of the specimens so comparisons are made in the context of the different tests setups at the same age, with no reference to 28-day strengths.

5.1 Results from the experimental output

5.1.1 Specimen CMK1-5-A

The first specimen of mixture CMK reached a maximum applied load of 37.087kN at a displacement of 3.675mm (Figure 5-1). Upon reaching approximately 73% of the peak strength, internal cracking and pullout of the steel fibers could be observed on the ascending branch of the force – displacement curve. A distinct “breaking” sound also signaled the engagement of the fiber reinforcement. At peak strength the major horizontal crack appeared at the free end of the embedded test bar. One end of the crack path intercepted one of the circular openings and proceeded horizontally while the other end followed an upwards inclined path. Shortly after the appearance of the horizontal crack, a longitudinal splitting crack path appeared along the length of the test bar.

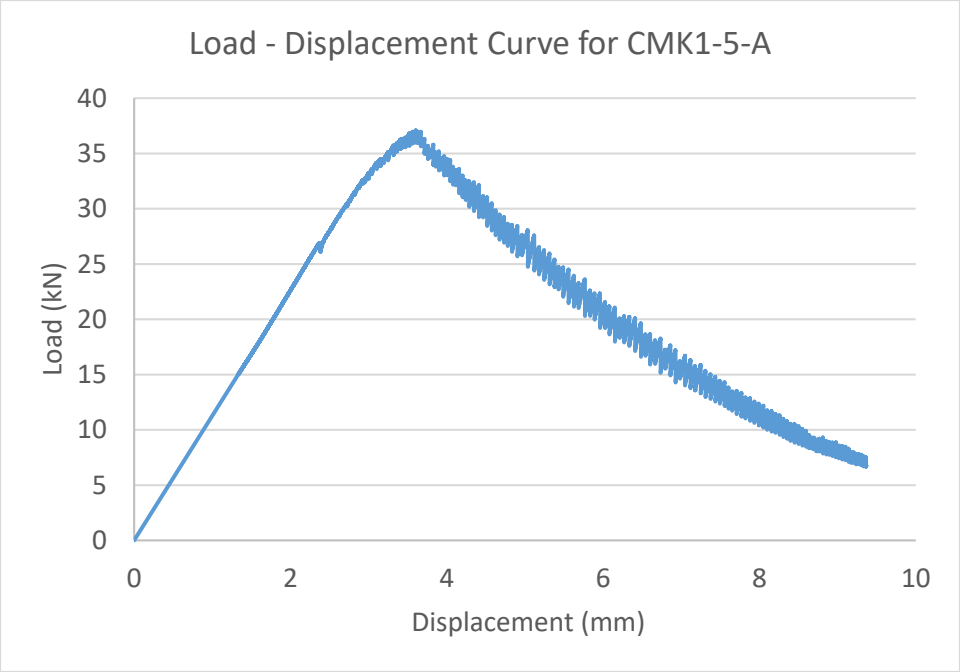

Figure 5-1 Load - Displacement Curve for Specimen CMK1-5-A.

Figure 5-2 plots the evolution of bar translation (in orange) and the concrete upwards translation (in grey) measured with the DT setup as shown in Fig. 4-22. The difference between the two curves quantifies the reinforcement slip, which is measured over a gauge length of 10mm for the concrete surface and 15mm for the bar displacement. Also plotted in light blue is the longitudinal crack opening measured over a gauge length of 8mm centered with respect to the vertical bar – so this really is an approximation of the splitting crack width (at a distance of 20mm from the loaded end of the bar anchorage). It is noted that transverse crack opening is related through the rib profile with the vertical translation of the bar. Note that the crack opening at peak stress is about 0.25mm, however, this is hardly visible but at the top part of the specimen in Figure 5-4 which refers to peak response. The difference in the values between the loading system and the vertical translation of the reinforcement is owing to displacements and deformations occurring outside the gauge lengths of the DTs (eg. bar elongation above the point of measurement of the DT and horizontal cracks below the end of anchorage (Figure 4-23).

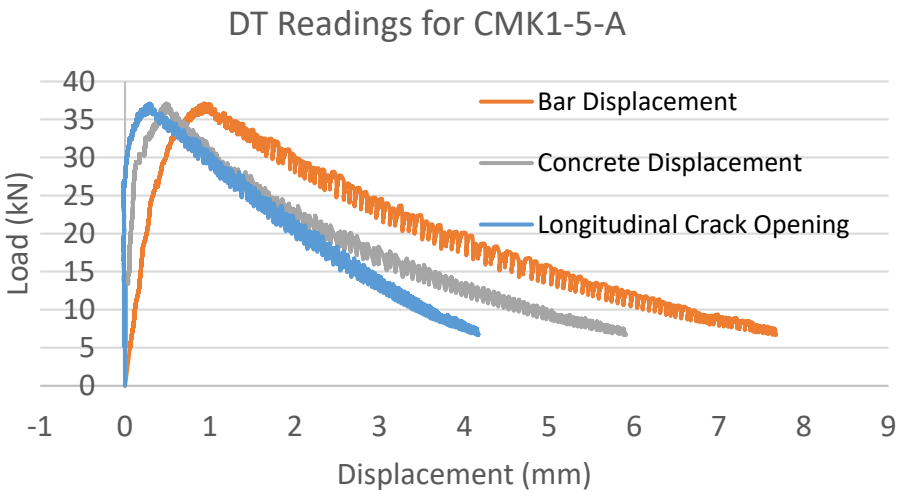

Figure 5-2 Displacement output from DTs for Speciment CMK1-5-A.

Average bond stress is obtained by dividing the developed bar force with the contact perimeter of the bar ($=5\pi\cdot(D_b)^2$) $=4020$ mm^2. As mentioned already this is only an indication of the bond intensity – pointwise, the local bond stress differs from this average value. Figure 5-3 shows the corresponding bond stress – slip relationship obtained from the force and displacement output of the experiment.

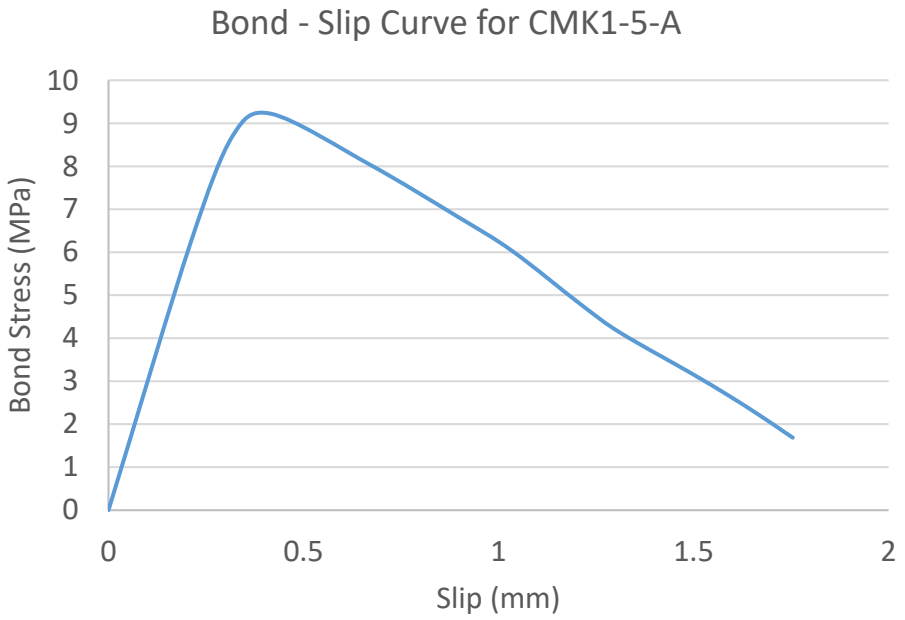

Figure 5-3 Bond Stress – Slip Curve for Specimen CMK1-5-A.

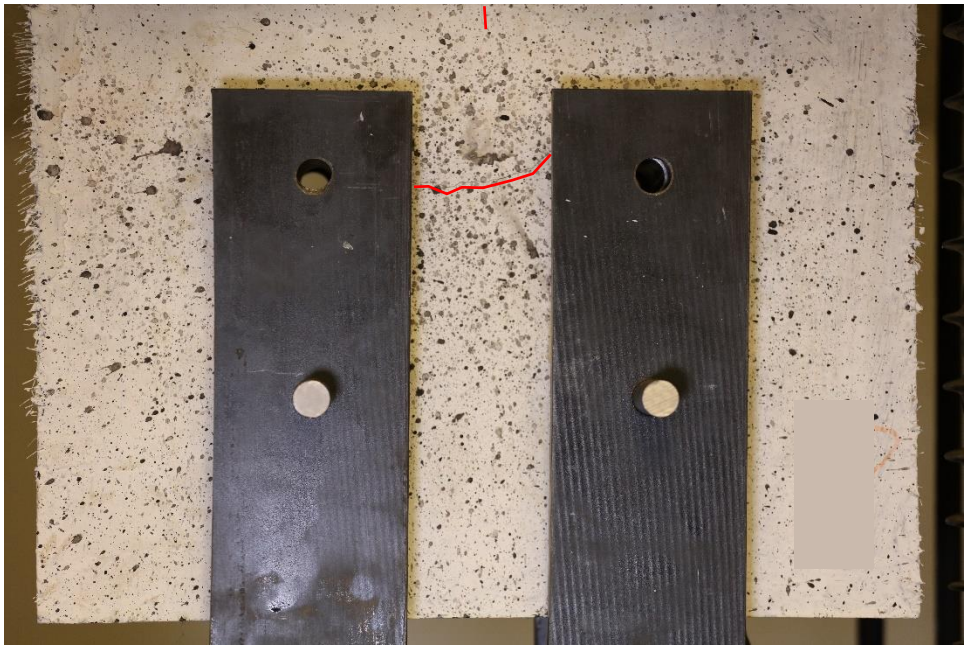

Figure 5-4 Surface cracking at peak strength for specimen CMK1-5-A.

Figure 5-5 Surface cracking at termination of the experiment for specimen CMK1-5-A.

In the following sections the same information for all test specimens is processed. Results are presented using the same sequence as in the case of Specimen CMK1-5-A, however discussion of the test observations and collective evaluation of the results will be presented in Section 5-2.

5.1.2 Specimen CMK1-5-B

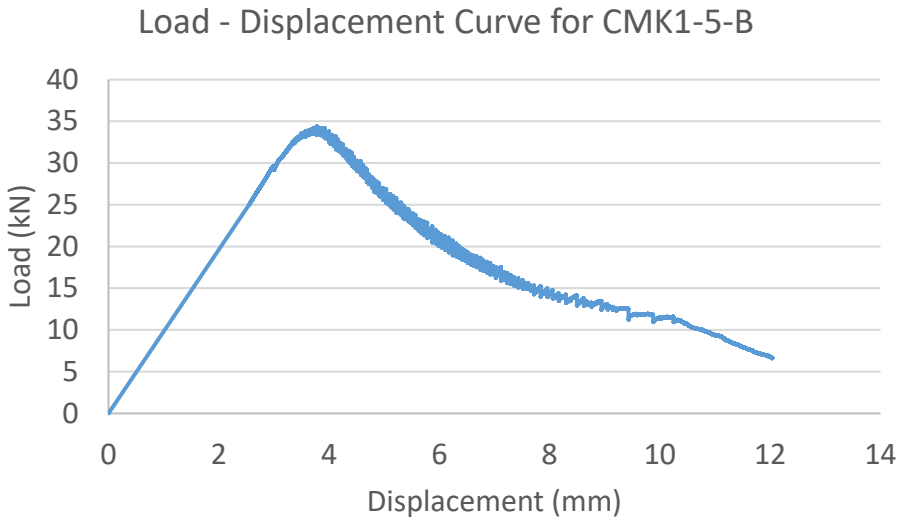

Figure 5-6 Load - Displacement Curve for Specimen CMK1-5-B.

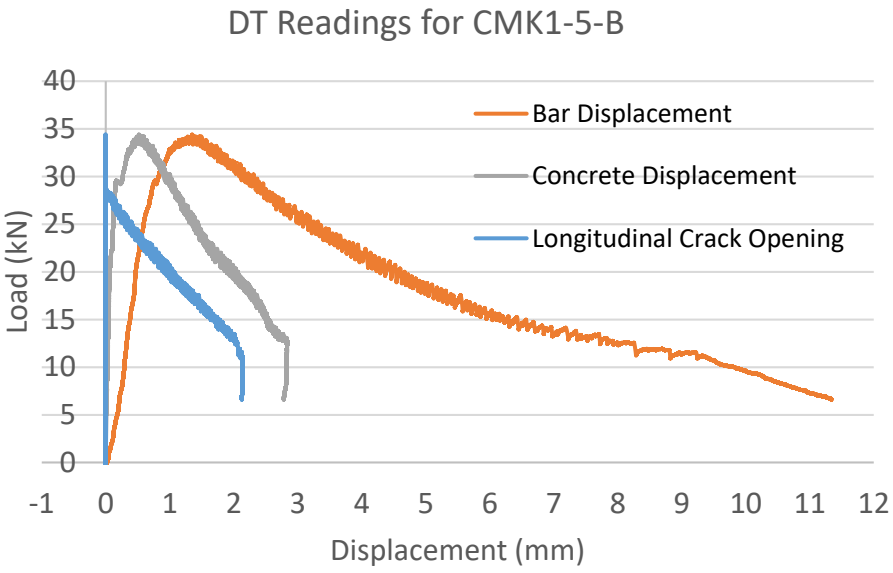

Figure 5-7 Displacement output from DTs for Speciment CMK1-5-B.

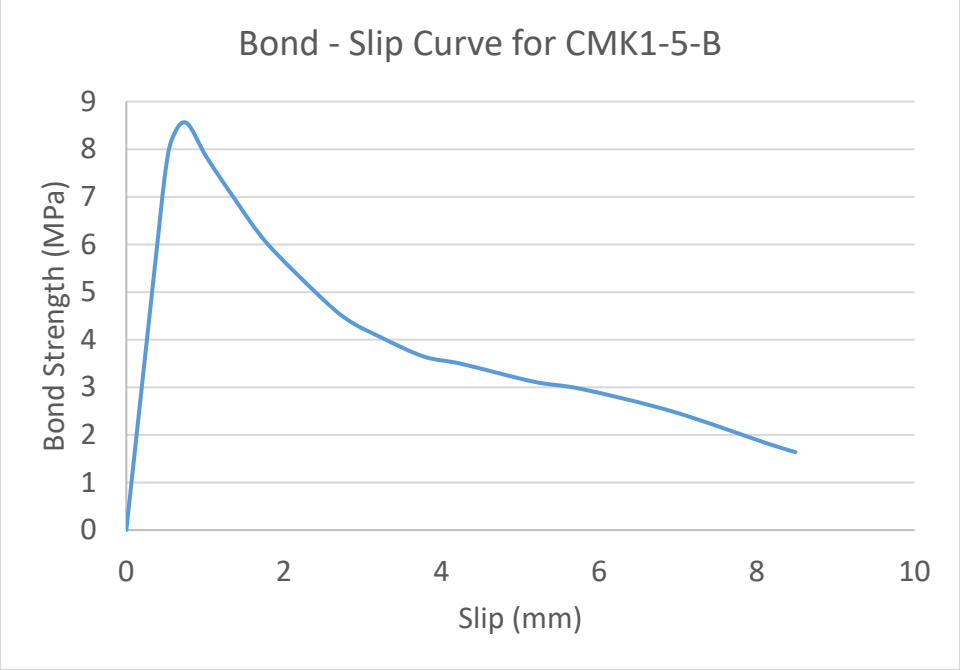

Figure 5-8 Bond Stress – Slip Curve for Specimen CMK1-5-B.

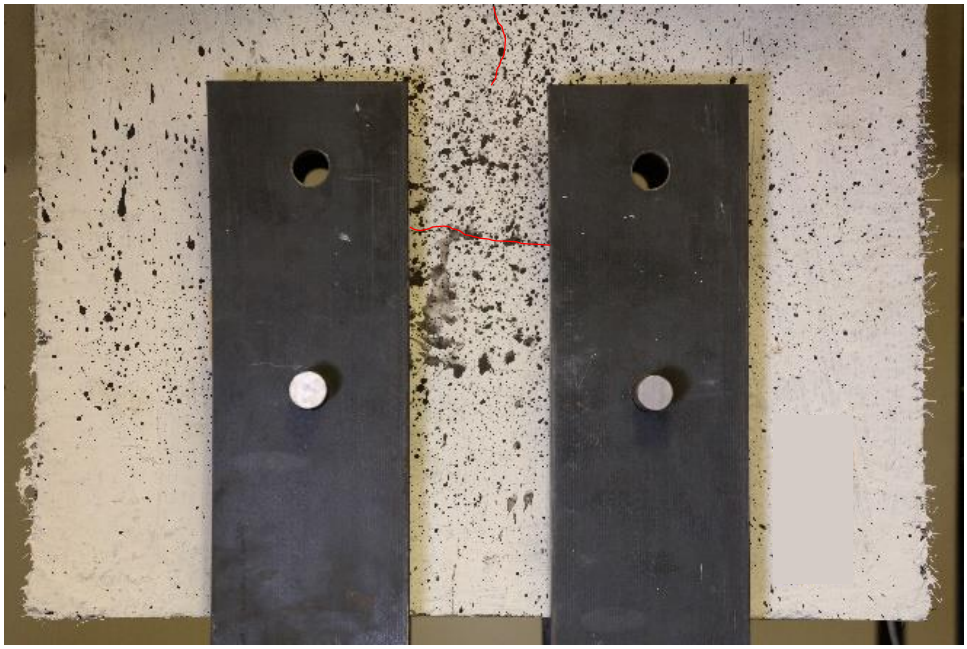

Figure 5-9 Surface cracking at peak strength for specimen CMK1-5-B.

Figure 5-10 Surface cracking at termination of the experiment for specimen CMK1-5-B.

5.1.3 Specimen CMK2-5-A

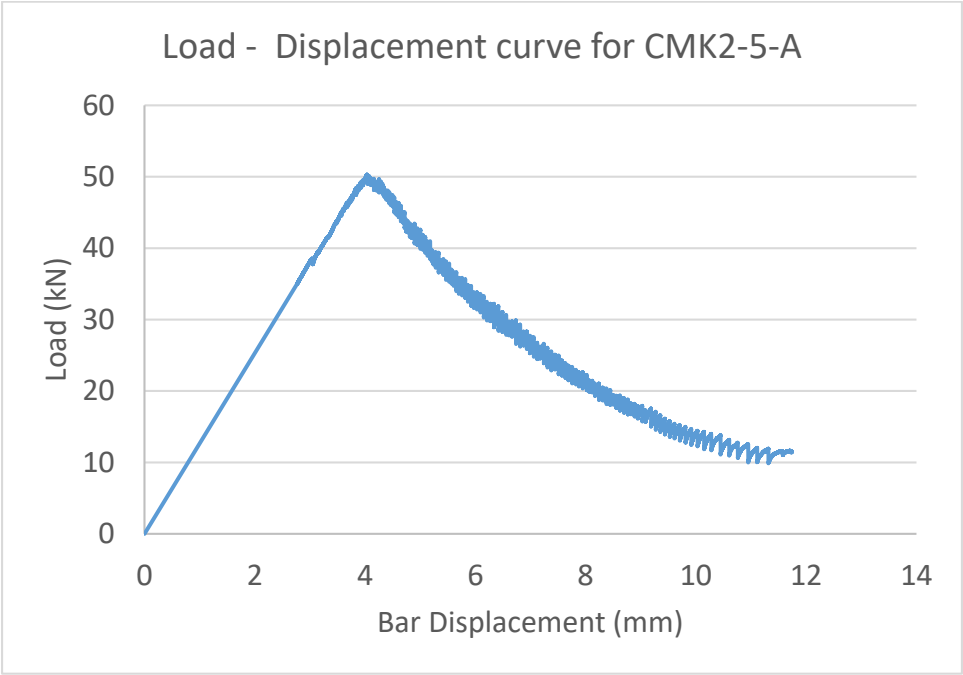

Figure 5-11 Load - Displacement Curve for Specimen CMK2-5-A.

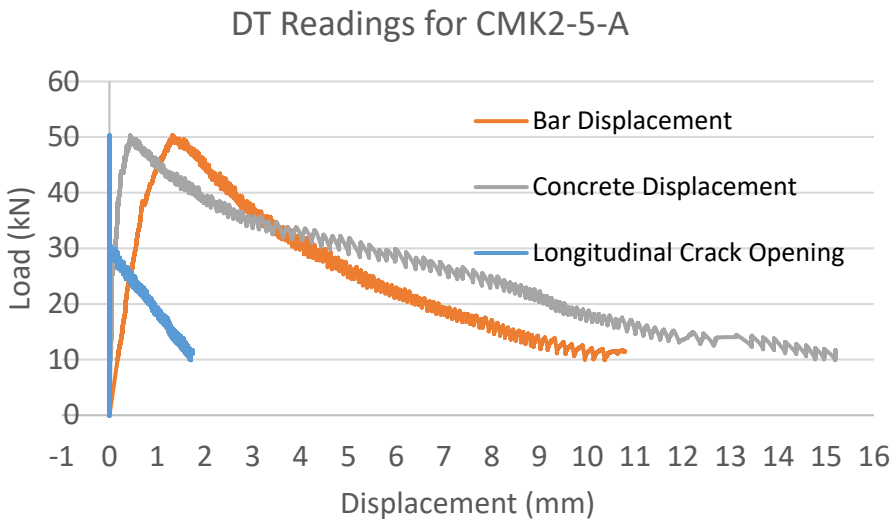

Figure 5-12 Displacement output from DTs for Speciment CMK2-5-A.

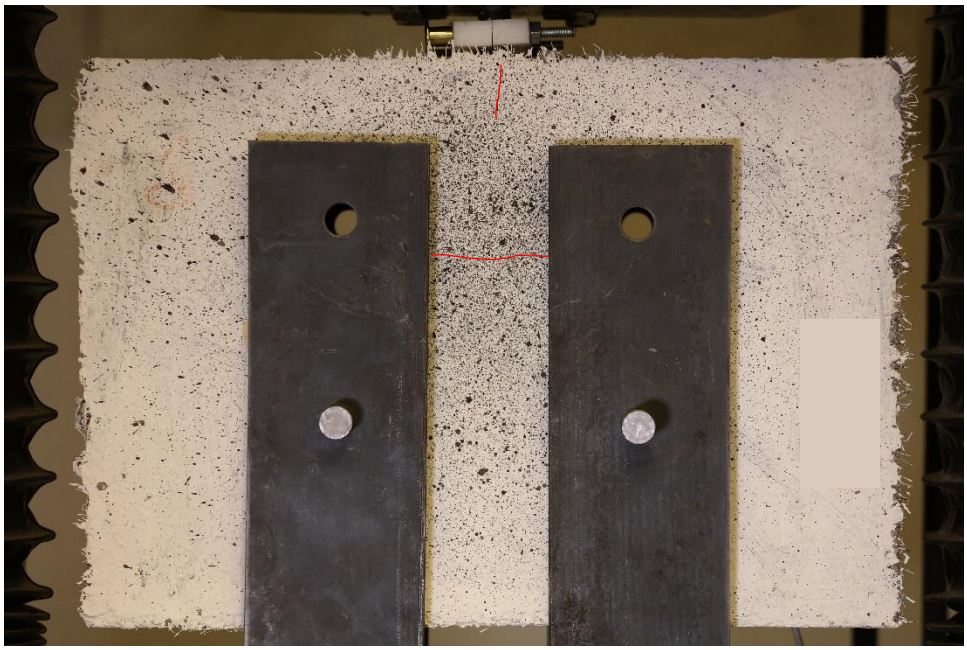

Figure 5-13 Surface cracking at peak strength for specimen CMK2-5-A.

Figure 5-14 Surface cracking at termination of the experiment for specimen CMK2-5-A.

5.1.4 Specimen CMK2-5-B

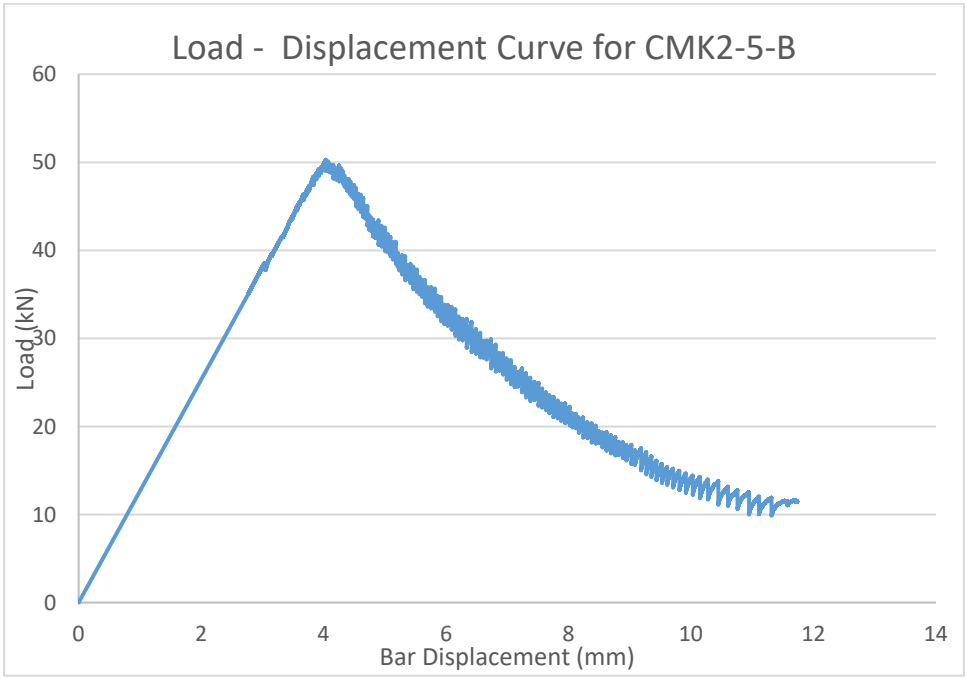

Figure 5-15 Load - Displacement Curve for Specimen CMK2-5-B.

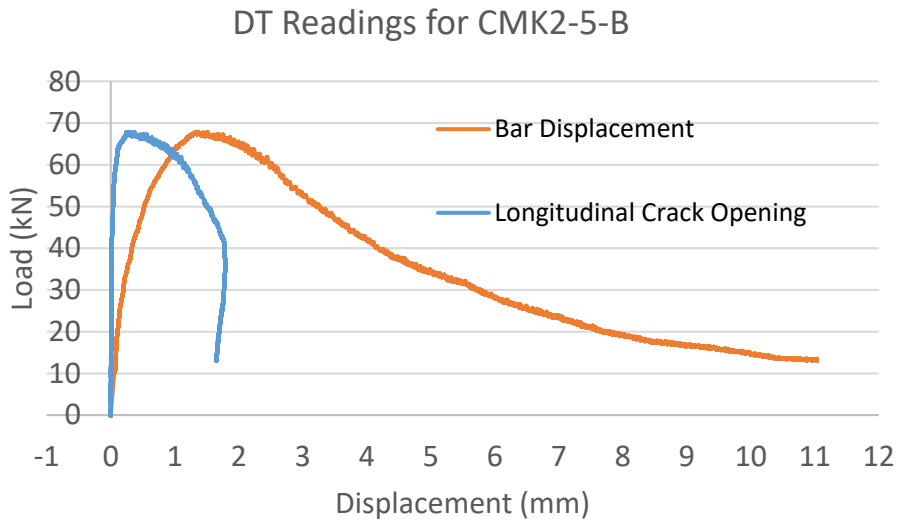

Figure 5-16 Displacement output from DTs for Speciment CMK2-5-B.

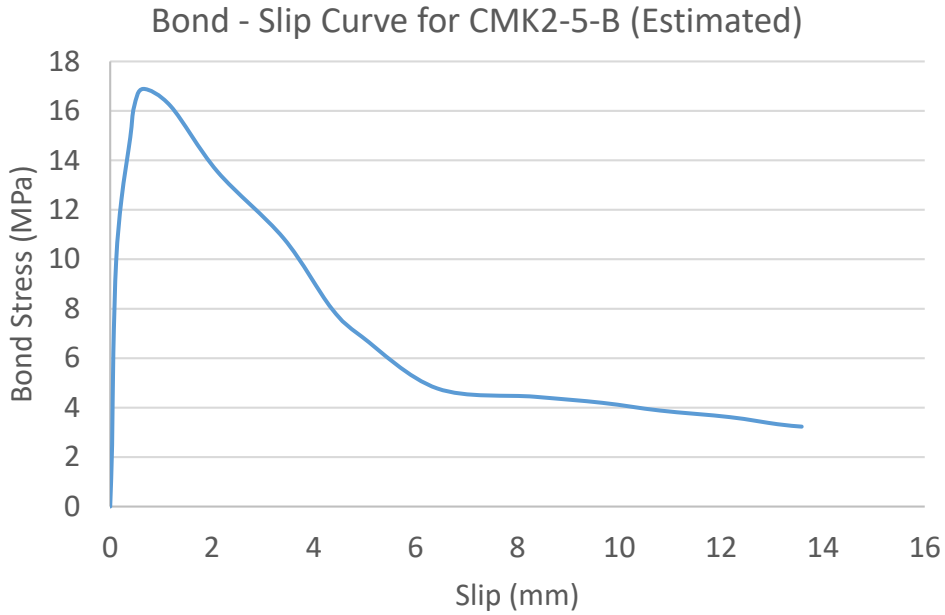

Figure 5-17 Bond Stress – Slip Curve for Specimen CMK2-5-B.

Figure 5-18 Surface cracking at peak strength for specimen CMK2-5-B.

Figure 5-19 Surface cracking at termination of the experiment for specimen CMK2-5-B.

5.1.5 Specimen CMF1-5-A

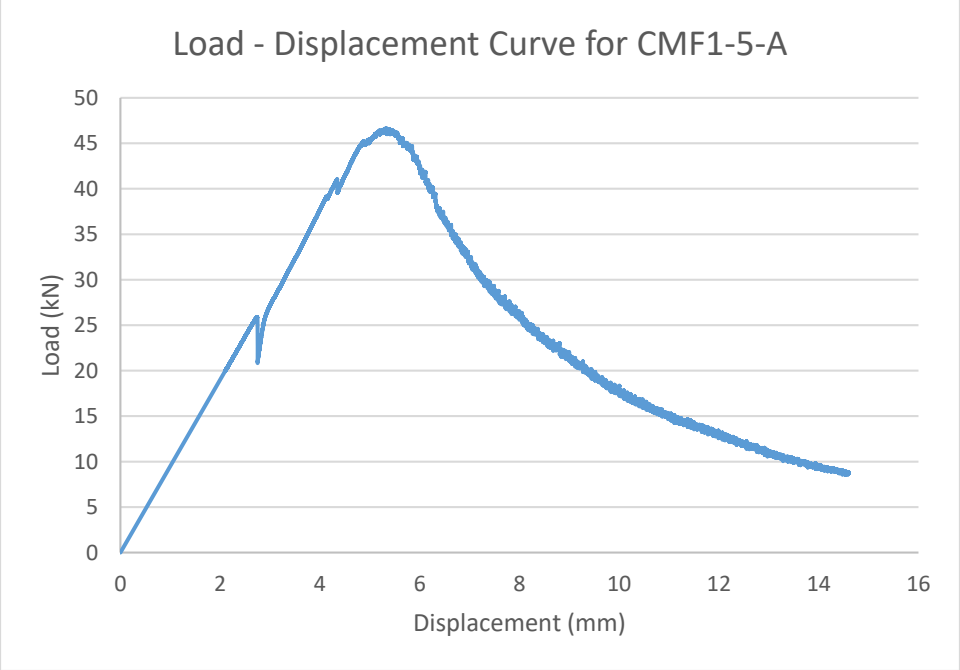

Figure 5-20 Load - Displacement Curve for Specimen CMF1-5-A.

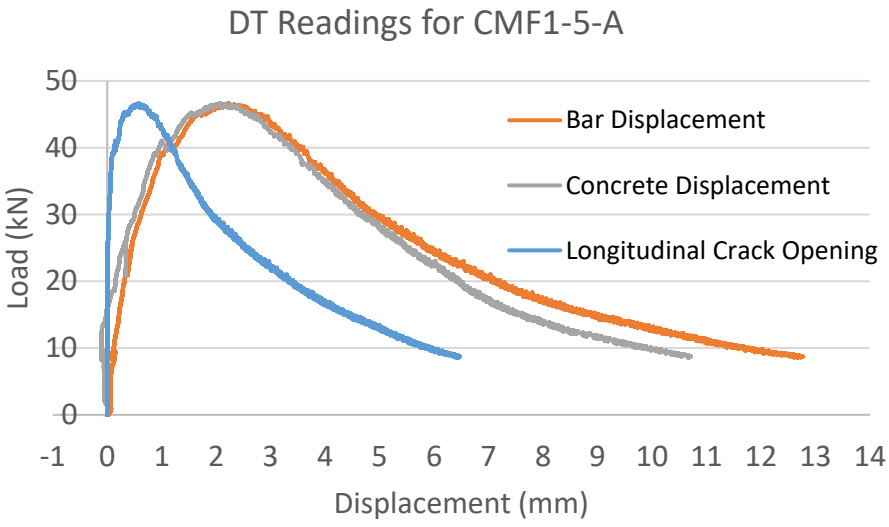

Figure 5-21 Displacement output from DTs for Speciment CMF1-5-A.

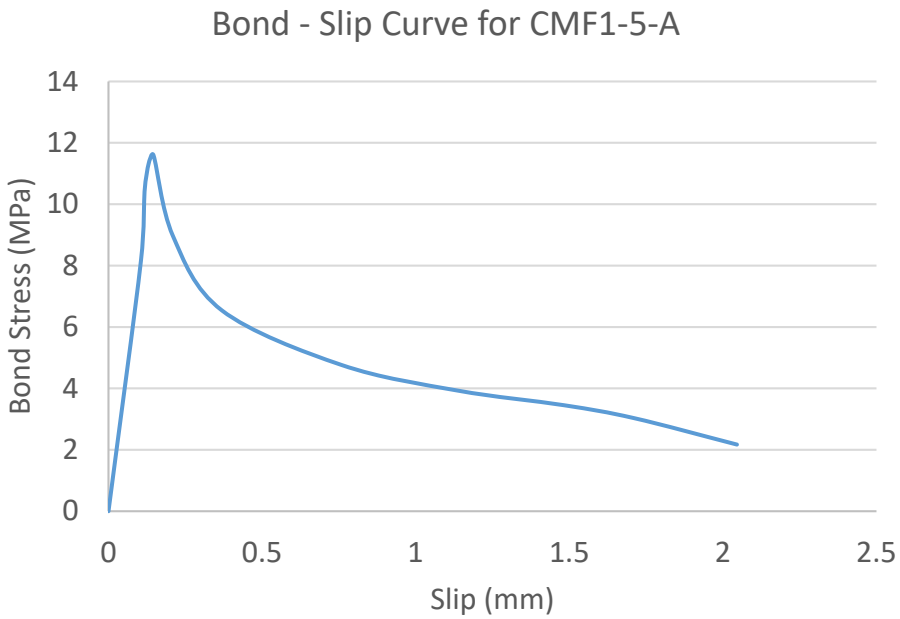

Figure 5-22 Bond Stress – Slip Curve for Specimen CMF1-5-A.

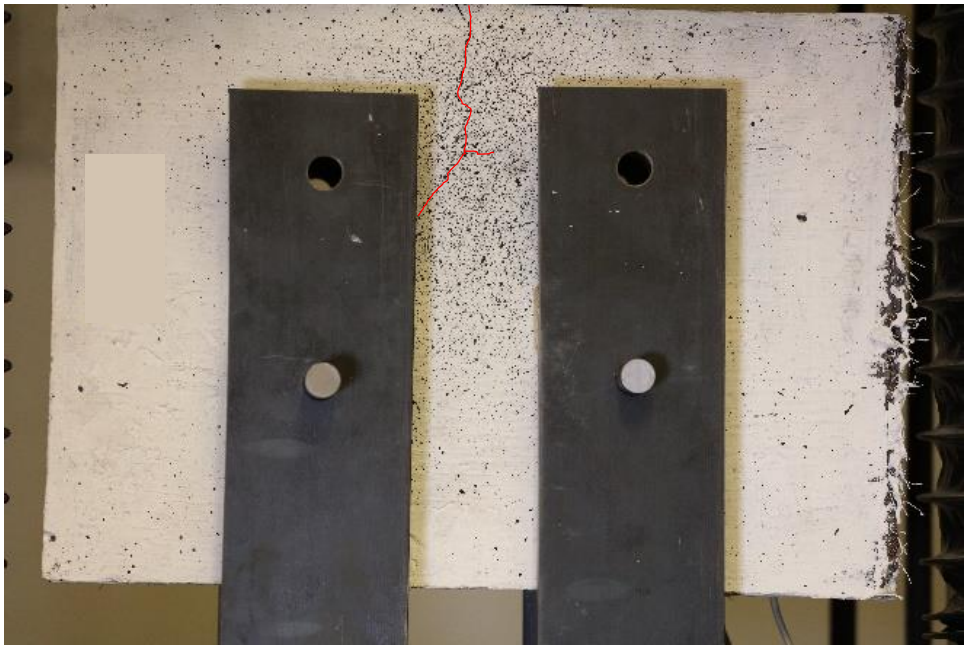

Figure 5-23 Surface cracking at peak strength for specimen CMF1-5-A.

Figure 5-24 Surface cracking at termination of the experiment for specimen CMF1-5-A.

5.1.6 Specimen CMF1-5-B

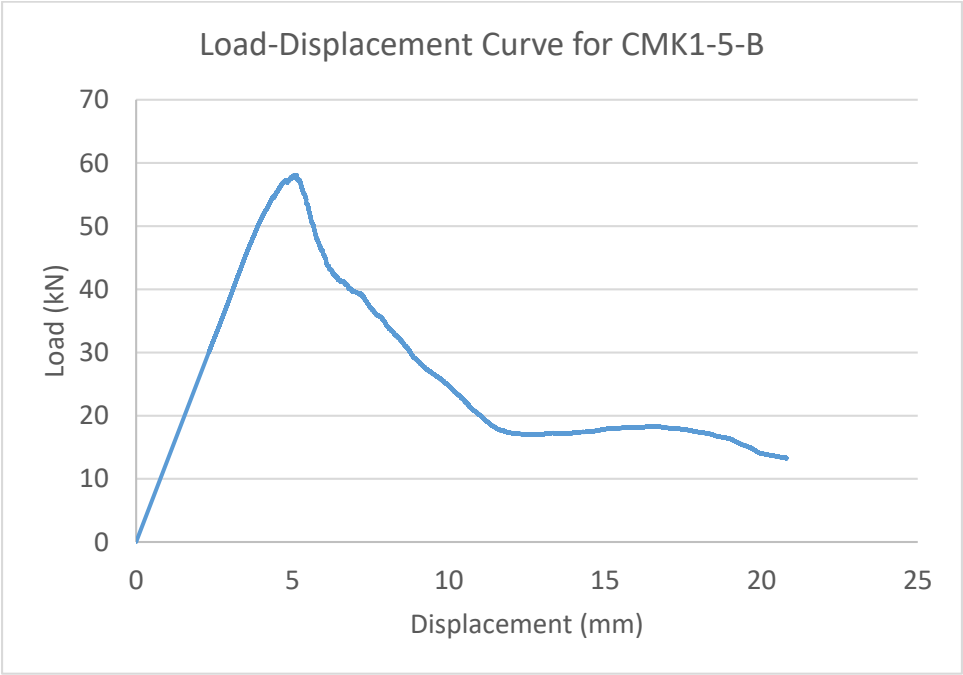

Figure 5-25 Load - Displacement Curve for Specimen CMF1-5-B.

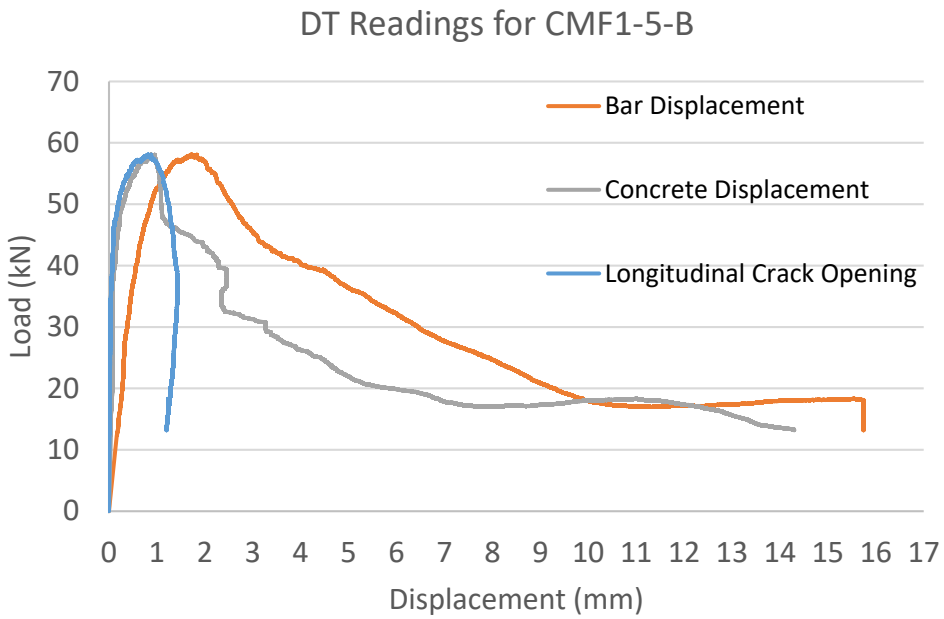

Figure 5-26 Displacement output from DTs for Speciment CMF1-5-B.

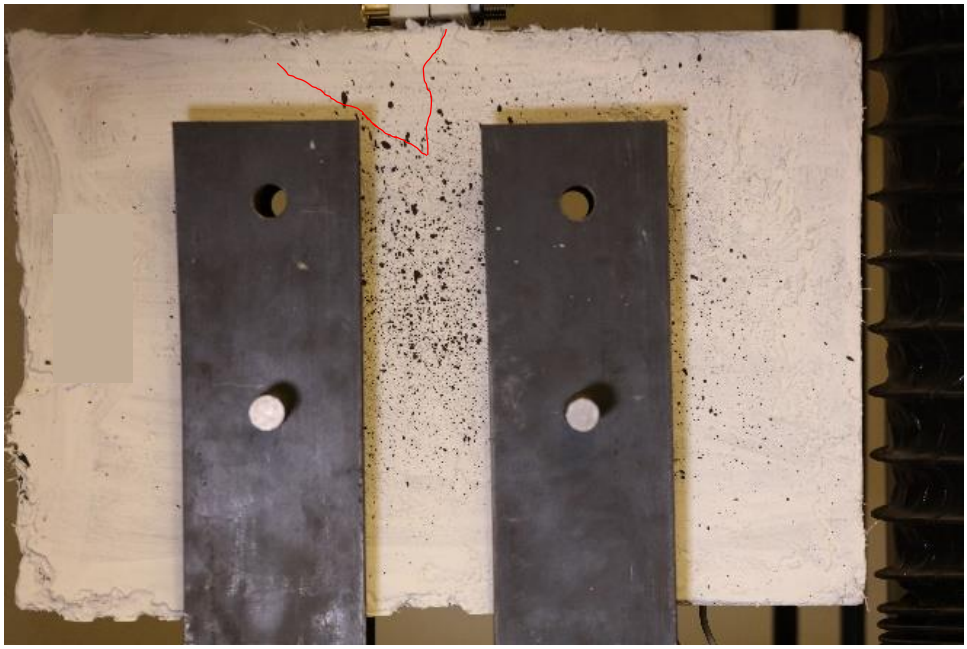

Figure 5-27 Surface cracking at peak strength for specimen CMF1-5-B.

Figure 5-28 Surface cracking at termination of the experiment for specimen CMF1-5-B.

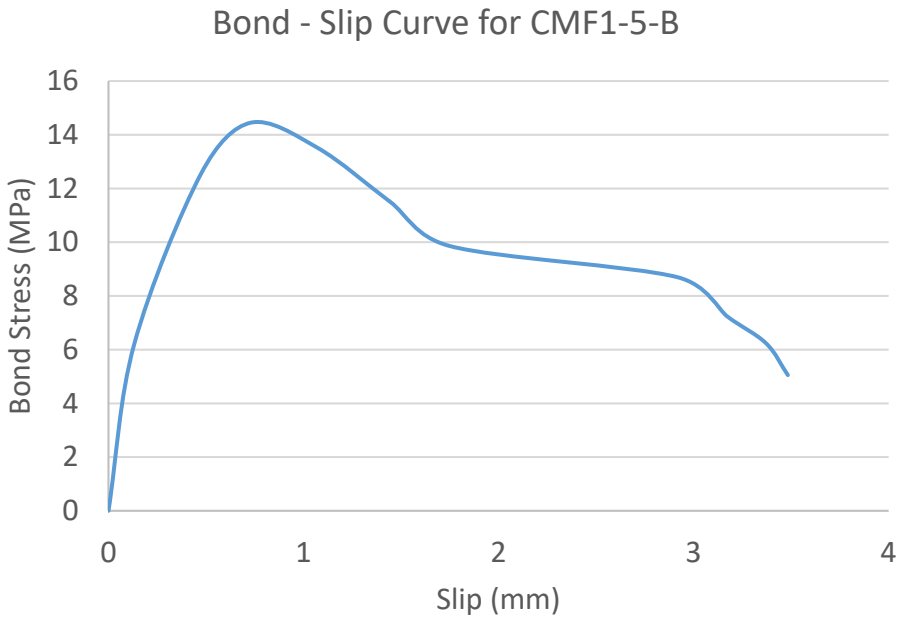

Figure 5-29 Bond Stress – Slip Curve for Specimen CMF1-5-B.

5.1.7 Specimen CMF2-5-A

5.1.7.1 CMF2-5-A (Part 1)

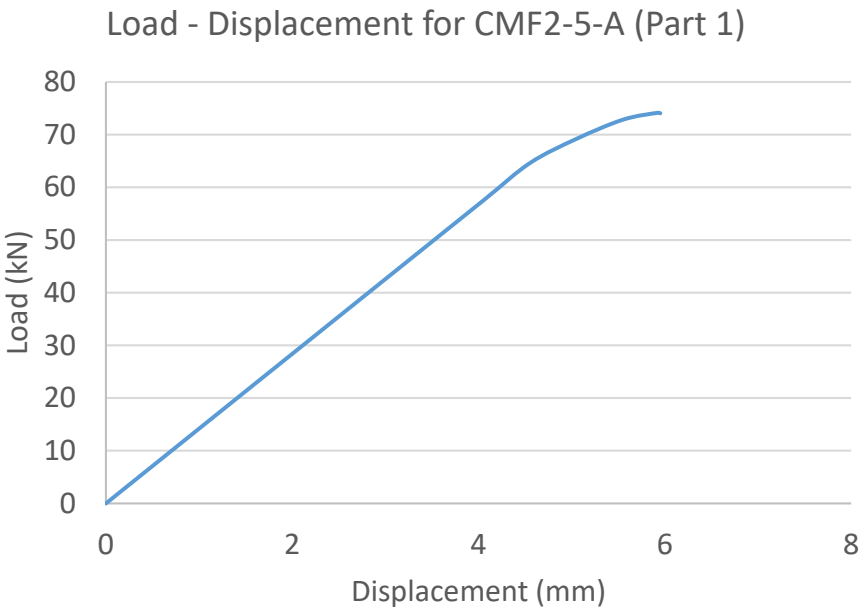

Figure 5-30 Load - Displacement Curve for Specimen CMK2-5-A (Part 1).

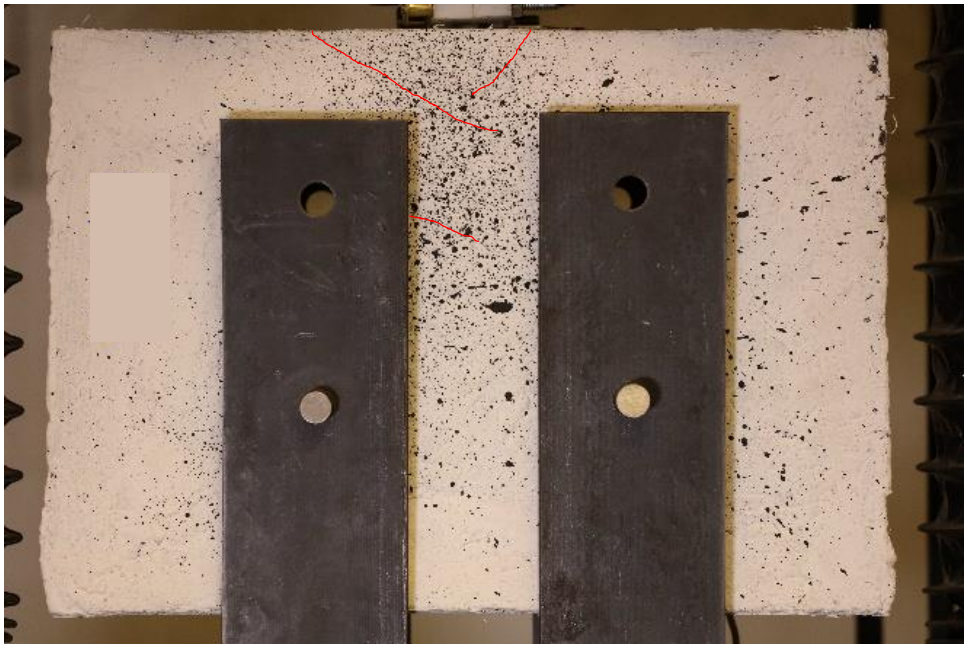

Figure 5-31 Surface cracking at peak strength for specimen CMF2-5-A (Part 1).

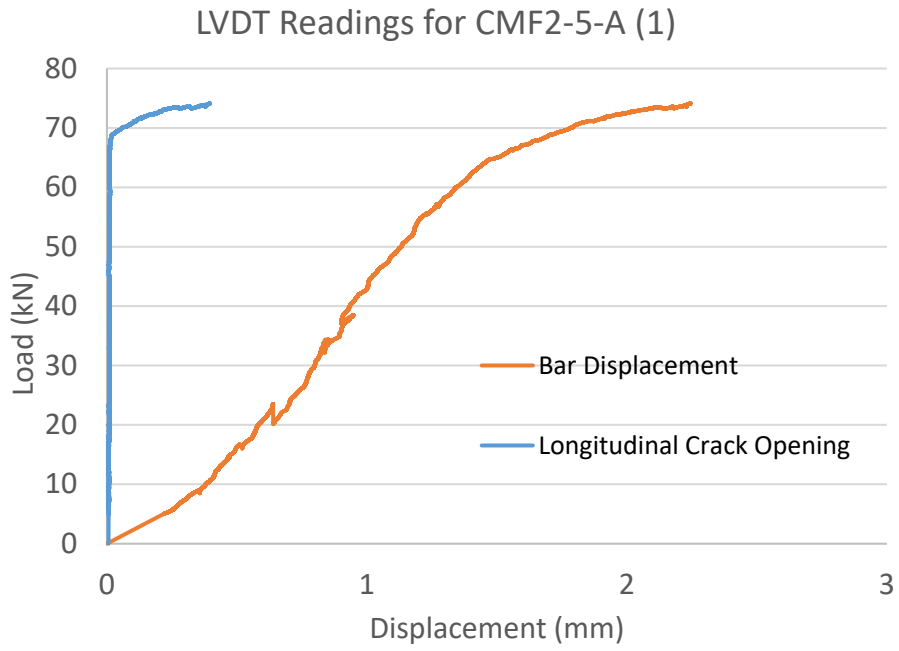

Figure 5-32 Displacement output from DTs for Speciment CMK2-5-A (Part 1).

5.1.7.2 CMF2-5-A (Part 2)

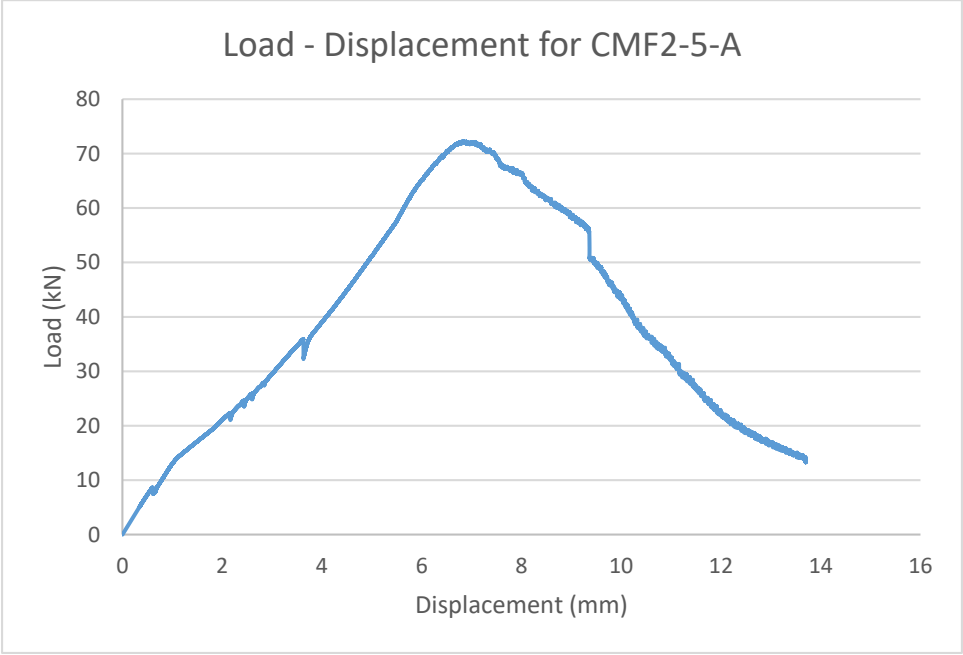

Figure 5-33 Load - Displacement Curve for Specimen CMK2-5-A (Part 2).

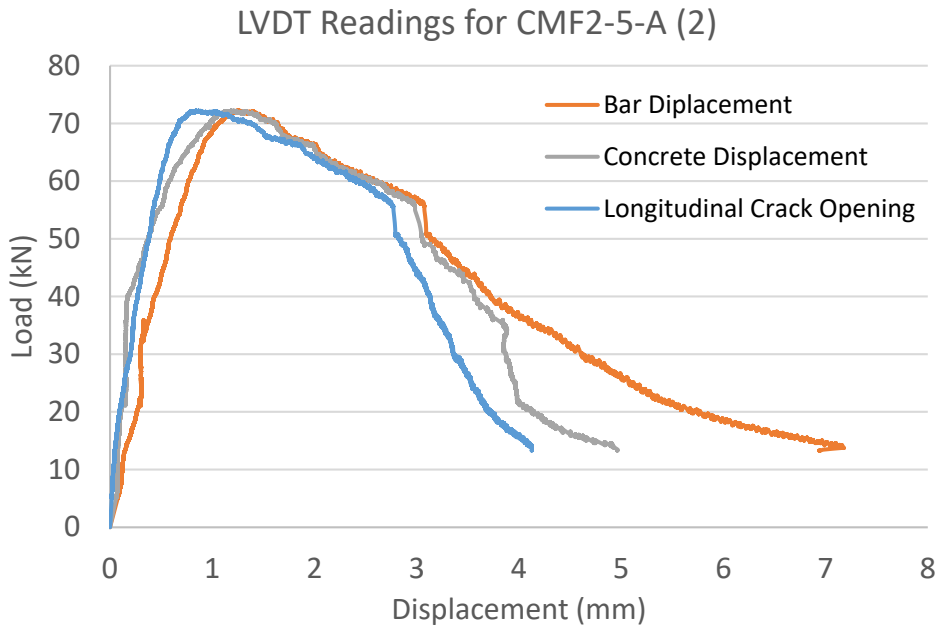

Figure 5-34 Displacement output from DTs for Speciment CMF2-5-A (Part 2).

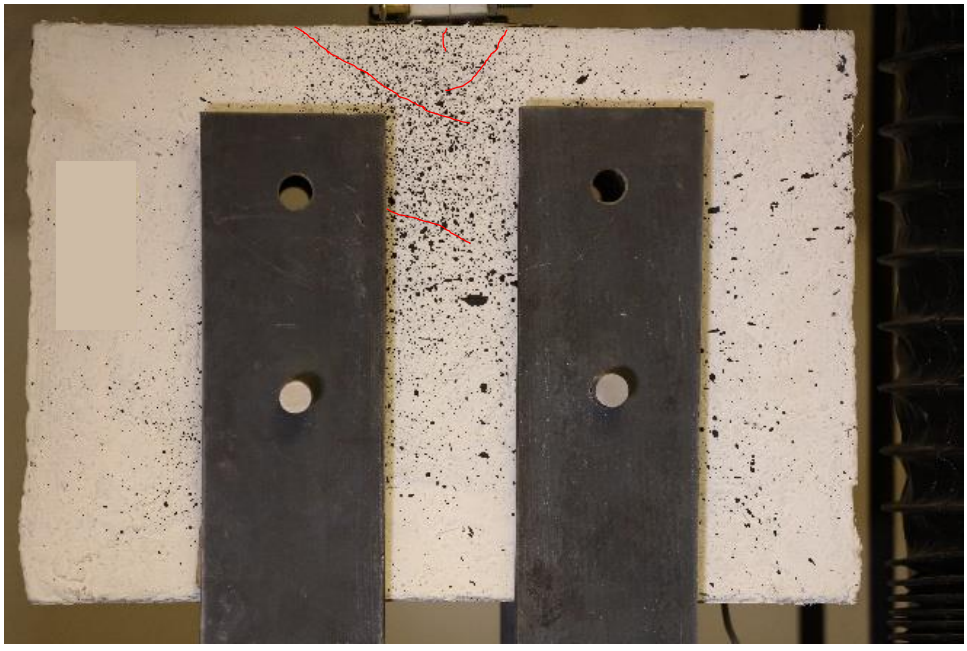

Figure 5-35 Surface cracking at peak strength for specimen CMF2-5-A (Part 2).

Figure 5-36 Surface cracking at termination of the experiment for specimen CMF2-5-A (Part 2).

5.1.8 Specimen IHNJ1-5-A

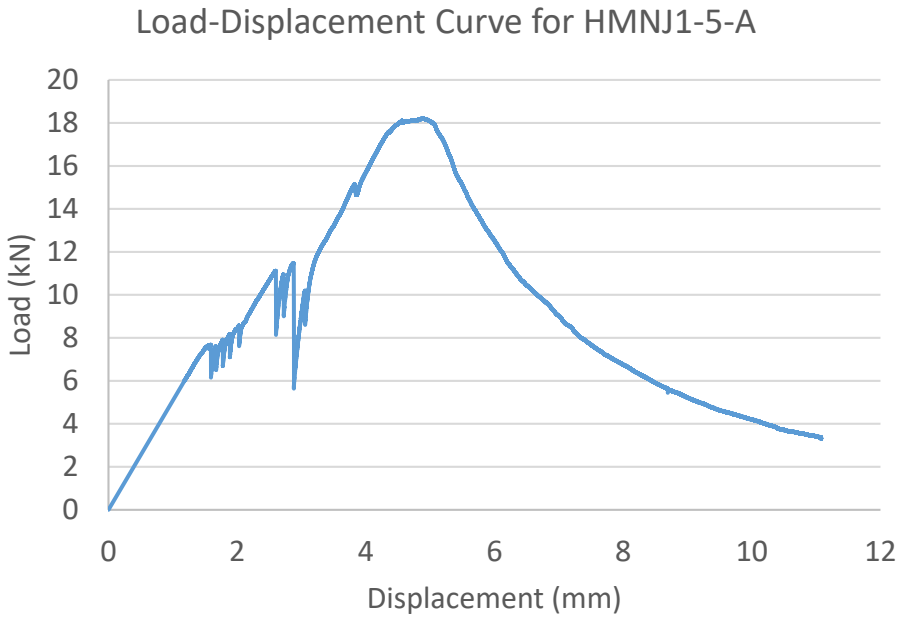

Figure 5-37 Load - Displacement Curve for Specimen IHNJ1-5-A.

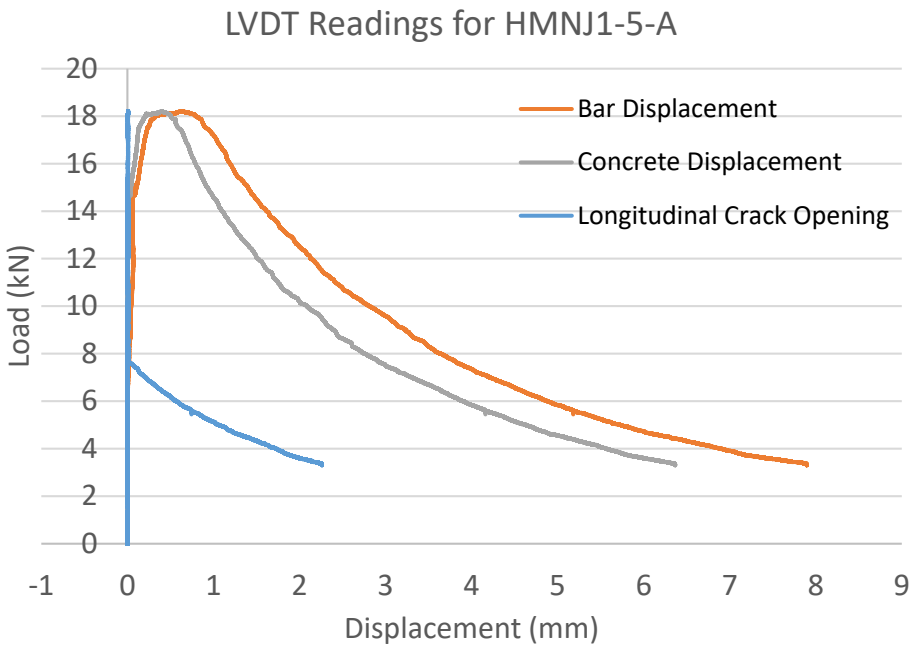

Figure 5-38 Displacement output from DTs for Speciment IHNJ1-5-A.

Figure 5-39 Surface cracking at peak strength for specimen IHNJ1-5-A.

Figure 5-40 Surface cracking at termination of the experiment for specimen IHNJ1-5-A.

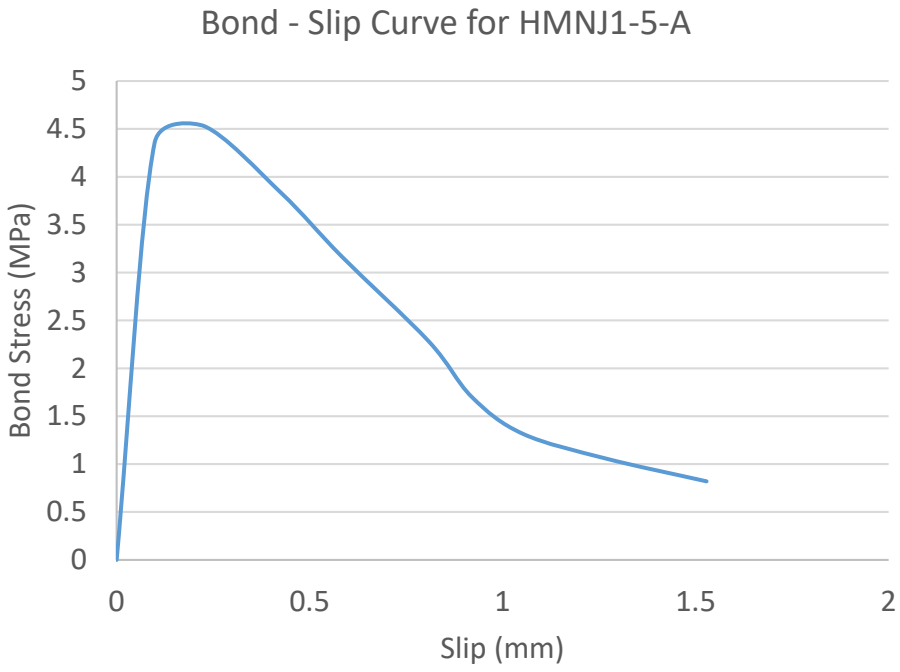

Figure 5-41 Bond Stress – Slip Curve for Specimen IHNJ1-5-A.

5.1.9 Specimen IHNJ1-5-B

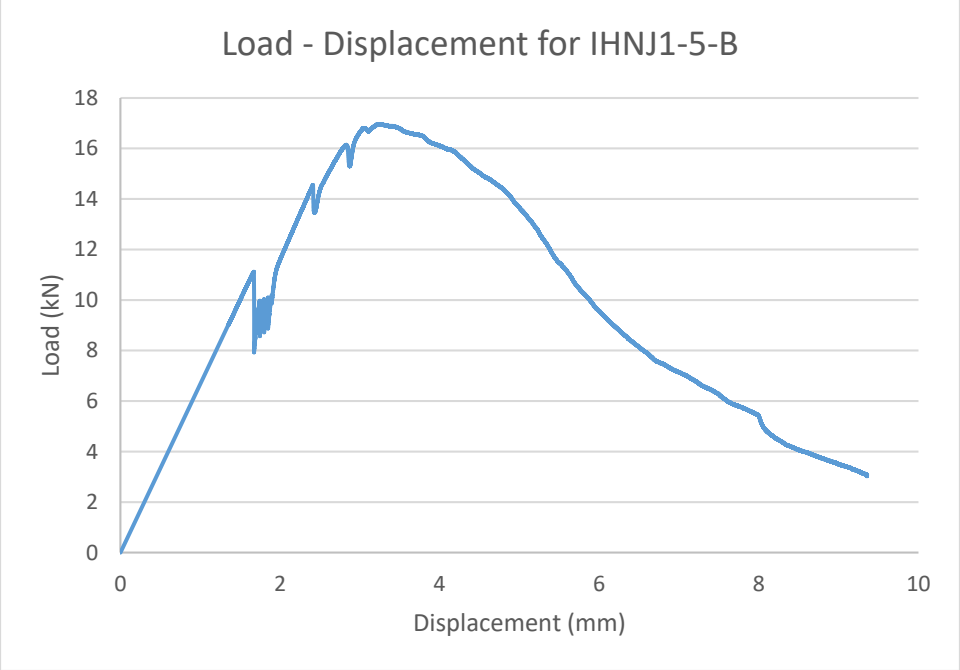

Figure 5-42 Load - Displacement Curve for Specimen IHNJ1-5-B.

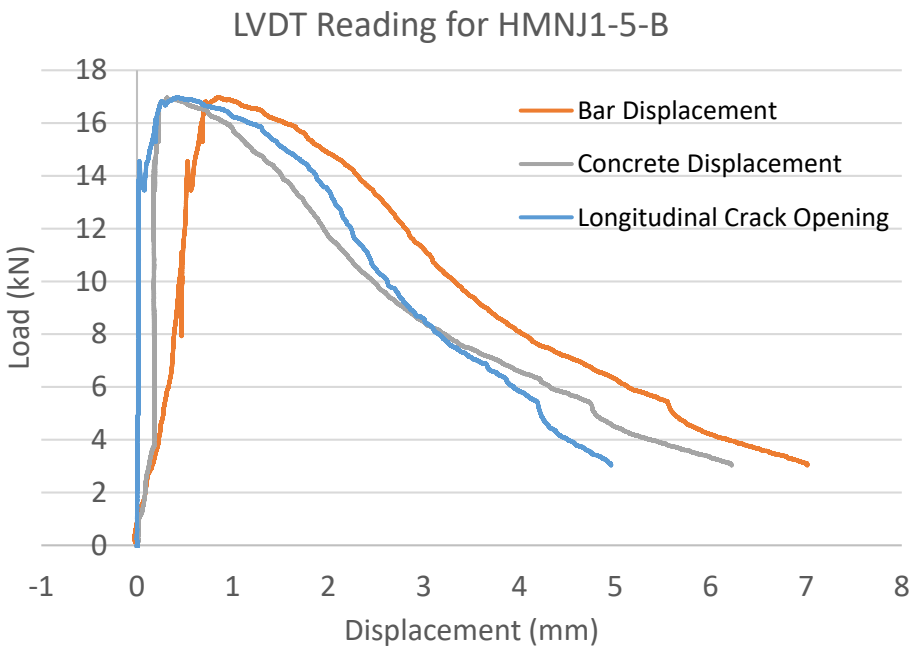

Figure 5-43 Displacement output from DTs for Speciment IHNJ1-5-B.

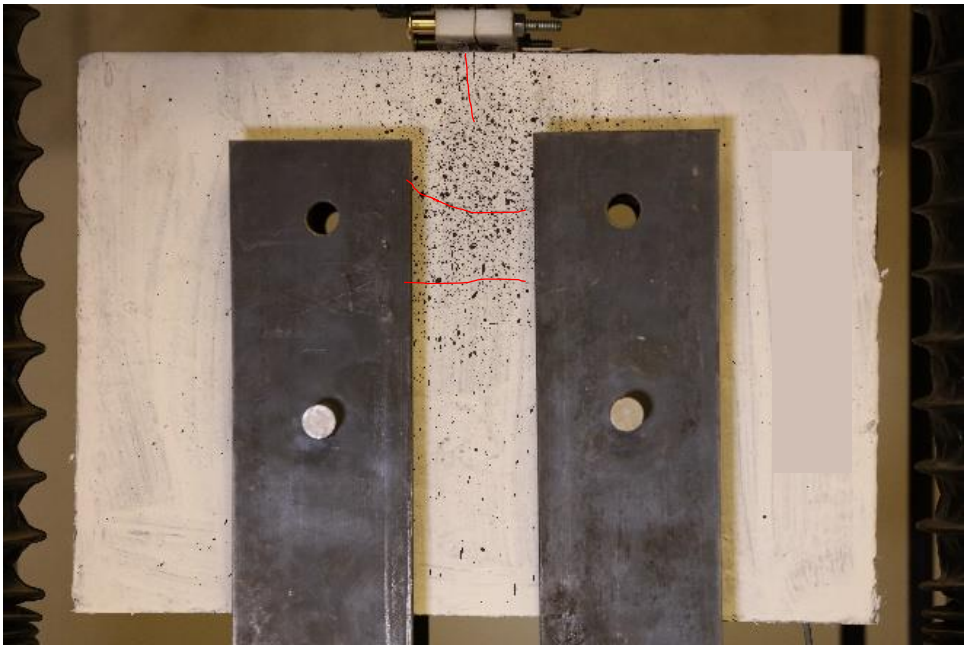

Figure 5-44 Surface cracking at peak strength for specimen IHNJ1-5-B.

Figure 5-45 Surface cracking at termination of the experiment for specimen IHNJ1-5-B.

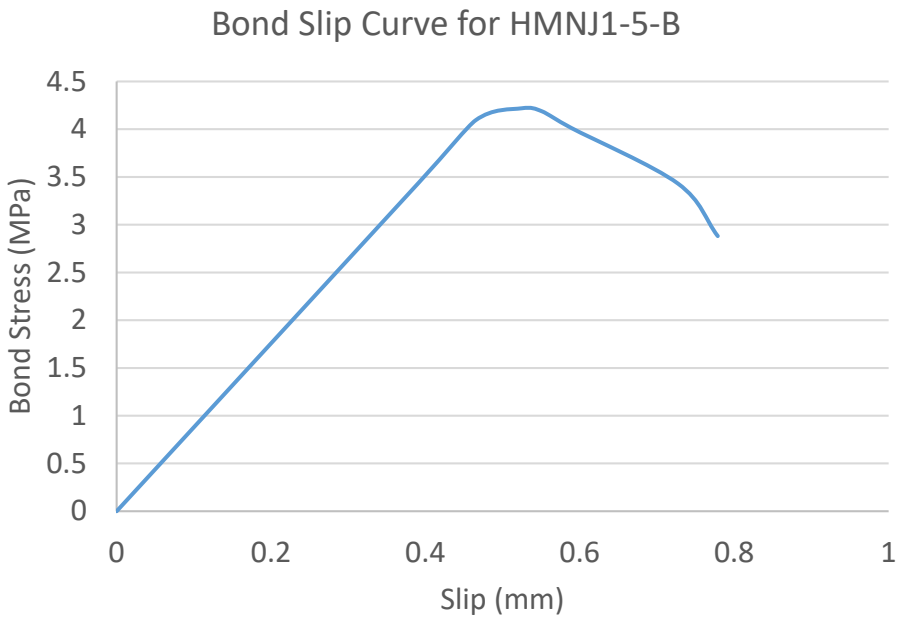

Figure 5-46 Bond Stress – Slip Curve for Specimen IHNJ1-5-B.

5.1.10 Specimen IHNJ2-5-A

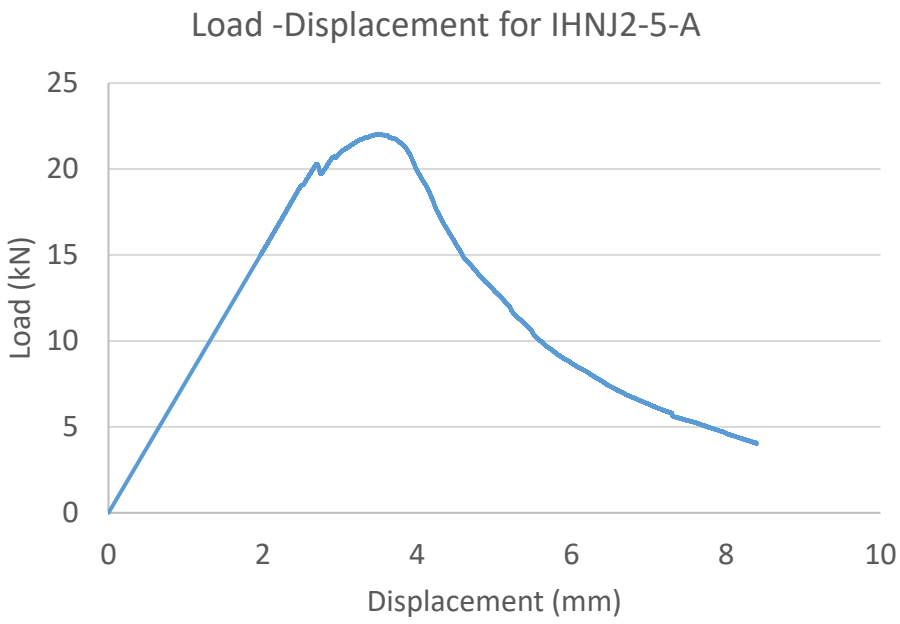

Figure 5-47 Load - Displacement Curve for Specimen IHNJ2-5-A.

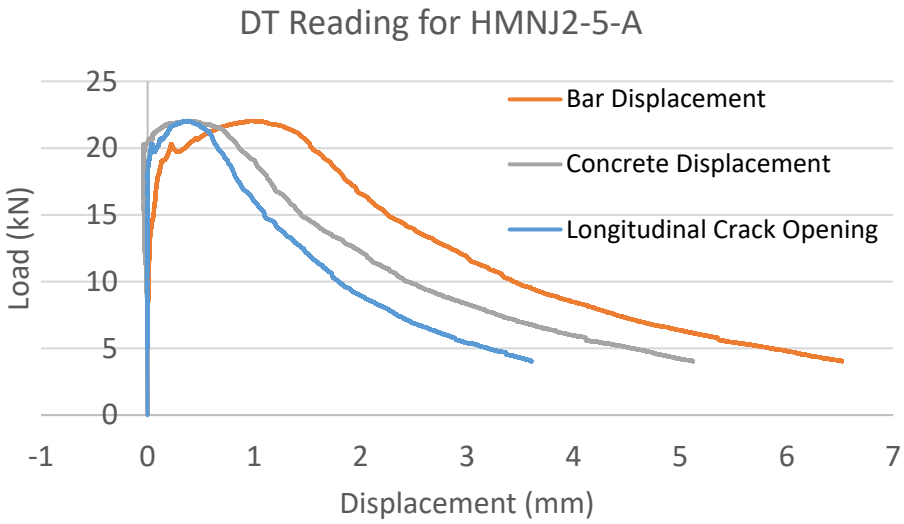

Figure 5-48 Displacement output from DTs for Speciment IHNJ2-5-A.

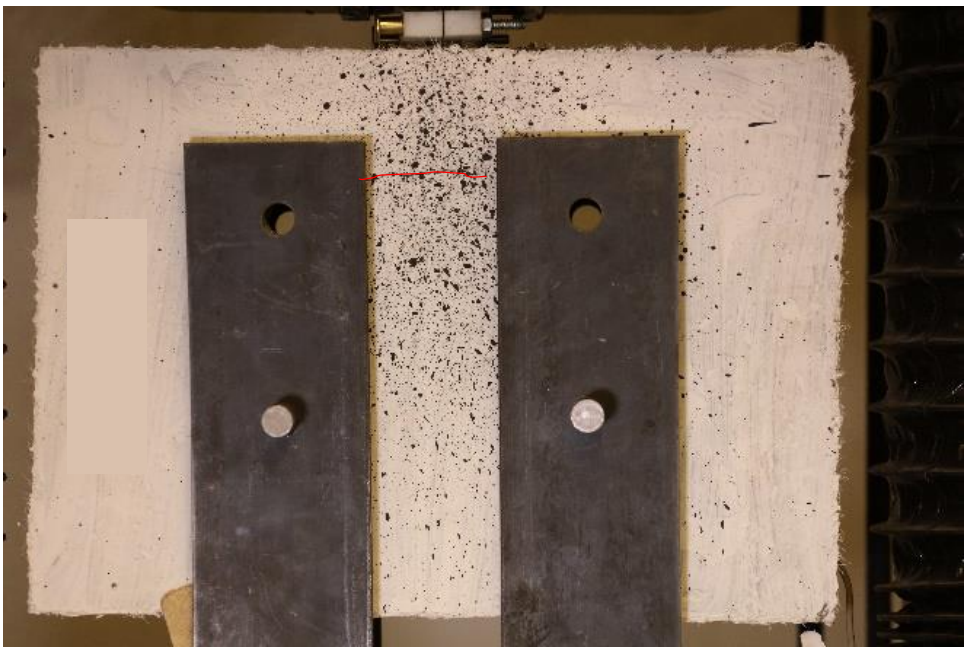

Figure 5-49 Surface cracking at peak strength for specimen IHNJ2-5-A.

Figure 5-50 Surface cracking at termination of the experiment for specimen IHNJ2-5-A.

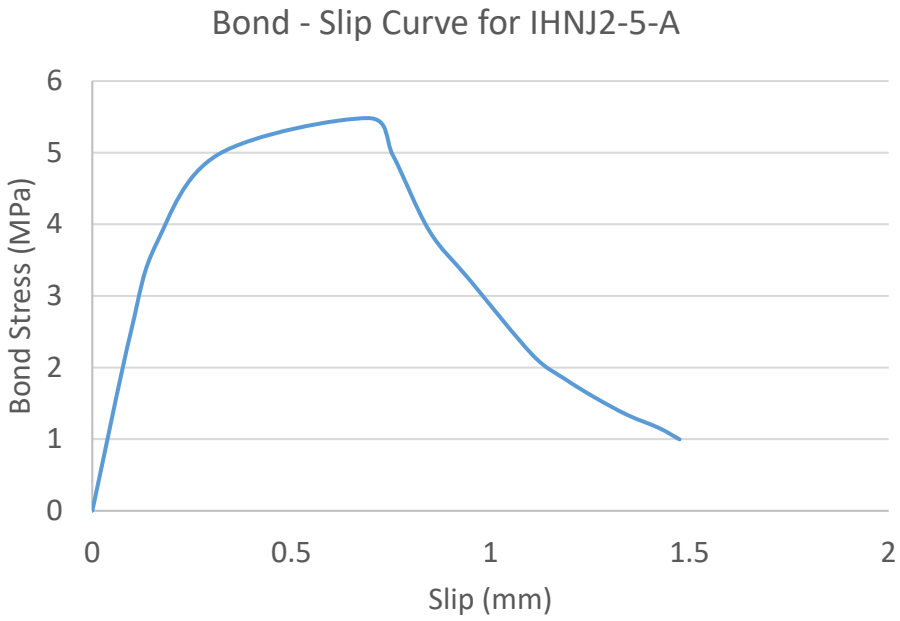

Figure 5-51 Bond Stress – Slip Curve for Specimen IHNJ2-5-A.

5.1.11 Specimen IHNJ2-5-B

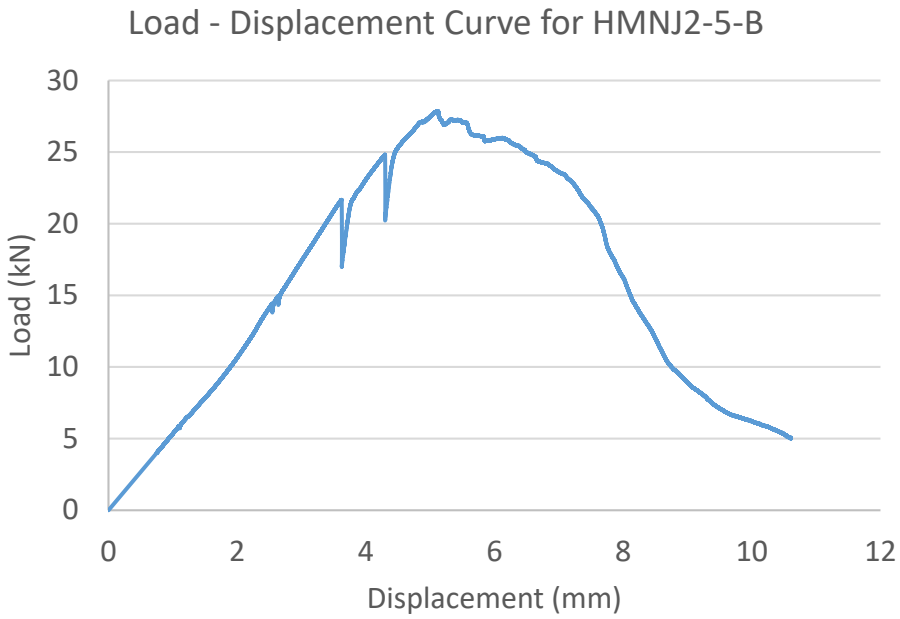

Figure 5-52 Load - Displacement Curve for Specimen IHNJ2-5-B.

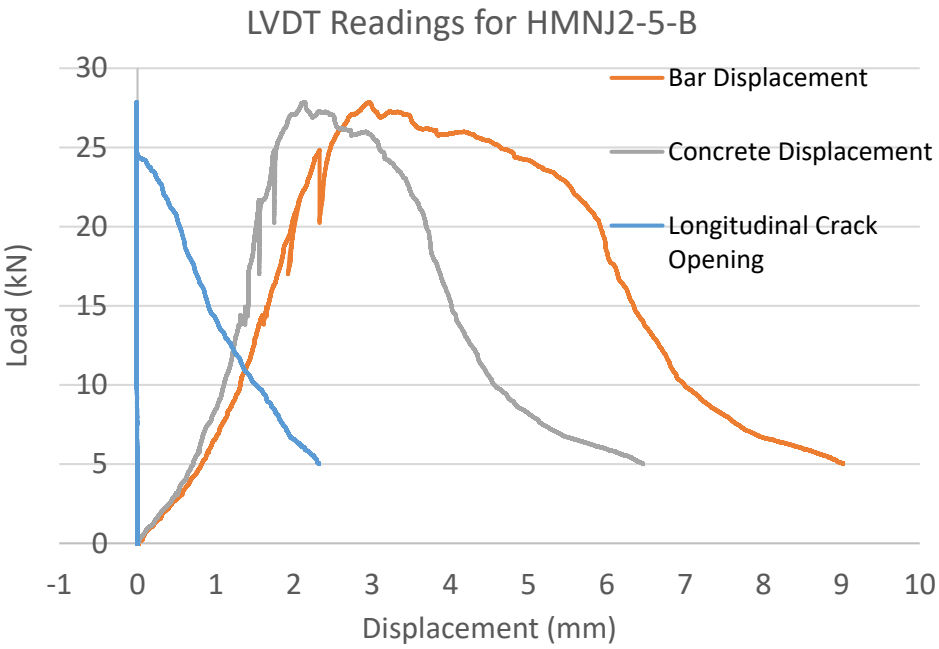

Figure 5-53 Displacement output from DTs for Speciment IHNJ2-5-B.

Figure 5-54 Surface cracking at peak strength for specimen IHNJ2-5-B.

Figure 5-55 Surface cracking at termination of the experiment for specimen IHNJ2-5-B.

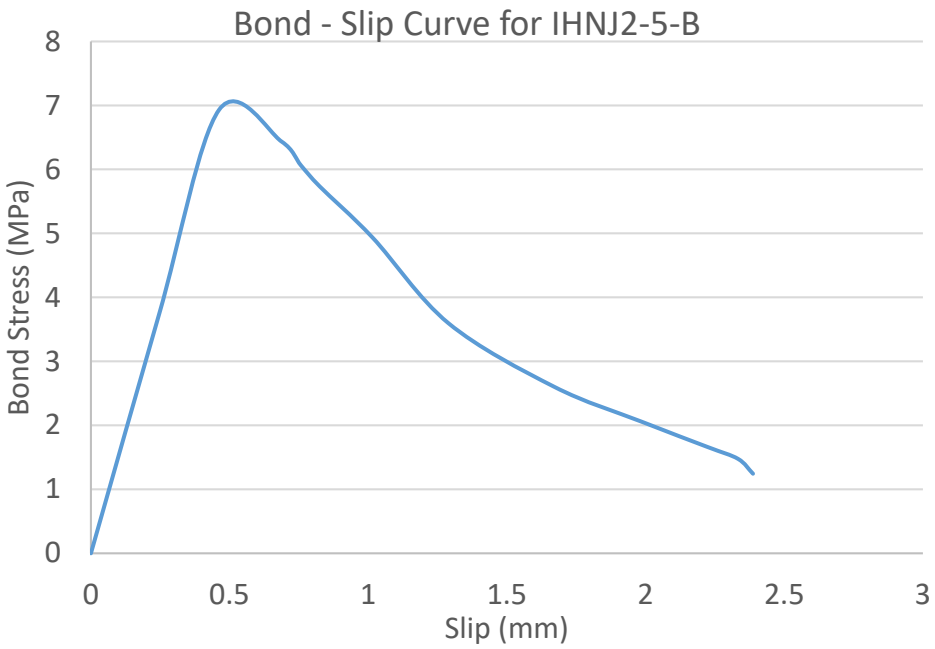

Figure 5-56 Bond Stress – Slip Curve for Specimen IHNJ2-5-B.

5.1.12 Specimen IHRT2-5-A

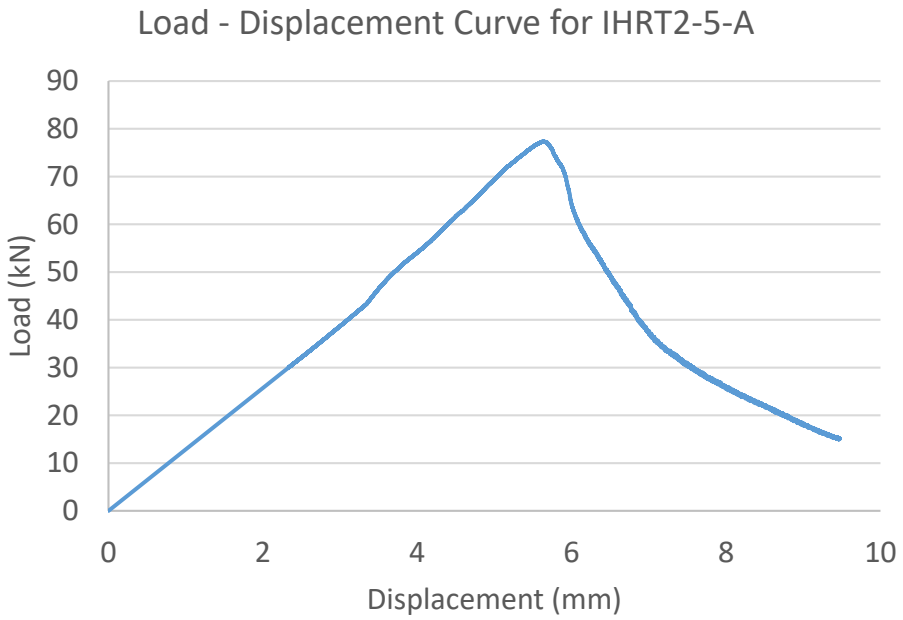

Figure 5-57 Load - Displacement Curve for Specimen IHRT2-5-A.

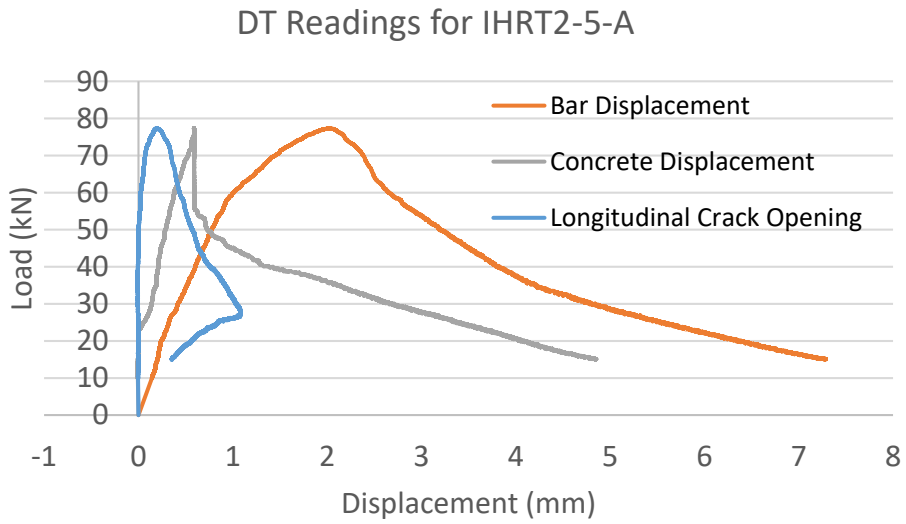

Figure 5-58 Displacement output from DTs for Speciment IHRT2-5-A.

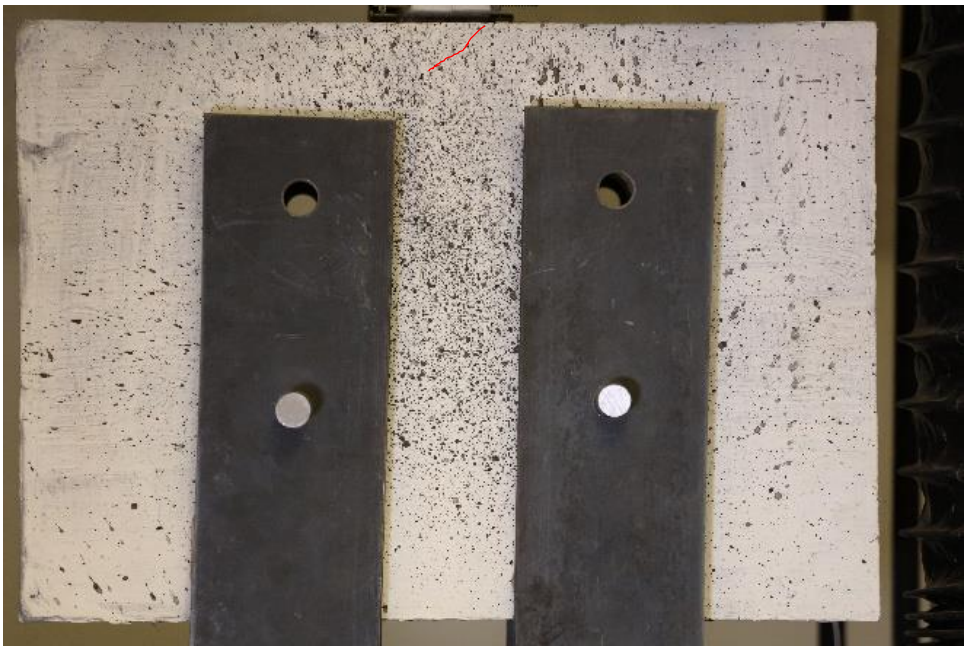

Figure 5-59 Surface cracking at peak strength for specimen IHRT2-5-A.

Figure 5-60 Surface cracking at termination of the experiment for specimen IHRT2-5-A.

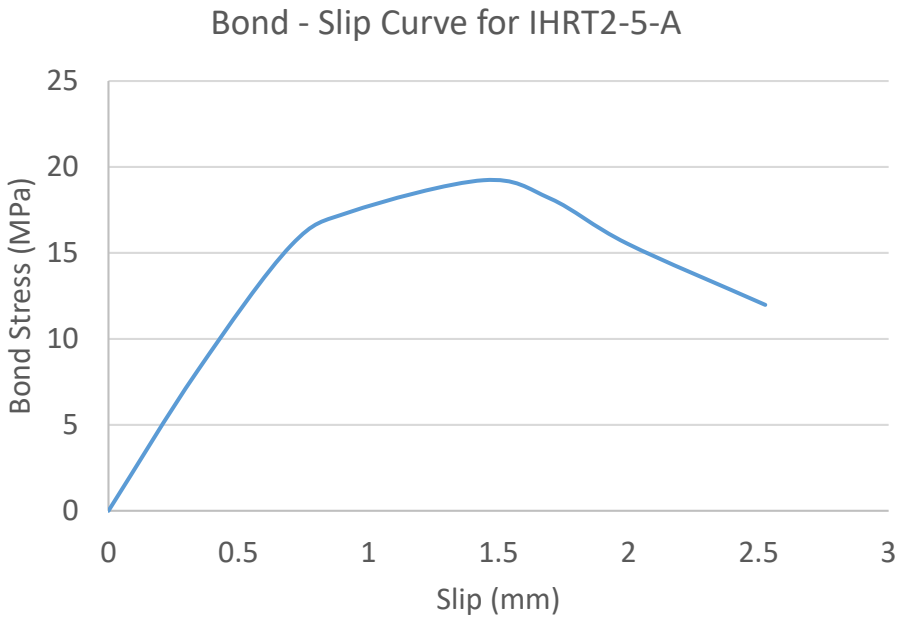

Figure 5-61 Bond Stress – Slip Curve for Specimen IHRT2-5-A.

5.1.13 Specimen IHRT2-5- B

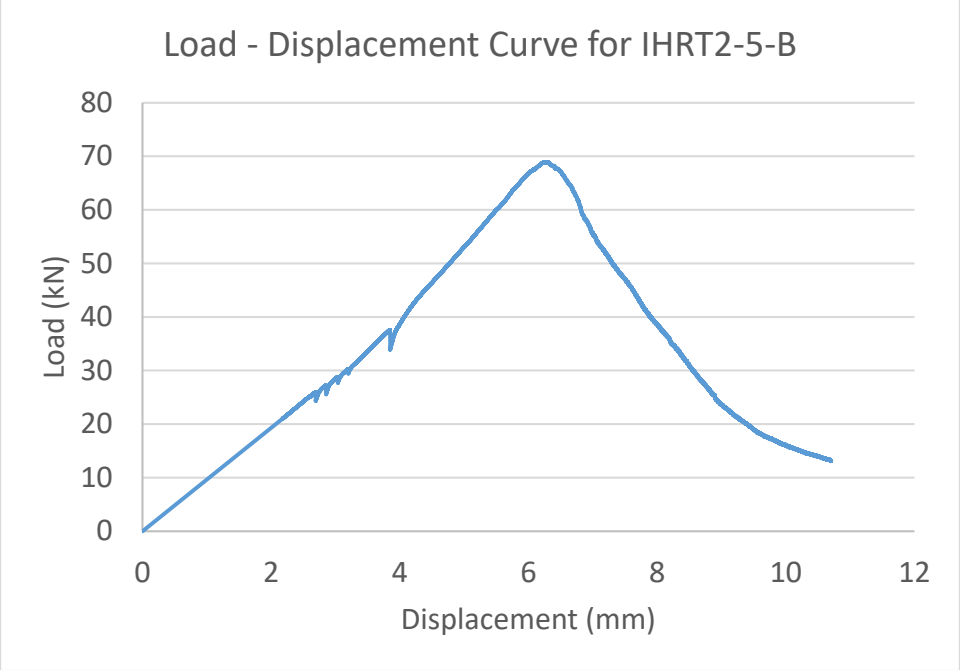

Figure 5-62 Load - Displacement Curve for Specimen IHRT2-5-B.

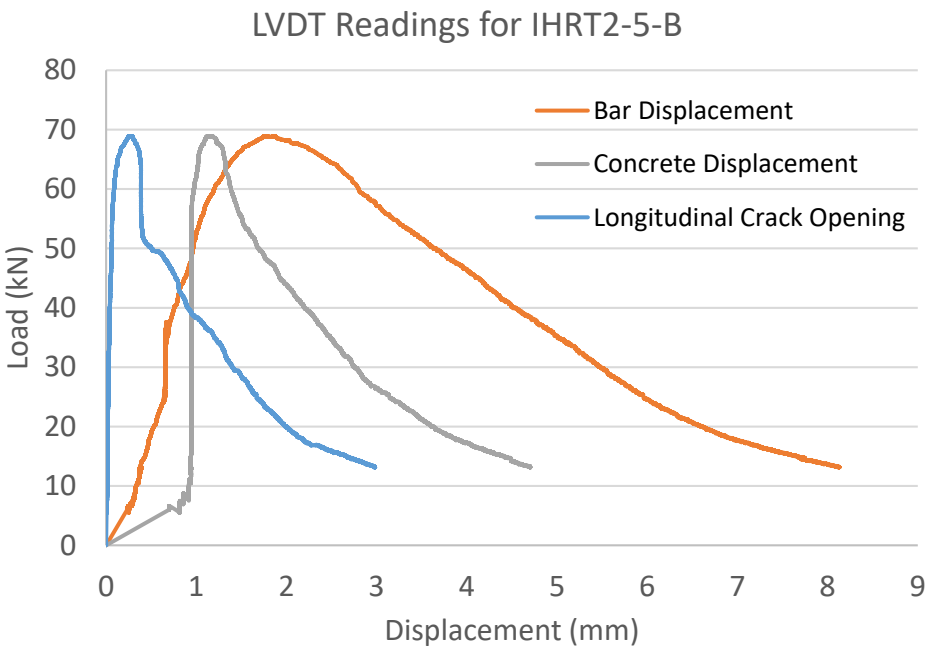

Figure 5-63 Displacement output from DTs for Speciment IHRT2-5-B.

Figure 5-64 Surface cracking at peak strength for specimen IHRT2-5-B.

Figure 5-65 Surface cracking at termination of the experiment for specimen IHRT2-5-B.

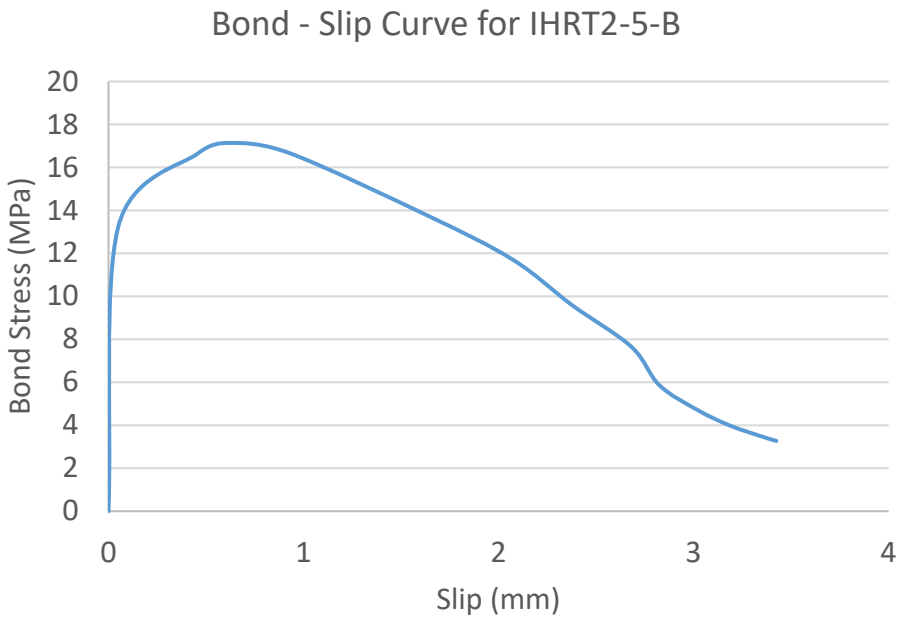

Figure 5-66 Bond Stress – Slip Curve for Specimen IHRT2-5-B.

5.2 Discussion of Experimental Results – and Comparisons

5.2.1 Overview of specimen behavior

A summary is provided for the individual behavior of the specimens belonging to their respective material categories, based on the information provided in Section 5.1. The characteristic of the force – displacement responses are discussed, along with the observed failure mode and cracking propagation. The maximum splitting crack measurements obtained from the attached DT's and the constitutive bond – slip properties are also examined in this section.

5.2.1.1 CMK material

Among the specimens of the CMK material, the average strength for the specimens with $1 \cdot D_b$ (CMK1-5-A, CMK1-5-B) was 35.75kN, whereas for the case of $2 \cdot D_b$ (CMK2-5-A, CMK2-5-B) the average strength was 59.11kN. Greater variations between the specimens of the larger cover were observed. Incidentally, higher concentrations of fiber reinforcement accompanied the specimen with the greater strength (CMK2-5-B) in the region surrounding the bar, while on specimen CMK2-5-A, the fibers were more scattered and randomly aligned (see Appendix II, Tables A1 and A2). This suggests that the ultimate response of the specimen was affected by the distribution and orientation of the fibers around the test bar.

Specimen CMK1-5-B followed the force – displacement response of specimen CMK1-5-A (Figure 5-6). At approximately 80% of the total strength, internal cracking commenced, signified with the first vertical inconsistency (and the accompanying “breaking” sound) in the ascending branch of the strength curve, with the fibers intercepting the opening cracks as the load increases. Contrary to specimen CMK1-5-A, in this specimen a splitting crack preceded the appearance of the horizontal crack at the free end of the bar, justifying the assumption that the random orientation and sparse allocation of fibers around the bar altered the mode of failure in this specimen (Figure 5-10). The horizontal crack reached the circular opening on one side of the specimen, while proceeding downwards in-between the circular openings from the other side. The maximum widths of the splitting crack as measured by the corresponding DTs were, 4.14mm and 2.12mm for the specimens CMK1-5-A and CMK1-5-B, respectively.

Both specimens with the larger cover of $2 \cdot D_b$ demonstrate a similar force – displacement response (Figs. Figure 5-11 and Figure 5-15). The ascending branch was interrupted for the first time by ensuing internal cracking, while fibers proceed to engage the concrete as the loading increases. Cracking in specimen CMK2-5-A was initiated via the simultaneous appearance of the major horizontal crack (cone failure) at the free end of the bar and the splitting crack along the bar length (Figure 5-19). It is noted here that the splitting crack displayed an inclination towards one side of the specimen. At approximately 30% of the specimen strength, the controlling mechanism of failure shifted and the splitting crack increased, with the upper segment on one side of the crack to dislocate eccentrically from the specimen. In specimen CMK2-5-B, cracking ensued eccentrically, with the conical cracking surface appearing at approximately the midspan between the circular opening and the bar. The base of the crack appeared at approximately 20mm above the free end of the bar. A concurring, eccentric splitting crack ensued at a location between the bar axis and the base of the conical failure surface. Multiple inclined crack patterns could be observed in the area between the circular openings. Towards the end of the experiment, a significant portion of the specimen defined by the controlling (cone) crack surface attempted to disconnect completely from the concrete body. The maximum widths of the splitting crack as measured by the corresponding DT were 1.74mm and 1.78mm for the specimens CMK2-5-A and CMK2-5-B, respectively.

The bond – slip relationships were obtained by calculating the average bond stress from the corresponding loading measurements while the slip was calculated by subtracting the displacement measurement of the bar from the concrete surface, as obtained from the attached DTs. The average peak bond stress f_b for specimens CMK1-5-A and CMK1-5-B was 8.89MPa

while for the specimens comprising the $2 \cdot D_b$ cover, the average peak response was 14.695MPa. For specimen CMK2-5-A, the displacement measures from the concrete surface became greater than the displacement of the bar, due to the concrete segment becoming detached from the body and being pushed upwards; in this case it was not possible to obtain the bond – slip relationship. The average peak slip values for the two former specimens was 0.6mm whereas for the latter case, the slip was 0.67mm. Considerable variation in slip was indicated by the specimens with $1 \cdot D_b$ cover with the ultimate value for specimen CMK1-5-A to be 1.75mm whereas for CMK1-5-B the ultimate slip was 8.49mm. Additionally, it is worth mentioning that the descending branch of the bond – slip constitutive law for specimen CMK1-5-A formed a convex curve as the slip increases whereas the other specimens of this material series employ a concave curve in the corresponding branch. The convex curve indicated the superiority of the conical failure mode whereas the concave curve is attributed to splitting failure, an outcome that was additionally demonstrated in the formation of the crack patterns.

5.2.1.2 CMF material

The average strength for the specimens with $1 \cdot D_b$ (CMF1-5-A, CMF1-5-B) was 52.37kN while the specimen with $2 \cdot D_b$ (CMF2-5-A) reached failure at 72.241kN. Great peak strength variations could be observed between the specimens of $1 \cdot D_b$ in this case, which can be validated by their corresponding unique failure mechanisms. In specimen CMF1-5-A, cracking was initiated by the appearance of a splitting crack that extended towards the free end of the bar. Inclined cracking expanded from the free end of the bar, towards the surfaces of the cylindrical supports. The engagement of the fibers can be witnessed through the force – displacement curve of the specimen where discontinuities ensue in the ascending branch. A major initial drop at approximately 57% of the ascending branch signified the realignment of the cylindrical supports in the setup, while the branch resumes its ascend following the same stiffness. At strength levels of approximately 85% of the peak load, the fibers had fully engaged the concrete and consistent breakages appeared on the force – displacement curve, as the fibers bridging the corresponding openings approached failure. Towards the end of the experiment, the previously secondary inclined crack originating at the free end of the bar had surpassed the splitting crack and has denoted the primary failure surface of the specimen (Figure 5-24).

Specimen CMF1-5-B however displayed a decreased percentage of fiber breakage. As it can be noted from Figure 5-25, the force – displacement curve contained fewer discontinuities belonging to the fiber failure when compared to that of specimen CMF1-5-A. This phenomenon can be

explained by the different failure mechanism that governed this experiment. The primary cracking surface was defined by the major splitting crack appearing in alignment with the bar axis, while a secondary upwards inclined crack appeared at an offset of the free end of the bar (Figure 5-27). Proceeding into the descending branch, the opening of the splitting crack increases slightly, as the test bar began to slowly pull out of the concrete. Minimal surface cracking could be observed on this specimen (Figure 5-28). Intense deformation appeared on the concrete top surface in the immediate periphery of the bar. It is worth noting that upon reaching the descending branch, the force was stabilized at a plateau of 30% of the peak strength before the experiment was terminated. The maximum widths of the splitting crack as measured by the corresponding DT were 6.4mm and 1.45mm for the specimens CMF1-5-A and CMF1-5-B, respectively.

Due to an accident that occurred during the experiment for specimen CMF2-5-A was divided into two parts: In Part 1, the specimen reached a maximum of 74.144kN before being suddenly interrupted by the rupture of the bottom supporting bar (Figure 5-30). Inclined cracking patterns had already appeared in the specimen surface, delineating a segment of conical shape located eccentrically, between one of the circular openings and the test bar (Figure 5-31). Horizontal cracking could be also observed closer to the free end of the bar. After replacing the damaged component from the mechanical base, Part 2 commenced, and the specimen was loaded anew, reaching a maximum of 72.241kN (Figure 5-33), before developing a distinct conical failure surface. The controlling crack surface appeared within the conical surface defined previously in Part 1 (Figure 5-34). Towards the end of the experiment, the top surface of the specimen attempted to completely dislocate from the concrete body (Figure 5-35). The maximum widths of the splitting crack as measured by the corresponding DT were 0.35mm and 4.14mm for the specimens CMF2-5-A (Part 1) and CMF2-5-A (Part 2), respectively.

The average peak bond stress f_b for specimens CMKF1-5-A and CMF1-5-B was 13.025MPa whereas no bond – slip could be obtained from specimen CMF2-5-A due to the rupture of the supporting bar. The average bond strength was obtained from the peak load value as 18.17MPa. With cracks having formed throughout the specimen volume, measurements from the DTs followed inconsistent displacements due to the repositioning of the specimen fragments. The average slip at peak bond stress was 0.445mm. Once more, significant variation emerged in the slip measurements, with the peak slip value for specimen CMF1-5-A to be 0.15mm while for specimen CMF1-5-B the peak slip reached to 0.74mm. The respective ultimate slip measurements were 2.04mm and 3.5mm. The descending branch formed the similar concave pattern with the latter case to reach the plateau at approximately 65% of the peak bond strength,

reflecting the stabilization encountered in the force – displacement relationship. In both cases, the splitting crack dominated the failure mode of the specimen with the exception that in the latter case, the failure mode shifted into pullout, as the splitting crack measurements decreased towards the end of the specimen.

5.2.1.3 IHNJ material

The average strength for the specimens with $1 \cdot D_b$ (IHNJ1-5-A, IHNJ1-5-B) was 17.59kN while the specimen with $2 \cdot D_b$ (IHNJ2-5-A, IHNJ2-5-B) reached failure at 25kN. Higher consistency in strength measurements could be observed in this specimen series. Uniform distributions of the synthetic fibers were observed along the delineated crack paths.

Specimens IHNK1-5-A and IHNJ1-5-B displayed similar force – displacement responses, combined with comparable crack patterns. Fiber engagement was emphasized in the ascending branch of the strength curve, with breakage occurring at load levels of 40 to 60% of the peak response (Figs. Figure 5-37 and Figure 5-42). This can be explained by the weaker tensile strength of the synthetic material contained in the fibrous reinforcement. Load discontinuities (fiber failure) congregated in the ascending branch while no noticeable discontinuities appearing at the onset of the descending branch. Owing to the more uniform dispersion of the fibers over the specimen volume, a greater quantity of fibrous reinforcement was engaged as the cracking surface increased in dimensions. Surface cracks appeared at the free end of the bar, resembling the conic failure zone encountered in pullout experiments whereas a concurring splitting crack appeared in alignment with the bar axis. The conical crack extended beyond the bar anchorage and traversed through the circular openings, which transferred the failure surface in the plane defined by the opening centroids. At strength levels of approximately 25% of the peak strength, the conical failure zone had dominated over the splitting crack and a significant portion of the upper segment of the specimen began to dislocate completely (Figs. Figure 5-40 and Figure 5-45). The maximum widths of the splitting crack as measured by the corresponding DT were 2.25mm and 4.95mm for the specimens IHNJ1-5-A and IHNJ1-5-B, respectively.

Specimen IHNJ2-5-A exhibited a somewhat different response than specimen IHNJ2-5-B which can be attributed to lower peak strength measured in the force – displacement curve. While discontinuities appeared in the latter case, resembling the response obtained from the specimens with smaller cover thickness, in the case of IHNJ2-5-A, the ascending branch demonstrated fewer drops in strength due to fiber breakage/pullout. Surface cracks congregated around the free end of the bar followed by a splitting crack starting from the top surface. The major crack developed

at an upwards offset of the free end and expanded towards the side surfaces of the specimen (Figure 5-50). In the case of IHNJ2-5-B, the controlling crack surface occurred at a plane that traversed one of the circular openings and reached the top surface of the specimen (Figure 5-55). Multiple secondary splitting cracks appeared in close proximity with the test bar. The maximum widths of the splitting crack as measured by the corresponding DT were 3.59mm and 2.32mm for the specimens IHNJ2-5-A and IHNJ2-5-B, respectively.

The average peak bond stress f_b for specimens IHNJ1-5-A and IHNJ1-5-B was 4.375MPa while for IHNJ2-5-A and IHNJ2-5-B the average strength was 6.205MPa. The respective peak slip values were 0.23mm and 0.73mm. Small variation was noted in this specimen series with corresponding average ultimate values reaching up to 1.53mm and 0.79mm. For the case of specimen IHNJ1-5-A, the descending branch followed a mild decrease towards the ultimate value, suggesting the simultaneous increase of both the conical and splitting cracks. For the case of IHNJ1-5-A, the conical crack dominated the failure mode and the descending branch (forming a somewhat convex curve) was interrupted at a lower ultimate slip. Specimen IHNJ2-5-B displayed a hardening segment that reached up to the maximum bond stress before dropping suddenly into a concave pattern in the descending branch. The latter branch resembled the failure curve of an unconfined concrete specimen, which was suggested by the almost completely horizontal failure plane that controlled the response. The failure plane was located at an offset from the free end of the bar, indicating possible sporadic concentration of fiber reinforcement in that area. The last specimen of this series developed a hardening branch before reaching the peak bond strength before proceeding into a mild softening branch. At approximately 70% of the peak value, bond stress dropped suddenly and the experiment was terminated shortly after. The mild slope in the first segment of the descending branch indicated the domination of the conical failure plane which exhausted the deformation capacity of the concrete section by reaching the top surface of the specimen, at which point the specimen fragment in the upper part of the cracking surface began to dislocate. A contributing factor to this failure response was the presence of the circular opening that diminished the tensile capacity of the specimen in the corresponding plane.

5.2.1.4 IHRT material

The average strength of the specimens (IHRT2-5-A, IHRT2-5-B) was 73.13kN. The force – displacement curves obtained from these specimens displayed smoother lines, with discontinuities occurring towards the end of the descending branch. In the case of IHRT2-5-A, cut-offs appeared at approximately 50% of the ascending branch, owing to readjustments of the

cylindrical supports. Crack patterns displayed analogous behavior between the specimens, with major conical cracks proliferating at an offset above the free end of the bar, followed by arched splitting cracks starting from the top surface (Figures Figure 5-60 and Figure 5-65). The origin of the splitting cracks occurred at a side offset from the bar axis. The conical failure plane extended outside the anchorage towards the circular openings that alter the orientation of the crack path. The maximum widths of the splitting crack as measured by the corresponding DT were 0.96mm and 2.98mm for the specimens IHRT2-5-A and IHRT2-5-B, respectively.

The average peak bond stress f_b for specimens IHRT2-5-A and IHRT2-5-B was 18.18MPa, which was the highest measured value in this experimental program. The average slip values at the peak bond strength and at the termination of the experiment were 1.03mm and 2.97mm, with the ultimate slip measurement for the latter specimen to be approximately double the ultimate slip of the former specimen. Both specimens were controlled by the major conical crack appearing at an offset from the test bar axis, with the latter specimen of the two to undergo a commensurate contribution from both the conical and the splitting crack, reaching an ultimate slip of 3.42mm. This can be emphasized by the gradual descend observed in the softening branch of the bond – slip relationship. In the former specimen, however, bond stress followed a hardening branch prior to reaching the maximum bond stress, after which point, the descending branch proceeded to an ultimate slip at approximately 2.53mm. It is worth noting at this point, that bond – slip relationships that contained both a hardening and a softening branch (indicative of the domination of the conical crack) reached lower values of ultimate slip while bond – slip relationships that dropped immediately into descending branches of concave form (indicative of splitting crack domination) reached higher values of relative slip between steel and concrete.

5.2.2 Comparisons between specimens

In this section the experimental data is compared across the specimens in reference to the two parameters of this study: the concrete cover and the UHPC material properties. Table 5-1 provides the collection of the peak responses from the force – displacement relationships of all specimens along with the peak measurements from the bond – slip law. The splitting cracks measurements at the peak strength, obtained from the attached DTs is shown as well as the failure mode indicator letter. Indicator “C” stands for conical failure, indicator “S” for splitting failure and “P” for pullout failure. The order of the indicators displays the failure mode dominance. Sign “-” denotes the existence of multiple failure patterns with the preceding phenomenon to be the

dominant failure mode. Sign “+” denotes multiple failure modes with approximately equivalent contributions to the failure response.

Table 5-1 Collection of experimental results from all specimens.

Specimen ID	P_{peak} (kN)	$\Delta_{@peak}$ (mm)	$f_{b,\,peak}$ (MPa)	$Slip_{@peak}$ (mm)	Δ_{Vcrack} (mm)	Failure Mode
CMK1-5-A	37.1	3.67	9.22	0.42	4.14	C+S
CMK1-5-B	34.41	3.77	8.55	0.76	2.12	P+S-C
CMK2-5-A	50.30	4.00	12.5	-	1.74	C-S-P
CMK2-5-B	67.91	5.43	16.89	0.65	1.78	P+S-C
CMF1-5-A	46.63	5.37	11.6	0.15	6.4	S-C
CMF1-5-B	58.11	5.10	14.45	0.73	1.45	P-S
CMF2-5-A (Part 1)	74.14	5.92	18.44	-	0.35	-
CMF2-5-A (Part 2)	72.24	5.54	17.9	-	4.14	P+C-S
IHNJ1-5-A	18.22	3.76	4.53	0.23	2.25	C+S-P
IHNJ1-5-B	16.97	3.27	4.22	0.52	4.59	C-S
IHNJ2-5-A	22.04	3.58	5.48	0.69	3.59	C-S
IHNJ2-5-B	27.87	4.57	6.93	0.46	2.32	C
IHRT2-5-A	77.34	5.10	19.23	1.44	0.96	C-S
IHRT2-5-B	68.92	4.94	17.13	0.62	2.98	C+S

5.2.2.1 Contribution of concrete cover

A clear increase in bar development capacity was observed in specimens with a cover of $2{\cdot}D_b$ over specimens with a cover of $1{\cdot}D_b$. Peak strengths were increased by an average of 59% (65% for CMK, 70% for CMF, 42% for IHNJ) with a 100% increase of the available cover, with the greatest increase to be attributed to the CMF material, most likely because better advantage of the long length fibers of this material was possible. The same percentage of strength increase occurred in the average bond strength values. The increase of the cover displayed the least influence, albeit considerable, in the case of the IHNJ, in which synthetic fiber were used. Materials containing steel fibers showed the largest effect in bond strength increase, with the mixture containing longer fibers with hooked ends to be the most affected. The above information supports the following conclusions:

- The increase in available concrete cover provided an improvement in the overall development capacity of the test anchorage. Provided that an increase in cover was accompanied by an increase of the fiber reinforcement ratio of the concrete section, the effective confining pressure on the anchored bar was consequently increased.
- The observed limit in the relative strength gain (59% increase in strength for 100% increase of cover) that beyond that point there was an alteration of failure whereby the anchorage is no longer the critical component of the test setup, but instead, failure was transferred outside the anchorage zone to the weakest tensile trajectory in the FRC matrix.
- UHPC materials constructed with synthetic fibers showed the least influence by the increase of the cover. This may be attributed to the more uniform distribution of the fibers per sectional area which accounts for less variation in the fiber reinforcement ratio of the increased section. It is also likely that confining pressure in the cover rendered local pullout failure the weakest link of bar behavior on account of the relatively low tensile strength of the material matrix used.
- UHPC materials constructed with steel fibers show greater influence by the increase of the cover for the case of inclusion of longer fibers with hooked ends. While longer lengths provide for better anchorage for the fibers, the modification of hooked ends further increased the fiber bond strength by interlocking against the surrounding concrete. Complementary studies concerning the bond capacity of deformed fiber reinforcement are recommended to reinforce this assumption.
- Bond strength was increased correspondingly with greater cover. While the measurements obtained from the above experiments represented the average bond stress along the bar length, the observed strength increases provided a dependable estimation of the local bond strength, due to the small embedment length of the test bar.

5.2.2.2 Contribution of the UHPC material synthesis

Greater tensile strengths have been observed for materials containing steel fiber reinforcement instead of synthetic. The maximum obtained tensile strength (77.34kN) was obtained by specimen IHRT2-5-A whereas the minimum obtained tensile strength (16.97kN) was obtained by specimen IHNJ1-5-B. Greater ultimate displacement values were observed in the specimens constructed with the CMF material, reaching up to 20.7mm total displacement for specimen CMF1-5-B. The average ultimate displacements for specimens of the CMK series were 10.65mm and 12.48mm for the cases of $1 \cdot D_b$ and $2 \cdot D_b$, respectively. For the CMF series, the average ultimate displacements for specimens with $1 \cdot D_b$ cover was 17.83mm and $2 \cdot D_b$,13.7mm. For the IHNJ

series, the average ultimate displacements for specimens with $1 \cdot D_b$ cover was 10.18mm and $2 \cdot D_b$, 9.48mm. The average ultimate displacements for the specimens of the IHRT series was 10.07mm. It should be noted that the tests were terminated upon reaching a residual load equal approximately to 20% of the peak strength of each respective specimen.

One major difference in the force – displacement response of the steel fiber reinforced specimens, from the PVA reinforced specimens, was the onset of fiber pullout at the end of the ascending branch for the former case. In the latter case, fibers began debonding at approximately 60% of the peak tensile strength in the ascending branch. This phenomenon can be explained by the lower tensile capacity of the synthetic fibers, which began to debond prematurely, until sufficient fiber area is engaged through the propagation of the cracking planes. Steel fibers reached failure at higher values of applied loading and exhibit “rigid” behavior in the softening branch of the force – displacement response. This behavior could be observed by the irregularities accumulating at the descending branches of the steel fiber reinforced specimens, particularly towards the end of the experiment, where crack widths increased significantly. Highly consistent behavior was observed in the CMK and IHRT mixtures, in which the fibers demonstrated almost identical patterns of engagement. In the case of the IHRT specimens, the initial stiffness differed between the two specimens, as a result of self-adjustments of the experimental setup. Specimens from the CMF series displayed the most irregularities in their strength responses. A difference of 12kN in tensile strength was measured between the specimens of $1 \cdot D_b$ cover whereas the stiffness between specimens CMF1-5-B and CMF2-5-A (Part 1) were almost identical. Incidentally, the initial stiffness of CMF2-5-A (Part 2) resembled the one from CMF1-5-A. While the initial stiffnesses did not differ significantly, in the case of the IHNJ specimen series, the ascending branches showed several horizontal translations and irregularities in the applied load. These translations were a result of the initially weaker fiber area reaching failure before sufficient fibers are engaged. This effect was diminished considerably as the load approached the peak strength and consequently entered in the softening branch.

5.2.2.3 Contribution of the test setup

The importance of the test setup in the determination of local bond – slip relationships has been discussed extensively in Chapter 3 of this study. In the current section, comparison is made between the bond – slip relationships obtained from the data gathered from this experimental program, as displayed in 5.1, with the corresponding data obtained from companion four-point bending tests conducted by Saikali (2019). The four-point bending specimens examined were

constructed with the same batches used for the CMK, CMF and IHRT mixtures. For ease of reference, the bond – slip constitutive relationships obtained from the above experiments are summarized in Figure 5-67. Figures Figure 5-68 to Figure 5-72 show the corresponding bond stress – slip relationship from the beam specimens from Saikali (2019). As explained in the work of Saikali (2019), the beam specimens are identified with a five-character code name, followed by an alphabetical letter indicating the number of the specimens with the same constitution. The first character corresponds to the material recipe where "K" stands for mixture CMK, "F" for CMF and "I" for IHRT. Annotation "E1" indicates an embedment length of $5 \cdot D_b$, and annotations "C1" and "C2" indicate cover lengths of $1 \cdot D_b$ and $2 \cdot D_b$, respectively. For ease of reference, the beam specimens are renamed in accordance to the specimen identification codes used in this study, as displayed in Table 5-2.

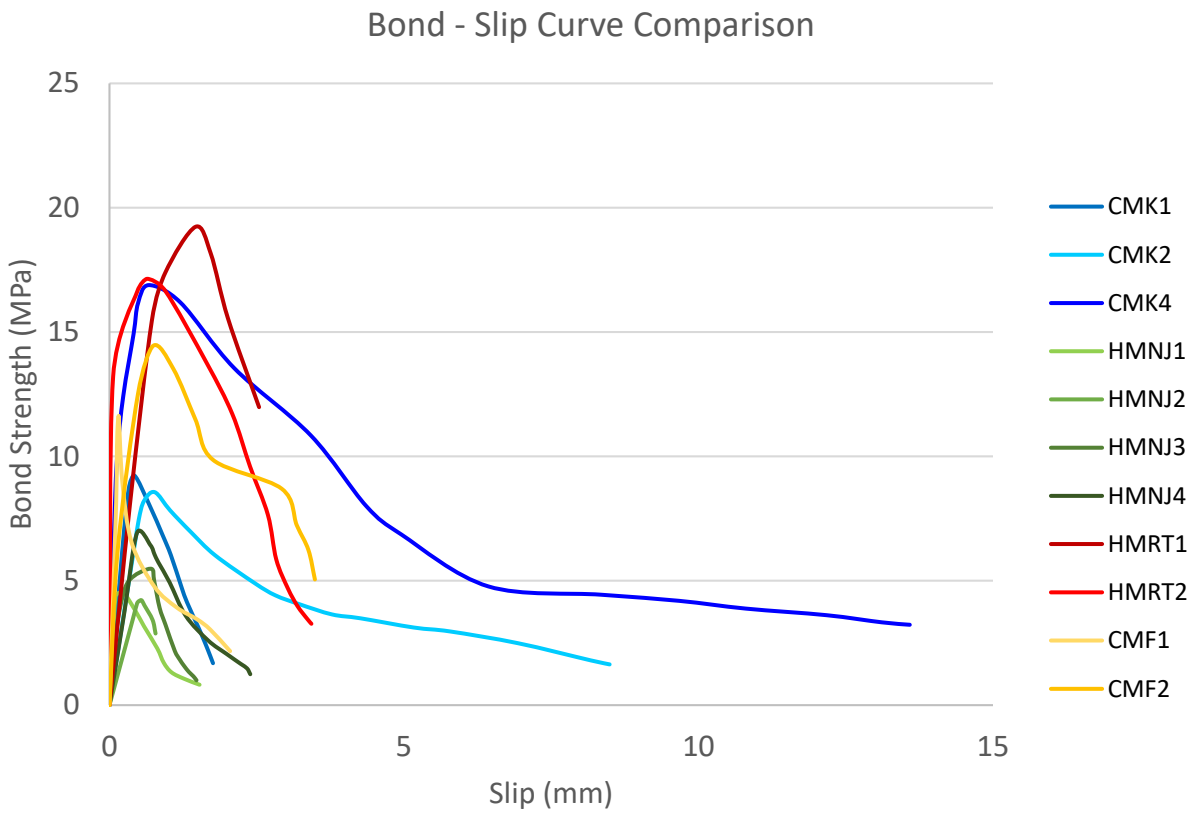

Figure 5-67 Collection of the bond – slip constitutive relationships for all specimens conducted in this study.

Table 5-2 Correlation of specimen identification names with Saikali (2019).

Tsiotsias' DTP Specimen IDs	Saikali's Renamed Specimen IDs	Saikali's Beam Specimen IDs
CMK1-5 CMK2-5	CMK1-5B CMK2-5B	KE1C1 KE1C2
CMF1-5 CMF2-5	CMF1-5B CMF2-5-B	FE1C1 FE1C2
IHRT2-5	IHRT2-5B	IE1C2

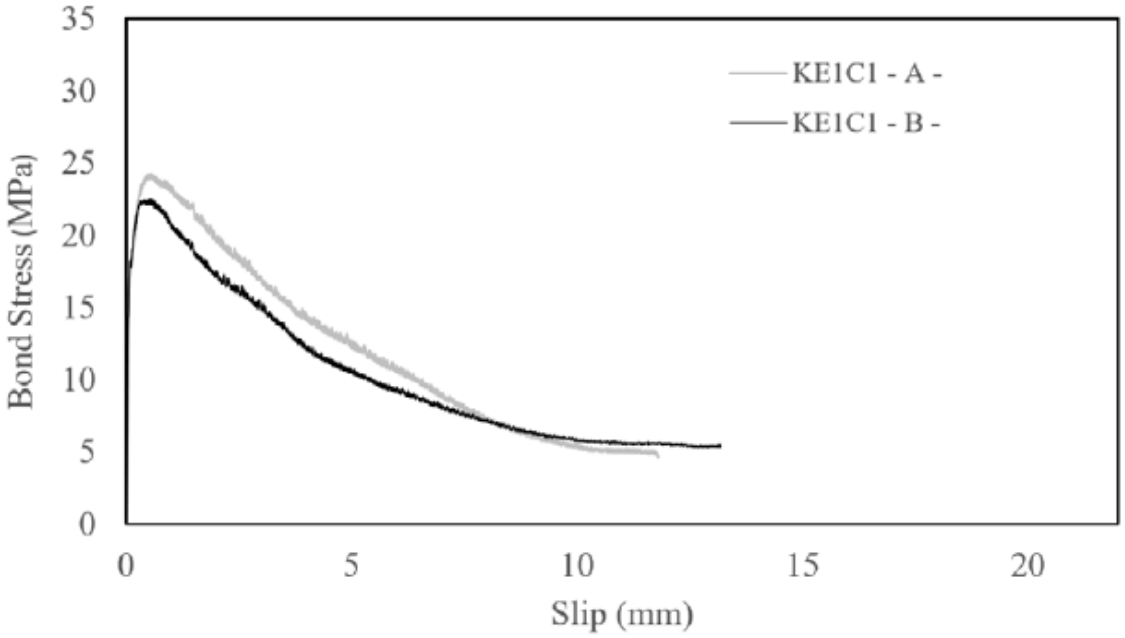

Figure 5-68 Bond – slip constitutive relationships from the CMK1-5B series, obtained from Saikali (2019).

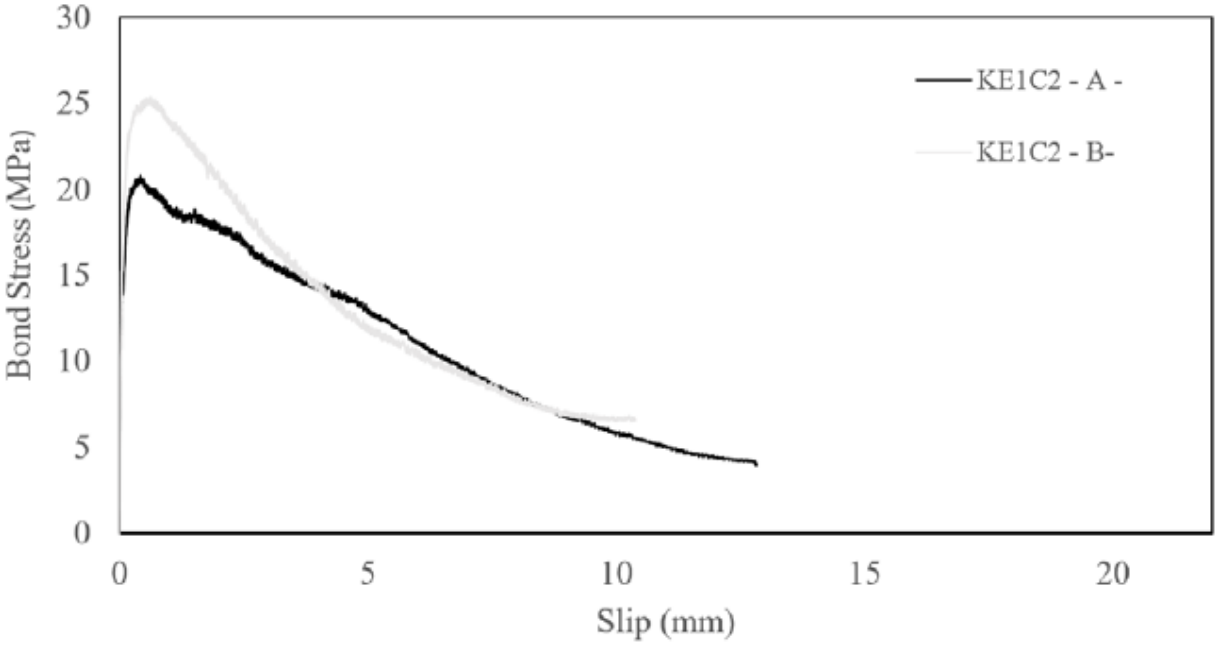

Figure 5-69 Bond – slip constitutive relationships from the CMK2-5B series, obtained from Saikali (2019).

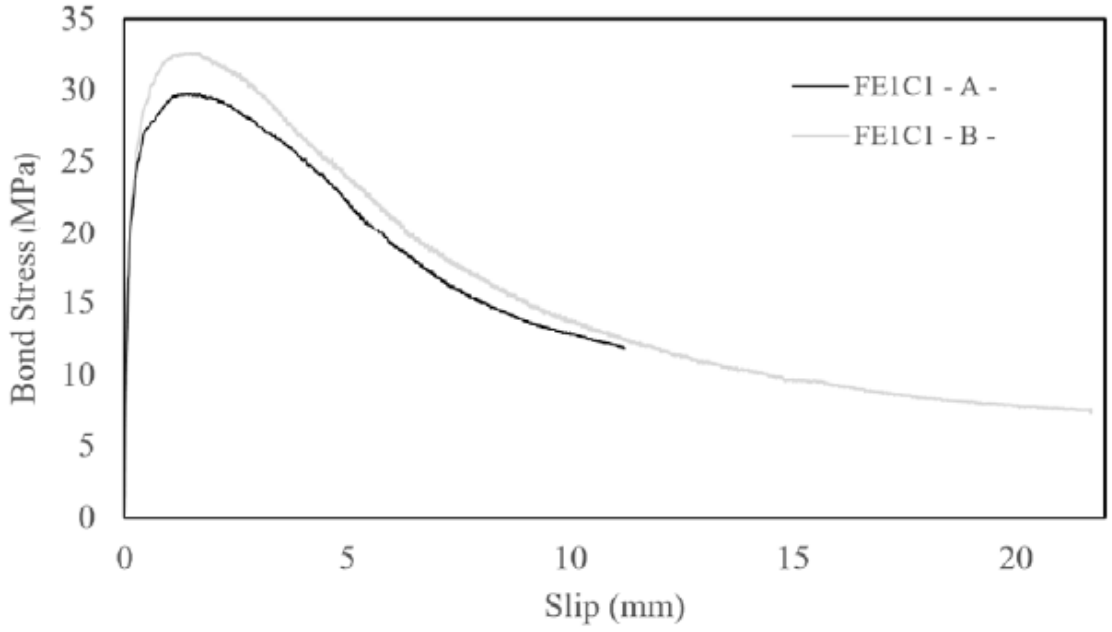

Figure 5-70 Bond – slip constitutive relationships from the CMF1-5B series, obtained from Saikali (2019).

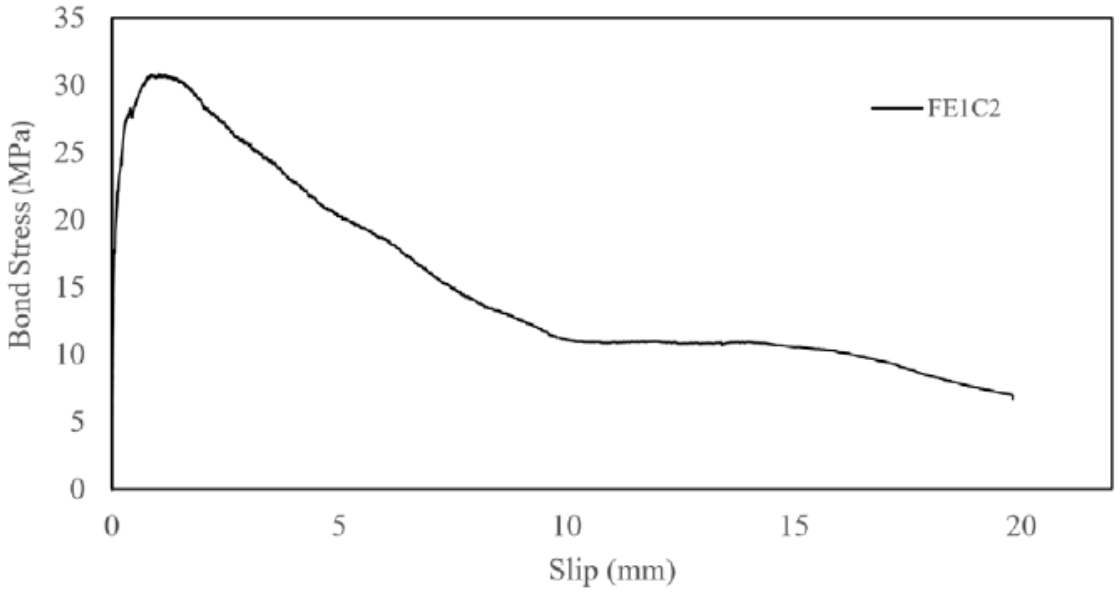

Figure 5-71 Bond – slip constitutive relationship from the CMF2-5B series, obtained from Saikali (2019).

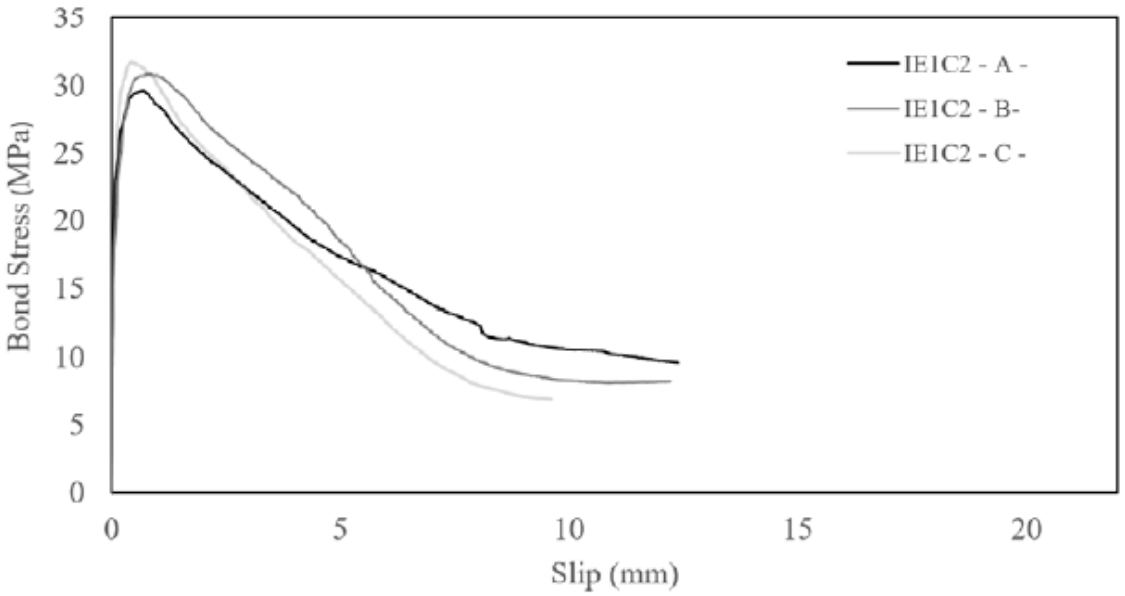

Figure 5-72 Bond – slip constitutive relationships from the IHRT2-5B series, obtained from Saikali (2019).

Table 5-3 provides the accumulation of the peak bond stresses, the relative slip at peak strength and the ultimate relative slip per specimen, in comparison with the respective beam specimens constructed by Saikali (2019), and Table 5-4 provides the averages of the aforementioned values. A systematic difference in the bond strength values was observed between the corresponding specimens of the two studies, with the beam specimens reaching far higher bond strengths as compared with the Modified Tension Pullout specimens studied here. Specimens constructed with material CMK showed 2.58 times higher bond strength for beam specimens with $1 \cdot D_b$ cover whereas beam specimens with $2 \cdot D_b$ bond strength was measured as 1.56 times higher. Relative slip values at peak bond stress remained in similar values, with greater scatter observed in the specimens of this study. Incidentally, ultimate relative slip measurements were higher by a factor of 2.4 for the case of $1 \cdot D_b$ DTP specimens and lower by a factor of 0.88 for the case of $2 \cdot D_b$ specimens of the same setup. The greatest difference between specimens of the same setup in terms of ultimate relative slip was seen for specimens CMK1-5-A and CMK1-5-B. Beam specimens with $1 \cdot D_b$ cover constructed with the CMF material showed higher values in bond strength by a factor of 2.4 when compared with the corresponding DTP specimens and in specimens with $2 \cdot D_b$ cover bond strength was higher by a factor of 1.7. Relative slip measurements at peak bond stress and ultimate state were higher in the beam specimens by factors of 3.3 and 6.0. Lastly, in the case of the in-house material mixture as composed by Saikali (2019), bond strength in beam specimens exceeded the capacity of the DTP specimens by a factor of 1.65, whereas the relative slip at peak bond stress was measured as lower by a factor of 0.58. Ultimate relative slip was 2.78 times higher in the beam specimens.

Table 5-3 Comparison of peak bond stress, peak relative slip and ultimate relative slip per specimen, with Saikali (2019).

Specimen ID	$f_{b,peak}$**(MPa)**	**Slip@**$_{peak}$ **(mm)**	**Slip**$_u$ **(mm)**
[Tsiotsias (2019) / Saikali (2019)]			
CMK1-5-A / KE1C1-A-	9.22 / 24.25	0.42 / 0.56	1.75 / 7.41
CMK1-5-B / KE1C1-B-	8.55 / 22.5	0.76 / 0.52	8.49 / 7.11
CMK2-5-A / KE1C2-A-	12.5 / 20.79	- / 0.42	- / 7.15
CMK2-5-B / KE1C2-B-	16.89 / 25.25	0.65 / 0.62	13.58 / 5.98
CMF1-5-A / FE1C1-A-	11.6 / 29.72	0.15 / 1.39	2.05 / 12.04
CMF1-5-B / FE1C1-B-	14.45 / 32.59	0.73 / 1.58	3.5 / 19.00
CMF2-5-A / FE1C2	18.17 / 30.86	- / 1.04	- / 17.25

IHRT2-5-A / IE1C2-A-	19.23 / 29.62	1.46 / 0.71	2.53 / 12.38
IHRT2-5-B / IE1C2-B-	17.13 / 30.72	0.62 / 0.73	3.42 / 8.51
- / IE1C2-C-	- / 31.73	- / 0.44	- / 7.28

Table 5-4 Comparison of average peak bond stress, average peak slip values and average ultimate slip values with Saikali (2019).

Specimen ID	**Average $f_{b,peak}$(MPa)**	**Average Slip@$_{peak}$ (mm)**	**Average Slip$_u$ (mm)**
[Tsiotsias (2019) / Saikali (2019)]			
CMK1-5-A / KE1C1-A- CMK1-5-B / KE1C1-B-	8.9 / 23	0.6 / 0.5	5.12 / 12.5
CMK2-5-A / KE1C2-A- CMK2-5-B / KE1C2-B-	14.7 / 23	0.67 / 0.52	13.58/ 12.0
CMF1-5-A / FE1C1-A- CMF1-5-A / FE1C1-A-	13.025/ 31.16	0.45 / 1.49	2.77 / 16.5
CMF2-5-A / FE1C2	18.17/ 30.86	- / 1.04	- / 20
IHRT2-5-A / IE1C2-A- IHRT2-5-B / IE1C2-B- - / IE1C2-C-	18.18 / 30	1.55 / 0.9	2.975 / 10

A summary of the observations stated above support the following conclusions:

- The bond strength obtained from beam specimens, including all material properties, was higher than that obtained from DTP specimens: values differed by a factor of 2.48 for the case of $1{\cdot}D_b$ cover and 1.64 for $2{\cdot}D_b$ cover when compared to DTP specimens.
- The favorable effect attributed to the flexural response of beam specimens was reduced for greater values of cover.
- The effect of cover increase was less discernible in the case of beam specimens. Whereas doubling of the cover increased the observed peak bond stress by an average factor of 1.5 for the case of DTP specimens, this effect does not appear as prominently in the case of the beam specimens.
- Scatter were observed in the relative slip measurements at peak bond strength for the case of materials CMK and CMF. Whereas for material CMK the peak relative slip

resulted in comparable values between beam and DTP specimens, for material CMF the relative slip at peak was measured as 3.32 times higher in the case of beam specimens. Extraneous effects in the flexural response due to the inclusion of longer fibers are suggested in this outcome. However, relative slip at peak bond strength is obtained as 172% greater for DTP specimens constructed with the IHRT material.

- Ultimate relative slip measurements highly depend on the controlling mode of failure, with pullout and splitting failures producing greater ultimate slip values followed by conical failures outside the range of the anchorage.
- Fiber length and orientation significantly affect ultimate slip measurements. Great scatter in ultimate slip measurements was observed between specimens with different material properties, whereas beam specimens lead to greater absolute values of ultimate slip, on average.

Table 5-5 Compressive strength of material mixtures (from Eshghi (2019), Saikali (2019)).

Specimen ID	Compressive strength f_c (MPa)
CMK (Commercial K)	122.6
CMF (Commercial F)	128.36
IHNJ1-5 (M5)	65.44
IHNJ2-5 (M2)	55.04
IHRT (IE1C2 – Batch C2)	125.04

Table 5-6 contains the normalized bond strength with the tensile and compressive strengths of the specimens, in comparison the equivalent normalized bond strength obtained from Saikali (2019). Table 5-7 denotes the averages of these values. The tensile strengths were obtained from dogbone specimens in direct tension denoted in Table 4-10, whereas the compressive strengths are shown in Table 5-5.

In the absence of dogbone specimens for the case of mixture IHRT, the tensile strength of the flexural specimens with one-way fiber arrangement was used, along with a corresponding reduction factor L. Factor L is calculated as the average ratio of the dogbone tensile strength over the flexural (one-way) tensile strength for all specimens of the study. Therefore, for materials CMK and CMF:

$$\text{L} = \text{Average}\{5.3/35.4, 8/36.18\} = \text{Average}\{0.15, 0.22\} = 0.185$$

$$\text{Tensile strength for IHNJ mixture: } f_t = 11.3 \cdot 0.185 = 2.09 MPa \quad [5\text{-}1]$$

$$\text{Tensile strength for IHRT mixture: } f_t = 28.83 \cdot 0.185 = 5.33 MPa$$

Table 5-6 Comparison of the normalized bond strength with tensile and compressive strengths measurements, as obtained by Saikali (2019).

Specimen ID		$f_{b,peak} / f_t$		$f_{b,peak} / \sqrt{f_c}$	
Tsiotsias (2019)	**Saikali (2019)**	**Tsiotsias (2019)**	**Saikali (2019)**	**Tsiotsias (2019)**	**Saikali (2019)**
CMK1-5-A	KE1C1-A	1.74	4.58	0.83	2.19
CMK1-5-B	KE1C1-B	1.61	4.25	0.77	2.03
CMK2-5-A	KE1C2-A	2.36	3.9	1.16	1.88
CMK2-5-B	KE1C2-B	3.19	4.76	1.53	2.28
CMF1-5-A	FE1C1-A	1.45	3.72	1.02	2.62
CMF1-5-B	FE1C1-B	1.81	4.07	1.28	2.88
CMF2-5-A	FE1C2	2.27	3.86	1.60	2.72
IHNJ1-5-A	-	2.17	-	0.56	-
IHNJ1-5-B	-	2.02	-	0.52	-
IHNJ2-5-A	-	2.62	-	0.74	-
IHNJ2-5-B	-	3.32	-	0.93	-
IHRT2-5-A	IE1C2-A	3.61	5.56	1.72	2.65
IHRT2-5-B	IE1C2-B	3.21	5.76	1.53	2.75
-	IE1C2-C	-	5.95	-	2.84

Table 5-7 Comparison of the average normalized bond strength with tensile and compressive strength measurements, as obtained by Saikali (2019) and Eshghi (2018).

Specimen ID		$f_{b,peak} / f_t$		$f_{b,peak} / \sqrt{f_c}$	
Tsiotsias (2019)	**Saikali (2019)**	**Tsiotsias (2019)**	**Saikali (2019)**	**Tsiotsias (2019)**	**Saikali (2019)**
CMK1-5	KE1C1	1.68	4.34	0.8	2.08

CMK2-5	KE1C2	2.77	4.34	1.33	2.08
CMF1-5	FE1C1	1.63	3.9	1.15	2.75
CMF2-5	FE1C2	2.27	3.86	1.6	2.72
IHNJ1-5	-	2.1	-	0.58	-
IHNJ2-5	-	2.97	-	0.825	-
IHRT2-5	IE1C2	3.4	5.61	1.63	2.68

Figures Figure 5-73 and Figure 5-74 display the distribution of the normalized bond strength of all specimens to the concrete tensile strength and to the square root of the compressive strength, respectively, with reference to the available concrete cover. Each point annotation ascribes to specimens belonging to each of the material categories used in this study, in comparison with the beam specimens examined by Saikali (2019).

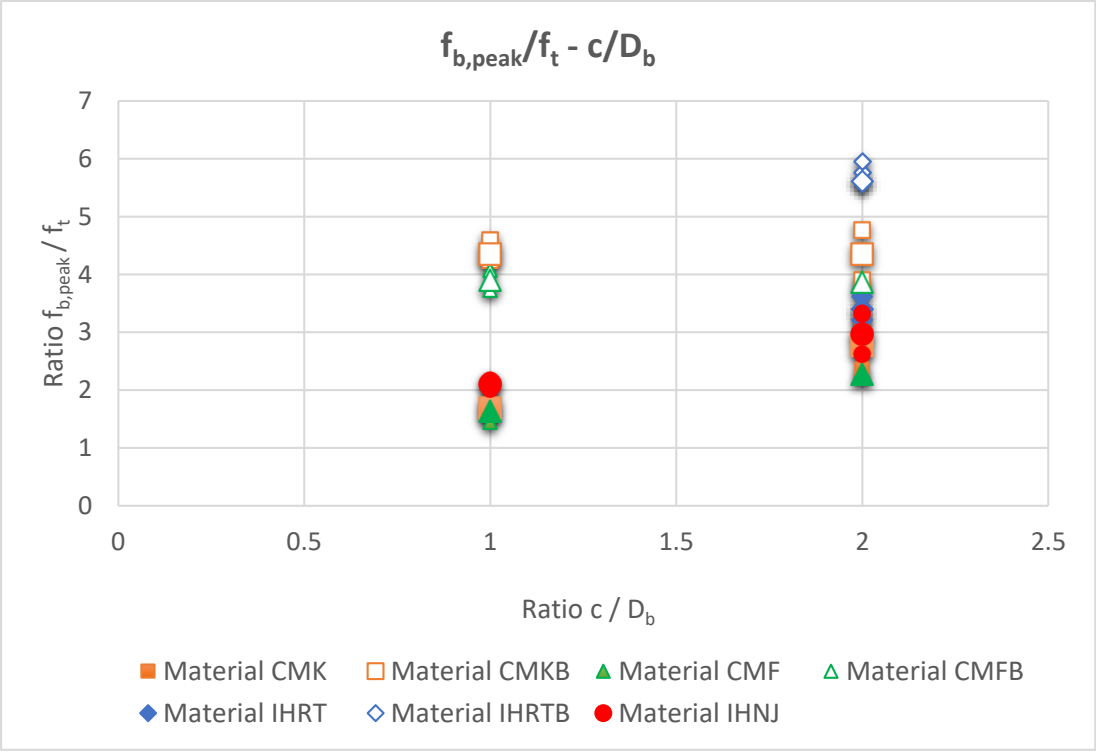

Figure 5-73 Distribution of the normalized bond strength to the tensile strength of concrete in reference to the specimen cover.

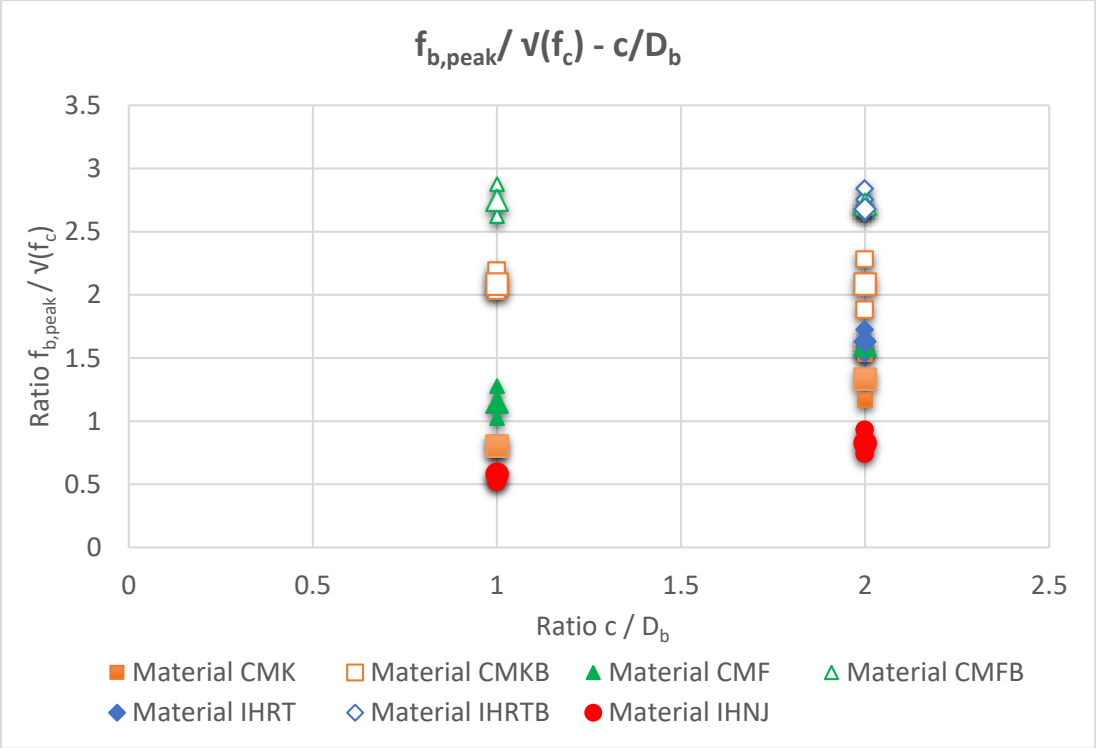

Figure 5-74 Distribution of the normalized bond strength to the square root of the compressive strength of concrete in reference to the specimen cover.

Noticeable differences can be observed between specimens of the same material properties between the setups of the DTP test and four-point bending test. An increase in the normalized bond stress is delineated between specimens of the DTP test with higher concrete cover, whereas in the case of beam specimens, the effect of the cover thickness is negligible. The specimens constructed with synthetic fibers (ECC material) are at the lower levels of bond values. Greatest variability can be additionally observed between specimens of the larger cover thickness in the case of Figure 5-73.

It may be concluded from Figure 5-74, that the approximation of bond strength with the square root of the compressive strength of concrete approaches the unit value for specimens with smaller covers. However, beam specimens appear to overestimate the bond strength with an average ratio exceeding the value of 2. Specimens with synthetic fibers display the least influence from the increase of the cover, however leading to ratios lower than 1.0. A reduction factor can be consequently used in the case of ECC materials, to account for the lower strength of the synthetic fibers.

5.3 Digital Image Correlation (DIC) Analysis

During the implementation of the experiments, each specimen was photographed with a time lapse of five seconds in order to perform a Digital Image Correlation (DIC) analysis. The DIC analysis was completed using the MATLAB module, GeoPIV-RG (Stanier et al. 2015). Each image illustrates the speckled surface of the respective specimens along progressive stages of the experiment. For each specimen, 16 distinct points of interest (POIs) are selected from the surface and optimized into horizontal and vertical layers. An extensive horizontal layer is located approximately at the midspan of the embedded bar and two vertical layers cross the unobstructed surface between the steel plates. The selected points of interest are shown separately for each analysis. The output of the program contains the horizontal (x-axis) and vertical (y-axis) displacements of the POIs, as well as the relative distances between the POIs of corresponding layers depict the identification number of each layer and the POIs that belong to each layer.

The photogrammetric analysis is distinguished in two parts: 1) One complete analysis comprising images from the entire extent of the force-displacement curve, presented in 7 to 10 progressive stages. 2) Three individual analyses comprising images at the following locations: 30% of the peak strength on the ascending branch, 70% of the peak strength on the ascending branch, the peak strength and 70% of the peak strength on the descending branch. For the latter approach, the points of interest are selected anew for each case of analysis. The aim of this analysis is to provide a more accurate representation of the distribution of strains and the displacements of the surface points, in lieu of the subjectivity of the results obtained by the linear transducers.

Table 5-8 Allocation of Points of Interest per separate layer

Layer ID	POI sequence in Layer	Distance from top (mm)
Layer #1	1,2	10-20
Layer #2	3,4,5,6,7,8,9	30-40
Layer #3	10,11	50-60
Layer #4	12,13	70-80
Layer #5	14,15,16	130

5.3.1 Specimen CMK1-5-A

The output for each analysis using the GeoPIV-RG is organized in five distinct diagrams. In the first diagram (D1), the strain levels ε_{xx} are shown along the path defined by points 3-4-5-6-7-8-9 (Layer 2). Strains along this path-line are calculated by taking the difference in the horizontal displacements between successive points. In the second diagram (D2), the horizontal strains ε_{xx} are calculated and compared between two points of each layer. The points were chosen to have approximately equivalent horizontal distances between them. The pairs used in this diagram are 1-2, 5-7, 10-11, 12-13 and 14-16. In the third diagram (D3), the vertical strains ε_{yy} on the left strand of the vertical path line are calculated, using the vertical displacement of the included pairs, namely 1-5, 5-10, 10-12 and 12-14. Diagram four (D4), follows the exact same arrangement as D3 but using the pairs 2-7, 7-11, 11-13 and 13-16. Finally, in diagram five (D5) the vertical strains ε_{yy} are calculated for the three equidistant path-lines denoted by the pairs, 5-14, 6-15 and 7-16. Table 5-9 provides a summary of the diagrams, along with their POI allocation. Points denoted by "-" are used in pairs. Points that correspond to diagrams describing ε_{yy} are paired with the points directly below them.

Table 5-9 Allocation of points of interest in diagrams

Layer ID	**D1**	**D2**	**D3**	**D4**	**D5**
	ε_{xx}	**ε_{xx}**	**ε_{yy} (Left)**	**ε_{yy} (Right)**	**ε_{yy}**
Layer #1	-	1-2	1	2	-
Layer #2	3-4-5-6-7-8-9	5-7	5	7	5, 6, 7
Layer #3	-	10-11	10	11	-
Layer #4	-	12-13	12	13	-
Layer #5	-	14-16	14	16	14,15,16

5.3.1.1 Complete analysis

The locations of the 16 points of interest for the complete analysis are shown in Figure 5-75.

Figure 5-75 Locations of points of interest for specimen CMK1-5-A (Complete analysis).

A total of eight stages were used to analyze the surface displacements of specimen CMK1-5-A. The stages were selected from milestone points along the force – displacement curve depicted in Figure 5-1 that incorporate the complete response the specimen. The peak stress location is included among these stages.

-Demonstration of ε_{xx} along Layer 2

Figure 5-76 shows the distribution of horizontal strains ε_{xx} along the corresponding path-line, located at approximately the midspan of the length of the embedded test bar. In the depicted diagram, the horizontal axis relates to the stage of the analysis, or an equivalent “time” along the force – displacement response, with the final stage coinciding with the termination of the experiment. The vertical axis quantifies the strain levels, with each colored column depicting the strain level of a particular pair of POIs. It can be observed that towards the final stage of the analysis, the strain levels of ε_{xx56} the maximum value of 0.15 while the adjacent strains remain under values 0.008. Strain ε_{xx56} therefore, illustrates the location and extent of the splitting crack

at a distance of approximately 30-40mm from the top surface. Variations in the distance from the top surface are unavoidable, depending on the availability of compatible “speckles”.

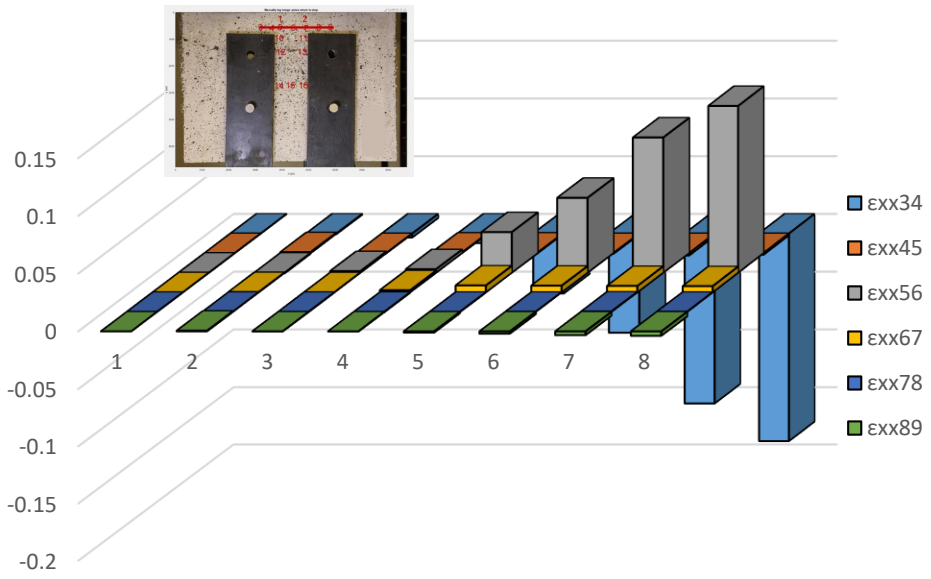

Figure 5-76 Demonstration of ε_{xx} along Layer 2 (CMK1-5-A – Complete analysis).

Figure 5-77 shows the distribution of horizontal strains ε_{xx} between layers, with each colored horizontal bar representing one specific layer along the extend of the analysis. The horizontal bars are arranged by height, so that top measurement belongs to Layer #1 and the bottom measurement belongs to Layer #5. In this diagram, the horizontal axis displays the strain levels of ε_{xx}, the vertical layer shows the stages in sequence of execution and each bar shows the horizontal strains of the representative pair of points. It can be observed that, during stage 8, in Layer #1 of the specimen (located at approximately 10-20mm from the top of the specimen) the horizontal strain ε_{xx12} is 0.1, in Layer #2 (30-40mm from the top surface) the strain ε_{xx57} is 0.073 and in Layer #3 (50-60mm from the top surface) the strain ε_{xx1110} is 0.048. This diagram can be used to define the splitting crack profile along the length of the embedded bar.

-Comparison of ε_{xx} between horizontal layers

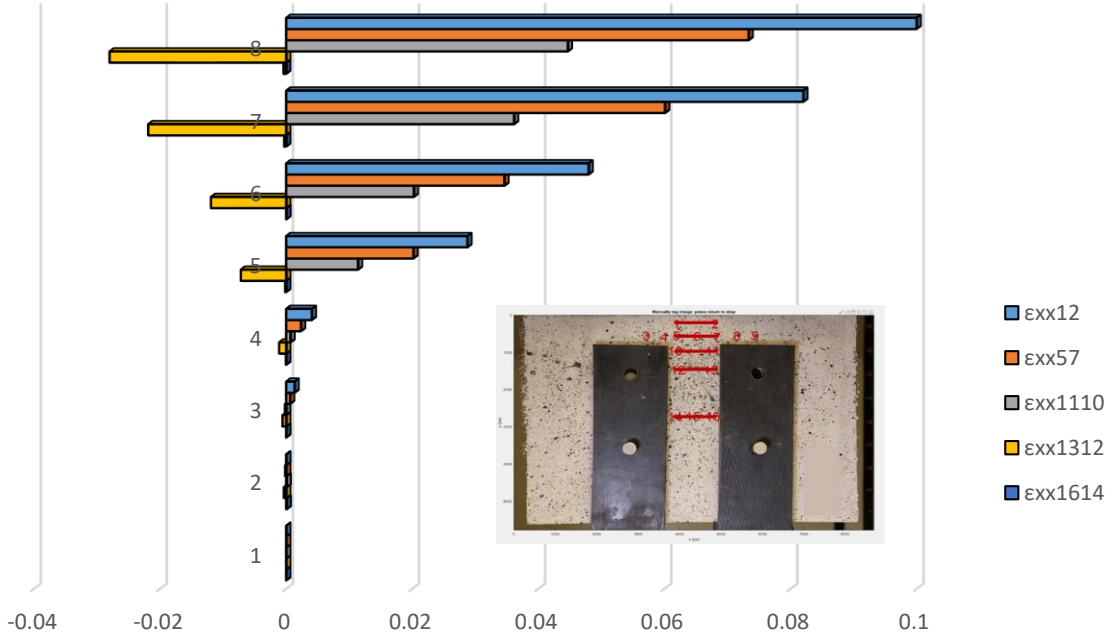

Figure 5-77 Comparison of ε_{xx} between horizontal layers (CMK1-5-A – Complete analysis).

-Comparison of ε_{yy} along vertical layers on each side

Figures Figure 5-78 and Figure 5-79 shows the vertical strains ε_{yy} denoted in the pathways 1-5-10-12-14 and 2-7-11-13-16, respectively. Each bar corresponds to the vertical strain levels between the two paired points and are arranged by height, in a similar manner as in Figure 5-77. The axes are also arranged in the same manner as in Figure 5-77. These diagrams can be used to describe the vertical strain levels along the height of the specimen and to create the crack width of the conical failure plane and measure the width of the crack in two separate locations.

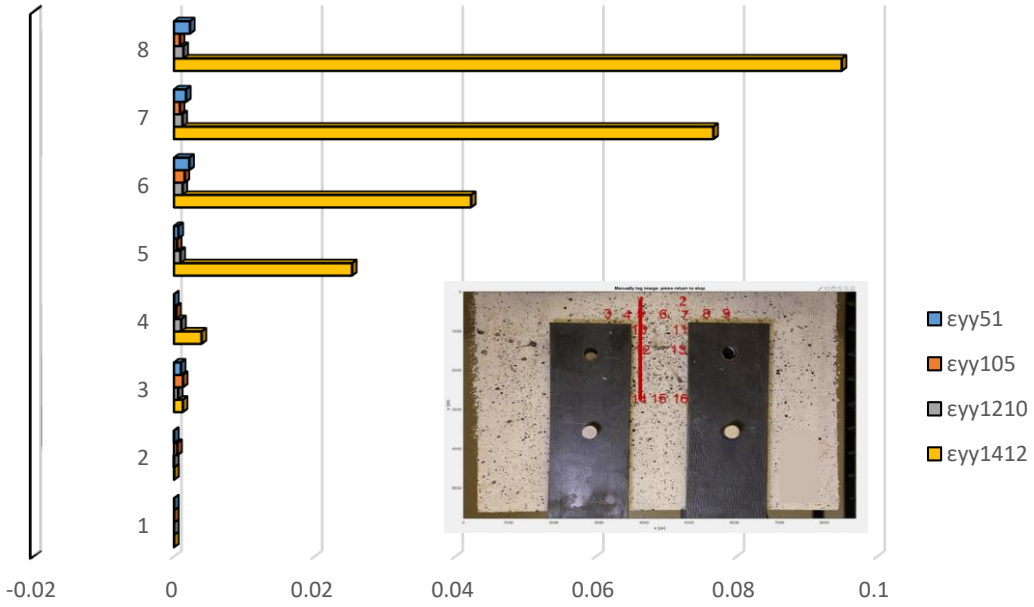

Figure 5-78 Demonstration of ε_{yy} on left vertical layer (CMK1-5-A – Complete analysis).

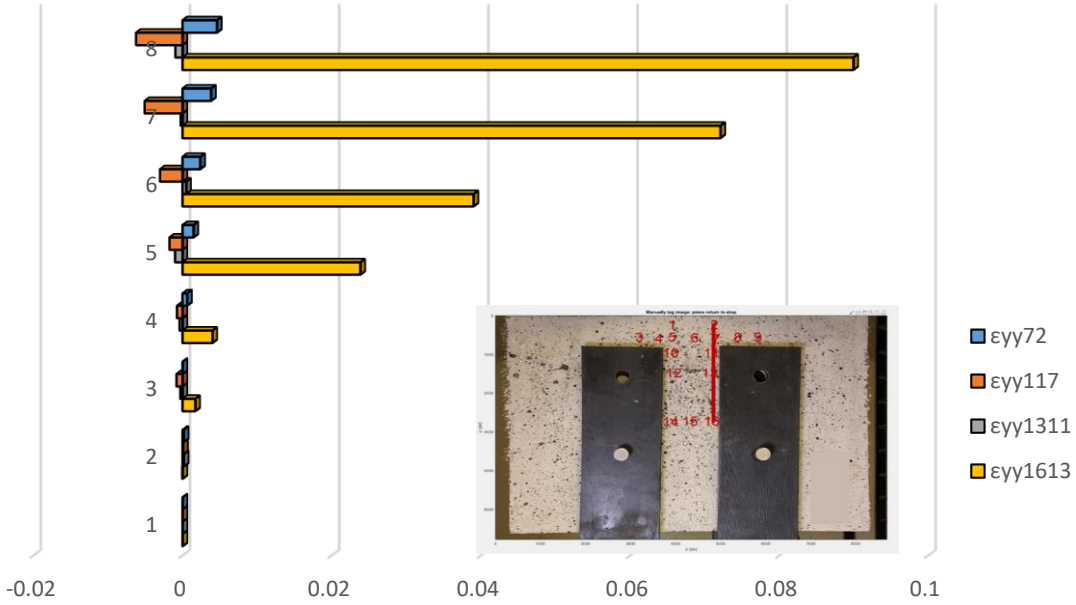

Figure 5-79 Demonstration of ε_{yy} on right vertical layer (CMK1-5-A – Complete analysis).

-Comparison of ε_{yy} between three equidistant layers

Figure 5-80 shows the distribution of the vertical strains ε_{yy} along three equidistant vertical layers. Each of colored bars corresponds to one of the vertical pathways 5-14, 6-15 and 7-16 and are located side by side, in the same manner as the pathways are located in the specimen. The horizontal axis of the diagram depicts the stage progression during the analysis and the vertical axis quantifies the strain levels for ε_{yy}. This diagram can be used to describe the vertical strain levels along the unobstructed horizontal path of the specimen and determine the crack profile of the conical failure zone.

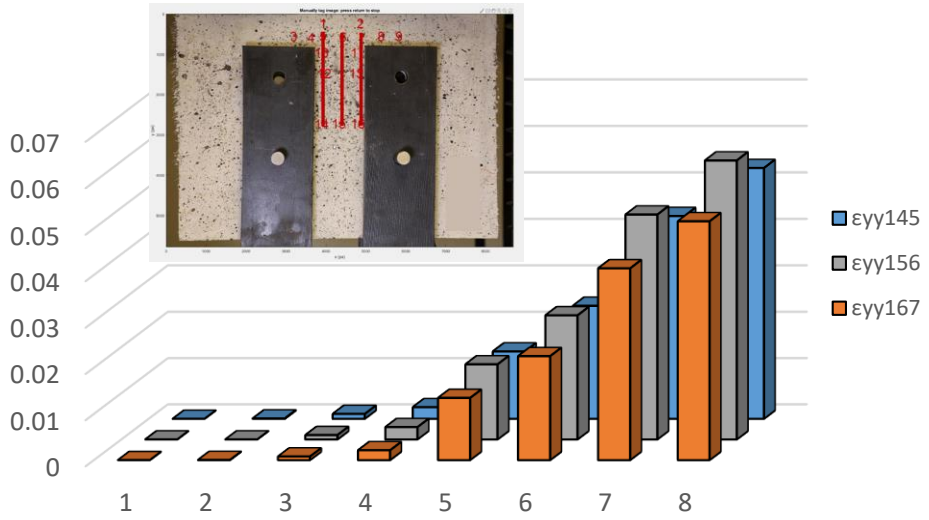

Figure 5-80 Comparison of ε_{yy} between three equidistant layers (CMK1-5-A – Complete analysis).

In the following sections, the above process is repeated three separate times. Each time, the locations of the points of interest is selected anew, at locations in the closest possible proximity of the points selected in the complete analysis. Only four stages are used in total, as explained in 5.3. The diagrams are arranged in the same manner as above and the results are presented individually for each analysis. Due to the great volume of the output produced for all specimens, the remaining diagrams obtained from the DIC analysis of the remaining specimens are placed in Appendix I. The discussion and comparison of the accumulated results is completed in 5.3.2.

5.3.1.2 Detailed analysis in three milestone points – Case 1

Figure 5-81 Locations of POIs for specimen CMK1-5-A (Three milestones – Case 1)

-Demonstration of ε_{xx} along Layer 2

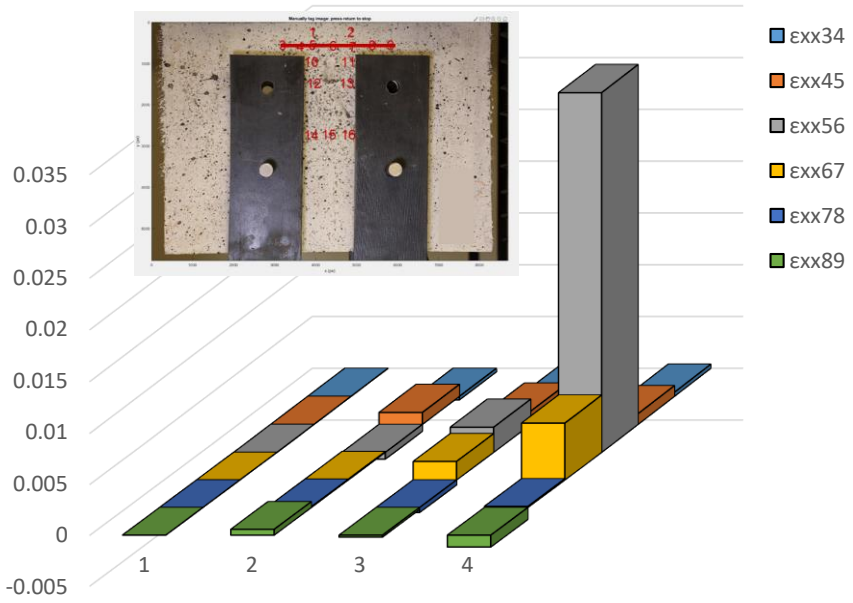

Figure 5-82 Demonstration of ε_{xx} along Layer 2 (CMK1-5-A - Case 1).

-Comparison of ε_{xx} between horizontal layers

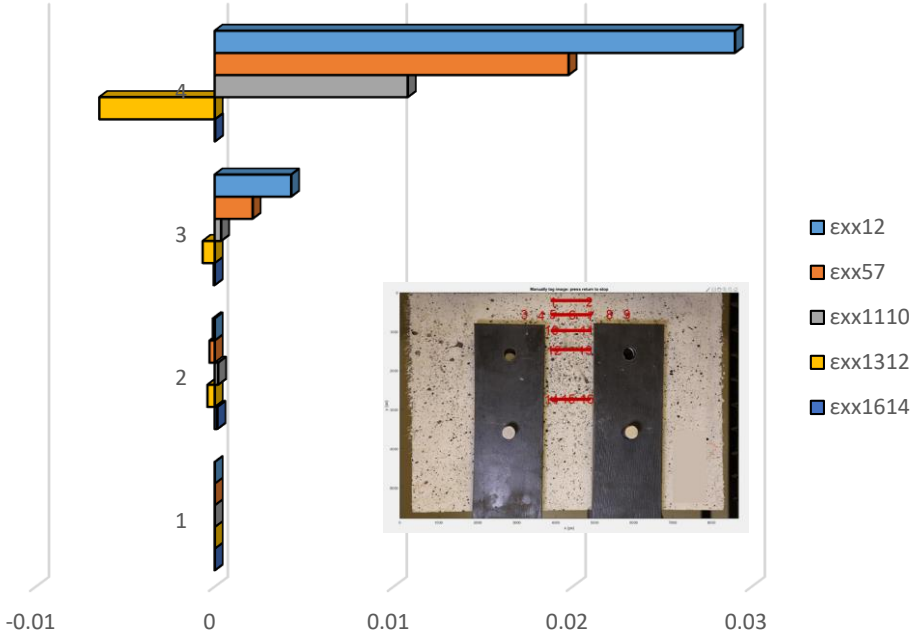

Figure 5-83 Comparison of ε_{xx} between horizontal layers (CMK1-5-A - Case 1).

-Comparison of ε_{yy} along vertical layers on each side

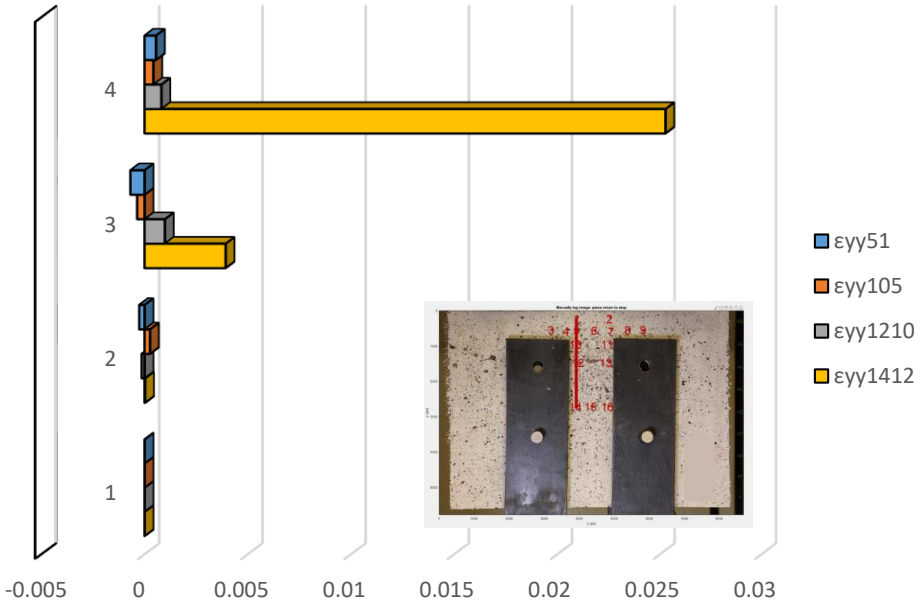

Figure 5-84 Demonstration of εyy on left vertical layer (CMK1-5-A - Case 1).

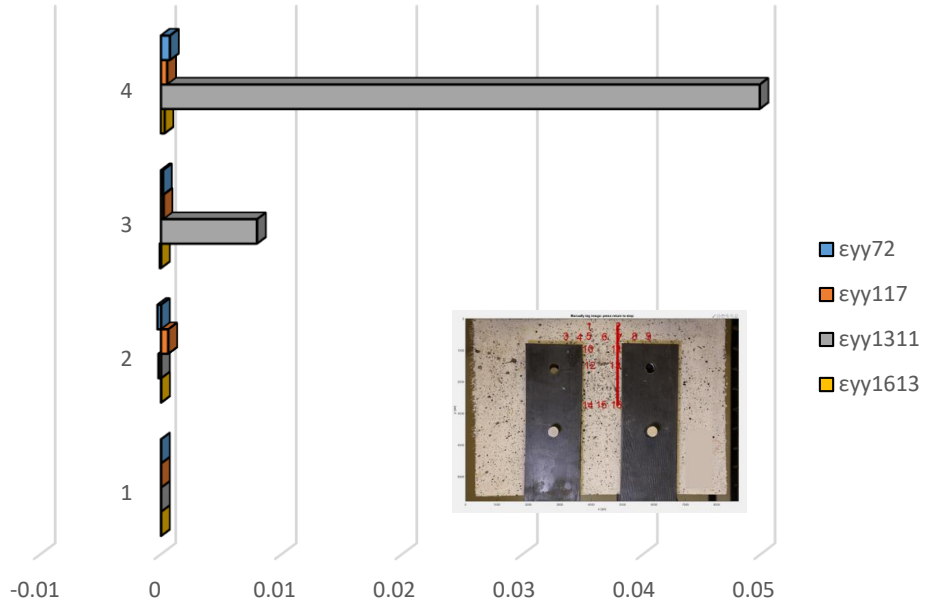

Figure 5-85 Demonstration of ε_{yy} on right vertical layer (CMK1-5-A - Case 1).

-Comparison of ε_{yy} between three equidistant layers

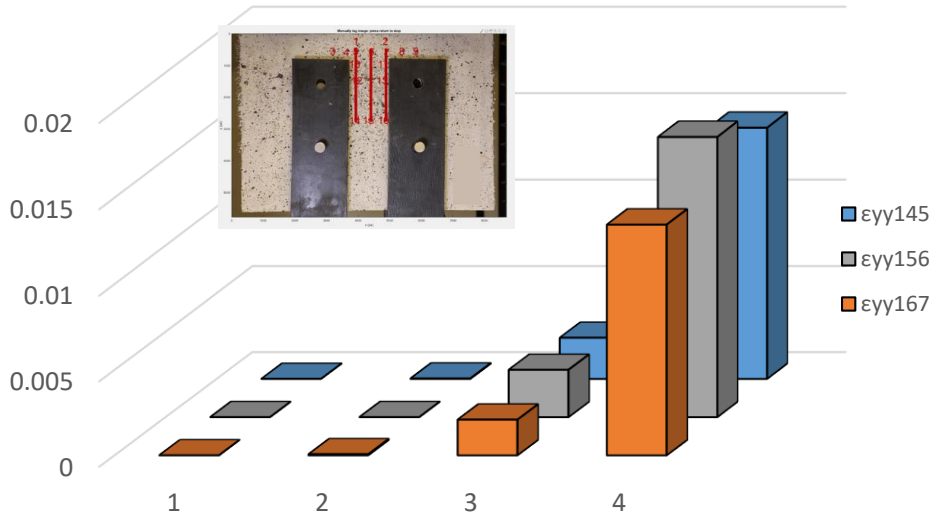

Figure 5-86 Comparison of ε_{yy} between three equidistant layers (CMK1-5-A - Case 1).

5.3.1.3 Detailed analysis in three milestone points – Case 2

Figure 5-87 Locations of POIs for specimen CMK1-5-A (Three milestones – Case 2)

-Demonstration of ε_{xx} along Layer 2

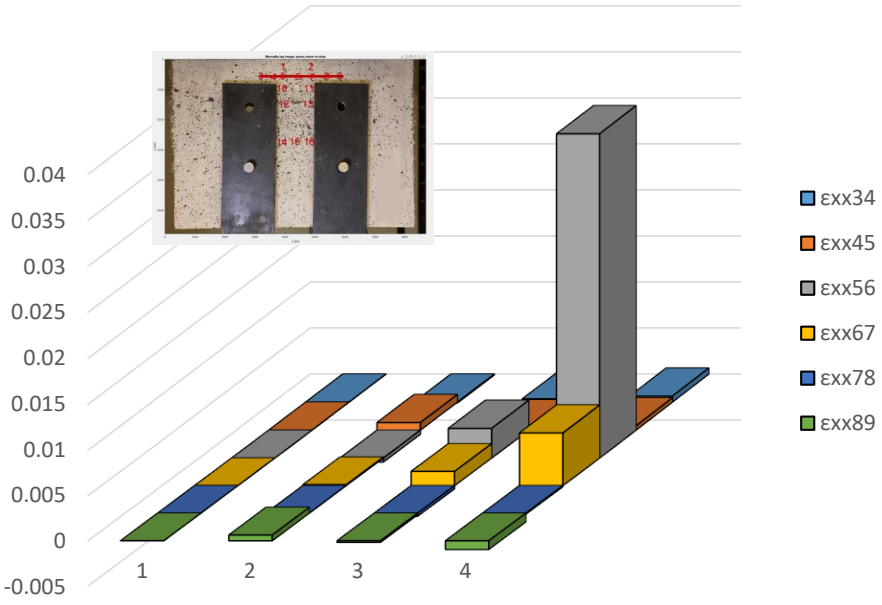

Figure 5-88 Demonstration of ε_{xx} along Layer 2 (CMK1-5-A - Case 2).

-Comparison of ε_{xx} between horizontal layers

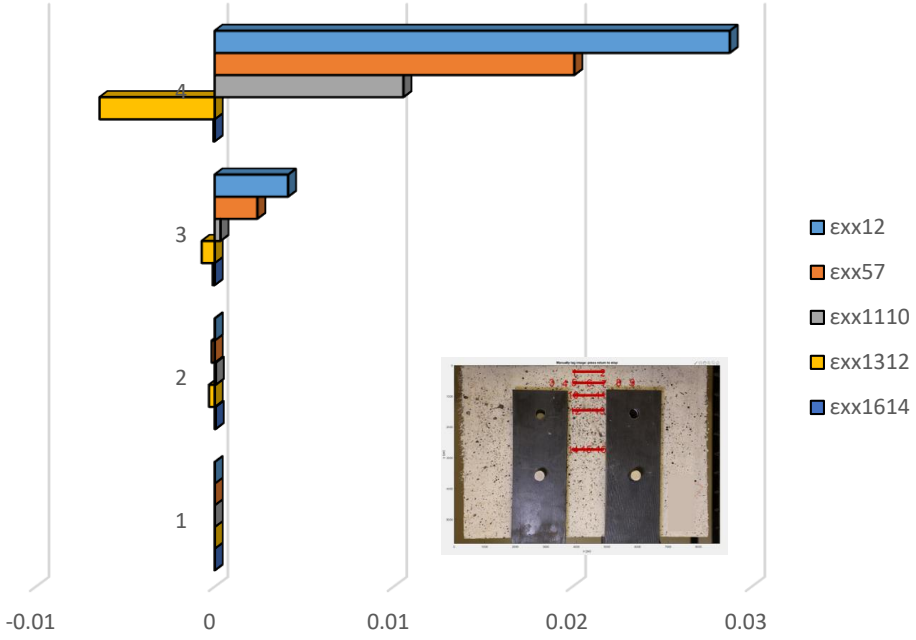

Figure 5-89 Comparison of ε_{xx} between horizontal layers (CMK1-5-A - Case 2).

-Comparison of ε_{yy} along vertical layers on each side

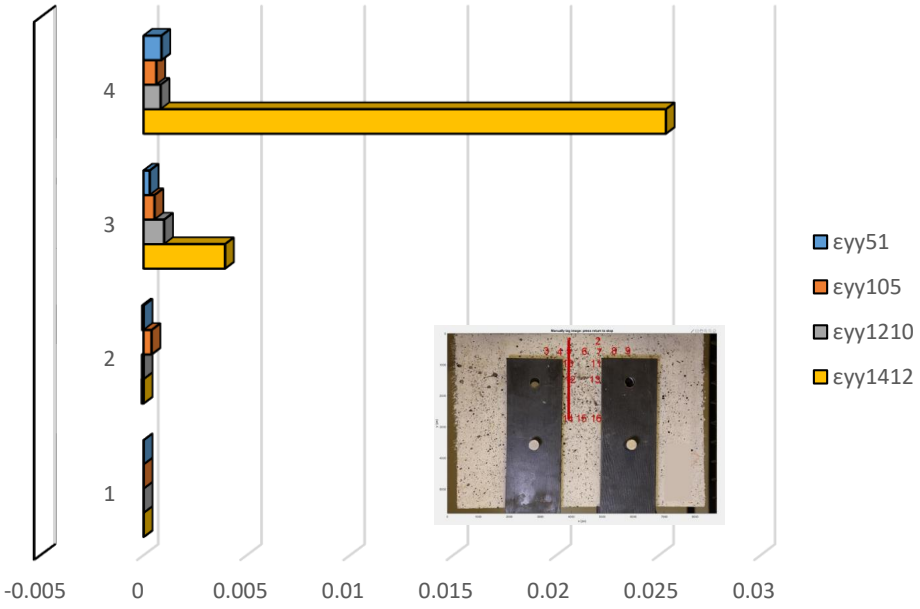

Figure 5-90 Demonstration of ε_{yy} on left vertical layer (CMK1-5-A - Case 2).

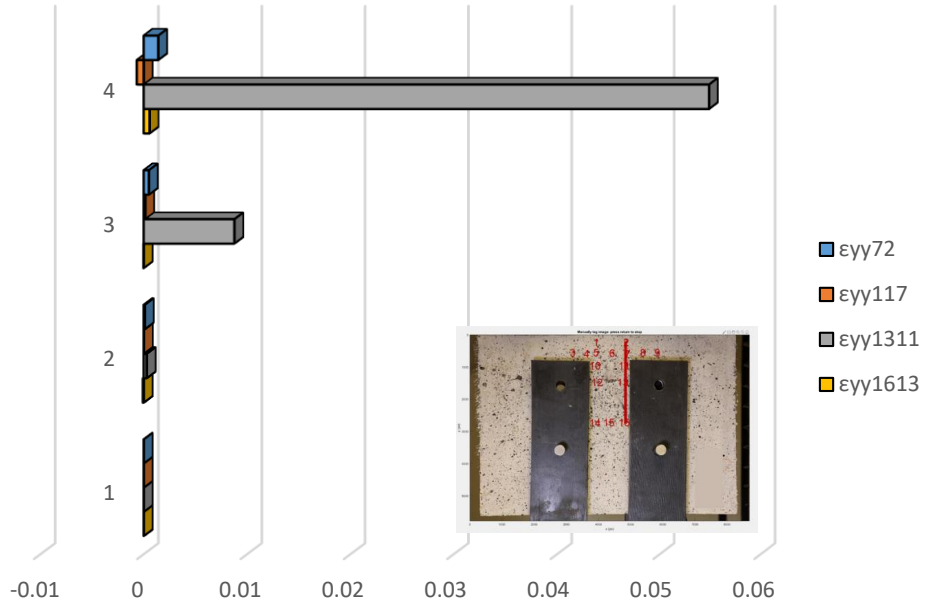

Figure 5-91 Demonstration of ε_{yy} on right vertical layer (CMK1-5-A - Case 2).

-Comparison of ε_{yy} between three equidistant layers

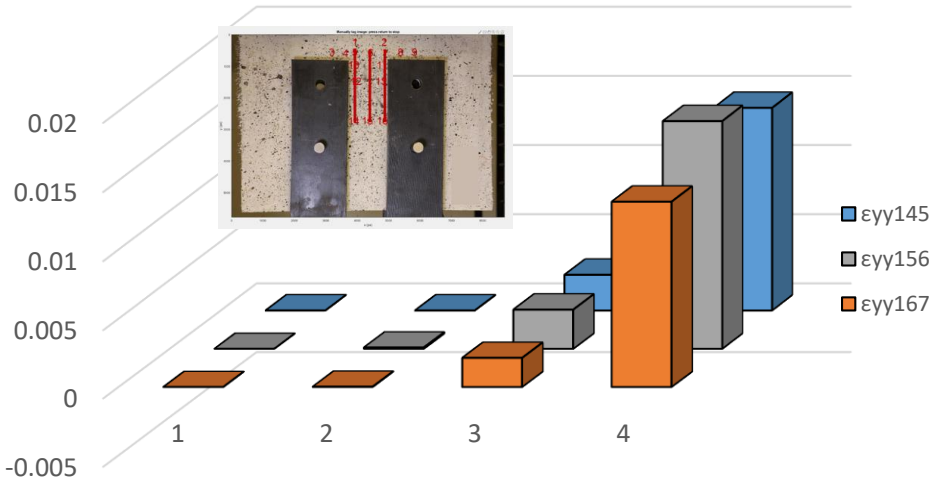

Figure 5-92 Comparison of ε_{yy} between three equidistant layers (CMK1-5-A - Case 2).

5.3.1.4 Detailed analysis in three milestone points – Case 3

Figure 5-93 Locations of POIs for specimen CMK1-5-A (Three milestones – Case 3)

-Demonstration of ε_{xx} along Layer 2

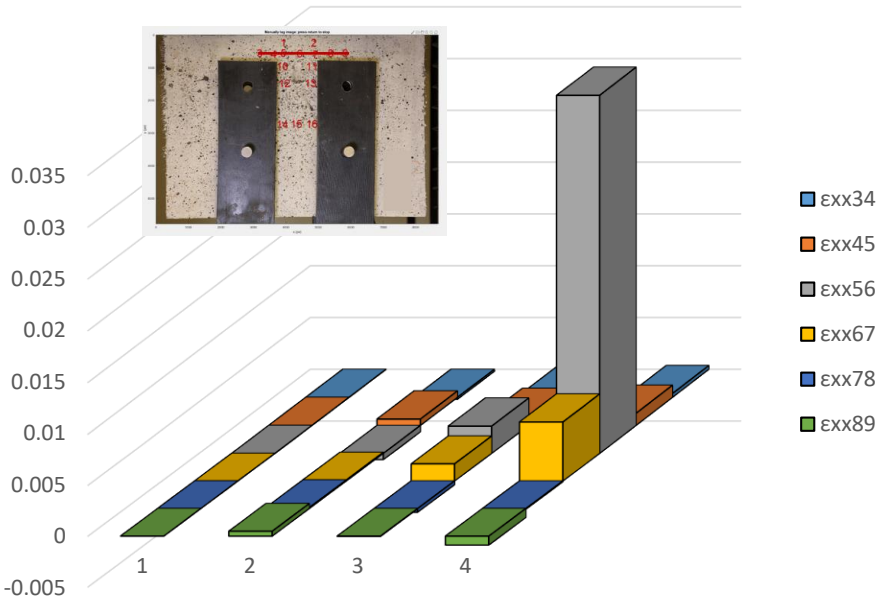

Figure 5-94 Demonstration of ε_{xx} along Layer 2 (CMK1-5-A - Case 3).

-Comparison of ε_{xx} between horizontal layers

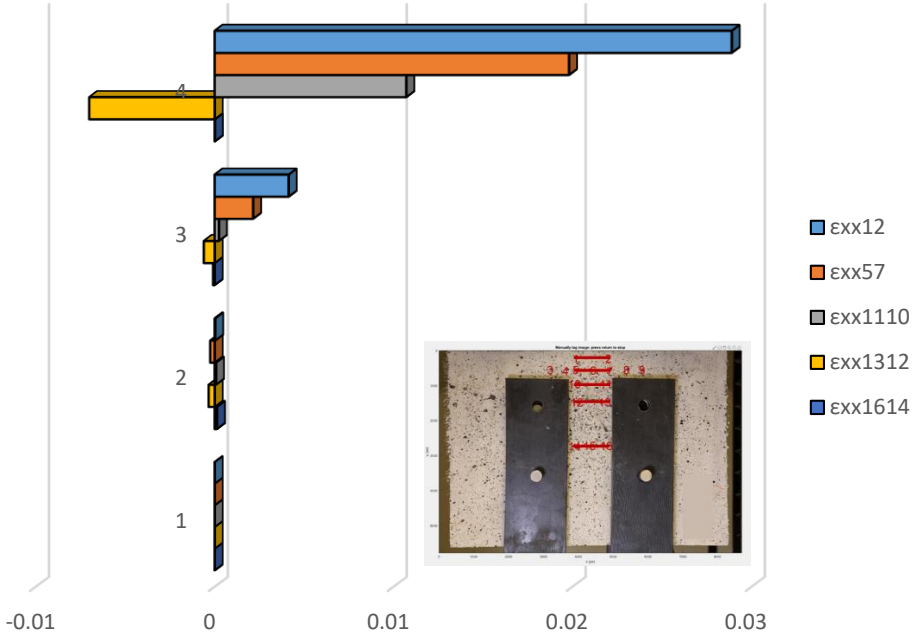

Figure 5-95 Comparison of ε_{xx} between horizontal layers (CMK1-5-A - Case 3).

-Comparison of ε_{yy} along vertical layers on each side

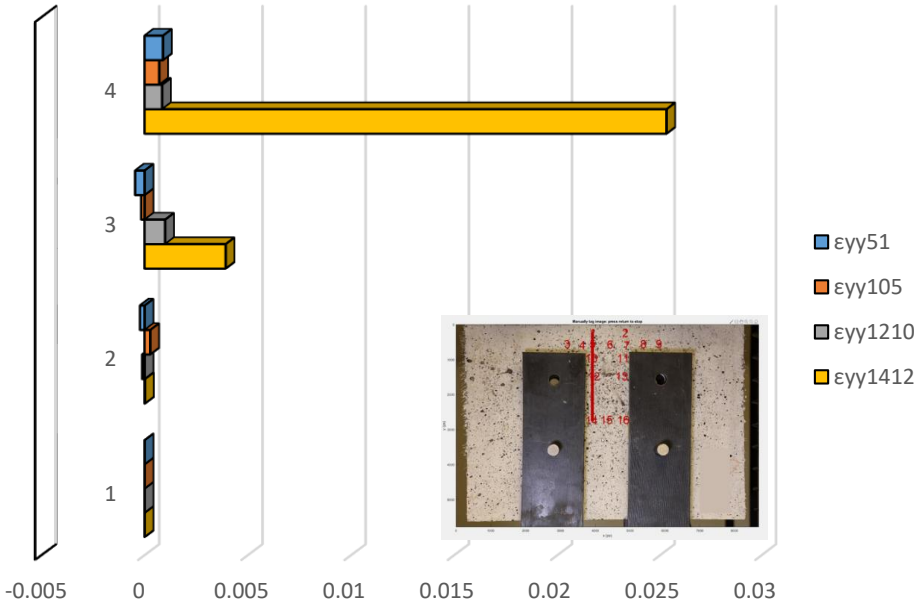

Figure 5-96 Demonstration of ε_{yy} on left vertical layer (CMK1-5-A - Case 3).

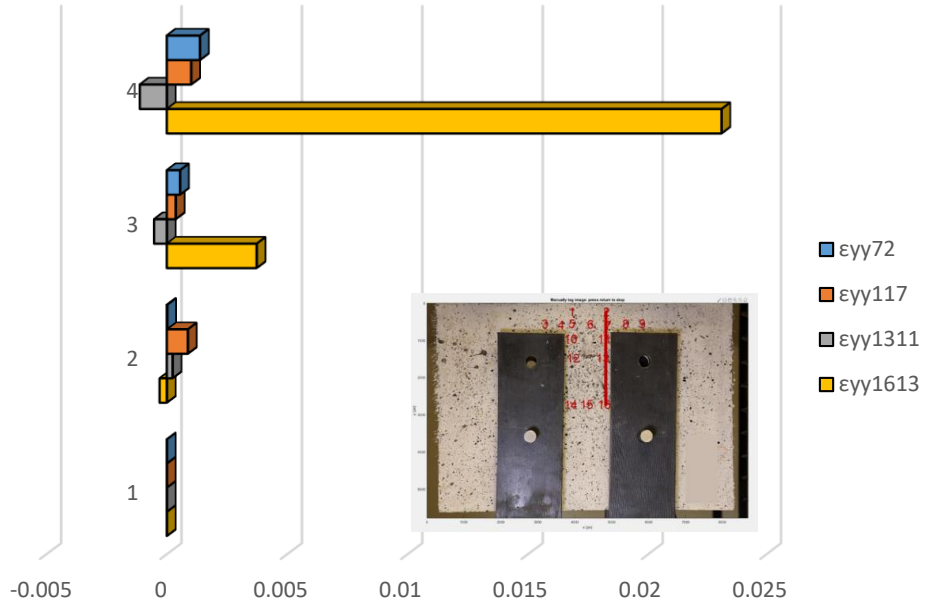

Figure 5-97 Demonstration of ε_{yy} on right vertical layer (CMK1-5-A - Case 3).

-Comparison of ε_{yy} between three equidistant layers

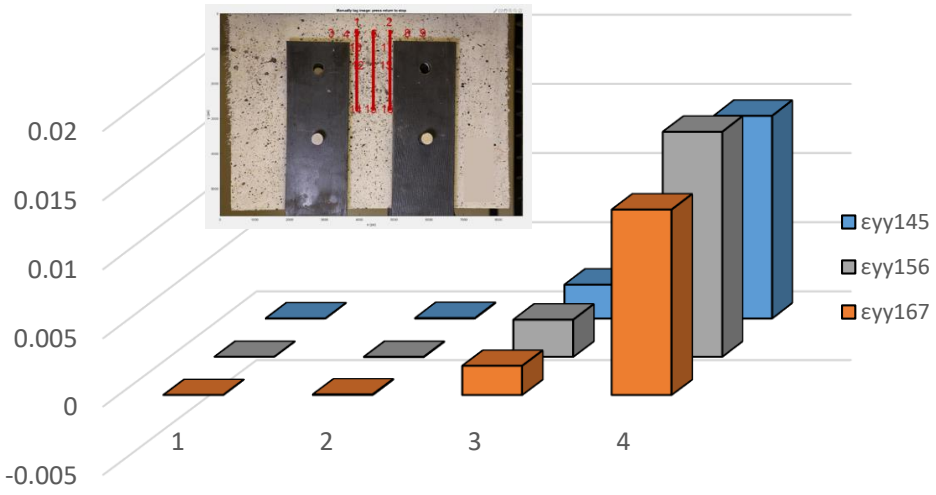

Figure 5-98 Comparison of ε_{yy} between three equidistant layers (CMK1-5-A - Case 3).

5.3.2 Comparisons between specimens

Table 5-10 displays the distribution of ε_{xx} at the ultimate point along Layer 2 as obtained from diagram framework D1, for all specimens. The red lines distinguishing strains ε_{xx56} and ε_{xx67} correspond to the zone engaged by the pulled bar. Significantly greater values are observed in the zone denoted by the red lines whereas in the zones on either side of the bar region the strains remain in relatively low values. Increased transverse strains of negative sign appear on the left side of the specimen front face, indicating the dislocation of parts of the specimen when separated from the main body of the specimen by a crack. The maximum tensile strain is obtained from specimen CMF1-5-A (0.264), in which the principal failure mechanism is splitting of the concrete. A closer interrogation of the accumulated results suggests that the splitting failure mechanism yields the greatest transverse strains, followed by the conical failure and pullout failure, respectively. The minimum strain is obtained from specimen CMF1-5-B. This observation is in accordance with the premise that the combination of long steel fibers with hooked ends with straight steel fibers provides the most scatter in the overall response of the specimen.

Table 5-10 Distribution of ultimate ε_{xx} along Layer 2, obtained from diagram D1.

Specimen ID	ε_{xx34}	ε_{xx45}	ε_{xx56}	ε_{xx67}	ε_{xx78}	ε_{xx89}	**Failure mode**
CMK1-5-A	-0.18	0.001	0.144	0.005	0.0	-0.004	C+S
CMK1-5-B	-0.125	-0.001	0.0	0.1	-0.001	0.006	P+S-C
CMK2-5-A	-0.154	0.0	-0.001	0.22	0.0	0.0	C-S-P
CMK2-5-B	-0.06	0.0	0.05	0.01	-0.001	0.02	P+S-C
CMF1-5-A	-0.24	0.001	0.264	0.0	-0.007	-0.006	S-C
CMF1-5-B	-0.02	0.004	0.014	0.003	0.0	0.001	P-S
CMF2-5-A (Part 1)	-0.006	0.004	0.004	0.005	0.003	0.001	-
CMF2-5-A (Part 2)	0.01	0.01	0.04	0.0	0.003	0.002	P+C-S
IHNJ1-5-A	-0.17	-0.002	-0.002	0.213	0.001	-0.003	C+S-P
IHNJ1-5-B	-0.08	-0.002	-0.001	0.167	0.0	0.0	C-S
IHNJ2-5-A	-0.118	-0.003	-0.003	0.13	0.005	0.0	C-S
IHNJ2-5-B	-0.12	-0.001	0.084	0.0012	0.0	0.0	C
IHRT2-5-A	-0.094	0.0	0.088	0.005	0.0014	-0.001	C-S
IHRT2-5-B	-0.15	-0.002	0.128	0.013	0.0	0.002	C+S

Table 5-11 shows the ultimate splitting crack values as obtained from the DT setup and the DIC analysis, according to diagram D2. The red vertical lines bound the points of interest within the embedded bar length. A relative compatibility can be observed in the acquired crack widths between the DT setup and the DIC analysis, with the majority of the former underestimating the expansion of the crack width. In the case of the DIC measurements, the splitting crack profile is delineated along the test bar axis and its extent may be determined. Negative values are observed in the locations surrounding the free end of the bar, indicating the intervention of the conical crack surface or points of interest that enclosed by arched splitting crack surfaces.

Table 5-11 Ultimate splitting crack values obtained from the DTs and diagram D2.

Specimen ID	Δ_{Vcrack} (mm)	Δ_{V12} – DIC (mm)	Δ_{V57} – DIC (mm)	Δ_{V1110} – DIC (mm)	Δ_{V1312} – DIC (mm)	Δ_{V1614} – DIC (mm)
CMK1-5-A	4.14	4.63	3.42	2.00	-1.99	-0.02
CMK1-5-B	2.12	3.2	2.8	1.58	-0.99	-0.018
CMK2-5-A	1.74	4.23	3.14	2.14	-1.56	-0.025
CMK2-5-B	1.78	2.94	2.24	0.93	-0.02	0.218
CMF1-5-A	6.4	5.76	4.52	1.84	0.83	-0.04
CMF1-5-B	1.45	0.64	0.36	0.38	0.19	0.06
CMF2-5-A (Part 1)	0.35	0.29	0.13	0.195	0	-0.01
CMF2-5-A (Part 2)	4.14	2.18	0.62	0.62	0.027	0
IHNJ1-5-A	2.25	5.56	4.21	1.97	0.49	0
IHNJ1-5-B	4.59	4.18	2.32	0.56	0	0.016
IHNJ2-5-A	3.59	3.6	2.48	0.79	-0.01	0
IHNJ2-5-B	2.32	2.57	2.08	0.53	0.18	0
IHRT2-5-A	0.96	3.24	1.98	0.705	-0.02	0
IHRT2-5-B	2.98	4.05	2.48	1.124	-0.03	-0.0154

Tables Table 5-12 and Table 5-13 show the ultimate crack width measured along the left and right vertical lines of points, respectively, as obtained from the corresponding diagrams. The red line designates the end of the anchorage length. A noticeable increase in strains can be observed in the proximity of the free end of the bar, owing to the occurrence of the crack immediately below the bar end. Tensile strain levels of considerable intensity envelop the concrete surrounding the

bar, reaching values that exceed the tensile strain capacity of conventional concrete. Consequently, the assumption that the strain of concrete does not contribute to bond strength, as included in Eqn. [2-1], no longer provides an accurate representation of the mechanisms that develop in UHPC materials. The inclusion of the concrete strain ε_c alters the solution to the fundamental differential equation that describes the bond strength of the steel-to-concrete interface, thus calling for a revised mathematical approach for the definition of bond behavior.

Table 5-12 Distribution of ultimate ε_{yy} along left vertical lane, obtained from diagram D3.

Specimen ID	ε_{yy15}	ε_{yy510}	ε_{yy1210}	ε_{yy1412}
CMK1-5-A	0.002	0.0008	0.0013	0.095
CMK1-5-B	0.0	0.0	0.0015	0.071
CMK2-5-A	0.0	0.001	-0.002	0.126
CMK2-5-B	0.004	0.004	0.24	0.003
CMF1-5-A	-0.14	0.007	0.012	0.14
CMF1-5-B	0.007	0.017	0.003	0.001
CMF2-5-A (Part 1)	-0.002	0.015	0.001	0.005
CMF2-5-A (Part 2)	-0.128	0.06	0.0036	0.0044
IHNJ1-5-A	0.0	0.003	-0.005	0.14
IHNJ1-5-B	-0.002	0.01	0.212	0.0075
IHNJ2-5-A	0.0	0.003	0.214	0.0
IHNJ2-5-B	-0.244	0.012	0.005	0.001
IHRT2-5-A	-0.002	0.004	0.19	-0.002
IHRT2-5-B	-0.006	0.003	0.266	0.0

Table 5-13 Distribution of ultimate ε_{yy} along right vertical lane, obtained from diagram D4.

Specimen ID	ε_{yy27}	ε_{yy117}	ε_{yy1311}	ε_{yy1613}
CMK1-5-A	0.004	-0.006	-0.001	0.09
CMK1-5-B	0.0017	-0.001	0.0126	0.06

CMK2-5-A	0.0	0.0	0.002	0.057
CMK2-5-B	0.63	-0.21	0.005	0.015
CMF1-5-A	0.002	-0.011	-0.015	0.15
CMF1-5-B	0.0	0.005	0.003	0.002
CMF2-5-A (Part 1)	0.006	0.008	0.0016	0.005
CMF2-5-A (Part 2)	0.078	0.005	0.005	0.006
IHNJ1-5-A	0.002	0.0	0.003	0.14
IHNJ1-5-B	0.0	0.002	0.22	0.007
IHNJ2-5-A	0.001	-0.001	0.207	0.0
IHNJ2-5-B	0.006	0.212	0.0	0.005
IHRT2-5-A	0.0014	0.16	0.006	-0.002
IHRT2-5-B	-0.005	0.0	0.2	0.0

Table 5-14 Ultimate horizontal crack profile in reference to the splitting crack from the DTs, obtained from diagram D5.

Specimen ID	Δ_{Vcrack} (mm)	$Slip_u$ (mm)	$\frac{\Delta_{Vcrack}}{Slip_u}$	Δ_{V145} – DIC (mm)	Δ_{V156} – DIC (mm)	Δ_{V167} – DIC (mm)	Failure mode
CMK1-5-A	4.14	1.76	2.35	5.87	6.48	5.69	C+S
CMK1-5-B	2.12	8.49	0.25	2.94	3.315	2.98	P+S-C
CMK2-5-A	1.74	-	-	5.63	6.32	2.68	C-S-P
CMK2-5-B	1.78	13.58	0.13	7.57	8.41	-5.21	P+S-C
CMF1-5-A	6.4	2.05	3.12	8.04	8.46	7.2	S-C
CMF1-5-B	1.45	3.5	0.41	0.48	0.3	0.21	P-S
CMF2-5-A (Part 1)	0.35	-	-	0.55	0.62	0.44	-
CMF2-5-A (Part 2)	4.14	-	-	0.69	1.5	0.53	P+C-S
IHNJ1-5-A	2.25	1.82	1.24	6.57	7.5	6.36	C+S-P
IHNJ1-5-B	4.59	0.65	7.06	5.21	5.84	5.1	C-S
IHNJ2-5-A	3.59	1.5	2.39	5.78	6.3	5.4	C-S
IHNJ2-5-B	2.32	2.79	0.83	0.51	6.35	5.6	C
IHRT2-5-A	0.96	2.54	0.38	5.03	5.32	4.57	C-S
IHRT2-5-B	2.98	4.42	0.67	5.45	5.13	4.73	C+S

Table 5-14 shows the crack profile of the conical failure plane in comparison to the splitting crack and relative slip measurements obtained from the DT setup. The conical crack profile demonstrates the maximum width at the mid-span of the specimen, where the bar axis is located, with situational inclinations to one side in the case of internal eccentric stress fields. Crack widths are measured greater in specimens where the conical and splitting cracks are prevalent whereas the pullout failure mode yields the smaller crack widths. In the case of arched splitting cracks, the encompassing points of interest are accounted for both the conical and splitting failure modes, due to the overlapping of the relative displacements.

Chapter 6: Discussion of Results and Conclusions

The collective results of the experimental program on bond of reinforcement in UHPC was intended to provide data that would later support the development of analytical expressions for design on anchorages of reinforcement in this type of concrete, but would also be used to develop a local bond – slip law which could be used in detailed modeling of structural components comprising UHPC material.

Apart from this generic objective associated with the experimental investigation, the test program enables investigation of other open issues related to the problem of bond. Such issues are:

(a) What is the effect of specimen form on the collected bond slip data.

(b) How is bond strength related to the measured tensile strength, and what is the effect of the type of tensile test conducted.

(c) Whether the existing solutions of the differential equation of bond are valid when used with UHPC. If so, it is important to identify any possible differences from conventional concrete assumptions.

In light of the emerging answers to the above open questions, summarizing the findings of the work done and the evidence collected, this chapter aims to address the open questions regarding bond of ribbed reinforcement in UHPC.

6.1 Conclusions on the effect of specimen form

This thesis is motivated by recent advents in reinforced concrete technology to introduce distributed mass reinforcement in the form of fine diameter fibers in a densely packed cementitious matrix, as a means of increasing the tensile capacity and fracture energy of the material. Objective is to characterize and quantify the properties of reinforcement bond in strain-resilient fiber-reinforced cementitious composites as a first step in the direction of the implementation of these materials in construction. The ability of UHPC and ECC to sustain large tensile strains and to release more than tenfold the amount of fracture energy of conventional concrete at failure, is owing to the internal confining effect of the distributed fibers. This internal confinement provides a novel environment for the development of steel reinforcement, and is a very efficient means of altering the constitutive mechanics that govern bond behavior. On account

of the ample evidence that reinforcement bond strengths obtained from experiments are vastly affected by the setup used in testing, a concern in the present research project was to attempt to eliminate these influences in order to reduce the risk for unconservative designs when bond and development capacity of reinforcement are overestimated. For this reason, an alternative setup of the direct tension pullout test (DTP) is conceptualized and fabricated as part of this study. (Direct tension pullout was selected as it establishes the least favorable conditions for bond stress to develop, therefore it provides the least influence of extraneous effects). The problem is studied also using advanced nonlinear finite element modeling using the commercial software platform, ATENA (2016). Two different modelling approaches are implemented, of different degrees of complexity, to idealize the mechanistic stress transfer from reinforcement to concrete through the contact interface between the two materials (the two models are based on the bond – link element and a more advanced, three-dimensional interface surface). With these two models the experimental trends and in particular the effects of specimen morphology on the results are explored with the objective to identify the source of the discord between different experimental setups when it comes to the study of bond. Primary conclusions of the study are as follows:

1. Previous research on pullout experiments suggests that the DTP test is the most pertinent setup to determine the constitutive bond – slip relationship, because it eliminates the favorable effects of compressive stress fields around the bar. In fact, in this test arrangement, the cementitious matrix that surrounds the reinforcement is also in tension, which is a stress state that reproduces faithfully the stress conditions encountered in the tension zone of common structural members, particularly in the region where tension reinforcement may be anchored. This disposition of stresses enables more realistic modeling and lower bound (more conservative) estimations of bond strength and bar development capacity.
2. A preliminary finite element analysis using spring-like, unidirectional contact links to model bond is conducted to study the stress distribution of UHPC materials under direct tension pullout. The analysis results corroborate those obtained from the experiments, capturing adequately the strength and crack distribution observed in the subsequent tests.
3. The bond stress – slip relationship in conventional unconfined concrete is reduced immediately after reaching the peak bond strength (or, in other words, the precipitous post peak decay of bond is a result of the formation of a longitudinal splitting crack). In the case of UHPC / ECC, however, the post-peak development strength is reduced gradually until the end of the analysis (an indication of a higher fracture energy capacity).

4. The bond link model provided a reliable approximation of the actual pullout behavior. However, this modeling approach requires the estimation of the constitutive properties a priori, and does not allow the use of variable properties along the anchorage length. In addition, the influence of transverse stresses on the bar surface cannot be studied with this approach because the bond properties are specified uniquely in the input and are pressure and restraint insensitive.
5. Simulation of various commonly used test setups is conducted using the three-dimensional interface model to enable comparison of the results between tests and also to check the ability of this approach to reproduce the experimental sensitivities. Based on the obtained force – displacement response of the setups, the standard pullout arrangement yielded the highest tensile capacity and apparent bond energy and resilience to slip, and by extension less conservative bond strength – slip estimates.
6. The presence of inclined compressive stress fields emanating from the bearing plates and converging toward the end of the anchorage was observed in the conventional and eccentric pullout setups. Using pressure sensitive constitutive properties for the bar-concrete interface, it was verified through the F.E. model that bond strength estimates obtained from these setups were effectively twice as high as the values obtained from the same modeling of the direct tension pullout test.
7. Shear stresses of opposing direction were observed in the opposing sides of the eccentric pullout test, due to the creation of moments (from equilibrium of forces) towards the geometric center of the opposing plate.
8. Radial stresses generated by the bar bearing against the concrete are resolved in the concrete ring surrounding the bar. The dimensions of the ring are dependent on the smallest cover surface. In the case of the eccentric pullout test, the ring assumed the form of an ellipse.
9. Cracking emanates from the contact ribs of the bar propagating through the concrete cover in an inclined (conical) field away from the contact point. Once the tensile stresses exhaust the tensile strength of concrete, the crack path spreads further, eventually reaching the outer surface of the cover, macroscopically appearing in the form of a splitting crack parallel to the bar.

6.2 Conclusions based on the experimental program

A total of 13 specimens were constructed using advanced cementitious composites and tested in accordance with the customized DTP setup discussed above. Four types of cementitious fiber reinforced material were used, namely, two commercial mixtures (with brass coated steel fibers) and two mixes developed in-house (one with brass coated fibers and one with synthetic, PVA fibers). A parameter of study was the available cover thickness. Using various types of instrumentation, the force – displacement relationship, the constitutive bond – slip law and splitting crack opening were attained for all specimens. Digital image correlation analysis (DIC) was performed to obtain the strain levels in the horizontal and vertical direction on the front face of the specimens.

1. Based on the relative peak tensile strengths of the specimens, the presence of larger cover increased the total specimen strength by up to 70%. Bond strength increased proportionately, whereas the relative slip at peak strength demonstrated a higher dependence on the amount and orientation of the fiber reinforcement.
2. Synthetic fibers, while accounting for lower tensile strengths than steel fibers, provide a more uniform distribution of the fiber reinforcement, leading to more homogeneous material properties. Synthetic fiber pullout occurred with greater intensity and impact in the ascending branch of the force – displacement curve where the crack widths captured by the engaged fiber reinforcement would be considered low.
3. Among steel fiber mixtures, greater strengths were achieved for the in-house mixture containing only short and straight steel fibers but at a higher volumetric ratio than the commercial mixes. The inclusion of longer fibers with hooked ends along with short and straight steel fibers in one of the two commercial mixes provided a considerable increase in strength, however leading to more inconsistencies due to the uneven distribution of the fibers in certain locations of specimen. The mixture containing the longer fibers however reached ultimate displacements of at least 20% higher than the specimens from all other mixes.
4. Due to the passive internal confinement by the fibers, multiple modes of failure were observed to propagate simultaneously which would correspond to phenomena observed in confined anchorages of conventional concrete. Combined cone and pullout failures that followed an initial splitting crack formation were reported in the majority of the specimen.
5. The presence of fiber reinforcement in the engaged radial zone surrounding the pulled bar significantly influenced the controlling mode of failure. Greater density of fibers around

the bar reduced the expansion of the splitting crack and prevented the bar from pulling out of the specimen.

6. Strain distribution levels obtained from the DIC analysis in the horizontal direction have established the pattern of variation in the splitting crack measurements as collected by the DT setup on the specimen. Additionally, strain levels in the vertical (longitudinal) direction affirm that concrete strain in UHPC moderates the development of slip, altering the mathematical premise upon which the derivation of the original solutions of the differential equation of bond is based on.
7. Stark differences were observed in the magnitudes of bond strength obtained between otherwise identical material and contact lengths in different bond specimens (beam tests vs. DTP specimens having a length of anchorage of $5D_b$). The pattern of difference, whereby strength from DTP is less than half the value obtained from beam tests, follows consistently the corresponding differences between tensile strengths obtained from bending (4-point) tests and dog-bone material tests (where tensile strength obtained from dog-bone test is less than 1/3 the value obtained from prism flexural testing). This implies that the bending action interferes both with tensile strength and with the mechanics of the anchorage in a manner that yet poorly understood. Bond strength results from the DTP tests can be expressed as about equal to the $\sqrt{f_c'}$.

6.3 Future projects

Continuation of this research may be conducted through more detailed investigation of the experimental parameters used in this study. Mechanical characteristics, such as the embedment length and bar profile, should be examined further, to study the interrelation between the local and average bond – slip responses, as well as the effect of bar geometry on the obtained bond values. The initial conditions of the governing differential equation that describes bond behavior are, additionally, subject to reconsideration in the case of UHPC matrices. More specifically:

1. DTP specimens, following the modified setup designed in this study, with embedment lengths greater than 10Db should be examined experimentally. The higher available development length will allow for post-elastic phenomena in the bond – slip response to be observed in sequence, and the local bond – slip properties to be determined.
2. Test bars of various geometries and rib profiles should be examined in direct tension pullout using UHPC matrices. These include G-FRP bars, both in shorter and longer embedment lengths, as well as various cover thicknesses.

3. The analytical solution of the governing differential equation of bond should be reviewed, with the inclusion of the concrete tensile strain the strain compatibility equation. As it was justified from DIC analysis of this study, the UHPC matrix sustains strain levels of significant intensity, that are no longer negligible. The contribution of the concrete strain in the mathematical interpretation of bond would lead to a more coherent understanding of the inherent bond – slip law properties.
4. Revision of the detailing procedures in reinforced concrete members has become attainable through the application of UHPC. Due to greater tensile capacities and higher bond strength being developed in the presence of UHPC matrices, transverse reinforcement requirements may be reduced, and more effective design and formulation criteria are necessary for newly-formed code provisions.

Selected References

1. ACI 318 Committee, “Building Code Requirements for Structural Concrete (ACI 318-02) and Commentary (318R-02),” American Concrete Institute, Farmington Hills, MI, 2002, 443 pp.
2. ACI 318 Committee, “Building Code Requirements for Structural Concrete (ACI 318-14) and Commentary (318R-14),” American Concrete Institute Farmington Hills, MI, 2014.
3. ACI Committee 408. (2003). ACI 408R-03 Bond and Development of Straight Reinforcing Bars in Tension. *American Concrete Institute*, 1–49.
4. ASTM A944-99, 'Standard test method for comparing bond strength of steel reinforcing bars to concrete using beam-end specimens', ASTM (1999), pp 501-504.
5. Azizinamini, A., Pavel, R., Hatfield, E., & Ghosh, S. K. (1999). Behavior of lap-spliced reinforcing bars embedded in high-strength concrete. *ACI Structural Journal*, *96*(5), 826–835. https://doi.org/10.14359/737
6. Azizinamini, A., Stark, M., Roller, J. J., & Ghosh, S. K. (1993). Bond performance of reinforcing bars embedded in high-strength concrete. *ACI Structural Journal*, *90*(5), 554–561. https://doi.org/10.14359/3951
7. Bakis, C., Uppuluri, V., Nanni, A., and Boothby, T. (1998). “Analysis of bonding mechanisms of smooth and lugged FRP rods embedded in concrete.” Compos. Sci. Technol., 58(8), 1307–1319.
8. Bandelt, M. J., & Billington, S. L. (2016). Bond behavior of steel reinforcement in high-performance fiber-reinforced cementitious composite flexural members. *Materials and Structures/Materiaux et Constructions*, 49(1–2), 71–86. https://doi.org/10.1617/s11527-014-0475-4
9. Bandelt, M. J., & Billington, S. L. (2018). Simulation of deformation capacity in reinforced high- performance fiber-reinforced cementitious composite flexural members. *Journal of Structural Engineering*, *144*(10), 04018188. https://doi.org/10.1061/(ASCE)ST.1943-541X.0002174
10. Bandelt, M. J., Frank, T. E., Lepech, M. D., & Billington, S. L. (2017). Bond behavior and interface modeling of reinforced high-performance fiber-reinforced cementitious composites. *Cement and Concrete Composites*, *83*, 188–201. https://doi.org/10.1016/j.cemconcomp.2017.07.017

11. Bandelt, M. J., & Billington, S. L. (2014). Monotonic and Cyclic Bond-Slip Behavior of Ductile High-Performance Fiber-Reinforced Cement-Based Composites. *Proc. SHCC 3*, (1), 2–9. https://doi.org/10.13140/2.1.3342.6720
12. Berrocal, C. G., Fernandez, I., Lundgren, K., & Löfgren, I. (2017). Corrosion-induced cracking and bond behaviour of corroded reinforcement bars in SFRC. *Composites Part B: Engineering*, *113*, 123–137. https://doi.org/10.1016/j.compositesb.2017.01.020
13. Bonacci, B. J. F. (1994). Bar yield penetration in monotonically loaded anchorages, *120*(3), 965–986.
14. Bournas, D. A., & Triantafillou, T. C. (2011). Bond Strength of Lap-Spliced Bars in Concrete Confined with Composite Jackets. *Journal of Composites for Construction*, *15*(2), 156–167. https://doi.org/10.1061/(ASCE)CC.1943-5614.0000078
15. Cairns, J., and Plizzari, G. A. (2002). “Do we need a standard test for bond?” Proc., Bond in Concrete – From Research to Standards,L. Balazs, J. M. Bartos, J. Cairns, and A. Borosnyoi, eds., fib (federation internationale du beton), Budapest, 259–267.
16. Cairns, J., & Plizzari, G. A. (2003). Towards a Harmonised European bond test. Materials and Structures/Materiaux et Constructions, 36(262), 498–506. https://doi.org/10.1617/13887
17. Cattaneo, S., & Rosati, G. (2009). Bond between steel and self-consolidating concrete: experiments and modeling. *ACI Structural Journal*, *106*(4), 540–550.
18. CEN (2004) Eurocode 2: Design of concrete structures, Part 1-1: General rules and rules for buildings. CEN, Brussels, EN 1992-1-1:2004.
19. Chao, S. H. (2005). Bond Characterization of Reinforcing Bars and Prestressing Strands in High Performance Fiber Reinforced Cementitious Composites Under Monotonic and Cyclic Loading, (April), 1–9.
20. Chao, S. H., Naaman, A. E., & Parra-Montesinos, G. J. (2009). Bond behavior of reinforcing bars in tensile strain-hardening fiber-reinforced cement composites. *ACI Structural Journal*, *106*(6), 897–906. https://doi.org/10.14359/51663191
21. Chao, S.-H., Naaman, A. E., & Parra-Montesinos, G. J. (2010). Local bond stress-slip models for reinforcing bars and prestressing strands in high-performance fiber-reinforced cement composites. *ACI Special Publication*, *SP-272*(8), 151–172. Retrieved from http://www.concrete.org/PUBS/JOURNALS/OLJDetails.asp?Home=SP&ID=51664090

22. Ciampi, V., Eligehausen, R., Popov, E. P., & Bertero, V. V. (1982). Analytical Model for Concrete Anchorages of Reinforcing Bars under Generalized Excitations. *Report N° UCB/EERC-82/23*, 121. Retrieved from http://dx.doi.org/10.18419/opus-8475
23. Comité Euro-International du Béton. (1993). CEB-FIP model code 1990: Design code, Thomas Telford, London
24. Cox, J. V., & Herrmann, L. R. (1998). Development of a plasticity bond model for steel reinforcement. *Mechanics of Cohesive-Frictional Materials*, *3*(2), 155–180. https://doi.org/10.1002/(SICI)1099-1484(199804)3:2<155::AID-CFM45>3.0.CO;2-S
25. Červenka, V., Jendele, L., & Červenka, J. (2005). ATENA Program Documentation, Part 1: Theory. *Praha, Czech Republic*, 1–282.
26. Červenka, V., Jendele, L., & Červenka, J. (2005). ATENA Program Documentation, Part 2-2: User's Manual for ATENA 3D. *Praha, Czech Republic*, 1–282.
27. Červenka, V., Jendele, L., & Červenka, J. (2005). ATENA Program Documentation, Part 11: Troubleshooting Manual. *Praha, Czech Republic*, 1–282.
28. Červenka, V., Jendele, L., & Červenka, J. (2005). ATENA Program Documentation, Part 12: User's Manual for ATENA Studio. *Praha, Czech Republic*, 1–282.
29. CSA Committee A23.3-14 (2004). Design of Concrete Structures, Canadian Standards Association, Mississauga, Ontario, Canada, 214 pp.
30. Dagenais, M.-A., & Massicotte, B. (2015). Tension Lap Splices Strengthened with Ultrahigh-Performance Fiber-Reinforced Concrete. *Journal of Materials in Civil Engineering*, *27*(7), 04014206. https://doi.org/10.1061/(ASCE)MT.1943-5533.0001169
31. Dagenais, M.-A., & Massicotte, B. (2017). Cyclic Behavior of Lap Splices Strengthened with Ultrahigh Performance Fiber-Reinforced Concrete. *Journal of Structural Engineering*, *143*(2), 04016163. https://doi.org/10.1061/(ASCE)ST.1943-541X.0001652
32. Dagenais, M.-A., Massicotte, B., & Boucher-Proulx, G. (2018). Seismic Retrofitting of Rectangular Bridge Piers with Deficient Lap Splices Using Ultrahigh-Performance Fiber-Reinforced Concrete. *Journal of Bridge Engineering, ASCE*, *23*(2), 1–13. https://doi.org/10.1061/(ASCE)BE.1943-5592.0001173
33. Darwin, D.; Tholen, M. L.; Idun, E. K.; and Zuo, J., 1996a, "Splice Strength of High Relative Rib Area Reinforcing Bars," ACI Structural Journal, V. 93, No. 1, Jan.-Feb., pp. 95-107.
34. Darwin, D.; Zuo, J.; Tholen, M. L.; and Idun, E. K., 1996b, "Development Length Criteria for Conventional and High Relative Rib Area Reinforcing Bars," ACI Structural Journal, V. 93, No. 3, May-June, pp. 347-359.

35. Dinges, D., et al. (1985). "Untersuchung verschiedener Elementsteifig- keitsmatrizen auf ihre Eignung zur Berechnung von Stahlbeton- konstruktionen." final res. rep., 2nd Interimreport, Darmstadt (1982), 3rd Interimreport, Kassel/Darmstadt (1983).
36. Eleftheriou, T. E., Tastani, S. P., Pantazopoulou, S. J., & Asce, M. (2017). Development of Reinforcing Bars in SRCC Matrix: Modeling and Interpretation, 143(9), 1–16. https://doi.org/10.1061/(ASCE)ST.1943-541X.0001845.
37. Eligehausen, R., Popov, E. P., & Bertero, V. V. (1982). Local bond stress-slip relationships of deformed bars under generalized excitations. *Proceedings of the 7th European Conference on Earthquake Engineering.*, 69–80. https://doi.org/Report No. UCB/EERC-83/23
38. Eligehausen, R. and Mayer, U. (2000), Investigations on the influence of the relative rib area of reinforcing bars on the structural behavior of reinforced concrete members in the serviceability and ultimate limit state (Translation from German), 503, Deutscher Ausschuss für Stahlbeton, Beuth Berlin, Germany.
39. Eshghi, N. (2018). Behaviour and Analysis of Strain Hardening Fiber Reinforced Cementitious Composites Under Shear and Flexure. Dissertation, in Partial Fulfillment of the MASc requirements, Department of Civil Engineering, York University. https://yorkspace.library.yorku.ca/xmlui/handle/10315/34418
40. Ezeldin, A. S., & Balaguru, P. N. (1989). Bond behavior of normal and high-strength fiber reinforced concrete. *ACI Materials Journal*, *86*(5), 515–524. https://doi.org/10.14359/2141
41. Fehling, E., & Lorenz, P. (2013). Characterization of Rebars Anchorage in Uhpc, (1), 587–596.
42. *fib* Bulletin 10 (2000). “Bond of reinforcement in concrete.” Rep. by former CEB Task Group 2.5, Ch.7/TG 4.2/WP 7, International Federation for Concrete, Lausanne, Switzerland.
43. *fib* Bulletin 65 (2012). Model Code 2010 – Final Draft, Volumes 1 & 2. *Federation Internationalle du Beton,* Lausanne, Switzerland.
44. *fib* Bulletin 72 (2014). Bond and Anchorage of Reinforcement – Background to the fib Model Code 2010. *Federation Internationalle du Beton* (170 pages), Lausanne, **ISBN:** 978-2-88394-112-0.
45. Filippou, F., Popov, E., and Bertero, V. (1983). “Modeling of R/C joins under cyclic excitations.” J. Struct. Eng., 109(11), 2666–2684.

46. Georgiou, A. (2017). Characterization of the Structural Performance of Strain-Hardening Fiber Reinforced Cementitious Composites Doctor of Philosophy Dissertation Characterization of the Structural Performance of Strain-Hardening Composites.
47. Goto, Y. (1971). Cracks Formed in Concrete Around Deformed Tension Bars. *ACI Journal Proceedings*, *68*(4), 244–251. https://doi.org/10.14359/11325
48. Harajli, M. H. (2007). Numerical Bond Analysis Using Experimentally Derived Local Bond Laws: A Powerful Method for Evaluating the Bond Strength of Steel Bars. *Journal of Structural Engineering*, *133*(5), 695–705. https://doi.org/10.1061/(ASCE)0733-9445(2007)133:5(695)
49. Harajli, M. H., Hout, M., & Jalkh, W. (1995). Local bond stress-slip behavior of reinforcing bars embedded in plain and fibre concrete. *ACI Materials Journal*, *92*(4), 449–466. https://doi.org/10.12989/cac.2015.16.3.449
50. Hoshino, M. (1974). "Ein Beitrag zur Untersuchung des Spannungszustandes an Arbeitsfugen mit Spannglied-Kopplungen von abschnittsweise in Ortbeton hergestellten Spannbetonbriicken." Dissertation, presented to Technischeltoch Schale, Darmstadt, Germany, in partial fulfillment of the requirements for the degree of Doctor of Philosophy.
51. Keuser, M., Mehlhorn, G. (1987). Finite element models for bond problems. ASCE Journal of Structural Engineering, Vol. 113, No. 10, October, 1987.
52. Lagier, F., Massicotte, B., & Charron, J.-P. (2016). 3D Nonlinear finite-element modeling of lap splices in UHPFRC. *Journal of Structural Engineering*, *142*(11), 04016087. https://doi.org/10.1061/(ASCE)ST.1943-541X.0001549
53. Lagier, F., Massicotte, B., & Charron, J. P. (2015). Bond strength of tension lap splice specimens in UHPFRC. *Construction and Building Materials*, *93*, 84–94. https://doi.org/10.1016/j.conbuildmat.2015.05.009
54. Laura N. Lowes, J. P. M., & Sanjay, G. (2004). Concrete-Steel Bond Model for Use in Finite Element Modeling of Reinforced Concrete Structures. *Structural Journal*, *101*(4). https://doi.org/10.14359/13336
55. Lee, J. K. (2016). Bonding behavior of lap-spliced reinforcing bars embedded in Ultra-high Strength Concrete with steel fibers. *KSCE Journal of Civil Engineering*, *20*(1), 273–281. https://doi.org/10.1007/s12205-015-1396-7
56. Li, V. C., Mishra, D. K., & Wu, H. C. (1995). Matrix design for pseudo-strain-hardening fibre reinforced cementitious composites. *Materials and Structures*, *28*(10), 586–595. https://doi.org/10.1007/BF02473191

57. Lutz, L. A., & Gergely, P. (1967). Mechanics of Bond and Slip of Deformed Reinforcement. ACI Journal, (64), 711–721.
58. Malvar, L. J. (1992). Bond of reinforcement under controlled confinement. Materials Journal, 89(6), 593–601. https://doi.org/10.14359/4039
59. Massicotte, B., Dagenais, M.-A., & Lagier, F. (2013). Performance of UHPFRC jackets for the seismic strengthening of bridge piers. *RILEM-Fib-AFGC International Symposium on Ultra-High Performance Fibre-Reinforced*, (1), 89–98.
60. Naaman, A. E., & Reinhardt, H. W. (2006). Proposed classification of HPFRC composites based on their tensile response. *Materials and Structures/Materiaux et Constructions*, *39*(289), 547–555. https://doi.org/10.1617/s11527-006-9103-2
61. Naaman, A. E., & Najm, H. (1991). Bond-slip mechanisms of steel fibers in concrete. ACI Materials Journal, 88(2), 135–145. https://doi.org/10.14359/1896
62. Nammur, G., & Naaman, A. E. (1989). Bond Stress Model for Fiber Reinforced Concrete Based on, (86), 45–57.
63. Ngo, D., and Scordelis, A. C. (1967). "Finite element analysis of reinforced concrete beams." ACI-Journal, pp. 152-163.
64. Orangun, C. O., Jirsa, J. O., and Breen, J. E. (1975). ‘‘Strength of an- chored bars: A reevaluation of test data on development length and splices.’’ Research Rep. No. 154-3F, Center for Highway Research, Univ. of Texas, Austin, Tex.
65. Orangun, C. O., Jirsa, J. O., and Breen, J. E. (1977). ‘‘Reevaluation of test data on development length and splices.’’ ACI Mater. J., 74(3), 114–122.
66. Pantazopoulou, S. J. (2001). Modeling Cover -Cracking due to Reinforcement Corrosion in RC Structures, 2(April), 342–351.
67. Rehm G., Eligehausen R: Bond of ribbed bars under high-cycle repeated loads, ACI Journal 76(2), 297- 309.
68. RILEM/CEB/FIP, 'Bond test for reinforcing steel: 2. Pullout Test', Recommendation RC 6 (1978).
69. Saikali, R. (2019). Bond Behavior of Steel Reinforcing Bars Embedded in Ultra-High-Performance Steel Fiber Reinforced Concrete. Dissertation, in Partial Fulfillment of the MASc requirements, Department of Civil Engineering, York University. https://yorkspace.library.yorku.ca/xmlui/handle/10315/34418
70. Schafer, H. (1975). A contribution to the solution of contact problems with the aid of bond elements. In Computer methods in applied mechanics and engineering. Vol. 6, pp. 335-354, North-Holland Publishing Company, Amsterdam.

71. Stanier, S.A., Blaber, J., Take, W.A. and White, D.J. (2015). Improved image-based deformation measurement for geotechnical applications. Canadian Geotechnical Journal, doi: 10.1139/cgj-2015-0253.
72. Tepfers, R. (1973). ‘‘Theory of bond applied to overlapped tensile reinforcement splices for deformed bars.’’ Publ. No. 73:2, Chalmers University of Technology, Gothenburg, Sweden.
73. Timoshenko, S., and Goodier, J. N. (1970). Theory of elasticity, 3rd Ed., McGraw-Hill, New York.
74. Tassios, T. P. (1979): Properties of Bond between Concrete and Steel under Load Cycles Idealizing Seismic Actions. AICAP-CEB Symposium, Vol. 1 – State of the Art Reports (CEB Bulletin d’Information No. 131), Rome, Italy, 1979. pp. 67-122.
75. Tassios, T. P., and Yannopoulos, P. J. (1981). “Analytical studies on reinforced concrete members under cyclic loading based on bond-slip relationships.” ACI Mater. J., 78(3), 206–216.
76. Tastani, S. P., and Pantazopoulou, S. J. (2006). “Bond of G-FRP bars in concrete: Experimental study and analytical interpretation.” J. Compos. Constr., 10(5), 381–391.
77. Tastani, S. P., & Pantazopoulou, S. J. (2010). Direct Tension Pullout Bond Test: Experimental Results. Journal of Structural Engineering, 136(6), 731–743. https://doi.org/10.1061/(ASCE)ST.1943-541X.0000159
78. Tastani, S. P., & Pantazopoulou, S. J. (2013). Reinforcement and concrete bond: State determination along the development length. Journal of Structural Engineering (United States), 139(9), 1567–1581. https://doi.org/10.1061/(ASCE)ST.1943-541X.0000725
79. Tastani, S., Brokalaki, E., and Pantazopoulou, S. J. (2014), “State of Bond along Lap-Splices”, accepted for publication, ASCE J. of Structural Engineering, 141(10):1-14, (October) 10.1061/(ASCE)ST.1943-541X.0001243, 04015007.
80. Tepfers, R. (1973). A theory of bond applied to overlapped tensile reinforcement splices for deformed bars. Chalmers University of Technology.
81. Tepfers, R. (1979). Cracking of concrete cover along anchored deformed reinforcing bars. Magazine of Concrete Research, 31(106), 3–12. https://doi.org/10.1680/macr.1979.31.106.3
82. Vecchio, F., Collinsm M. (1986). “The modified compression field theory for reinforced concrete elements subjected to shear.” ACI J., 83(2), 219-231.

83. Wildermuth A and Hofmann J (2012) Effect of the bond behaviour of rebars and its evaluation by simplified test specimens. Proceedings of the 4th International Conference on Bond in Concrete, Brescia, Italy,1, 75– 80.
84. Wille, K., & Naaman, A. E. (2012). Pullout behavior of high-strength steel fibers embedded in ultra-high-performance concrete. *ACI Materials Journal*, *109*(4), 479–488. https://doi.org/10.14359/51683923
85. Wille, K., & Naaman, A. E. (2013). Effect of ultra-high-performance concrete on pullout behavior of high-strength brass-coated straight steel fibers. *ACI Materials Journal*, *110*(4), 451–461. https://doi.org/10.14359/51685792
86. Xu L, Pan J, Lu C, Yin W. Development mechanism of plastic hinge in rein- forced engineered cementitious composite beams under monotonic loading. Structural Concrete. 2018; 1–15. https://doi.org/10.1002/suco.201800009
87. Yuan, J., & Graybeal, B. (2015). Bond of reinforcement in ultra-high-performance concrete. *ACI Structural Journal*, *112*(6), 851–860. https://doi.org/10.14359/51687912
88. Ziari, A., & Kianoush, M. R. (2014). Finite-Element Parametric Study of Bond and Splitting Stresses in Reinforced Concrete Tie Members. *Journal of Structural Engineering*, *140*(5), 04013106. https://doi.org/10.1061/(ASCE)ST.1943-541X.0000903
89. Zuo, J., & Darwin, D. (2000). Splice strength of conventional and high relative rib area bars in normal and high-strength concrete. *ACI Structural Journal*, *97*(4), 630–641. https://doi.org/10.14359/7428

Appendix I

Specimen CMK1-5-B

Complete analysis

Figure A - 1 Locations of Points of Interest for specimen CMK1-5-B (Complete Analysis).

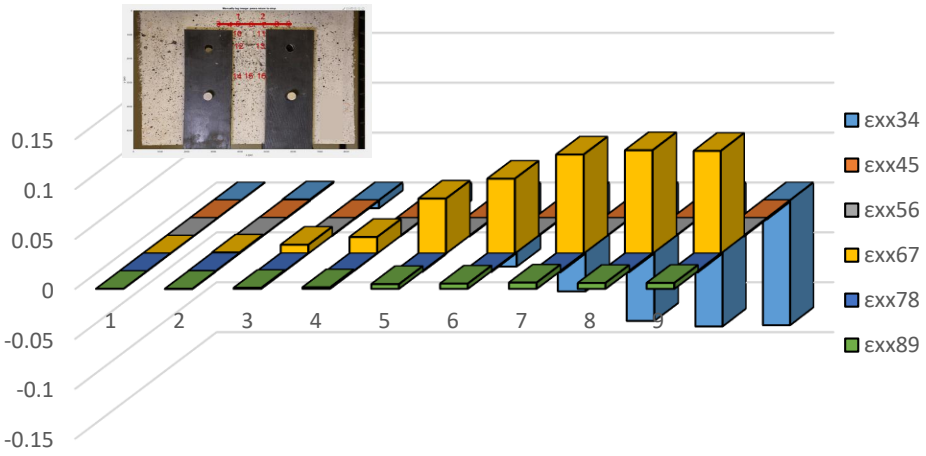

Figure A - 2 Demonstration of ε_{xx} along Layer 2 (CMK1-5-B – Complete analysis).

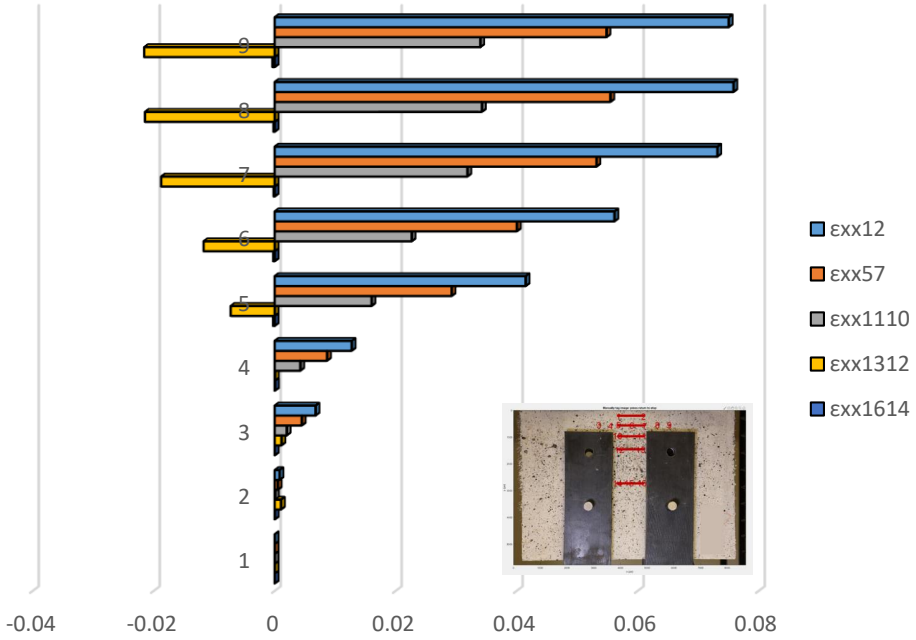

Figure A - 3 Comparison of ε_{xx} between horizontal layers (CMK1-5-B – Complete analysis).

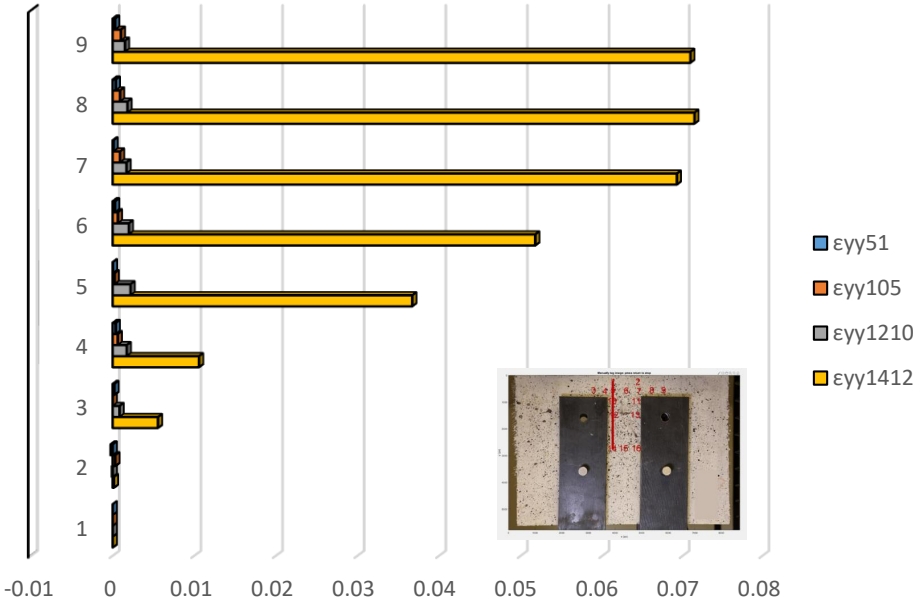

Figure A - 4 Demonstration of ε_{yy} on left vertical layer (CMK1-5-B – Complete analysis).

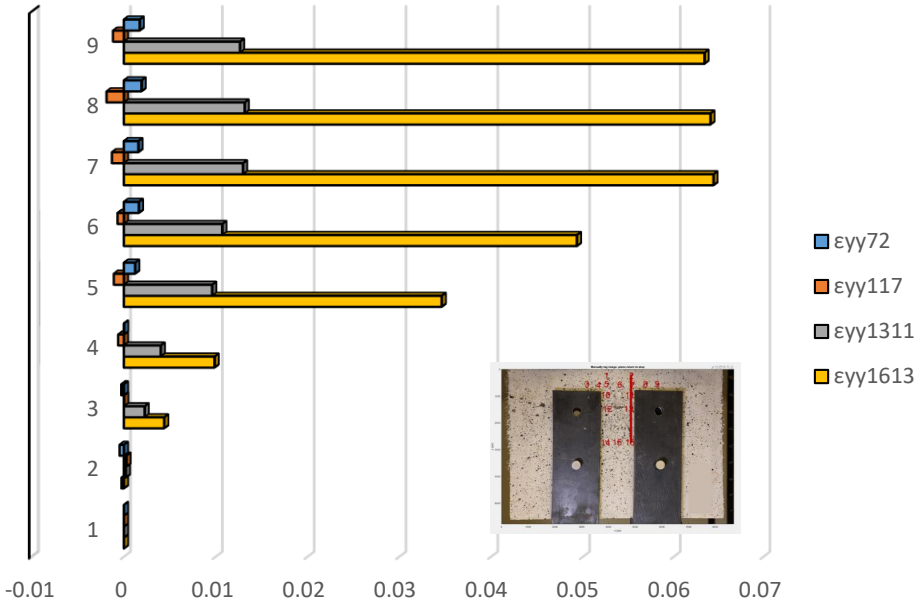

Figure A - 5 Demonstration of ε_{yy} on right vertical layer (CMK1-5-B – Complete analysis.

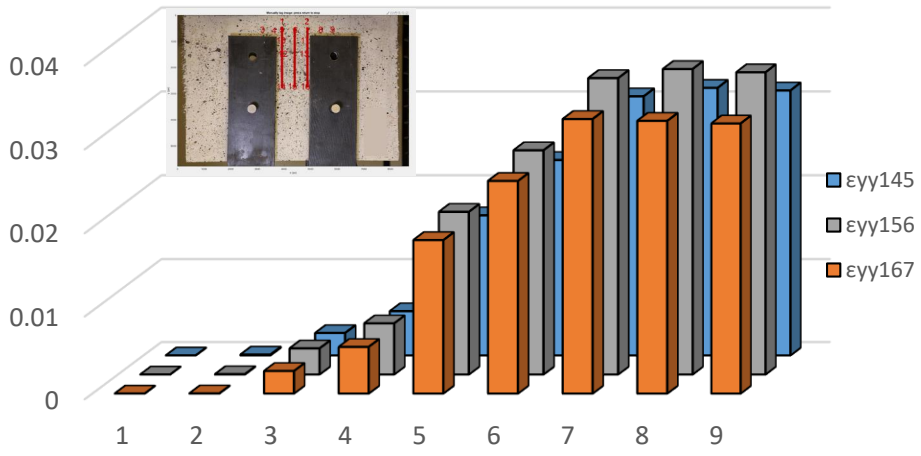

Figure A - 6 Comparison of ε_{yy} between three equidistant layers (CMK1-5-B – Complete analysis).

Detailed analysis in three milestone points – Case 1

Figure A - 7 Locations of POIs for specimen CMK1-5-B (Case 1).

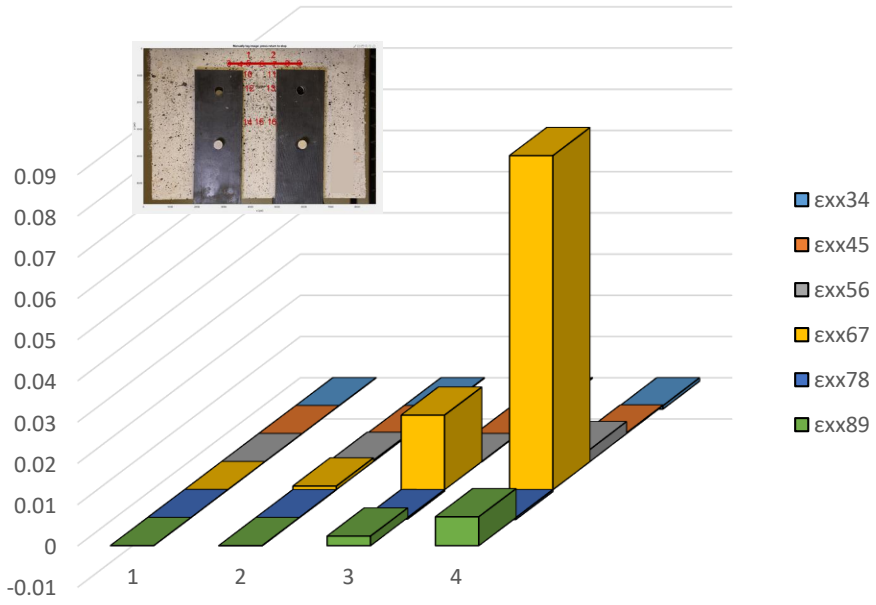

Figure A - 8 Demonstration of ε_{xx} along Layer 2 (CMK1-5-B – Case 1).

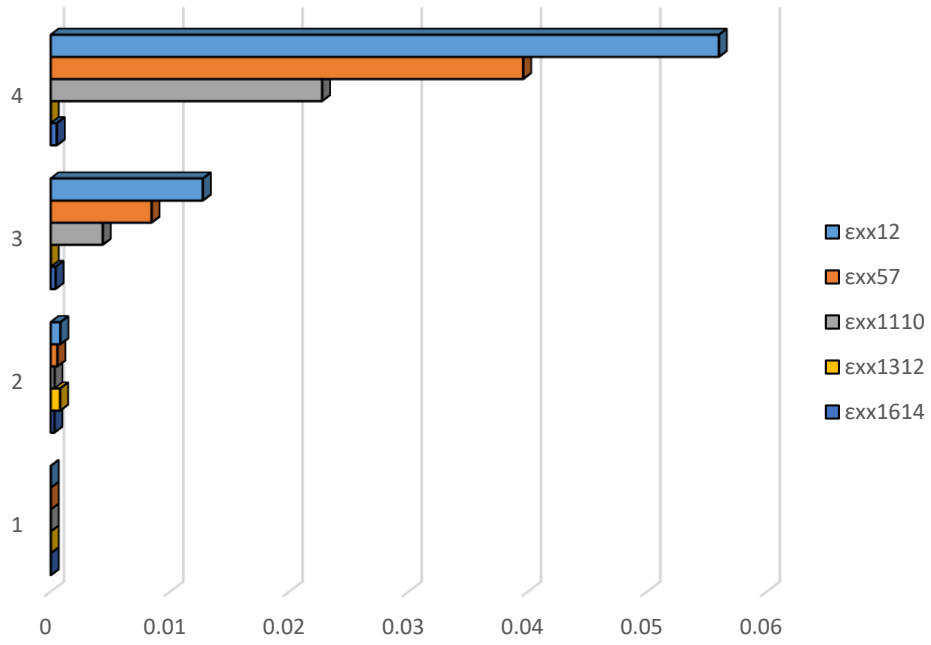

Figure A - 9 Comparison of ε_{xx} between horizontal layers (CMK1-5-B – Case 1).

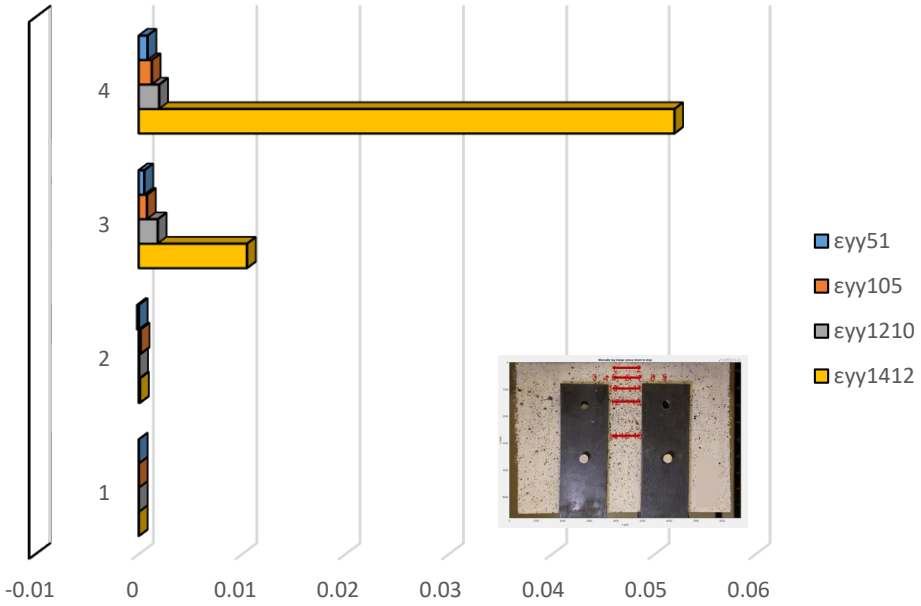

Figure A - 10 Demonstration of εyy on left vertical layer (CMK1-5-B – Case 1).

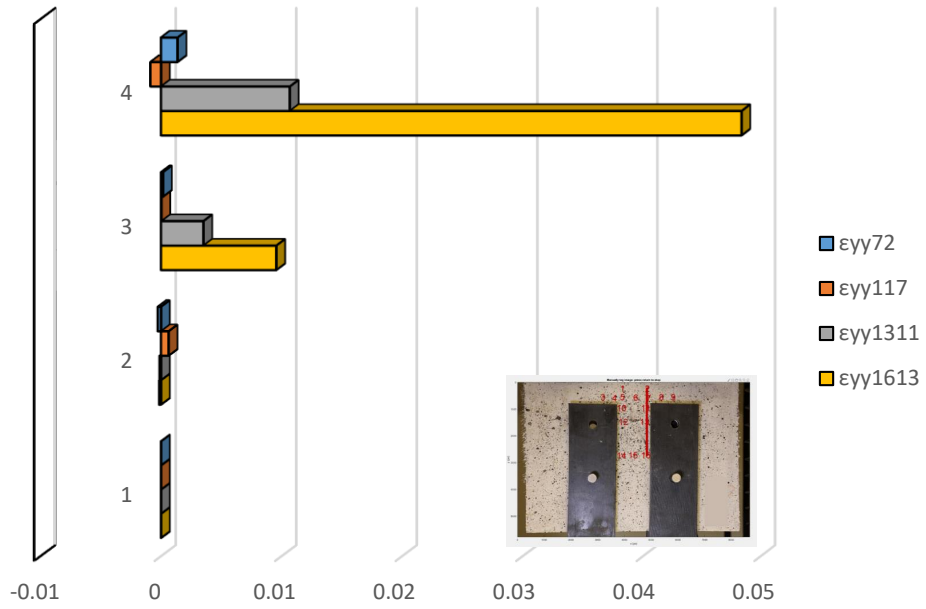

Figure A - 11 Demonstration of ε_{yy} on right vertical layer (CMK1-5-B – Case 1).

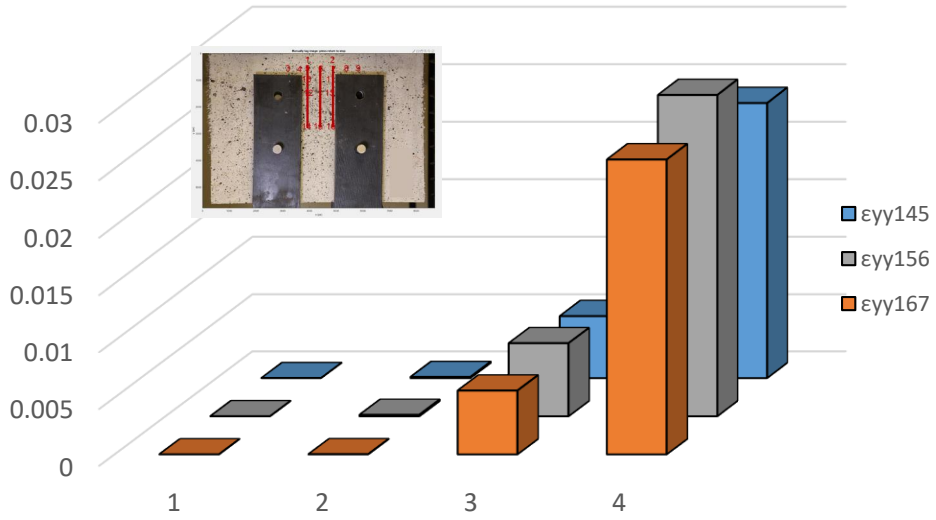

Figure A - 12 Comparison of ε_{yy} between three equidistant layers (CMK1-5-B – Case 1).

Detailed analysis in three milestone points – Case 2

Figure A - 13 Locations of POIs for specimen CMK1-5-B (Case 2).

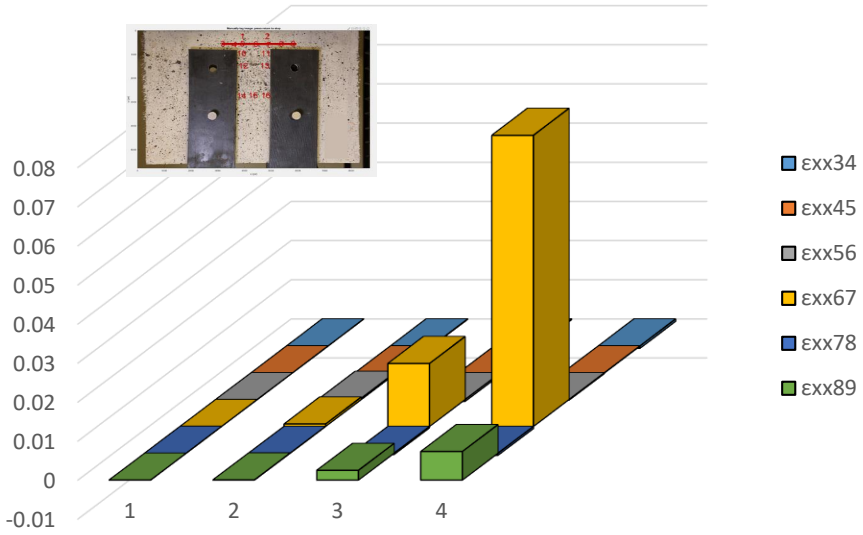

Figure A - 14 Demonstration of ε_{xx} along Layer 2 (CMK1-5-B – Case 2).

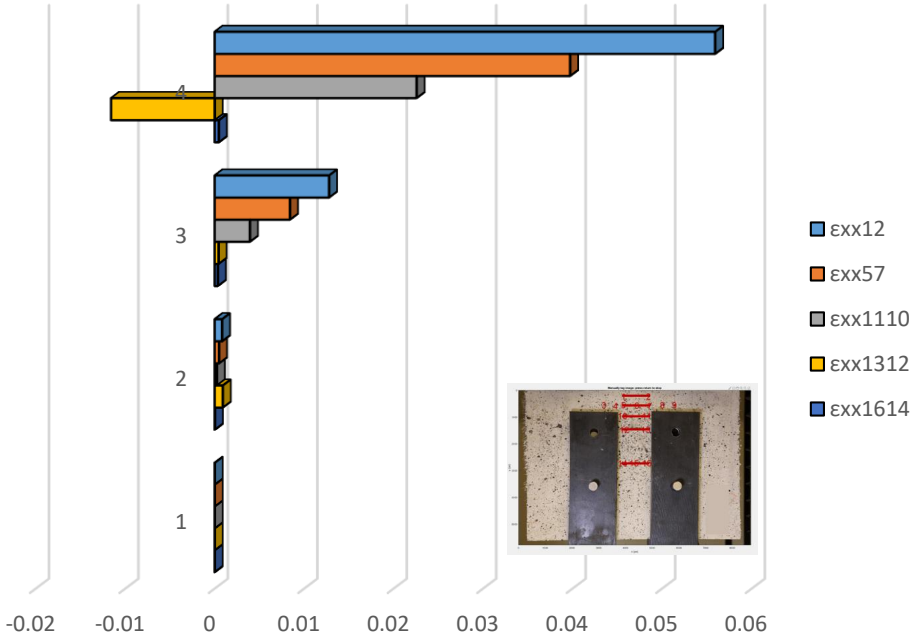

Figure A - 15 Comparison of ε_{xx} between horizontal layers (CMK1-5-B – Case 2).

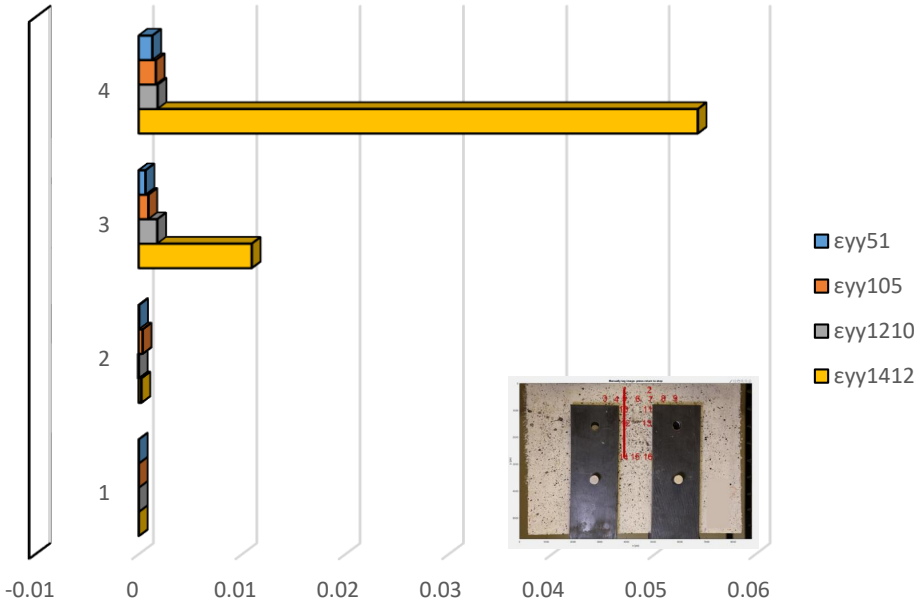

Figure A - 16 Demonstration of εyy on left vertical layer (CMK1-5-B – Case 2).

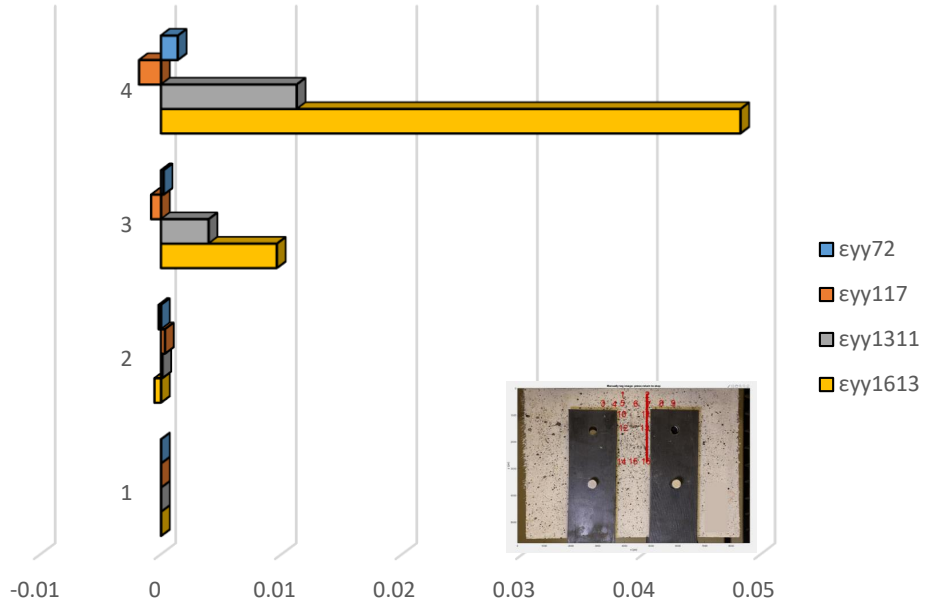

Figure A - 17 Demonstration of ε_{yy} on right vertical layer (CMK1-5-B – Case 2).

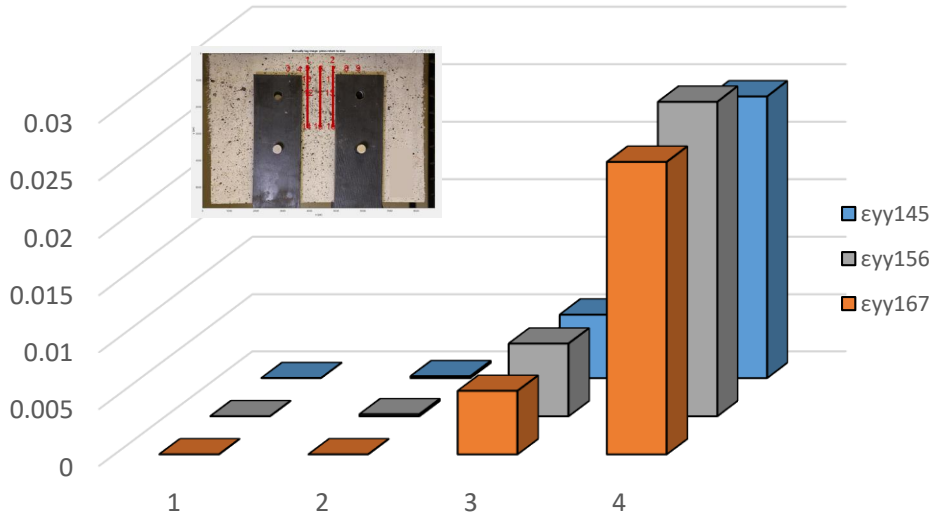

Figure A - 18 Comparison of ε_{yy} between three equidistant layers (CMK1-5-B – Case 2).

Detailed analysis in three milestone points – Case 3

Figure A - 19 Locations of POIs for specimen CMK1-5-B (Case 3)

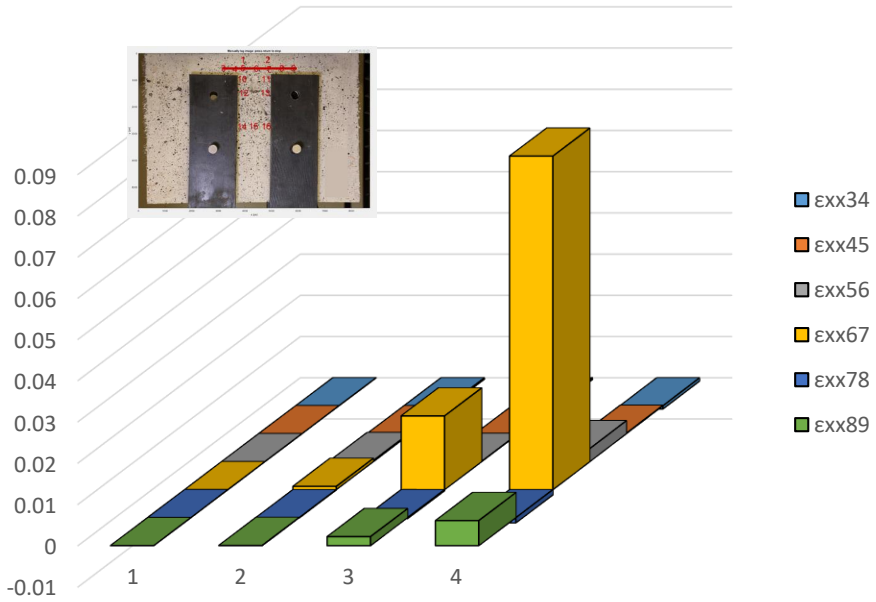

Figure A - 20 Demonstration of ε_{xx} along Layer 2 (CMK1-5-B – Case 3).

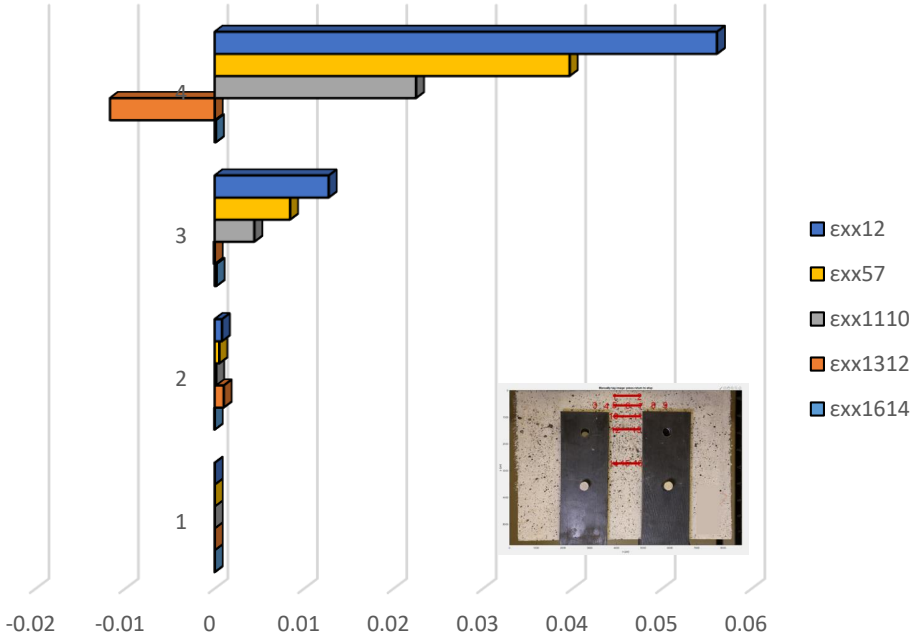

Figure A - 21 Comparison of ε_{xx} between horizontal layers (CMK1-5-B – Case 3).

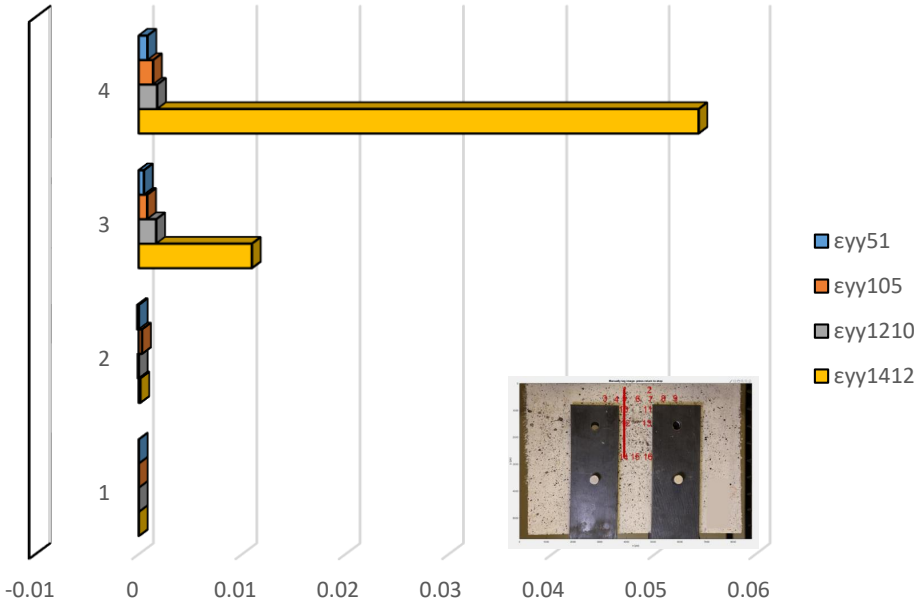

Figure A - 22 Demonstration of εyy on left vertical layer (CMK1-5-B – Case 3).

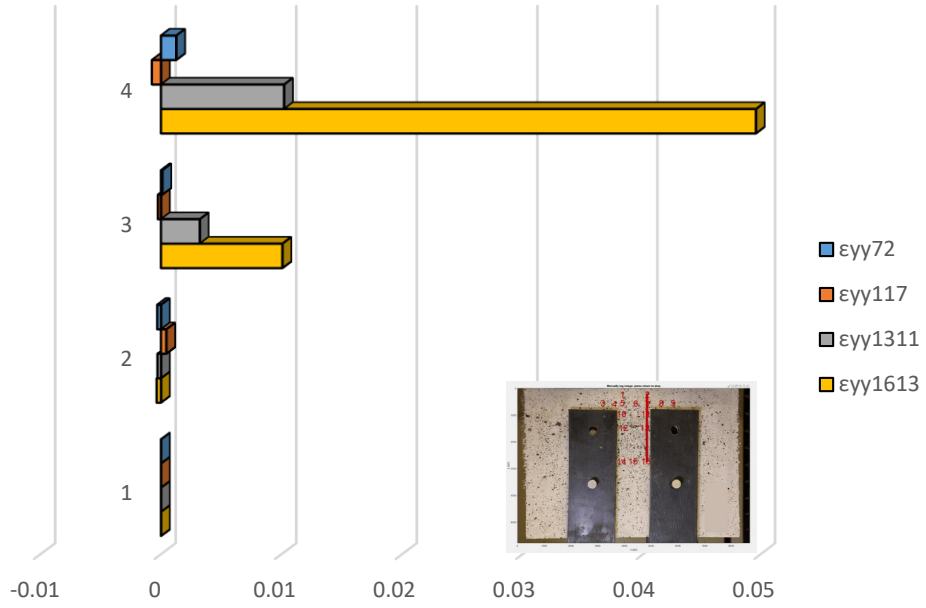

Figure A - 23 Demonstration of ε_{yy} on right vertical layer (CMK1-5-B – Case 3).

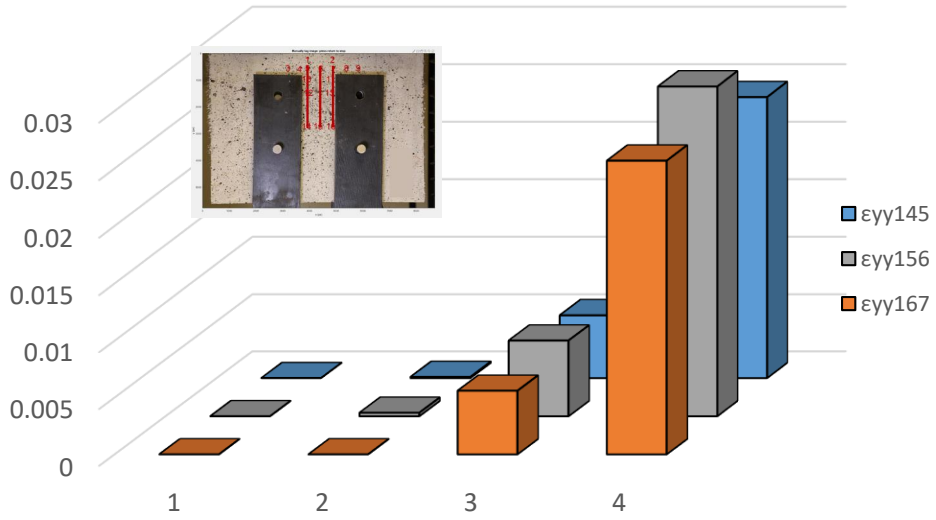

Figure A - 24 Comparison of ε_{yy} between three equidistant layers (CMK1-5-B – Case 3).

Specimen CMK2-5-A

Complete Analysis

Figure A - 25 Locations of Points of Interest for specimen CMK2-5-A (Complete Analysis).

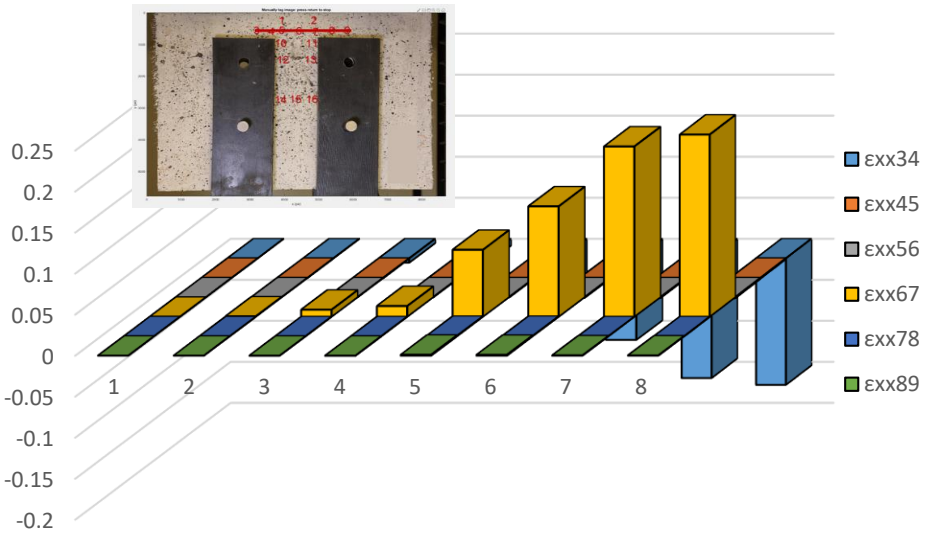

Figure A - 26 Demonstration of ε_{xx} along Layer 2 (CMK2-5-A – Complete analysis).

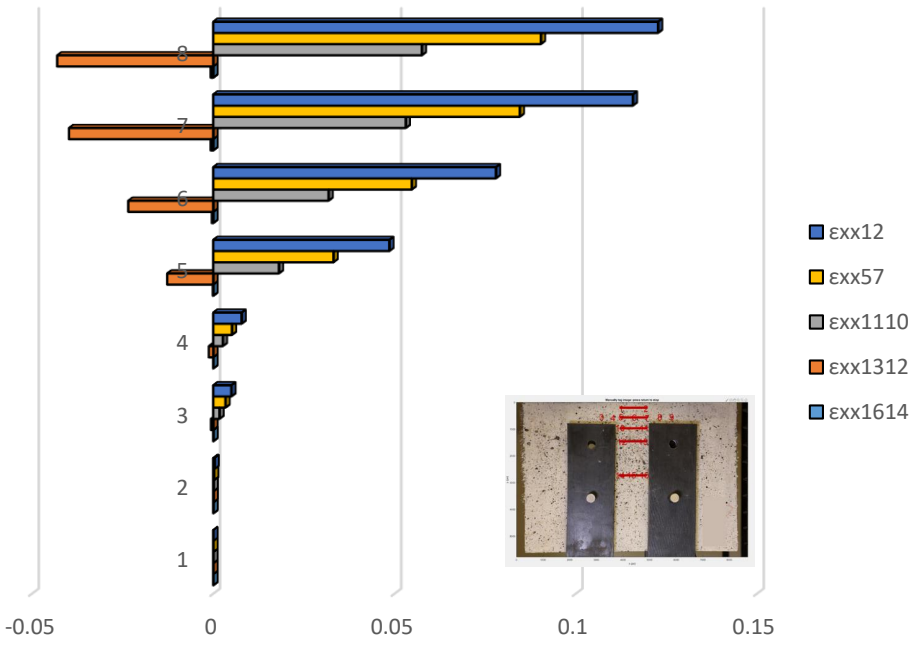

Figure A - 27 Comparison of ε_{xx} between horizontal layers (CMK2-5-A – Complete analysis).

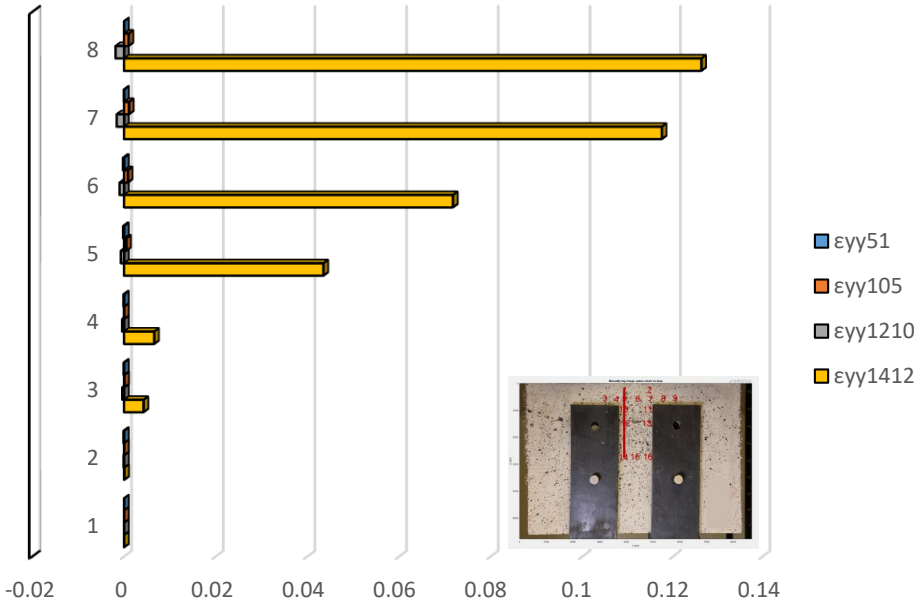

Figure A - 28 Demonstration of ε_{yy} on left vertical layer (CMK2-5-A – Complete analysis).

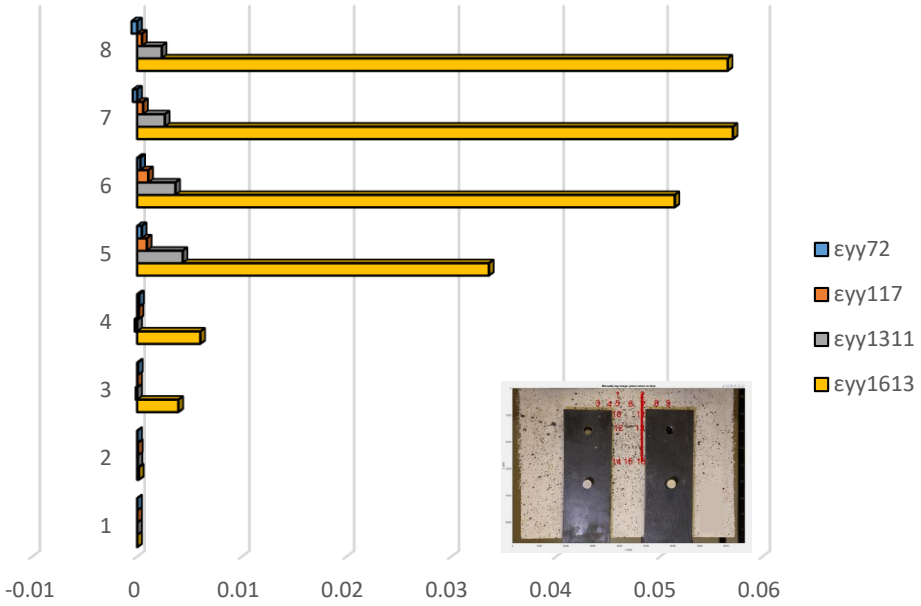

Figure A - 29 Demonstration of ε_{yy} on right vertical layer (CMK2-5-A – Complete analysis).

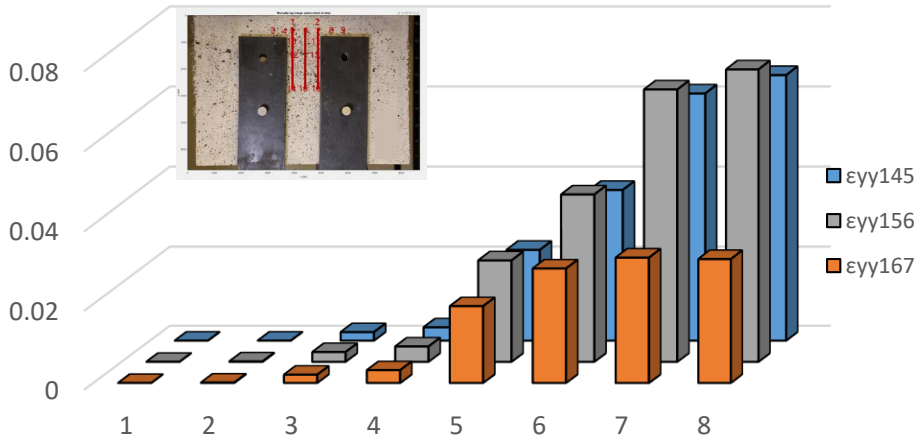

Figure A - 30 Comparison of ε_{yy} between three equidistant layers (CMK2-5-A – Complete analysis).

Detailed analysis in three milestone points – Case 1

Figure A - 31 Locations of POIs for specimen CMK2-5-A (Case 1)

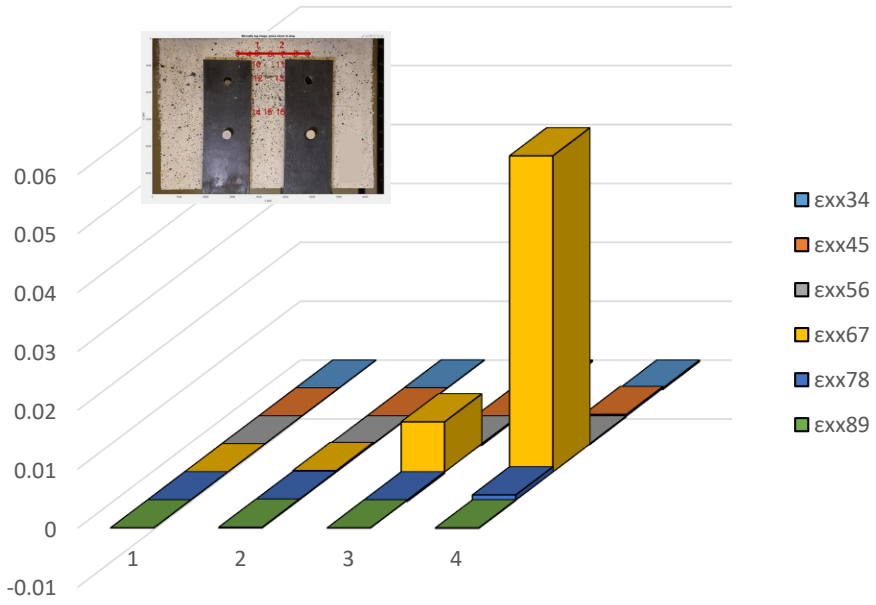

Figure A - 32 Demonstration of ε_{xx} along Layer 2 (CMK2-5-A – Case 1).

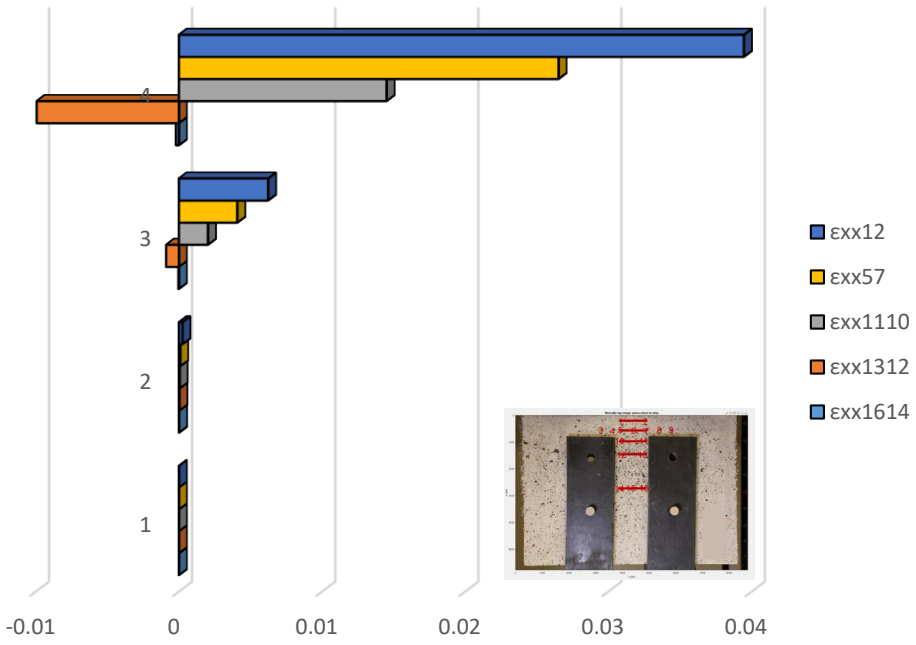

Figure A - 33 Comparison of ε_{xx} between horizontal layers (CMK2-5-A – Case 1).

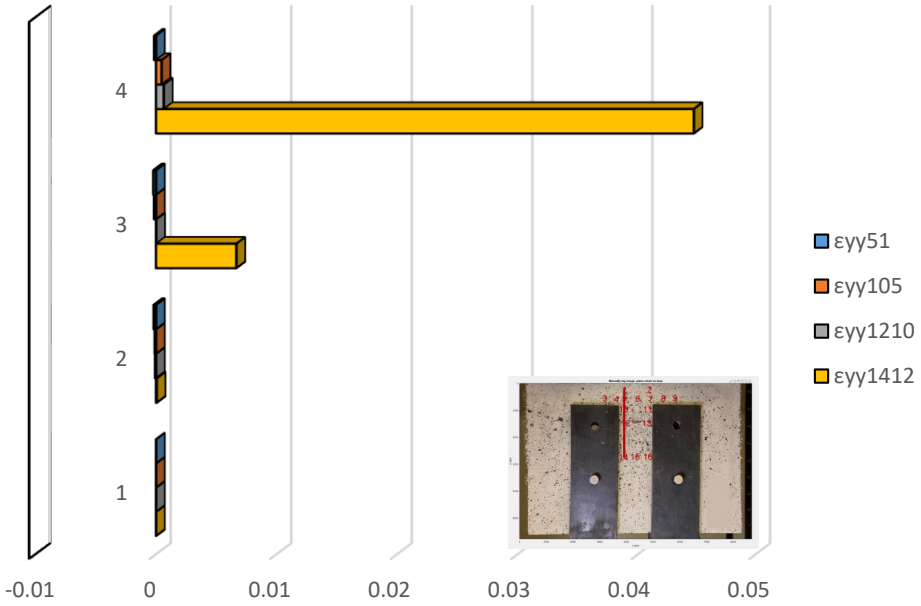

Figure A - 34 Demonstration of εyy on left vertical layer (CMK2-5-A – Case 1).

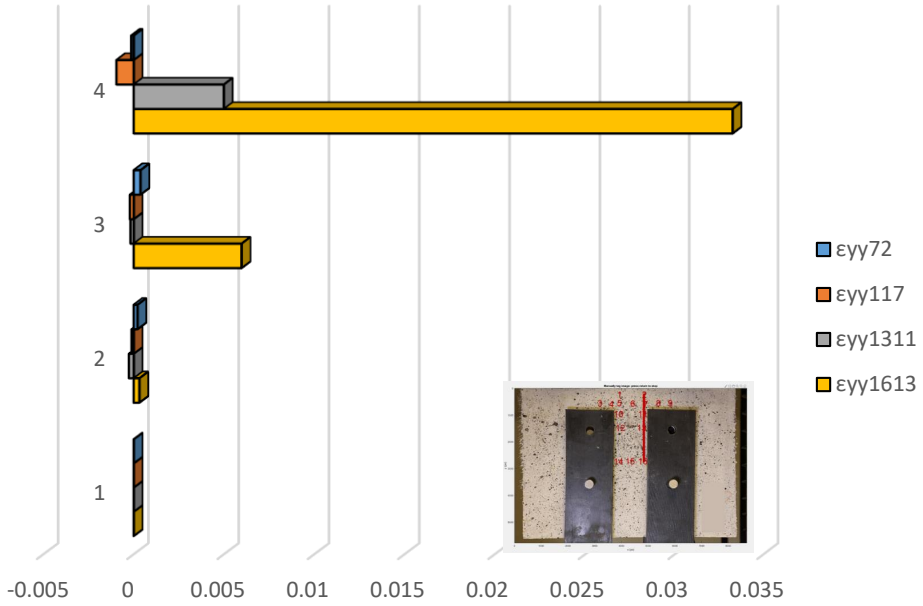

Figure A - 35 Demonstration of εyy on right vertical layer (CMK2-5-A – Case 1).

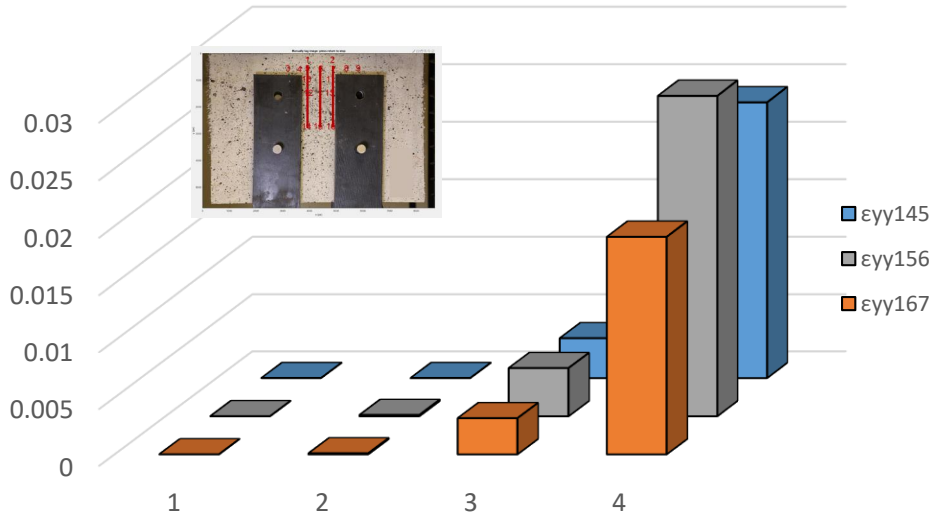

Figure A - 36 Comparison of ε_{yy} between three equidistant layers (CMK2-5-A – Case 1).

Detailed analysis in three milestone points – Case 2

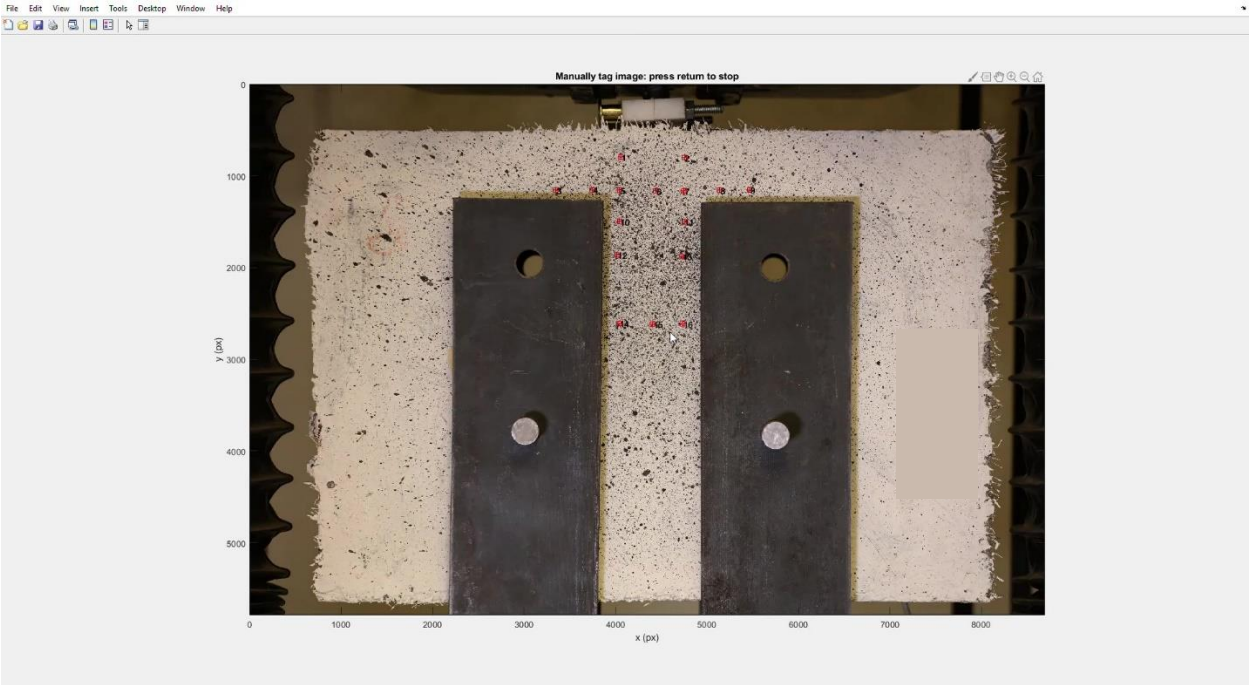

Figure A - 37 Locations of POIs for specimen CMK2-5-A (Case 2)

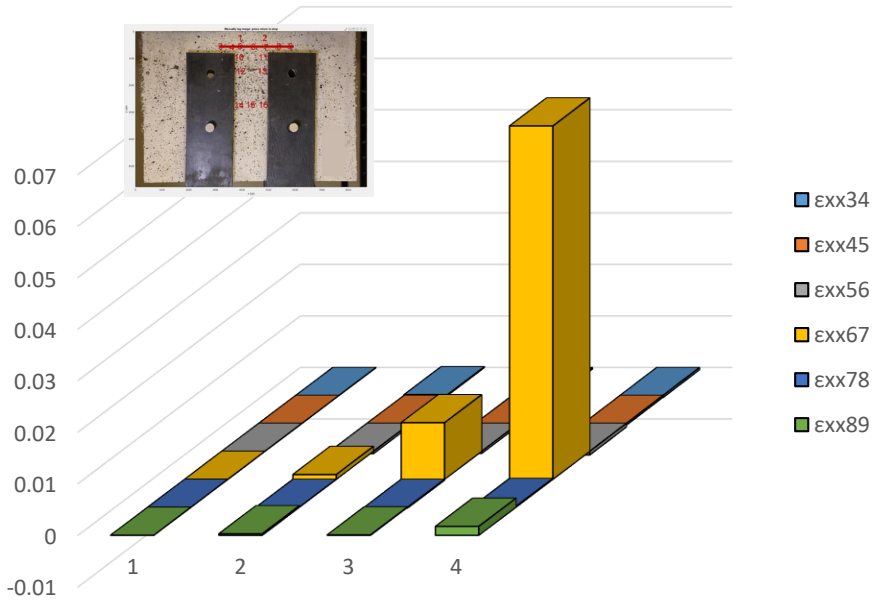

Figure A - 38 Demonstration of ε_{xx} along Layer 2 (CMK2-5-A – Case 2).

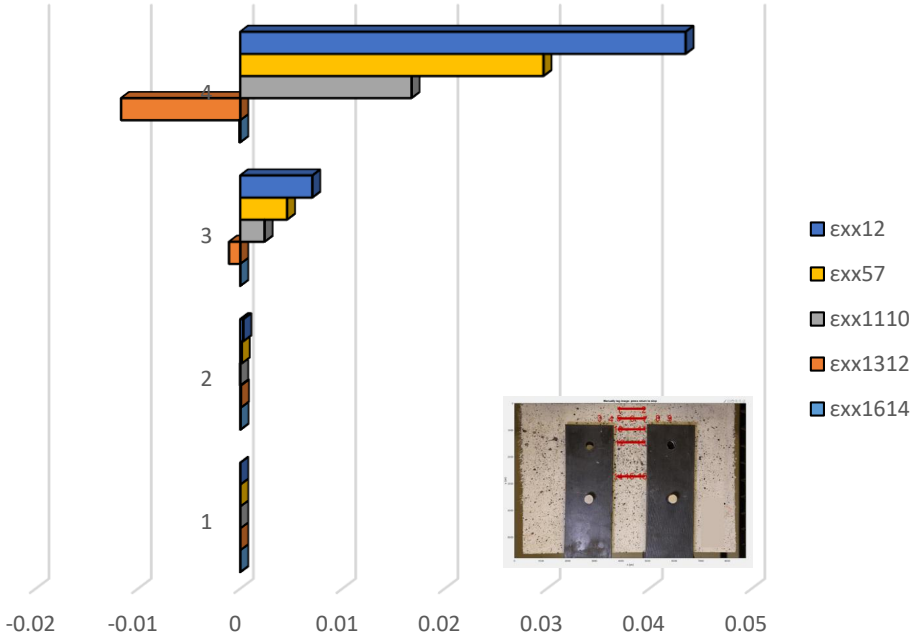

Figure A - 39 Comparison of ε_{xx} between horizontal layers (CMK2-5-A – Case 2).

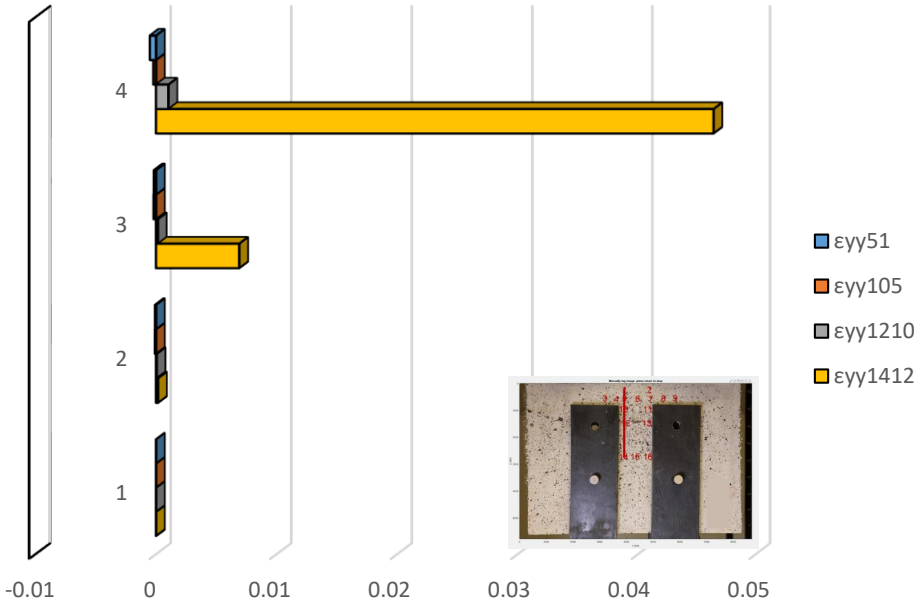

Figure A - 40 Demonstration of εyy on left vertical layer (CMK2-5-A – Case 2).

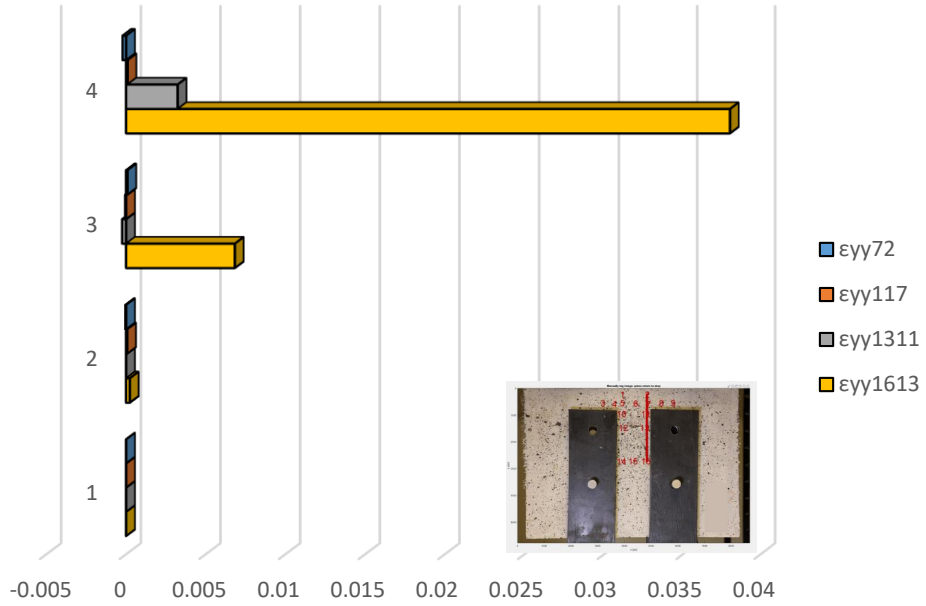

Figure A - 41 Demonstration of εyy on right vertical layer (CMK2-5-A – Case 2).

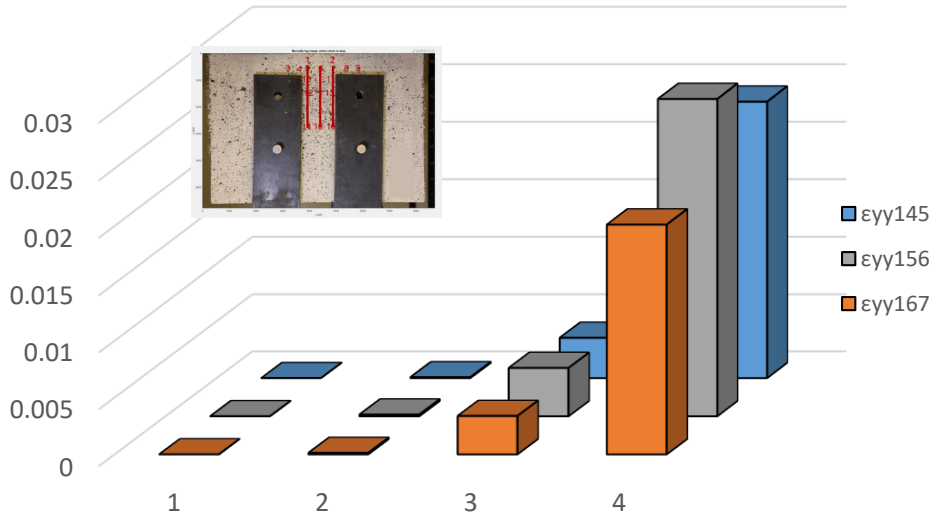

Figure A - 42 Comparison of ε_{yy} between three equidistant layers (CMK2-5-A – Case 2).

Detailed analysis in three milestone points – Case 3

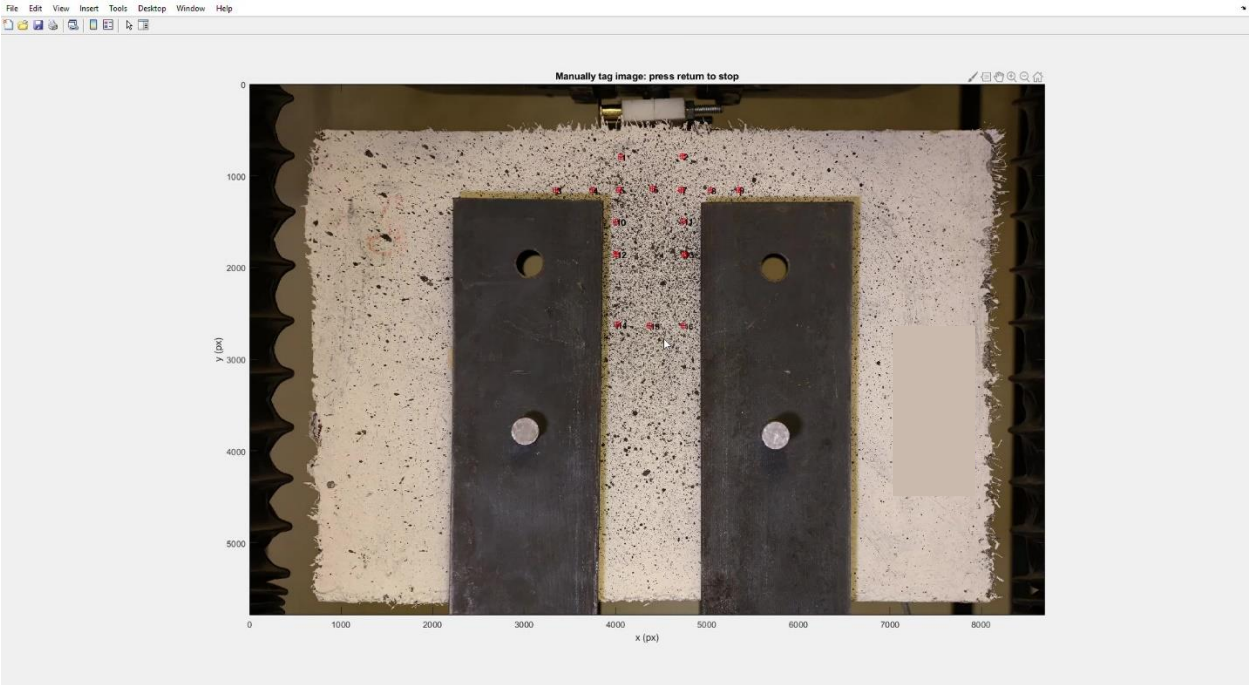

Figure A - 43 Locations of POIs for specimen CMK2-5-A (Case 3)

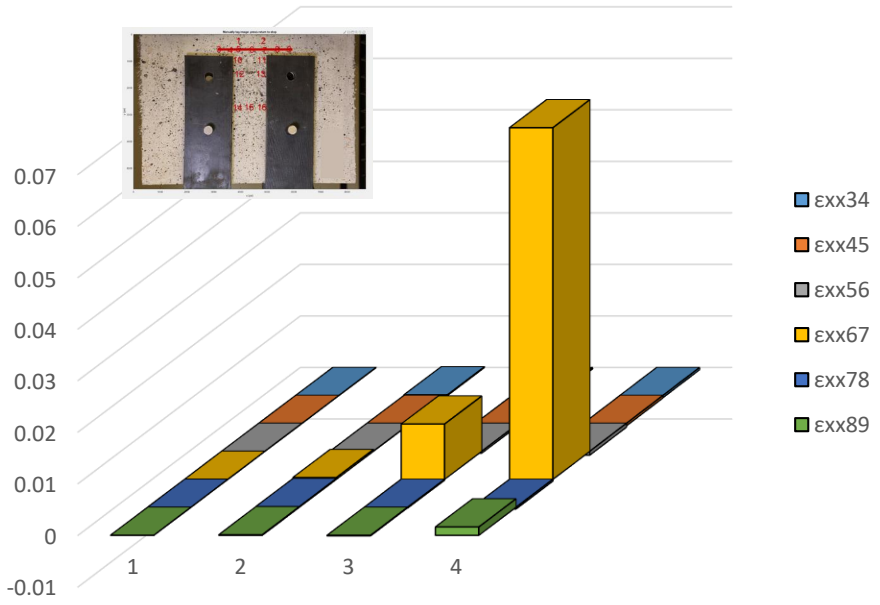

Figure A - 44 Demonstration of ε_{xx} along Layer 2 (CMK2-5-A – Case 3).

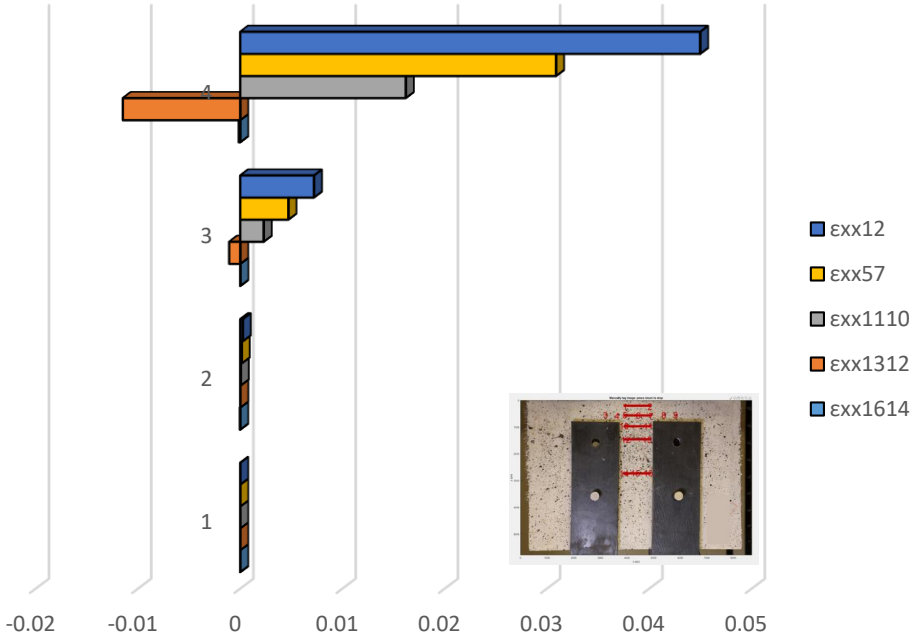

Figure A - 45 Comparison of ε_{xx} between horizontal layers (CMK2-5-A – Case 3).

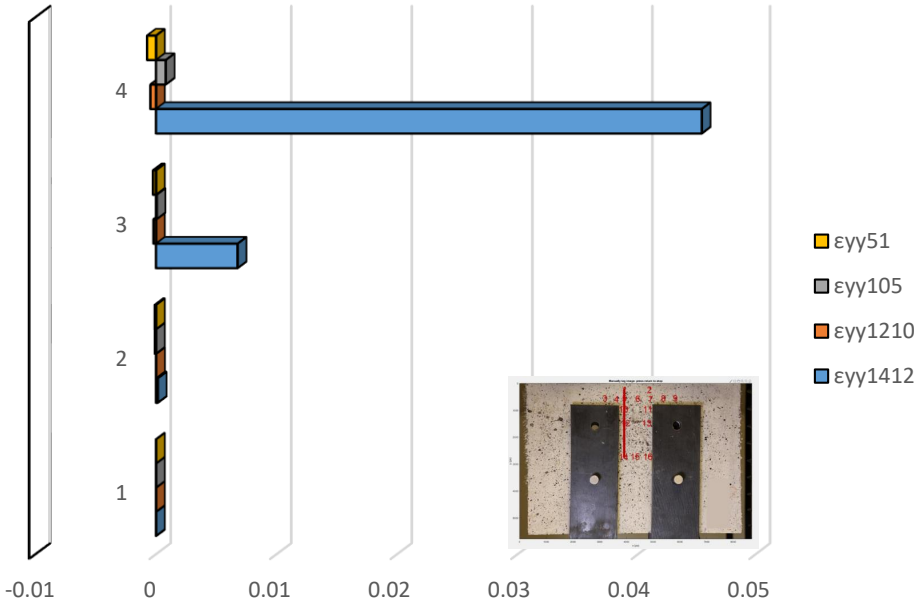

Figure A - 46 Demonstration of εyy on left vertical layer (CMK2-5-A – Case 3).

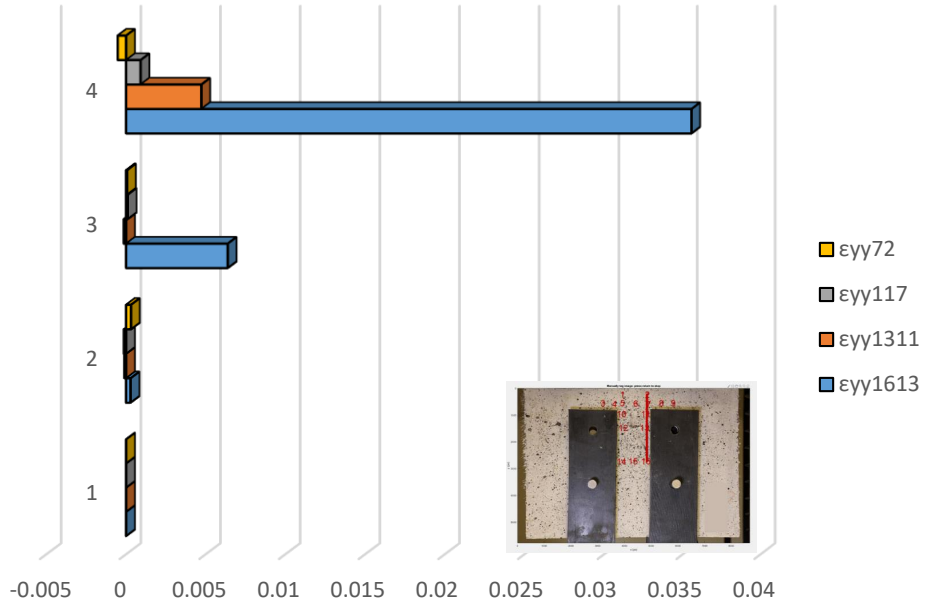

Figure A - 47 Demonstration of εyy on right vertical layer (CMK2-5-A – Case 3).

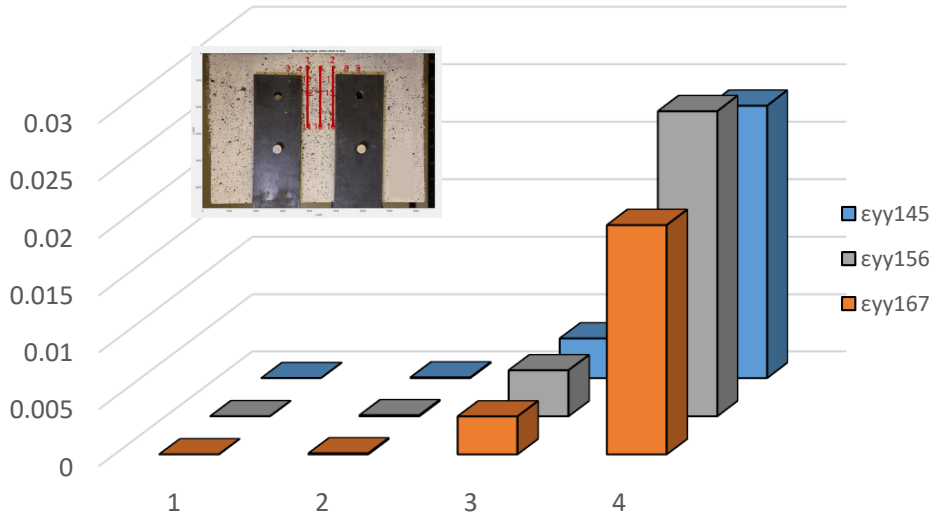

Figure A - 48 Comparison of ε_{yy} between three equidistant layers (CMK2-5-A – Case 3).

Specimen CMK2-5-B

Complete analysis

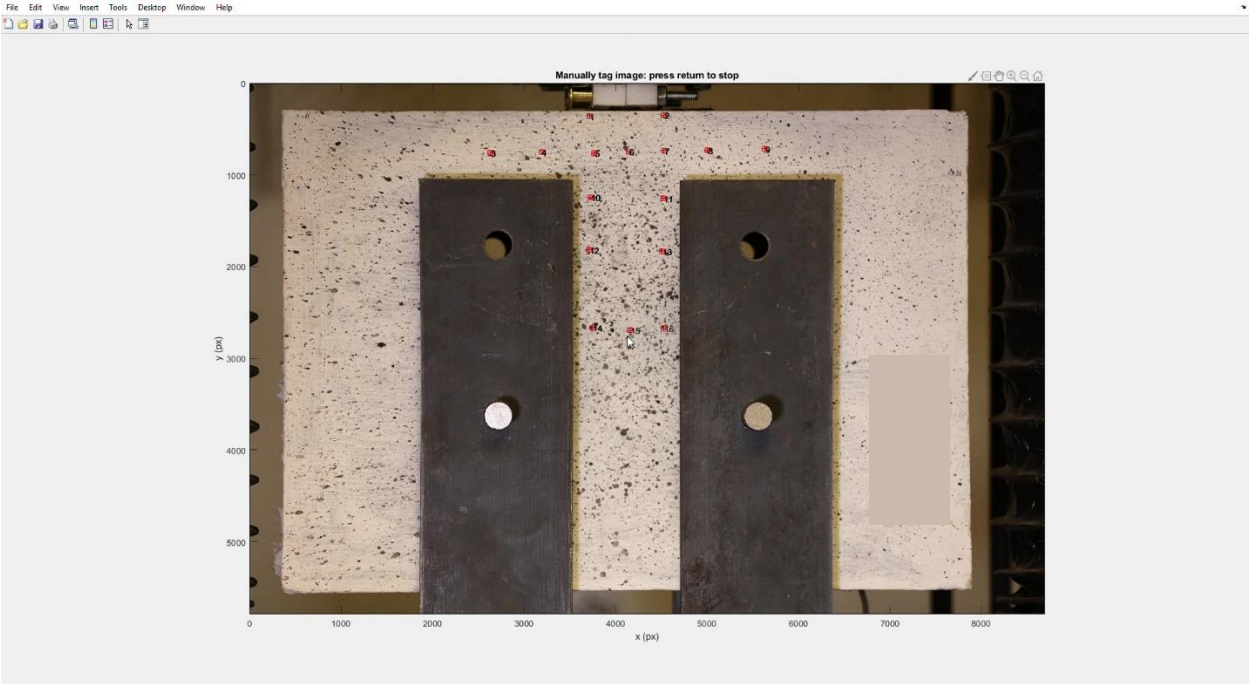

Figure A - 49 Locations of Points of Interest for specimen CMK2-5-B (Complete Analysis).

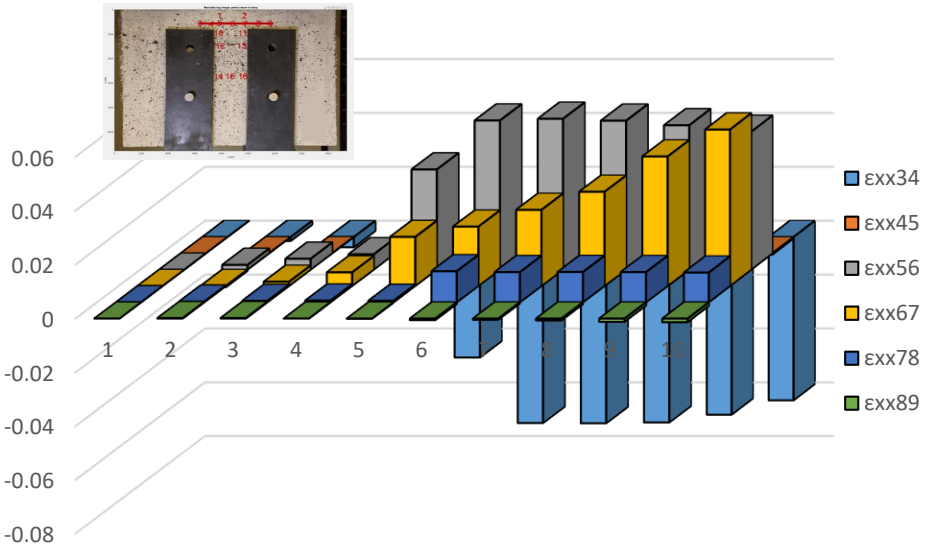

Figure A - 50 Demonstration of ε_{xx} along Layer 2 (CMK2-5-B – Complete analysis).

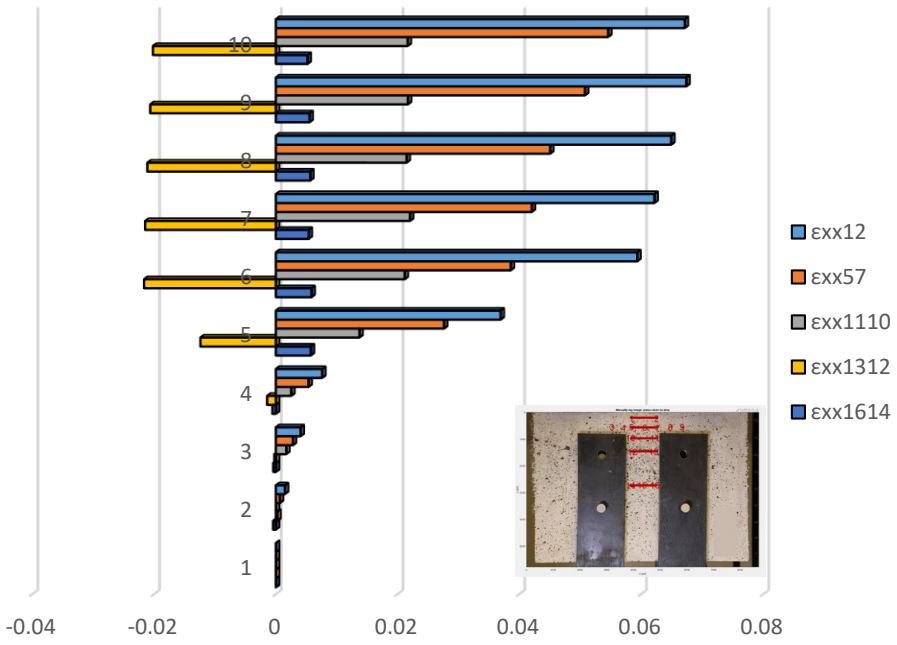

Figure A - 51 Comparison of ε_{xx} between horizontal layers (CMK2-5-B – Complete analysis).

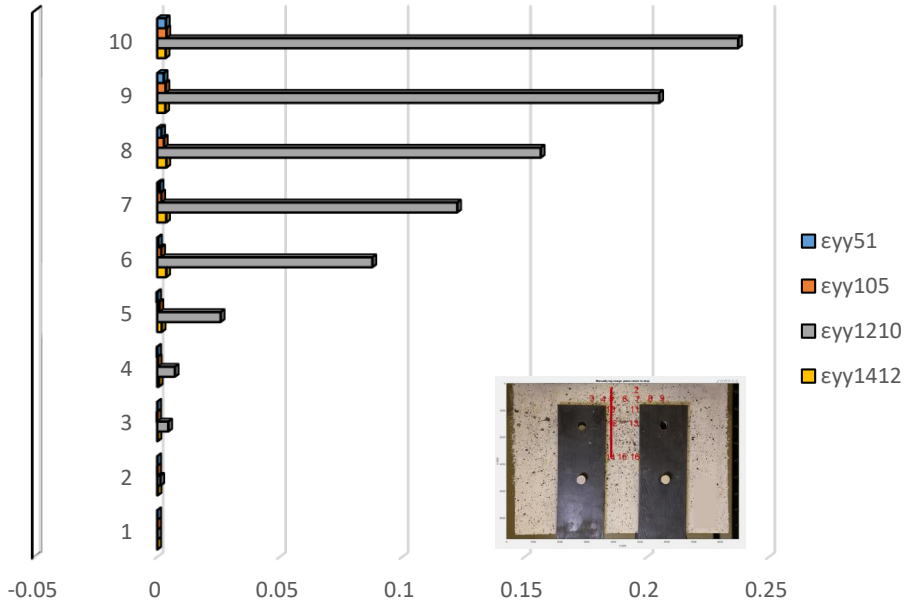

Figure A - 52 Demonstration of ε_{yy} on left vertical layer (CMK2-5-B – Complete analysis).

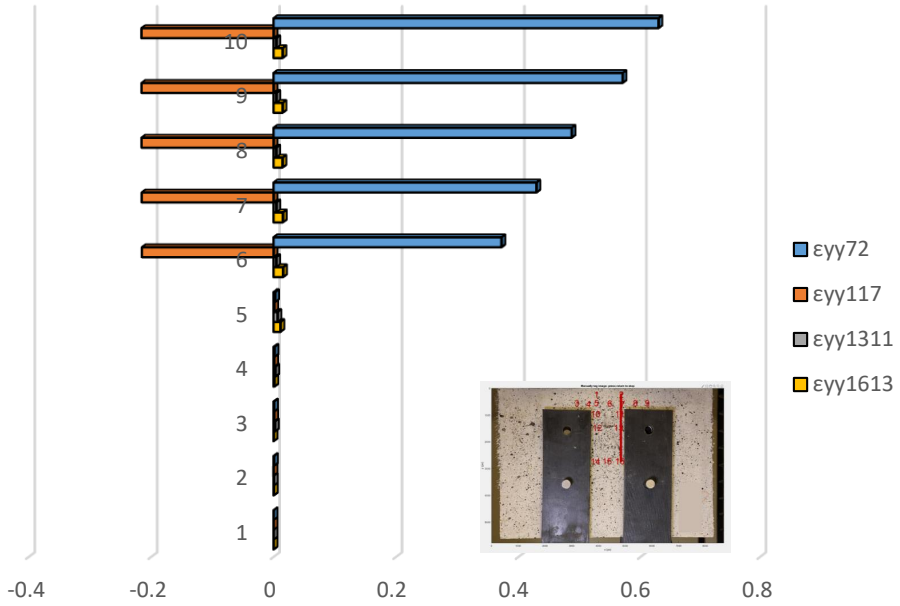

Figure A - 53 Demonstration of ε_{yy} on right vertical layer (CMK2-5-B – Complete analysis).

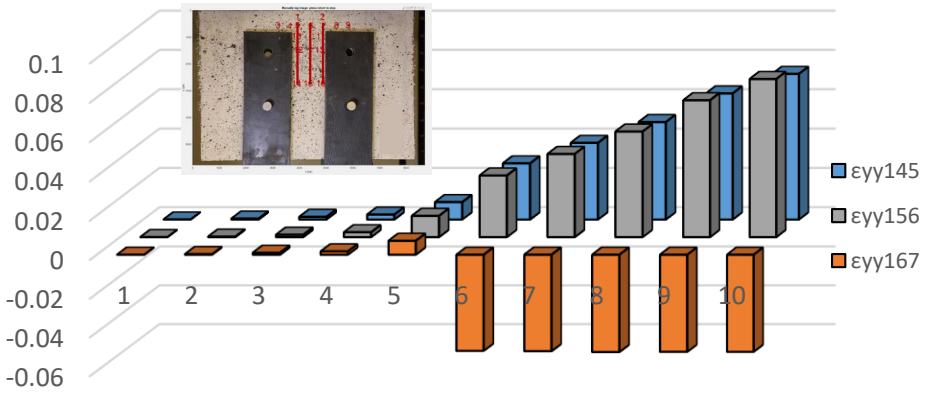

Figure A - 54 Comparison of ε_{yy} between three equidistant layers (CMK2-5-B – Complete analysis).

Detailed analysis in three milestone points – Case 1

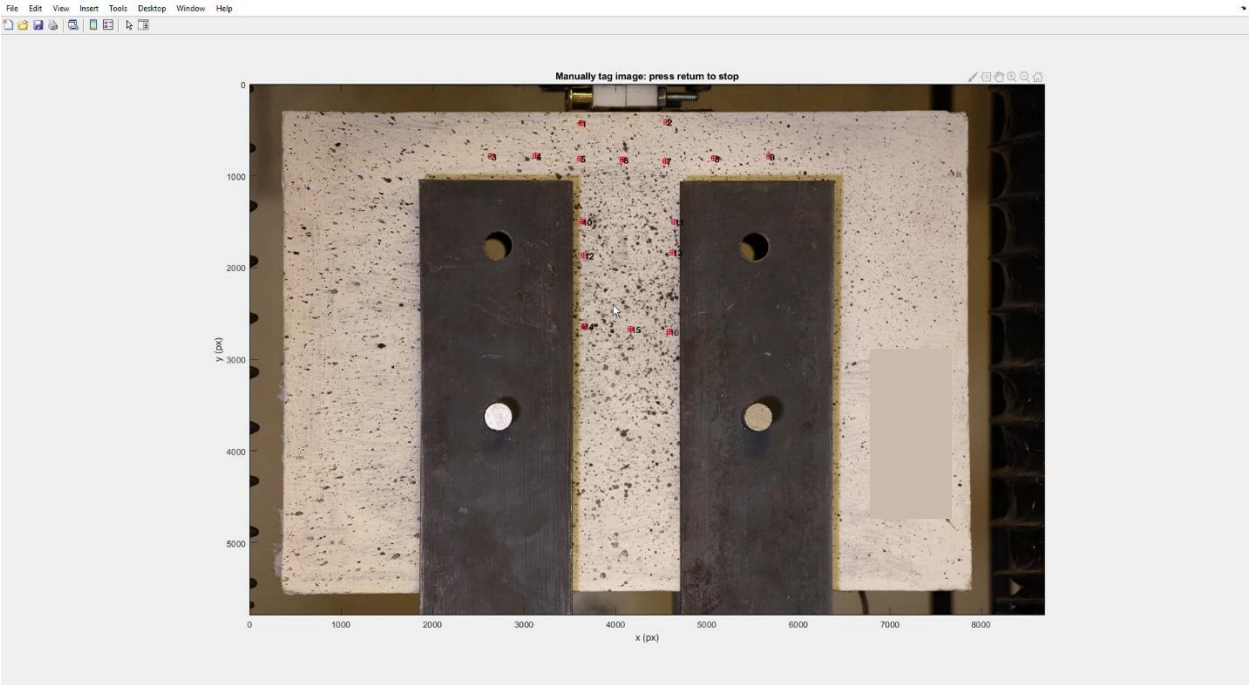

Figure A - 55 Locations of POIs for specimen CMK2-5-B (Case 1).

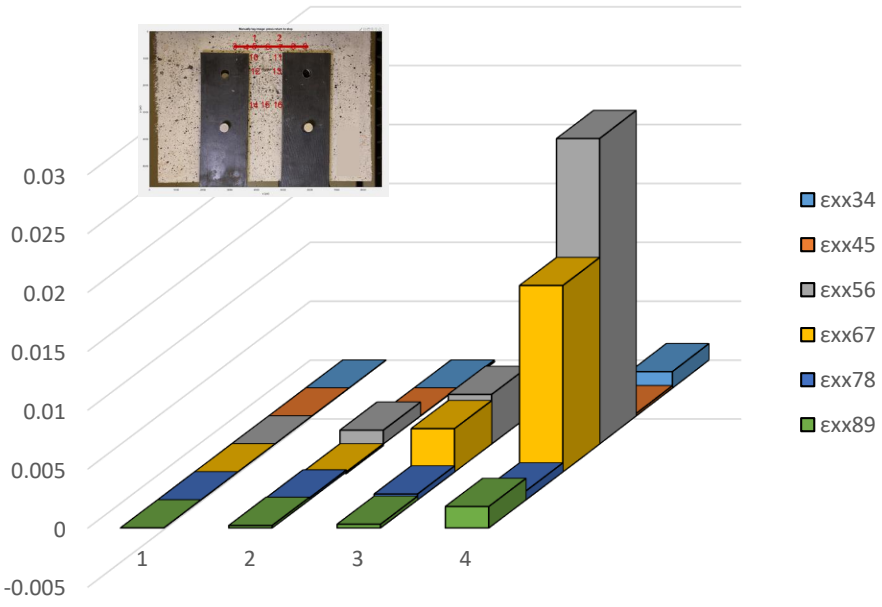

Figure A - 56 Demonstration of ε_{xx} along Layer 2 (CMK2-5-B – Case 1).

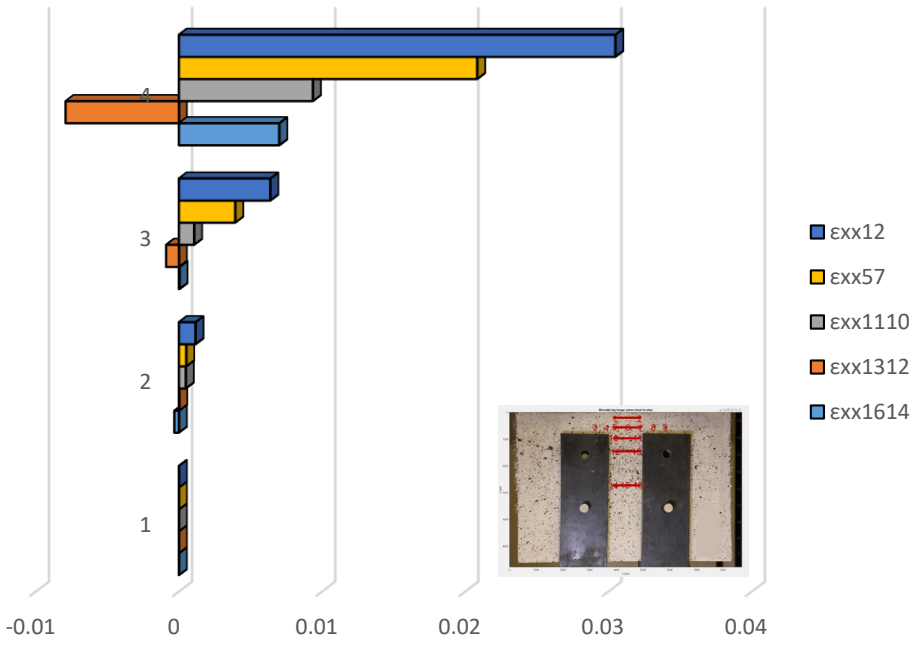

Figure A - 57 Comparison of ε_{xx} between horizontal layers (CMK2-5-B – Case 1).

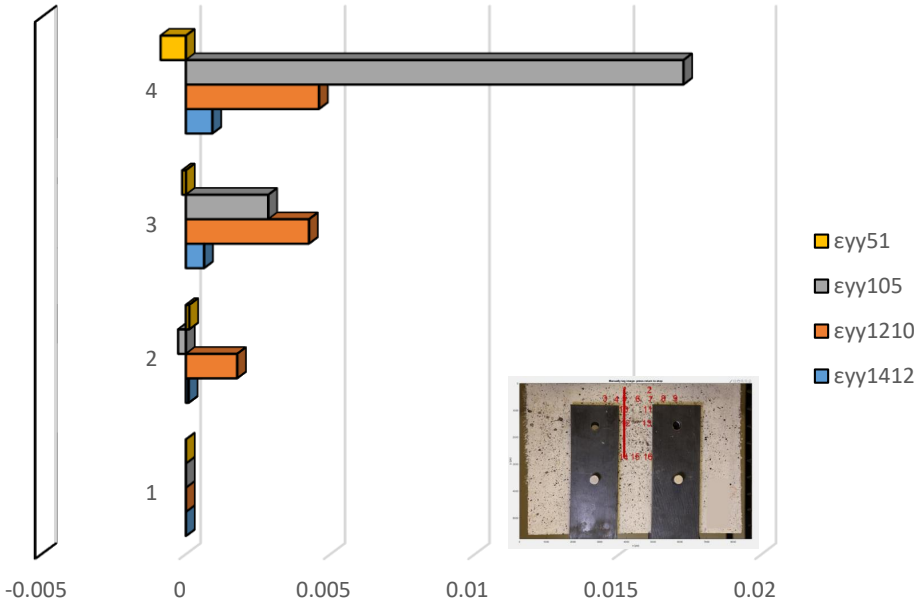

Figure A - 58 Demonstration of εyy on left vertical layer (CMK2-5-B – Case 1).

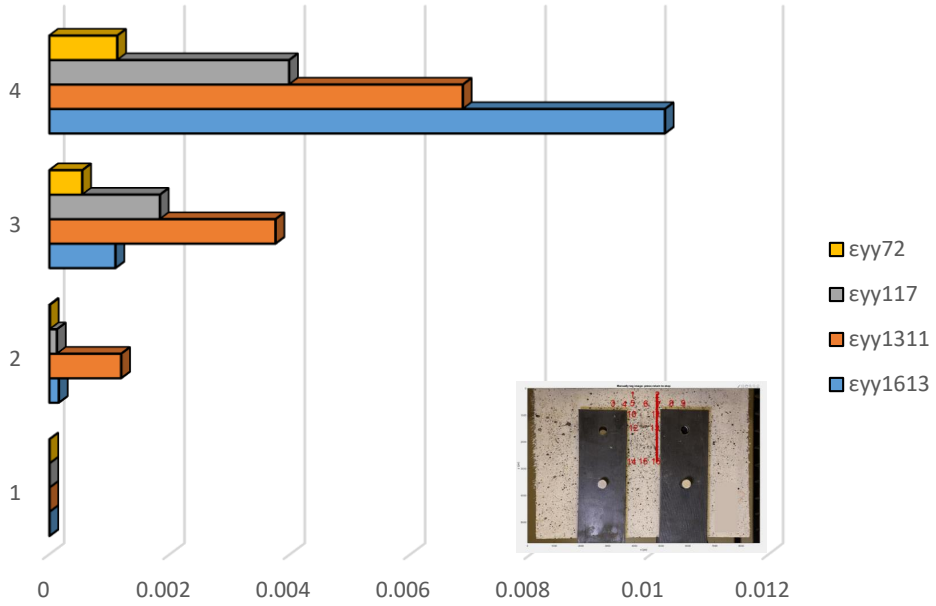

Figure A - 59 Demonstration of ε_{yy} on right vertical layer (CMK2-5-B – Case 1).

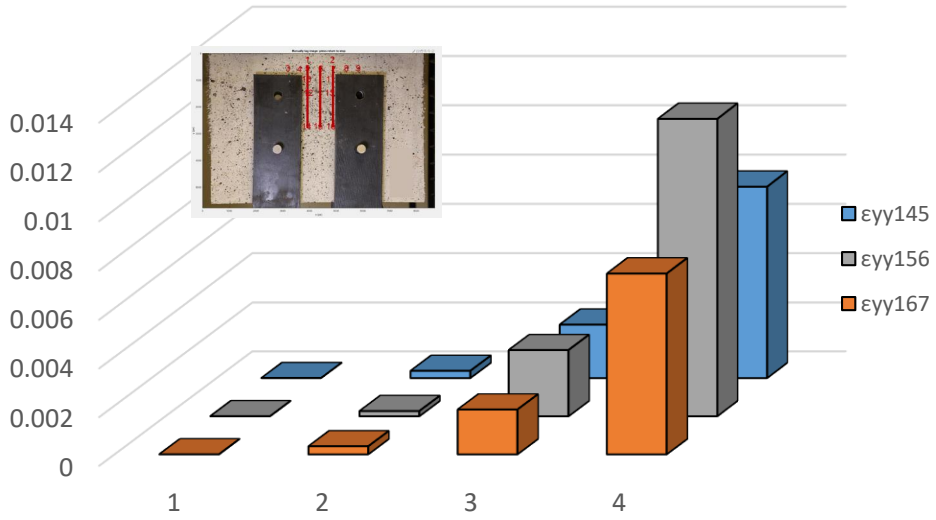

Figure A - 60 Comparison of ε_{yy} between three equidistant layers (CMK2-5-B – Case 1).

Detailed analysis in three milestone points – Case 2

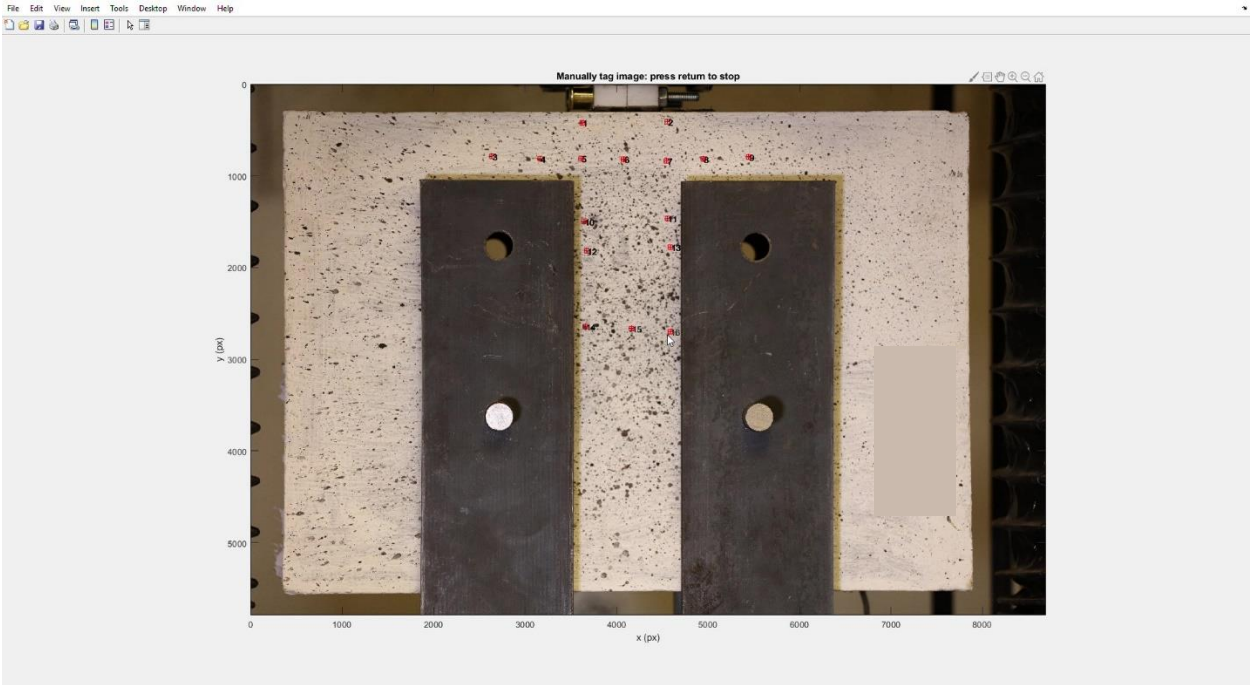

Figure A - 61 Locations of POIs for specimen CMK2-5-B (Case 2).

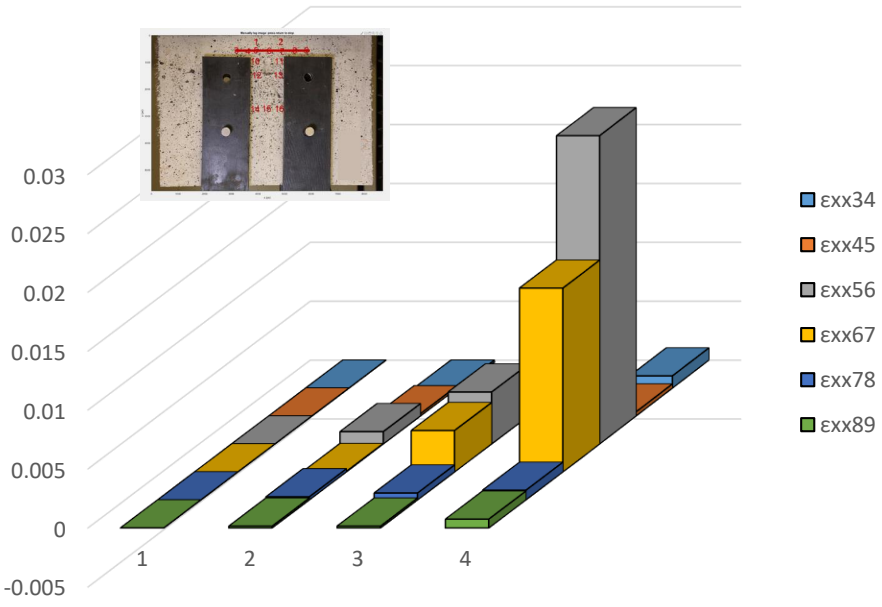

Figure A - 62 Demonstration of ε_{xx} along Layer 2 (CMK2-5-B – Case 2).

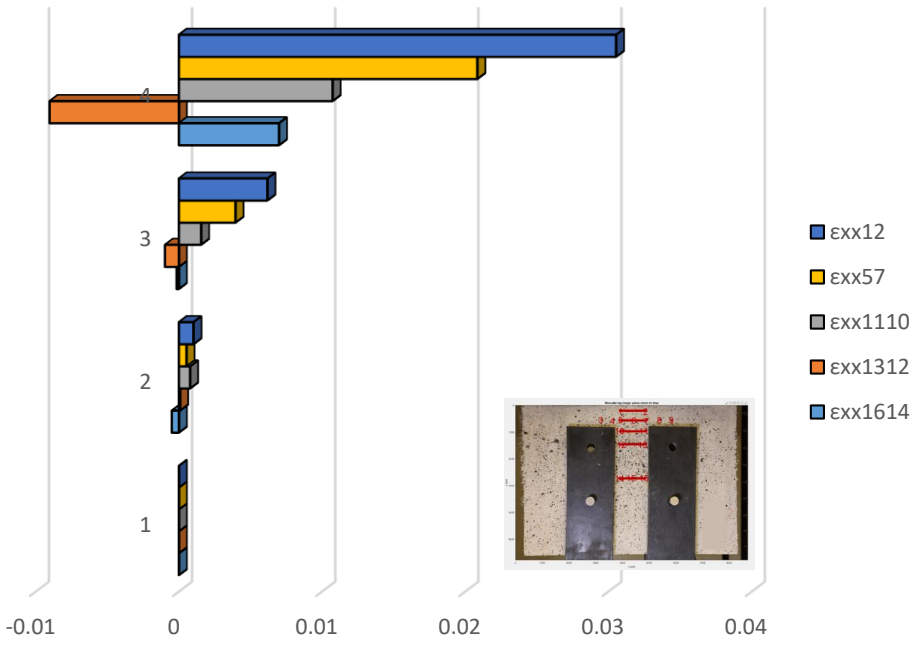

Figure A - 63 Comparison of ε_{xx} between horizontal layers (CMK2-5-B – Case 2).

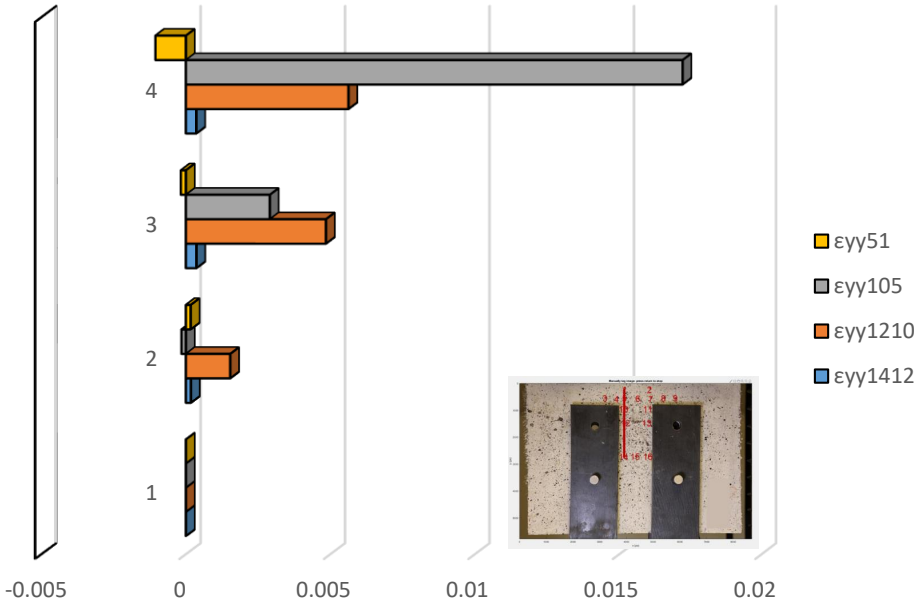

Figure A - 64 Demonstration of εyy on left vertical layer (CMK2-5-B – Case 2).

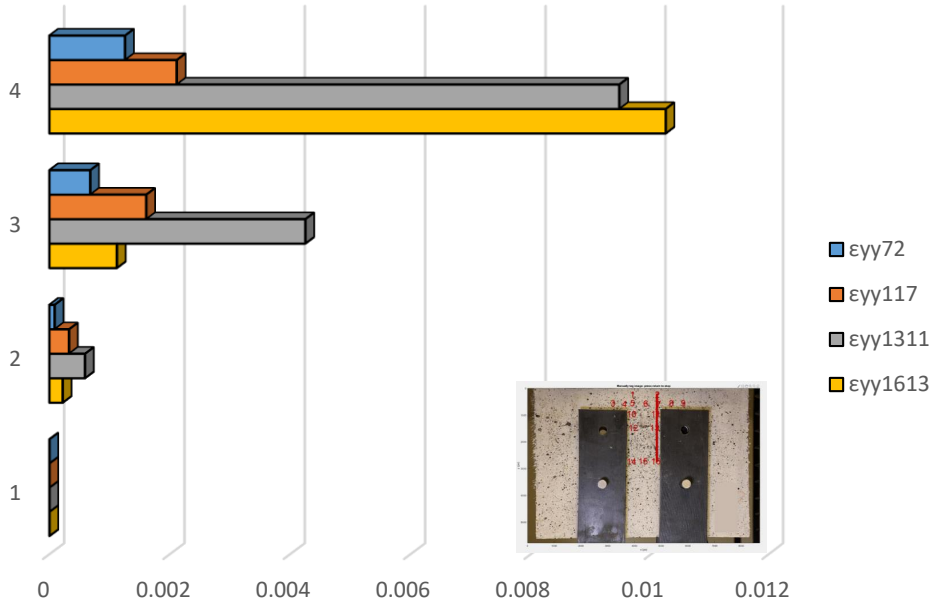

Figure A - 65 Demonstration of ε_{yy} on right vertical layer (CMK2-5-B – Case 2).

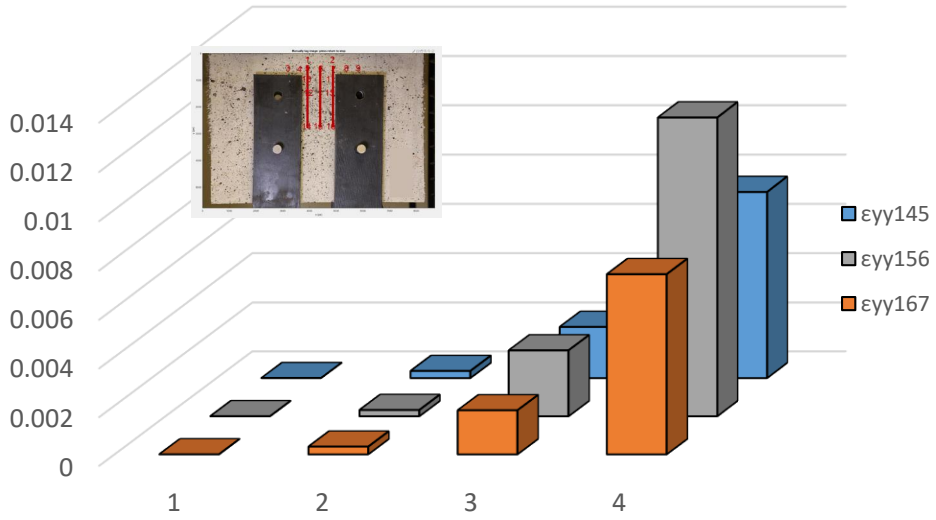

Figure A - 66 Comparison of ε_{yy} between three equidistant layers (CMK2-5-B – Case 2).

Detailed analysis in three milestone points – Case 3

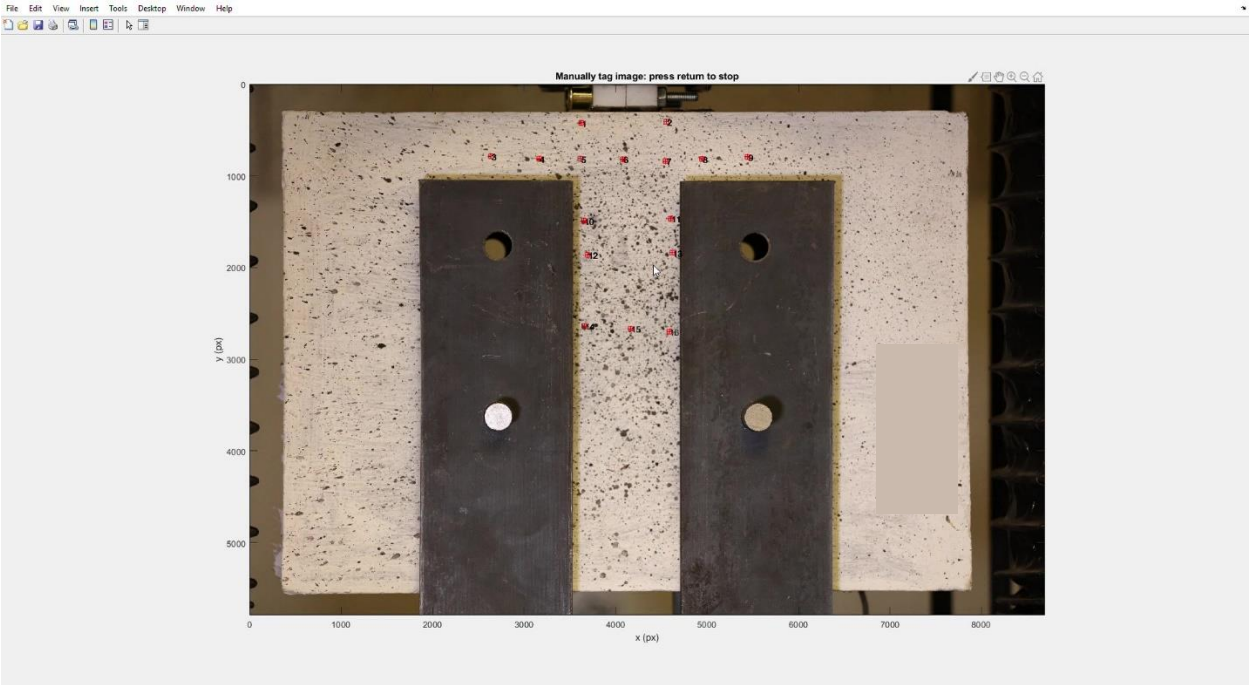

Figure A - 67 Locations of POIs for specimen CMK2-5-B (Case 3).

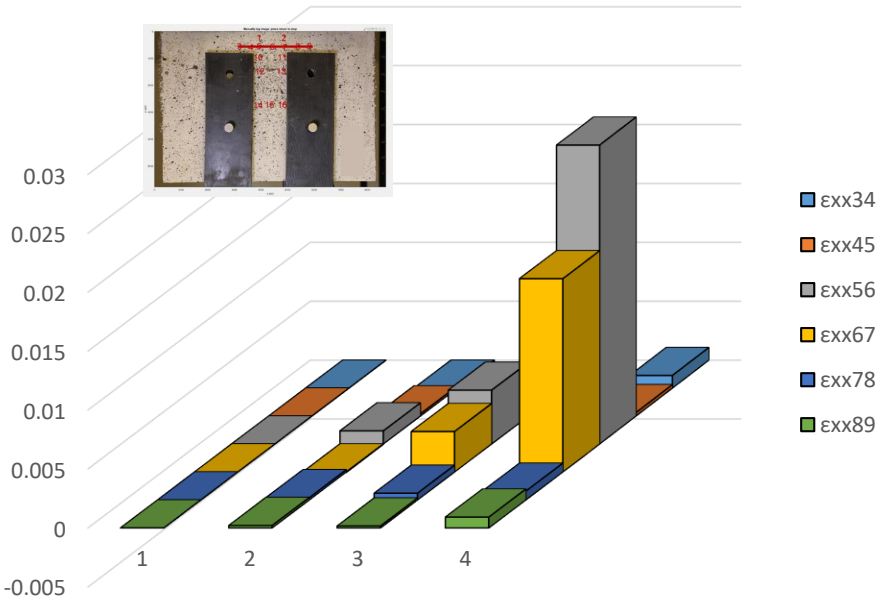

Figure A - 68 Demonstration of ε_{xx} along Layer 2 (CMK2-5-B – Case 3).

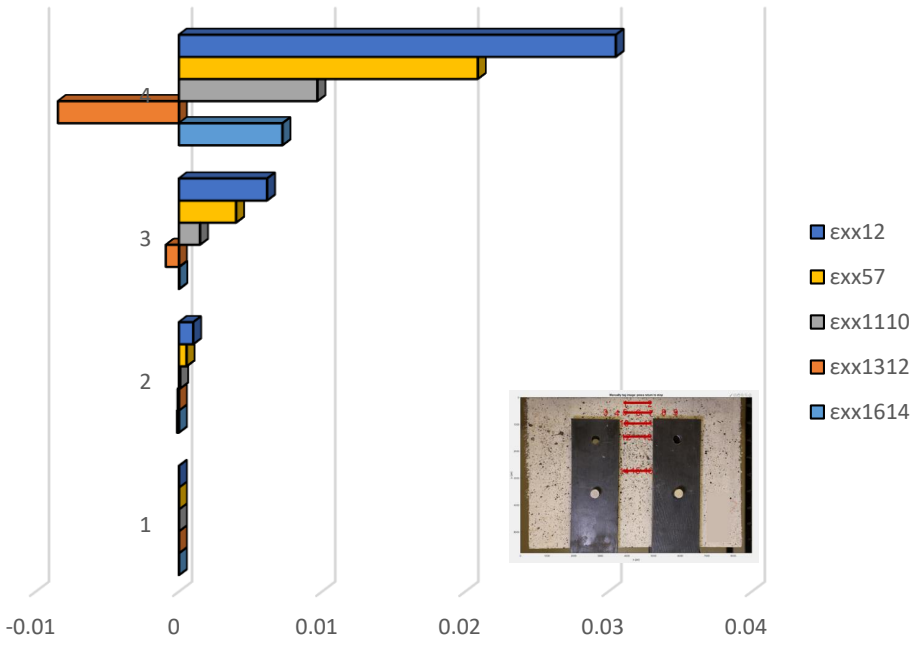

Figure A - 69 Comparison of ε_{xx} between horizontal layers (CMK2-5-B – Case 3).

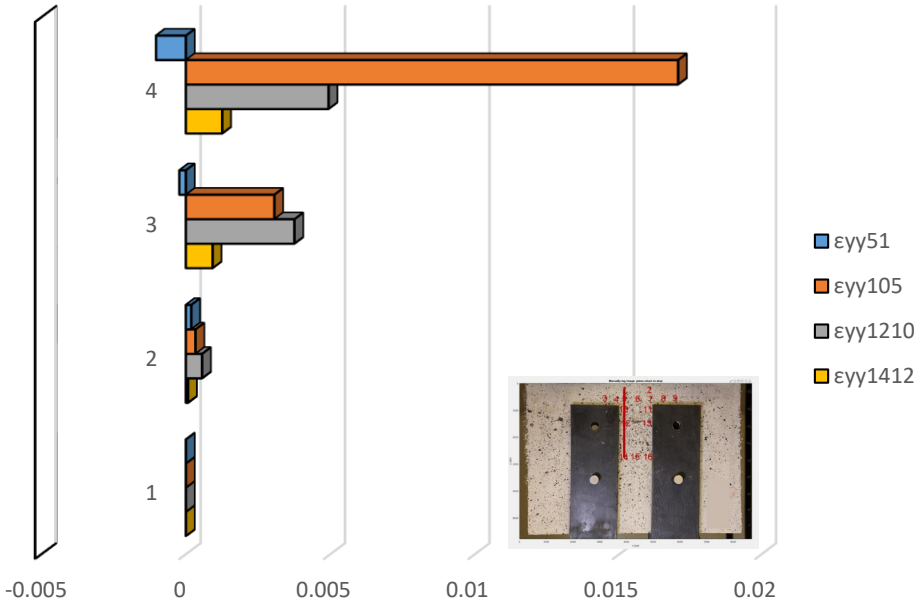

Figure A - 70 Demonstration of εyy on left vertical layer (CMK2-5-B – Case 3).

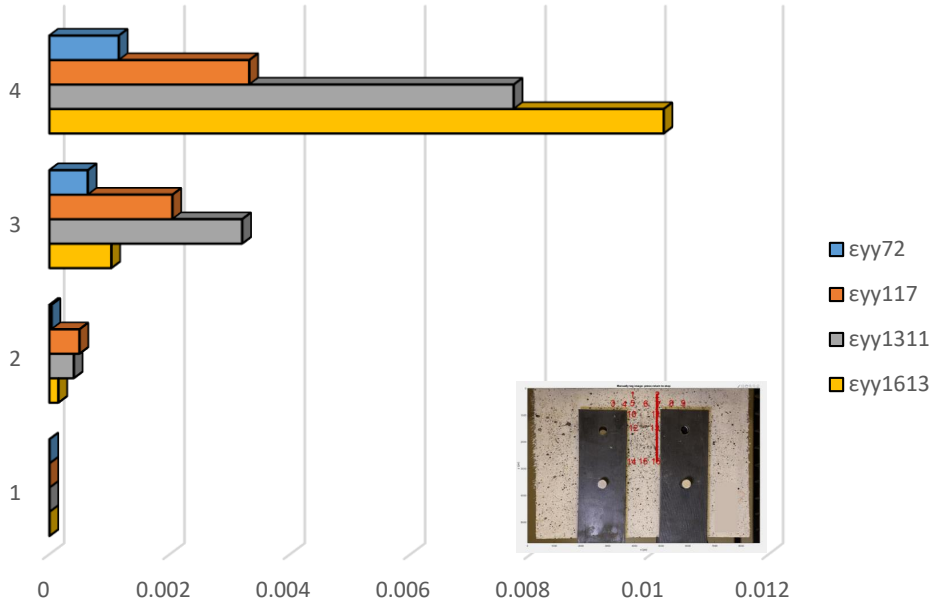

Figure A - 71 Demonstration of ε_{yy} on right vertical layer (CMK2-5-B – Case 3).

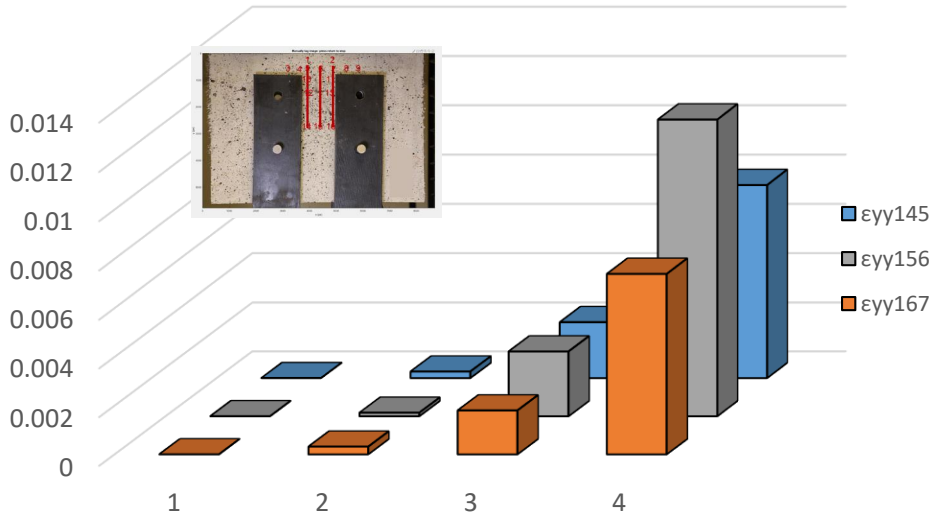

Figure A - 72 Comparison of ε_{yy} between three equidistant layers (CMK2-5-B – Case 3).

Specimen CMF1-5-A

Complete analysis

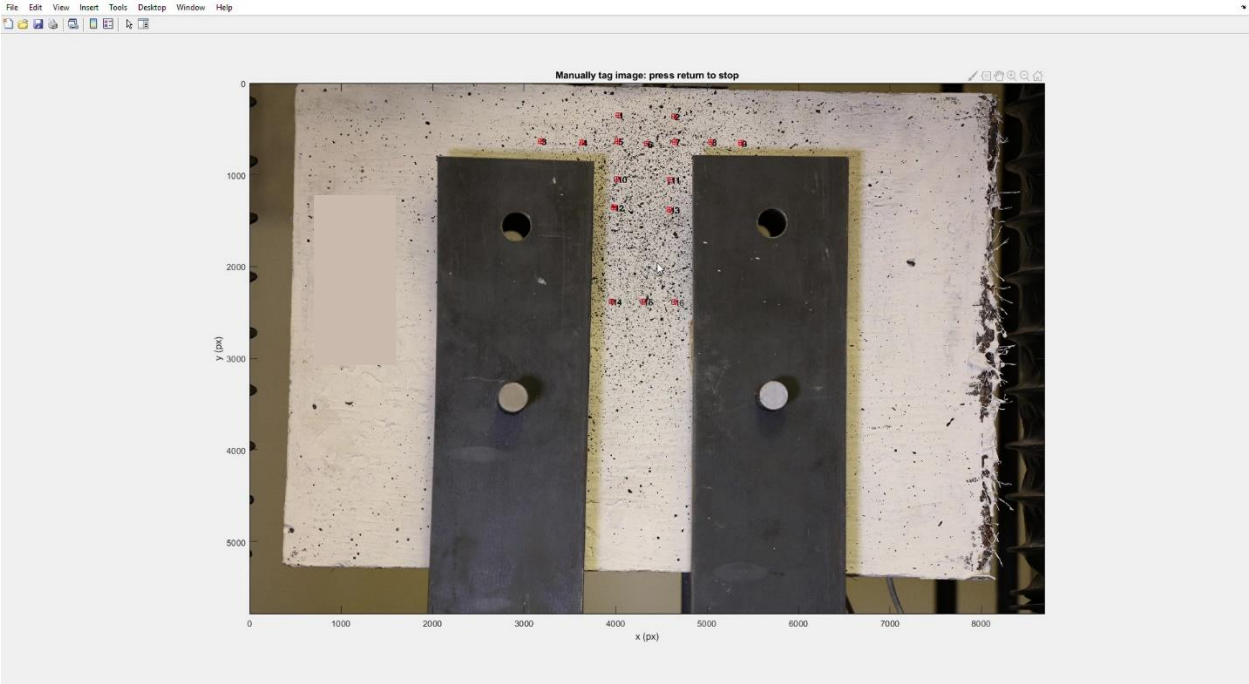

Figure A - 73 Locations of Points of Interest for specimen CMF1-5-A (Complete Analysis).

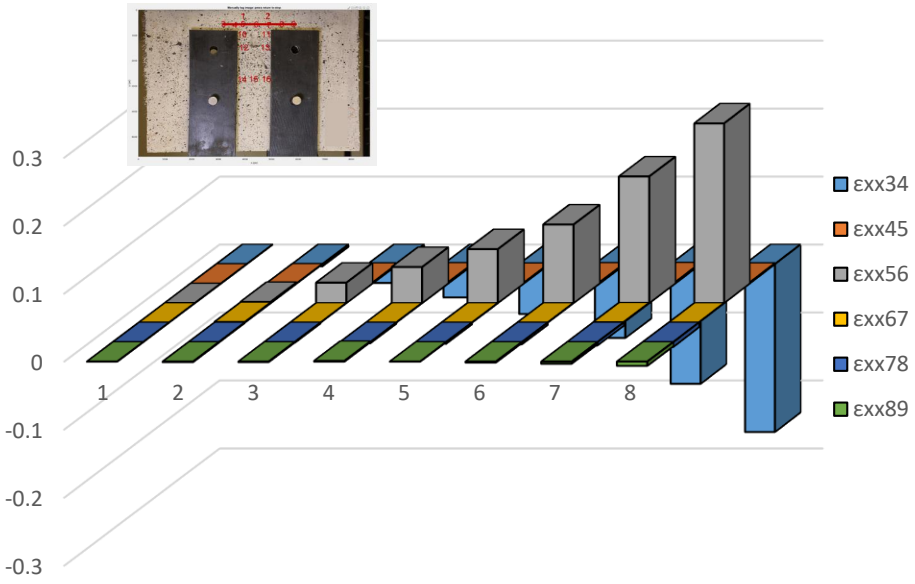

Figure A - 74 Demonstration of ε_{xx} along Layer 2 (CMF1-5-A – Complete analysis).

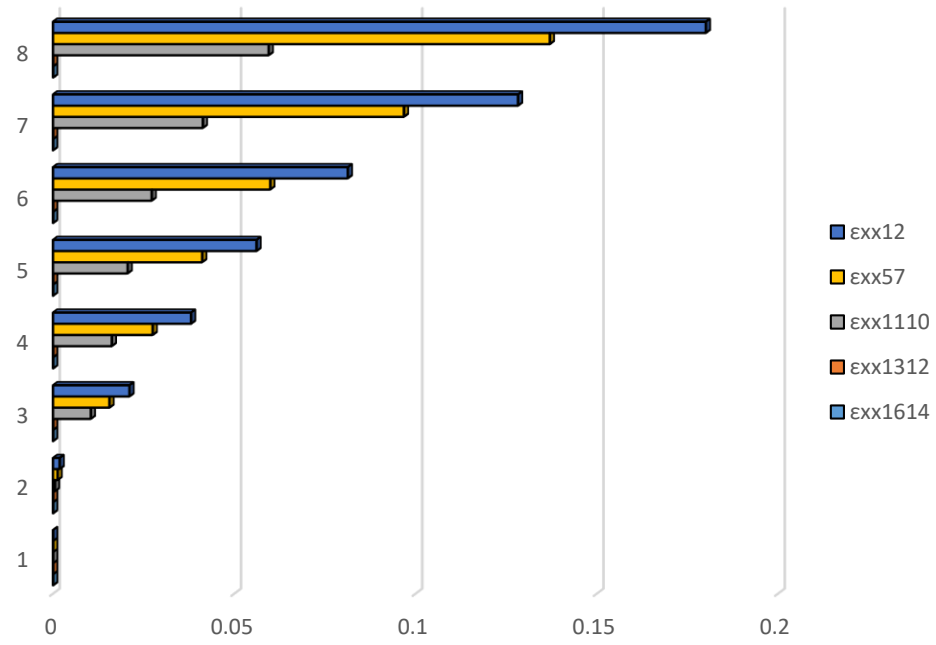

Figure A - 75 Comparison of ε_{xx} between horizontal layers (CMF1-5-A – Complete analysis).

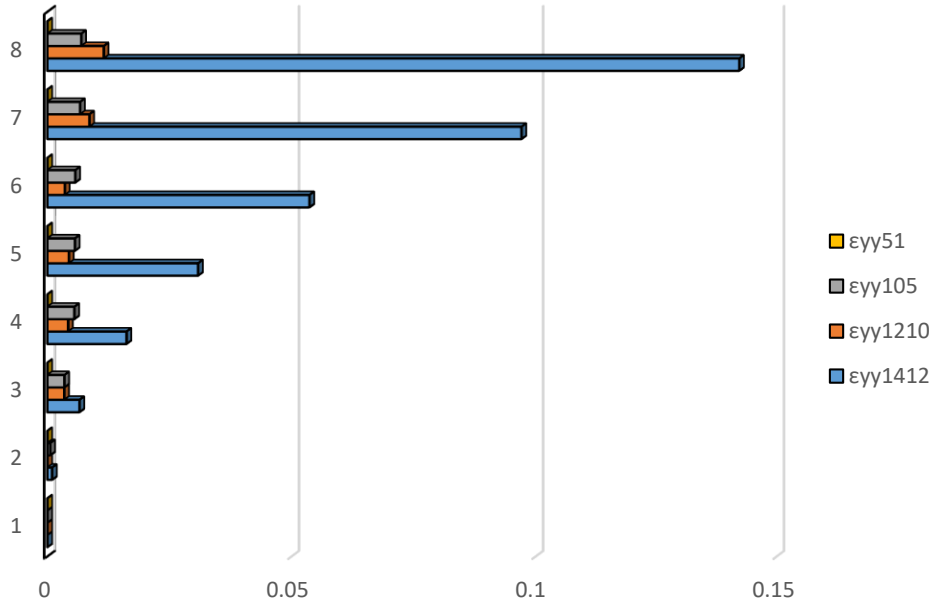

Figure A - 76 Demonstration of ε_{yy} on left vertical layer (CMF1-5-A – Complete analysis).

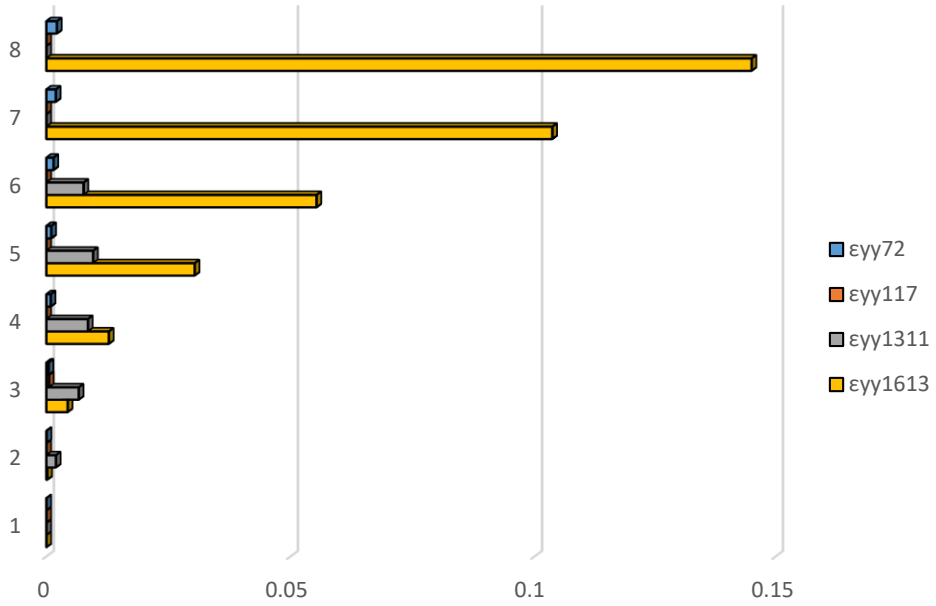

Figure A - 77 Demonstration of ε_{yy} on right vertical layer (CMF1-5-A – Complete analysis).

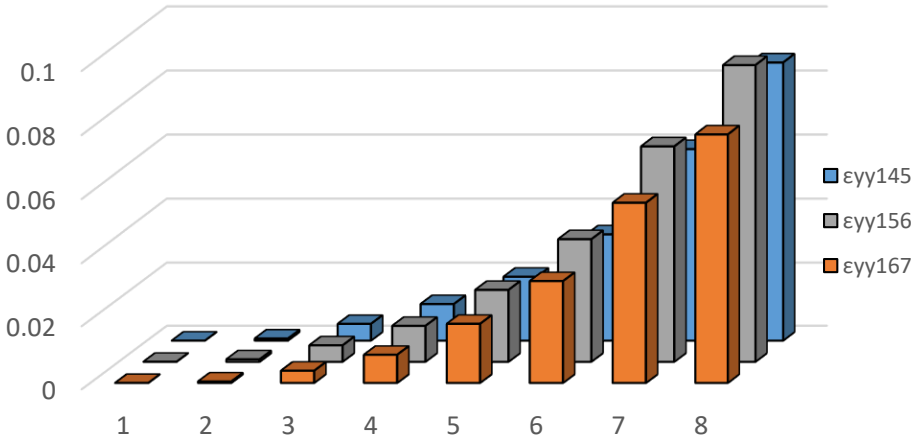

Figure A - 78 Comparison of ε_{yy} between three equidistant layers (CMF1-5-A – Complete analysis).

Detailed analysis in three milestone points – Case 1

Figure A - 79 Locations of POIs for specimen CMF1-5-A (Case 1).

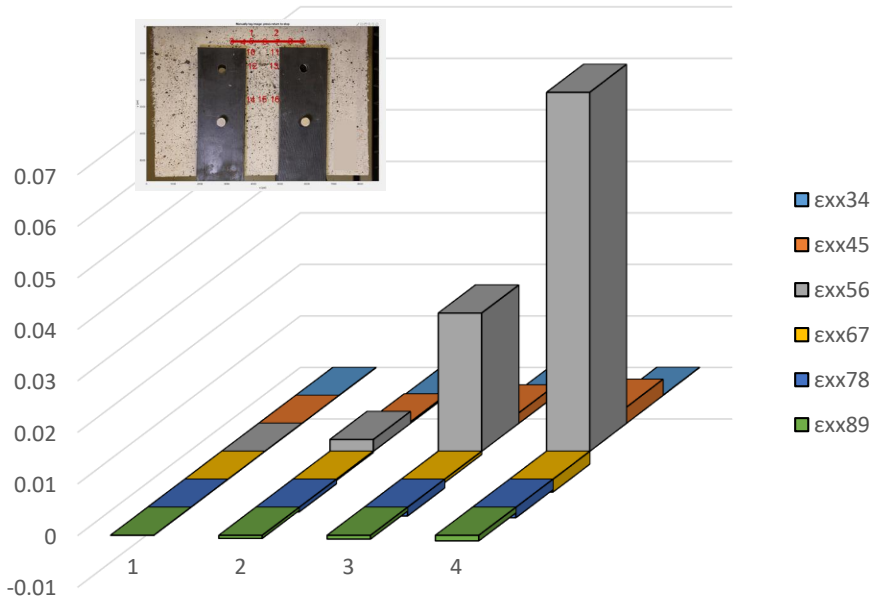

Figure A - 80 Demonstration of ε_{xx} along Layer 2 (CMF1-5-A – Case 1).

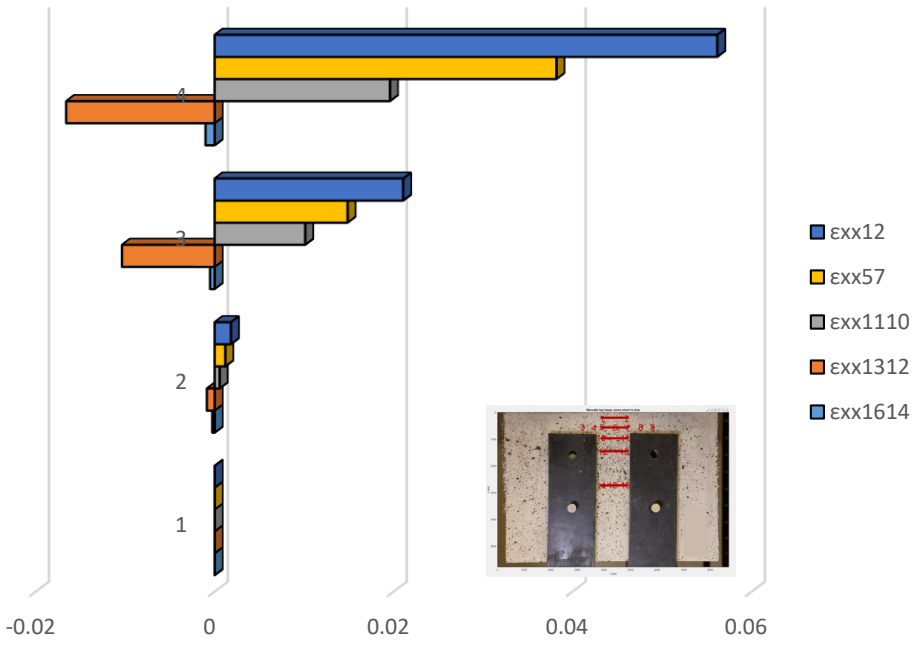

Figure A - 81 Comparison of ε_{xx} between horizontal layers (CMF1-5-A – Case 1).

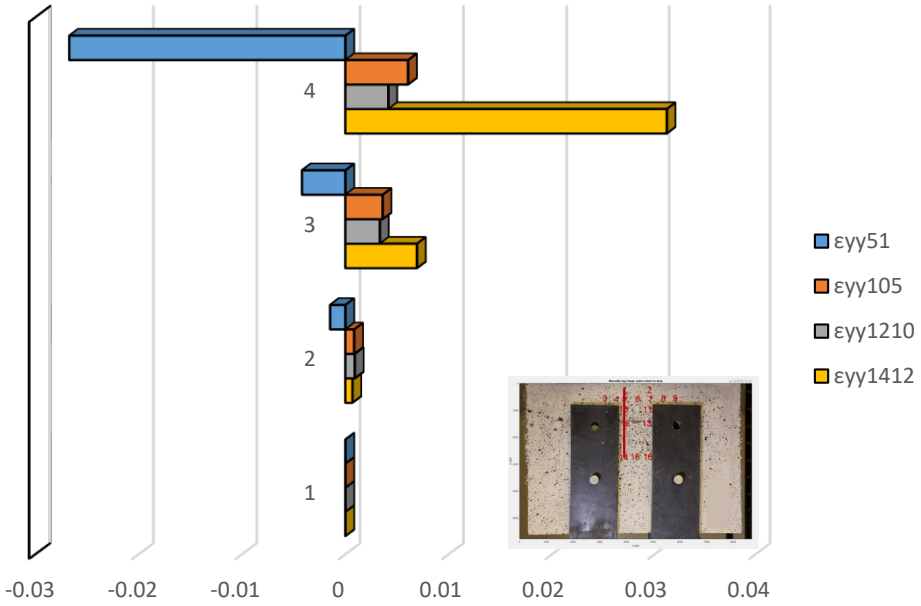

Figure A - 82 Demonstration of εyy on left vertical layer (CMF1-5-A – Case 1).

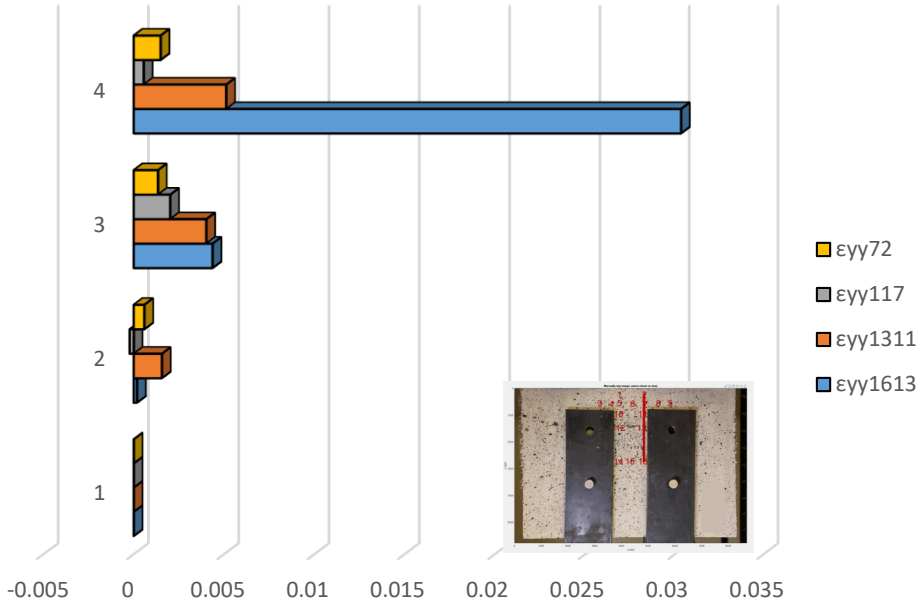

Figure A - 83 Demonstration of ε_{yy} on right vertical layer (CMF1-5-A – Case 1).

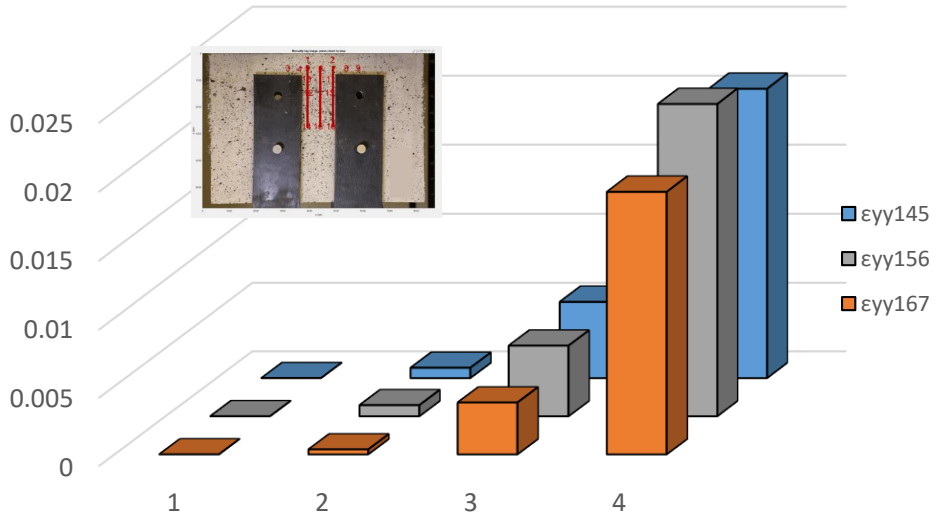

Figure A - 84 Comparison of ε_{yy} between three equidistant layers (CMF1-5-A – Case 1).

Detailed analysis in three milestone points – Case 2

Figure A - 85 Locations of POIs for specimen CMF1-5-A (Case 2).

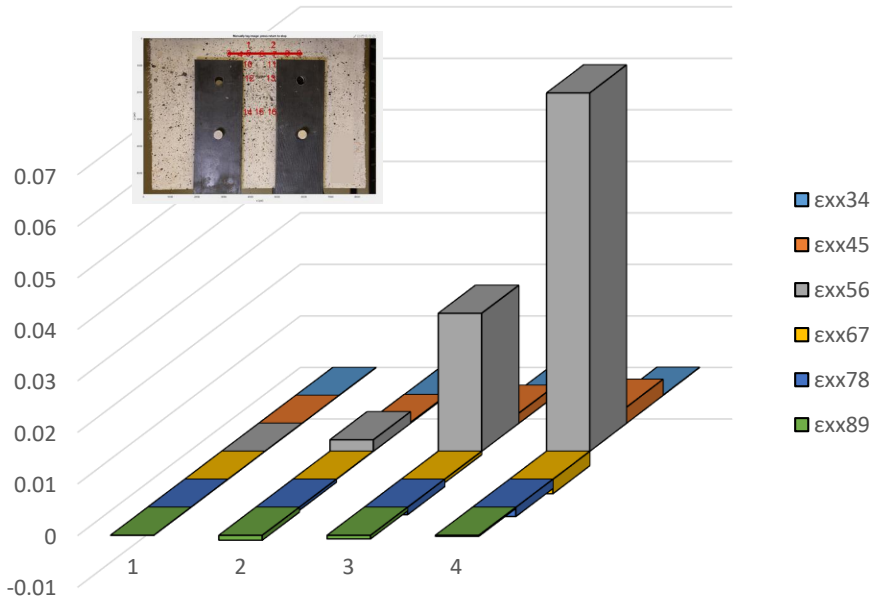

Figure A - 86 Demonstration of ε_{xx} along Layer 2 (CMF1-5-A – Case 2).

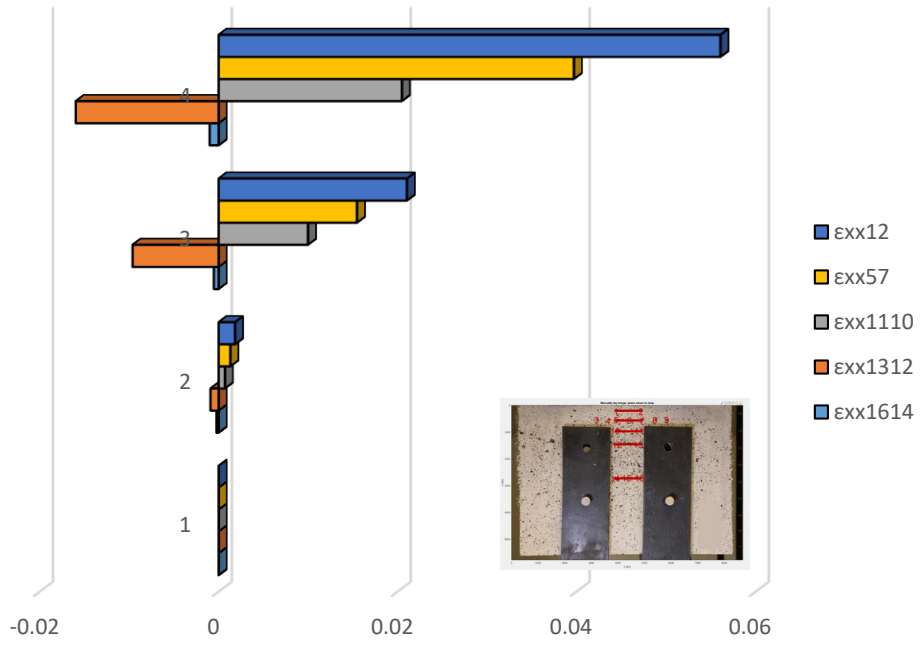

Figure A - 87 Comparison of ε_{xx} between horizontal layers (CMF1-5-A – Case 2).

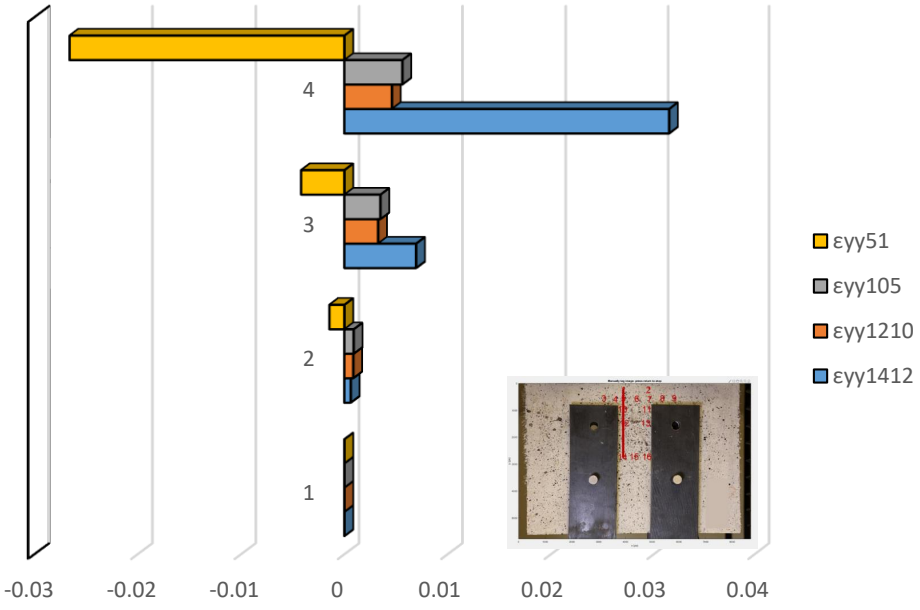

Figure A - 88 Demonstration of εyy on left vertical layer (CMF1-5-A – Case 2).

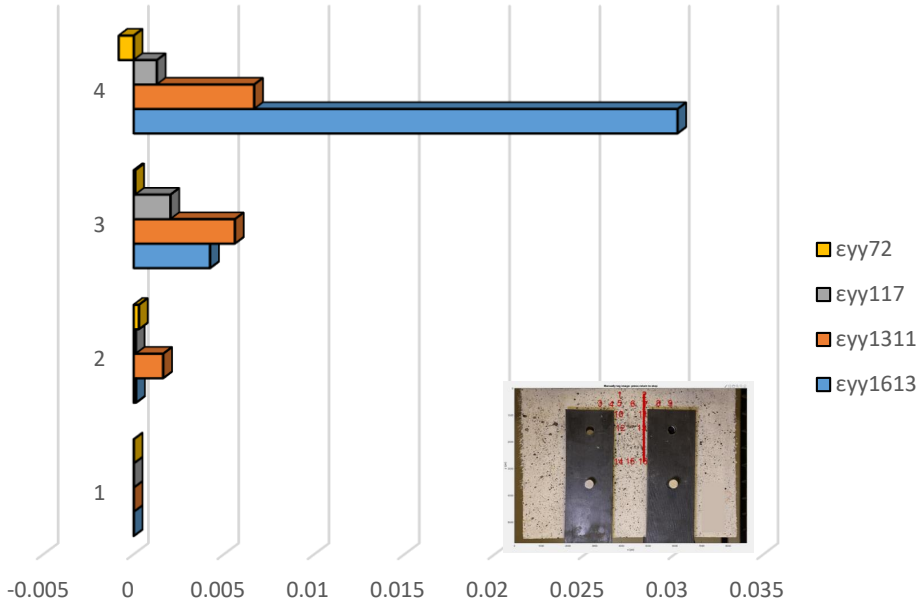

Figure A - 89 Demonstration of ε_{yy} on right vertical layer (CMF1-5-A – Case 2).

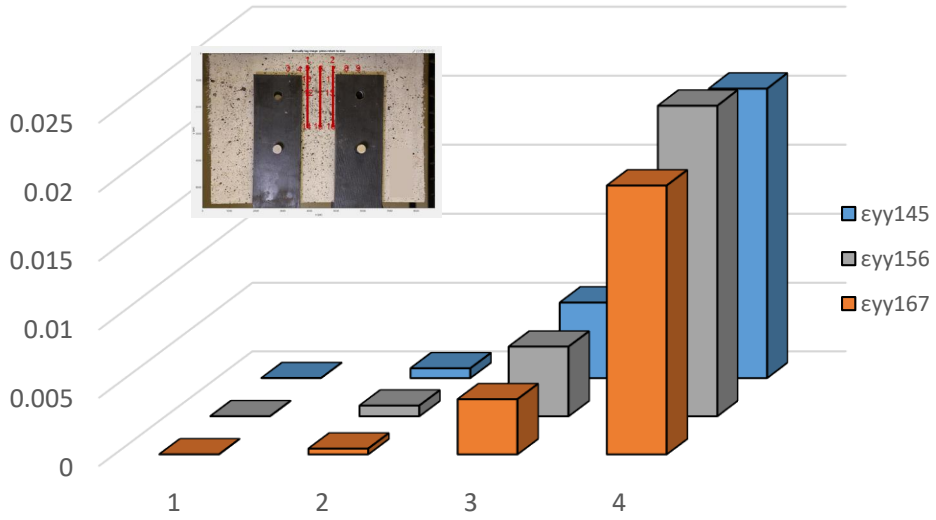

Figure A - 90 Comparison of ε_{yy} between three equidistant layers (CMF1-5-A – Case 2).

Detailed analysis in three milestone points – Case 3

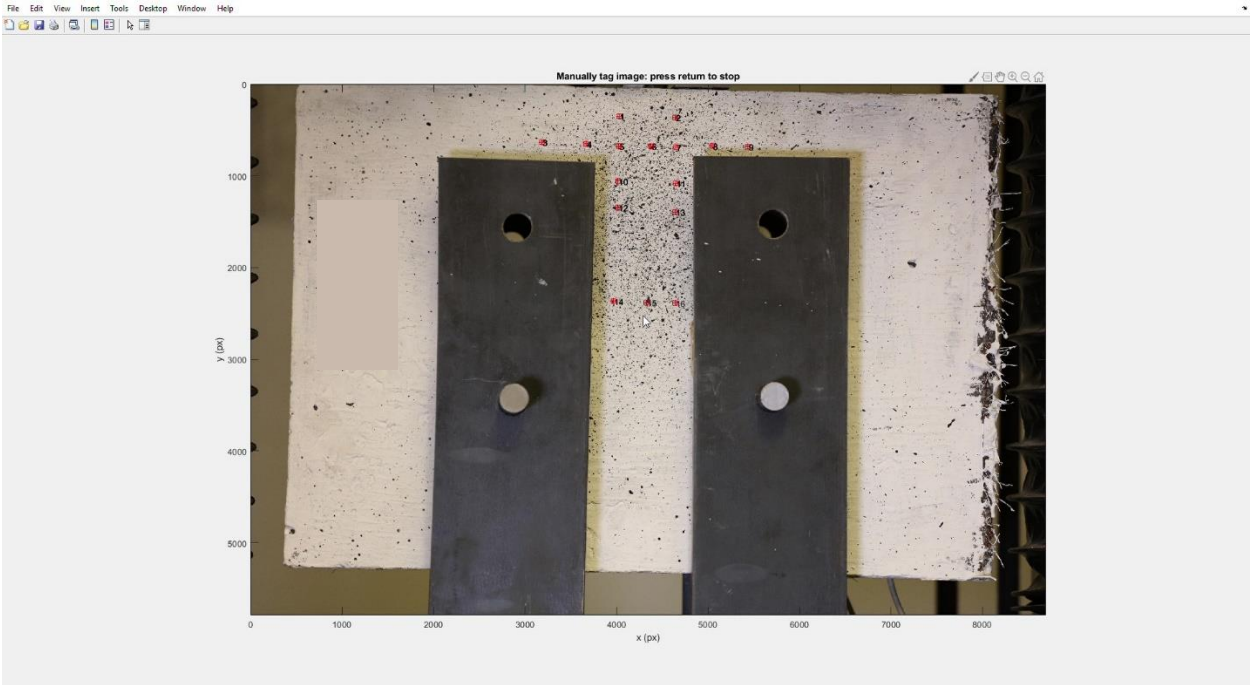

Figure A - 91 Locations of POIs for specimen CMF1-5-A (Case 3).

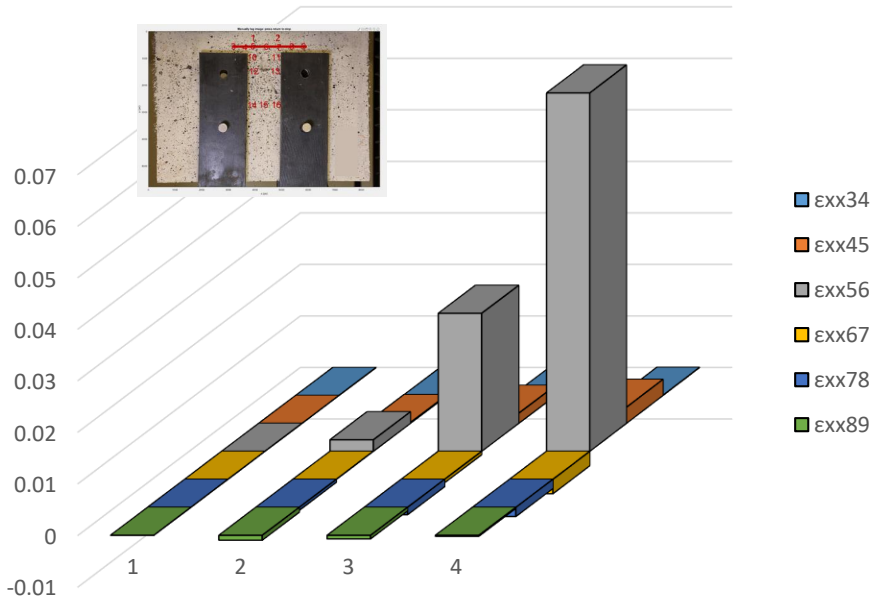

Figure A - 92 Demonstration of ε_{xx} along Layer 2 (CMF1-5-A – Case 3).

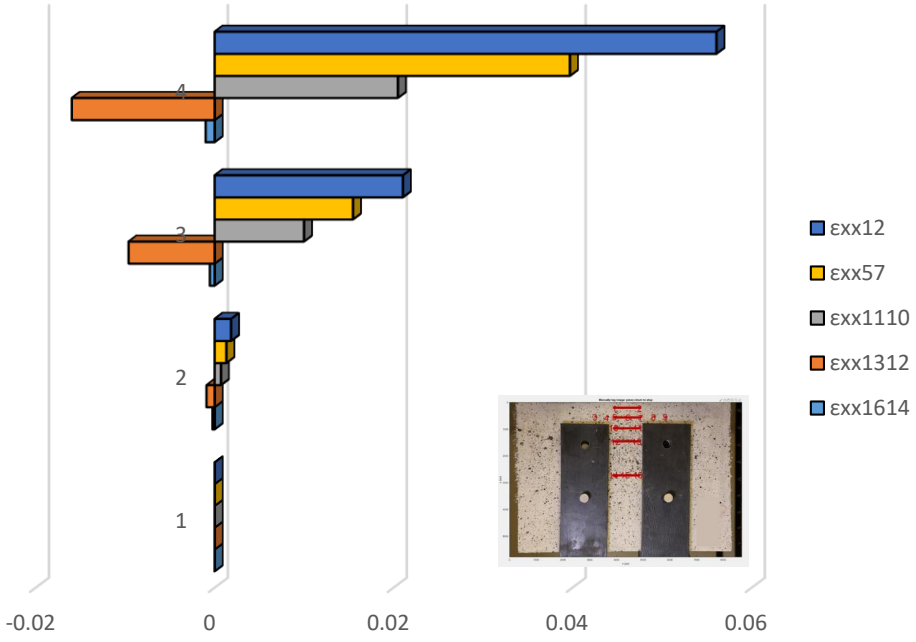

Figure A - 93 Comparison of ε_{xx} between horizontal layers (CMF1-5-A – Case 3).

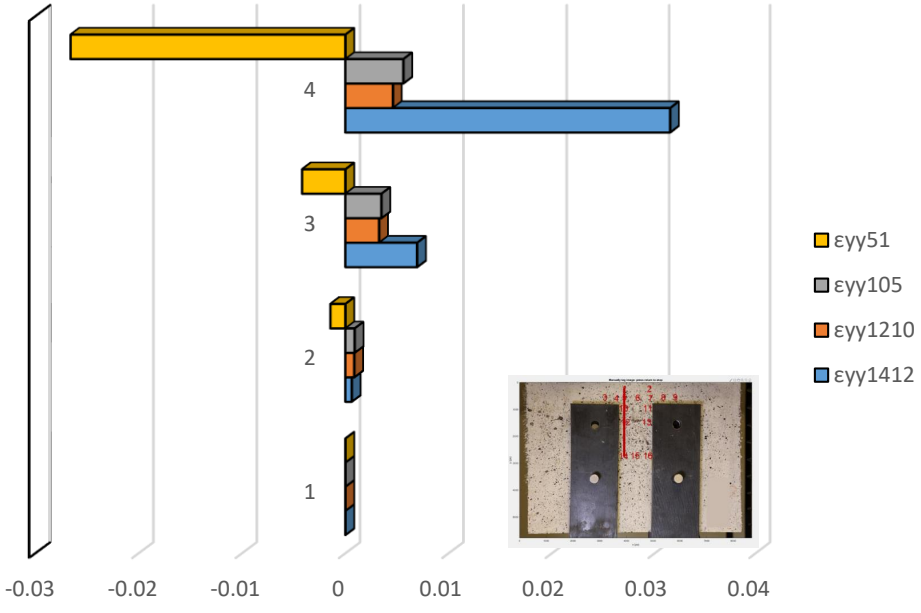

Figure A - 94 Demonstration of εyy on left vertical layer (CMF1-5-A – Case 3).

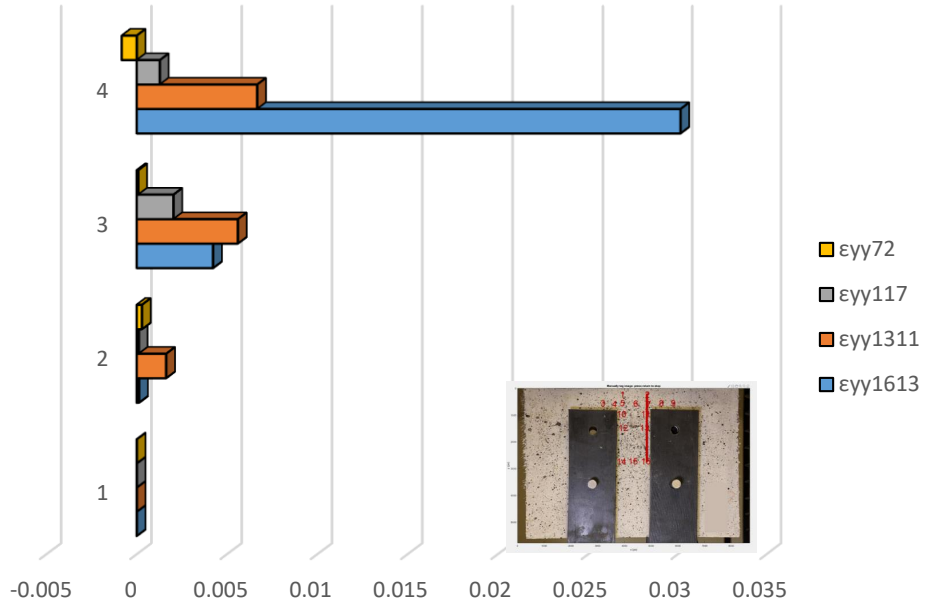

Figure A - 95 Demonstration of ε_{yy} on right vertical layer (CMF1-5-A – Case 3).

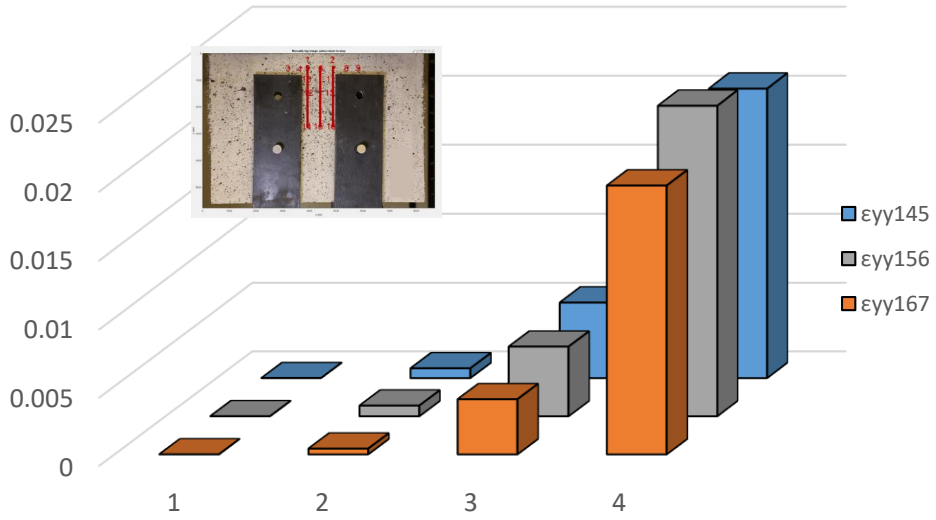

Figure A - 96 Comparison of ε_{yy} between three equidistant layers (CMF1-5-A – Case 3).

Specimen CMF1-5-B

Complete analysis

Figure A - 97 Locations of Points of Interest for specimen CMF1-5-B (Complete Analysis).

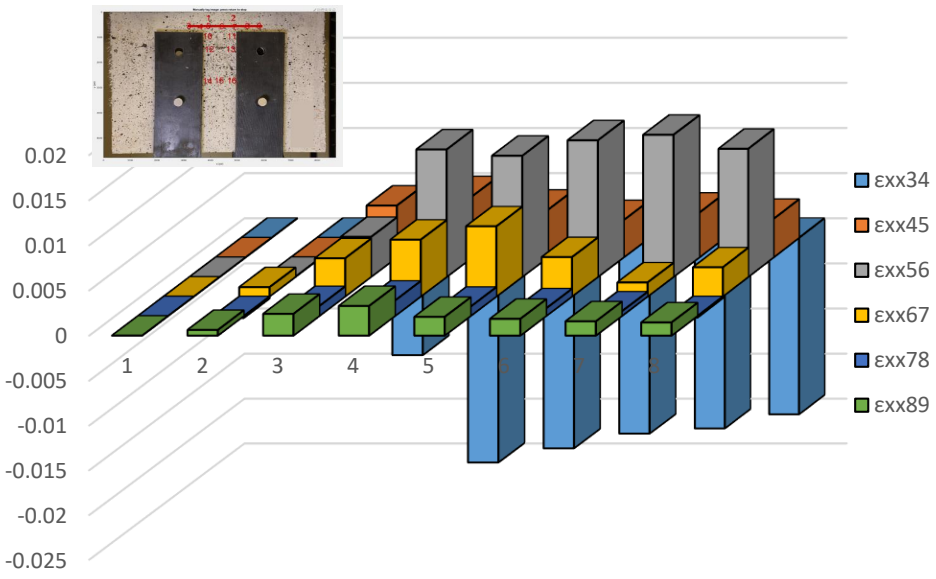

Figure A - 98 Demonstration of ε_{xx} along Layer 2 (CMF1-5-B – Complete analysis).

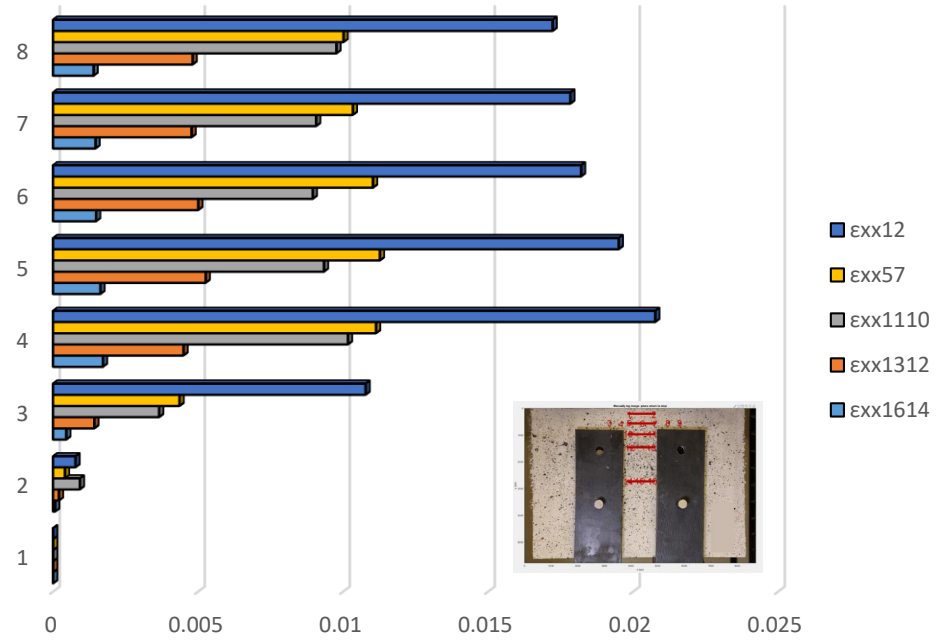

Figure A - 99 Comparison of ε_{xx} between horizontal layers (CMF1-5-B – Complete analysis).

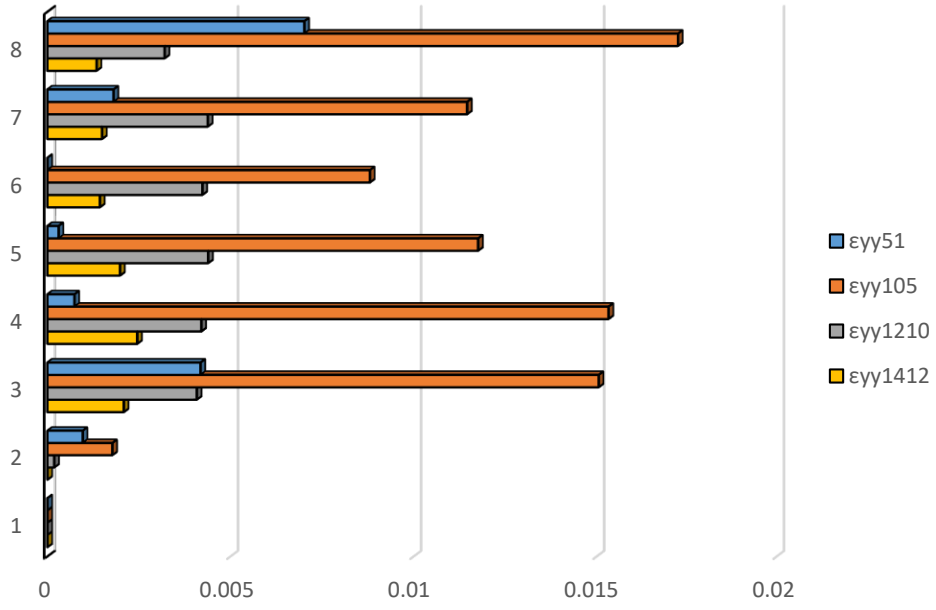

Figure A - 100 Demonstration of ε_{yy} on left vertical layer (CMF1-5-B – Complete analysis).

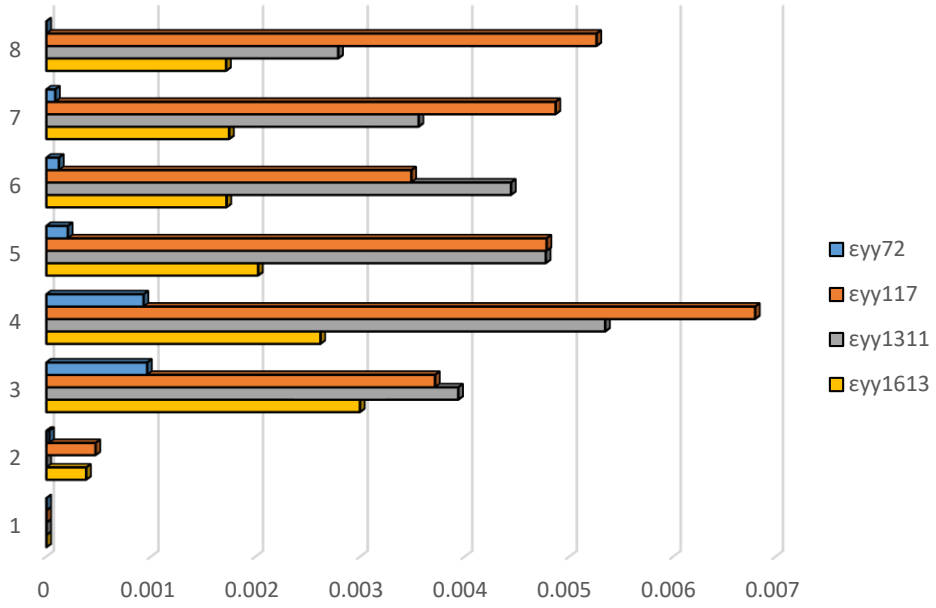

Figure A - 101 Demonstration of ε_{yy} on right vertical layer (CMF1-5-B – Complete analysis).

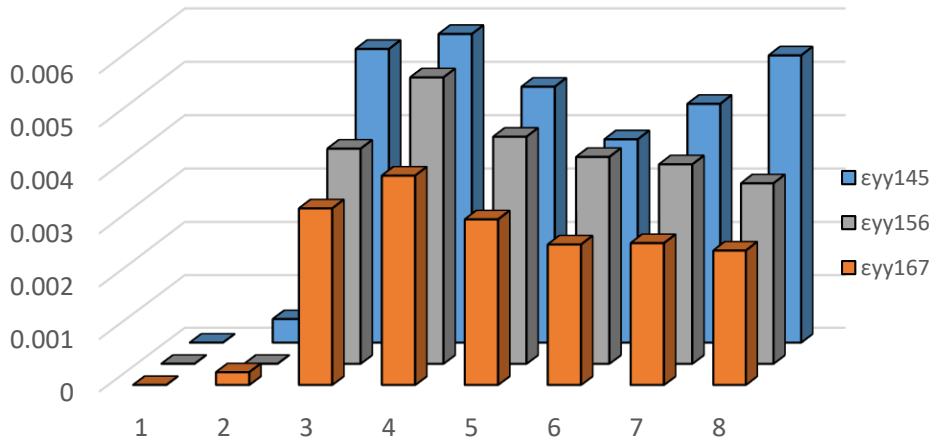

Figure A - 102 Comparison of ε_{yy} between three equidistant layers (CMF1-5-B – Complete analysis).

Detailed analysis in three milestone points – Case 1

Figure A - 103 Locations of POIs for specimen CMF1-5-B (Case 1)

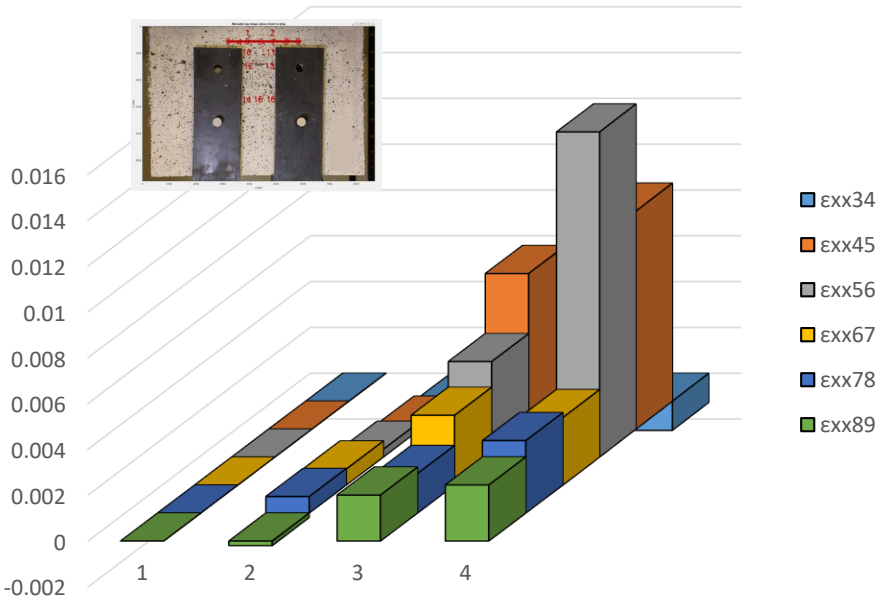

Figure A - 104 Demonstration of ε_{xx} along Layer 2 (CMF1-5-B – Case 1).

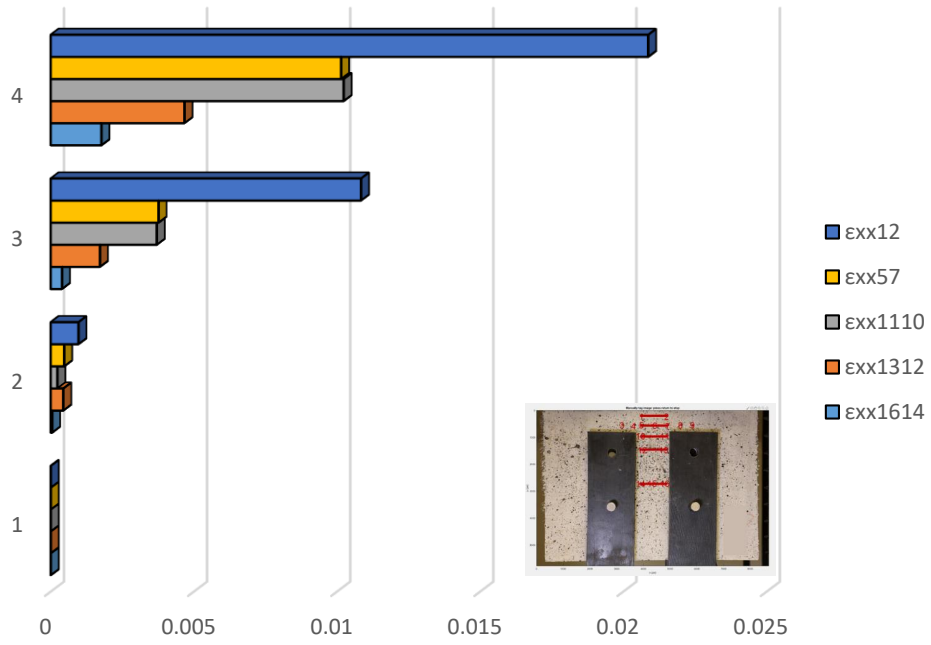

Figure A - 105 Comparison of ε_{xx} between horizontal layers (CMF1-5-B – Case 1).

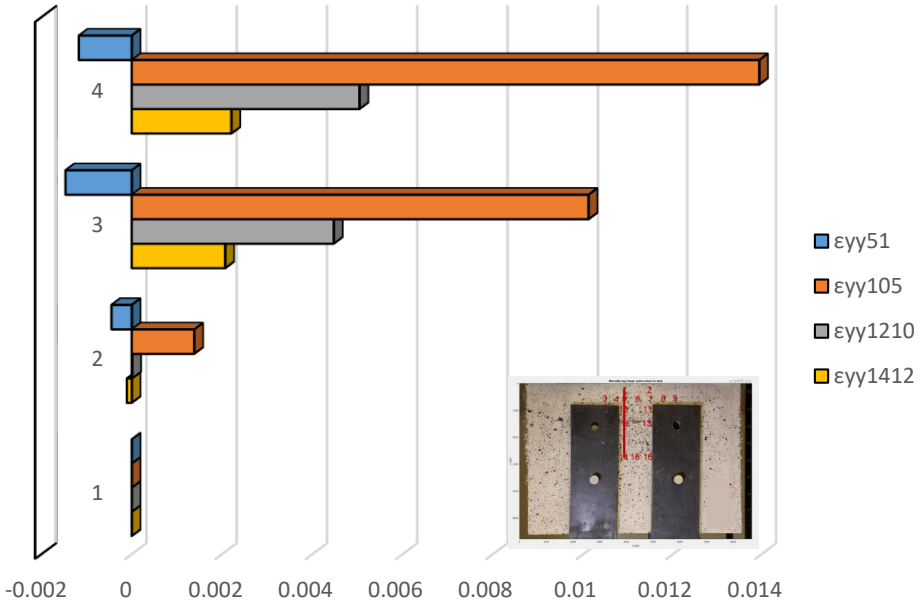

Figure A - 106 Demonstration of εyy on left vertical layer (CMF1-5-B – Case 1).

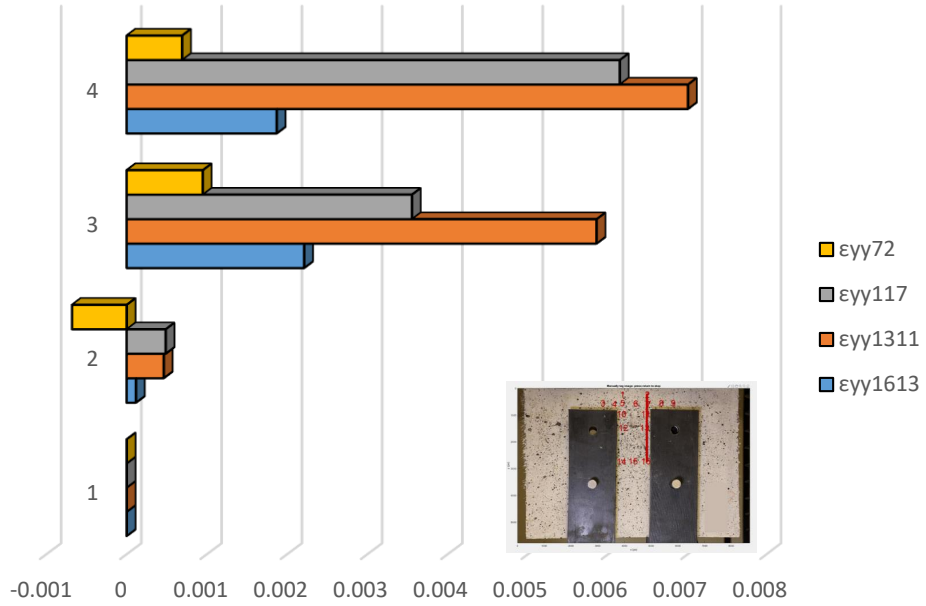

Figure A - 107 Demonstration of ε_{yy} on right vertical layer (CMF1-5-B – Case 1).

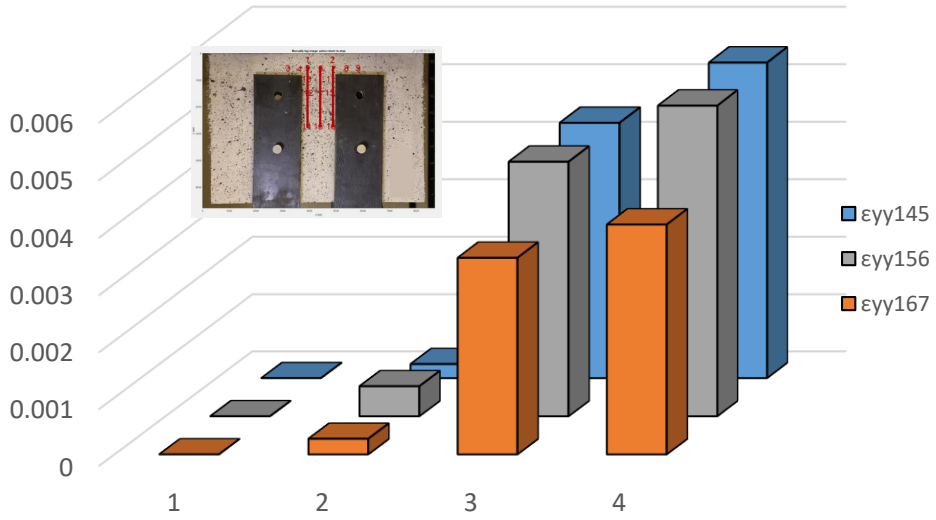

Figure A - 108 Comparison of ε_{yy} between three equidistant layers (CMF1-5-B – Case 1).

Detailed analysis in three milestone points – Case 2

Figure A - 109 Locations of POIs for specimen CMF1-5-B (Case 2).

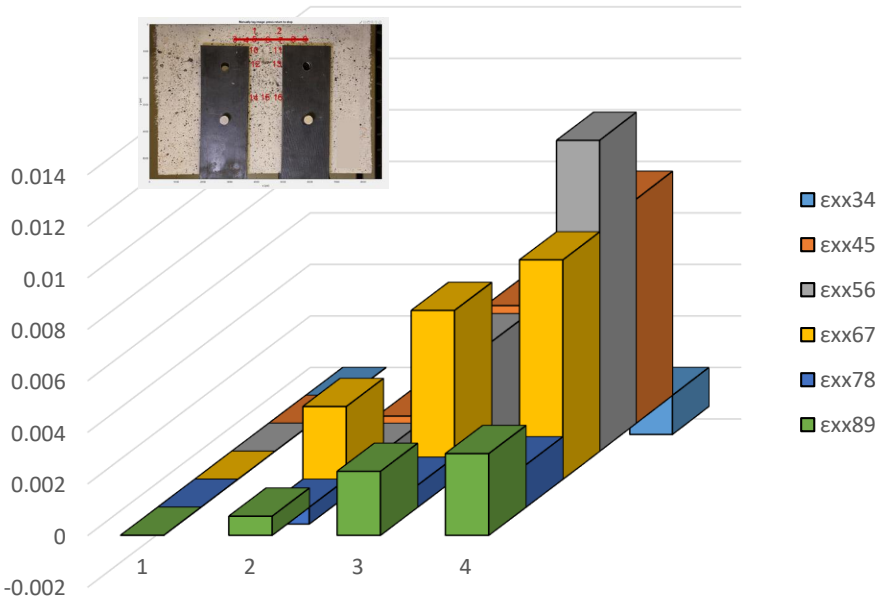

Figure A - 110 Demonstration of ε_{xx} along Layer 2 (CMF1-5-B – Case 2).

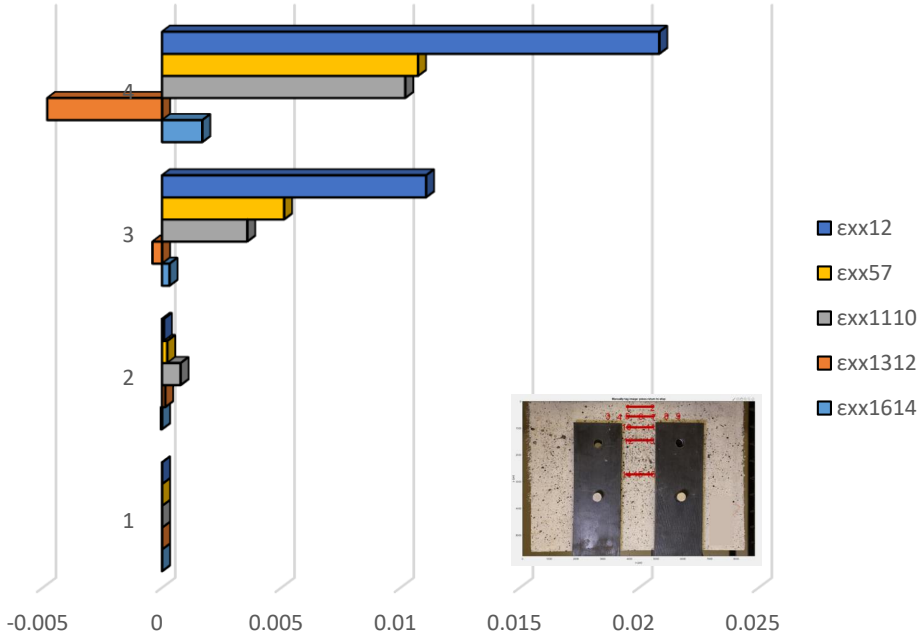

Figure A - 111 Comparison of ε_{xx} between horizontal layers (CMF1-5-B – Case 2).

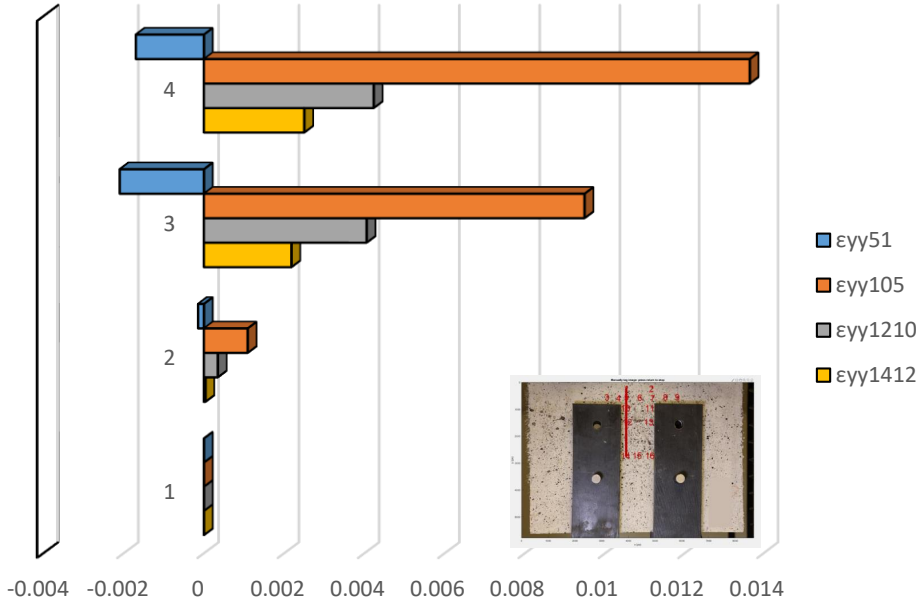

Figure A - 112 Demonstration of εyy on left vertical layer (CMF1-5-B – Case 2).

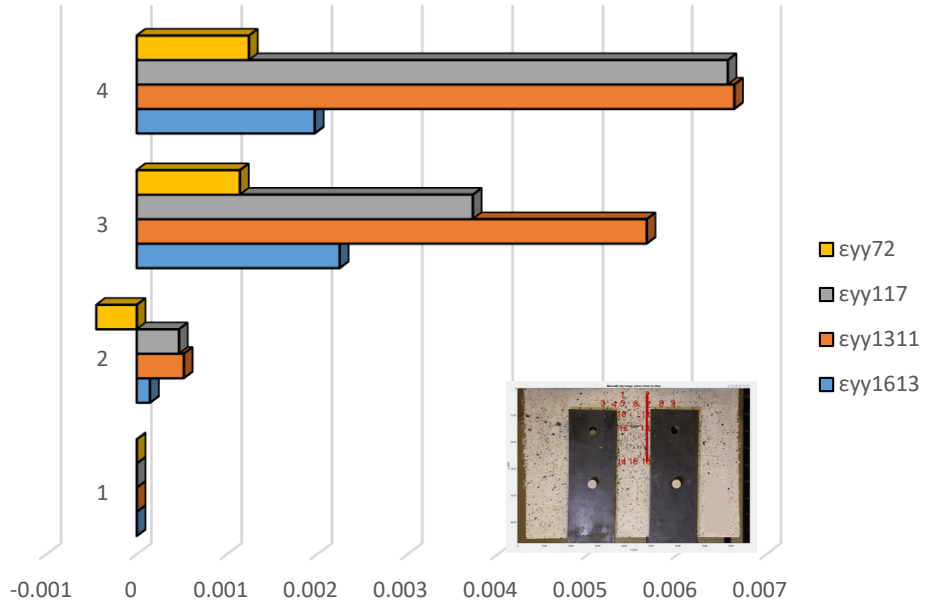

Figure A - 113 Demonstration of ε_{yy} on right vertical layer (CMF1-5-B – Case 2).

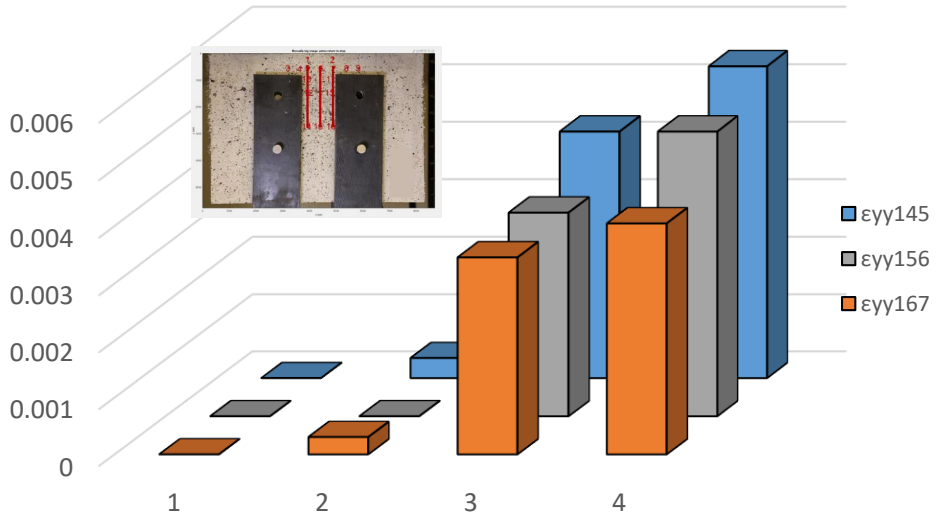

Figure A - 114 Comparison of ε_{yy} between three equidistant layers (CMF1-5-B – Case 2).

Detailed analysis in three milestone points – Case 3

Figure A - 115 Locations of POIs for specimen CMF1-5-B (Case 3).

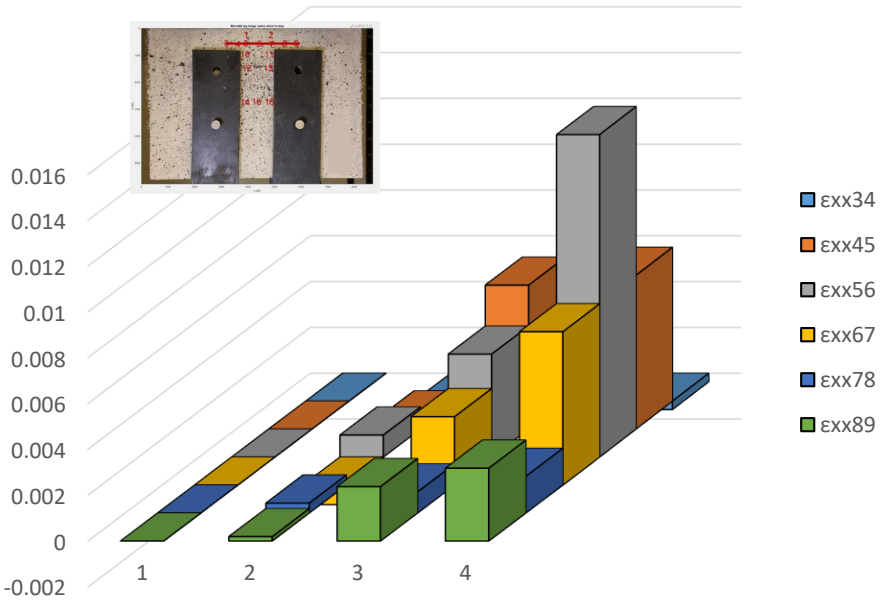

Figure A - 116 Demonstration of ε_{xx} along Layer 2 (CMF1-5-B – Case 3).

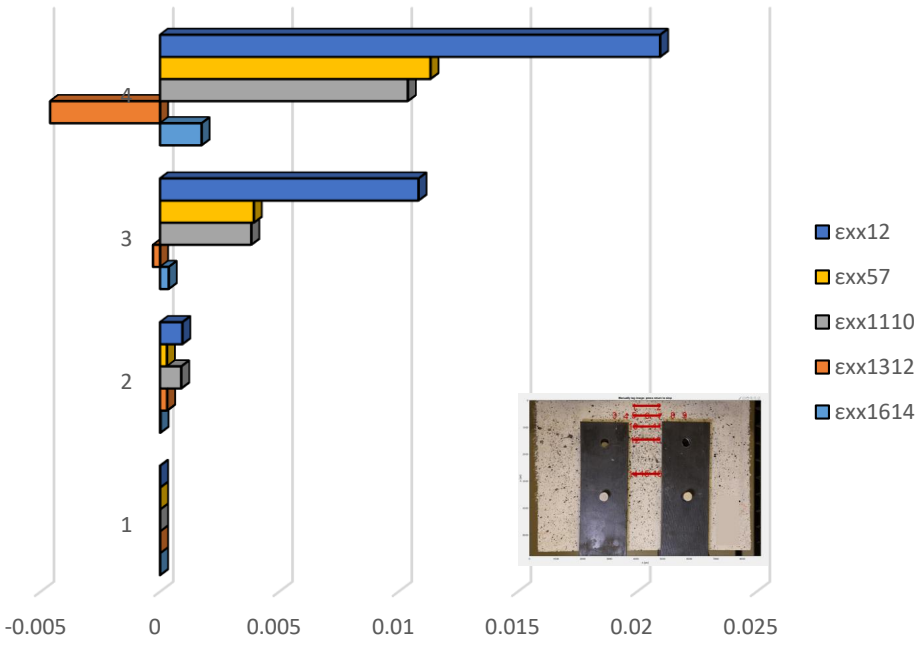

Figure A - 117 Comparison of ε_{xx} between horizontal layers (CMF1-5-B – Case 3).

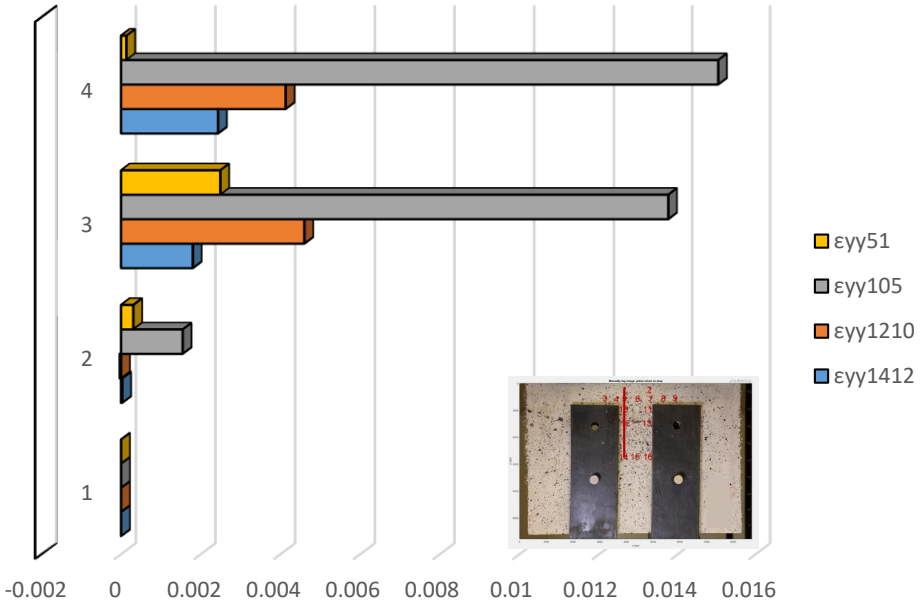

Figure A - 118 Demonstration of εyy on left vertical layer (CMF1-5-B – Case 3).

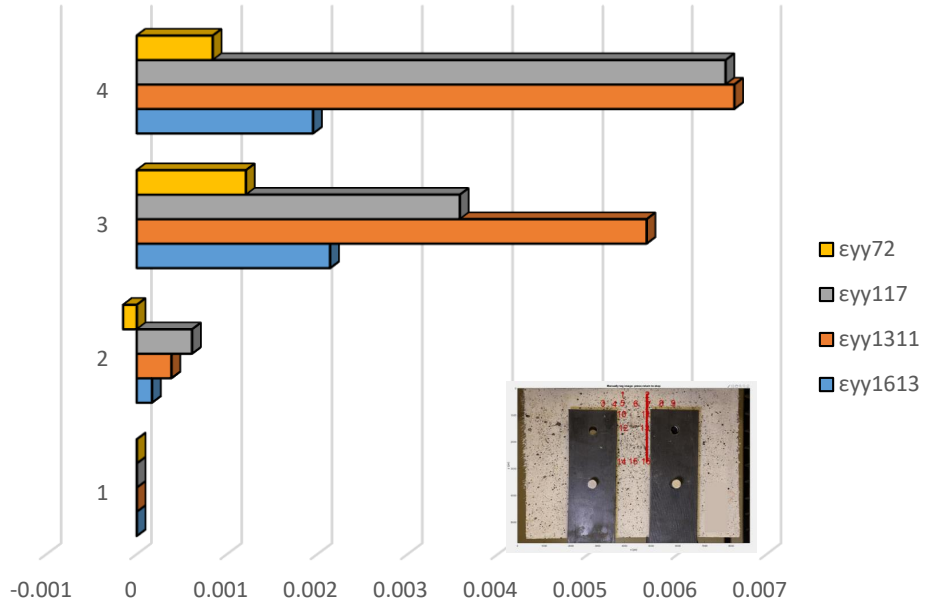

Figure A - 119 Demonstration of ε_{yy} on right vertical layer (CMF1-5-B – Case 3).

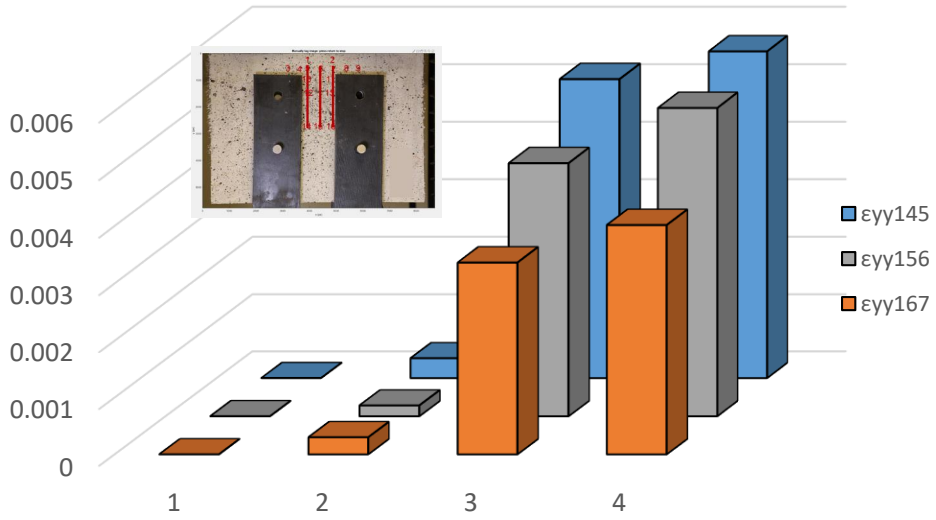

Figure A - 120 Comparison of ε_{yy} between three equidistant layers (CMF1-5-B – Case 3).

Specimen CMF2-5-A (Part 1)

Detailed analysis in three milestone points – Case 1

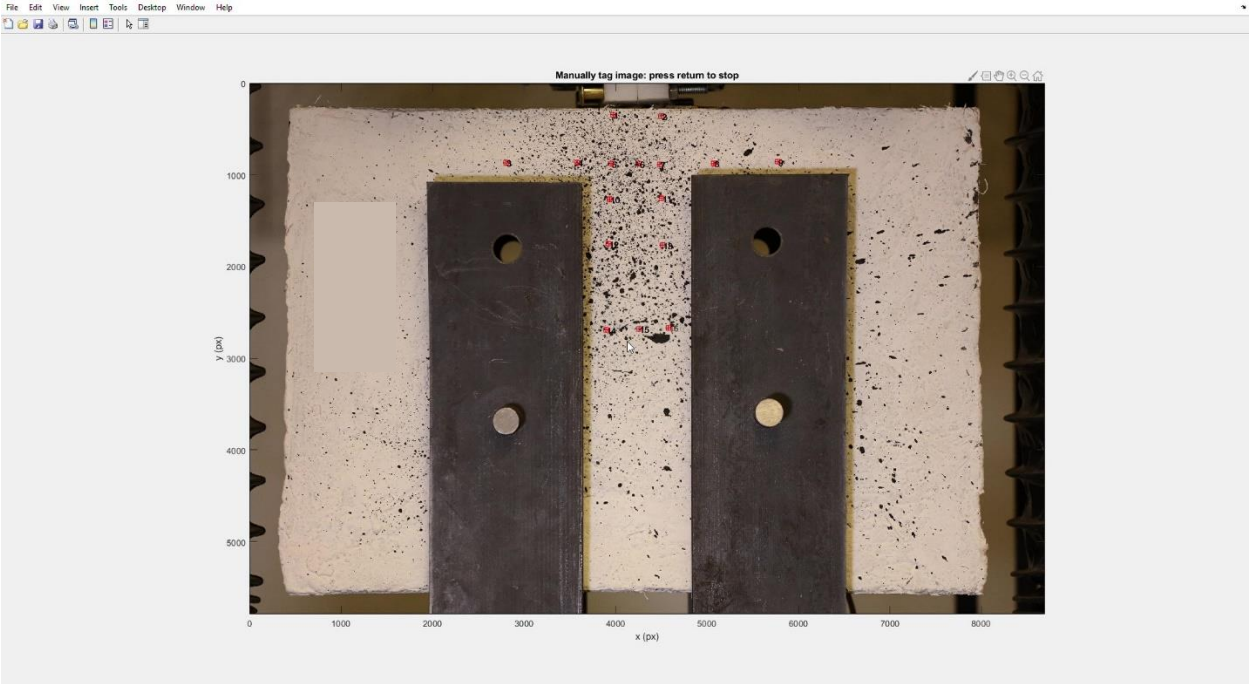

Figure A - 121 Locations of Points of Interest for Part 1 of specimen CMK2-5-A (Case 1).

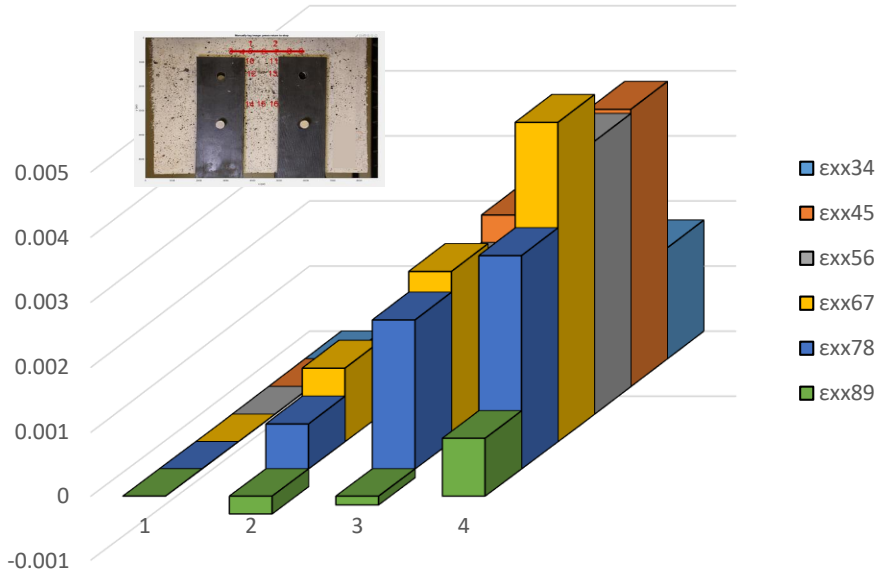

Figure A - 122 Demonstration of ε_{xx} along Layer 2 for Part 1 of specimen CMK2-5-A (Case 1).

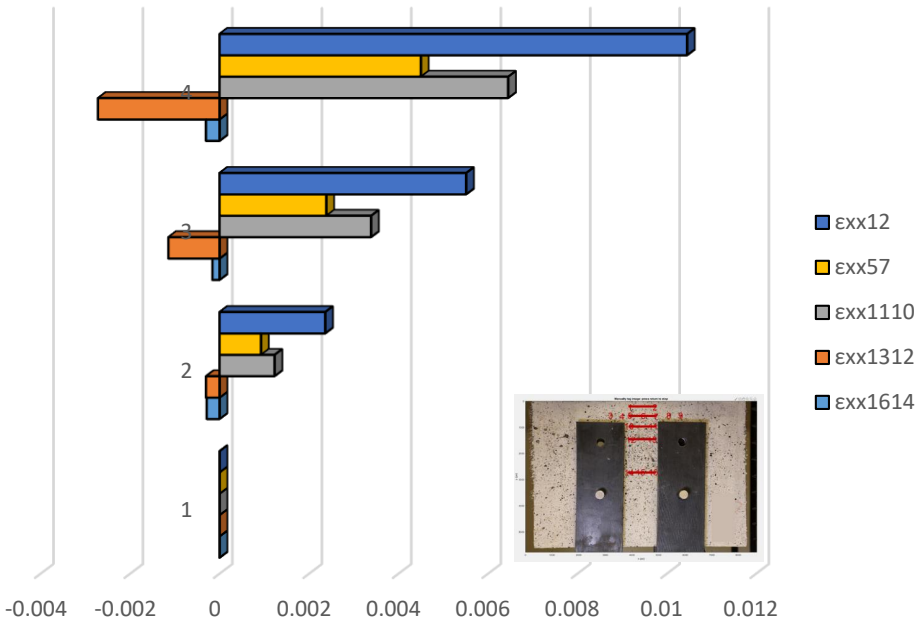

Figure A - 123 Comparison of ε_{xx} between horizontal layers for Part 1 of specimen CMK2-5-A (Case 1).

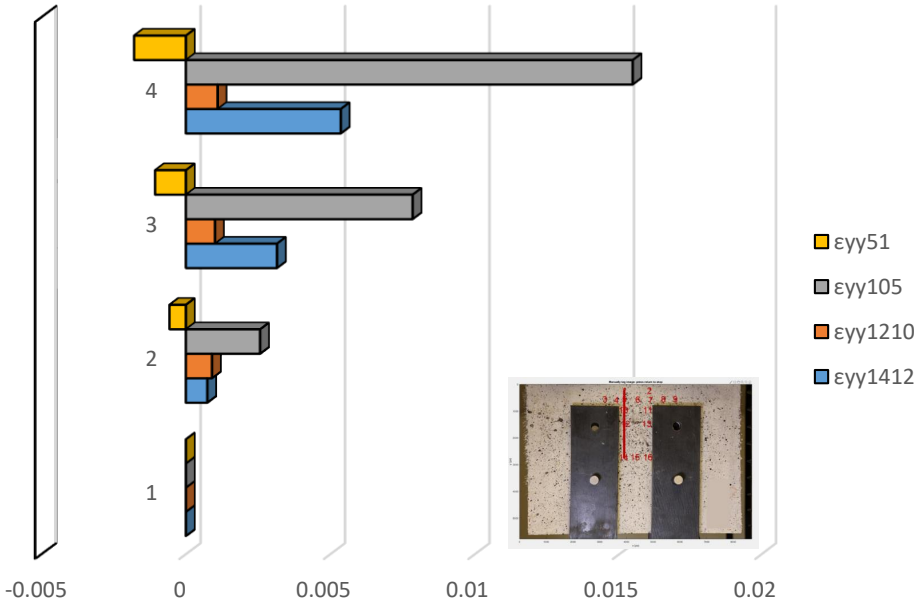

Figure A - 124 Demonstration of ε_{yy} on left vertical layer for Part 1 of specimen CMK2-5-A (Case 1).

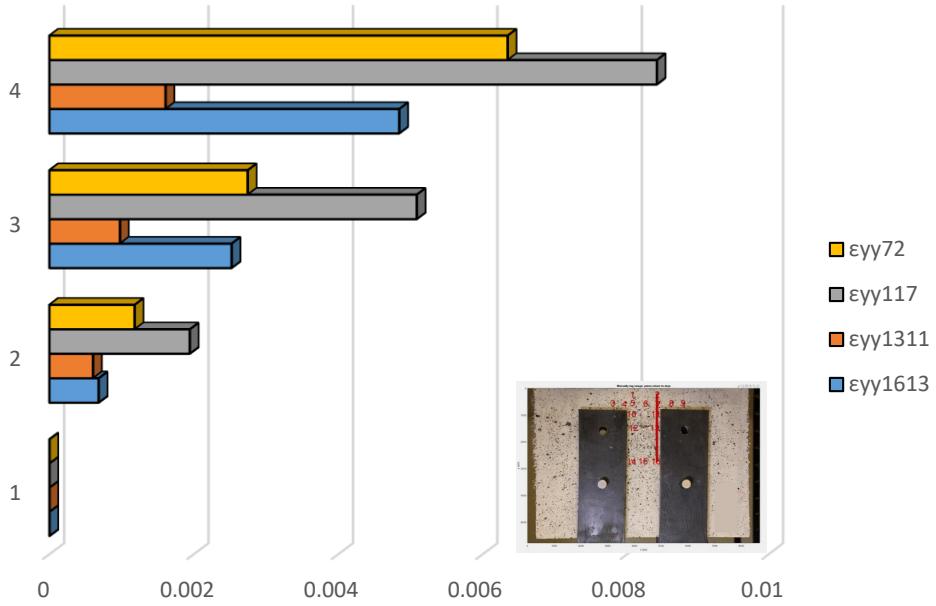

Figure A - 125 Demonstration of ε_{yy} on right vertical layer for Part 1 of specimen CMK2-5-A (Case 1).

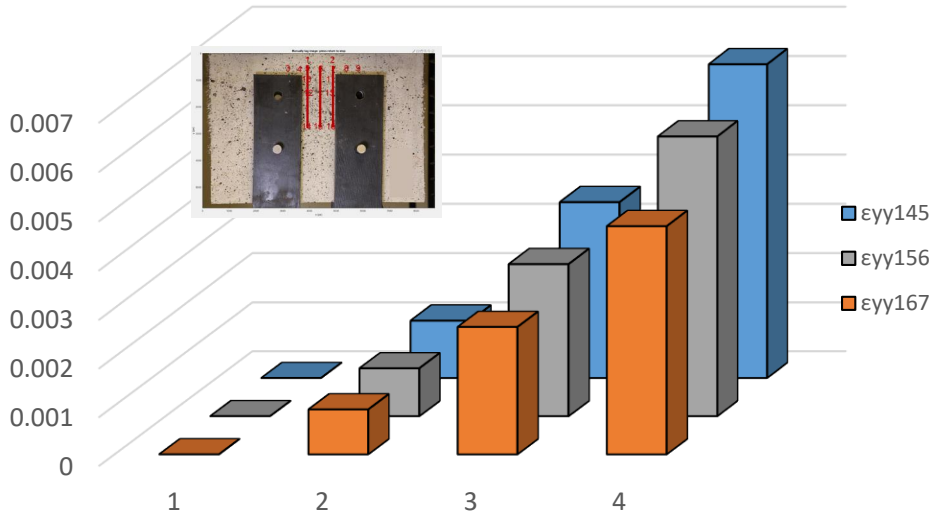

Figure A - 126 Comparison of ε_{yy} between three equidistant layers for Part 1 of specimen CMK2-5-A (Case 1).

Detailed analysis in three milestone points – Case 2

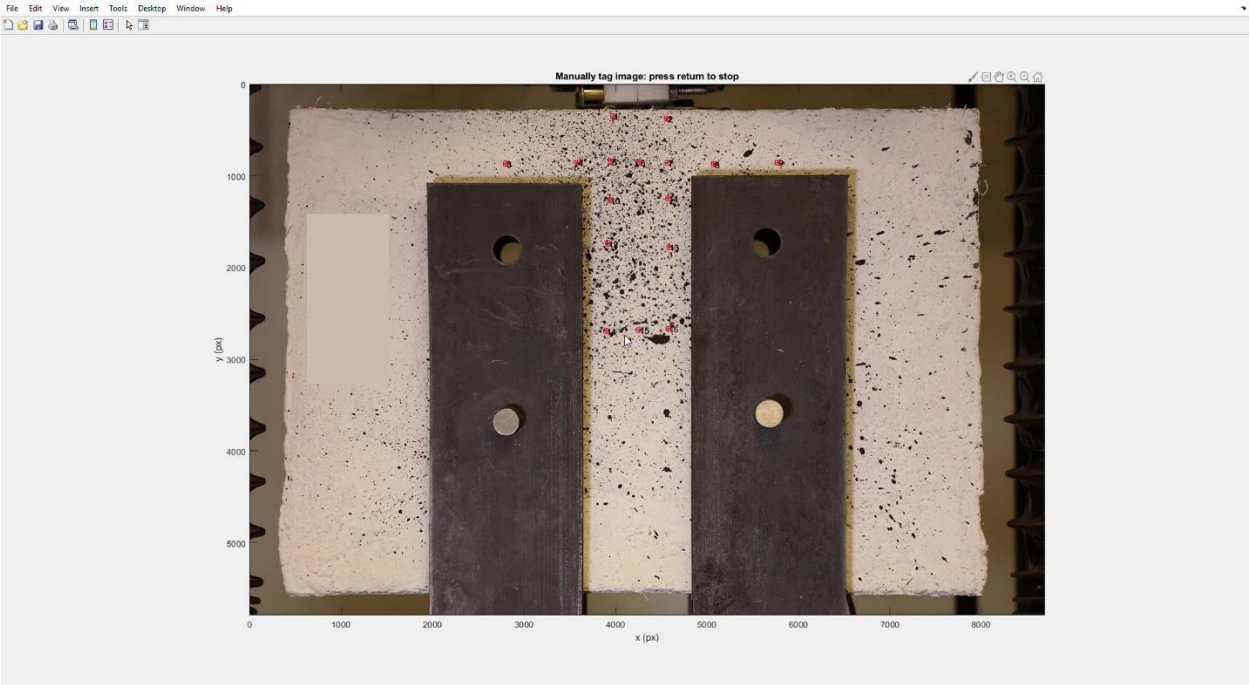

Figure A - 127 Locations of Points of Interest for Part 1 of specimen CMK2-5-A (Case 2).

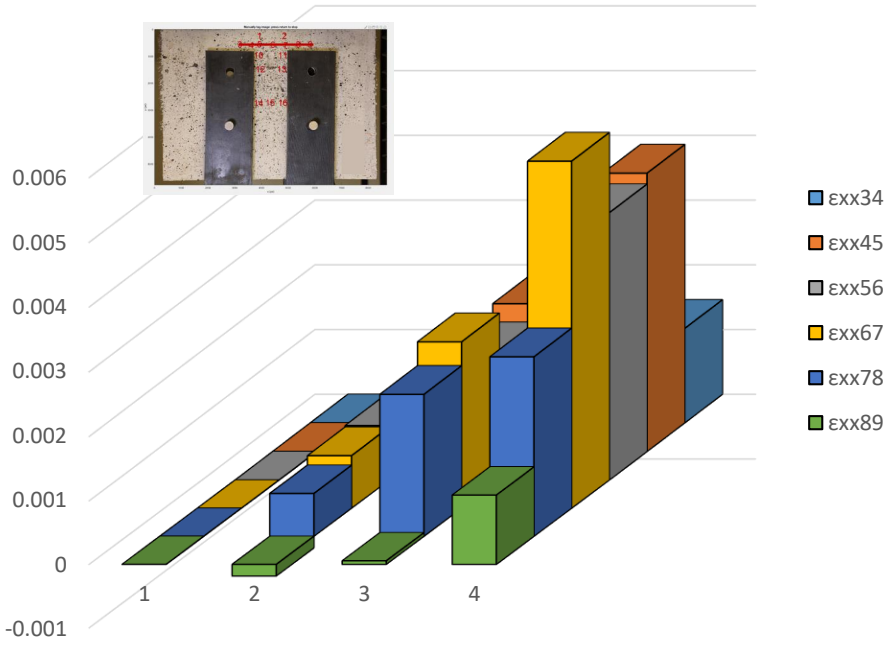

Figure A - 128 Demonstration of ε_{xx} along Layer 2 for Part 1 of specimen CMK2-5-A (Case 2).

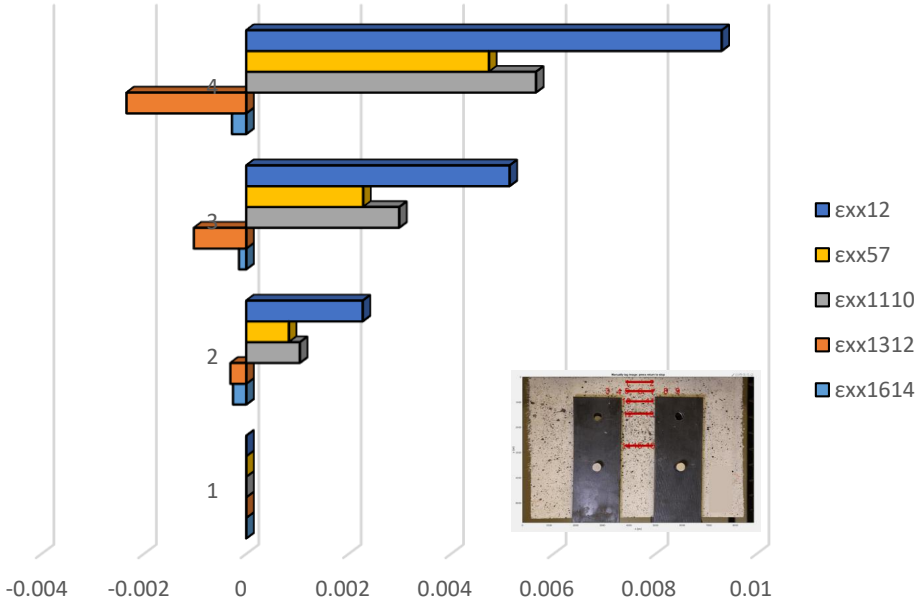

Figure A - 129 Comparison of ε_{xx} between horizontal layers for Part 1 of specimen CMK2-5-A (Case 2).

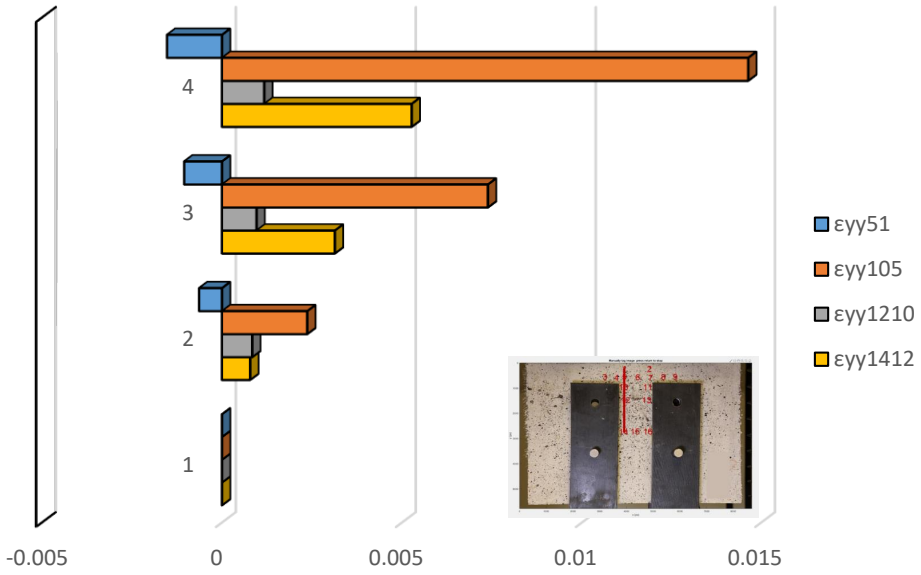

Figure A - 130 Demonstration of εyy on left vertical layer for Part 1 of specimen CMK2-5-A (Case 2).

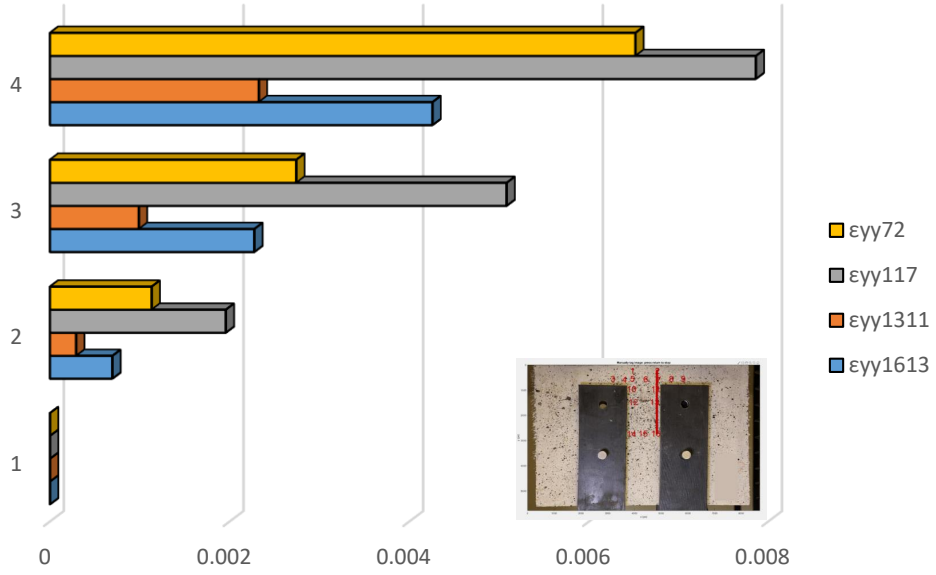

Figure A - 131 Demonstration of ε_{yy} on right vertical layer for Part 1 of specimen CMK2-5-A (Case 2).

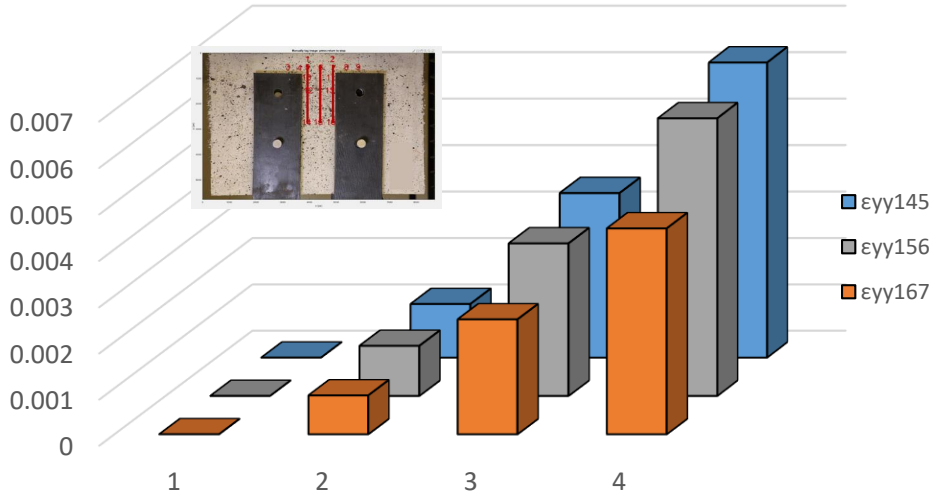

Figure A - 132 Comparison of ε_{yy} between three equidistant layers for Part 1 of specimen CMK2-5-A (Case 2).

Detailed analysis in three milestone points – Case 3

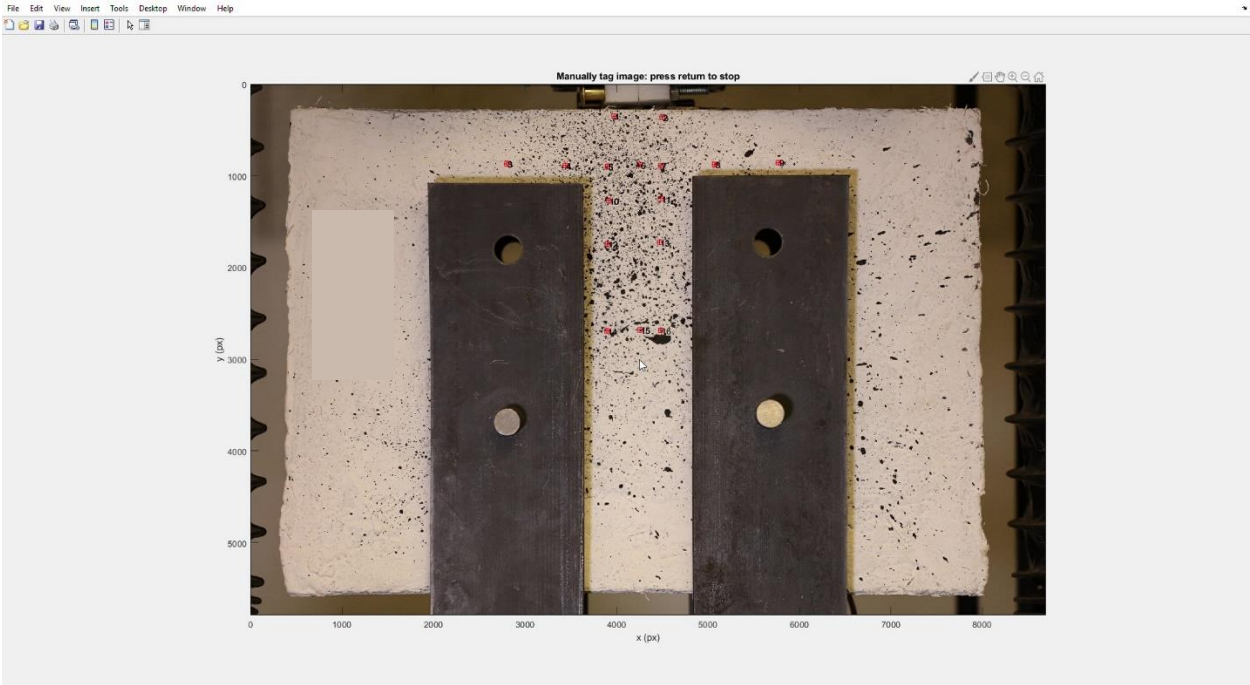

Figure A - 133 Locations of Points of Interest for Part 1 of specimen CMK2-5-A (Case 3).

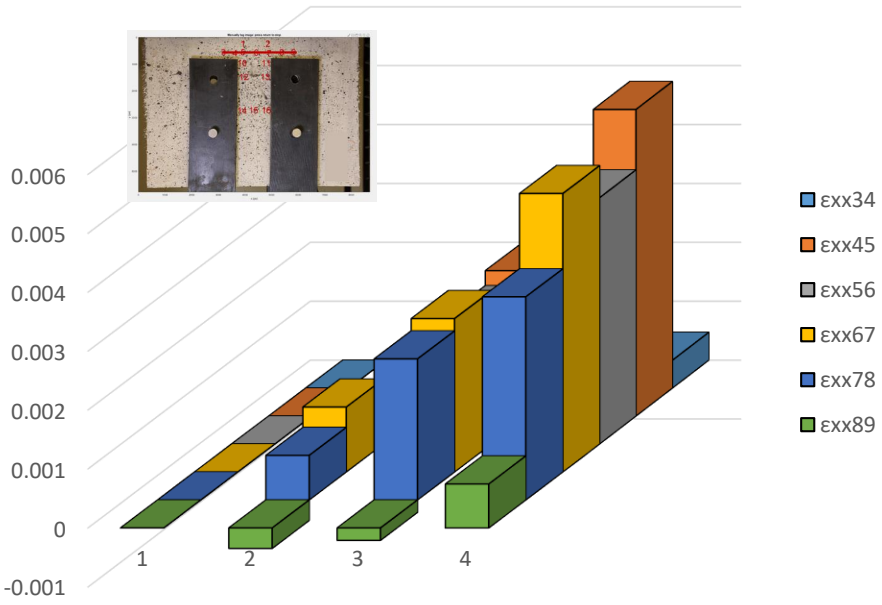

Figure A - 134 Demonstration of ε_{xx} along Layer 2 for Part 1 of specimen CMK2-5-A (Case 3).

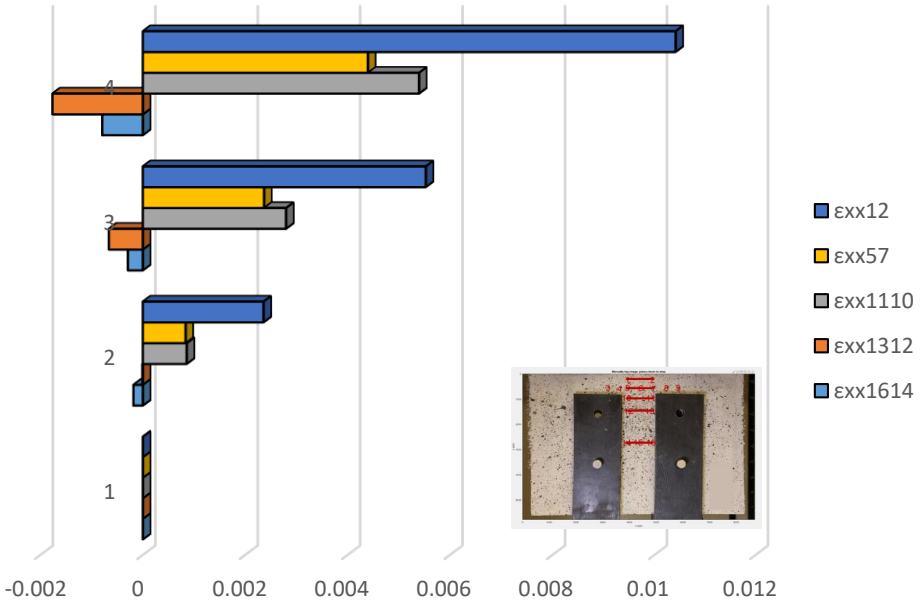

Figure A - 135 Comparison of ε_{xx} between horizontal layers for Part 1 of specimen CMK2-5-A (Case 3).

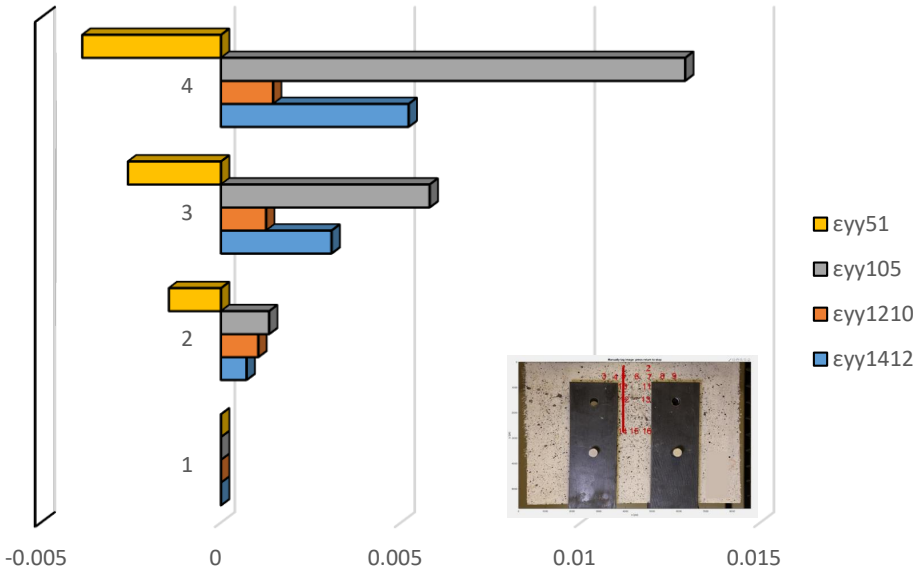

Figure A - 136 Demonstration of εyy on left vertical layer for Part 1 of specimen CMK2-5-A (Case 3).

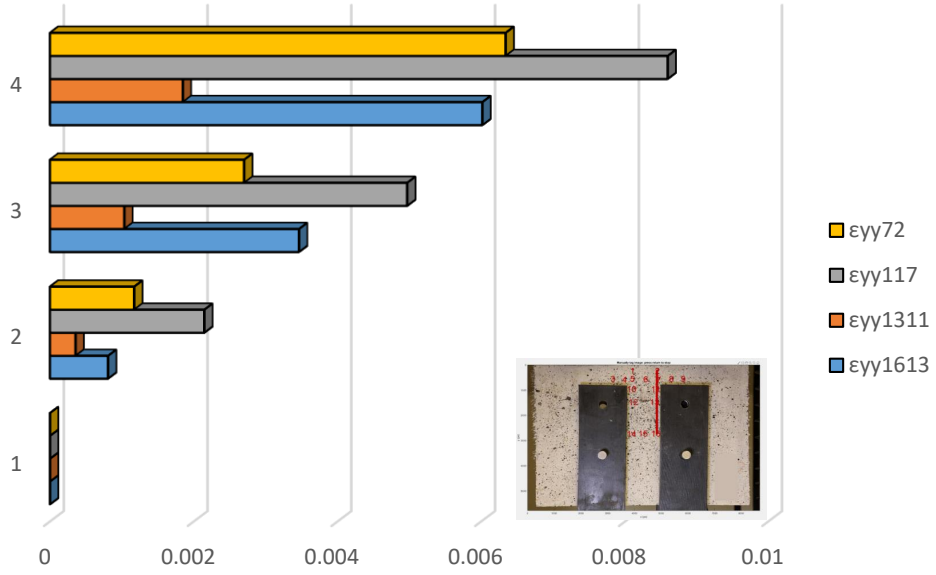

Figure A - 137 Demonstration of ε_{yy} on right vertical layer for Part 1 of specimen CMK2-5-A (Case 3).

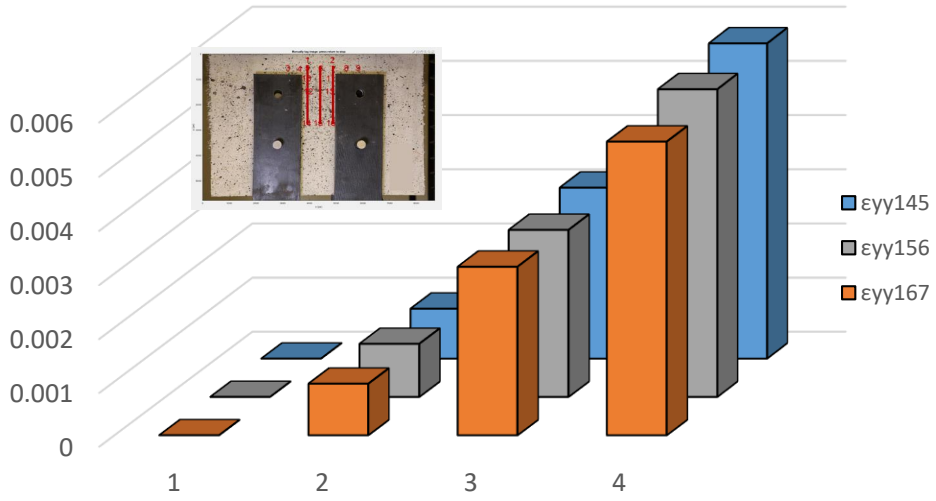

Figure A - 138 Comparison of ε_{yy} between three equidistant layers for Part 1 of specimen CMK2-5-A (Case 3).

Specimen CMF2-5-A (Part 2)

Complete analysis

Figure A - 139 Locations of points of interest for Part 2 of specimen CMF2-5-A (Complete analysis).

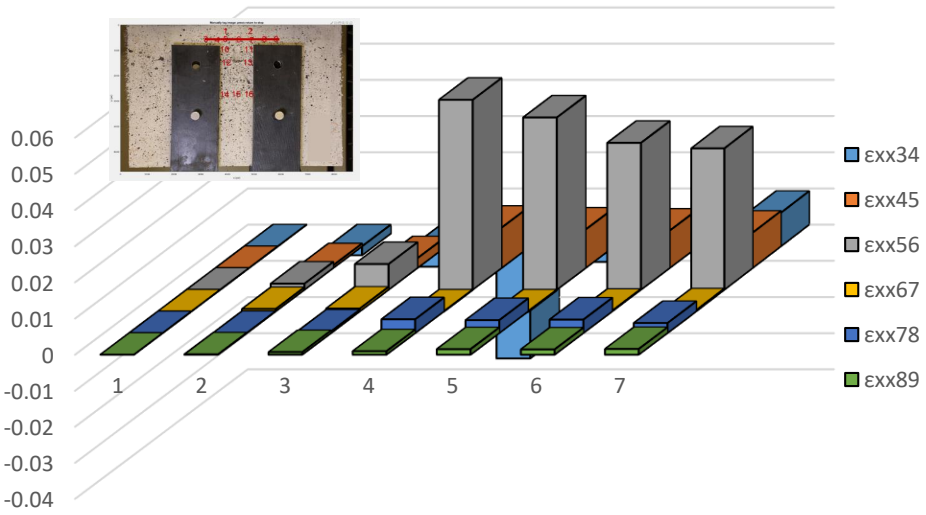

Figure A - 140 Demonstration of ε_{xx} along Layer 2 for Part 2 of specimen CMK2-5-A (Complete analysis).

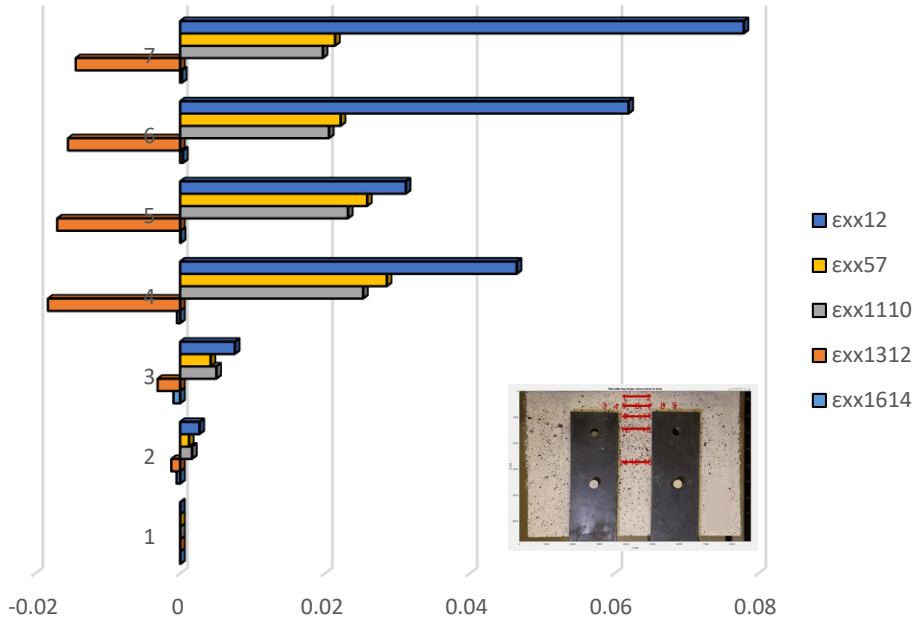

Figure A - 141 Comparison of ε_{xx} between horizontal layers for Part 2 of specimen CMK2-5-A (Complete analysis).

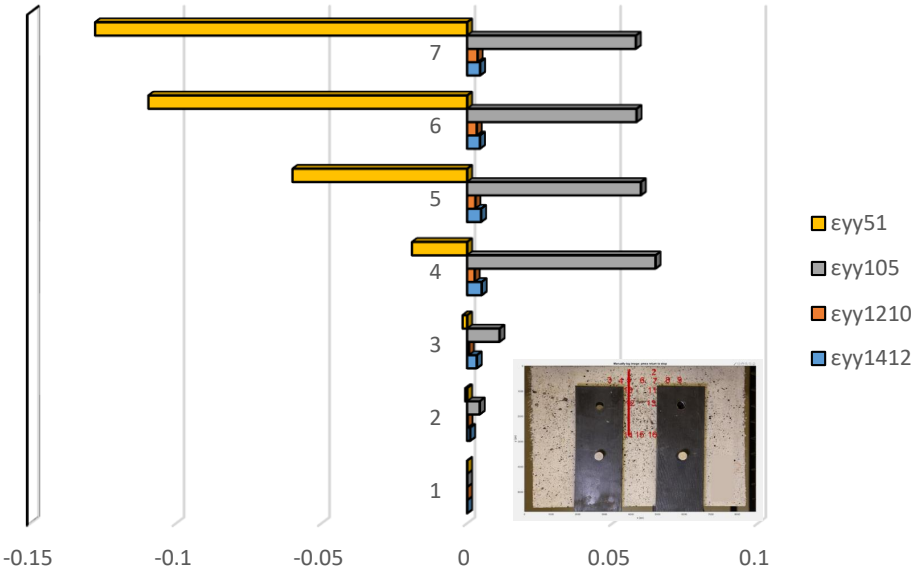

Figure A - 142 Demonstration of ε_{yy} on left vertical layer for Part 2 of specimen CMK2-5-A (Complete analysis).

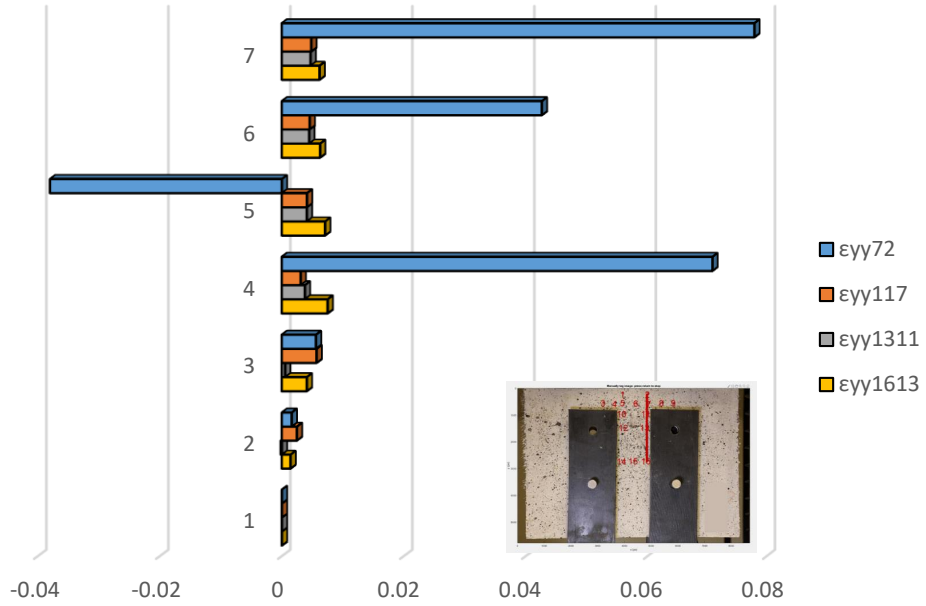

Figure A - 143 Demonstration of ε_{yy} on right vertical layer for Part 2 of specimen CMK2-5-A (Complete analysis).

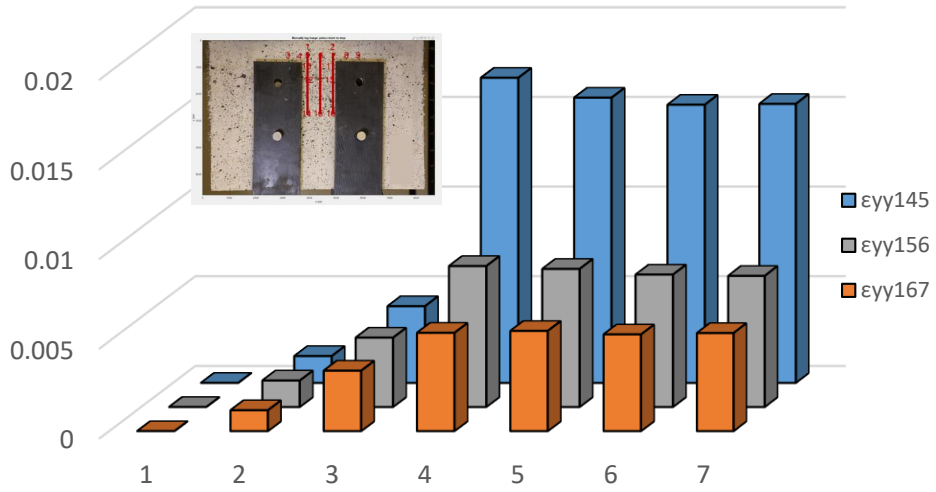

Figure A - 144 Comparison of ε_{yy} between three equidistant layers for Part 2 of specimen CMK2-5-A (Complete analysis).

Detailed analysis in three milestone points – Case 1

Figure A - 145 Locations of points of interest for Part 2 of specimen CMF2-5-A (Case 1).

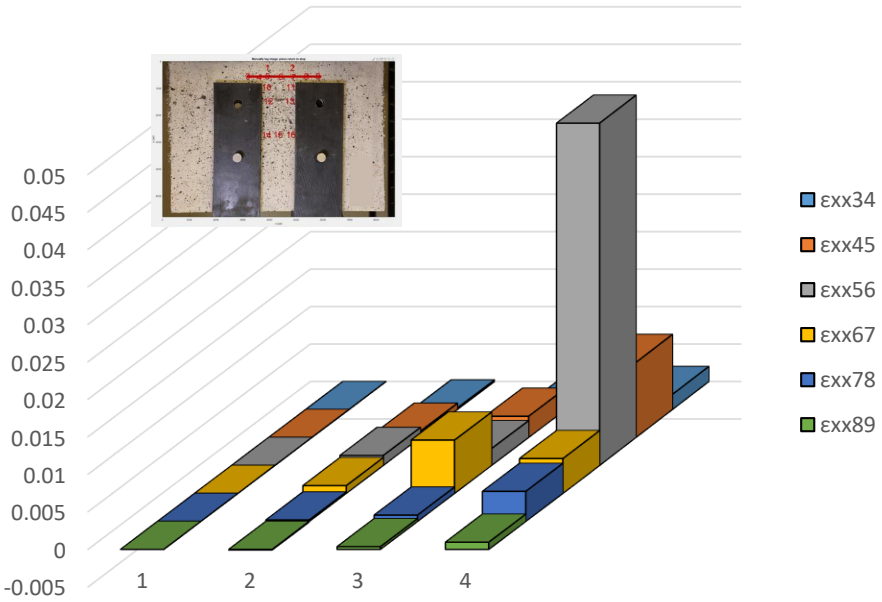

Figure A - 146 Demonstration of ε_{xx} along Layer 2 for Part 2 of specimen CMK2-5-A (Case 1).

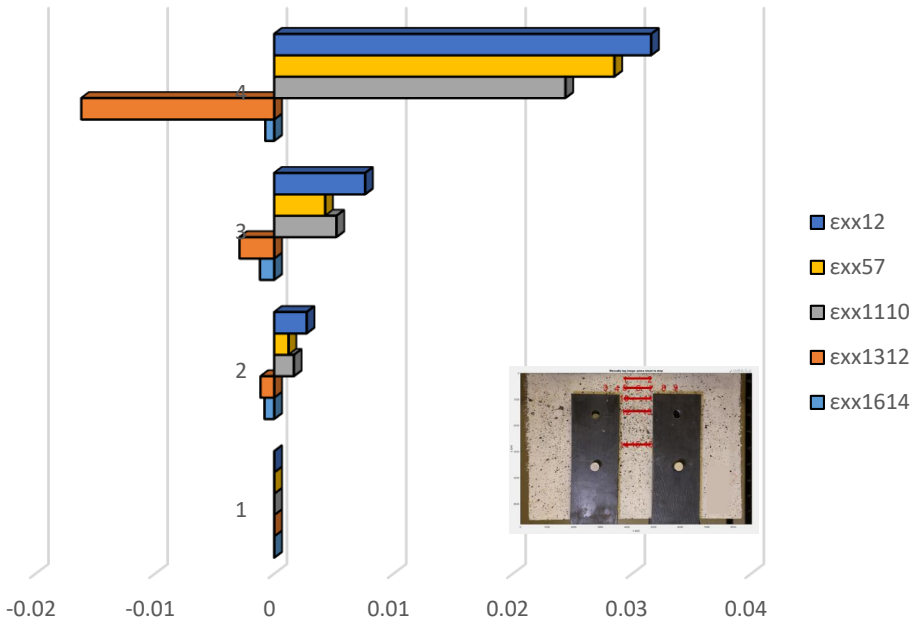

Figure A - 147 Comparison of ε_{xx} between horizontal layers for Part 2 of specimen CMK2-5-A (Case 1).

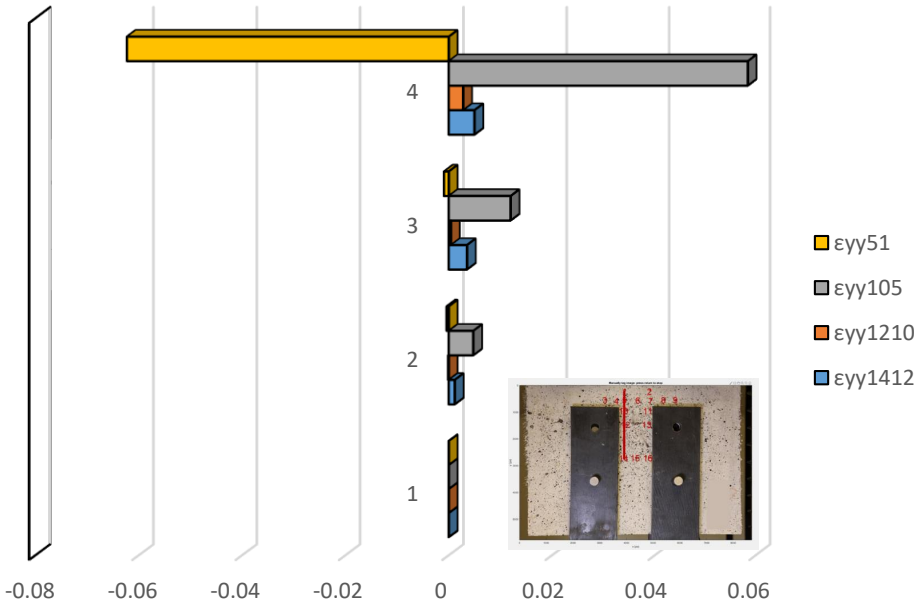

Figure A - 148 Demonstration of ε_{yy} on left vertical layer for Part 2 of specimen CMK2-5-A (Case 1).

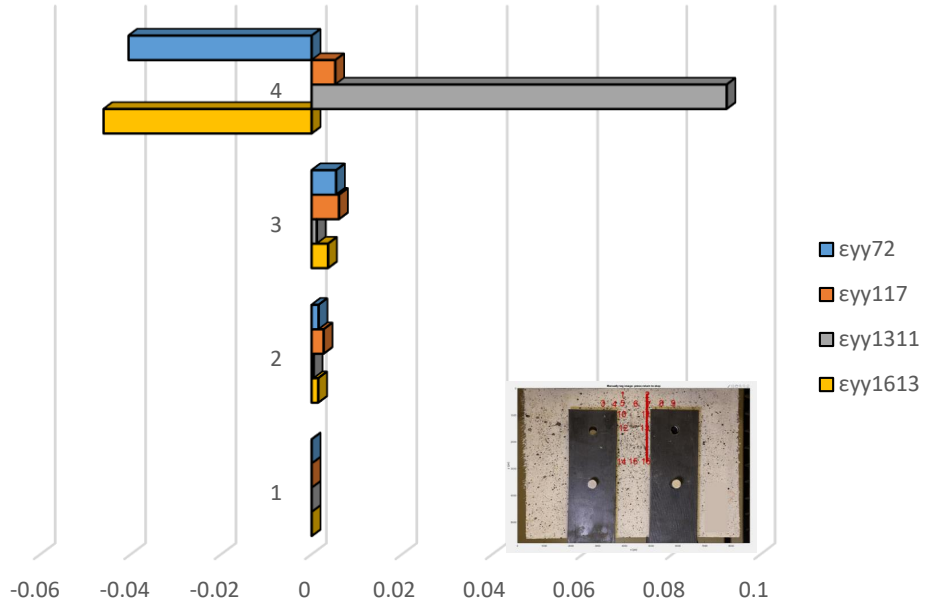

Figure A - 149 Demonstration of ε_{yy} on right vertical layer for Part 2 of specimen CMK2-5-A (Case 1).

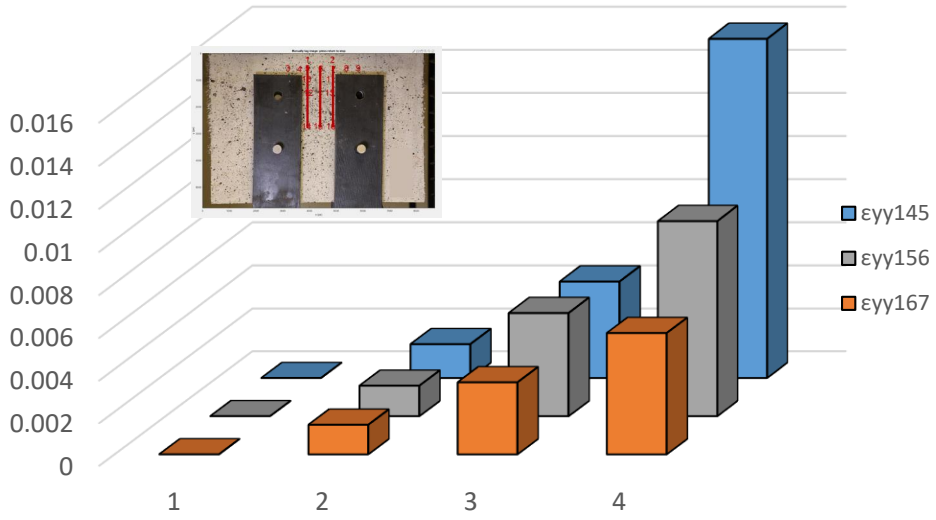

Figure A - 150 Comparison of ε_{yy} between three equidistant layers for Part 2 of specimen CMK2-5-A (Case 1).

Detailed analysis in three milestone points – Case 2

Figure A - 151 Locations of points of interest for Part 2 of specimen CMF2-5-A (Case 2).

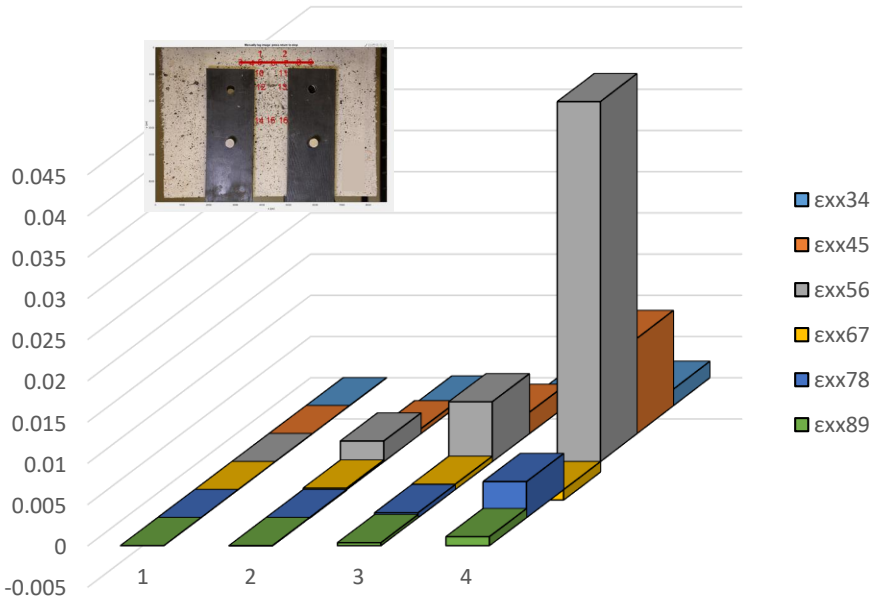

Figure A - 152 Demonstration of ε_{xx} along Layer 2 for Part 2 of specimen CMK2-5-A (Case 2).

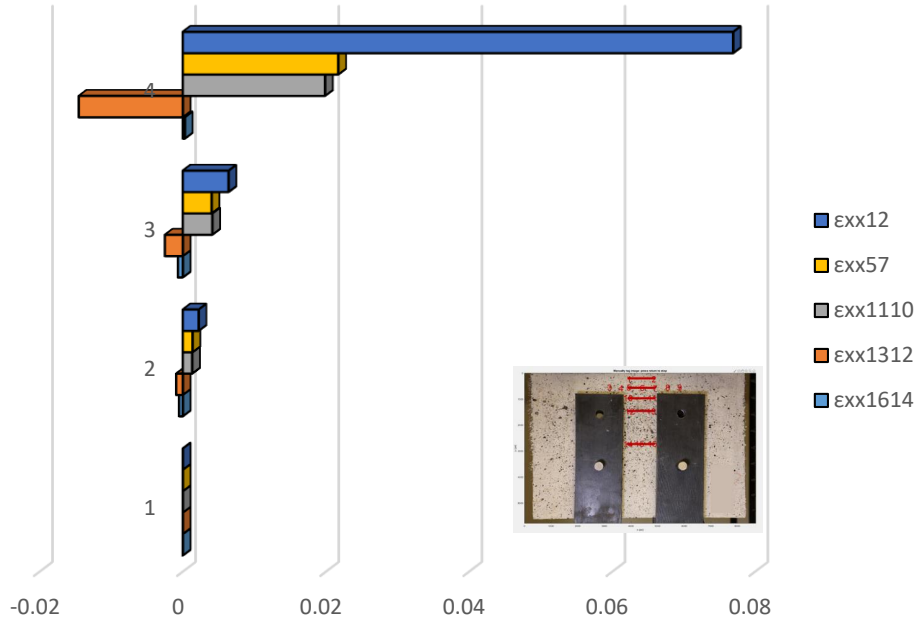

Figure A - 153 Comparison of ε_{xx} between horizontal layers for Part 2 of specimen CMK2-5-A (Case 2).

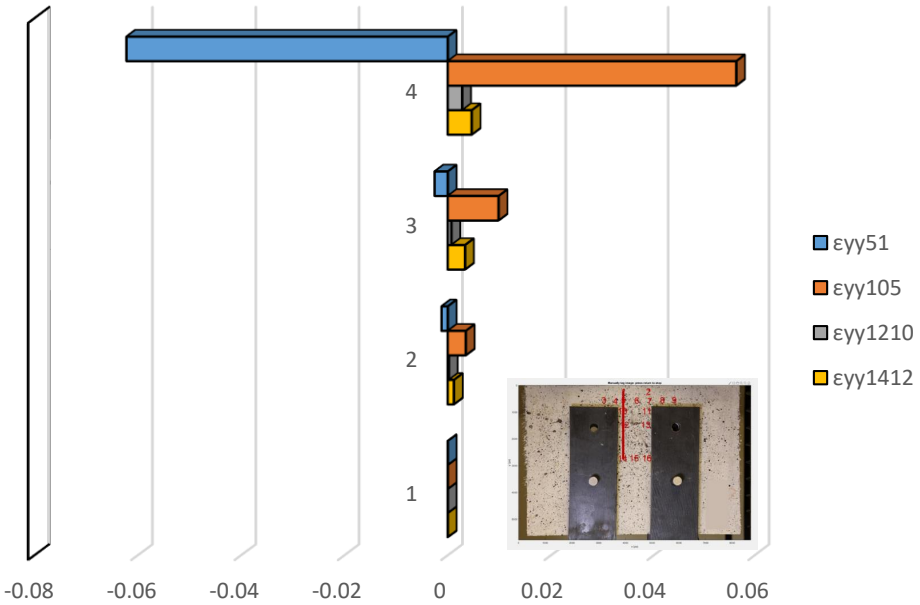

Figure A - 154 Demonstration of ε_{yy} on left vertical layer for Part 2 of specimen CMK2-5-A (Case 2).

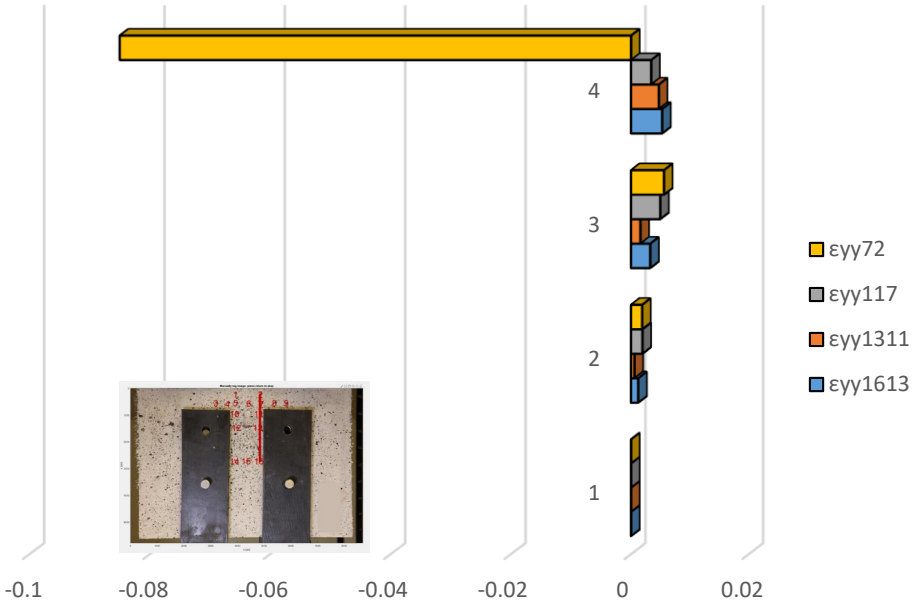

Figure A - 155 Demonstration of ε_{yy} on right vertical layer for Part 2 of specimen CMK2-5-A (Case 2).

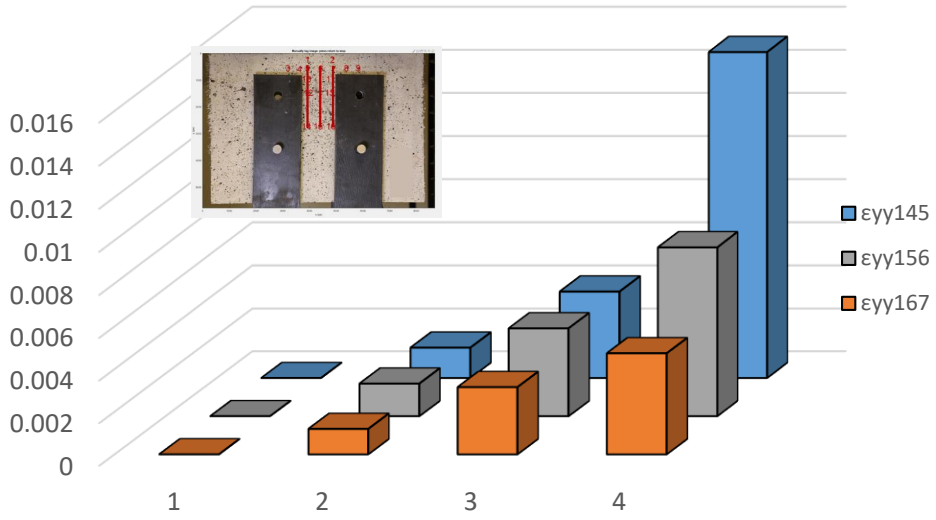

Figure A - 156 Comparison of ε_{yy} between three equidistant layers for Part 2 of specimen CMK2-5-A (Case 2).

Detailed analysis in three milestone points – Case 3

Figure A - 157 Locations of points of interest for Part 2 of specimen CMF2-5-A (Case 3).

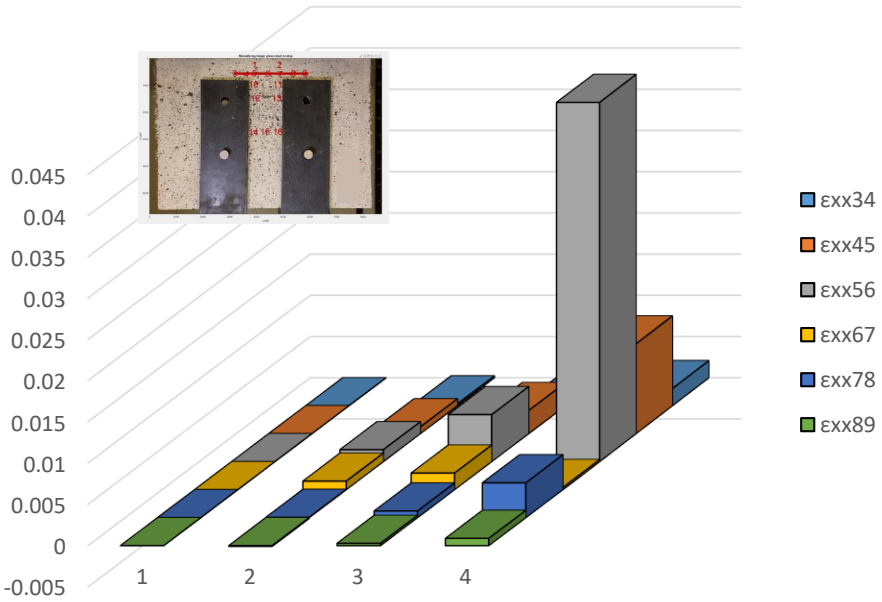

Figure A - 158 Demonstration of ε_{xx} along Layer 2 for Part 2 of specimen CMK2-5-A (Case 3).

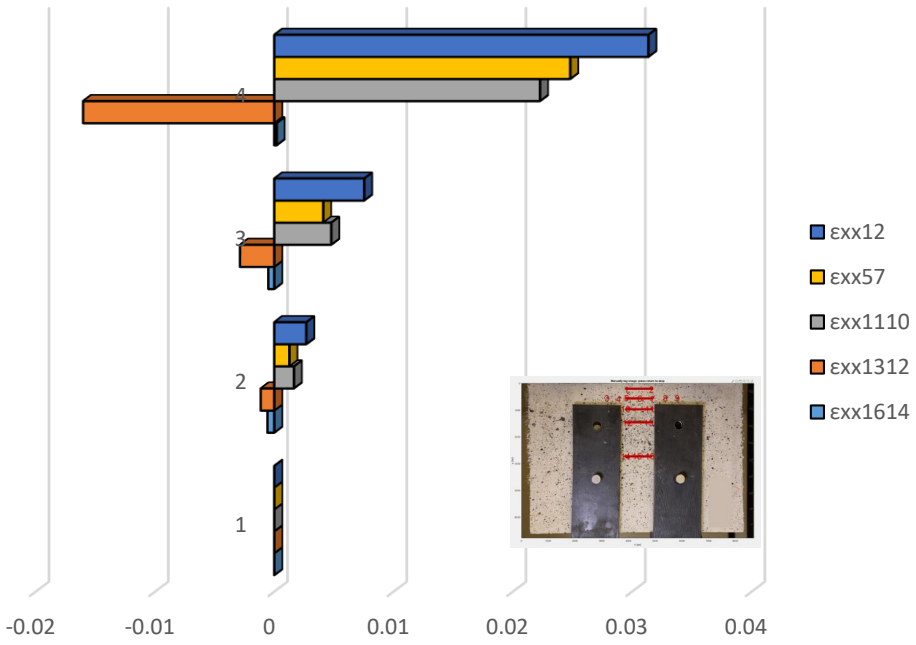

Figure A - 159 Comparison of ε_{xx} between horizontal layers for Part 2 of specimen CMK2-5-A (Case 3).

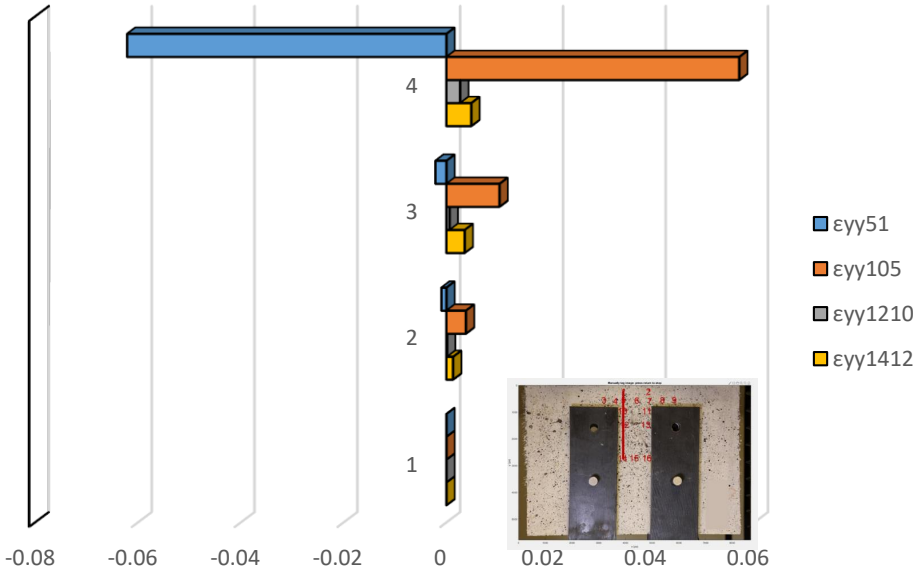

Figure A - 160 Demonstration of ε_{yy} on left vertical layer for Part 2 of specimen CMK2-5-A (Case 3).

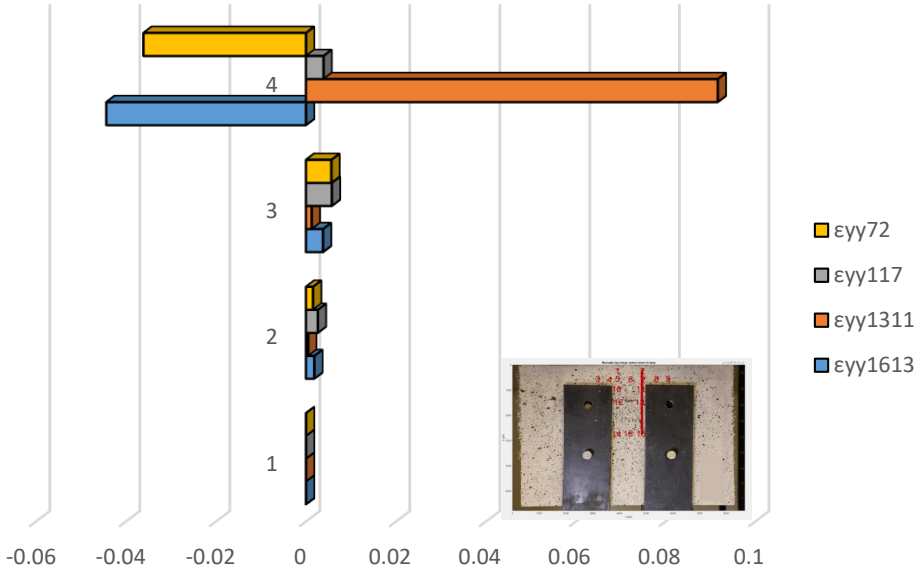

Figure A - 161 Demonstration of ε_{yy} on right vertical layer for Part 2 of specimen CMK2-5-A (Case 3).

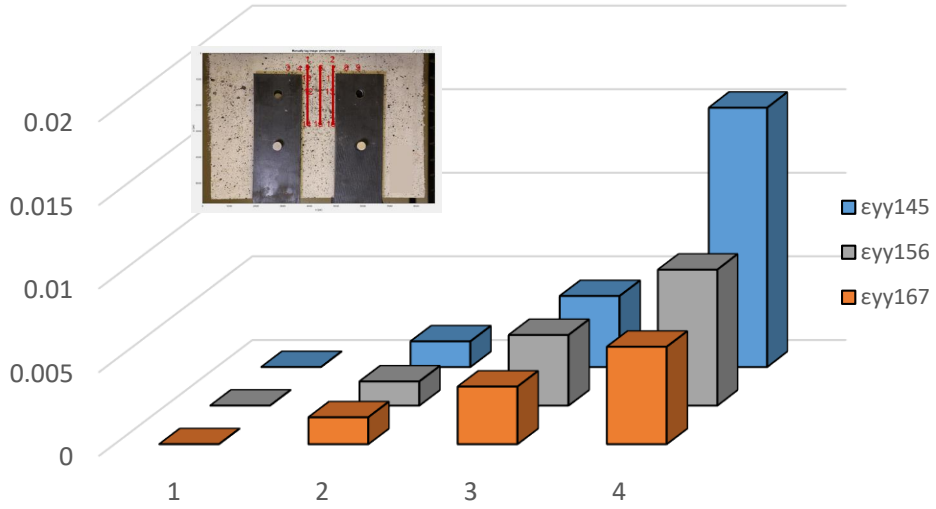

Figure A - 162 Comparison of ε_{yy} between three equidistant layers for Part 2 of specimen CMK2-5-A (Case 3).

Specimen IHNJ1-5-A

Complete analysis

Figure A - 163 Locations of Points of Interest for specimen IHNJ1-5-A (Complete Analysis).

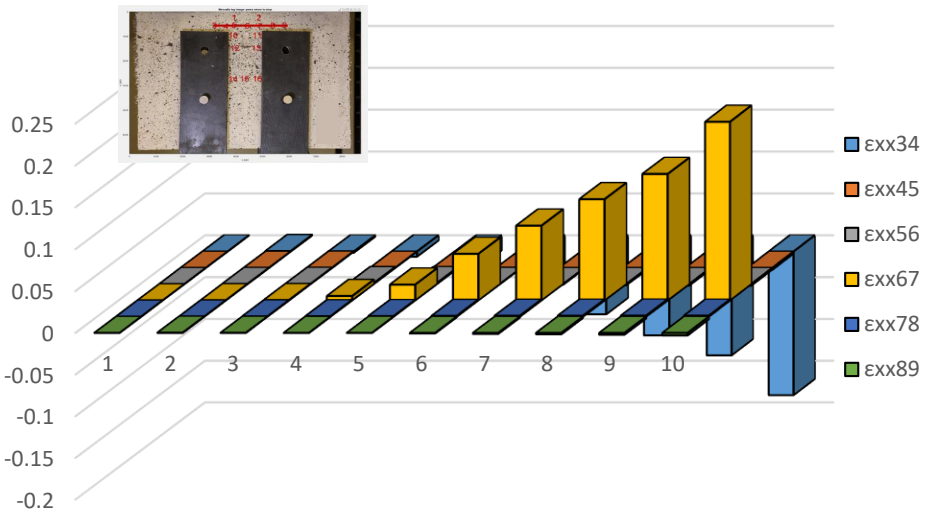

Figure A - 164 Demonstration of ε_{xx} along Layer 2 (IHNJ1-5-A – Complete analysis).

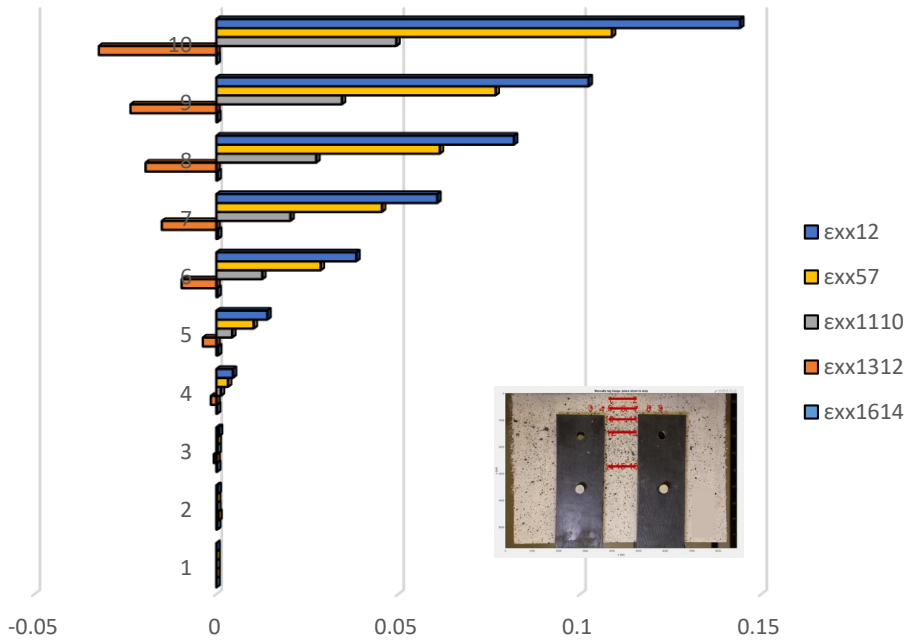

Figure A - 165 Comparison of ε_{xx} between horizontal layers (IHNJ1-5-A – Complete analysis).

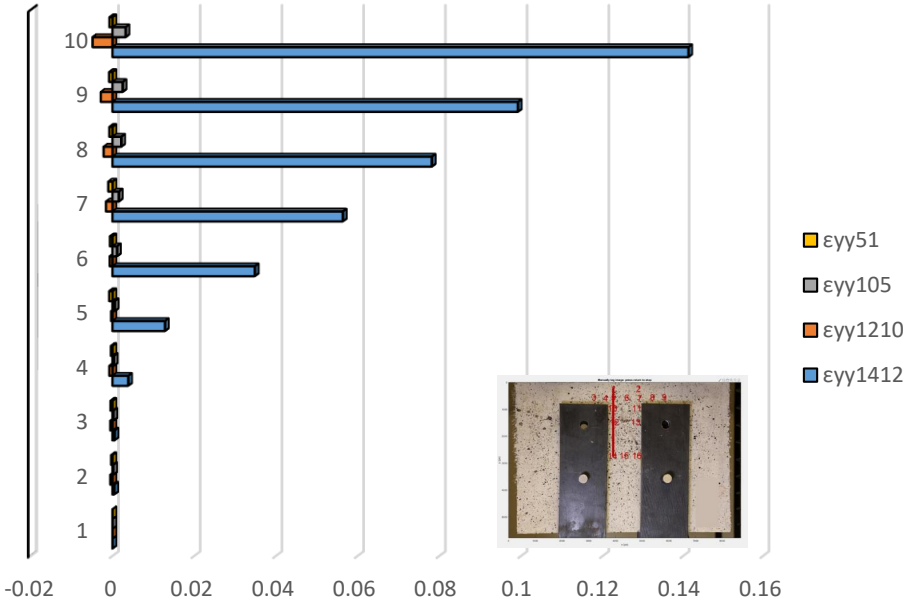

Figure A - 166 Demonstration of ε_{yy} on left vertical layer (IHNJ1-5-A – Complete analysis).

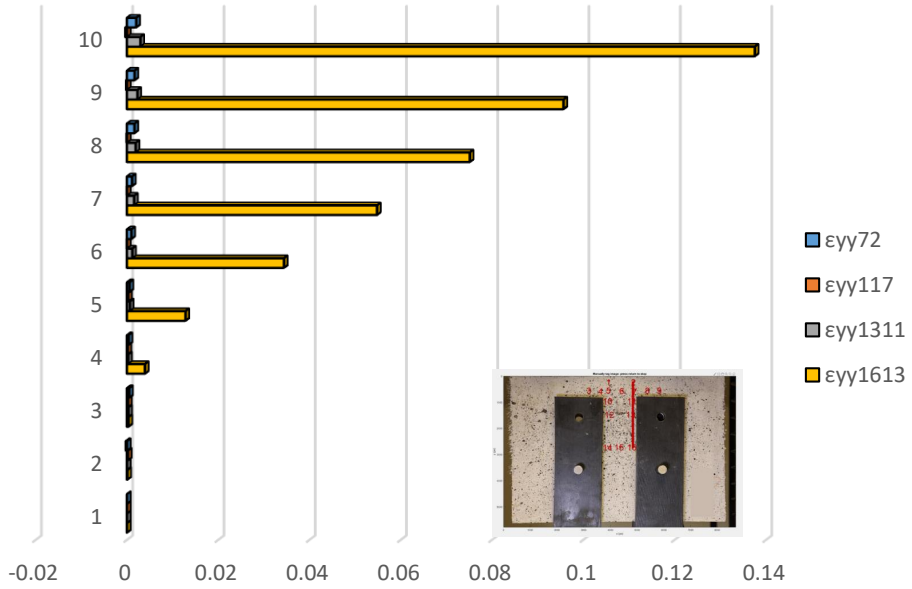

Figure A - 167 Demonstration of ε_{yy} on right vertical layer (IHNJ1-5-A – Complete analysis).

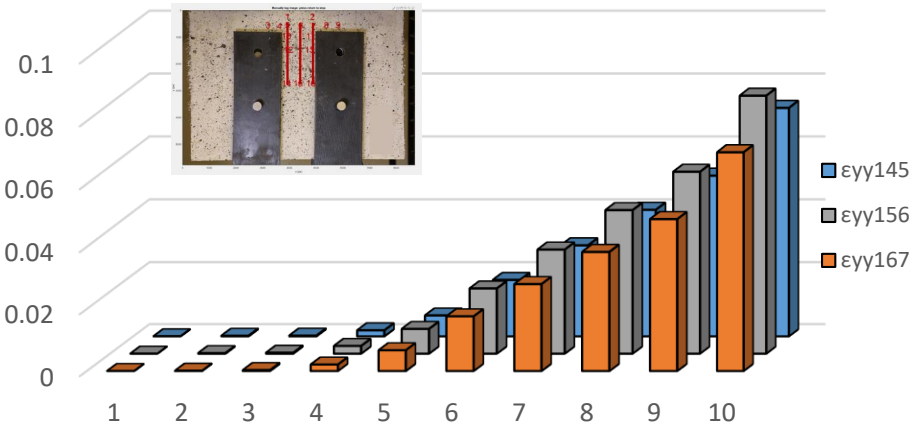

Figure A - 168 Comparison of ε_{yy} between three equidistant layers (IHNJ1-5-A – Complete analysis).

Detailed analysis in three milestone points – Case 1

Figure A - 169 Locations of POIs for specimen IHNJ1-5-A (Case 1)

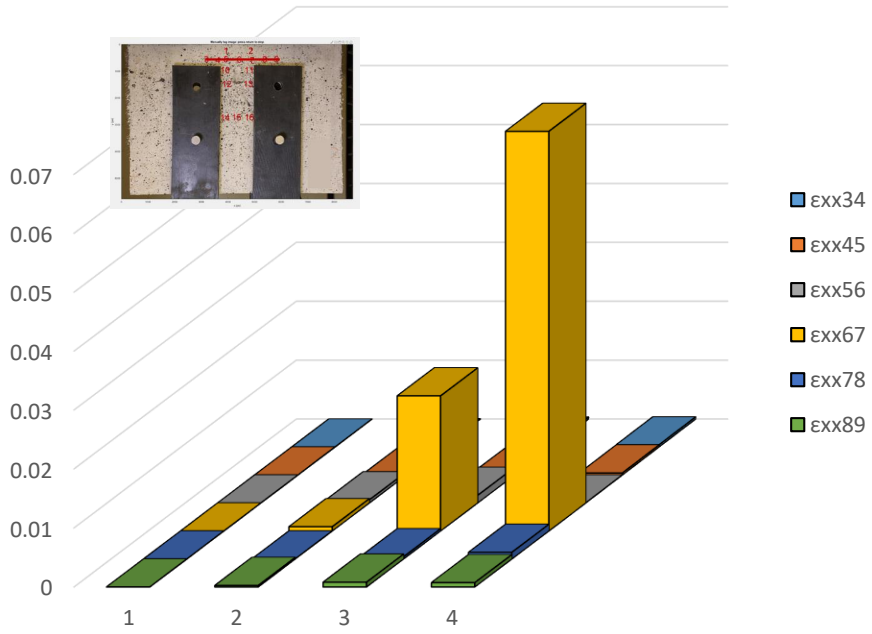

Figure A - 170 Demonstration of ε_{xx} along Layer 2 (IHNJ1-5-A – Case 1).

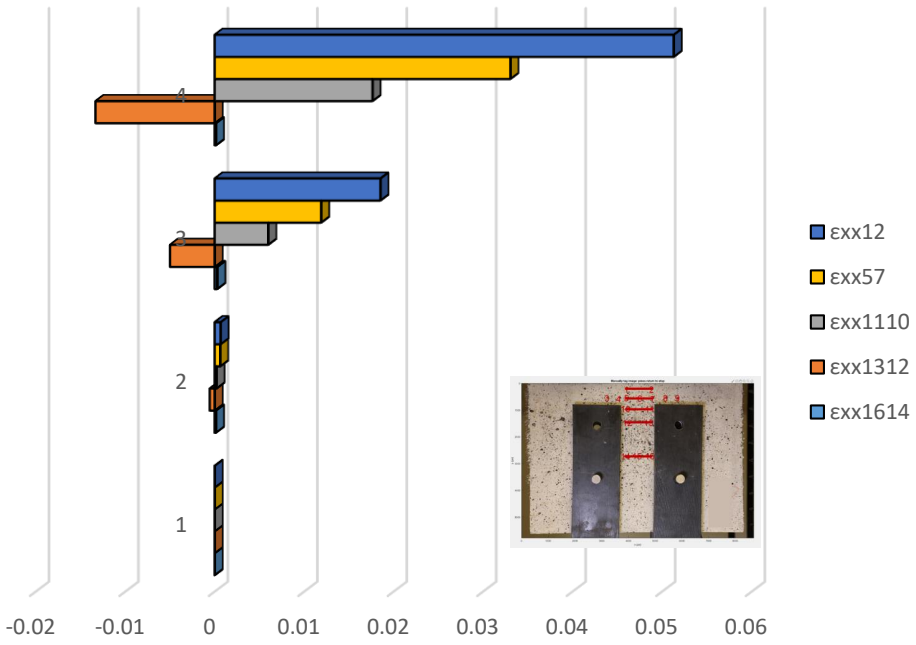

Figure A - 171 Comparison of ε_{xx} between horizontal layers (IHNJ1-5-A – Case 1).

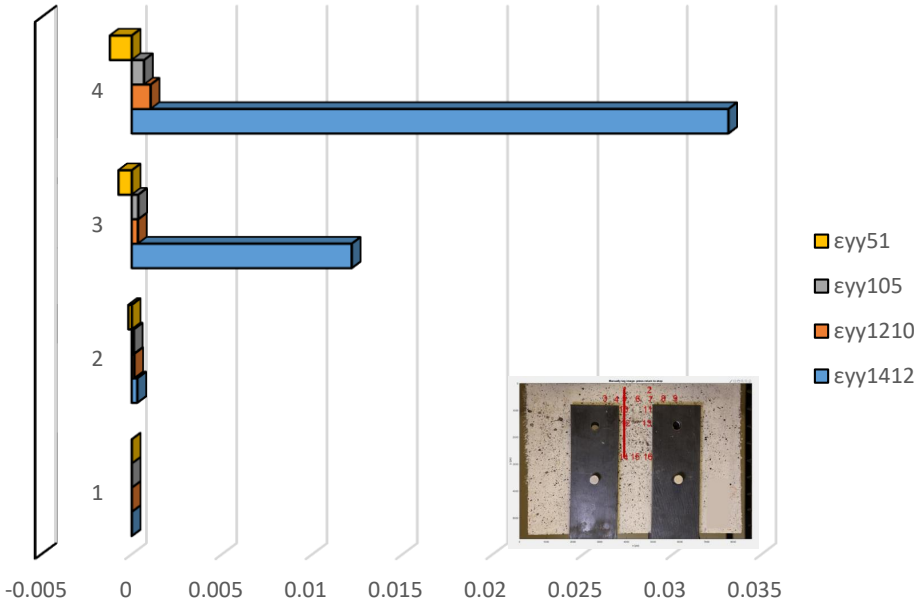

Figure A - 172 Demonstration of εyy on left vertical layer (IHNJ1-5-A – Case 1).

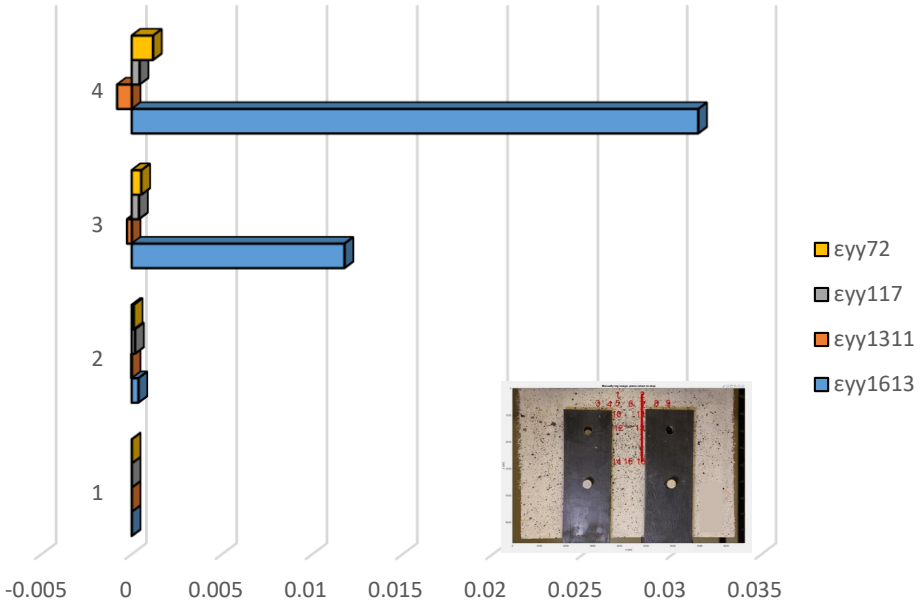

Figure A - 173 Demonstration of ε_{yy} on right vertical layer (IHNJ1-5-A – Case 1).

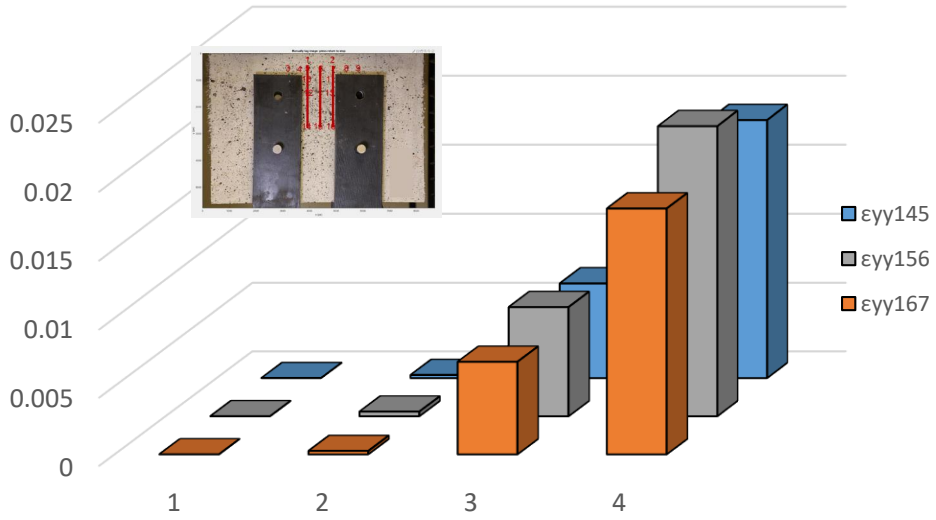

Figure A - 174 Comparison of ε_{yy} between three equidistant layers (IHNJ1-5-A – Case 1).

Detailed analysis in three milestone points – Case 2

Figure A - 175 Locations of POIs for specimen IHNJ1-5-A (Case 2)

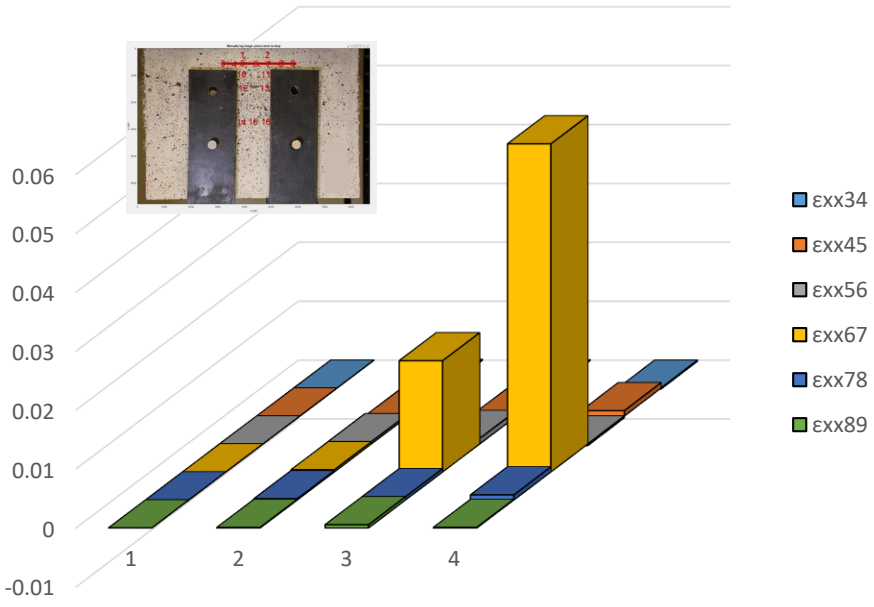

Figure A - 176 Demonstration of ε_{xx} along Layer 2 (IHNJ1-5-A – Case 2).

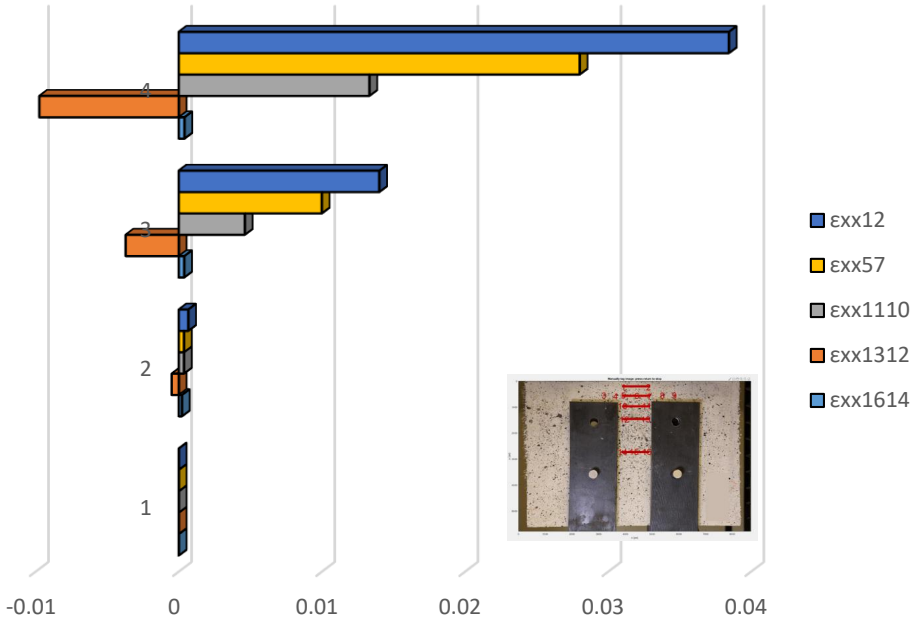

Figure A - 177 Comparison of ε_{xx} between horizontal layers (IHNJ1-5-A – Case 2).

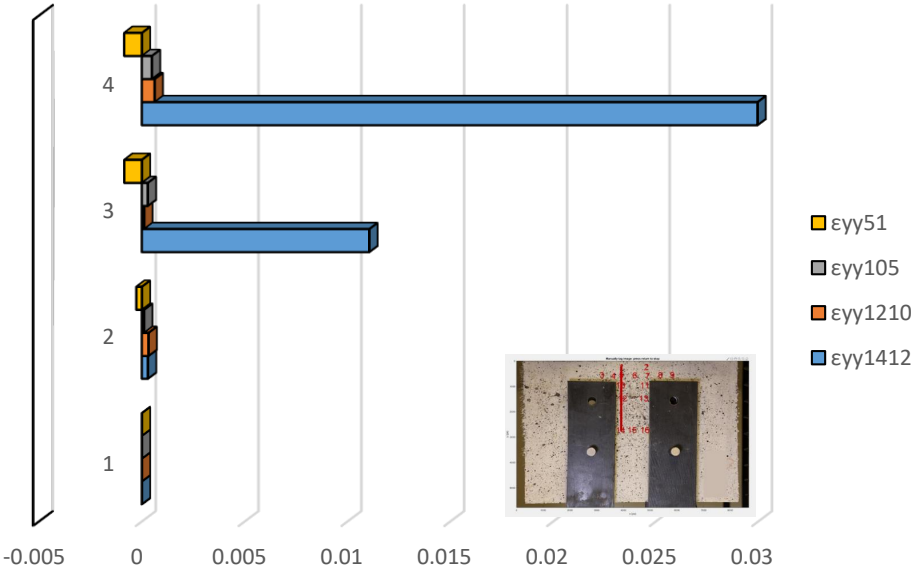

Figure A - 178 Demonstration of εyy on left vertical layer (IHNJ1-5-A – Case 2).

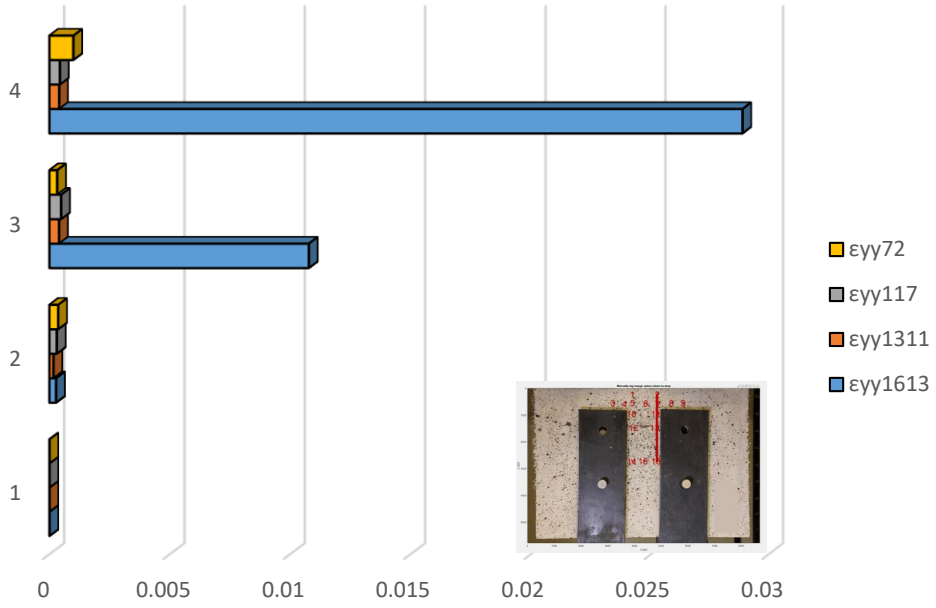

Figure A - 179 Demonstration of ε_{yy} on right vertical layer (IHNJ1-5-A – Case 2).

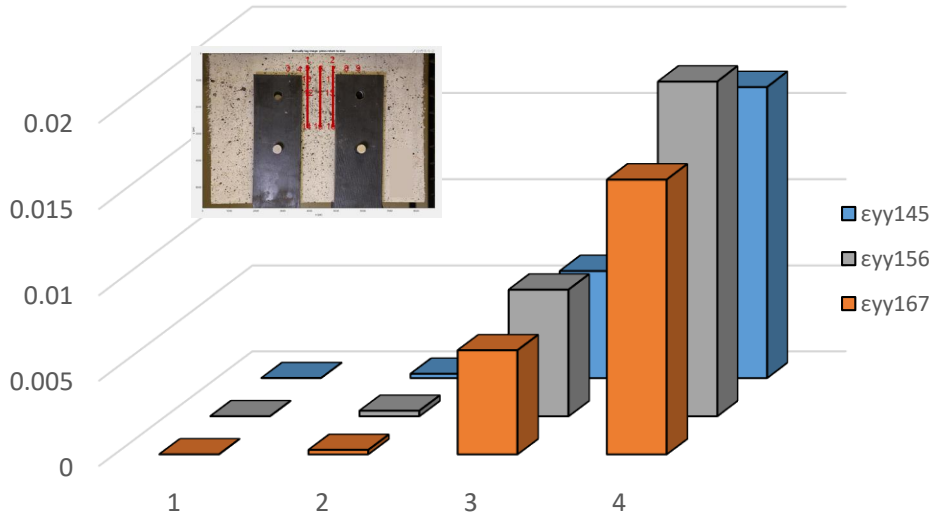

Figure A - 180 Comparison of ε_{yy} between three equidistant layers (IHNJ1-5-A – Case 2).

Detailed analysis in three milestone points – Case 3

Figure A - 181 Locations of POIs for specimen IHNJ1-5-A (Case 3)

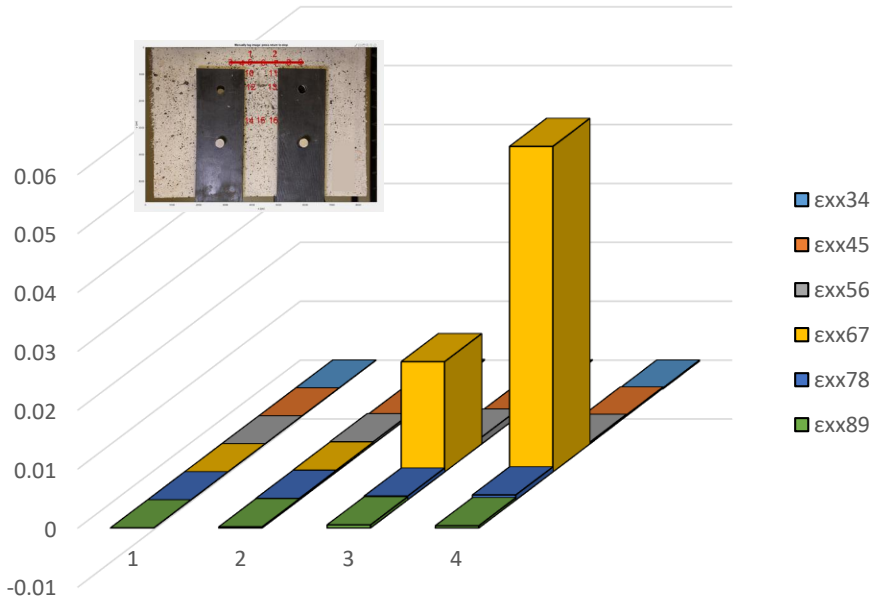

Figure A - 182 Demonstration of ε_{xx} along Layer 2 (IHNJ1-5-A – Case 3).

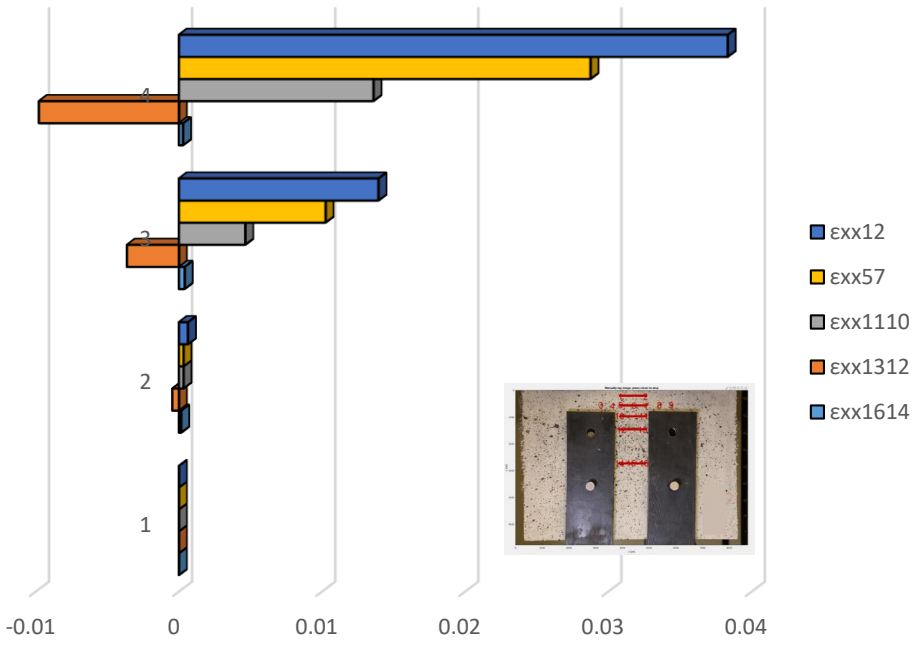

Figure A - 183 Comparison of ε_{xx} between horizontal layers (IHNJ1-5-A – Case 3).

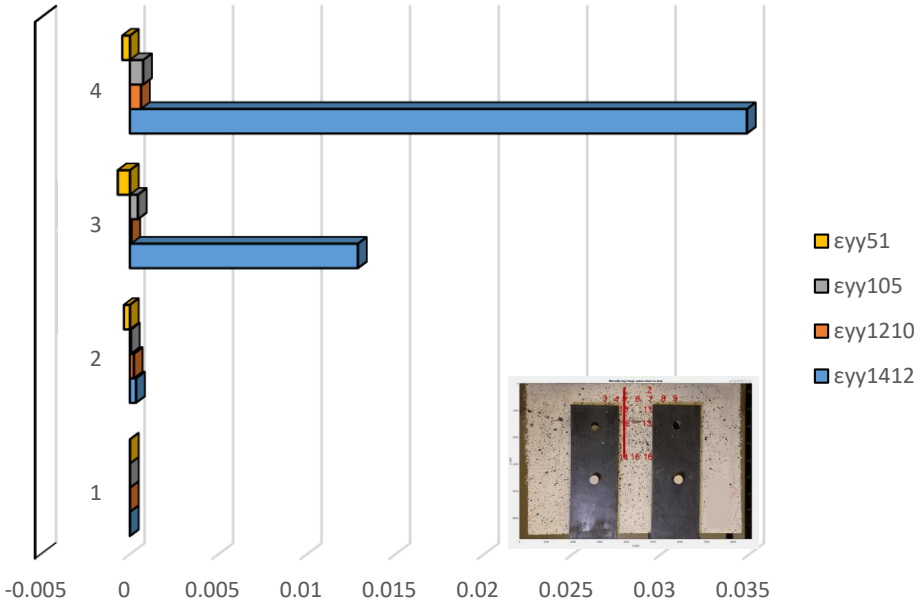

Figure A - 184 Demonstration of εyy on left vertical layer (IHNJ1-5-A – Case 3).

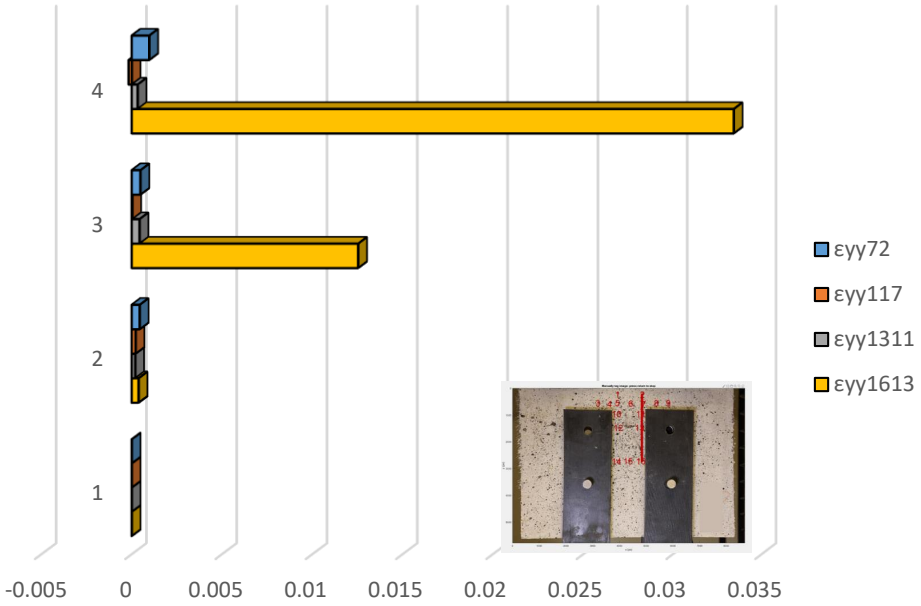

Figure A - 185 Demonstration of ε_{yy} on right vertical layer (IHNJ1-5-A – Case 3).

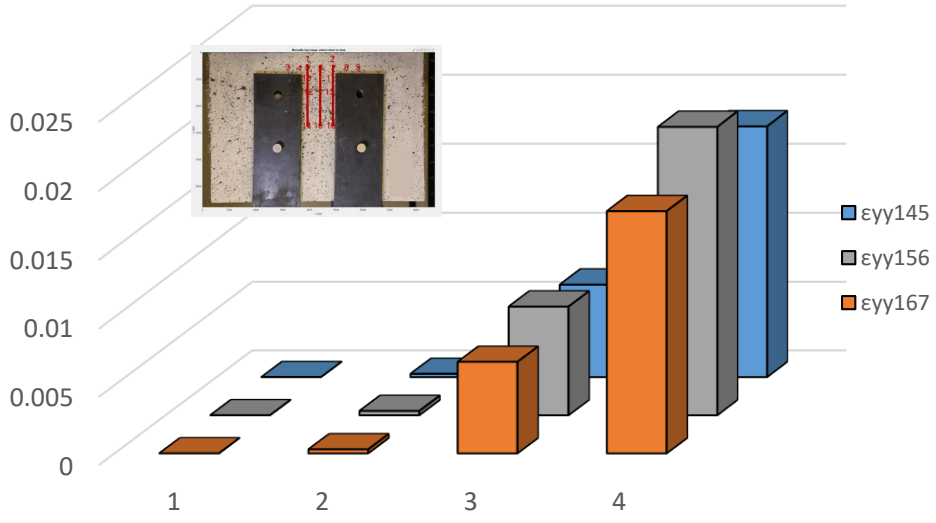

Figure A - 186 Comparison of ε_{yy} between three equidistant layers (IHNJ1-5-A – Case 1).

Specimen IHNJ1-5-B

Complete analysis

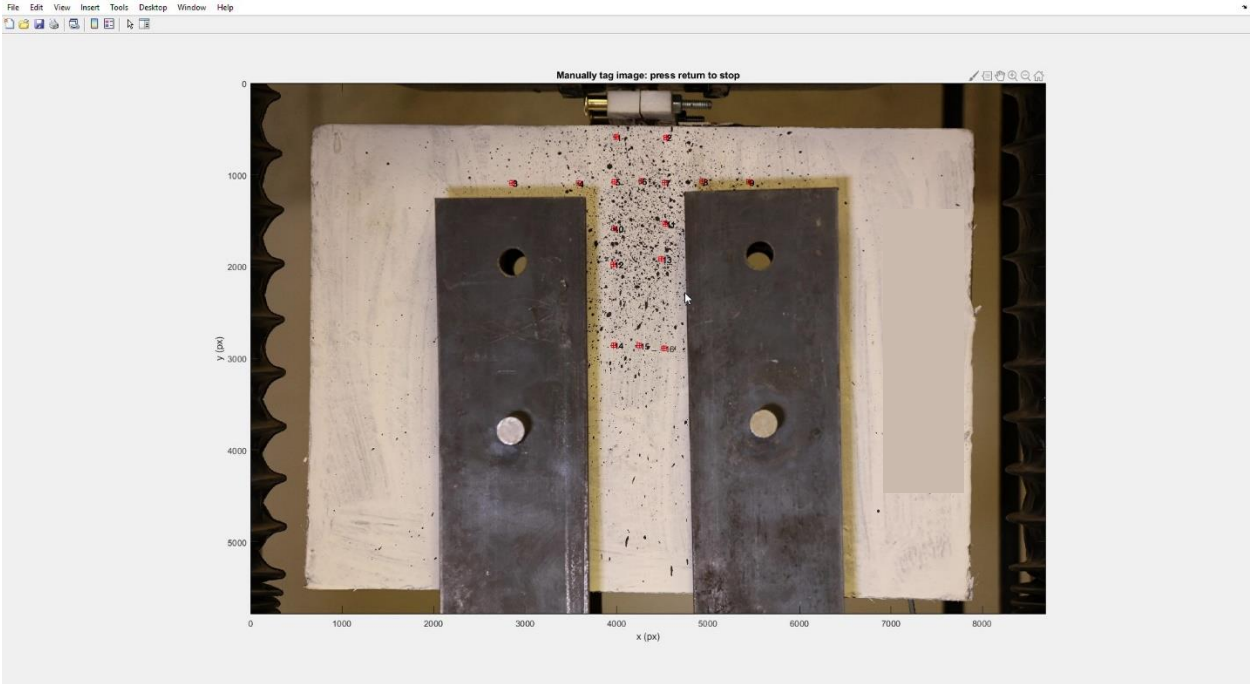

Figure A - 187 Locations of Points of Interest for specimen IHNJ1-5-B (Complete Analysis).

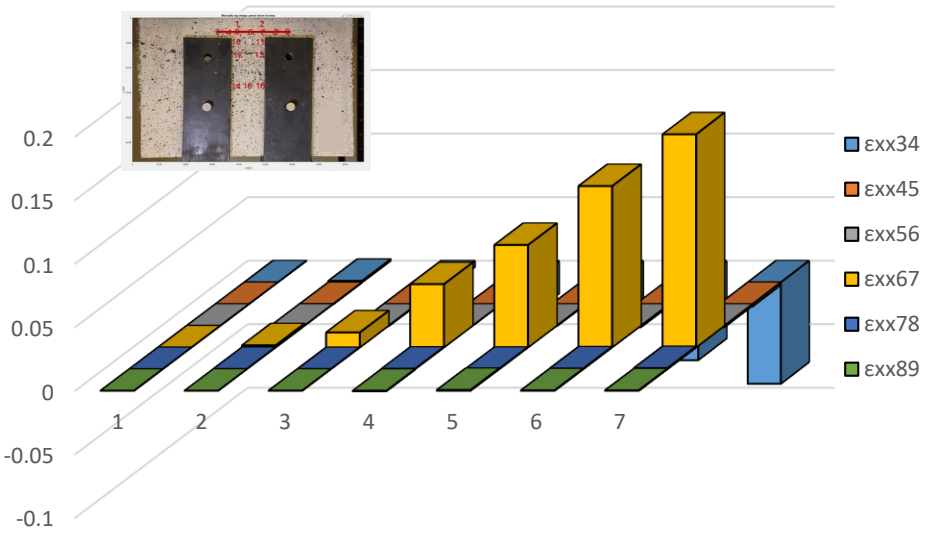

Figure A - 188 Demonstration of ε_{xx} along Layer 2 (IHNJ1-5-B – Complete analysis).

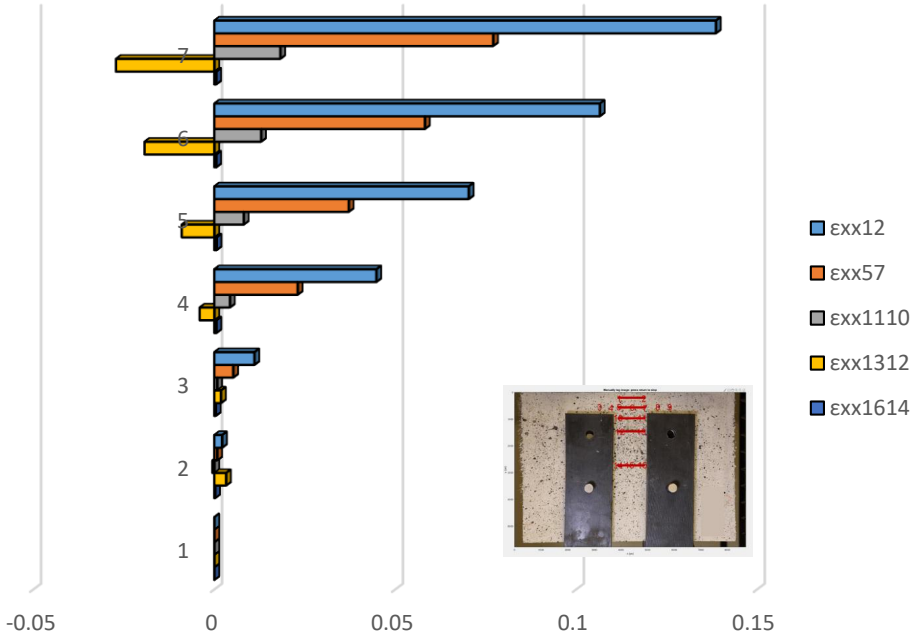

Figure A - 189 Comparison of ε_{xx} between horizontal layers (IHNJ1-5-B – Complete analysis).

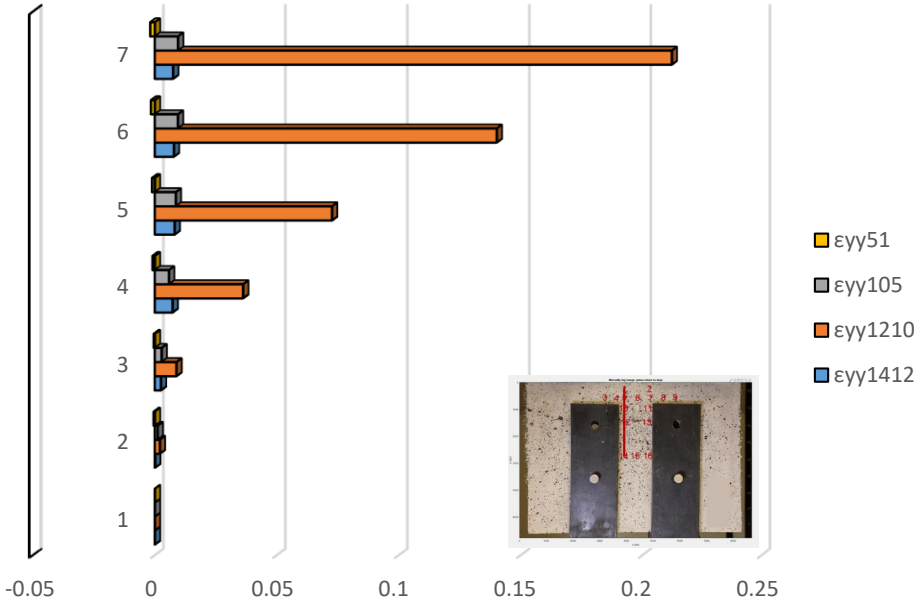

Figure A - 190 Demonstration of ε_{yy} on left vertical layer (IHNJ1-5-B – Complete analysis).

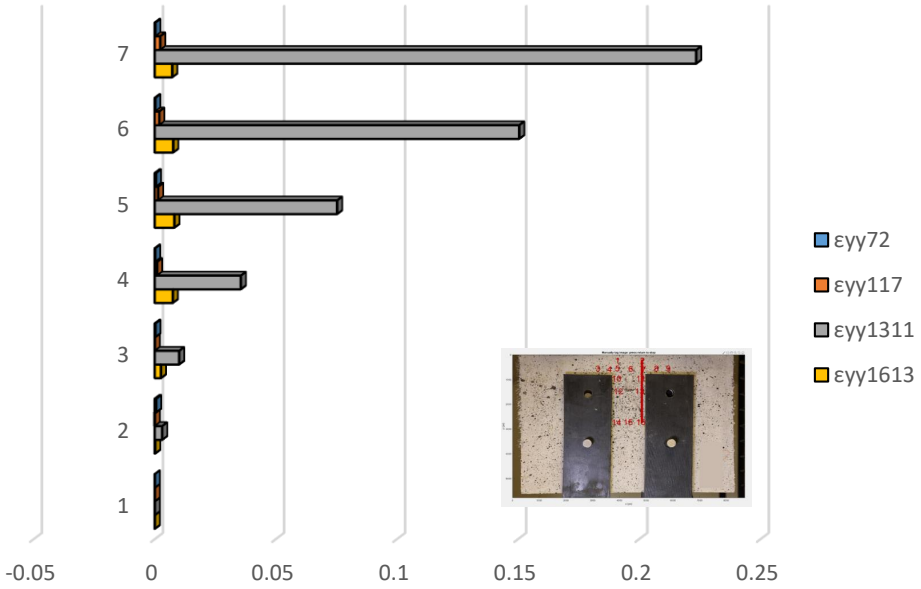

Figure A - 191 Demonstration of ε_{yy} on right vertical layer (IHNJ1-5-B – Complete analysis).

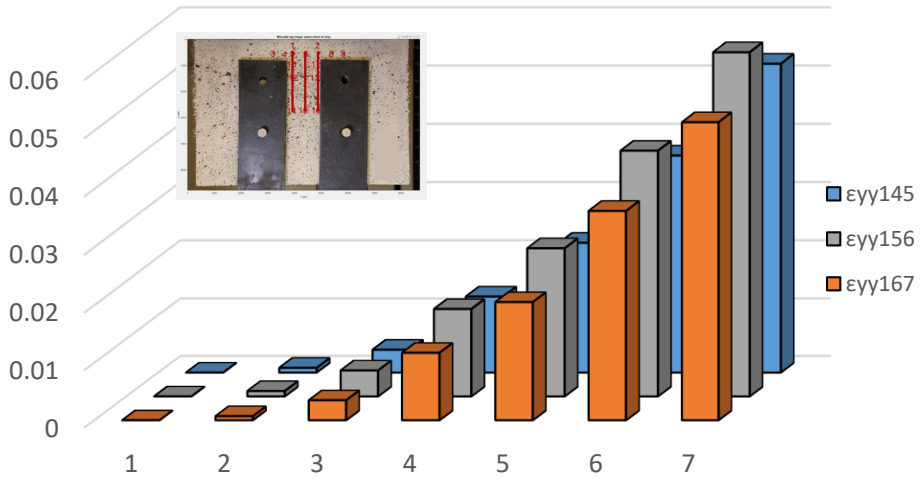

Figure A - 192 Comparison of ε_{yy} between three equidistant layers (IHNJ1-5-B – Complete analysis).

Detailed analysis in three milestone points – Case 1

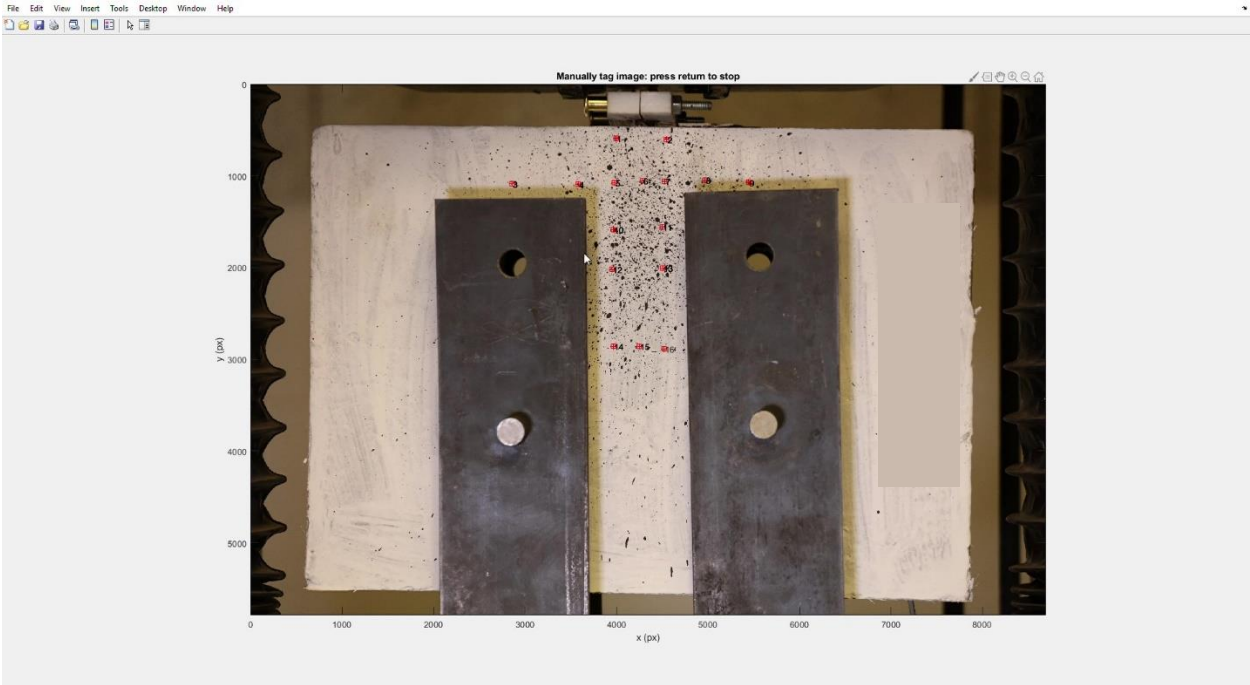

Figure A - 193 Locations of POIs for specimen IHNJ1-5-B (Case 1)

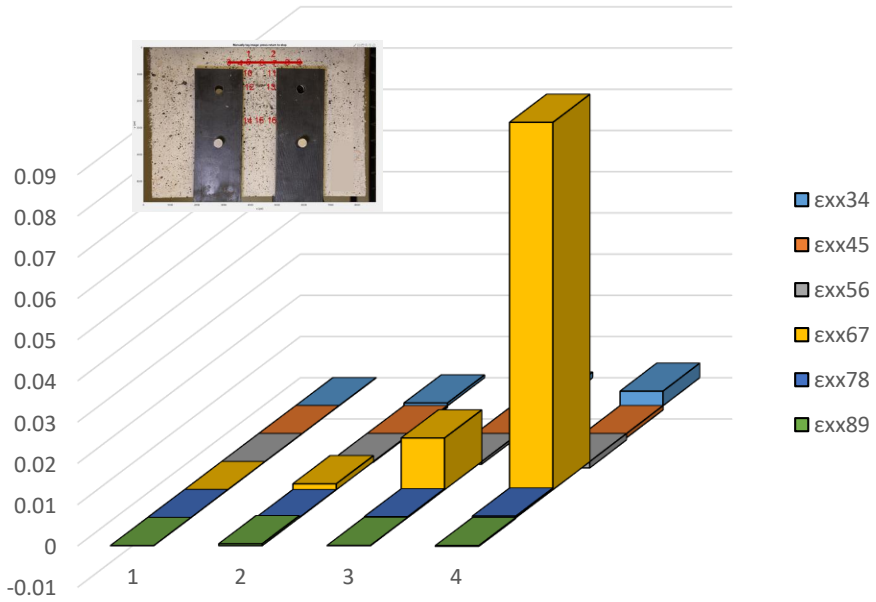

Figure A - 194 Demonstration of ε_{xx} along Layer 2 (IHNJ1-5-B – Case 1).

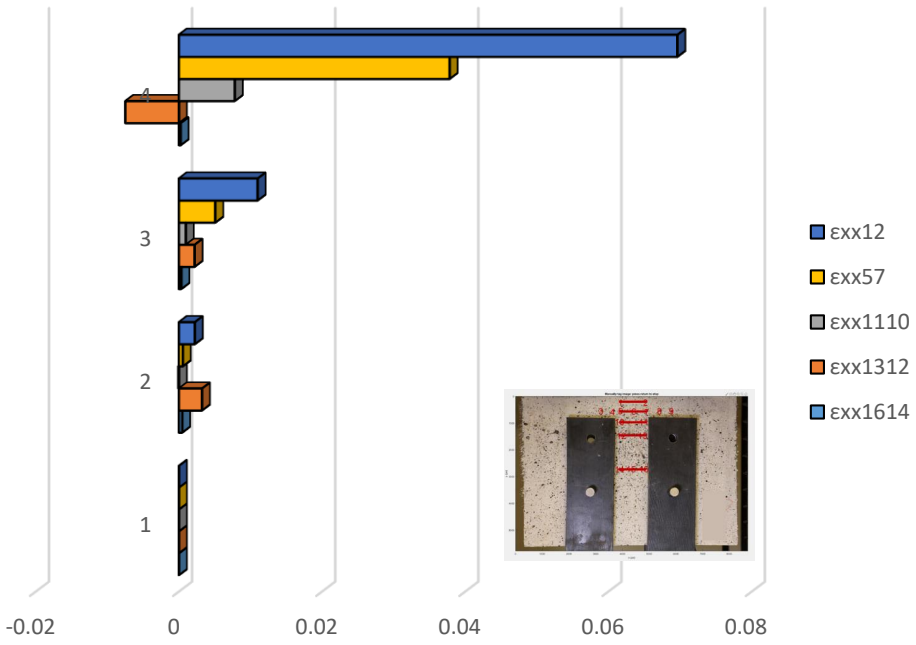

Figure A - 195 Comparison of ε_{xx} between horizontal layers (IHNJ1-5-B – Case 1)

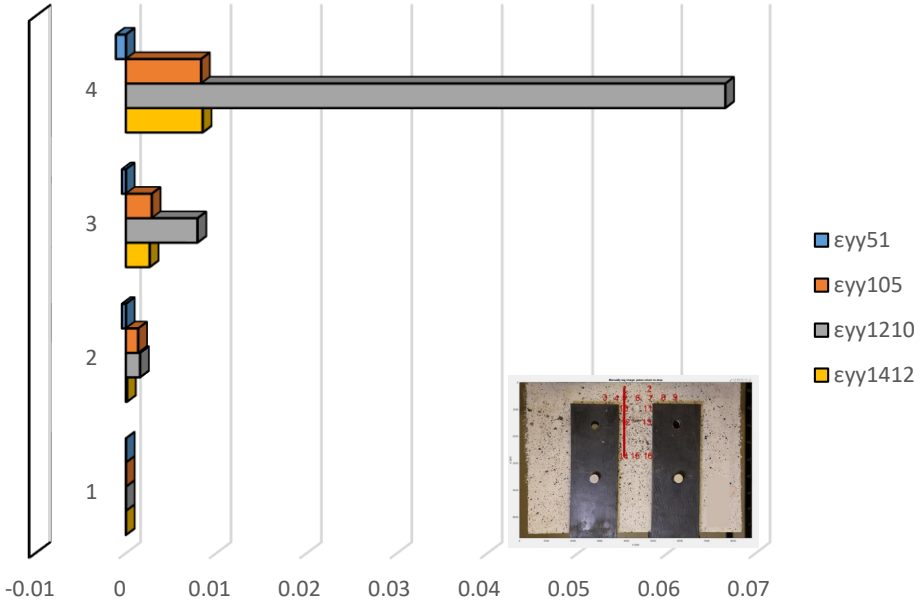

Figure A - 196 Demonstration of εyy on left vertical layer (IHNJ1-5-B – Case 1).

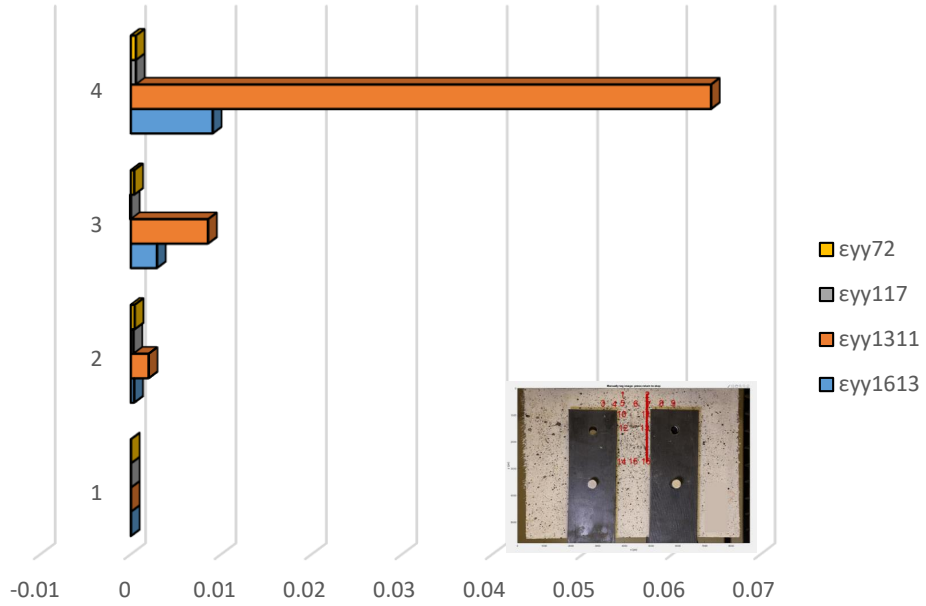

Figure A - 197 Demonstration of ε_{yy} on right vertical layer (IHNJ1-5-B – Case 1).

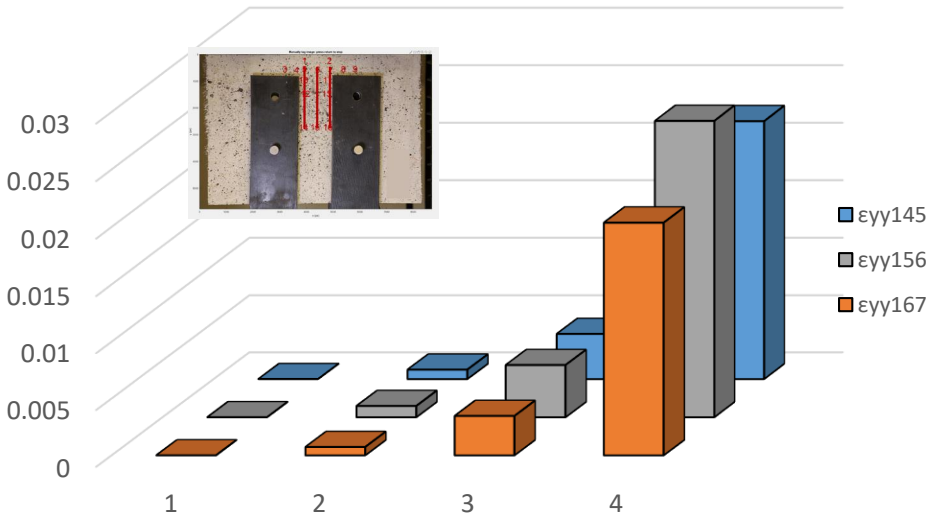

Figure A - 198 Comparison of ε_{yy} between three equidistant layers (IHNJ1-5-B – Case 1).

Detailed analysis in three milestone points – Case 2

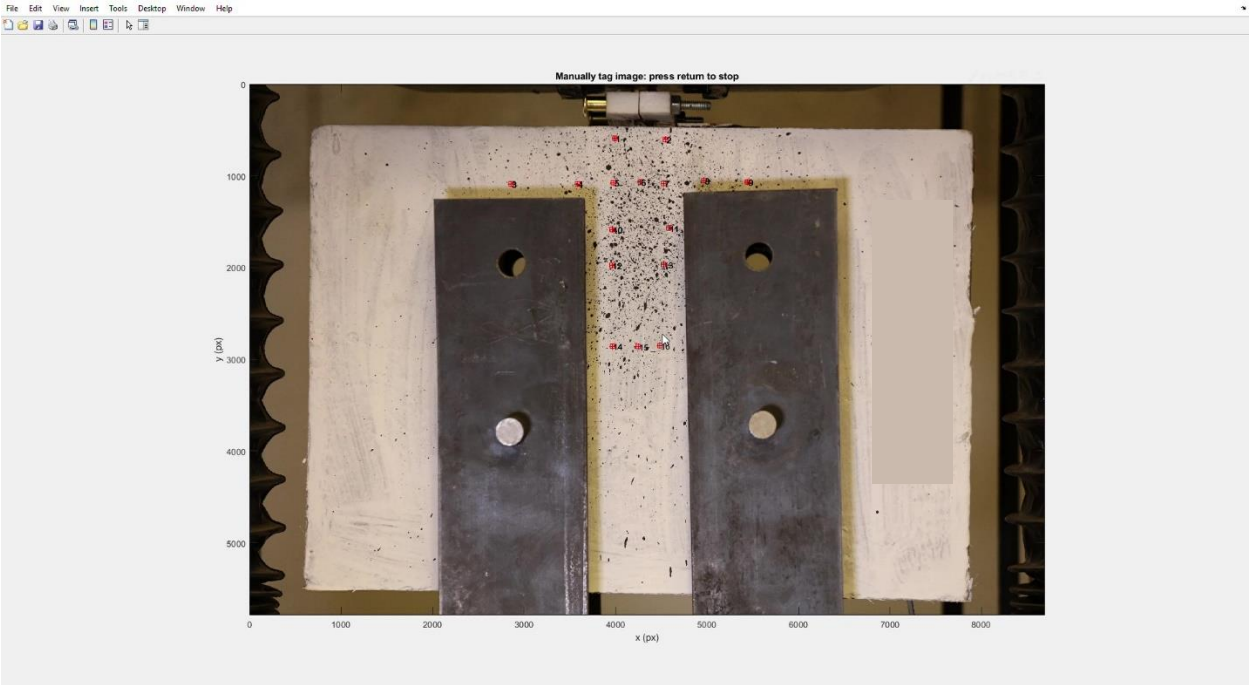

Figure A - 199 Locations of POIs for specimen IHNJ1-5-B (Case 2).

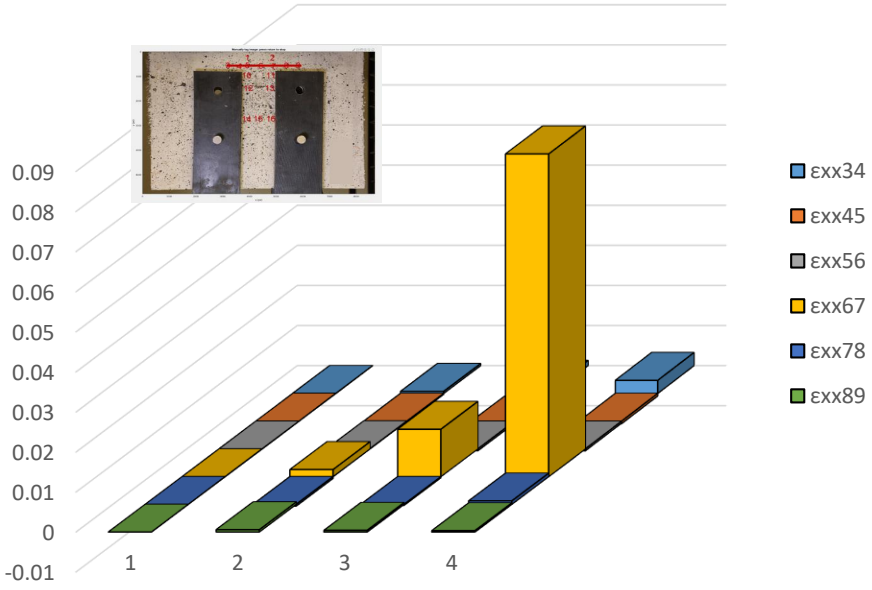

Figure A - 200 Demonstration of ε_{xx} along Layer 2 (IHNJ1-5-B – Case 2).

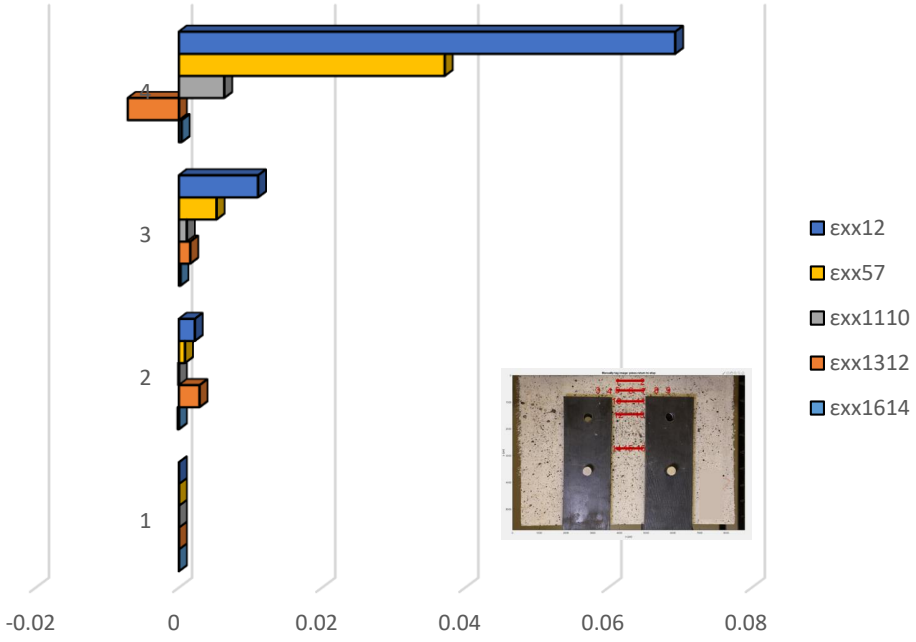

Figure A - 201 Comparison of ε_{xx} between horizontal layers (IHNJ1-5-B – Case 2)

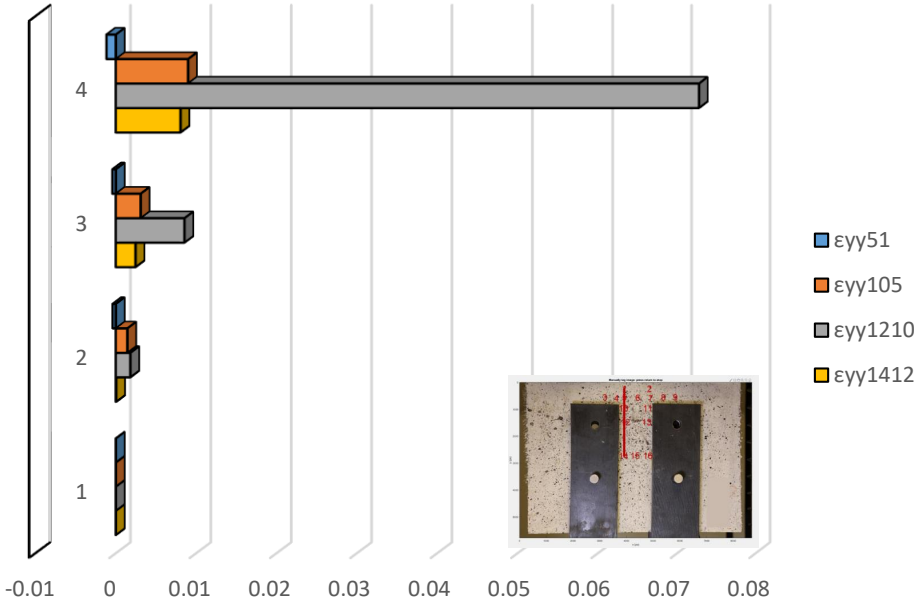

Figure A - 202 Demonstration of εyy on left vertical layer (IHNJ1-5-B – Case 2).

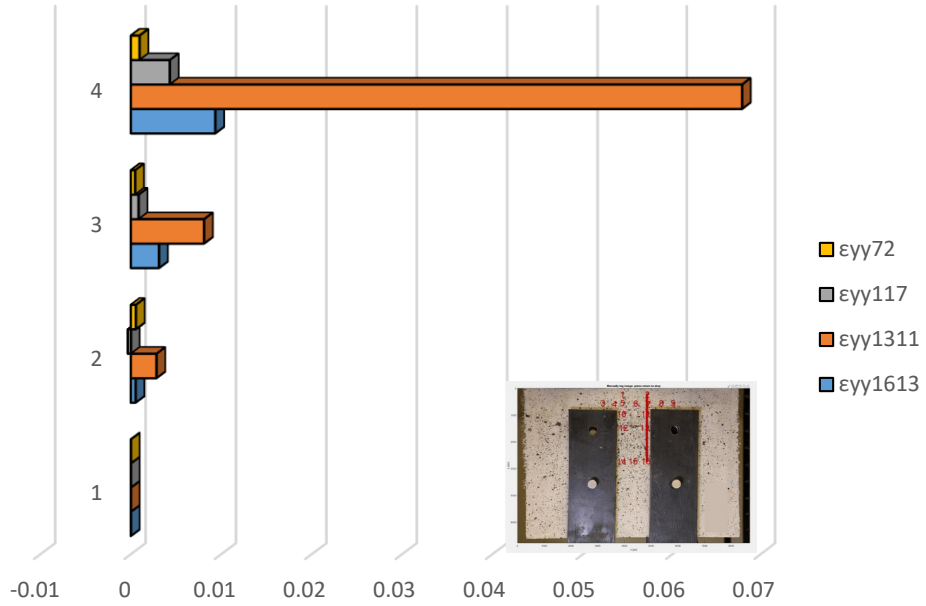

Figure A - 203 Demonstration of ε_{yy} on right vertical layer (IHNJ1-5-B – Case 2).

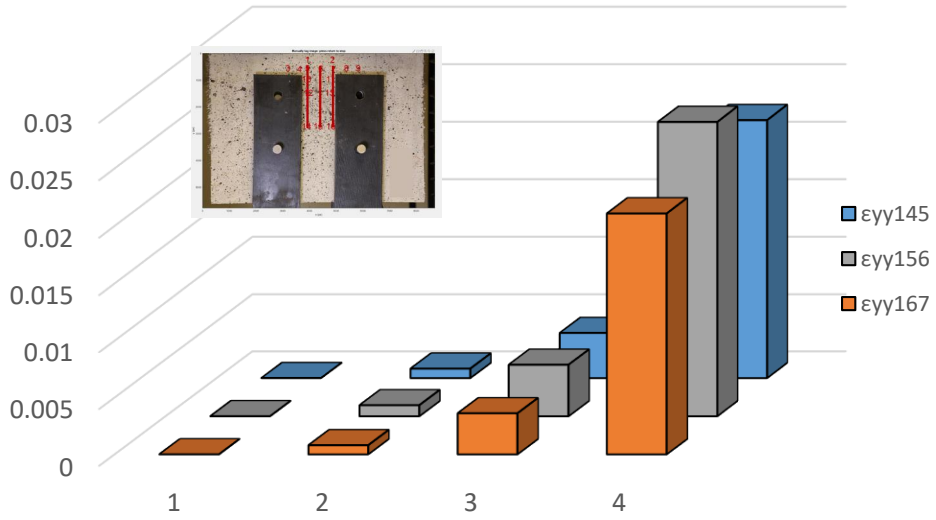

Figure A - 204 Comparison of ε_{yy} between three equidistant layers (IHNJ1-5-B – Case 2).

Detailed analysis in three milestone points – Case 3

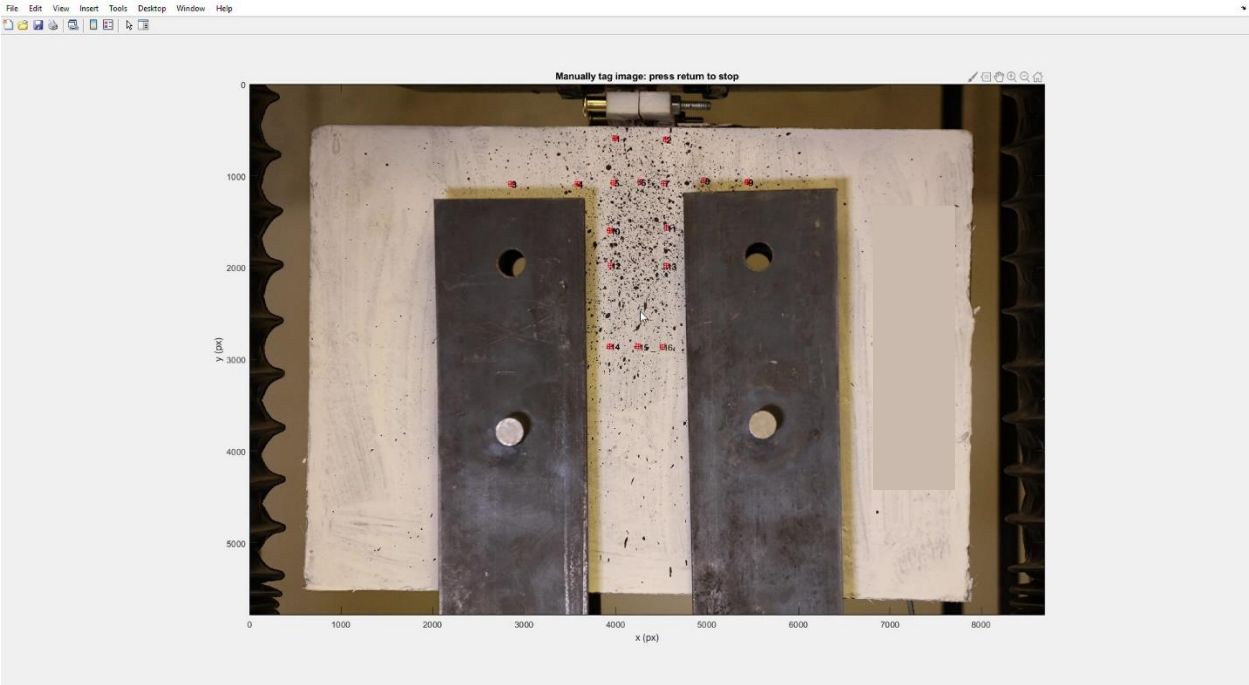

Figure A - 205 Locations of POIs for specimen IHNJ1-5-B (Case 3)

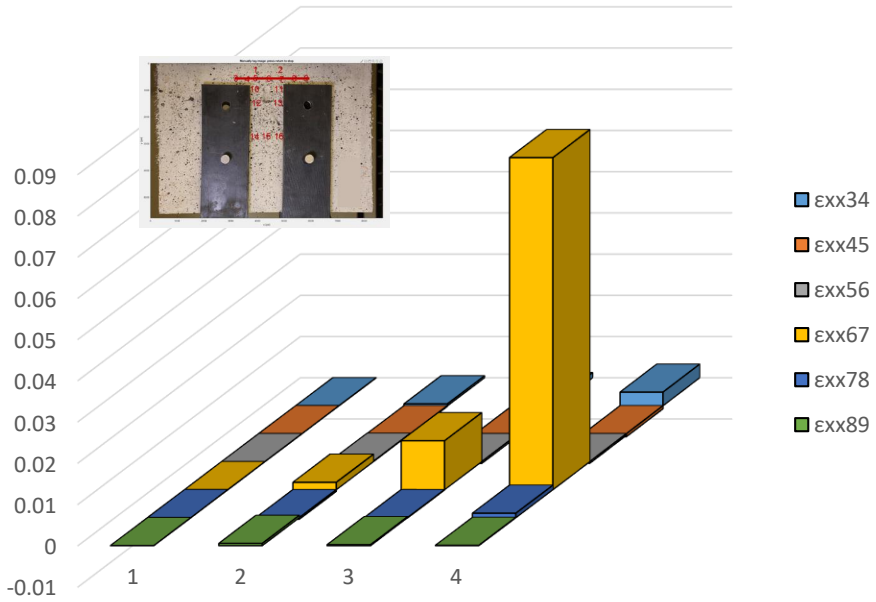

Figure A - 206 Demonstration of ε_{xx} along Layer 2 (IHNJ1-5-B – Case 3).

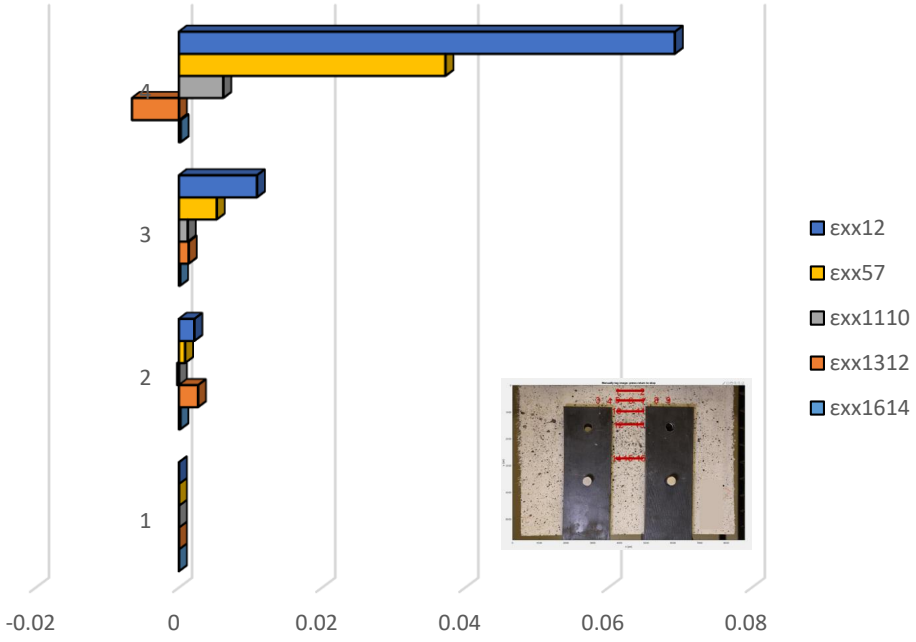

Figure A - 207 Comparison of ε_{xx} between horizontal layers (IHNJ1-5-B – Case 3)

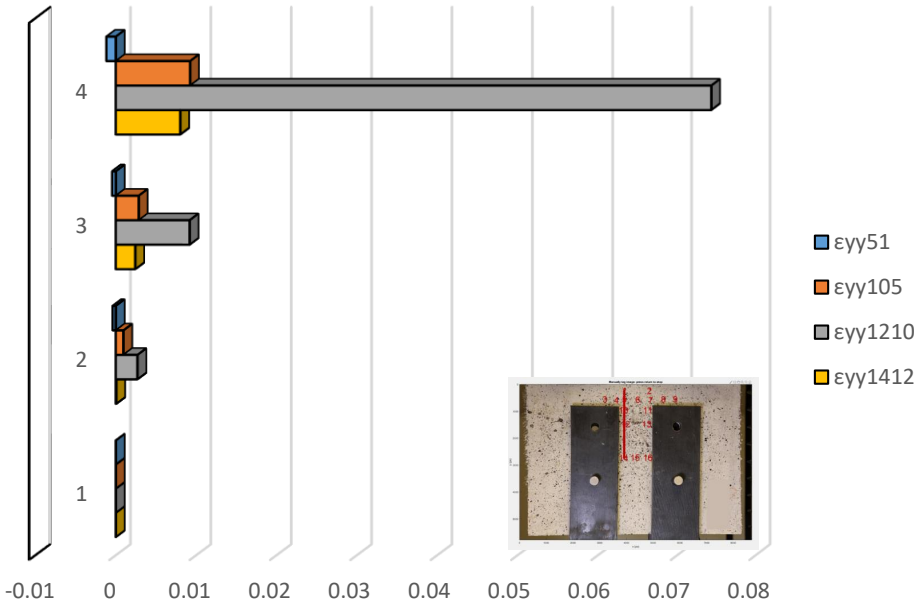

Figure A - 208 Demonstration of εyy on left vertical layer (IHNJ1-5-B – Case 3).

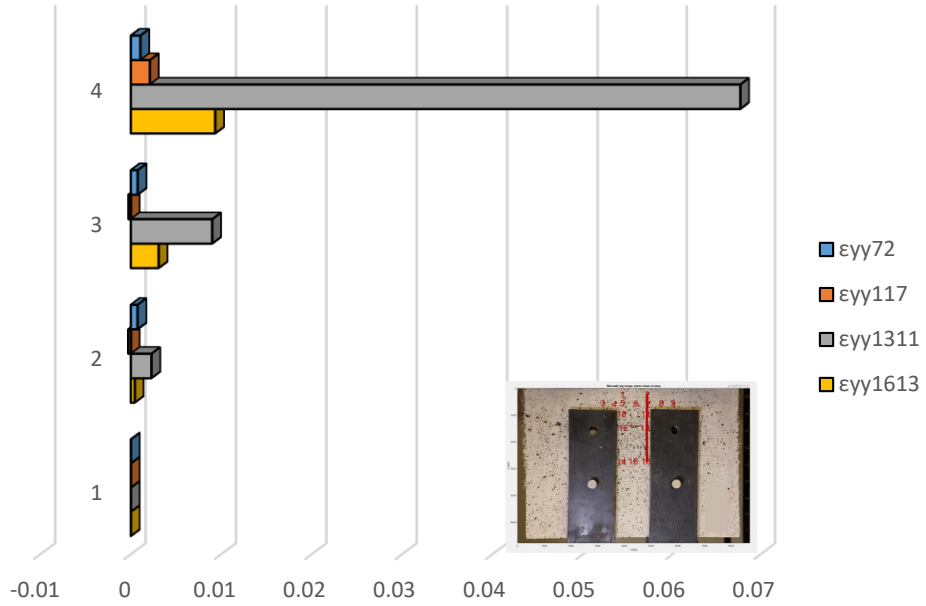

Figure A - 209 Demonstration of ε_{yy} on right vertical layer (IHNJ1-5-B – Case 3).

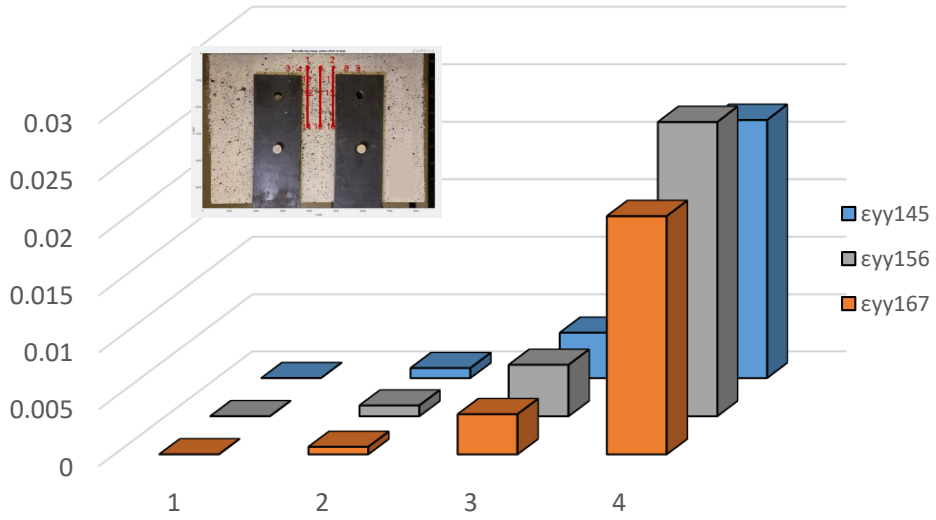

Figure A - 210 Comparison of ε_{yy} between three equidistant layers (IHNJ1-5-B – Case 3).

Specimen IHNJ2-5-A

Complete analysis

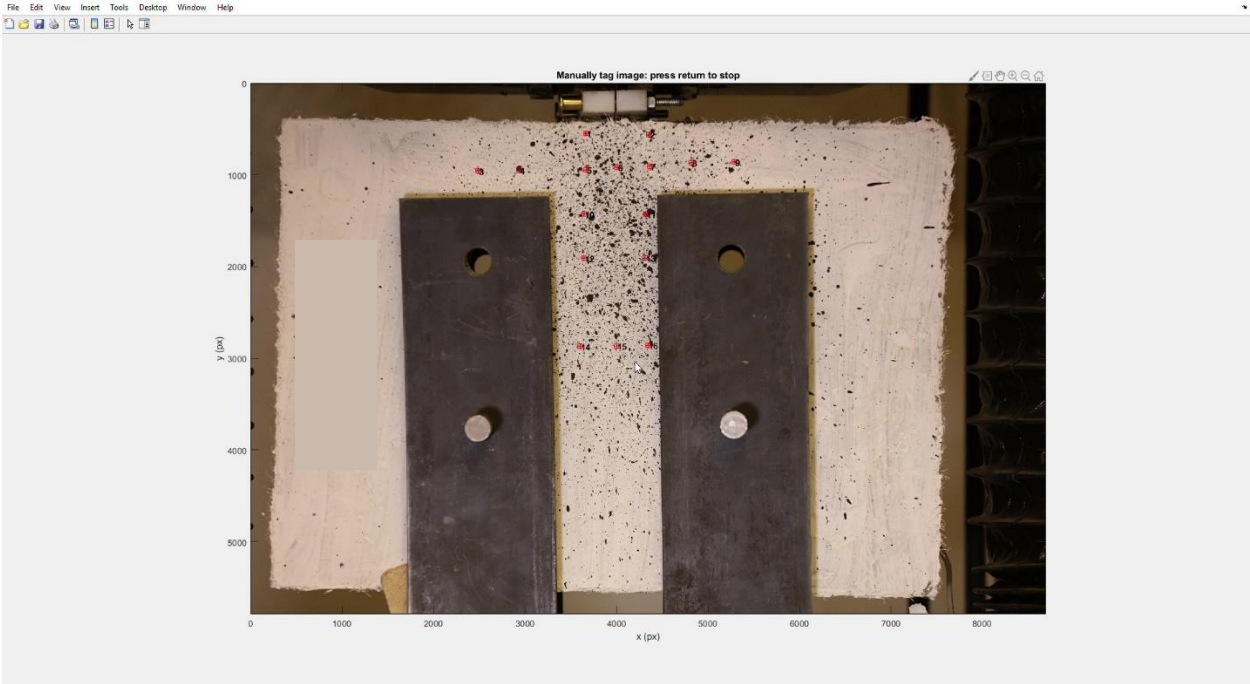

Figure A - 211 Locations of Points of Interest for specimen IHNJ2-5-A (Complete Analysis).

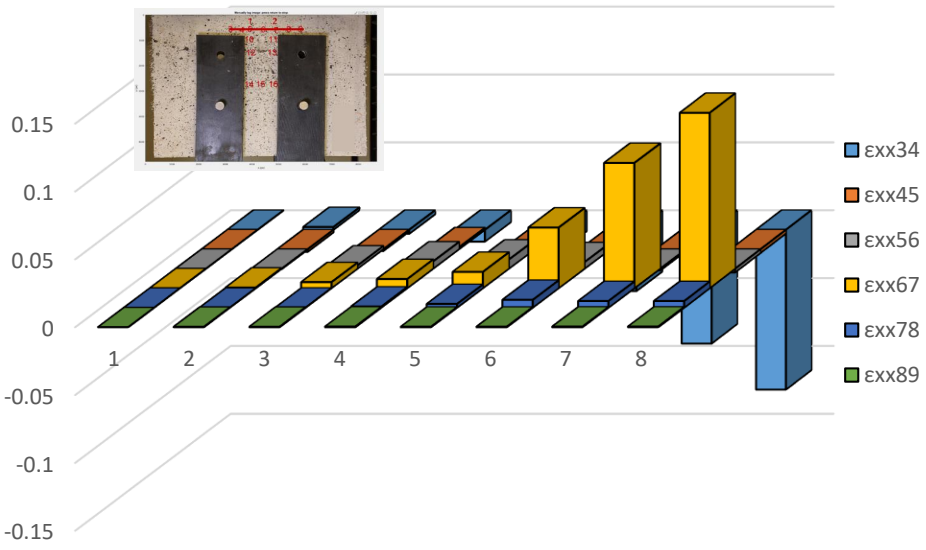

Figure A - 212 Demonstration of ε_{xx} along Layer 2 (IHNJ2-5-A – Complete analysis).

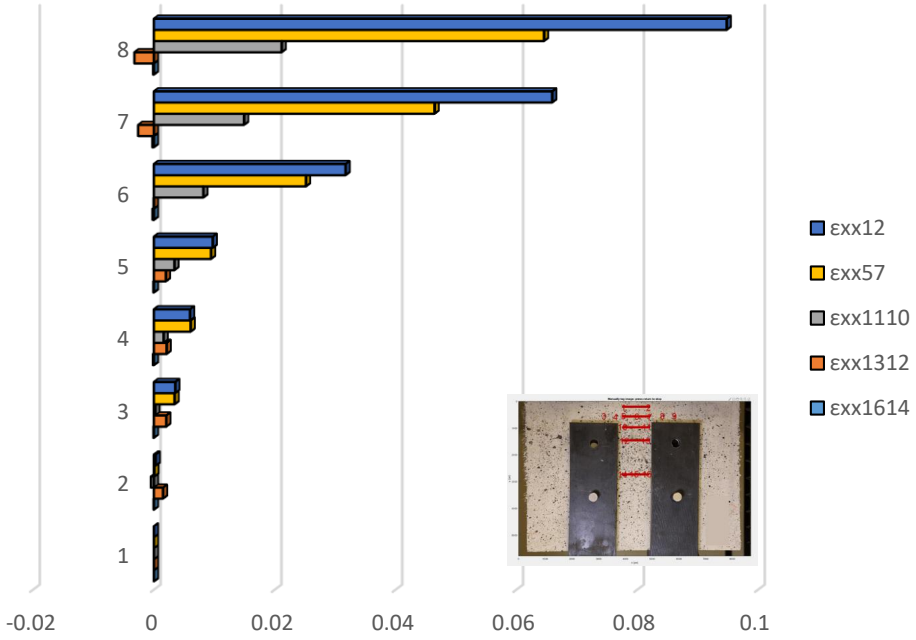

Figure A - 213 Comparison of ε_{xx} between horizontal layers (IHNJ2-5-A – Complete analysis).

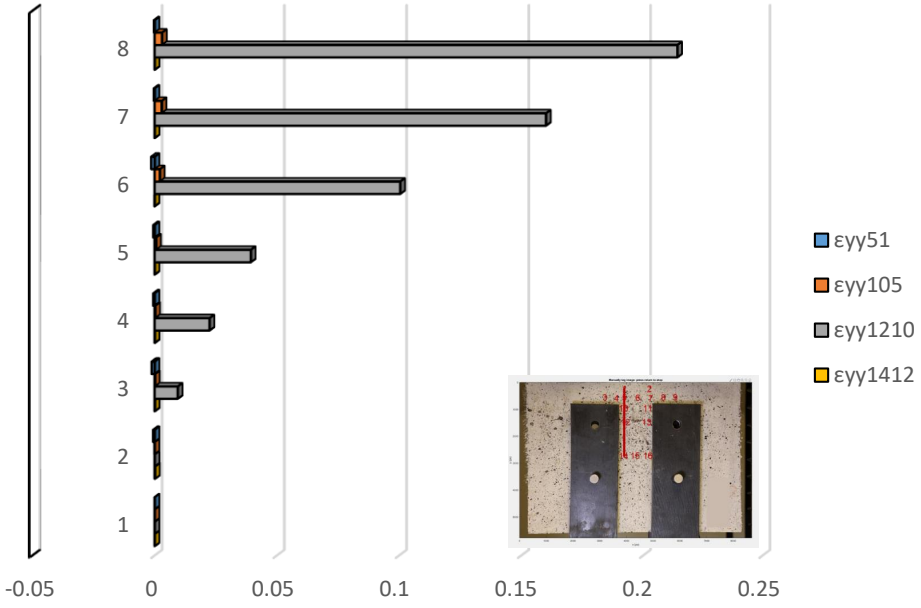

Figure A - 214 Demonstration of ε_{yy} on left vertical layer (IHNJ2-5-A – Complete analysis).

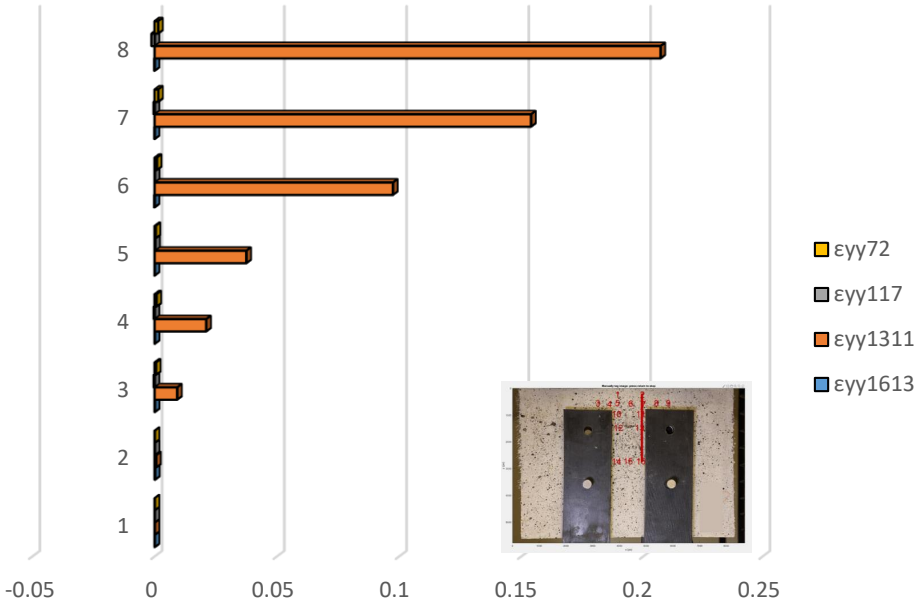

Figure A - 215 Demonstration of ε_{yy} on right vertical layer (IHNJ2-5-A – Complete analysis).

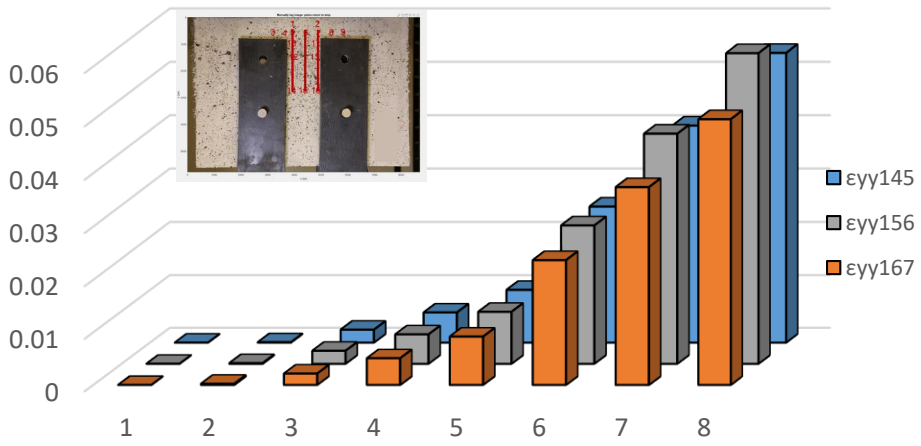

Figure A - 216 Comparison of ε_{yy} between three equidistant layers (IHNJ1-5-A – Complete analysis).

Detailed analysis in three milestone points – Case 1

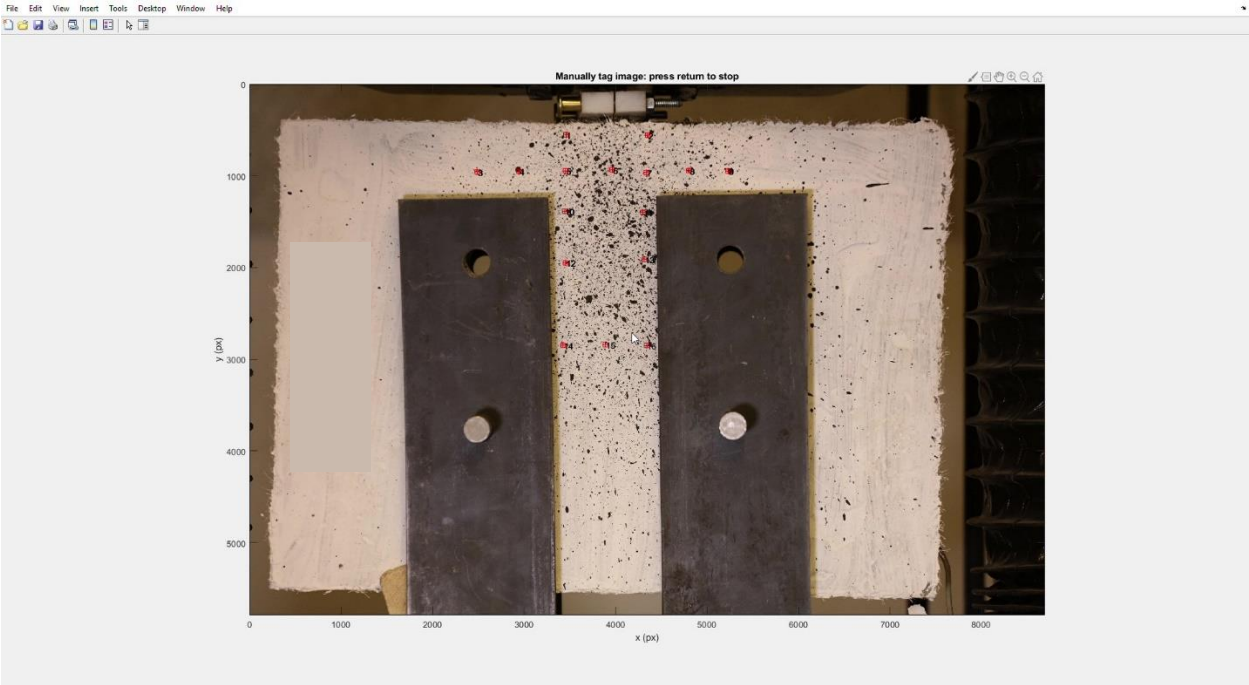

Figure A - 217 Locations of POIs for specimen IHNJ2-5-A (Case 1).

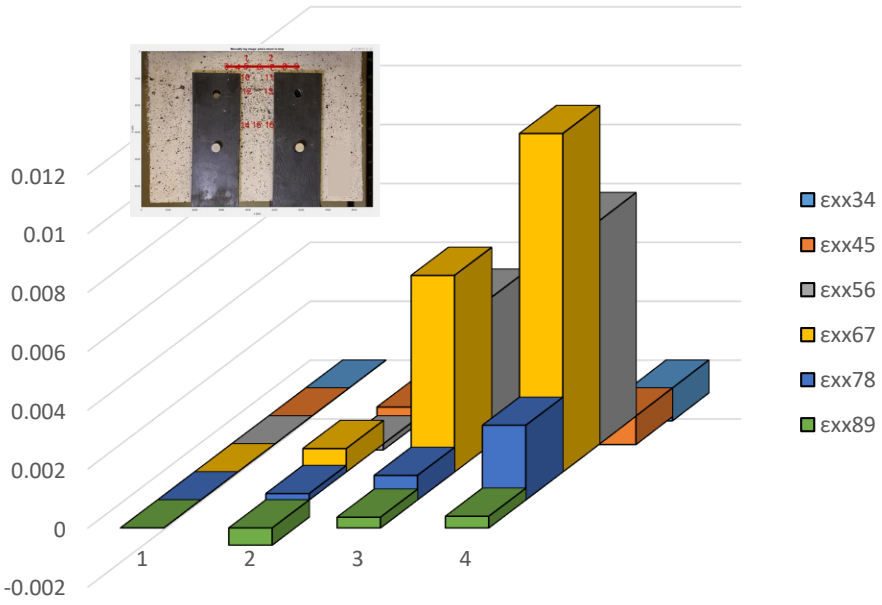

Figure A - 218 Demonstration of ε_{xx} along Layer 2 (IHNJ2-5-A – Case 1).

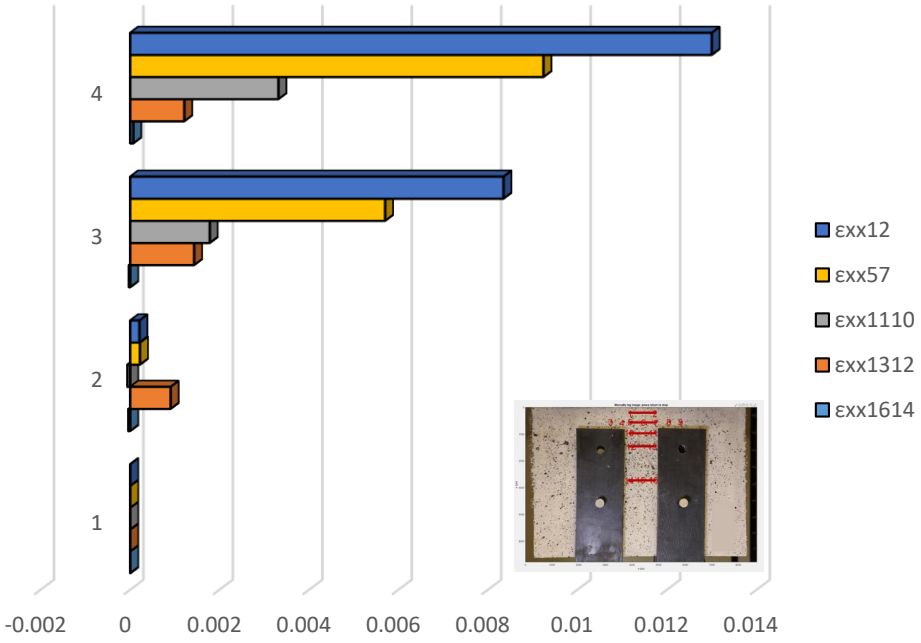

Figure A - 219 Comparison of ε_{xx} between horizontal layers (IHNJ2-5-A – Case 1).

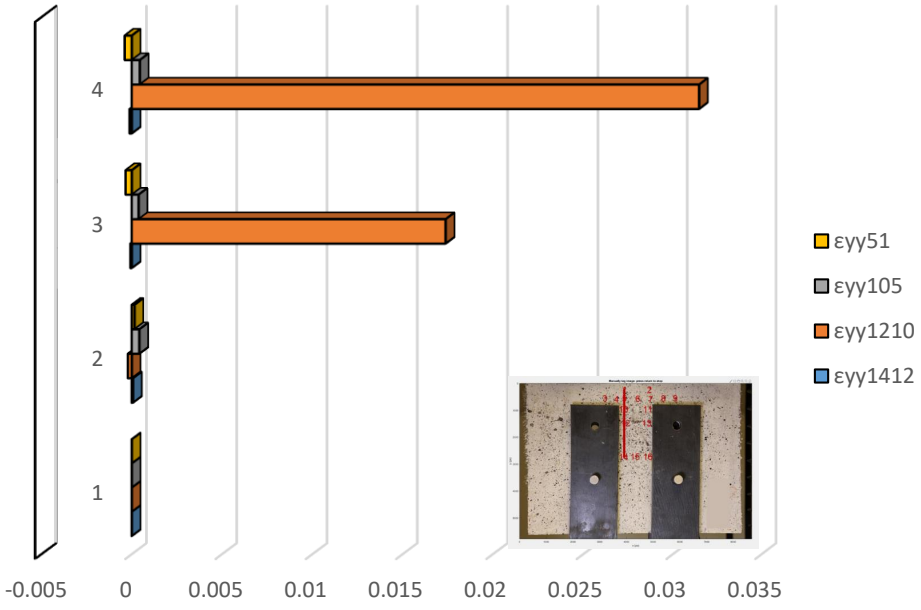

Figure A - 220 Demonstration of εyy on left vertical layer (IHNJ2-5-A – Case 1).

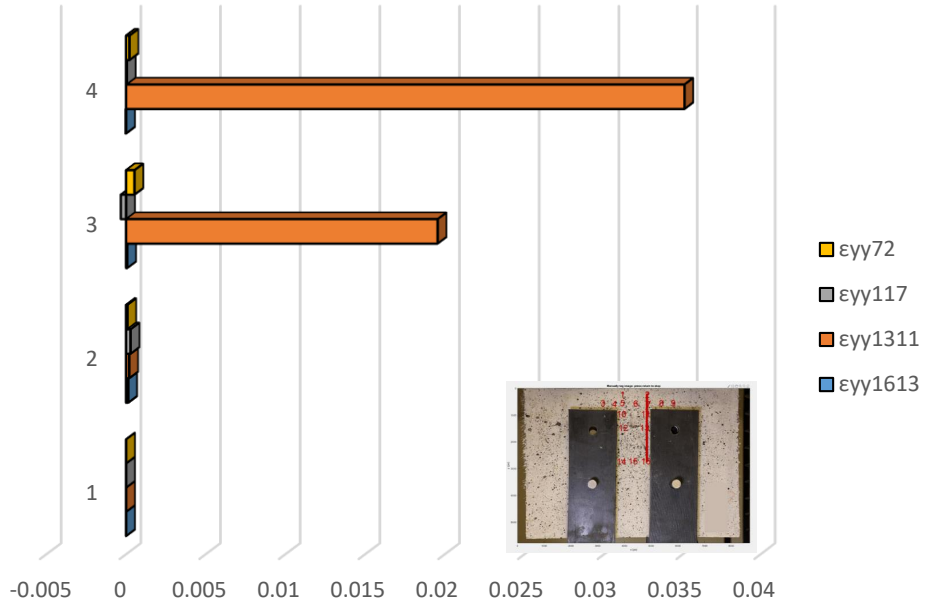

Figure A - 221 Demonstration of ε_{yy} on right vertical layer (IHNJ2-5-A – Case 1).

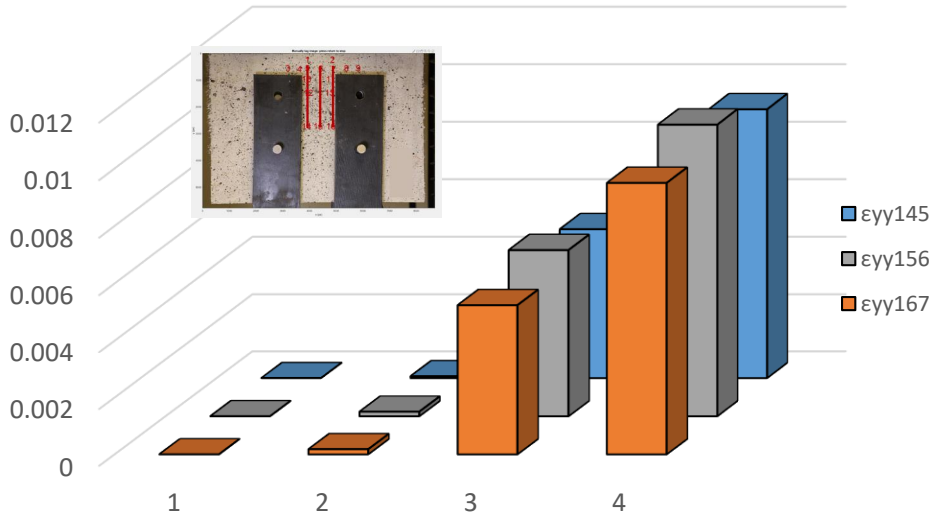

Figure A - 222 Comparison of ε_{yy} between three equidistant layers (IHNJ2-5-A – Case 1).

Detailed analysis in three milestone points – Case 2

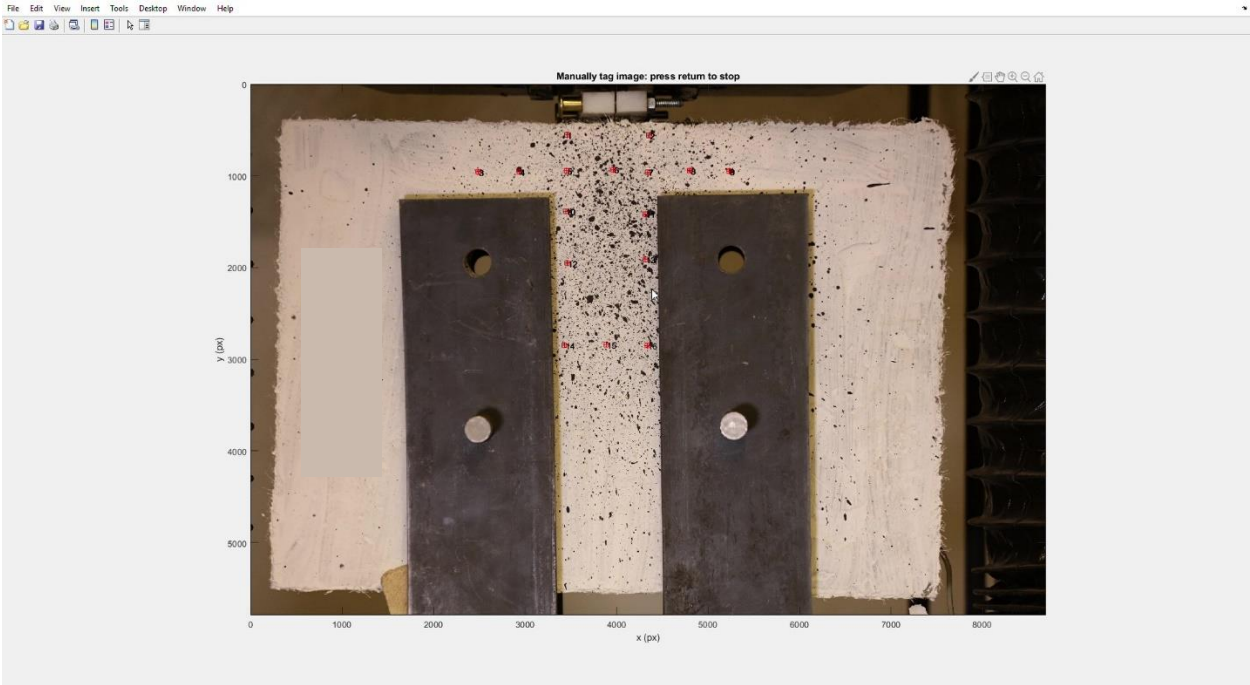

Figure A - 223 Locations of POIs for specimen IHNJ2-5-A (Case 2).

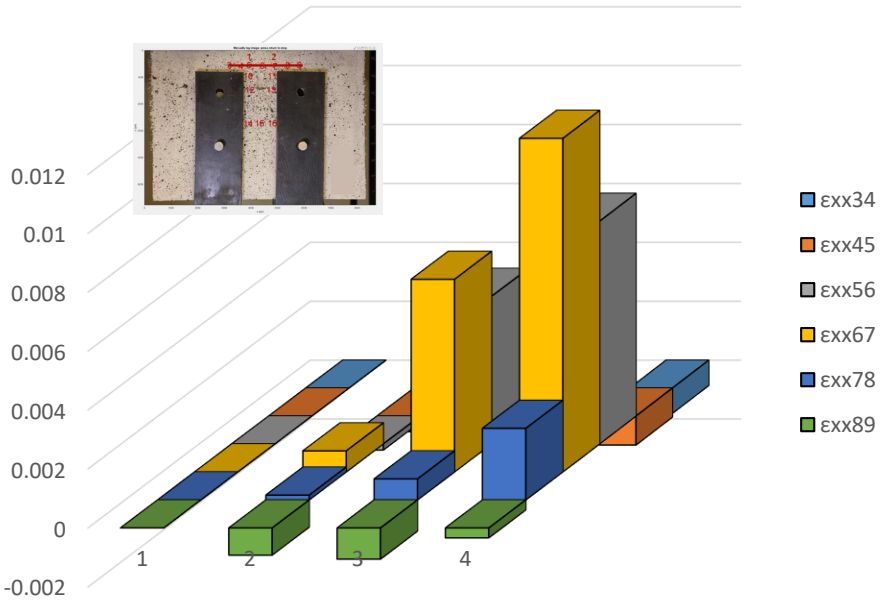

Figure A - 224 Demonstration of ε_{xx} along Layer 2 (IHNJ2-5-A – Case 2).

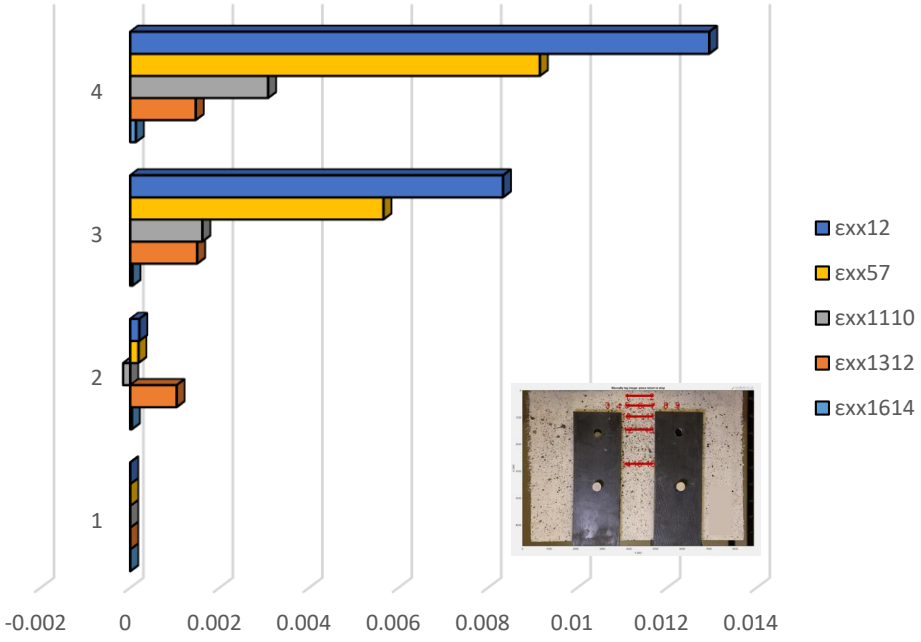

Figure A - 225 Comparison of ε_{xx} between horizontal layers (IHNJ2-5-A – Case 2).

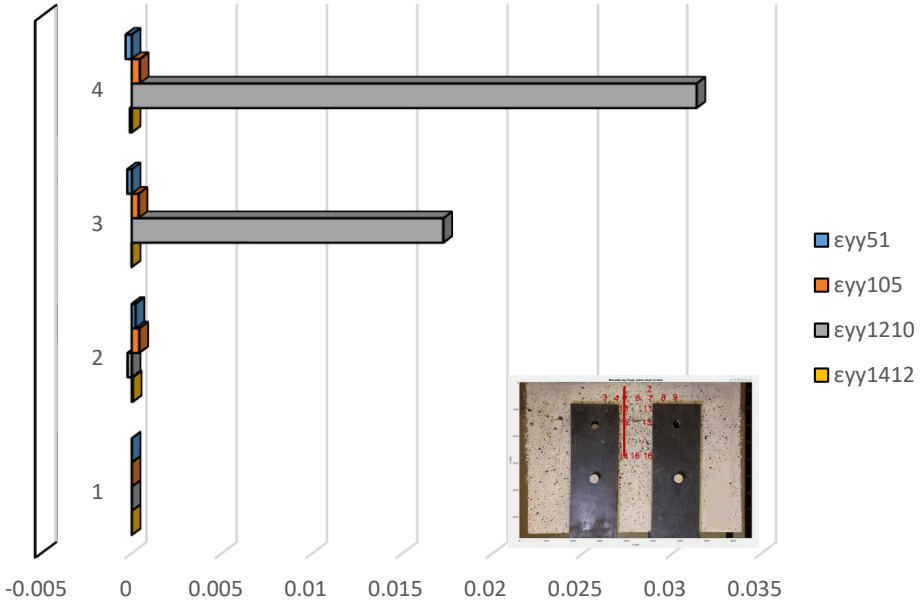

Figure A - 226 Demonstration of ε_{yy} on left vertical layer (IHNJ2-5-A – Case 2).

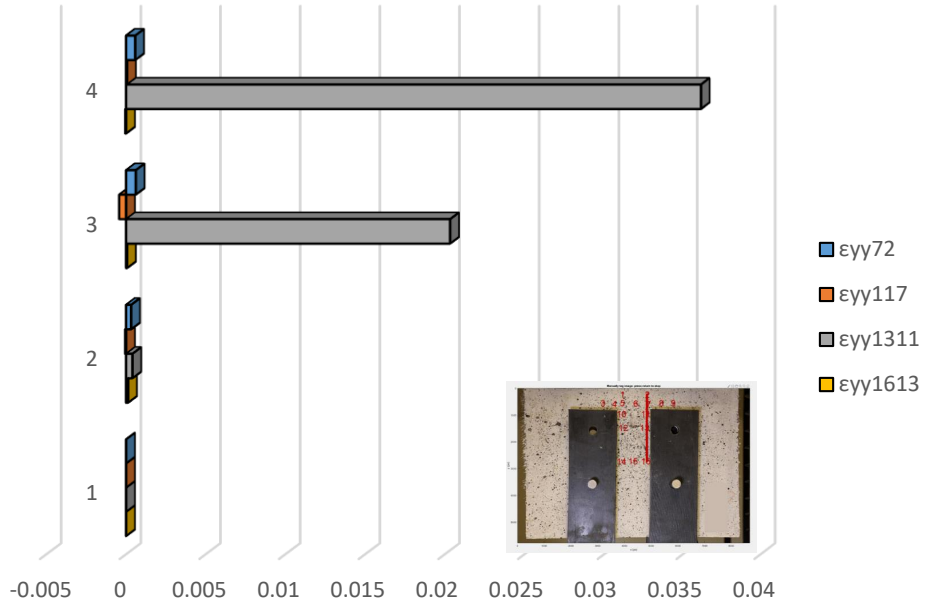

Figure A - 227 Demonstration of ε_{yy} on right vertical layer (IHNJ2-5-A – Case 2)

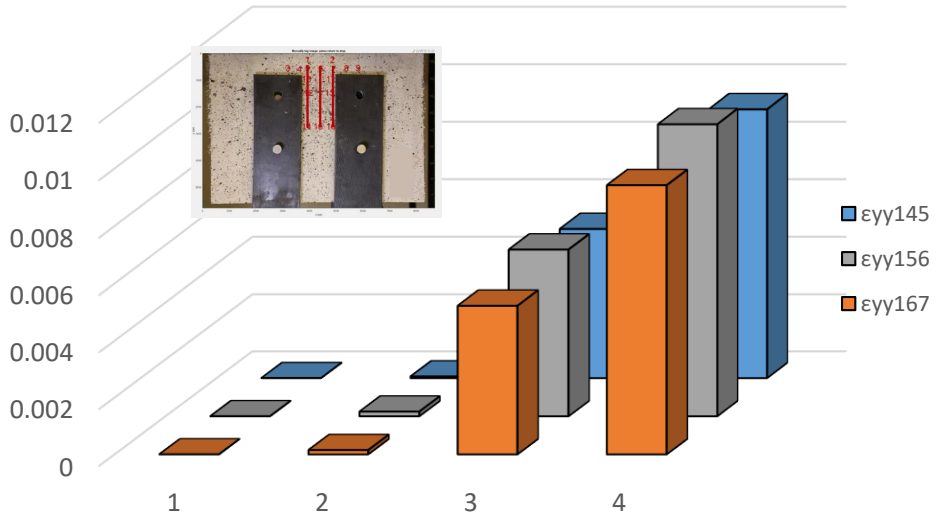

Figure A - 228 Comparison of ε_{yy} between three equidistant layers (IHNJ2-5-A – Case 2).

Detailed analysis in three milestone points – Case 3

Figure A - 229 Locations of POIs for specimen IHNJ2-5-A (Case 3).

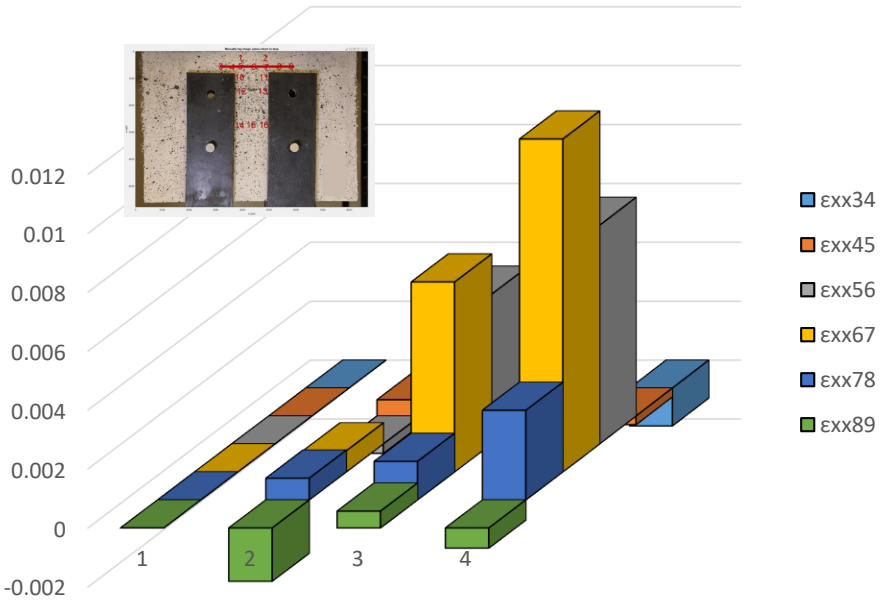

Figure A - 230 Demonstration of ε_{xx} along Layer 2 (IHNJ2-5-A – Case 3).

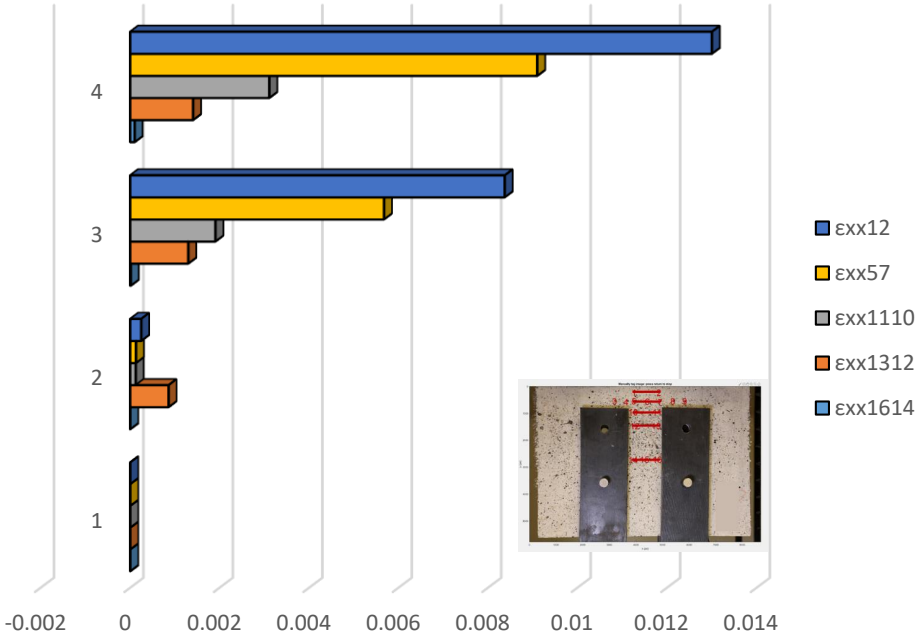

Figure A - 231 Comparison of ε_{xx} between horizontal layers (IHNJ2-5-A – Case 3)

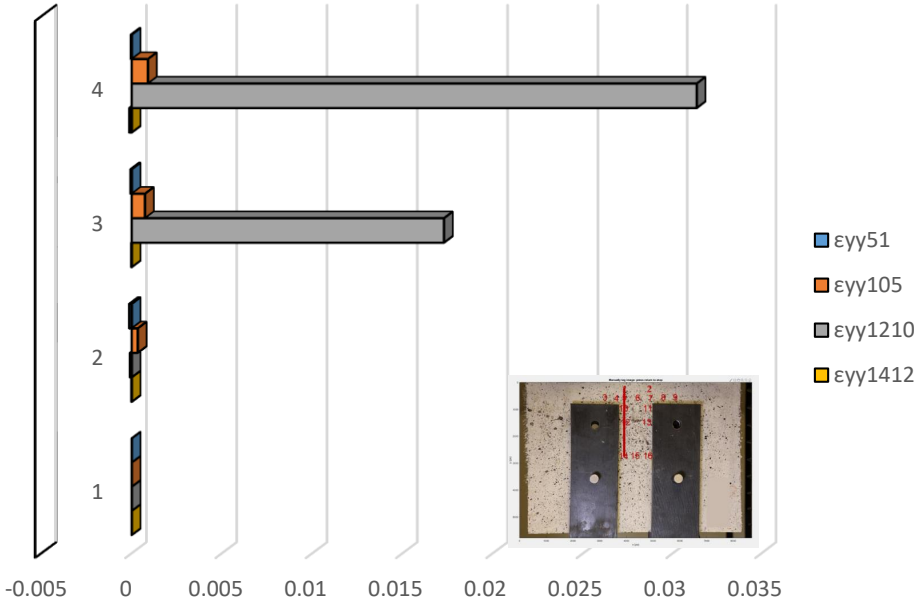

Figure A - 232 Demonstration of ε_{yy} on left vertical layer (IHNJ2-5-A – Case 3).

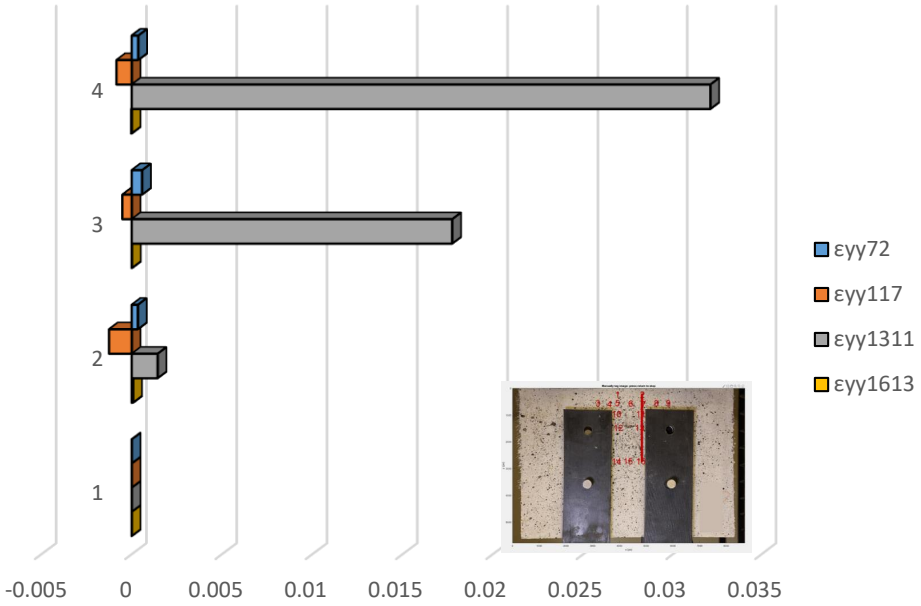

Figure A - 233 Demonstration of ε_{yy} on right vertical layer (IHNJ2-5-A – Case 3).

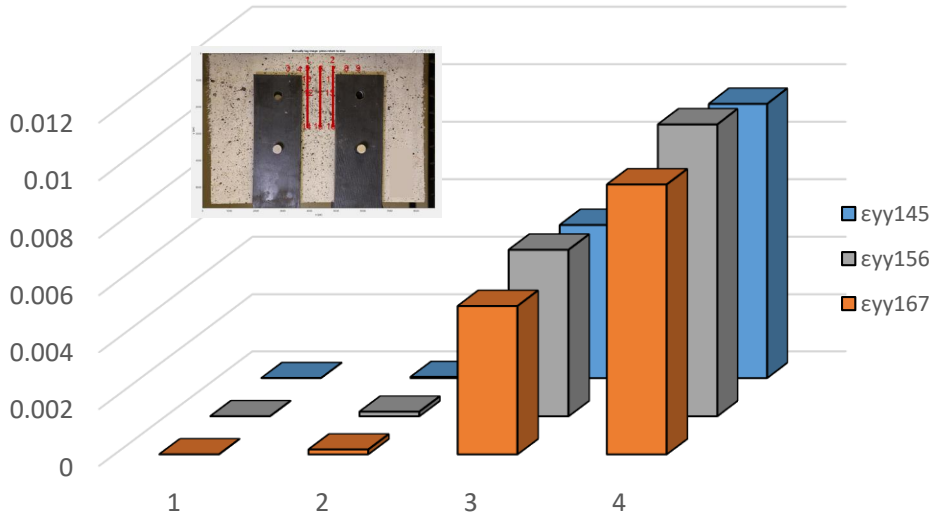

Figure A - 234 Comparison of ε_{yy} between three equidistant layers (IHNJ2-5-A – Case 3).

Specimen IHNJ2-5-B

Complete analysis

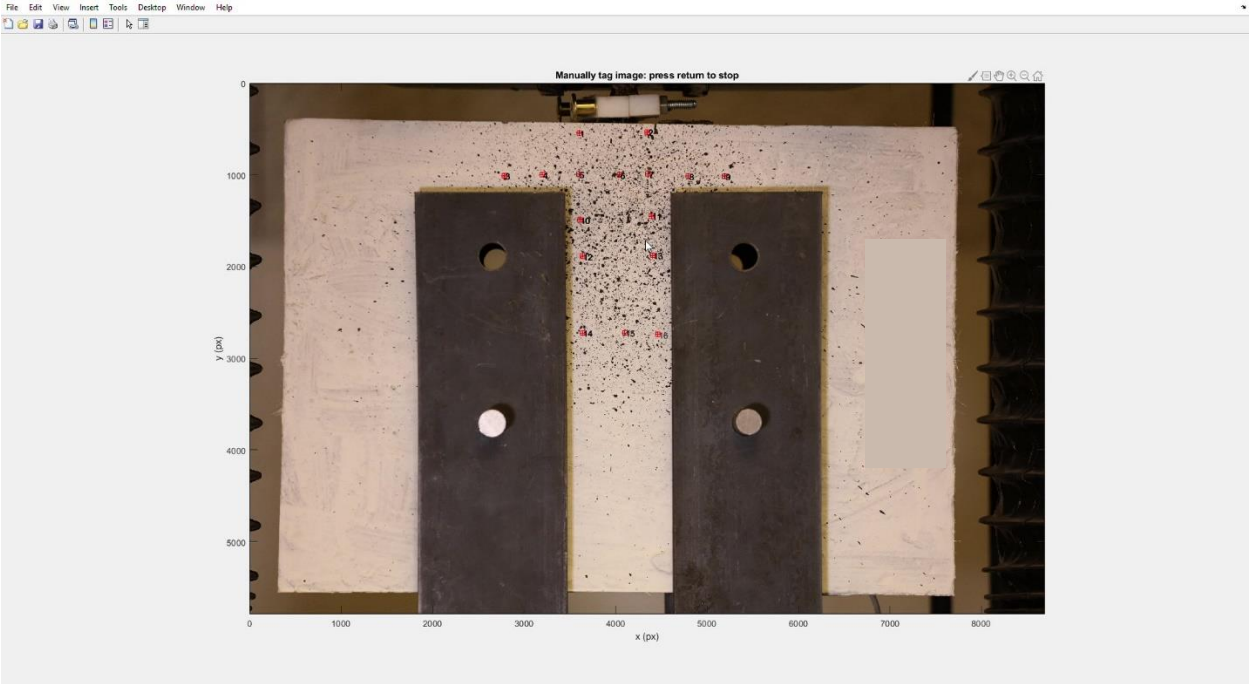

Figure A - 235 Locations of Points of Interest for specimen IHNJ2-5-B (Complete Analysis).

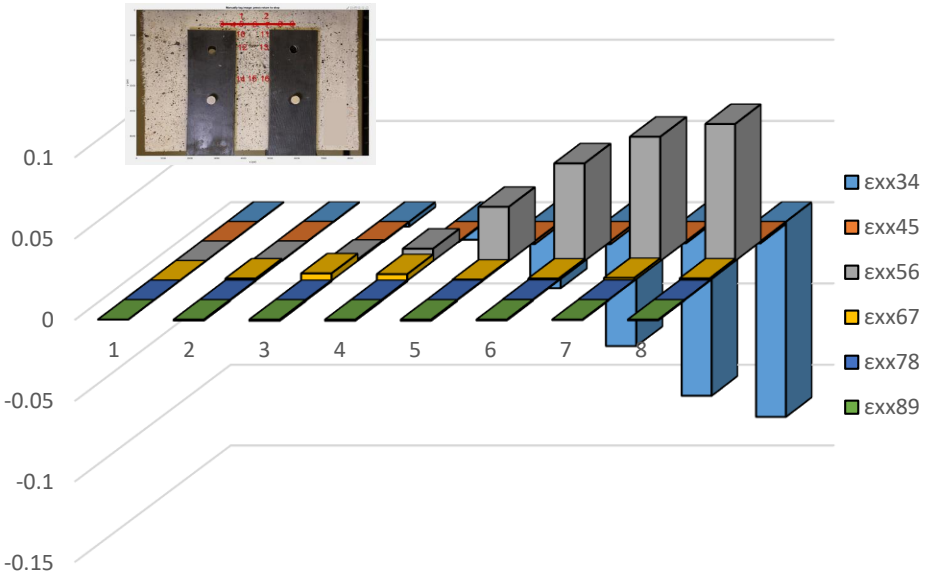

Figure A - 236 Demonstration of ε_{xx} along Layer 2 (IHNJ2-5-B – Complete analysis).

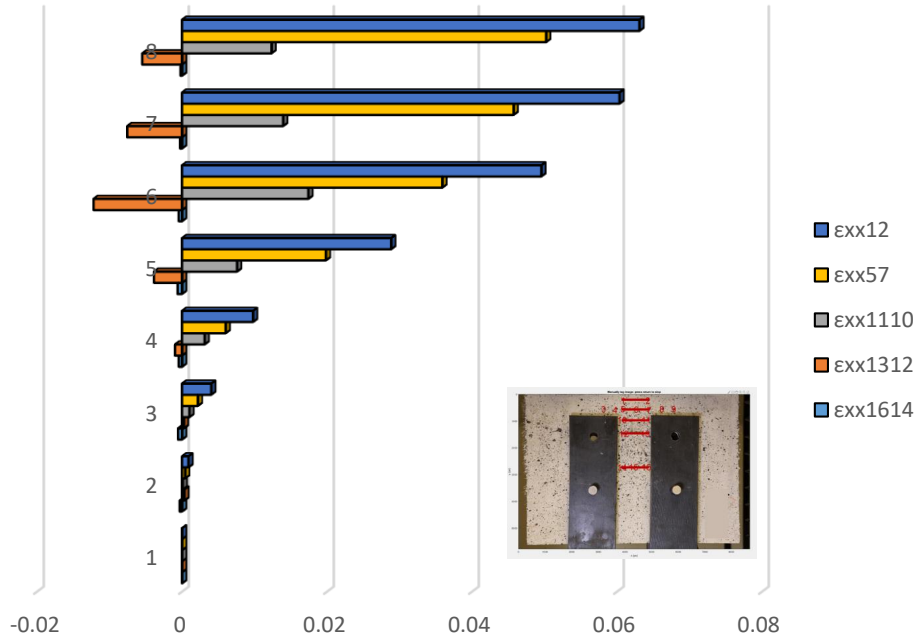

Figure A - 237 Comparison of ε_{xx} between horizontal layers (IHNJ2-5-B – Complete analysis).

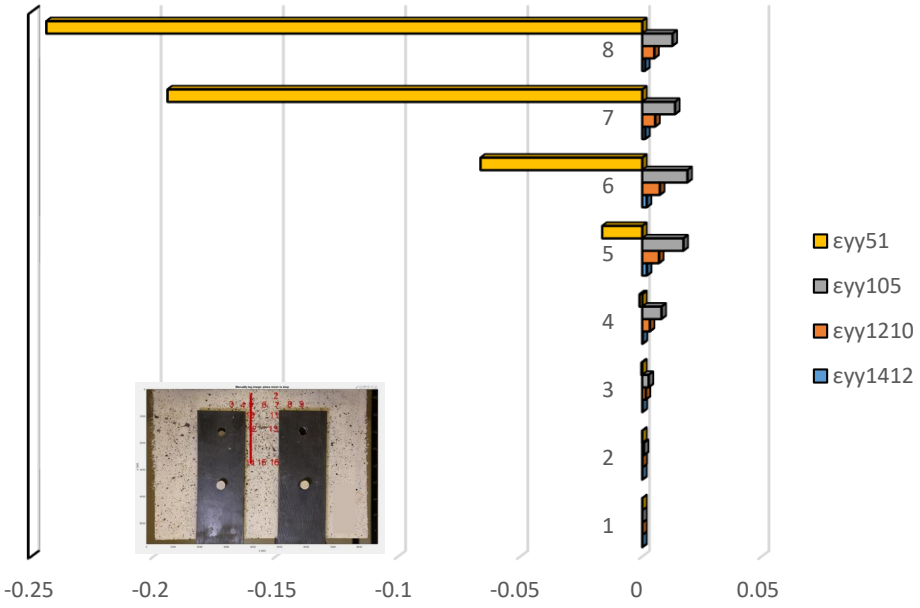

Figure A - 238 Demonstration of ε_{yy} on left vertical layer (IHNJ2-5-B – Complete analysis).

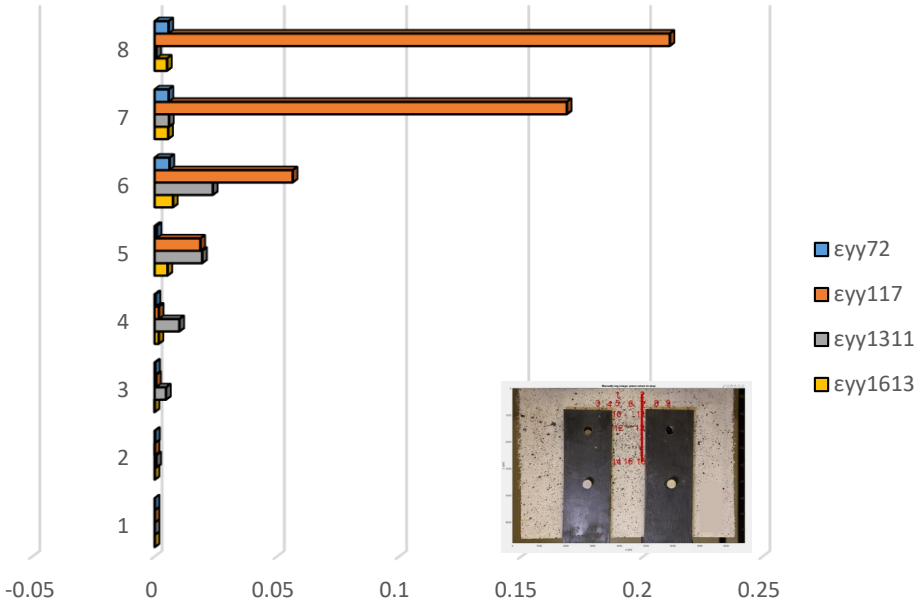

Figure A - 239 Demonstration of ε_{yy} on right vertical layer (IHNJ2-5-B – Complete analysis).

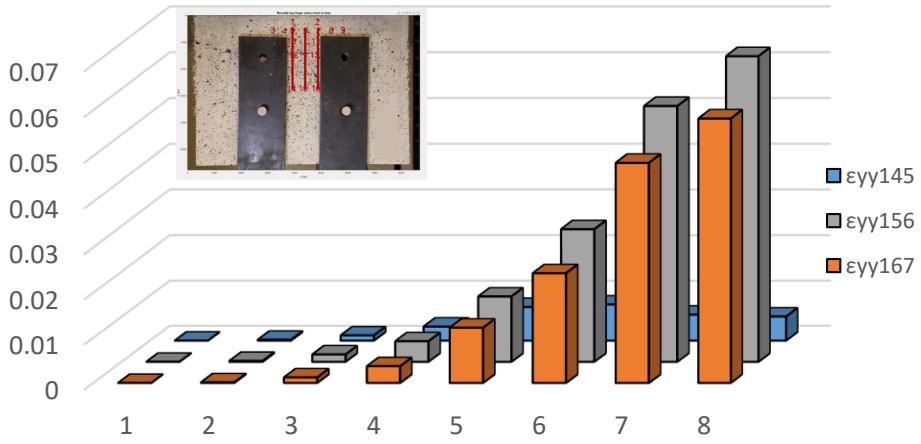

Figure A - 240 Comparison of ε_{yy} between three equidistant layers (IHNJ2-5-B – Complete analysis).

Detailed analysis in three milestone points – Case 1

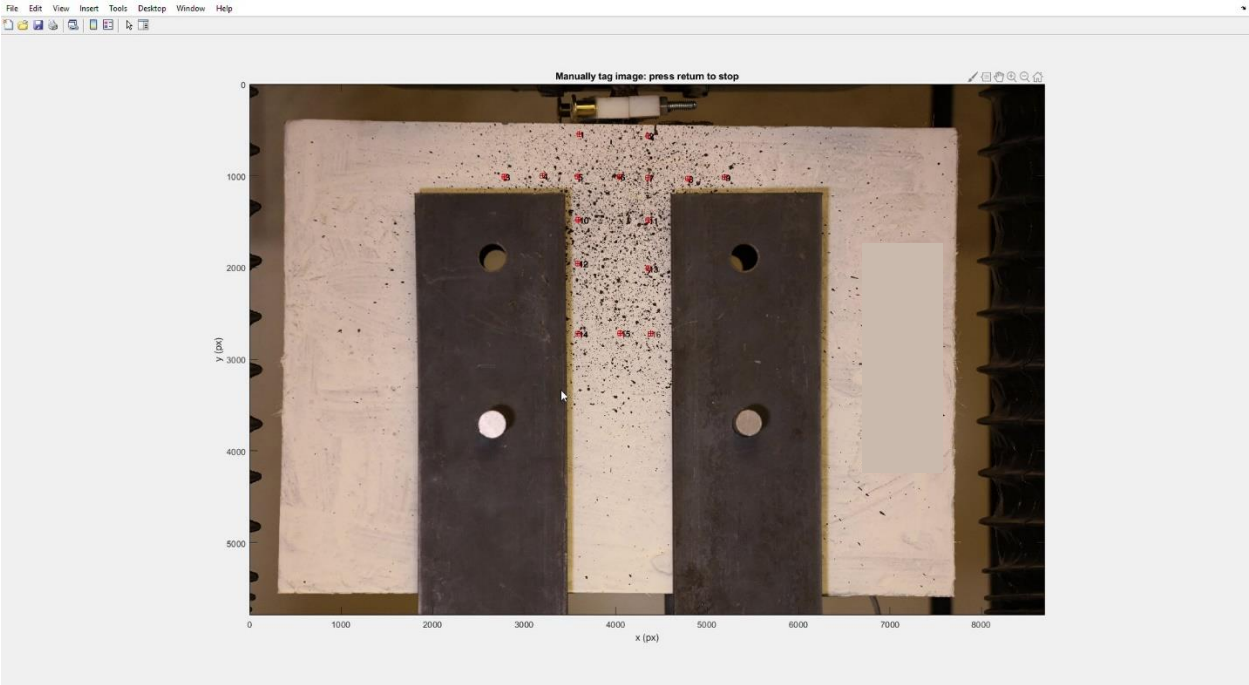

Figure A - 241 Locations of POIs for specimen IHNJ2-5-B (Case 1).

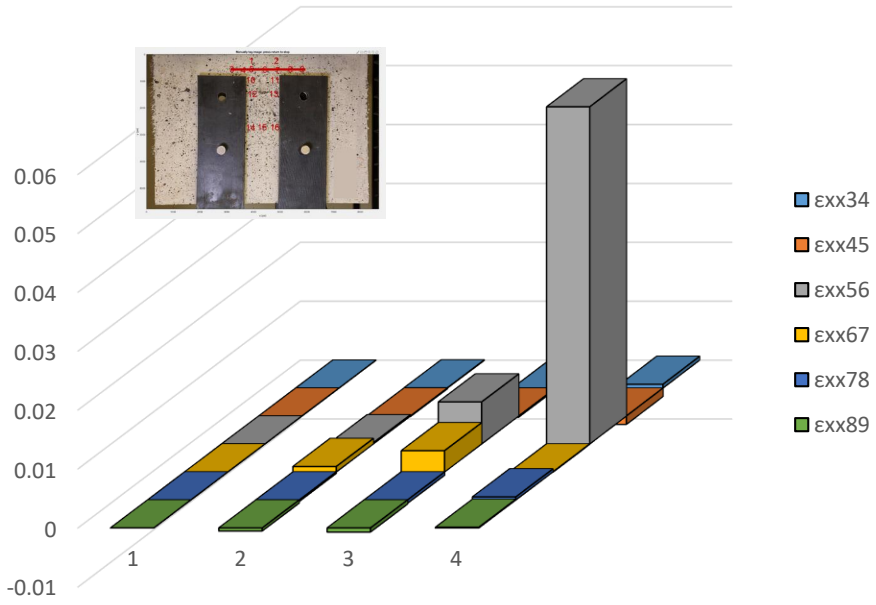

Figure A - 242 Demonstration of ε_{xx} along Layer 2 (IHNJ2-5-B – Case 1).

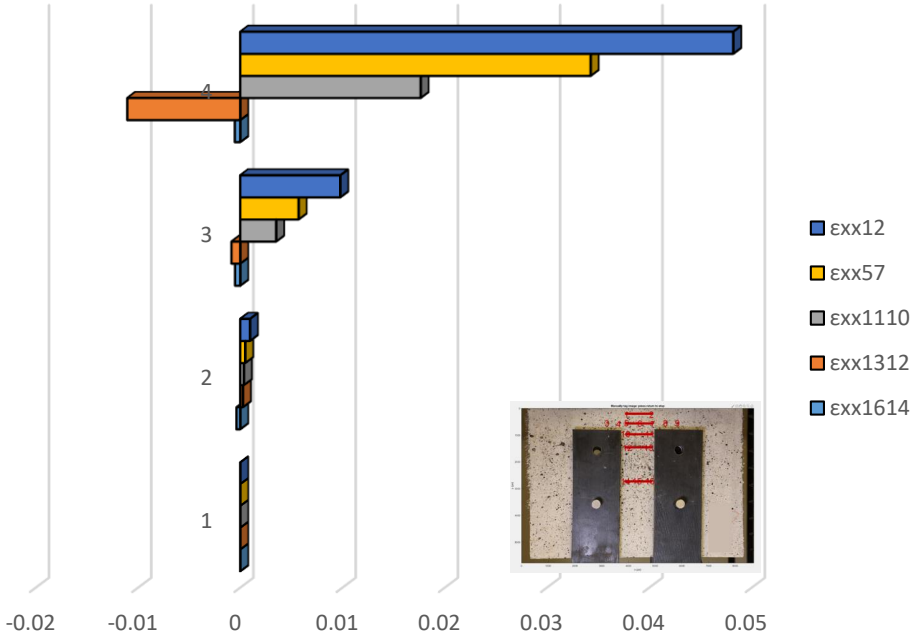

Figure A - 243 Comparison of ε_{xx} between horizontal layers (IHNJ2-5-B – Case 1).

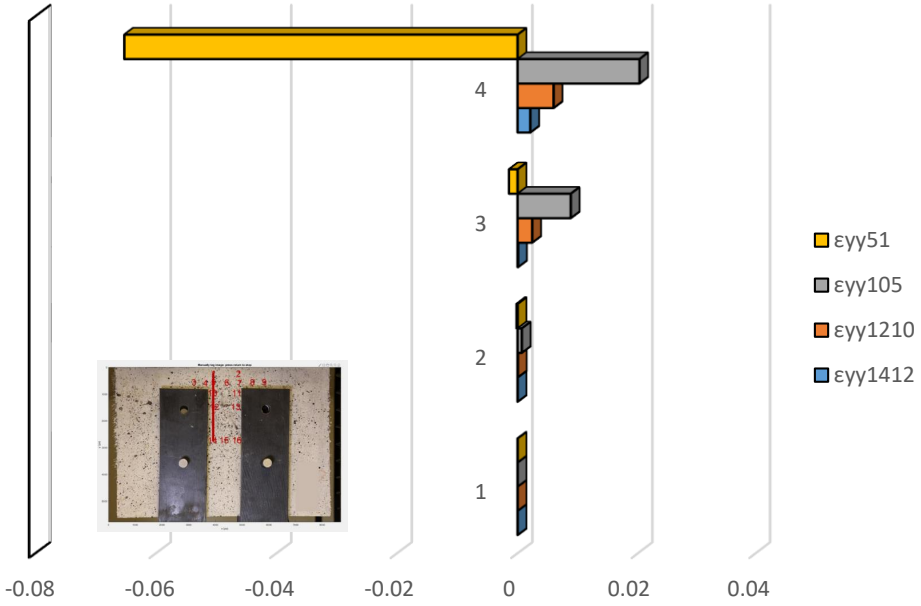

Figure A - 244 Demonstration of ε_{yy} on left vertical layer (IHNJ2-5-B – Case 1).

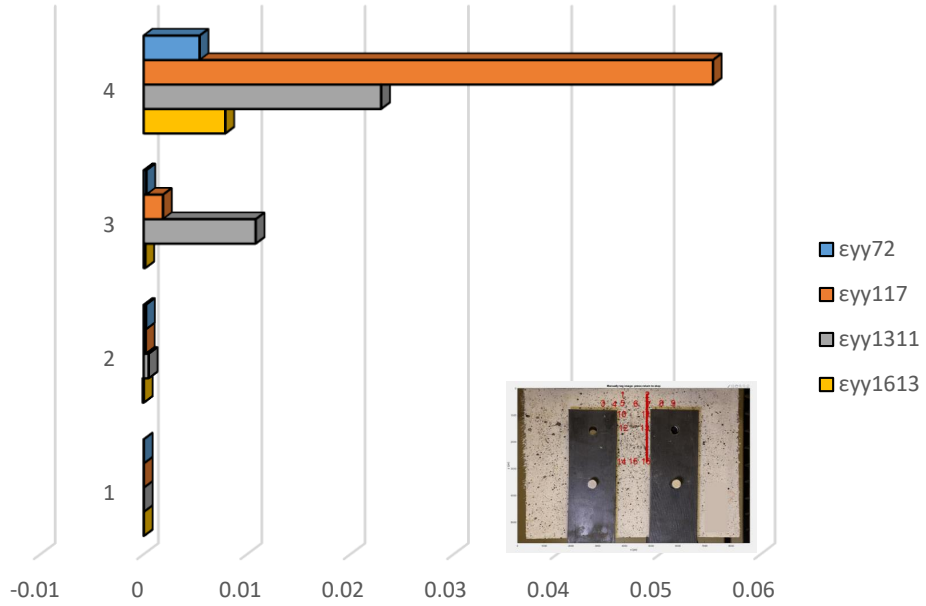

Figure A - 245 Demonstration of ε_{yy} on right vertical layer (IHNJ2-5-B – Case 1).

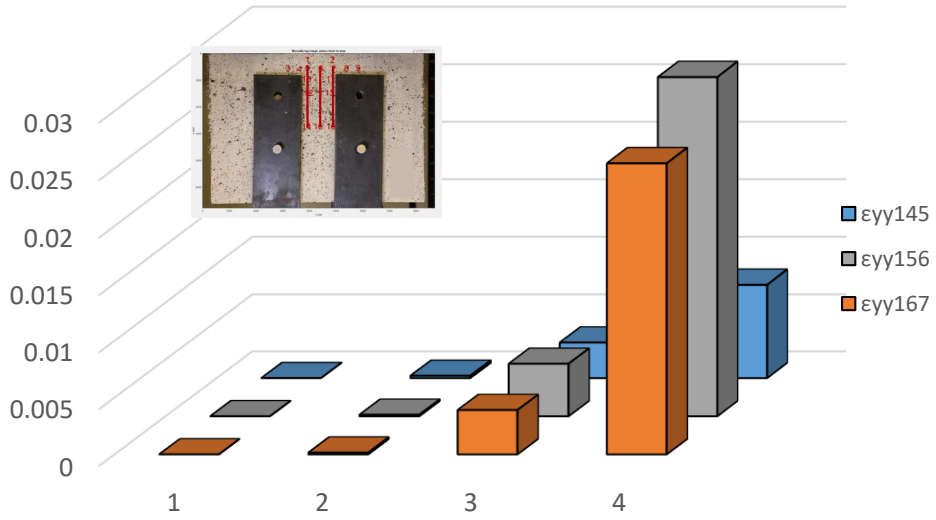

Figure A - 246 Comparison of ε_{yy} between three equidistant layers (IHNJ2-5-B – Case 1).

Detailed analysis in three milestone points – Case 2

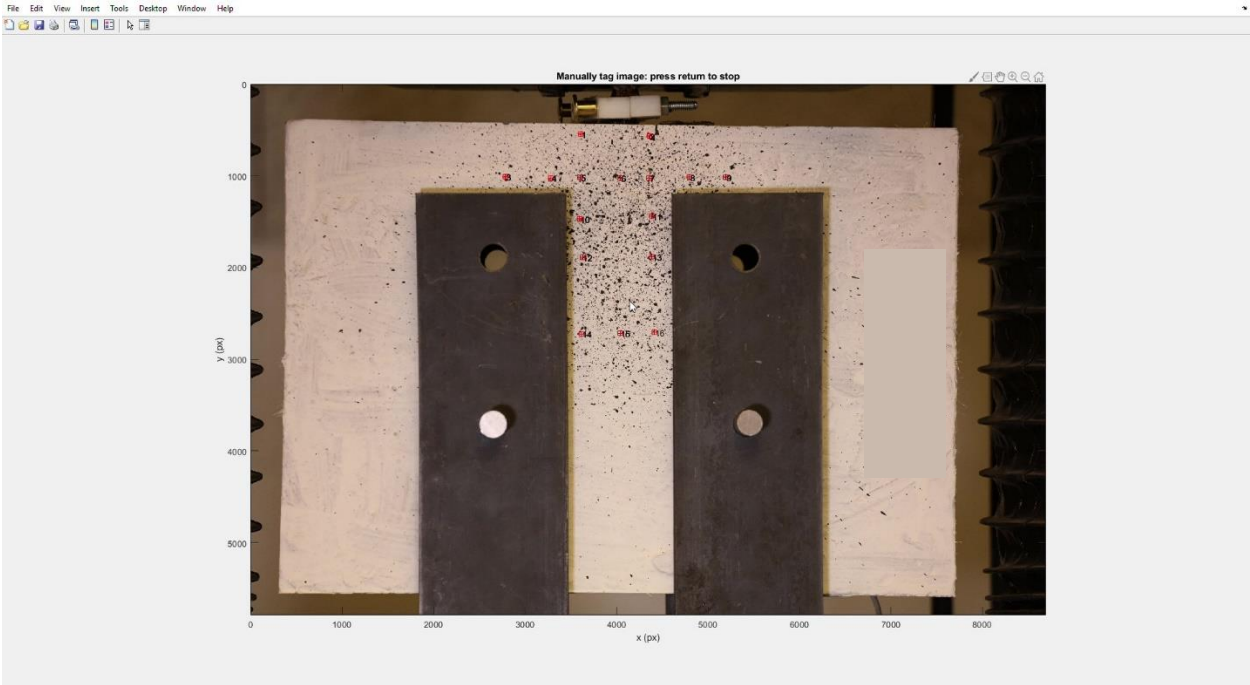

Figure A - 247 Locations of POIs for specimen IHNJ2-5-B (Case 2).

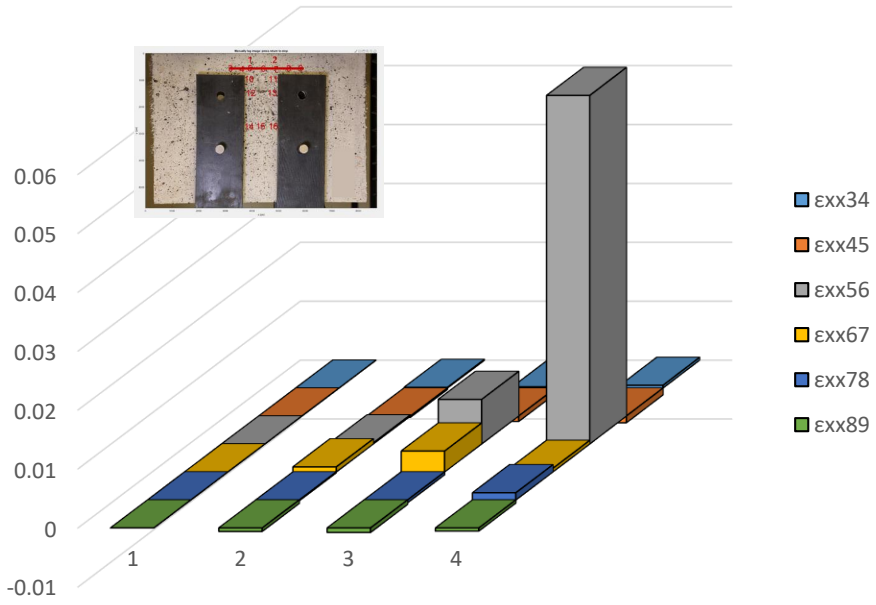

Figure A - 248 Demonstration of ε_{xx} along Layer 2 (IHNJ2-5-B – Case 1).

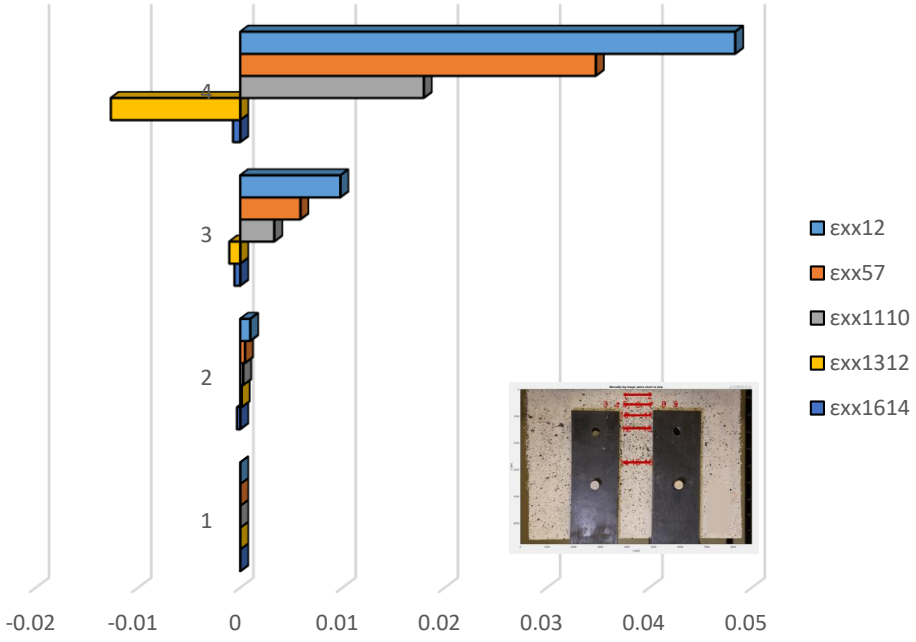

Figure A - 249 Comparison of ε_{xx} between horizontal layers (IHNJ2-5-B – Case 1).

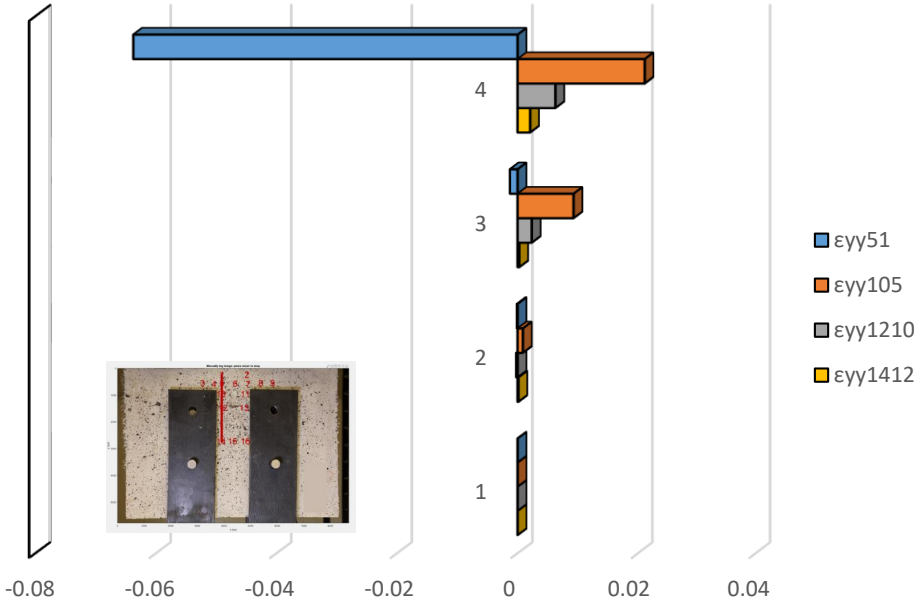

Figure A - 250 Demonstration of ε_{yy} on left vertical layer (IHNJ2-5-B – Case 2).

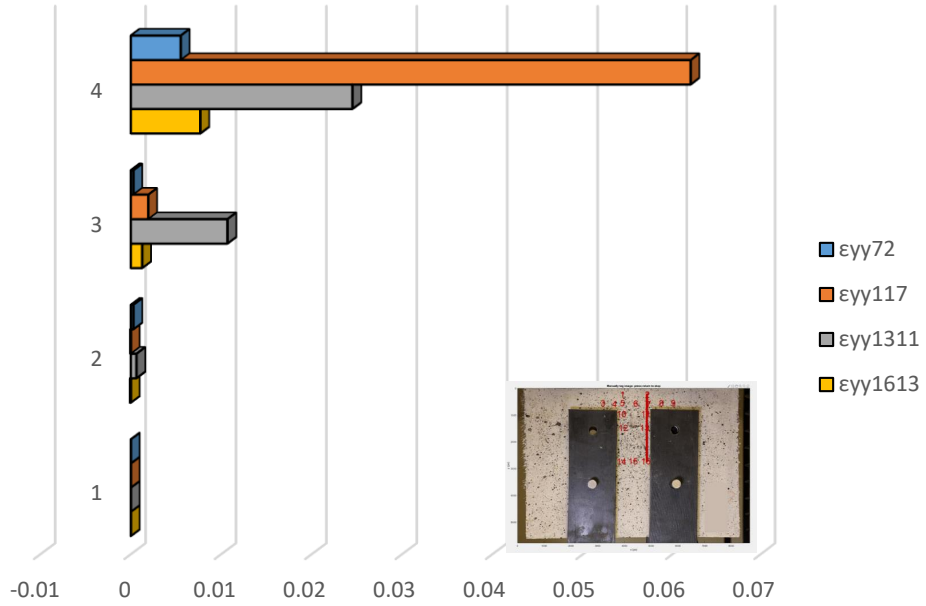

Figure A - 251 Demonstration of ε_{yy} on right vertical layer (IHNJ2-5-B – Case 2).

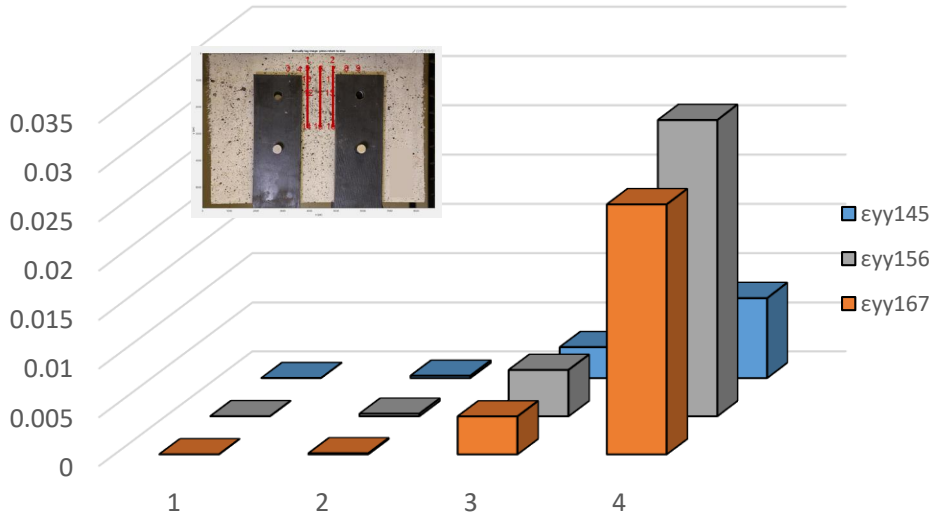

Figure A - 252 Comparison of ε_{yy} between three equidistant layers (IHNJ2-5-B – Case 2).

Detailed analysis in three milestone points – Case 3

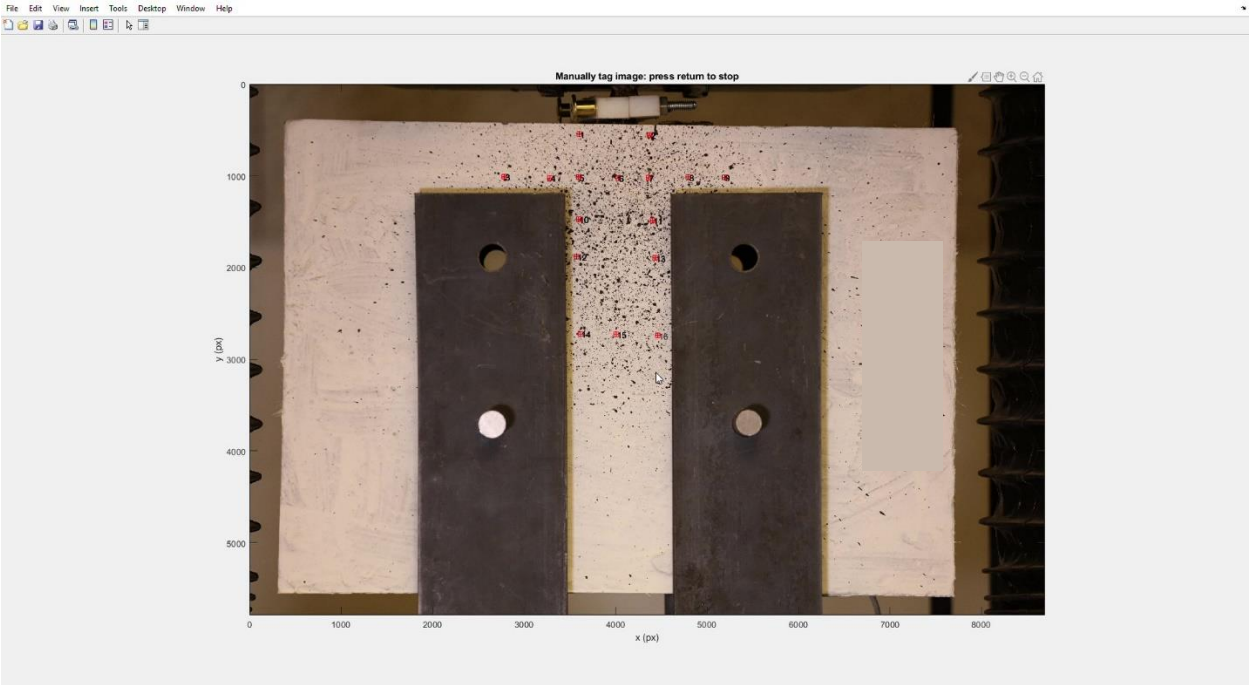

Figure A - 253 Locations of POIs for specimen IHNJ2-5-B (Case 3).

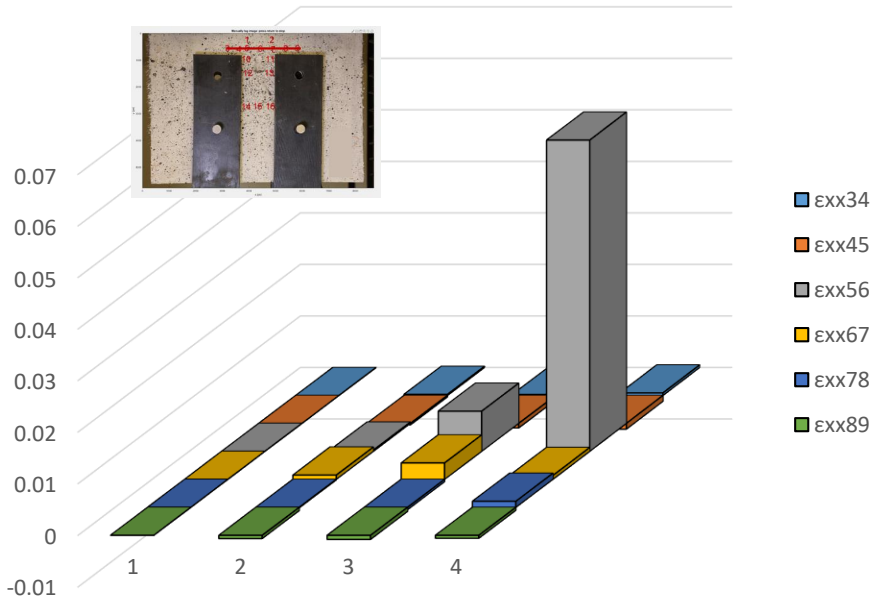

Figure A - 254 Demonstration of ε_{xx} along Layer 2 (IHNJ2-5-B – Case 3).

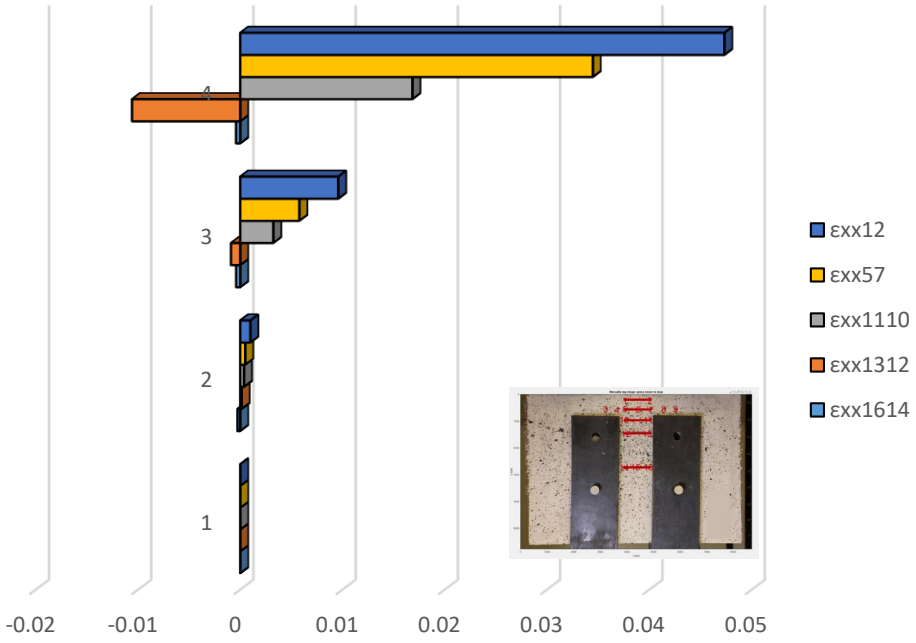

Figure A - 255 Comparison of ε_{xx} between horizontal layers (IHNJ2-5-B – Case 3).

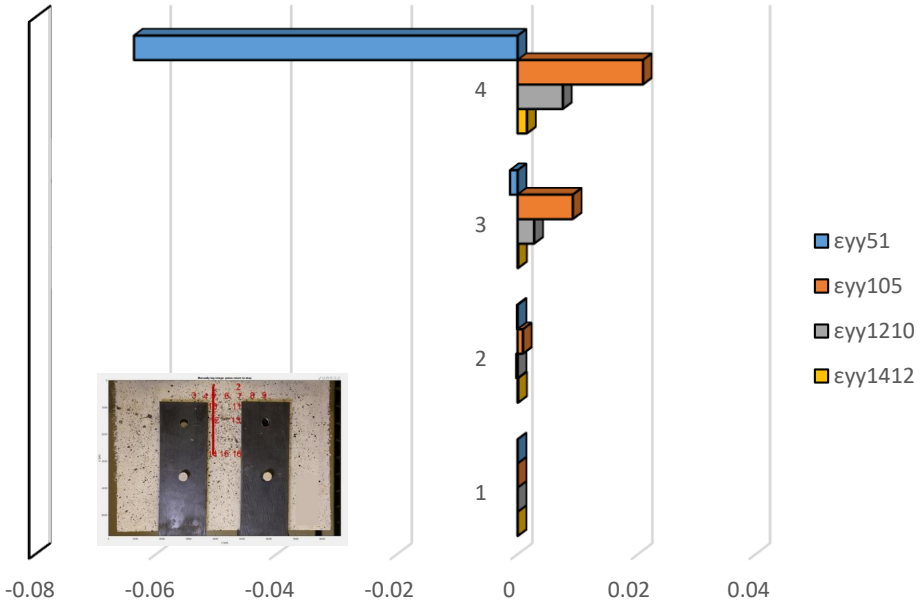

Figure A - 256 Demonstration of ε_{yy} on left vertical layer (IHNJ2-5-B – Case 3).

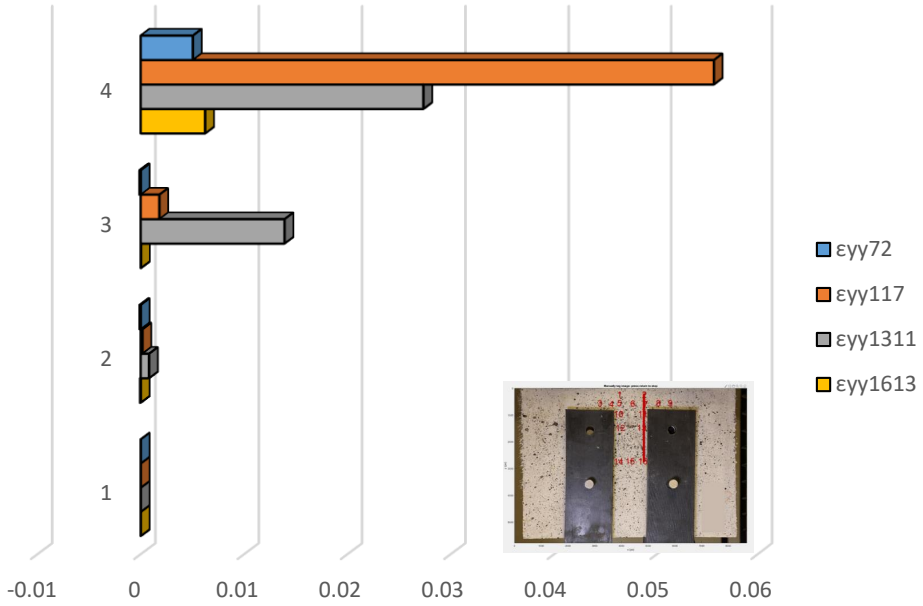

Figure A - 257 Demonstration of ε_{yy} on right vertical layer (IHNJ2-5-B – Case 3).

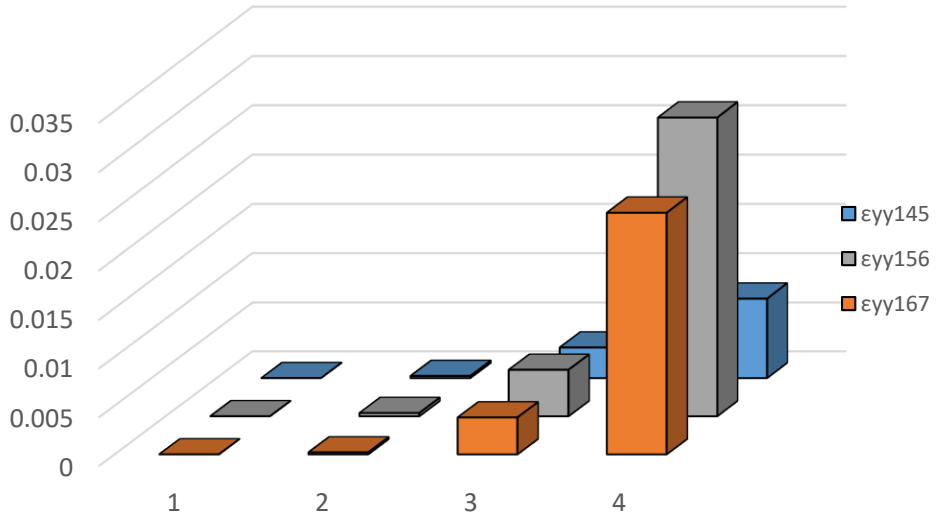

Figure A - 258 Comparison of ε_{yy} between three equidistant layers (IHNJ2-5-B – Case 3).

Specimen IHRT2-5-A

Complete analysis

Figure A - 259 Locations of Points of Interest for specimen IHRT2-5-A (Complete Analysis).

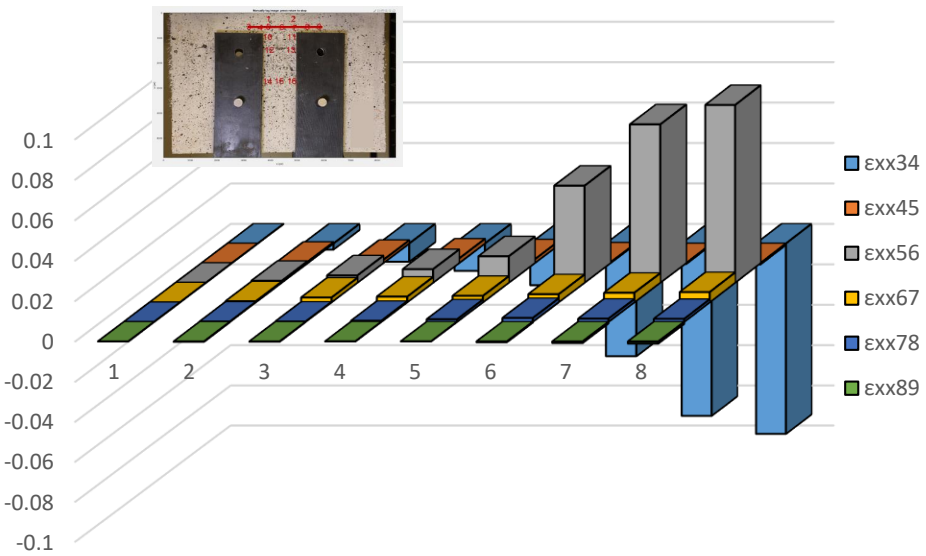

Figure A - 260 Demonstration of ε_{xx} along Layer 2 (IHRT2-5-A – Complete analysis).

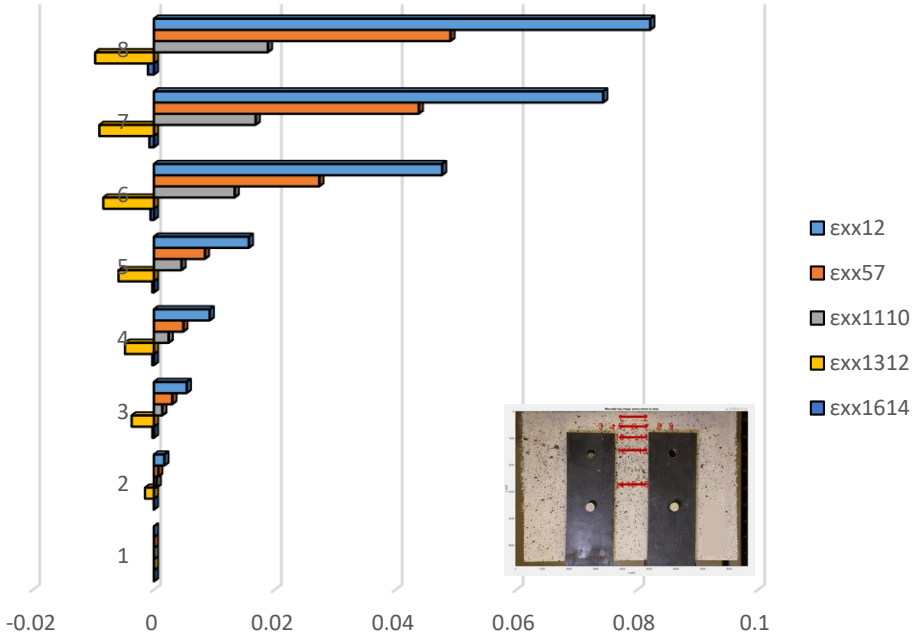

Figure A - 261 Comparison of ε_{xx} between horizontal layers (IHRT2-5-A – Complete analysis).

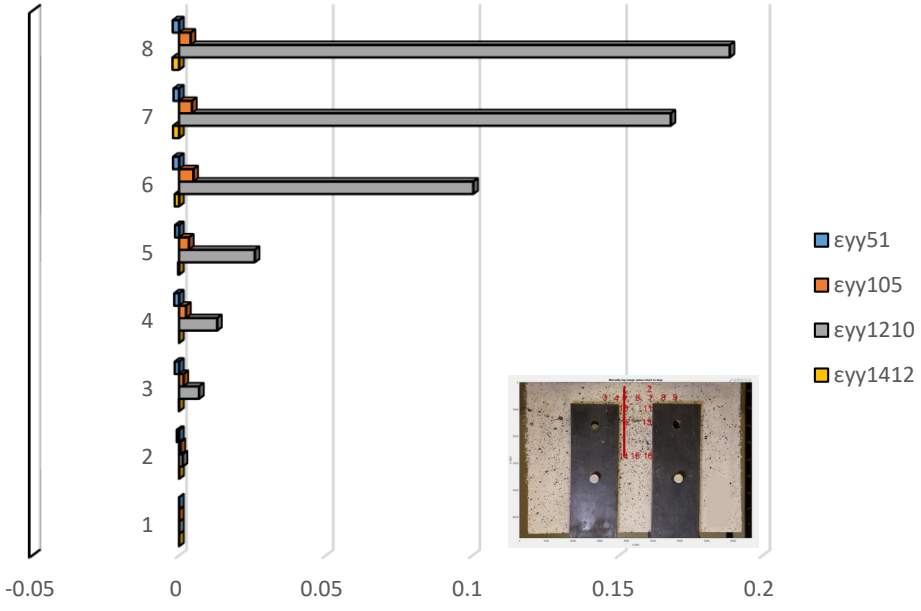

Figure A - 262 Demonstration of ε_{yy} on left vertical layer (IHRT2-5-A – Complete analysis).

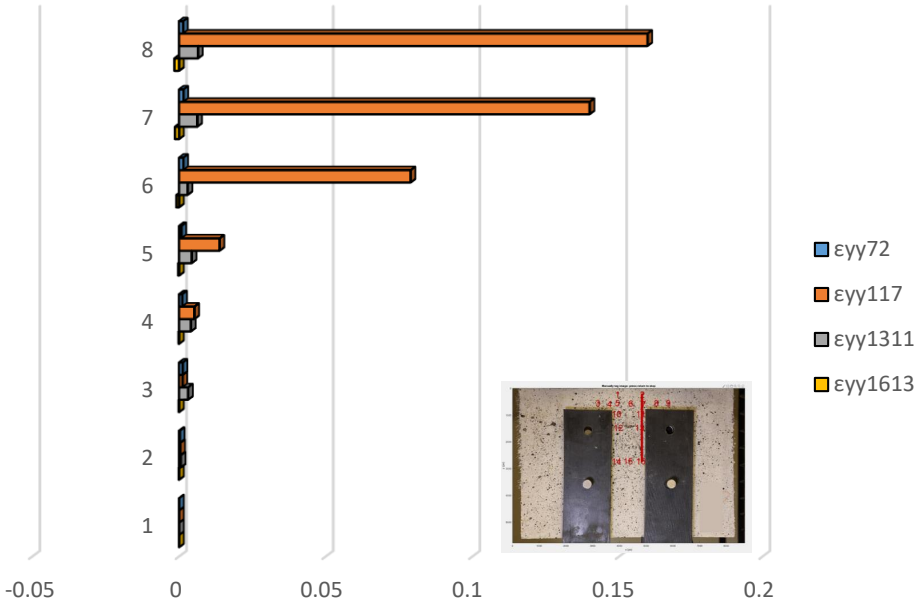

Figure A - 263 Demonstration of ε_{yy} on right vertical layer (IHRT2-5-A – Complete analysis).

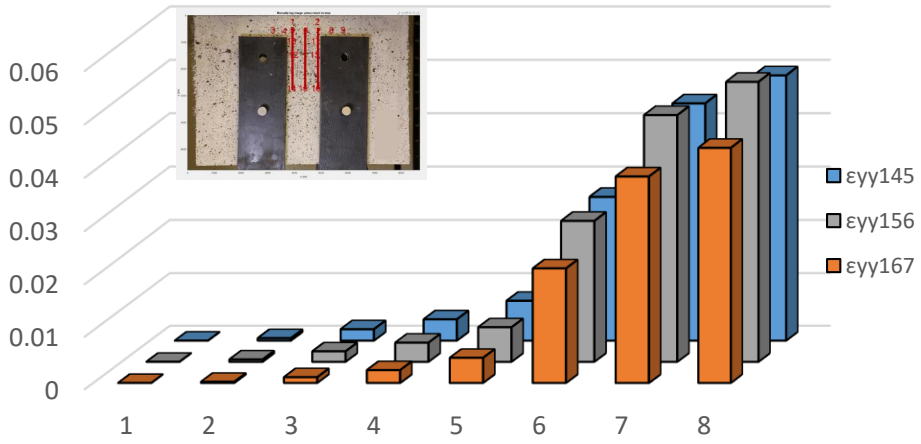

Figure A - 264 Comparison of ε_{yy} between three equidistant layers (IHRT2-5-A – Complete analysis).

Detailed analysis in three milestone points – Case 1

Figure A - 265 Locations of POIs for specimen IHRT2-5-A (Case 1).

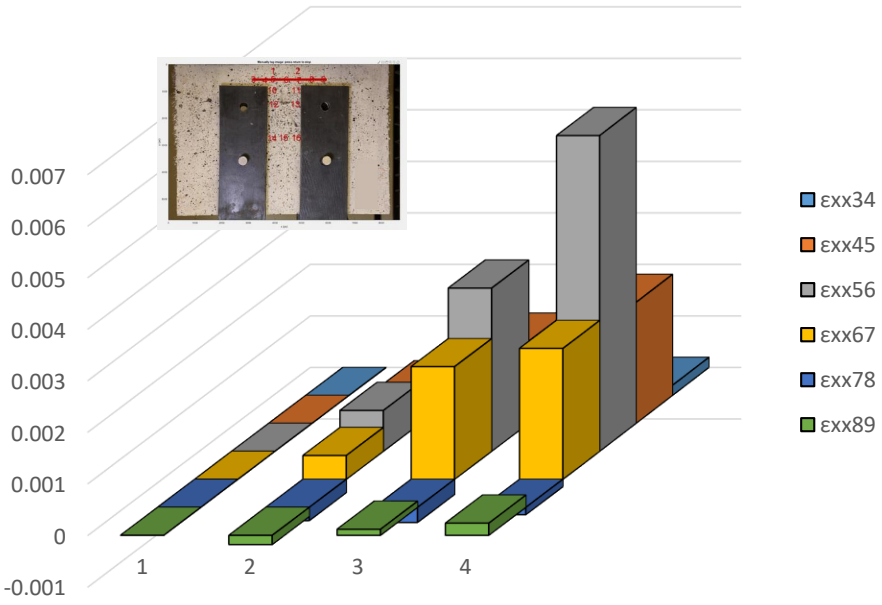

Figure A - 266 Demonstration of ε_{xx} along Layer 2 (IHRT2-5-A – Case 1).

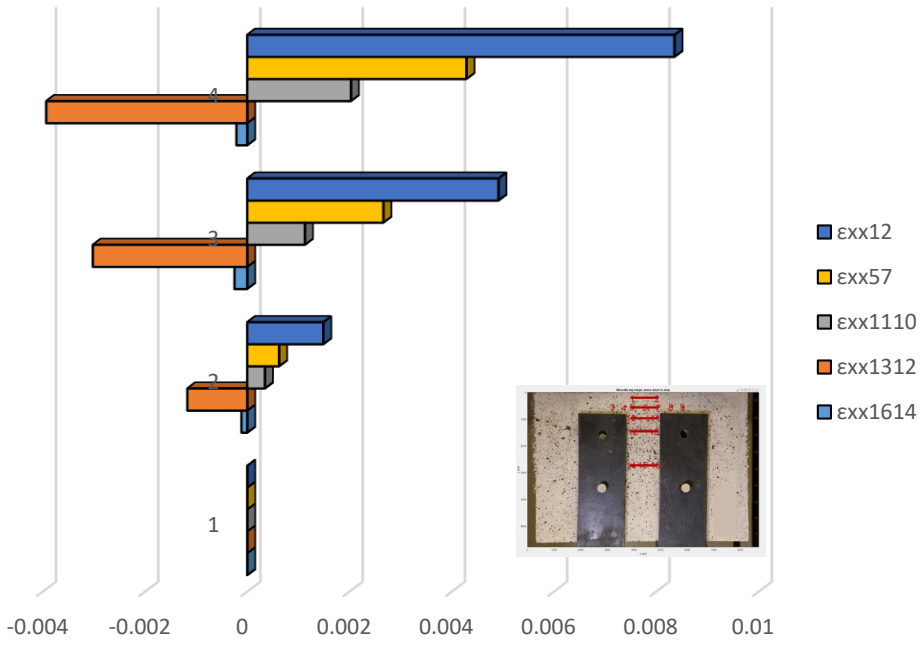

Figure A - 267 Comparison of ε_{xx} between horizontal layers (IHRT2-5-A – Case 1).

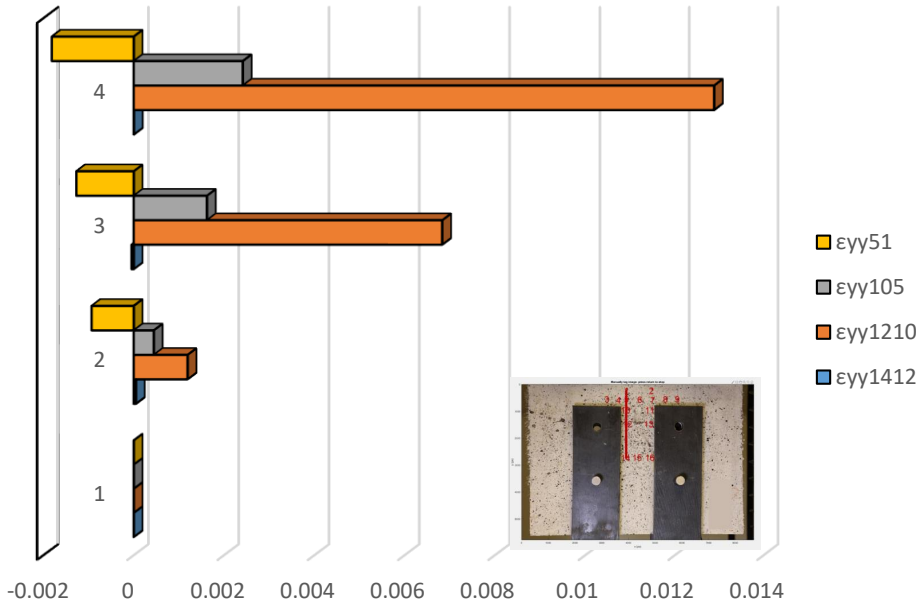

Figure A - 268 Demonstration of ε_{yy} on left vertical layer (IHRT2-5-A – Case 1).

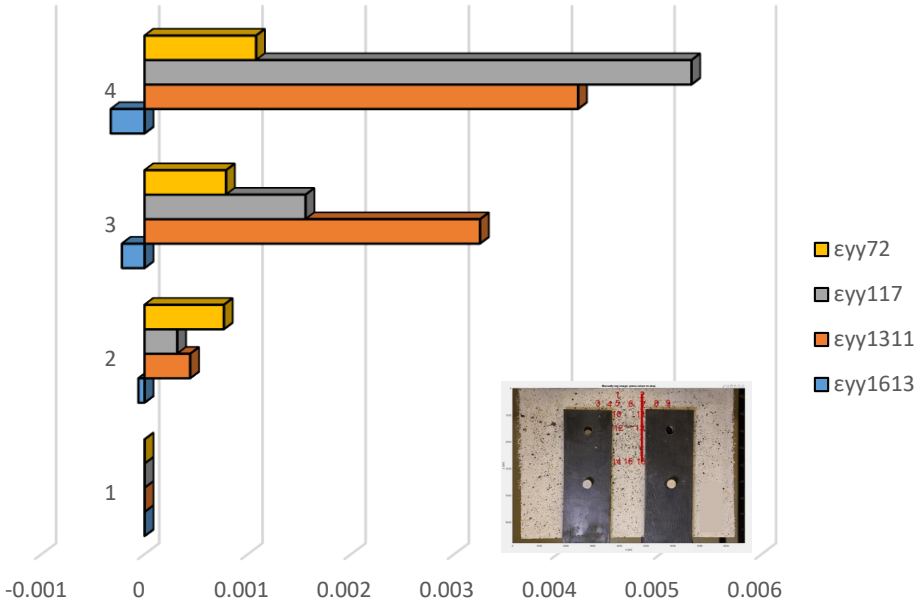

Figure A - 269 Demonstration of ε_{yy} on right vertical layer (IHRT2-5-A – Case 1).

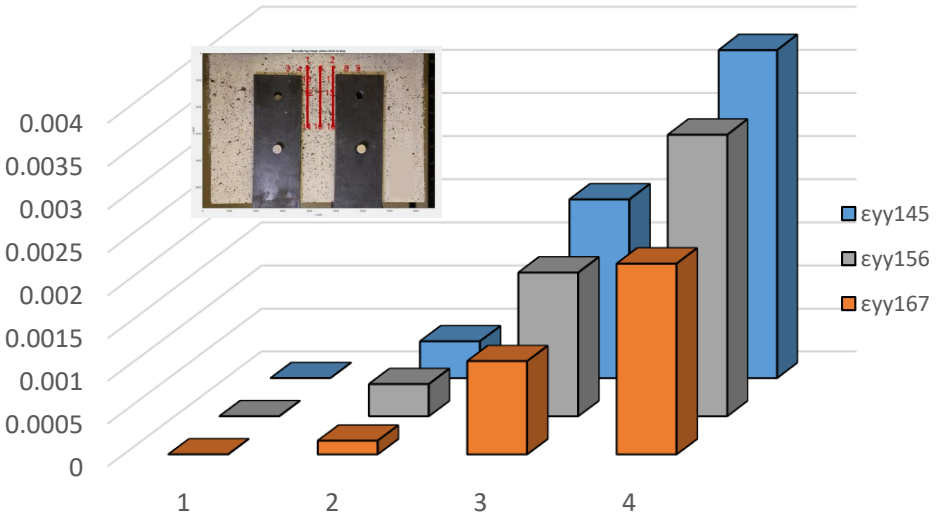

Figure A - 270 Comparison of ε_{yy} between three equidistant layers (IHRT2-5-A – Case 1).

Detailed analysis in three milestone points – Case 2

Figure A - 271 Locations of POIs for specimen IHRT2-5-A (Case 2).

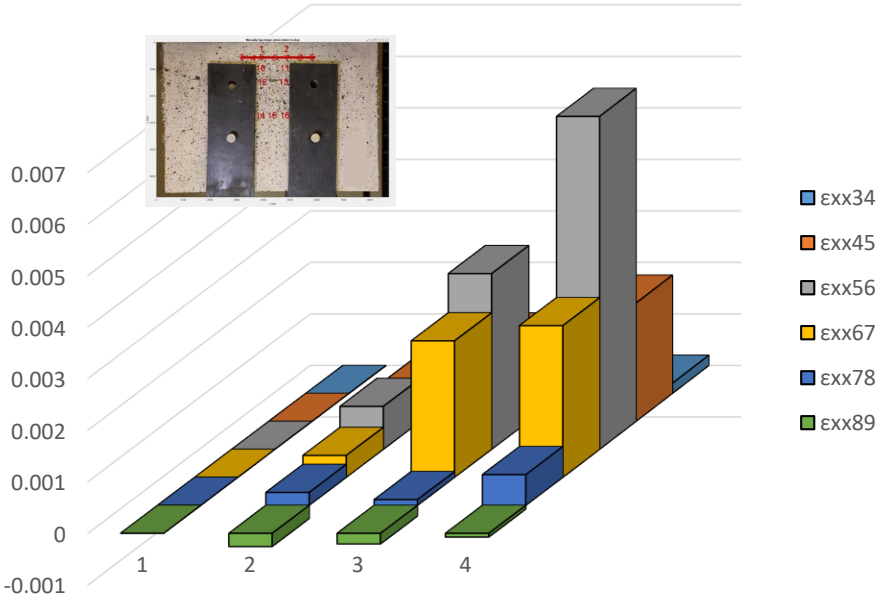

Figure A - 272 Demonstration of ε_{xx} along Layer 2 (IHRT2-5-A – Case 2).

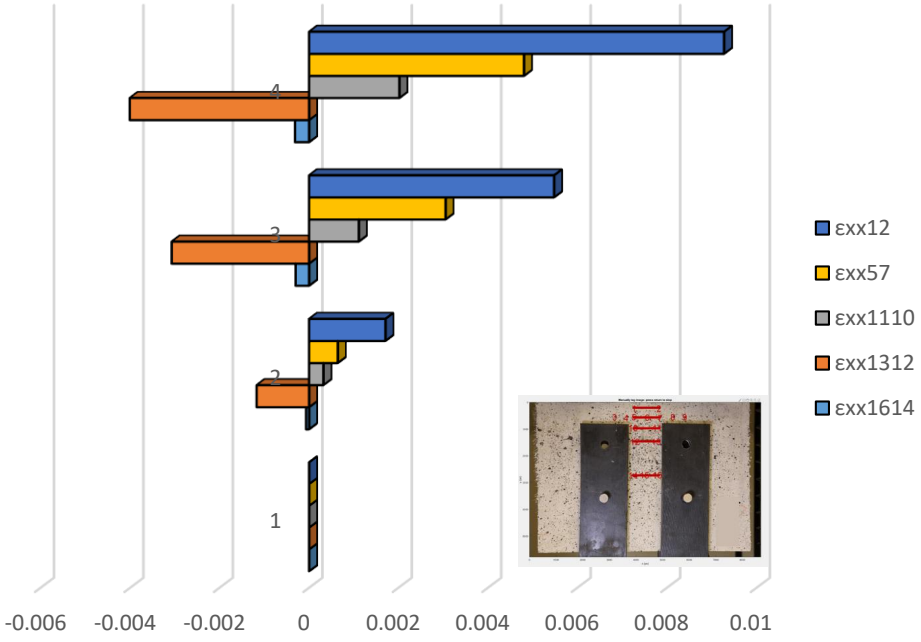

Figure A - 273 Comparison of ε_{xx} between horizontal layers (IHRT2-5-A – Case 2).

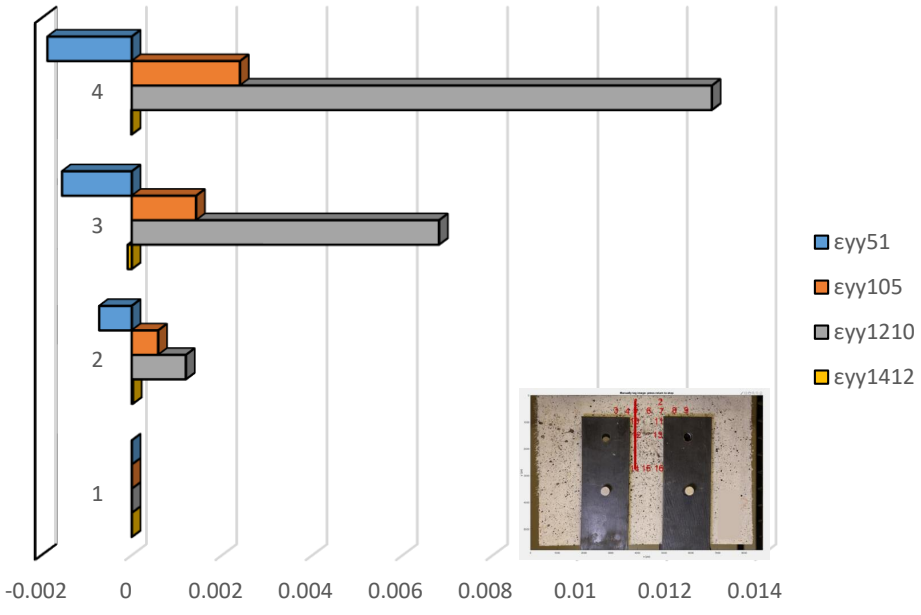

Figure A - 274 Demonstration of ε_{yy} on left vertical layer (IHRT2-5-A – Case 2).

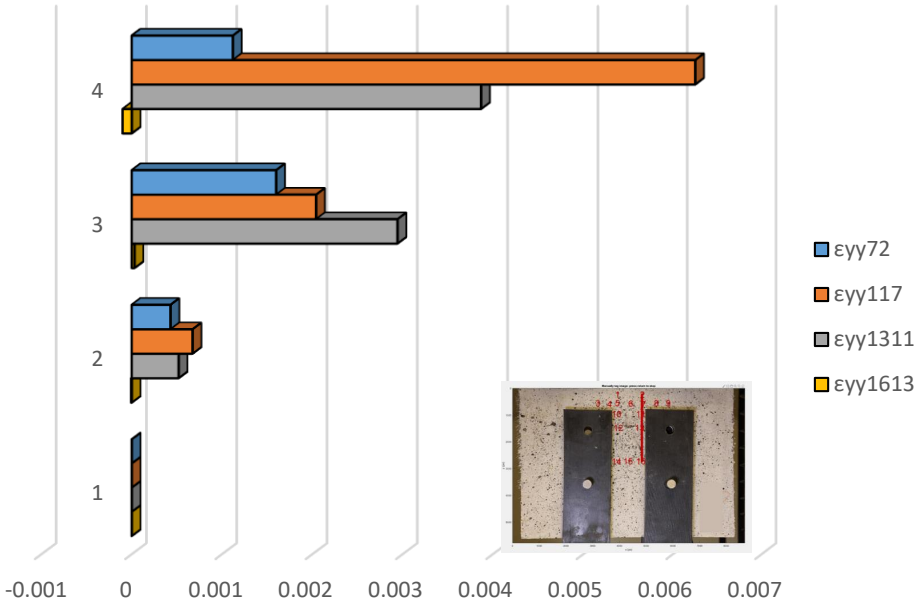

Figure A - 275 Demonstration of ε_{yy} on right vertical layer (IHRT2-5-A – Case 2).

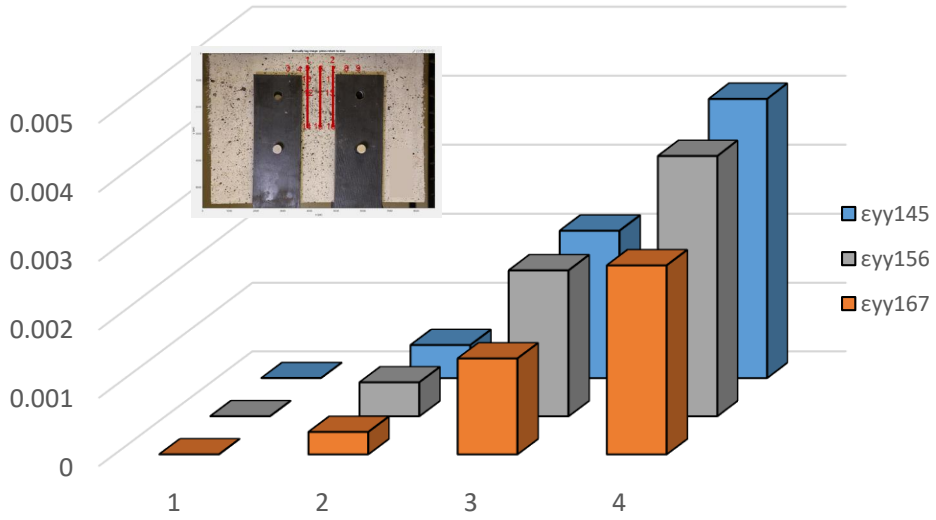

Figure A - 276 Comparison of ε_{yy} between three equidistant layers (IHRT2-5-A – Case 2).

Detailed analysis in three milestone points – Case 3

Figure A - 277 Locations of POIs for specimen IHRT2-5-A (Case 3).

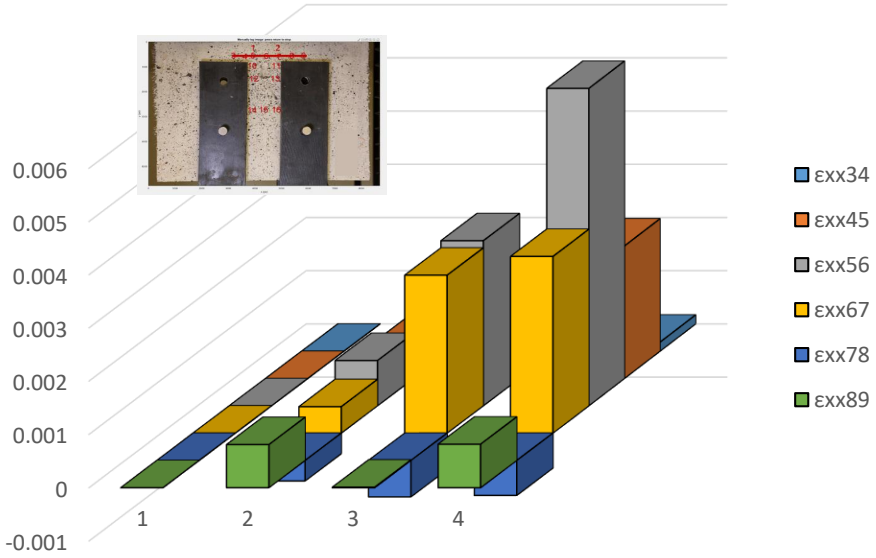

Figure A - 278 Demonstration of ε_{xx} along Layer 2 (IHRT2-5-A – Case 3).

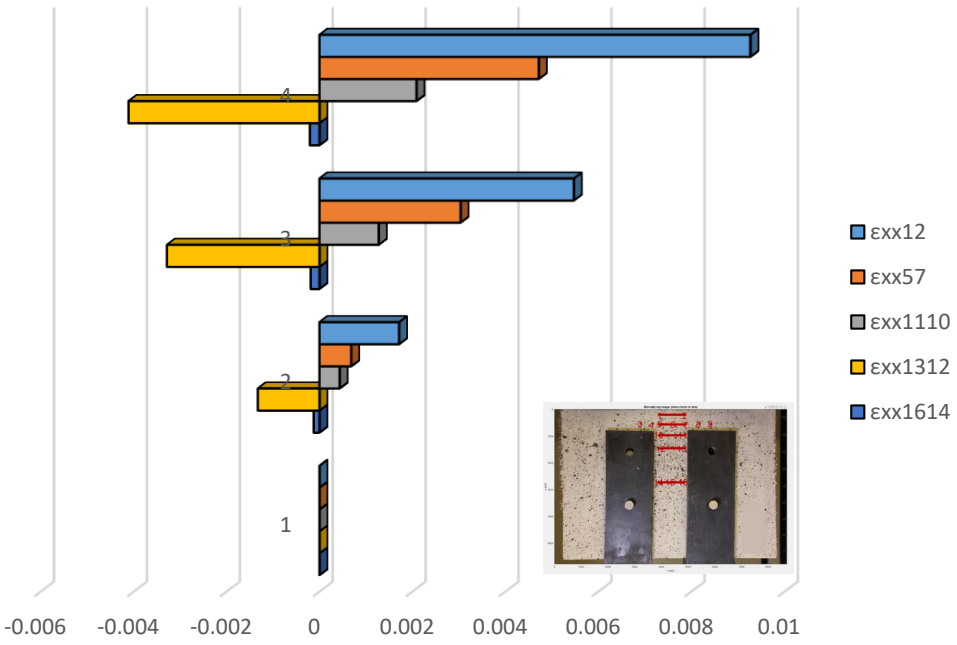

Figure A - 279 Comparison of ε_{xx} between horizontal layers (IHRT2-5-A – Case 3).

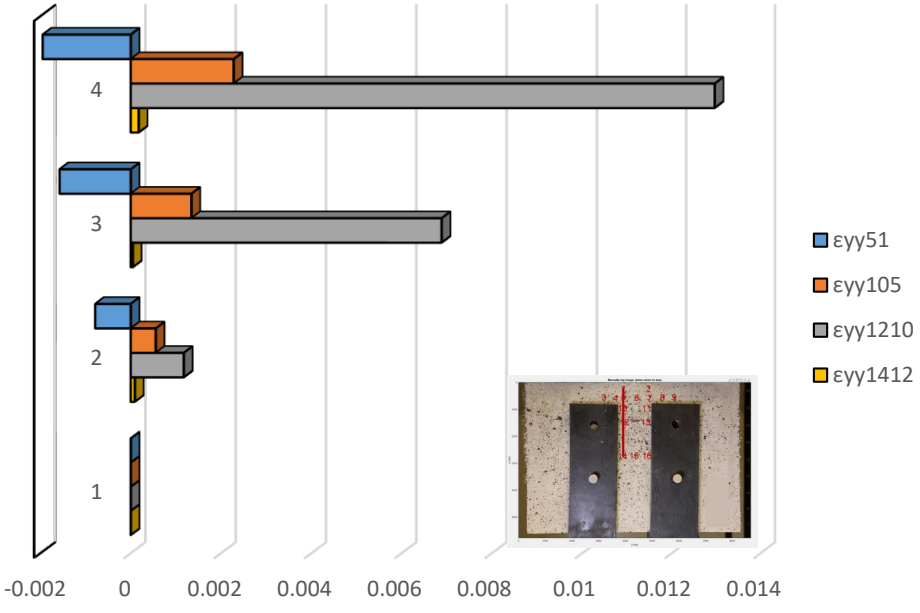

Figure A - 280 Demonstration of ε_{yy} on left vertical layer (IHRT2-5-A – Case 3).

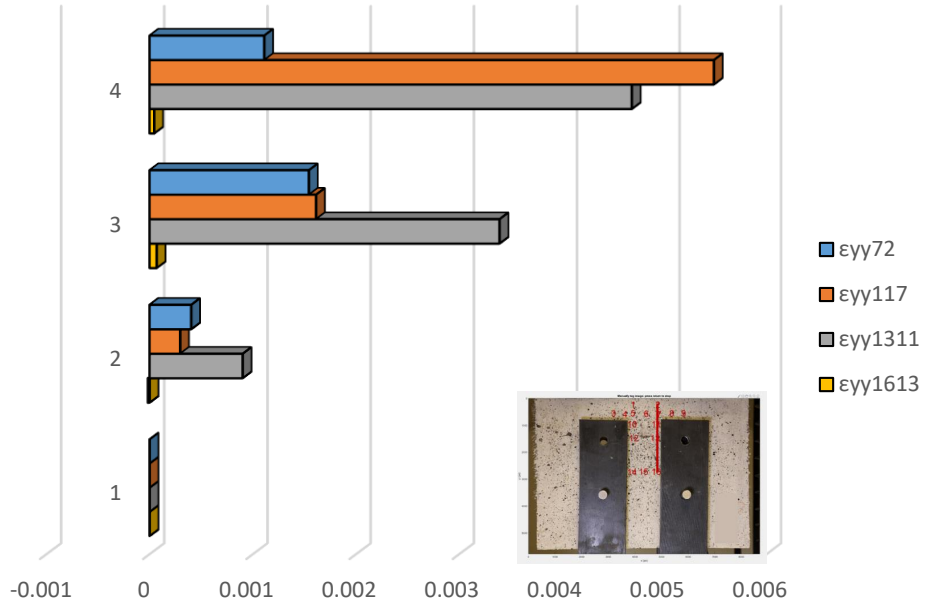

Figure A - 281 Demonstration of ε_{yy} on right vertical layer (IHRT2-5-A – Case 3).

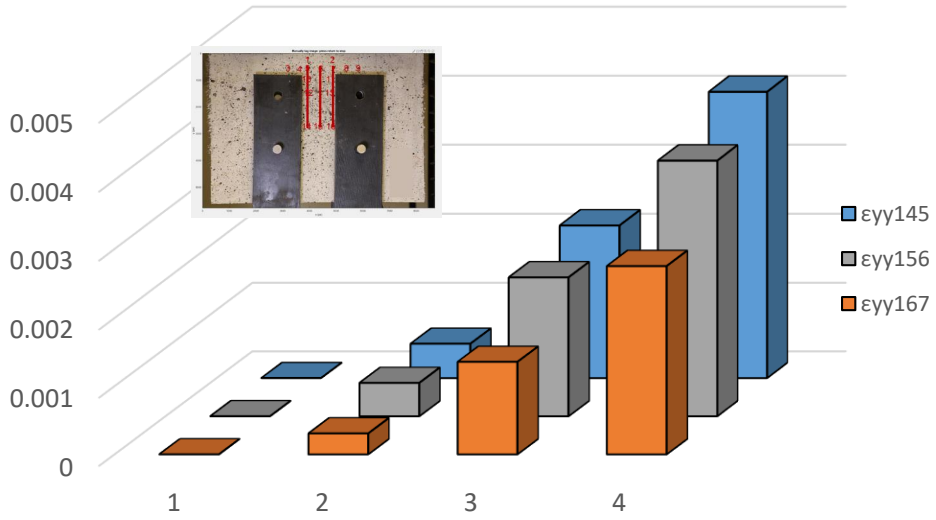

Figure A - 282 Comparison of ε_{yy} between three equidistant layers (IHRT2-5-A – Case 3).

Specimen IHRT2-5-B

Complete analysis

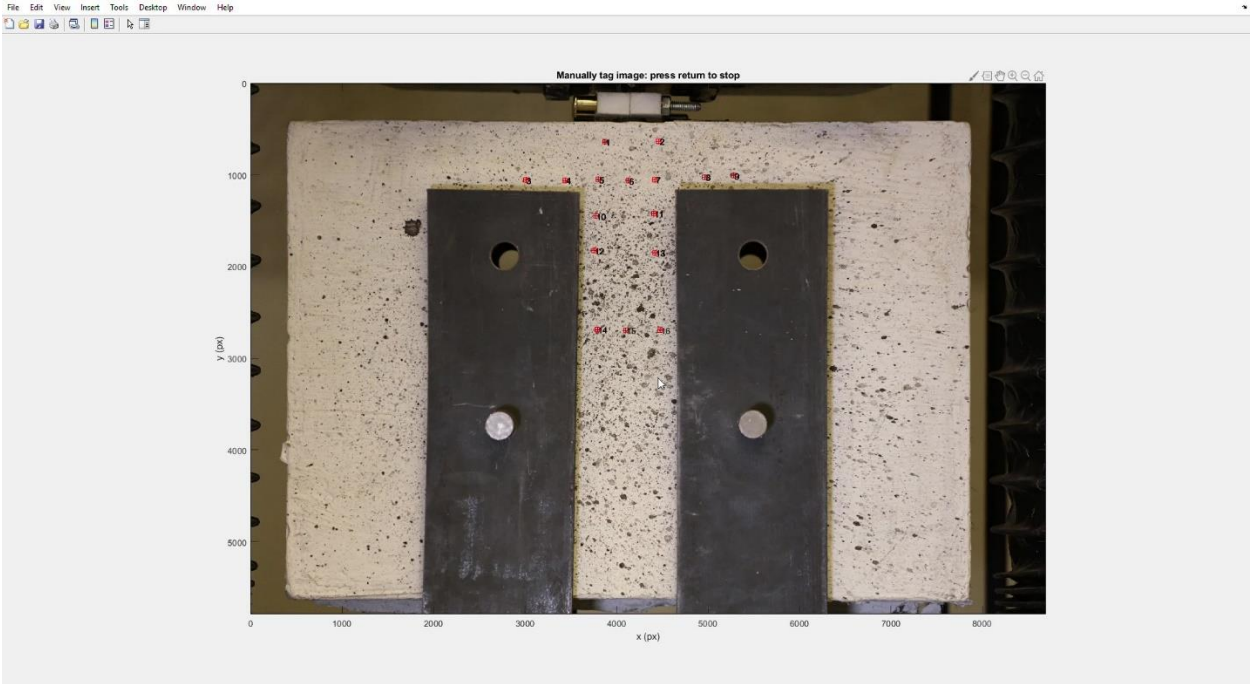

Figure A - 283 Locations of Points of Interest for specimen IHRT2-5-B (Complete Analysis).

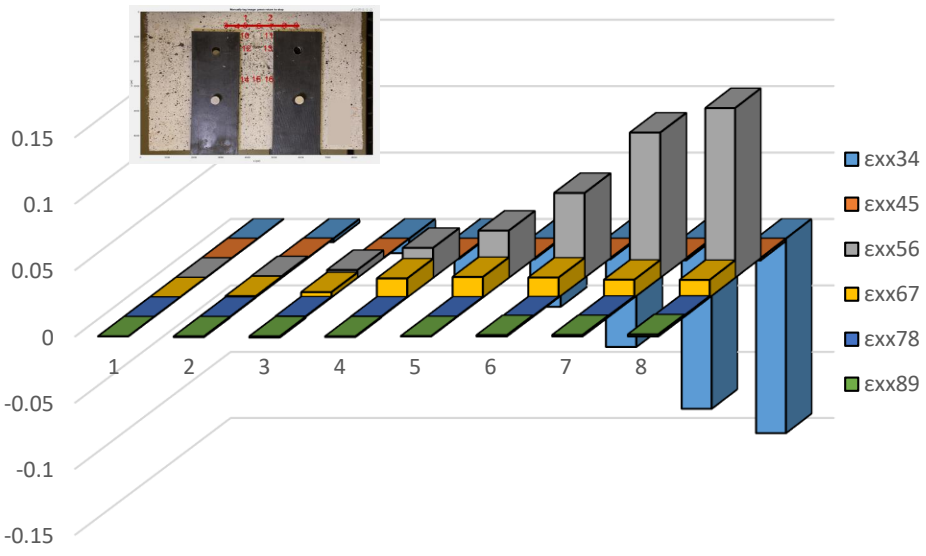

Figure A - 284 Demonstration of ε_{xx} along Layer 2 (IHRT2-5-B – Complete analysis).

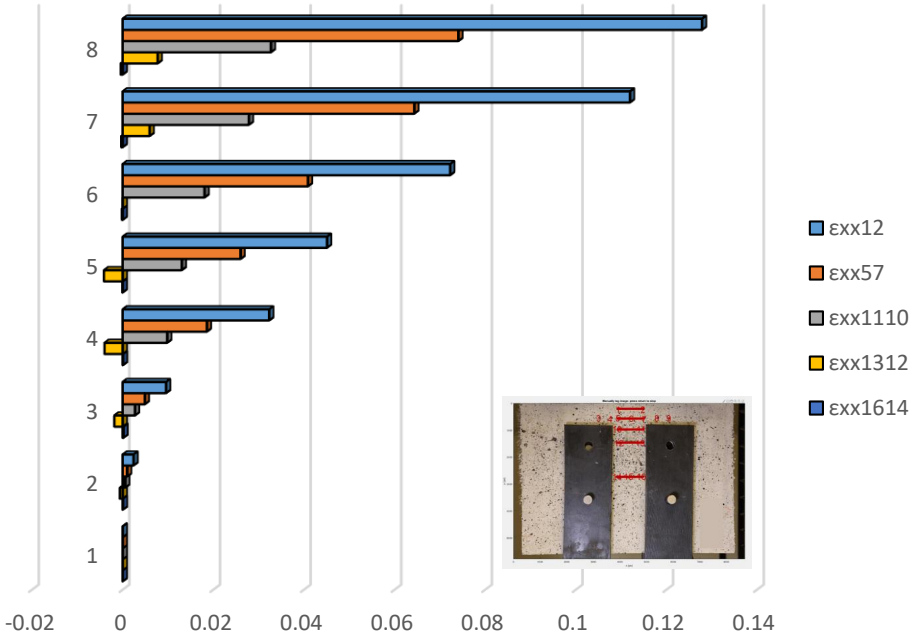

Figure A - 285 Comparison of ε_{xx} between horizontal layers (IHRT2-5-B – Complete analysis).

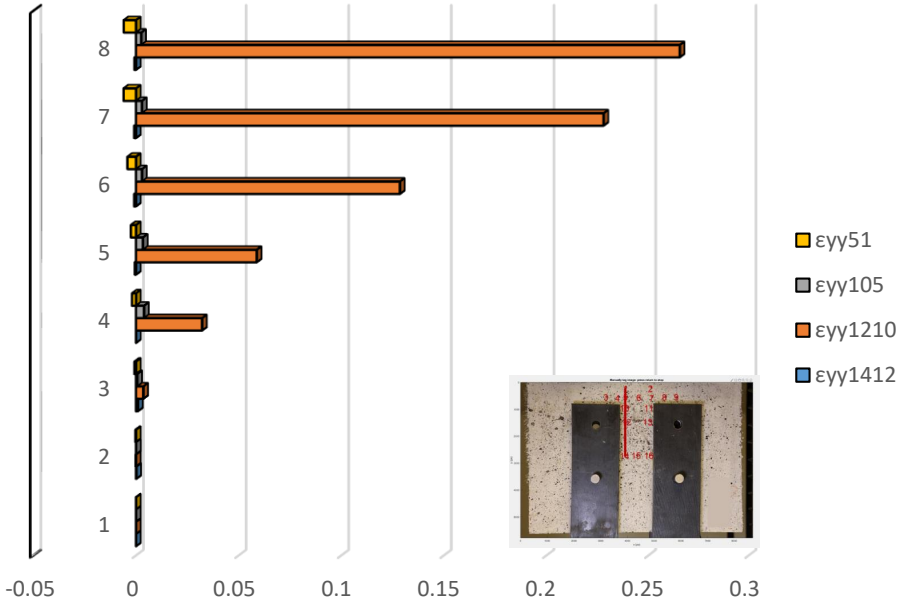

Figure A - 286 Demonstration of ε_{yy} on left vertical layer (IHRT2-5-B – Complete analysis).

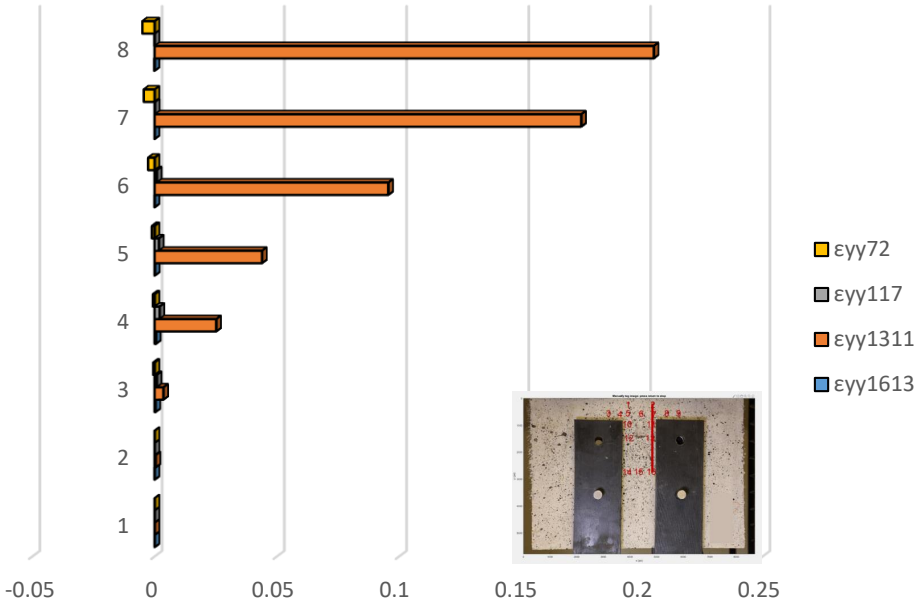

Figure A - 287 Demonstration of ε_{yy} on right vertical layer (IHRT2-5-B – Complete analysis).

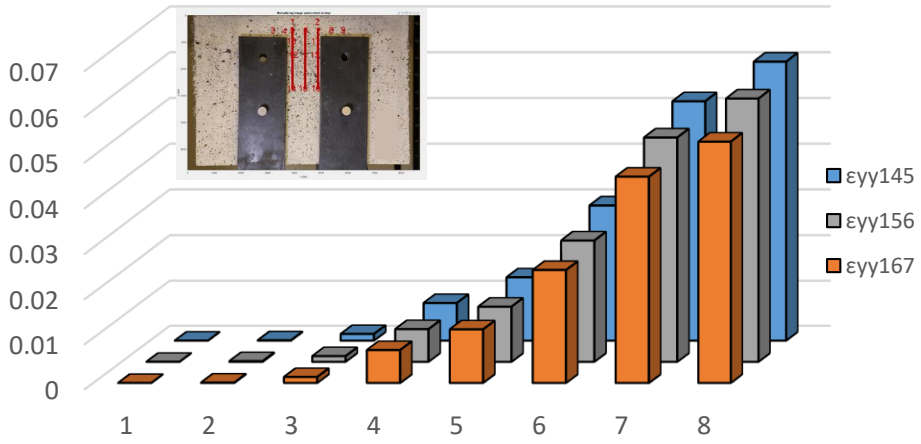

Figure A - 288 Comparison of ε_{yy} between three equidistant layers (IHRT2-5-B – Complete analysis).

Detailed analysis in three milestone points – Case 1

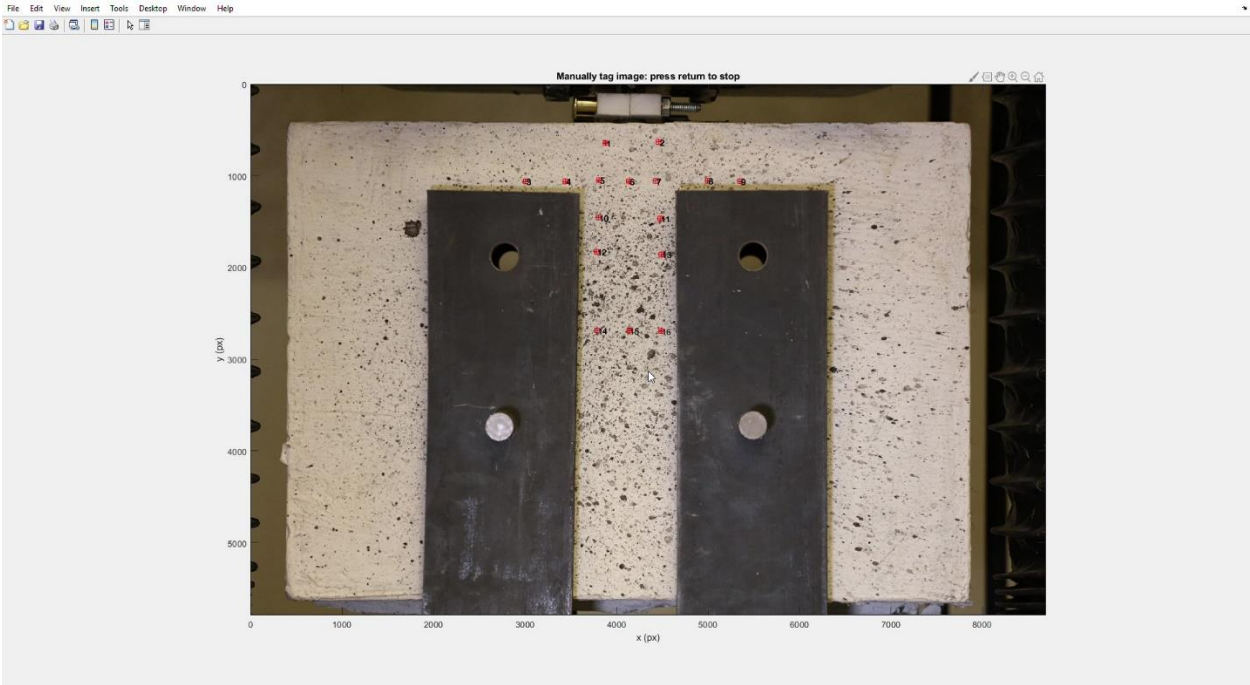

Figure A - 289 Locations of POIs for specimen IHRT2-5-B (Case 1).

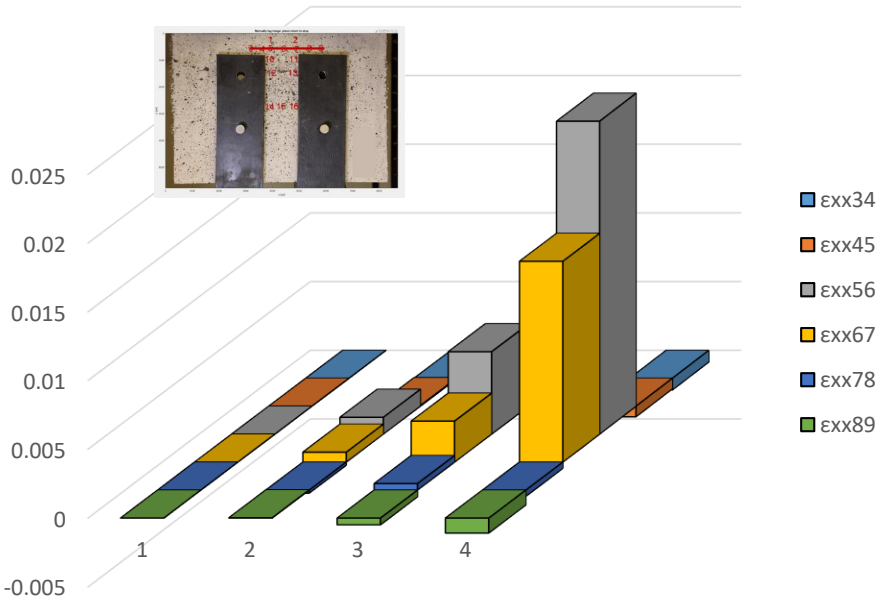

Figure A - 290 Demonstration of ε_{xx} along Layer 2 (IHRT2-5-B – Case 1).

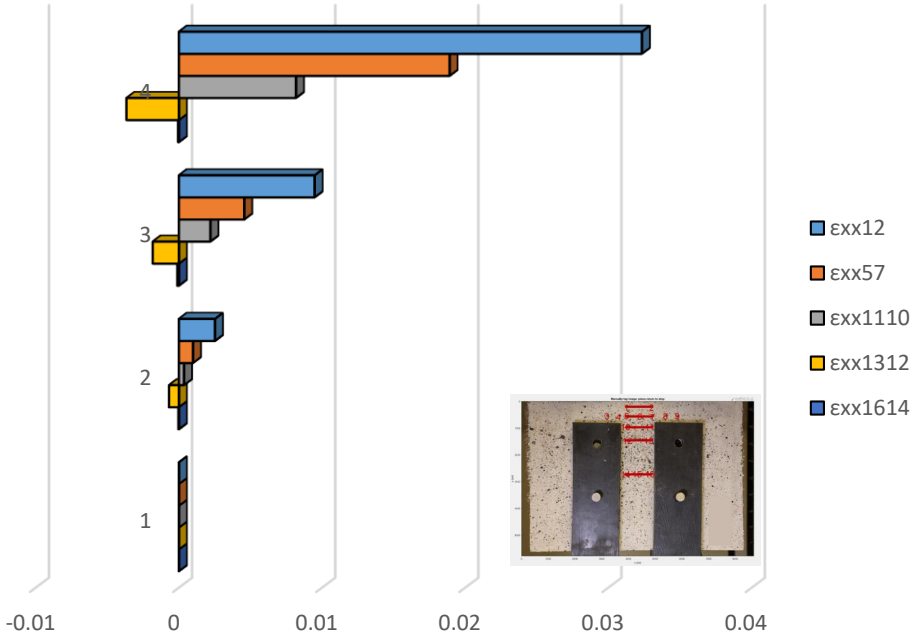

Figure A - 291 Comparison of ε_{xx} between horizontal layers (IHRT2-5-B – Case 1).

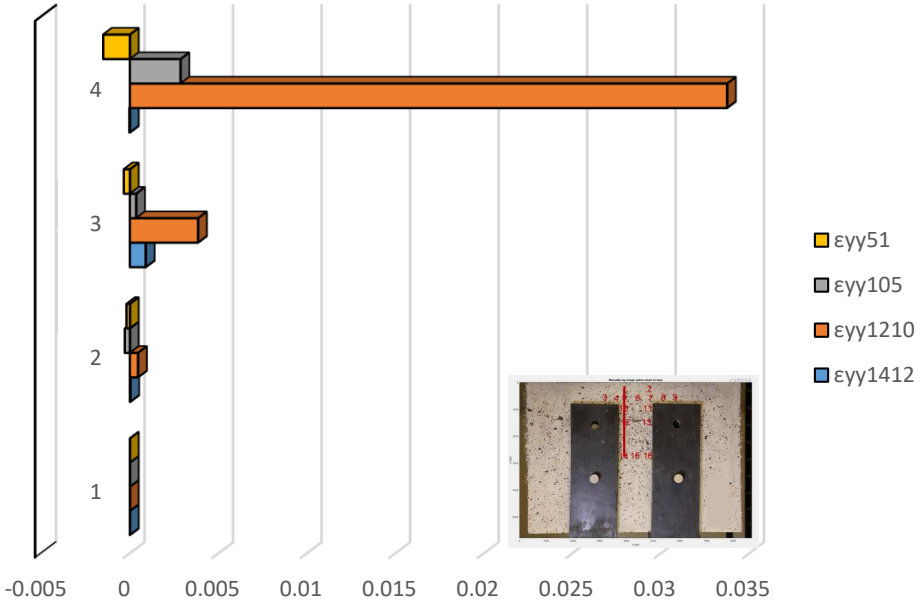

Figure A - 292 Demonstration of ε_{yy} on left vertical layer (IHRT2-5-B – Case 1).

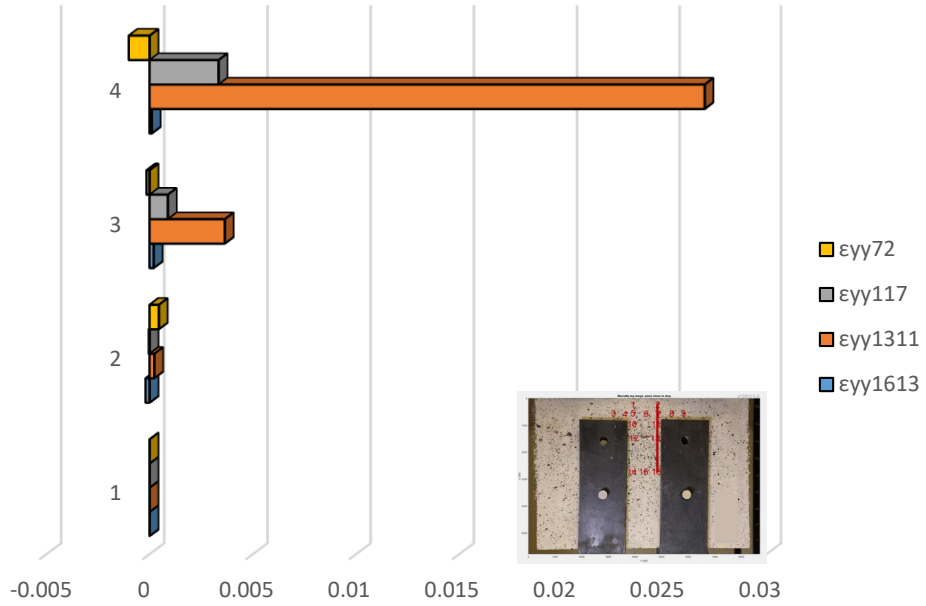

Figure A - 293 Demonstration of ε_{yy} on right vertical layer (IHRT2-5-B – Case 1).

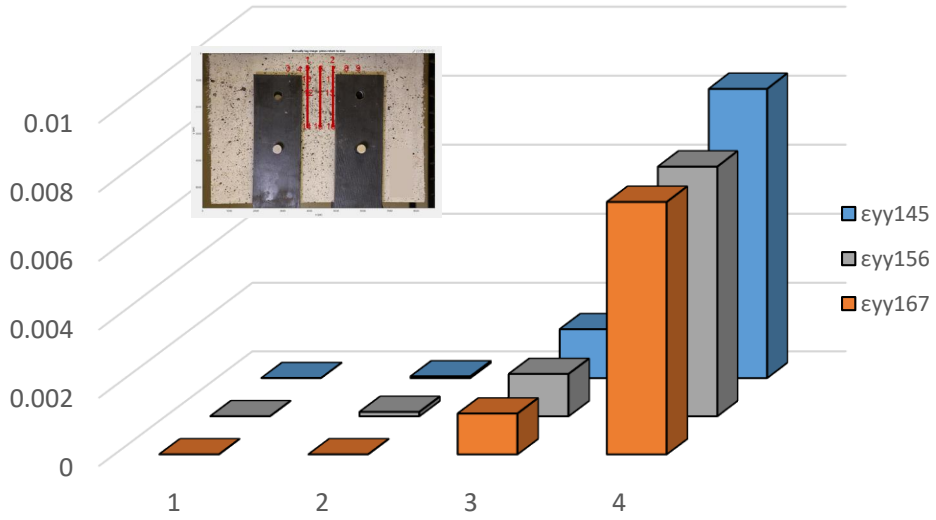

Figure A - 294 Comparison of ε_{yy} between three equidistant layers (IHRT2-5-B – Case 1).

Detailed analysis in three milestone points – Case 2

Figure A - 295 Locations of POIs for specimen IHRT2-5-B (Case 2).

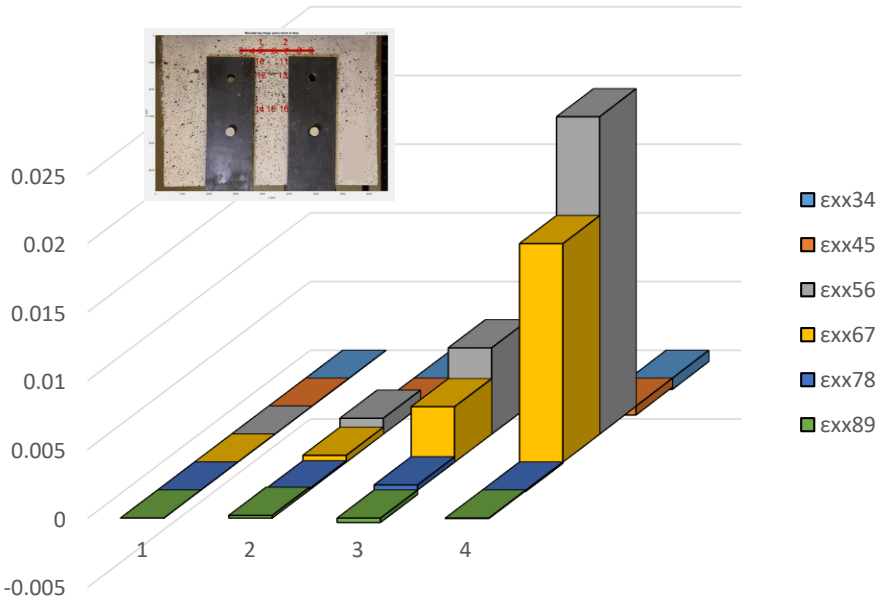

Figure A - 296 Demonstration of ε_{xx} along Layer 2 (IHRT2-5-B – Case 2).

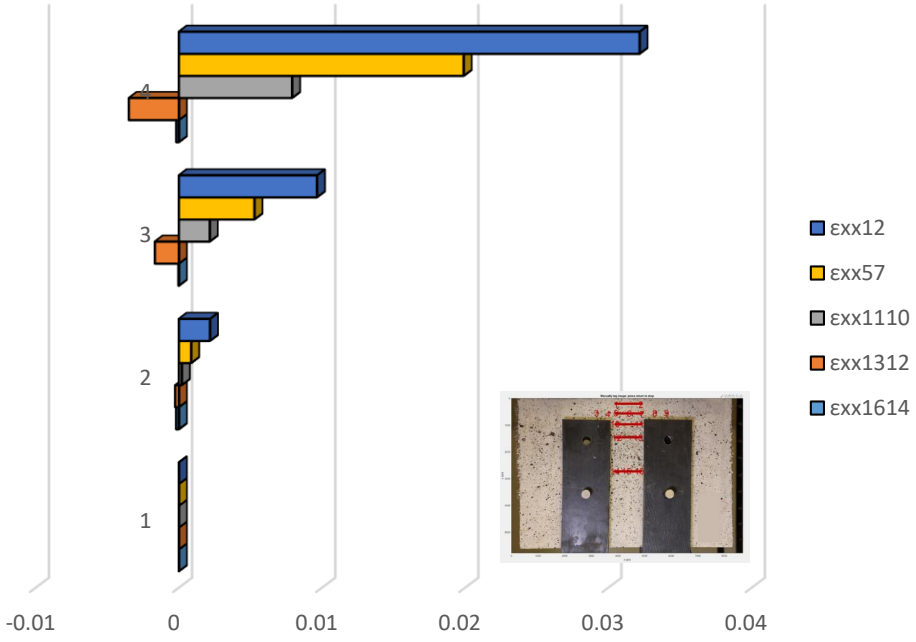

Figure A - 297 Comparison of ε_{xx} between horizontal layers (IHRT2-5-B – Case 2).

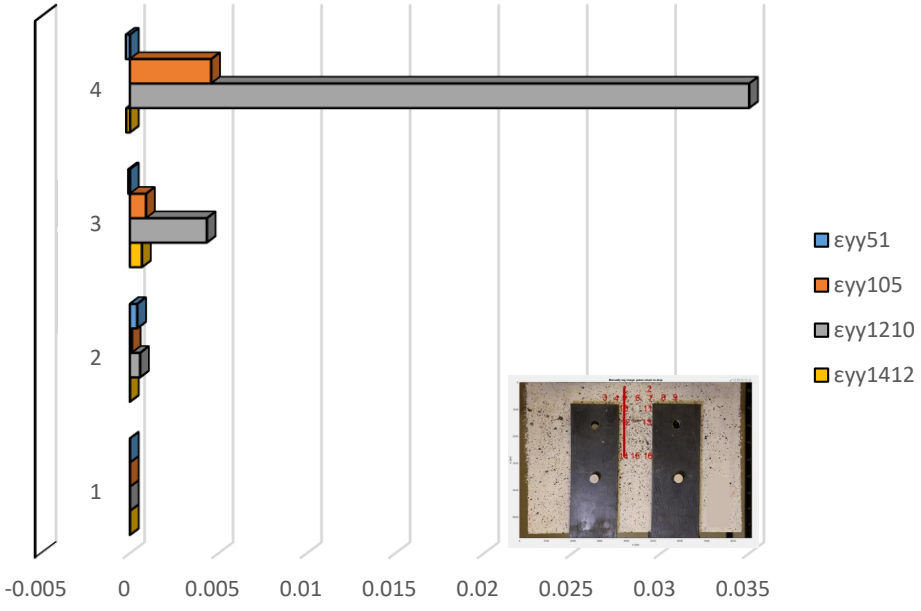

Figure A - 298 Demonstration of εyy on left vertical layer (IHRT2-5-B – Case 2).

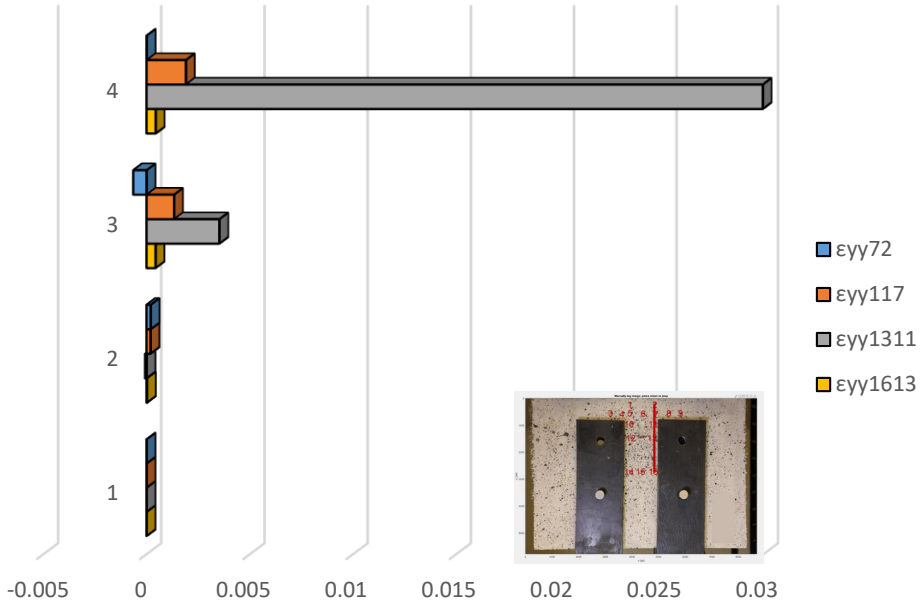

Figure A - 299 Demonstration of ε_{yy} on right vertical layer (IHRT2-5-B – Case 2).

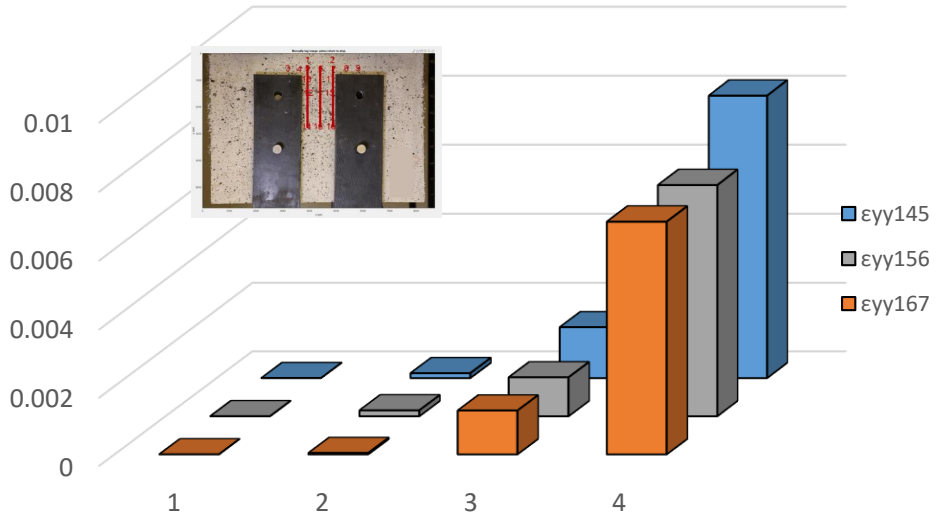

Figure A - 300 Comparison of ε_{yy} between three equidistant layers (IHRT2-5-B – Case 1).

Detailed analysis in three milestone points – Case 3

Figure A - 301 Locations of POIs for specimen IHRT2-5-B (Case 3).

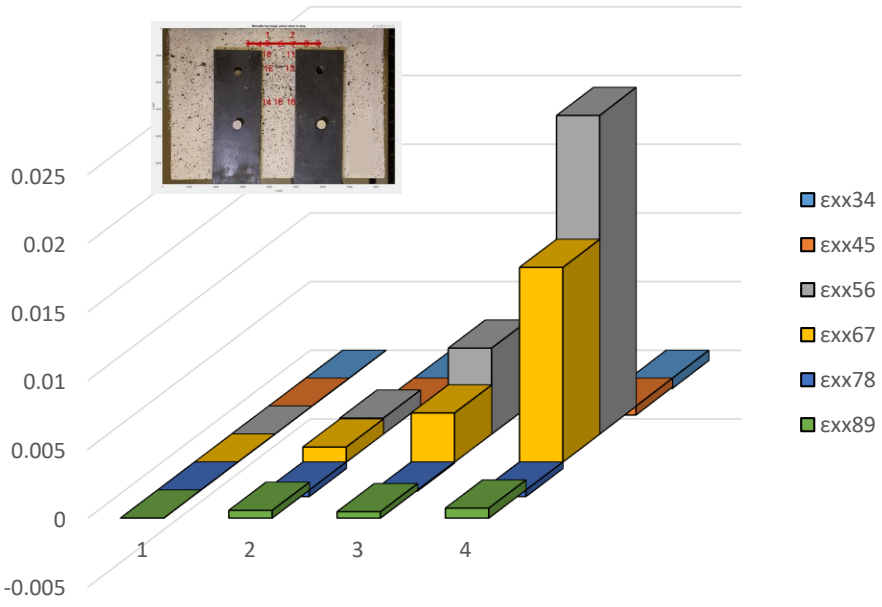

Figure A - 302 Demonstration of ε_{xx} along Layer 2 (IHRT2-5-B – Case 3).

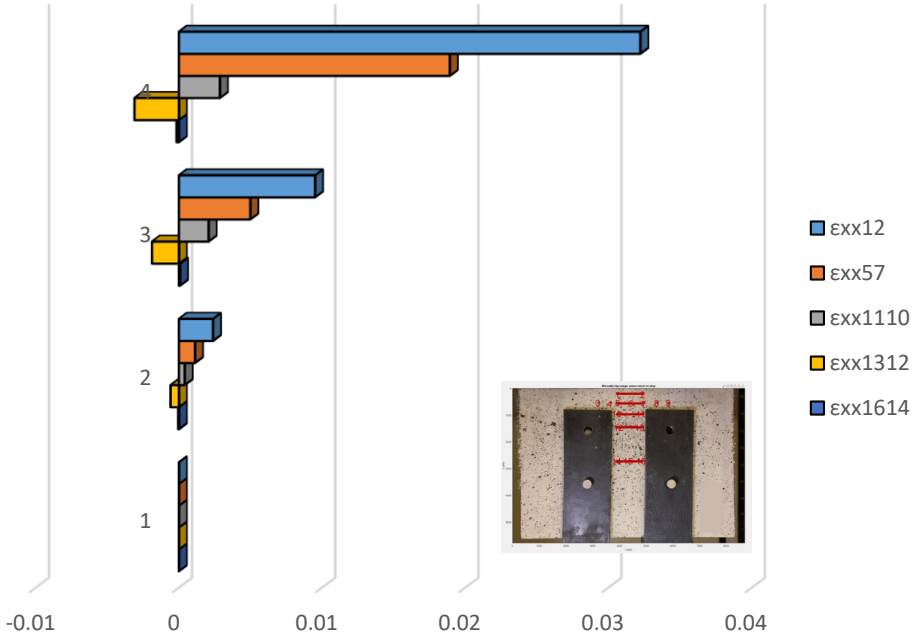

Figure A - 303 Comparison of ε_{xx} between horizontal layers (IHRT2-5-B – Case 3).

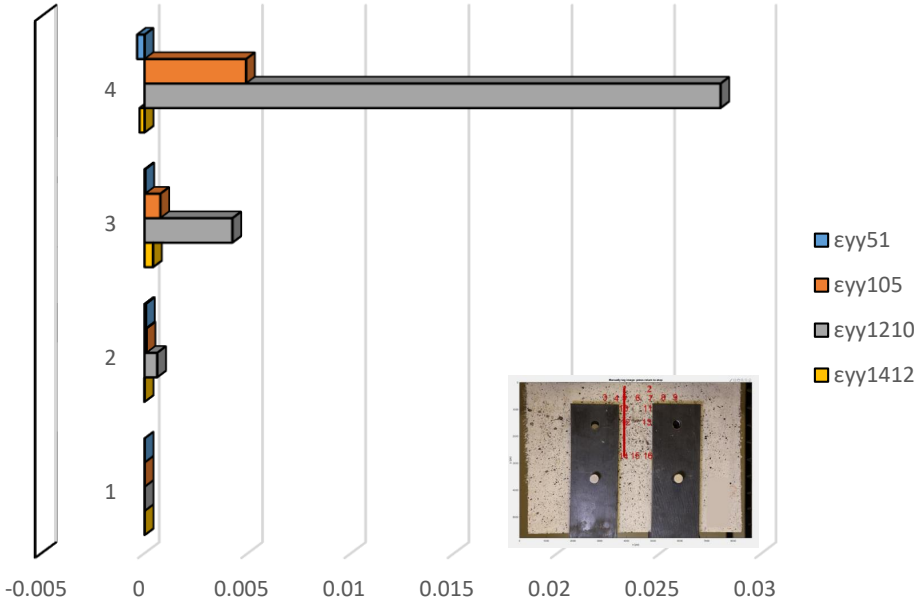

Figure A - 304 Demonstration of εyy on left vertical layer (IHRT2-5-B – Case 3).

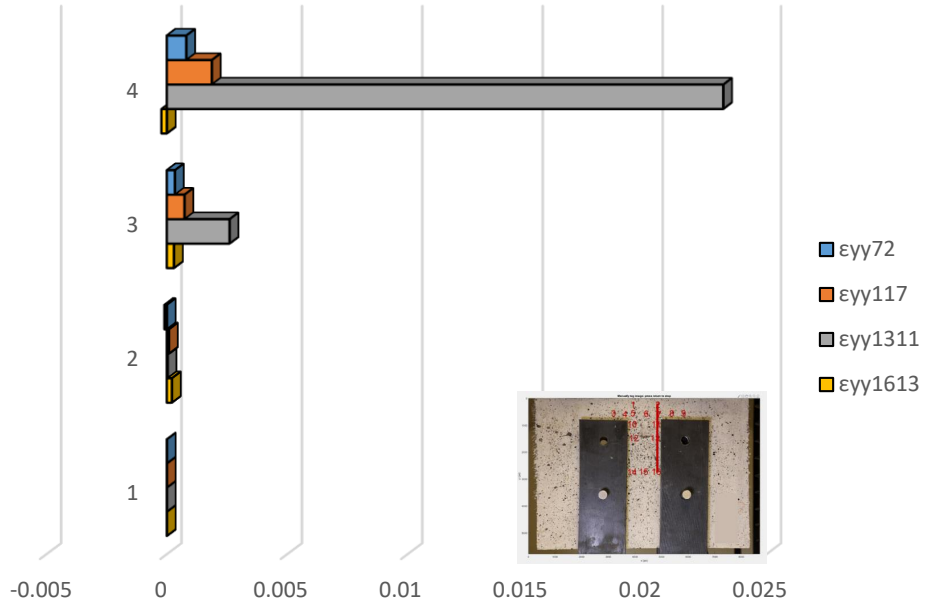

Figure A - 305 Demonstration of ε_{yy} on right vertical layer (IHRT2-5-B – Case 3).

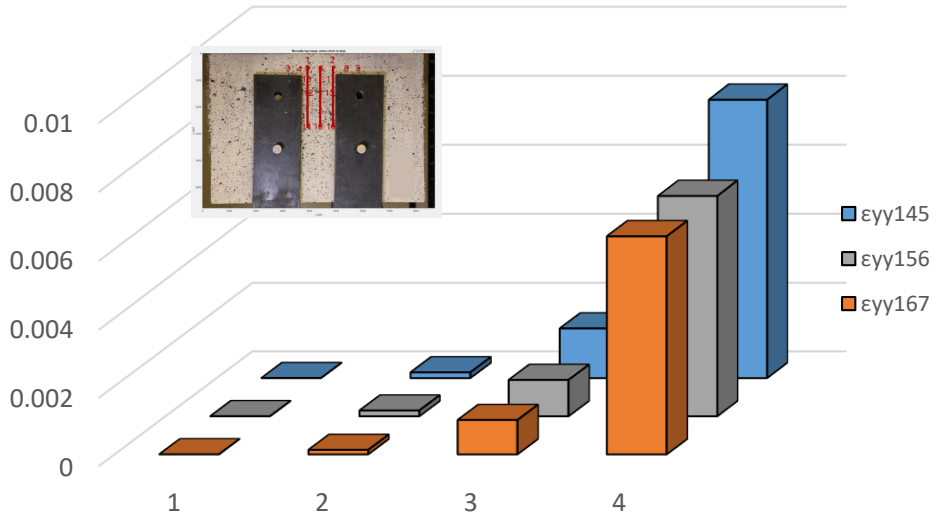

Figure A - 306 Comparison of ε_{yy} between three equidistant layers (IHRT2-5-B – Case 3).

Appendix II

Table A - 1 Crack distribution for specimen CMK1-5-A after the end of the experiment.

CMK1-5-A	
	
	
	

Table A - 2 Crack distribution for specimen CMK1-5-B after the end of the experiment

CMK1-5-B	
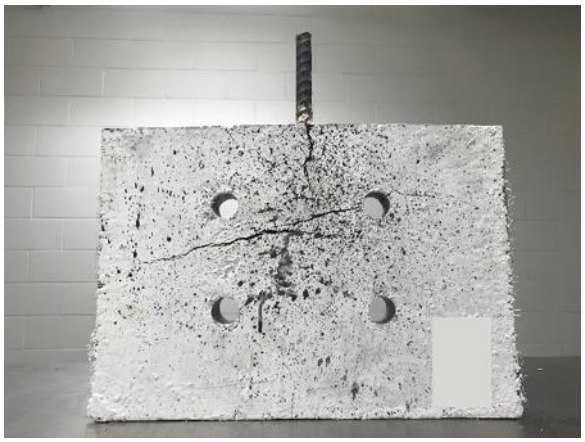	
	
	

Table A - 3 Crack distribution for specimen CMK2-5-A after the end of the experiment.

CMK2-5-A	
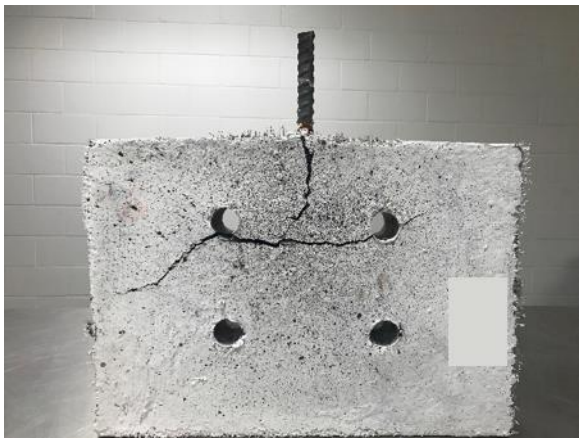	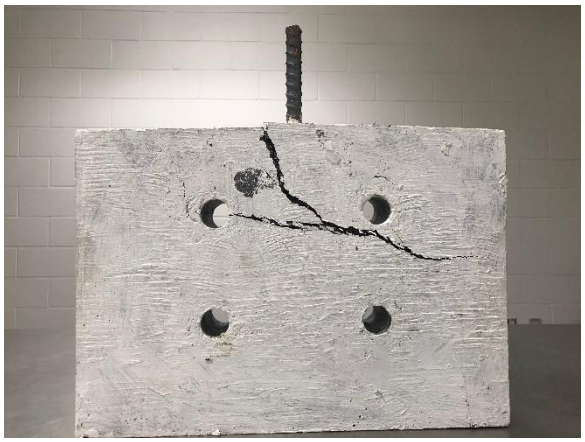
	
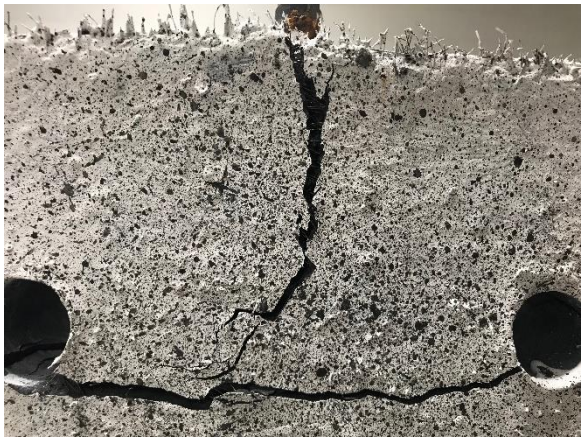	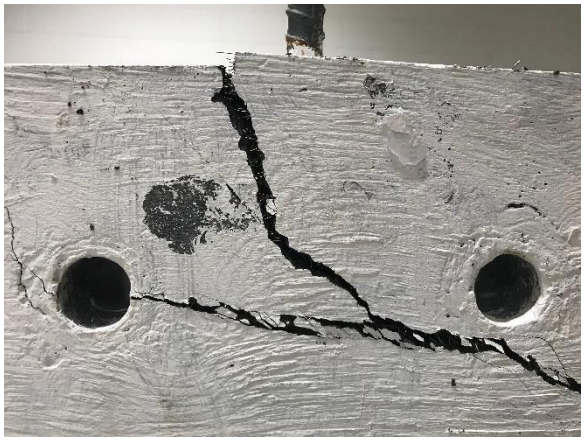

Table A - 4 Crack distribution for specimen CMK2-5-B after the end of the experiment.

CMK2-5-B	
	
	
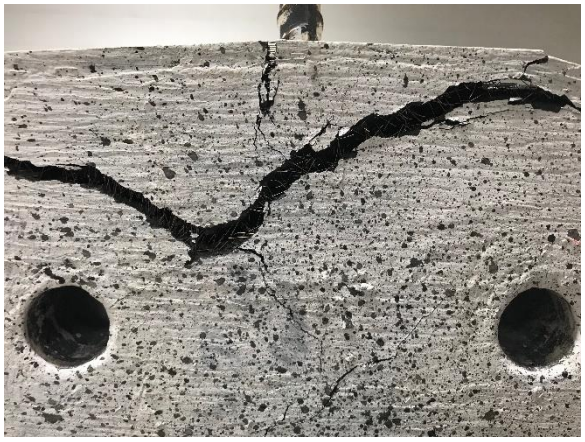	

Table A - 5 Crack distribution for specimen CMF1-5-A after the end of the experiment.

CMF1-5-A	
	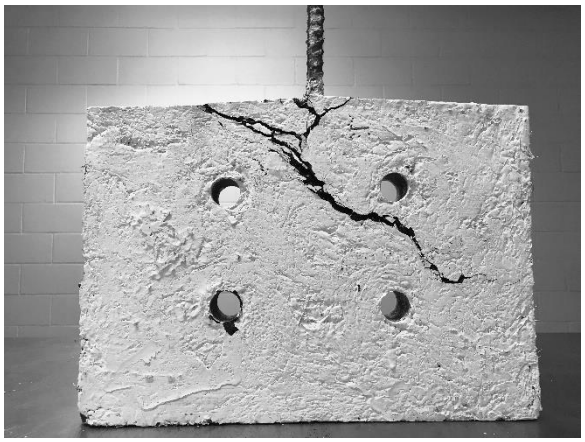
	
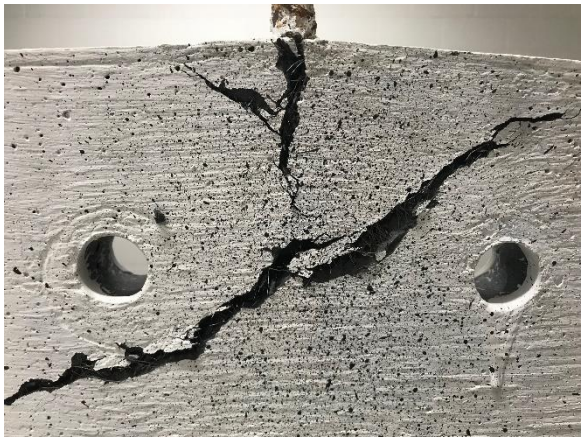	

Table A - 6 Crack distribution for specimen CMF1-5-B after the end of the experiment.

CMF1-5-B	
	
	
	

Table A - 7 Crack distribution for specimen CMF2-5-A after the end of the experiment.

CMF2-5-A	
	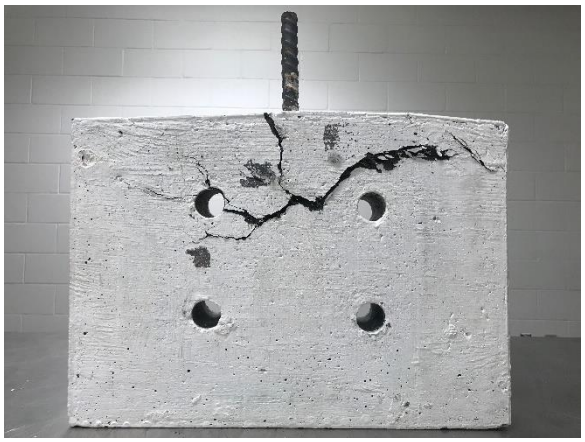
	
	

Table A - 8 Crack distribution for specimen IHNJ1-5-A after the end of the experiment.

IHNJ1-5-A	
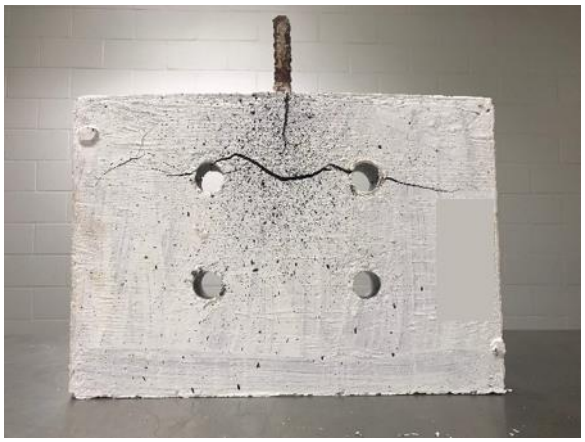	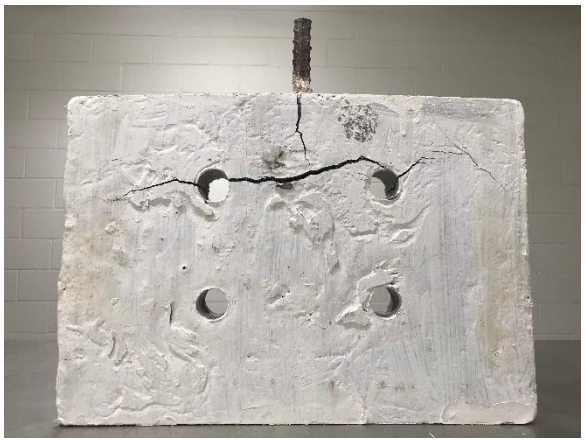
	
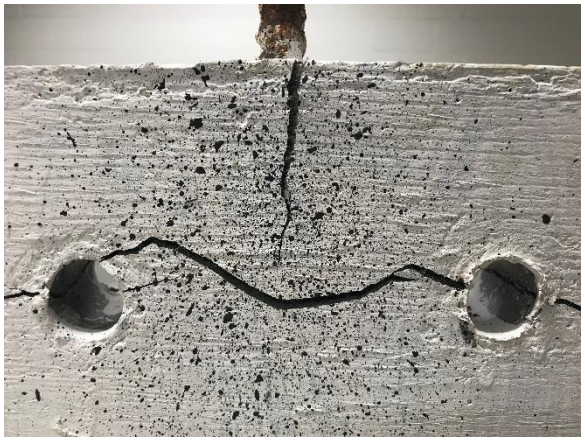	

Table A - 9 Crack distribution for specimen IHNJ1-5-B after the end of the experiment.

IHNJ1-5-B	
	
	
	

Table A - 10 Crack distribution for specimen IHNJ2-5-A after the end of the experiment.

IHNJ2-5-A	
	
	
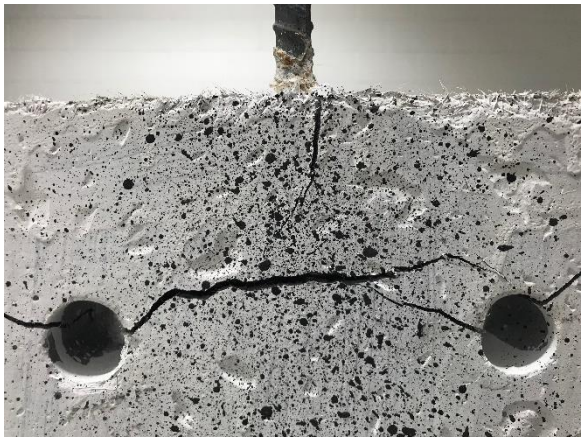	

Table A - 11 Crack distribution for specimen IHNJ2-5-B after the end of the experiment.

IHNJ2-5-B	
	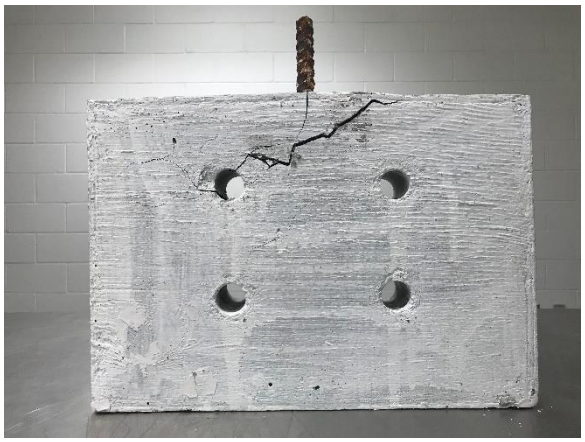
	
	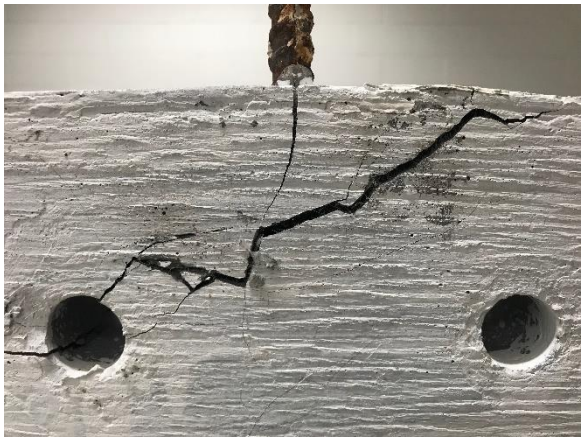

Table A - 12 Crack distribution for specimen IHRT2-5-A after the end of the experiment.

IHRT2-5-A	
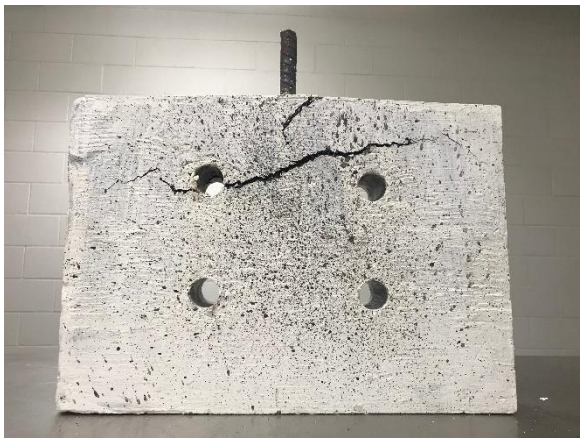	
	
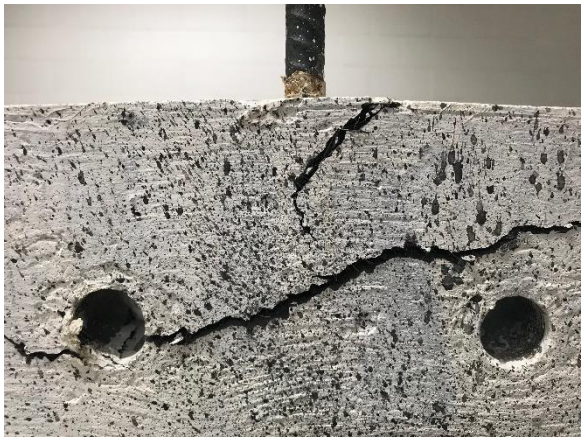	

Table A - 13 Crack distribution for specimen IHRT2-5-B after the end of the experiment.

IHRT2-5-B	
	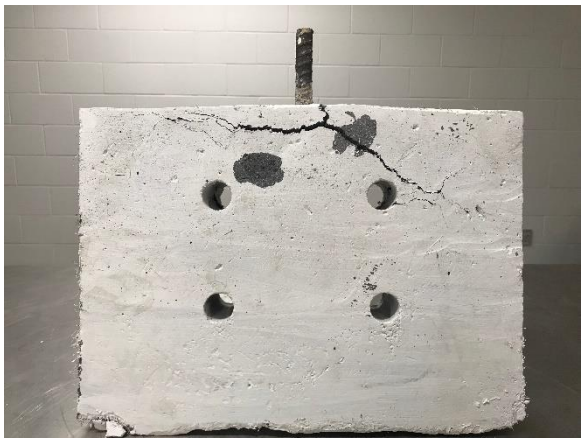
	
	

Appendix III

Table A - 14 Bond stages along the anchorage length, when concrete contribution to strain compatibility is neglected:

Schematic representation of the boundary values and distributions of *s(x)*, $\varepsilon_s(x)$

Solution of differential Eq. (15b) in combination with bond law (Eq. 2c)	• Ascending branch $s(x)=C_1e^{-\omega x}+C_2e^{\omega x}\;;\;\varepsilon_s(x)=C_1\omega\cdot e^{-\omega x}-C_2\omega\cdot e^{\omega x},\;\omega=\left(\frac{4f_b^{max}}{E_sD_bs_1}\right)^{0.5}$ • Maximum bond stress plateau • $s(x)=\frac{2f_b^{max}}{E_sD_b}x^2-C_3x+C_4\quad;\quad\varepsilon_s(x)=-\frac{4f_b^{max}}{E_sD_b}x+C_3$ • Descending branch $s(x)=C_5\cdot sin(ax)+C_6\cdot cos(ax)+\frac{f_b^{max}+k_bs_2}{k_b}\quad;\quad\varepsilon_s(x)=-C_5a\cdot cos(ax)+C_6a\cdot sin(ax),$ $a=\left(\frac{4k_b}{E_sD_b}\right)^{0.5}$ • Residual bond stress plateau $\varepsilon_s(x)=-\frac{4f_b^{res}}{E_sD_b}x+C_7\;;\;s(x)=\frac{2f_b^{res}}{E_sD_b}x^2-C_7x+C_8$
I: elastic bond	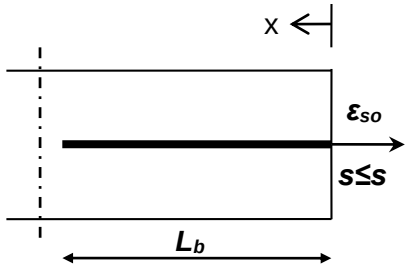 $0\le x\le L_b:$ $s(x)=\frac{\varepsilon_o}{\omega\left(1-e^{-2\omega L_b}\right)}\left(e^{-\omega x}+e^{\omega x-2\omega L_b}\right)\le s_1$ $\varepsilon_s(x)=\frac{\varepsilon_o}{1-e^{-2\omega L_b}}\left(e^{-\omega x}-e^{\omega x-2\omega L_b}\right)$

II: Plastified bond

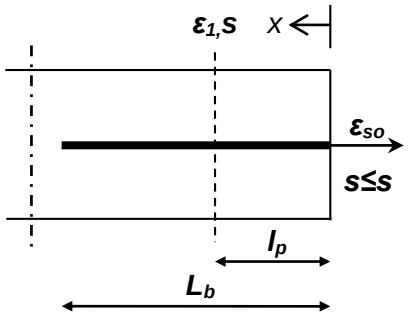

- $l_p \le x \le L_b$:

$$\varepsilon_s(x) = \frac{\varepsilon_1}{1-e^{-2\omega(L_b-l_p)}}\left(e^{-\omega(x-l_p)} - e^{\omega(x-l_p)-2\omega(L_b-l_p)}\right)$$

$$s(x) = \frac{\varepsilon_1}{\omega\left(1-e^{-2\omega(L_b-l_p)}\right)}\left(e^{-\omega(x-l_p)} + e^{\omega(x-l_p)-2\omega(L_b-l_p)}\right) \le s_1$$

- $0 \le x \le l_p$:

$$\varepsilon_s(x) = -\frac{4f_b^{max}}{E_s D_b}x + \varepsilon_{so} \quad \text{and} \quad s(x) = \frac{2f_b^{max}}{E_s D_b}(x^2 - l_p^2) - \varepsilon_{so}(x - l_p) + s_1 \le s_2$$

For $\varepsilon_s(l_p)=\varepsilon_1$ $\Rightarrow$ $l_p = L_b - \frac{1}{2\omega} ln\left(\frac{s_1\omega + \varepsilon_1}{s_1\omega - \varepsilon_1}\right)$; $\varepsilon_1 = -\frac{4f_b^{max}}{E_s D_b} l_p + \varepsilon_{so}$

III: Softening of Bond

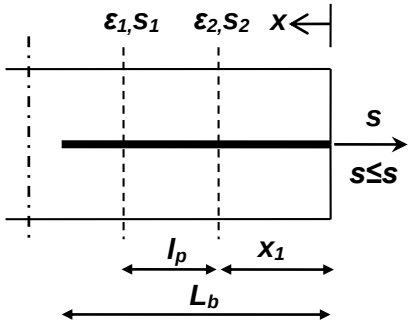

- $x_1 + l_p \le x \le L_b$:

$$\varepsilon_s(x) = \frac{\varepsilon_1}{1 - e^{-2\omega(L_b - l_p - x_1)}}\left(e^{-\omega(x - l_p - x_1)} - e^{\omega(x - l_p - x_1) - 2\omega(L_b - l_p - x_1)}\right)$$

$$s(x) = \frac{\varepsilon_1}{\omega\left(1 - e^{-2\omega(L_b - l_p - x_1)}\right)}\left(e^{-\omega(x - l_p - x_1)} + e^{\omega(x - l_p - x_1) - 2\omega(L_b - l_p - x_1)}\right)$$

- $x_1 \le x \le x_1 + l_p$:

$$\varepsilon_s(x) = -\frac{4 f_b^{max}}{E_s D_b}(x - x_1) + \varepsilon_2 \quad \text{and} \quad s(x) = \frac{2 f_b^{max}}{E_s D_b}(x - x_1)^2 - \varepsilon_2(x - x_1) + s_2$$

$$l_p = L_b - x_1 - \frac{1}{2\omega} ln\left(\frac{s_1\omega + \varepsilon_1}{s_1\omega - \varepsilon_1}\right),\ \varepsilon_1 = -\frac{4 f_b^{max}}{E_s D_b} l_p + \varepsilon_2 \text{ and } \varepsilon_2 = \left(-s_1 + s_2 + \frac{2 f_b^{max}}{E_s D_b} l_p^2\right) / l_p$$

- $0 \le x \le x_1$:

$$\varepsilon_s(x) = -C_5 a \cdot cos(ax) + C_6 a \cdot sin(ax)$$

$$s(x) = C_5 \cdot sin(ax) + C_6 \cdot cos(ax) + \frac{f_b^{max} + k_b s_2}{k_b} \text{ where } a = \left(\frac{4k_b}{E_s D_b}\right)^{0.5}$$

$$C_6 = \frac{s_2 + \frac{\varepsilon_2}{\alpha} tan(ax_1) - \frac{f_b^{max} + k_b s_2}{k_b}}{sin(ax_1)tan(ax_1) + cos(ax_1)}, \quad C_5 = \frac{C_6 a \cdot sin(ax_1) - \varepsilon_2}{\alpha \cdot cos(ax_1)}, \quad s_o = C_6 + \frac{f_b^{max} + k_b s_2}{k_b},$$

$$\varepsilon_{so} = -C_5 a$$

IV: Residual bond

- $x_2 \le x \le L_b$

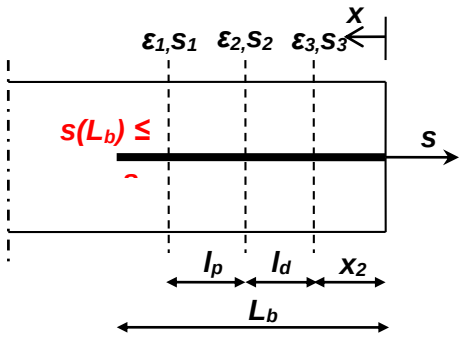

$$\varepsilon_s(x) = \frac{\varepsilon_1}{1 - e^{-2\omega(L_b - l_p - l_d - x_2)}} \left(e^{-\omega(x - l_p - l_d - x_2)} - e^{\omega(x - l_p - l_d - x_2) - 2\omega(L_b - l_p - l_d - x_2)} \right)$$

$$s(x) = \frac{\varepsilon_1}{\omega\left(1 - e^{-2\omega(L_b - l_p - l_d - x_2)}\right)} \left(e^{-\omega(x - l_p - l_d - x_2)} + e^{\omega(x - l_p - l_d - x_2) - 2\omega(L_b - l_p - l_d - x_2)} \right)$$

$$l_p + l_d + x_2 - L_b = \frac{1}{2\omega} ln \left(\frac{s_1\omega - \left(\frac{-s_1 + s_2}{l_p} - \frac{2 f_b^{max} l_p}{E_s D_b} \right)}{s_1\omega + \left(\frac{-s_1 + s_2}{l_p} - \frac{2 f_b^{max} l_p}{E_s D_b} \right)} \right) \quad ; \quad \varepsilon_2 = \frac{-s_1 + s_2 + \frac{2 f_b^{max} l_p^2}{E_s D_b}}{l_p};$$

$$\varepsilon_1 = -\frac{4 f_b^{max} l_p}{E_s D_b} + \varepsilon_2 \quad ; \quad \varepsilon_3 = -C_5 a \quad ; \quad \varepsilon_2 = -C_5 a \cdot cos(al_d) + C_6 a \cdot sin(al_d)$$

$$s_2 = C_5 sin(al_d) + C_6 cos(al_d) + \frac{f_b^{max} + k_b s_2}{k_b} \quad ; \quad s_3 = C_6 + \frac{f_b^{max} + k_b s_2}{k_b} \quad ; \quad C_3 = \varepsilon_2 \quad ; \quad C_4 = s_2$$

- $0 \le x \le x_2$

$$C_7 = \varepsilon_3 + \frac{4 f_b^{res}}{E_s D_b} x_2; \; C_8 = s_3 - \frac{2 f_b^{res}}{E_s D_b} x_2^2 + C_7 x_2 \quad ; \quad s_o = C_8 \quad ; \quad \varepsilon_{so} = C_7$$